TUDelft

Delft University of Technology

High-Entropy Liquid Electrolytes for Lithium Batteries

Wang, Q.

DOI

Publication date
2023

Document Version
Final published version

Citation (APA)

Important note
To cite this publication, please use the final published version (if applicable).
Please check the document version above.

High-Entropy Liquid Electrolytes for Lithium Batteries

Qidi WANG

2023

High-Entropy Liquid Electrolytes
for Lithium Batteries

Dissertation

For the purpose of obtaining the degree of doctor
at Technology University of Delft
by the authority of the Rector Magnificus prof. dr. ir. T.H.J.J. van der Hagen
chair of the Board for Doctorates
to be defended publicly on
Thursday 12 October 2023 at 12:30 o' clock

by

Qidi WANG

Master of Science in Material Science and Engineering
Tsinghua University, China
Born in Shandong, China

This dissertation has been approved by the promotors.

Composition of the doctoral committee:

Rector Magnificus	Chairperson
Prof. dr. ir. M. Wagemaker	Delft University of Technology, promotor
Dr. S. Ganapathy	Delft University of Technology, copromotor

Independent members:

Prof. dr. D. Aurbach	Bar-Ilan University, Israel
Prof. dr. B. Li	Tsinghua University, China
Prof. dr. A. Yamada	The University of Tokyo, Japan
Prof. dr. M. Tromp	University of Groningen, the Netherlands
Prof. dr. F. M. Mulder	Delft University of Technology, the Netherlands
Prof. dr. E. Brück	Delft University of Technology (reserve member)

TUDelft

Dedicated to my family

Contents

1. Introduction

1.1 Liquid electrolytes for lithium batteries

Lithium-ion batteries (LIBs) have afforded rapid advances in portable electronic devices and enabled the implementation of electric vehicles (EV)[1,2]. The increasing demand for advanced energy storage requires the optimization of current LIBs with the application of higher specific capacity electrodes, e.g., the nickel-rich oxide cathodes[3-5] paired with silicon-based[6] or Li metal anodes[7]. This leads to more aggressive interphases on both electrodes to ensure reversibility of the battery chemistries[8-11]. The Li-metal anode having the high theoretical capacity (3860 mAh g^{-1}, 10-times larger than that of the conventional graphite anode of 370 mAh g^{-1}), and low electrochemical redox potential (-3.040 V vs. standard hydrogen electrode), has gained increasing attention[7,12,13]. Similar to the graphite anode, the more negative electrochemical potential of Li metal leads to serious challenges on the electrode-electrolyte interphase. The extreme activity makes Li metal react with almost every component of the electrolytes in the battery[14]. A consequence of this is that a passivation layer forms on the metal surface, namely the solid electrolyte interphase (SEI)[8]. An effective SEI will passivate the Li-metal electrode, inhibiting its continuous chemical reaction with electrolyte while maintaining its electrochemical potential and activity, allowing Li^+ transport when batteries are operating[8,15]. This means that the presence of a favourable SEI is critical for enabling the reversible electrochemical reaction of Li metal, operating far away from the chemical equilibrium defined by its thermodynamics[9]. This imposes more stringent requirements on electrolyte design.

In order to increase cycling reversibility, various electrolyte modifications have been explored to enhance the SEI properties and improve the electrochemical performance of Li batteries (Fig. 1.1), including changing salt concentrations[16,17], using different combination of solvents or salts[18,19], developing new additives or solvents[20], and using diluent solvents[21,22]. Fig. 1.1 shows that conventional carbonate electrolytes exhibit an average Coulombic efficiency (CE) below 85%. Introducing the widely used fluoroethylene carbonate (FEC) additive, the CE increases to approximately 95%, which is known to induce F-rich SEI species but still far from the practical demand[23-26]. Ether-based electrolytes are more stable against reduction, resulting in a higher CE, especially by employing a high salt concentration (e.g., 5 M LiFSI of ~99%) inducing a salt-derived

SEI[16]. A similar effect is observed for locally concentrated electrolytes[21,27]. Additionally, highly fluorinated electrolytes, containing a substantial amount of fluorinated solvent with a low donor number (DN), contributes to a weaker solvation facilitating a salt-derived and F-rich SEI[20,28,29]. These electrolytes alter the solvation environment of Li ions, manipulating interphase properties to form anion-derived and/or LiF-abundant components that improve battery performance[25,30]. However, most electrolytes have a drawback in terms of lower ionic conductivity due to high viscosity, resulting in performance degradation of cycling at high rates[16,31]. Meanwhile, they also raise concerns about electrolyte cost and environmental sustainability due to the high fluorine[32,33]. Additionally, some electrolytes present a broad range of CEs, even when containing similar electrolyte components[23,34,35], which implies that the chemical build-up of the interphase driven by the decomposition of electrolytes may not directly determine the battery performance[22,30,36-39].
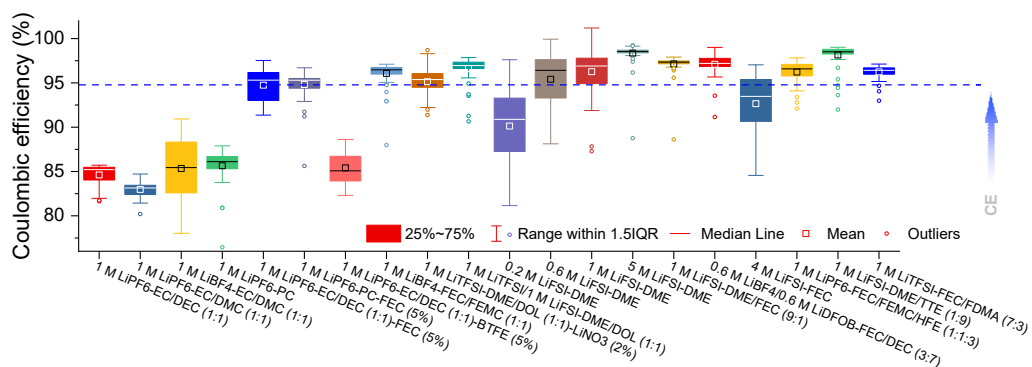
Fig. 1.1. Electrochemical cycling of various kinds of representative electrolytes, prepared and cycled under the same conditions. The CE of LiPF$_6$-EC/DEC/FEC electrolyte is indicated as a reference (bleu dotted line). The centre line of the box plot represents the median; lower and upper box limits represent the 25 and 75% quantiles, respectively; whiskers extend to box limit ±1.5×IQR (interquartile range); outlying points are plotted individually.

Understanding and controlling of the SEI are very important, but remain challenging due to its intricate chemical composition and structure[30,40]. The composition is very diverse consisting of mixed organic and inorganic species[41,42], and the structure is complicated due to the presence of crystalline/amorphous phases closely intertwined on the electrode surface[43,44]. To date, several techniques have been applied to characterize the

chemical composition and structure of the SEI, including nuclear magnetic resonance[45,46], cryogenic-electron microscopy[44,47], synchrotron-based X-ray diffraction[48] and titration gas chromatography[49], showing important insights. However, even these may be insufficient to allow an accurate understanding of interphase properties. This is mainly because these interphases are highly fragile and the damage to their spatial arrangement is inevitable during any ex-situ measurement. In addition, reliable in-situ/operando techniques to study these interphases in their native form are rare. This limited understanding and the resulting lack of design principles has further limited the development of advanced electrolytes. Therefore, exploring routes towards effective solid passivation layers and understanding the intricate relationships with electrolytes are essential to pursue.

1.2 Li-ion transfer across electrode-electrolyte interphases

The Li-ion transfer across the electrode-electrolyte interphase involves several processes (Fig. 1.2), which could hold the key to understand and tailor the performance of electrolytes. In general, there are two interfaces for the Li-ion transfer between the electrode and electrolyte. These are the solid-solid electrode-interphase interface, where the interphase includes the SEI in case of anodes and the cathode electrolyte interphase (CEI) in case of cathodes, as well as the solid-liquid interphase-electrolyte interface. At the electrode-interphase interface, the Li-ion transfer is governed by solid-solid ion diffusion (or solid-solid redox reactions followed by ion diffusion) as shown in Fig. 1.2. In this case, the interphase plays a more important role because it determines the kinetics of Li-ion transfer. For the interphase-electrolyte interface, the electrolyte dominates as the composition and structure of the interphase are derived from the decomposition of electrolytes and thus impacted by the nature of the electrolytes during the charge/discharge processes.

To have a comprehensive understanding on the Li-ion transfer, involving solvation sheath reorganization and electron transfer from electrode to Li-ion, a physical model is beneficial for quantitively evaluate the thermodynamics and kinetics of this process. Li-ion transfer process is to some extend similar to the electron transfer describe by Marcus theory, which is originally introduced by R. A. Marcus in 1956 as a method for calculating

the contribution of solvent reorientation of the outer coordination shell. Since then it has been extended to include the inner coordination shell and refined significantly for address a variety of different types of transformations, such as proton transfer[50], hydride transfer[51], and methyl transfer reactions[52].
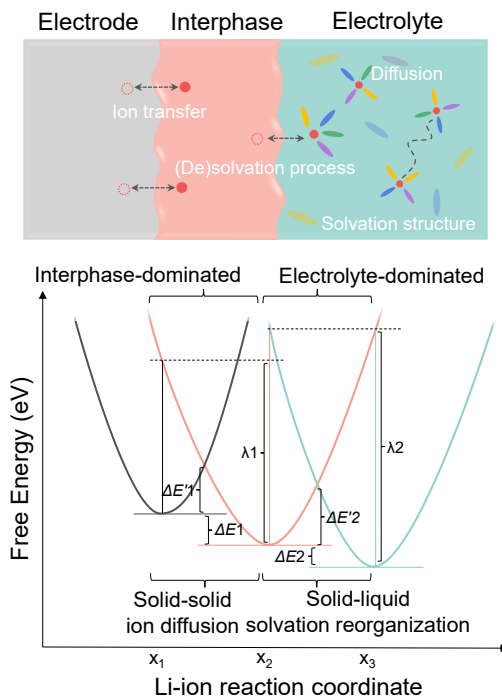
Fig. 1.2. Schematic diagram of the Li-ion transfer from electrode to electrolyte. The Li-ion reaction coordinate represents the surrounding coordinates of Li-ion as it transfers in the battery system from electrode to electrolyte. ΔE is the energy change moving along the parabolas between point x_i to x_{i+1}. $\Delta E'$ is the energy barrier and λ represents the reorganization energy.

The energy barrier for the electron transfer can be expressed as follows:

$$\Delta G^{\ddagger} = \frac{(\lambda + \Delta G^{\circ})^2}{4\lambda} \tag{1.1}$$

where $\Delta G^{\ddagger}$ is activation energy, namely the energy barrier of the formation of the transition state, ΔG° is Gibbs free energy change between reactant and product, λ is the reorganization energy, which refers to the energy it takes to force the reactants to have the same nuclear configuration as the products without letting the electron transfer. The

reorganization energy associated with the solvation sheath can be expressed through a dielectric continuum formulation:

$$\lambda = \frac{e^2}{4\pi\varepsilon_0}\left(\frac{1}{a_0} - \frac{1}{R}\right)\left(\frac{1}{\varepsilon_{op}} - \frac{1}{\varepsilon_s}\right) \tag{1.2}$$

where e is the charge of electron, ε_0 is the vacuum permittivity, a_0 is the solvated radius of cations, R is the separation distance, ε_{op} and ε_s is the optical and static dielectric constants[53].

Furthermore, the rate constant k_{ET} of this charge transfer process can be obtained by the following equation:

$$k_{ET} = A\ exp\left(-\frac{\Delta G^{\ddagger}}{K_B T}\right) \tag{1.3}$$

where A is a pre-factor related to the nature of the electron transfer reaction; K_B is the Boltzmann constant.

Therefore, the kinetics and the thermodynamics of a reaction can be linked by the activation energy using Marcus theory, which is promising to be applied in comprehending Li-ion transfer, spanning from the solvation sheath within the electrolyte to the electrode redox processes. While further work is required in the theoretical domain and corresponding experimental analysis for the quantitative, the Marcus theory framework, initially devised for elucidating electron transfer mechanisms based on ground-state energetics and self-exchange rates, can be a potential valuable tool for delineating Li-ion transfer process.

In Fig. 1.2, based on original model in Marcus theory, the schematic of energy landscape for Li-ion transfer from electrolyte to electrode is illustrated by three free-energy parabolas, where Li-ion transfer across the solid-solid and solid-liquid interfaces involves a pair of parabolas, respectively. The intersection of the parabolas represents an activation energy $\Delta E'$ between two processes, which is related to the reorganization energy λ according to equation 1.1. The λ in this case is related to the energy to reorganize the solvation sheath or surrounding coordination of Li-ion. The energy barrier ΔE represents the energy change between state x_i and x_{i+1}, which can determine the activation energy and influence the kinetics of the Li-ion transfer. Generally, $\Delta E'1$ is positively correlated to $\lambda 1$, and $\lambda 1$ is strongly influenced by properties of the interphase components. If a good

interphase with higher stability and higher ionic conductivity is formed on the surface of the electrode, λ1 will become smaller, and consequently $\Delta E'1$ will also become smaller, promoting Li-ion transfer[19,54]. With respect to the interphase-electrolyte interface, the solid-liquid solvation reorganization based on Marcus theory[53,55], can be used to describe the Li-ion diffusion across the interface. In this case λ2 is determined by both solute and solvent. For example, an irregular vibration mode or an asymmetrical solvation structure can result in a smaller λ2[56], therefore leading to a smaller $\Delta E'2$. In addition, the properties of the electrolyte can also play an important role in the formation of interphase that further influences λ1. Usually, a favourable interphase of both SEI on the anode and CEI on the cathode can be constructed by the decomposition of anionic groups of the salt, which show high stability and relatively fast Li-ion transfer. This leads to a smaller λ1, thereby promoting solid-solid ion diffusion. Furthermore, the weaker solvation structures of Li-ion coordinated to solvents that facilitate Li-ion de-solvation, can contribute to a smaller λ2, leading to a lower solid-liquid solvation reorganization energy. These two interfaces for Li-ion transfer provide a semi-empirical framework in evaluating different electrolytes and understanding the underlying mechanism, promoting the development of advanced electrolytes.

1.3 High entropy alloys/materials

Since the introduction of high entropy (HE) alloys, that have five or more principal elements in near-equiatomic concentration[57,58], this concept has generated a wide interest and significant attention in materials science and engineering because of their potentially desirable properties. Although the fundamental issues have not yet been completely resolved, such as the thermodynamic origin of phase selection, the designed HE alloys were reported to have superior mechanical and physical properties. For example, increasing configurational entropy can change the thermodynamic stability, mechanical and magnetic properties, as well as exhibit improved ionic transport properties of the materials[59-63].

Up to now, several principles have been found to underpin the special nature of such materials[59,64]. First of all, multi-component compositions offer thermodynamics that can

promote the formation of solid solutions; secondly, the local lattices of such materials should be highly distorted because of the highly disordered atomic arrangement and different atomic sizes; thirdly, the lattice distortion and cooperative interactions from various components can facilitate ions percolate with low activation energy; fourthly, the composite effect in addition to the basic features of each element, through interactions among all the elements can also contribute to macroscopic properties. Although a large number of HE materials have already been prepared and shown to possess exceptional properties, exceeding those of conventional materials, an enormous compositional space still remains to be explored. In addition, there is great potential for the design and application of the HE materials concept to other fields of interest.
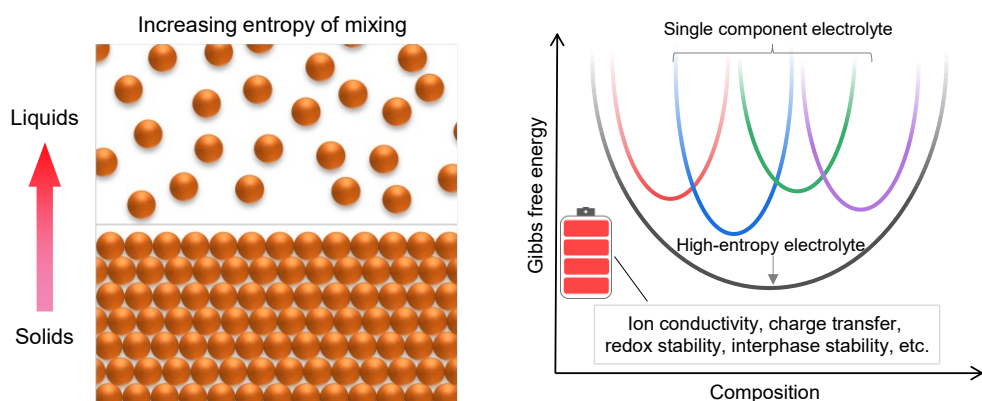
Fig. 1.3. Schematics of energy evolution in HE system. In contrast to the solid-state system, the liquid system exhibits greater chaos, contributing much more to the entropy.

Compared to solid systems, liquid systems present more chaos, consequently exhibiting a higher contribution from entropy (Fig. 1.3). Increasing the entropy in liquid electrolytes is straight forward by forming multi-component solutions, which does not require application of external forces through high temperature/pressure that are typically used to synthesize HE based solids. The electrolyte is an ion-conducting solution which acts as a conductive pathway to support ions transfer between cathode and anode in rechargeable batteries. Dissolving different salts in one or more solvents to form HE electrolytes would expect to result in more diverse ion migration properties because of their various localized interactions with both solvents and anionic groups. Potentially this

can be used to lower the average free energy, hence improve solubility and phase stability, and increase Li-ion conductivity of the electrolyte (Fig. 1.3). Therefore, the use of HE liquid electrolytes for Li batteries where by dissolving different kinds of salt in one or more solvents presents many possibilities.

1.4 High entropy liquid electrolytes

Entropy quantifies the level of chaos or uncertainty within a system. Similar to the concept of incorporating a variety of elements to create HE alloys/materials, increasing entropy within a liquid electrolyte involves diverse salts/solvents. Consequently, augmenting entropy within liquid electrolytes can yield two primary effects in liquid electrolyte. One of the aspects lies in the phase stabilization as illustrated in Fig. 1.4. In a system, the free energy changes at lowest mixing free energy ΔG_{mix} can be determined by:

$$\Delta G_{\text{mix}} = \Delta H_{\text{mix}} - T\Delta S_{\text{mix}} \tag{1.4}$$

where the ΔH_{mix} is enthalpy of mixing and ΔS_{mix} represents the entropy of mixing.

Specifically, ΔS_{mix} can be expressed in terms of the composition as follows:

$$\Delta S_{mix} = -nR \sum_i x_i ln x_i \tag{1.5}$$

where R is the gas constant, n is the total number of moles and x_i the mole fraction of component i. In the electrolyte, the solubility of the solutes is determined by the competition between ΔH_{mix} and ΔS_{mix}. Therefore, in HE system, thermodynamic phase formation can be modified by increasing entropy of mixing (ΔS_{mix}), to decrease the Gibbs free energy of mixing (ΔG_{mix}), thus facilitating formation of uniform solution.

Another aspect of entropy that plays an important role in electrolyte is the synergistic (Cocktail) effect. The property of this multi-component solution is certainly influenced by the specific compositions. Besides the properties of the individual component, the interaction among the components should also be considered. Accordingly, a synergistic solution mixture leads to the macroscopic performance that exceeds the sum of the effects of the constituent components through the intermolecular interaction and solvation disorder, depending on the composition, structure and properties of each component. This effect also motivates further interest to investigate unexplored compositions.
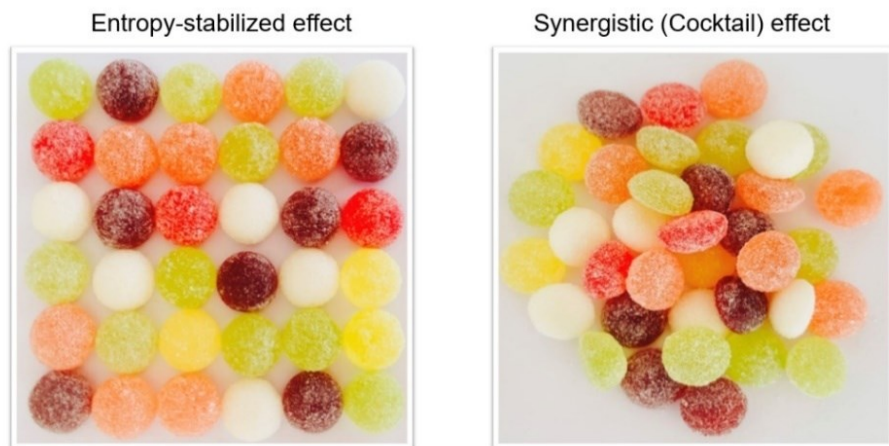
Fig. 1.4. Schematics of the impacts of HE in liquid electrolyte. There are two related but distinct characteristics on the influence of entropy: one is the entropy-stabilized effect, the other is the synergistic (cocktail) effect.

Introducing multiple principal solutes or solvents to create new liquid systems, namely HE solutions, should be expected to possess exceptional properties benefiting from both phase stabilization and the synergistic effect from increased entropy. This is proposed to be promising strategy to introduce diverse properties in electrolytes, which are decisive for the solvation sheath structure, ionic transport, and interphase composition/structure and its stability in electrolytes, impacting the performance of the Li batteries and beyond.

1.5 Outline of this thesis

Liquid electrolytes, consisting of salts and solvents, are an important class of functional solutions for batteries. Various combinations of these have the ability to influence properties which are decisive for the solvation sheath structure, ionic transport and interphase composition/structure and its stability. Because of the higher degree of chaos and mobility of the liquid state, further increasing the number of salt and/or solvent species to increase the entropy of mixing could provide new opportunities to develop multi-component electrolytes as a composition-rich class of materials for Li batteries. This thesis aims at exploration and development HE liquid electrolytes, to improve key Li-ion battery

properties such as cycle life and conductivity. Through investigating the prototype, HE electrolytes, systematic understanding of their potential characteristics, including solvation composition and structure, interphase property, have been revealed, providing rational guidance for the design and development of high-performance electrolytes for high-energy batteries.

This thesis consists of five main sections, which are independent but also relevant to each other as shown in Fig. 1.5.
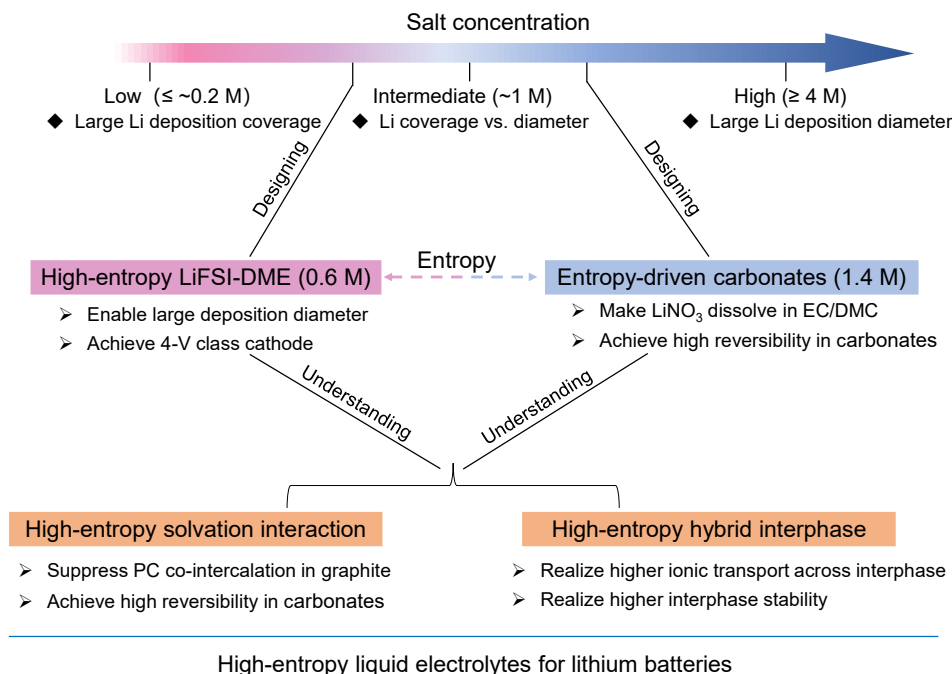
Fig. 1.5. Framework of this thesis.

Chapter 2 is a fundamental study on clarifying the impact of the electrolyte salt concentration on the compactness and reversibility of Li-metal deposits. It provides a picture in the relationship between Li microstructure and interphase for Li-metal batteries. Higher nucleation densities are formed in relatively low concentration electrolytes, which have the advantage of a higher Li deposition coverage. However, it goes along with the formation of an organic-rich unstable SEI which is unfavourable for the reversibility during (dis)charging. On the other hand, the growth of large deposits benefiting from the formation of an inorganic-rich stable SEI is observed in higher concentrations, but the

initial small nucleation density prevents full coverage of the current collector, thus compromises the plated Li-metal density. Taking advantage of this paradox, a nanostructured substrate is rationally applied that increases the nucleation density, realizing a higher deposition coverage and thus more compact plating at intermediate concentration (~1.0 M) electrolytes, leading to the extended reversible cycling of the batteries.

Based on the insights gained in Chapter 2, Chapter 3 exploits the HE strategy in low-concentration (0.6 M) electrolytes, demonstrating the substantial impact of raising the entropy of electrolytes by introducing multiple salts. Unlike what is seen for conventional single–salt liquid electrolytes, the participation of several anionic groups in the HE electrolyte induces a larger diversity in solvation structures, facilitating improved Li-ion diffusivity and the formation of more stable passivation layers on the surface of the electrodes. In comparison to the single salt electrolytes, this low-concentration dimethyl ether electrolyte with four-salts species shows an improved capacity retention of >80% over 600 cycles for nickel-rich cathodes charged to 4.3 V and >95% over 500 cycles in Li iron phosphate cathodes as well as the enhanced power density. This enables application of ether solvents, despite their poor oxidation stability, in high-voltage Li batteries with a low salt concentration.

This HE strategy is extended to raise the solubility of $LiNO_3$ (up to ~0.1 M) in commercial carbonate electrolytes (e.g., EC/DMC), forming an entropy-driven electrolyte as shown in Chapter 4. These HE electrolytes significantly enhance the cycling and rate performance of Li batteries. For Li-metal anodes the reversibility exceeds 99%, which extends the cycle life of batteries even under aggressive cycling conditions. For commercial batteries, combining a graphite anode with a $LiNi_{0.8}Co_{0.1}Mn_{0.1}O_2$ cathode, more than 1000 charge-discharge cycles are achieved while maintaining a capacity retention of more than 90%. These performance improvements to regular commercial electrolytes are rationalized by the unique features of the solvation structure HE electrolytes. The weaker solvation interaction induced by the higher disorder results in improved Li-ion kinetics, and the altered solvation composition leads to stabilized interphases. Finally, the higher entropy, induced by the presence of multiple salts, enables

a decrease in melting temperature of the electrolytes and thus enables lower battery operation temperatures without changing the solvents.

In Chapter 5 the solvation interaction of the HE electrolytes, specifically examining the co-intercalation of propylene carbonate (PC) solvent in graphite-containing anodes is studied. A combination of cryogenic electron microscopy and a range of spectroscopic techniques are used to investigate the evolution of electrode-electrolyte interphases, bringing forward the opportunities to improve the SEI properties by using these HE multi-salt electrolytes. By formulating an electrolyte with a conventional 1 M salt concentration and combining multiple commercial Li salts, the solvation interaction with the Li ions changes fundamentally. The participation of several salts results in a weaker solvation interaction, and an anion-rich solvation sheath, despite the relatively low total salt concentration. This induces a conformal, inorganic-rich SEI that effectively passivates the surface of the electrode, preventing solvent co-intercalation. This electrolyte improves the cycling and rate performance of graphite-based anodes (graphite, Si/graphite composites of ~450 mAh g^{-1} and ~1000 mAh g^{-1}) in combination with nickel-rich layered cathodes.

This leads to the final part of this thesis Chapter 6, where a detailed investigation of multi-component electrolytes, that are multi-salt vs. multi-solvent electrolytes, has been studied. Results reveal that various salts can balance Li-solvent/salt interactions to improve ionic conductivities in electrolytes and boost the formation of multi-component hybrid interphase layers, not various solvents. The local disorder introduced into the hybrid interphase exhibits a substantial enhancement of ion transport with a lower migration barrier, leading to good compatibility between the electrodes and electrolytes at high charge/discharge rates. Simultaneously, this comprehensive analysis further reveals that the formed hybrid interphases driven by various salts present an enhanced electrochemical/chemical stability to support both the long cycling life and long calendar aging life. These findings provide a practical route to achieve highly performing batteries.

References

1   J. B. Goodenough & Y. Kim. Challenges for Rechargeable Li Batteries. *Chemistry of Materials* **22**, 587-603, (2010).

2   B. Dunn, H. Kamath & J.-M. Tarascon. Electrical Energy Storage for the Grid: A Battery of Choices. *Science* **334**, 928-935, (2011).

3   W. Li, B. Song & A. Manthiram. High-voltage positive electrode materials for lithium-ion batteries. *Chemical Society Reviews* **46**, 3006-3059, (2017).

4   Y. Liu, B. Li, J. Liu, S. Li & S. Yang. Pre-planted nucleation seeds for rechargeable metallic lithium anodes. *Journal of Materials Chemistry A* **5**, 18862-18869, (2017).

5   N. Nitta, F. Wu, J. T. Lee & G. Yushin. Li-ion battery materials: present and future. *Materials Today* **18**, 252-264, (2015).

6   M. N. Obrovac & L. Christensen. Structural Changes in Silicon Anodes during Lithium Insertion/Extraction. *Electrochemical and Solid-State Letters* **7**, A93, (2004).

7   X.-B. Cheng, R. Zhang, C.-Z. Zhao & Q. Zhang. Toward Safe Lithium Metal Anode in Rechargeable Batteries: A Review. *Chemical Reviews* **117**, 10403-10473, (2017).

8   E. Peled. The Electrochemical Behavior of Alkali and Alkaline Earth Metals in Nonaqueous Battery Systems—The Solid Electrolyte Interphase Model. *Journal of The Electrochemical Society* **126**, 2047, (1979).

9   D. Larcher & J. M. Tarascon. Towards greener and more sustainable batteries for electrical energy storage. *Nature Chemistry* **7**, 19-29, (2015).

10   J. W. Choi & D. Aurbach. Promise and reality of post-lithium-ion batteries with high energy densities. *Nature Reviews Materials* **1**, 16013, (2016).

11   M. Li, C. Wang, Z. Chen, K. Xu & J. Lu. New Concepts in Electrolytes. *Chemical Reviews* **120**, 6783-6819, (2020).

12   D. Lin, Y. Liu & Y. Cui. Reviving the lithium metal anode for high-energy batteries. *Nature Nanotechnology* **12**, 194-206, (2017).

13   M. Armand & J. M. Tarascon. Building better batteries. *Nature* **451**, 652-657, (2008).

14   M. Winter, B. Barnett & K. Xu. Before Li Ion Batteries. *Chemical Reviews* **118**, 11433-11456, (2018).

15   E. Peled & S. Menkin. Review—SEI: Past, Present and Future. *Journal of The Electrochemical Society* **164**, A1703, (2017).

16 Q. Wang, C. Zhao, S. Wang, J. Wang, M. Liu, S. Ganapathy, X. Bai, B. Li & M. Wagemaker. Clarifying the Relationship between the Lithium Deposition Coverage and Microstructure in Lithium Metal Batteries. *Journal of the American Chemical Society* **144**, 21961-21971, (2022).

17 J. Wang, Y. Yamada, K. Sodeyama, C. H. Chiang, Y. Tateyama & A. Yamada. Superconcentrated electrolytes for a high-voltage lithium-ion battery. *Nature Communications* **7**, 12032, (2016).

18 K. Xu. Electrolytes and Interphases in Li-Ion Batteries and Beyond. *Chemical Reviews* **114**, 11503-11618, (2014).

19 K. Xu. Nonaqueous Liquid Electrolytes for Lithium-Based Rechargeable Batteries. *Chemical Reviews* **104**, 4303-4418, (2004).

20 Q. Wang, Z. Yao, C. Zhao, T. Verhallen, D. P. Tabor, M. Liu, F. Ooms, F. Kang, A. Aspuru-Guzik, Y.-S. Hu, M. Wagemaker & B. Li. Interface chemistry of an amide electrolyte for highly reversible lithium metal batteries. *Nature Communications* **11**, 4188, (2020).

21 S. Chen, J. Zheng, L. Yu, X. Ren, M. H. Engelhard, C. Niu, H. Lee, W. Xu, J. Xiao, J. Liu & J.-G. Zhang. High-Efficiency Lithium Metal Batteries with Fire-Retardant Electrolytes. *Joule* **2**, 1548-1558, (2018).

22 X. Cao, H. Jia, W. Xu & J.-G. Zhang. Review—Localized High-Concentration Electrolytes for Lithium Batteries. *Journal of The Electrochemical Society* **168**, 010522, (2021).

23 X.-Q. Zhang, X.-B. Cheng, X. Chen, C. Yan & Q. Zhang. Fluoroethylene Carbonate Additives to Render Uniform Li Deposits in Lithium Metal Batteries. *Advanced Functional Materials* **27**, 1605989, (2017).

24 I. A. Shkrob, J. F. Wishart & D. P. Abraham. What Makes Fluoroethylene Carbonate Different? *The Journal of Physical Chemistry C* **119**, 14954-14964, (2015).

25 Q. Zhao, S. Stalin & L. A. Archer. Stabilizing metal battery anodes through the design of solid electrolyte interphases. *Joule* **5**, 1119-1142, (2021).

26 D. Aurbach, Y. Ein-Ely & A. Zaban. The Surface Chemistry of Lithium Electrodes in Alkyl Carbonate Solutions. *Journal of The Electrochemical Society* **141**, L1, (1994).

27 Y. Yamada & A. Yamada. Review—Superconcentrated Electrolytes for Lithium Batteries. *Journal of The Electrochemical Society* **162**, A2406-A2423, (2015).

28 X. Fan, L. Chen, O. Borodin, X. Ji, J. Chen, S. Hou, T. Deng, J. Zheng, C. Yang, S.-C. Liou, K. Amine, K. Xu & C. Wang. Non-flammable electrolyte enables Li-metal batteries with aggressive cathode chemistries. *Nature Nanotechnology* **13**, 715-722, (2018).

29 Z. Yu, P. E. Rudnicki, Z. Zhang, Z. Huang, H. Celik, S. T. Oyakhire, Y. Chen, X. Kong, S. C. Kim, X. Xiao, H. Wang, Y. Zheng, G. A. Kamat, M. S. Kim, S. F. Bent, J. Qin, Y. Cui & Z.

Bao. Rational solvent molecule tuning for high-performance lithium metal battery electrolytes. *Nature Energy* **7**, 94-106, (2022).

30 K. Xu. Interfaces and interphases in batteries. *Journal of Power Sources* **559**, 232652, (2023).

31 Y. Yamada, K. Furukawa, K. Sodeyama, K. Kikuchi, M. Yaegashi, Y. Tateyama & A. Yamada. Unusual Stability of Acetonitrile-Based Superconcentrated Electrolytes for Fast-Charging Lithium-Ion Batteries. *Journal of the American Chemical Society* **136**, 5039-5046, (2014).

32 J. Han, L. Kiss, H. Mei, A. M. Remete, M. Ponikvar-Svet, D. M. Sedgwick, R. Roman, S. Fustero, H. Moriwaki & V. A. Soloshonok. Chemical Aspects of Human and Environmental Overload with Fluorine. *Chemical Reviews* **121**, 4678-4742, (2021).

33 G. Hernández, R. Mogensen, R. Younesi & J. Mindemark. Fluorine-Free Electrolytes for Lithium and Sodium Batteries. *Batteries & Supercaps* **5**, e202100373, (2022).

34 S. Jiao, X. Ren, R. Cao, M. H. Engelhard, Y. Liu, D. Hu, D. Mei, J. Zheng, W. Zhao, Q. Li, N. Liu, B. D. Adams, C. Ma, J. Liu, J.-G. Zhang & W. Xu. Stable cycling of high-voltage lithium metal batteries in ether electrolytes. *Nature Energy* **3**, 739-746, (2018).

35 S. Ko, T. Obukata, T. Shimada, N. Takenaka, M. Nakayama, A. Yamada & Y. Yamada. Electrode potential influences the reversibility of lithium-metal anodes. *Nature Energy* **7**, 1217-1224, (2022).

36 L. Suo, O. Borodin, T. Gao, M. Olguin, J. Ho, X. Fan, C. Luo, C. Wang & K. Xu. "Water-in-salt" electrolyte enables high-voltage aqueous lithium-ion chemistries. *Science* **350**, 938-943, (2015).

37 C. Wang, Y. S. Meng & K. Xu. Perspective—Fluorinating Interphases. *Journal of The Electrochemical Society* **166**, A5184, (2019).

38 Y.-X. Yao, X. Chen, C. Yan, X.-Q. Zhang, W.-L. Cai, J.-Q. Huang & Q. Zhang. Regulating Interfacial Chemistry in Lithium-Ion Batteries by a Weakly Solvating Electrolyte. *Angewandte Chemie International Edition* **60**, 4090-4097, (2021).

39 M. S. Kim, Z. Zhang, P. E. Rudnicki, Z. Yu, J. Wang, H. Wang, S. T. Oyakhire, Y. Chen, S. C. Kim, W. Zhang, D. T. Boyle, X. Kong, R. Xu, Z. Huang, W. Huang, S. F. Bent, L.-W. Wang, J. Qin, Z. Bao & Y. Cui. Suspension electrolyte with modified Li+ solvation environment for lithium metal batteries. *Nature Materials* **21**, 445-454, (2022).

40 M. Winter. The Solid Electrolyte Interphase – The Most Important and the Least Understood Solid Electrolyte in Rechargeable Li Batteries. *Zeitschrift für physikalische Chemie* **223**, 1395-1406, (2009).

41 K. Xu, G. V. Zhuang, J. L. Allen, U. Lee, S. S. Zhang, P. N. Ross, Jr. & T. R. Jow. Syntheses and Characterization of Lithium Alkyl Mono- and Dicarbonates as Components of Surface Films in Li-Ion Batteries. *The Journal of Physical Chemistry B* **110**, 7708-7719, (2006).

42 G. M. Hobold, A. Khurram & B. M. Gallant. Operando Gas Monitoring of Solid Electrolyte Interphase Reactions on Lithium. *Chemistry of Materials* **32**, 2341-2352, (2020).

43 P. Lu & S. J. Harris. Lithium transport within the solid electrolyte interphase. *Electrochemistry Communications* **13**, 1035-1037, (2011).

44 M. J. Zachman, Z. Tu, S. Choudhury, L. A. Archer & L. F. Kourkoutis. Cryo-STEM mapping of solid–liquid interfaces and dendrites in lithium-metal batteries. *Nature* **560**, 345-349, (2018).

45 B. M. Meyer, N. Leifer, S. Sakamoto, S. G. Greenbaum & C. P. Grey. High Field Multinuclear NMR Investigation of the SEI Layer in Lithium Rechargeable Batteries. *Electrochemical and Solid-State Letters* **8**, A145, (2005).

46 M. A. Hope, B. L. D. Rinkel, A. B. Gunnarsdóttir, K. Märker, S. Menkin, S. Paul, I. V. Sergeyev & C. P. Grey. Selective NMR observation of the SEI–metal interface by dynamic nuclear polarisation from lithium metal. *Nature Communications* **11**, 2224, (2020).

47 Y. Li, Y. Li, A. Pei, K. Yan, Y. Sun, C.-L. Wu, L.-M. Joubert, R. Chin, A. L. Koh, Y. Yu, J. Perrino, B. Butz, S. Chu & Y. Cui. Atomic structure of sensitive battery materials and interfaces revealed by cryo–electron microscopy. *Science* **358**, 506-510, (2017).

48 Z. Shadike, H. Lee, O. Borodin, X. Cao, X. Fan, X. Wang, R. Lin, S.-M. Bak, S. Ghose, K. Xu, C. Wang, J. Liu, J. Xiao, X.-Q. Yang & E. Hu. Identification of LiH and nanocrystalline LiF in the solid–electrolyte interphase of lithium metal anodes. *Nature Nanotechnology* **16**, 549-554, (2021).

49 C. Fang, J. Li, M. Zhang, Y. Zhang, F. Yang, J. Z. Lee, M.-H. Lee, J. Alvarado, M. A. Schroeder, Y. Yang, B. Lu, N. Williams, M. Ceja, L. Yang, M. Cai, J. Gu, K. Xu, X. Wang & Y. S. Meng. Quantifying inactive lithium in lithium metal batteries. *Nature* **572**, 511-515, (2019).

50 W. J. Albery. The Application of the Marcus Relation to Reactions in Solution. *Annual Review of Physical Chemistry* **31**, 227-263, (1980).

51 I.-S. Han Lee, E. H. Jeoung & M. M. Kreevoy. Primary Kinetic Isotope Effects on Hydride Transfer from 1,3-Dimethyl-2-phenylbenzimidazoline to NAD+ Analogues. *Journal of the American Chemical Society* **123**, 7492-7496, (2001).

52 R. A. Marcus. Theory of Rates of SN2 Reactions and Relation to Those of Outer Sphere Bond Rupture Electron Transfers. *The Journal of Physical Chemistry A* **101**, 4072-4087, (1997).

1

53   Y.-P. Liu & M. D. Newton. Reorganization Energy for Electron Transfer at Film-Modified Electrode Surfaces: A Dielectric Continuum Model. *The Journal of Physical Chemistry* **98**, 7162-7169, (1994).

54   K. Hayashi, Y. Nemoto, S. Tobishima & J. Yamaki. Mixed solvent electrolyte for high voltage lithium metal secondary cells. *Electrochimica Acta* **44**, 2337-2344, (1999).

55   R. A. Marcus & N. Sutin. Electron transfers in chemistry and biology. *Biochimica et Biophysica Acta (BBA) - Reviews on Bioenergetics* **811**, 265-322, (1985).

56   S. Hou, X. Ji, K. Gaskell, P. F. Wang, L. Wang, J. Xu, R. Sun, O. Borodin & C. Wang. Solvation sheath reorganization enables divalent metal batteries with fast interfacial charge transfer kinetics. *Science* **374**, 172-178, (2021).

57   J. W. Yeh, S. K. Chen, S. J. Lin, J. Y. Gan, T. S. Chin, T. T. Shun, C. H. Tsau & S. Y. Chang. Nanostructured High-Entropy Alloys with Multiple Principal Elements: Novel Alloy Design Concepts and Outcomes. *Advanced Engineering Materials* **6**, 299-303, (2004).

58   B. Cantor, I. T. H. Chang, P. Knight & A. J. B. Vincent. Microstructural development in equiatomic multicomponent alloys. *Materials Science and Engineering: A* **375-377**, 213-218, (2004).

59   M.-H. Tsai & J.-W. Yeh. High-Entropy Alloys: A Critical Review. *Materials Research Letters* **2**, 107-123, (2014).

60   E. P. George, D. Raabe & R. O. Ritchie. High-entropy alloys. *Nature Reviews Materials* **4**, 515-534, (2019).

61   D. Bérardan, S. Franger, A. K. Meena & N. Dragoe. Room temperature lithium superionic conductivity in high entropy oxides. *Journal of Materials Chemistry A* **4**, 9536-9541, (2016).

62   M. P. Stockham, B. Dong & P. R. Slater. High entropy lithium garnets – Testing the compositional flexibility of the lithium garnet system. *Journal of Solid State Chemistry* **308**, 122944, (2022).

63   Y. Zeng, B. Ouyang, J. Liu, Y.-W. Byeon, Z. Cai, L. J. Miara, Y. Wang & G. Ceder. High-entropy mechanism to boost ionic conductivity. *Science* **378**, 1320-1324, (2022).

64   L. R. Owen & N. G. Jones. Lattice distortions in high-entropy alloys. *Journal of Materials Research* **33**, 2954-2969, (2018).

2. Clarifying the relationship between lithium deposition coverage and microstructure in lithium metal batteries

Abstract

Improving the reversibility of the lithium (Li)-metal battery is one of the challenges in current battery research. This requires better fundamental understanding of the evolution of the Li deposition morphology, which is very complex due to the various parameters involved in different systems. Here, we clarify the fundamental origins of the Li deposition coverage in achieving highly reversible and compact Li deposits, providing a comprehensive picture in the relationship between Li microstructure and solid electrolyte interphase (SEI) for Li-metal batteries. Systematic variation of the salt concentration offers a framework that brings forward the different aspects that play a role in the cycling reversibility. The higher nucleation densities are formed in the lower concentration electrolytes, which have the advantage of a higher Li deposition coverage, however, it goes along with the formation of an organic-rich instable SEI which is unfavourable for the reversibility during (dis)charging. On the other hand, the growth of large deposits benefiting from the formation of an inorganic-rich stable SEI is observed in the higher concentrations, but the initial small nucleation density prevents full coverage of the current collector, thus compromises the plated Li-metal density. Taking advantages of the paradox, a nanostructured substrate is rationally applied that increases the nucleation density realizing a higher deposition coverage and thus more compact plating at intermediate concentration (~1.0 M) electrolytes, leading to the extended reversible cycling of the batteries.

2.1 Introduction

Since the first commercial lithium(Li)-ion batteries (LIBs) appeared in the early 1990s, they have been widely used to power mobile electronic devices[1,2]. The increase in energy density and reduction in price of LIBs has enabled the introduction of electrical vehicles, however, to push this further, higher energy densities are required to increase the driving range. In this context, Li metal is interesting, having the highest theoretical specific capacity (3,860 mAh g^{-1}) and lowest potential (-3.04 V vs. the standard hydrogen electrode, SHE). It is therefore intensively studied to break the specific energy bottleneck of current LIBs[3,4]. However, even after decades of intensive research, its poor electrochemical reversibility and consequentially short cycle life, remain the challenges that prevent commercialization[5-7].

It is widely accepted that the electrochemical reversibility is correlated with the evolution of the Li-metal morphology and the solid electrolyte interface (SEI) on the Li-metal surface. Heterogeneous Li-metal plating results in high-surface-area "mossy" or "whisker-like" morphologies, where the high Fermi energy level of Li metal causes irreversible reactions with the electrolyte that generate the SEI, which leads to loss of active Li, both as SEI species and as "dead" Li, the latter referring to the formation of electronically disconnected Li-metal particles[8-10]. Ideally, Li metal is electrochemically plated as a compact layer, having a small interface area with the electrolyte, where a flexible and stable SEI prevents further electrolyte decomposition. To achieve this, many strategies have been reported, of which the external strategies, including applying pressure[11-14], increasing temperature[15-18], aiming at physically generating a more compact deposition morphology. On the other hand, internal strategies are being investigated, where formulating electrolyte compositions aims at tuning both Li-metal morphology and SEI through electrochemical processes[19,20]. Generally, highly concentrated electrolytes (≥ 4 mol/liter (M))[21-24] and the functional additives or alternative salts/solvents[25-28] are employed to induce compact Li-metal plating through the formation of a stable SEI with good Li-ion conductivity. However, the large variety of systems studied, make it difficult to establish a coherent perception on how the Li-metal microstructural evolution and SEI composition/structure interact, and how these impact the reversibility upon cycling. An

2

opportunity to gain comprehensive understanding is variation of the salt concentration, being one of the very basic parameters that can be used to modify the electrolyte, determining the Li-ion mass transport through the electrolyte, and through its solvation characteristics, also influences the SEI composition and structure, both of which play important roles in the evolution of Li-metal microstructure.

In this work, we embark on a systematic study of the relationship between Li-metal microstructure and the SEI composition driven from electrolytes with varying concentrations. Different concentration of lithium bis(fluorosulfonyl)imide (LiFSI) salt was dissolved in a 1,2-Dimethoxyethane (DME) solvent, where the high donor number makes DME effective in the dissociation of alkali metal salts, enabling the study of a wide salt concentration range in the same system. This allows us to elucidate the influence of electrolyte properties on the microstructure of electrodeposited Li metal to explore the advantages and disadvantages of lower and higher salts concentration with respect to the resulting SEI and Li deposition morphology. These results indicate the importance of achieving a high Li deposition coverage, which can be achieved at lower salt concentrations, thereby marrying the advantages of low and high molarity salts towards higher reversibility for Li-metal batteries.

2.2 Impact of electrolyte concentrations on Li-metal morphology

The reversibility of the Li-metal plating/stripping in LiFSI DME electrolytes with different molarity is evaluated in Li||Cu cells. During the first 100 cycles at a current density of 0.5 mA cm^{-2} for 1.0 mAh cm^{-2}, the average Coulombic efficiency (CE) increases with the salt concentration (Fig. 2.1a and Fig. S2.1), along with a decrease in the CE fluctuation (Fig. 2.1b). A similar overall trend is observed for higher current densities of 1.0 mA cm^{-2}, 3 mA cm^{-2} and 5 mA cm^{-2} for 1.0 mAh cm^{-2} (Figs. S2.2-S2.5). The stability and overpotential are also evaluated in Li||Li symmetric cells (Figs. S2.6 and S2.7) where the reduced overpotential with increasing molarity appears to be a consequence of the reduced interfacial charge transfer resistance after the formation of the SEI (Fig. S2.8). The Li-ion transference number (t_{Li^+}) of the electrolytes is obtained via the method of
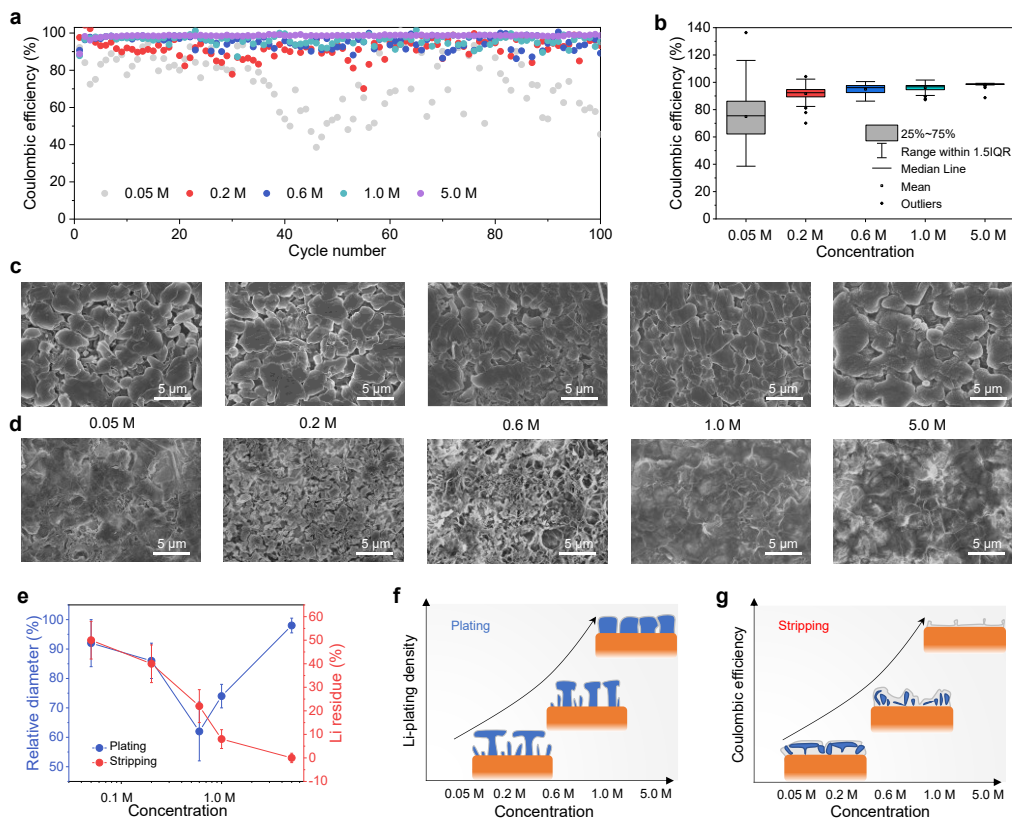
Fig. 2.1. Electrochemical cycling and Li-metal microstructure. a, CE in Li∥Cu cells for the LiFSI DME electrolyte with different molarities (0.05, 0.2, 0.6, 1.0, and 5.0 M). **b**, Box plot obtained on the basis of **a** showing statistics of the CE. The center line of the box plot represents the median; lower and upper box limits represent the 25% and 75% quantiles, respectively; whiskers extend to box limit $\pm 1.5 \times$ IQR (interquartile range); outlying points plotted individually. **c**, SEM images of Li deposited at 0.5 mA cm^{-2} for 2 h (1 mAh cm^{-2}) after the plating under the different electrolyte concentrations. **d**, SEM images of the Cu substrate after cycles, ending with Li stripping to 1.0 V vs. Li/Li$^+$ under the different electrolyte concentrations. The scale bars in **c** and **d** are 5 μm. **e**, Estimation of the average diameter of Li-metal deposits determined by SEM after plating, obtained from the images shown in **c** and **d**. The relative diameter is normalized by the largest average particle size among five different electrolytes, and the Li residual is estimated by the surface coverage. **f, g**, Schematic evolution of the Li-metal morphology in Li∥Cu cells as a function of concentration based on the SEM images for (**f**) discharge and (**g**) charge.

Abraham et al[29], resulting in the largest value for the 1.0 M salt electrolyte (Figs. S2.9-S2.13 and Table S2.1). A larger t_{Li^+} is considered favourable as it extends Sand's time,

i.e., the time until the Li ions in the electrolyte located near the surface of the Li metal are depleted, which is associated with the initiation of dendrite growth[3,9].

Scanning electron microscopy (SEM) was used to study the morphology of the plated/stripped Li deposits on Cu in Li‖Cu cells after plating at a current density of 0.5 mA cm^{-2} to an areal capacity of 1.0 mAh cm^{-2} (Fig. 2.1c) and after stripping to 1.0 V vs. Li/Li$^+$ (Fig. 2.1d). From the top-view SEM images, it is observed that the Li deposits in the dilute electrolytes, 0.05 M and 0.2 M, exhibit a similar diameter compared to that in the concentrated 5.0 M electrolyte. Moreover, with molarity increasing, the average diameter of Li deposits first appears to decrease until 0.6 M, and then increase while it increases to 5.0 M, as shown in Fig. 2.1e. To get a full understanding of their morphology, SEM on cross-sections was carried out so that the morphology as a function of depth can be investigated (Fig. S2.14). For the dilute electrolytes (0.05 M and 0.2 M) the deposited Li metal is more porous with smaller, whisker-like Li deposits near the current collector, whereas more compact deposition present at the top results in mushroom-like structures, which explains the larger relative diameter observed from the top-view SEM images. In contrast, when the molarity increases, larger columnar deposits form, leading to the larger diameter of the Li deposits. Therefore, the similar diameter in the top-view images of Li metal deposits in dilute and highly concentrated electrolytes represent different growth mechanism and morphology as illustrated in Fig. 2.1f. To investigate the morphology after stripping, SEM images after charging the Li‖Cu cells were collected (Fig. 2.1d). As the concentration increases, less Li residues can be observed on the Cu surface (Fig. 2.1e), which is schematically shown in Fig. 2.1g. The columnar Li deposits that occur at higher concentrations tend to decrease the formation of Li residual which is favourable for the high reversibility, however, the gaps between the columnar deposits can limit its deposit density.

2.3 Microstructure evolution and Li species quantification

^{7}Li solid-state NMR as a non-invasive method can provide quantitative and temporal information on Li metal deposition, where the development of operando probes allows to monitor processes of Li plating/stripping during an electrochemical measurement by

recording spectra at intervals[30-35]. The chemical shifts in ^{7}Li solid-state NMR can be used to differentiate metallic Li and diamagnetic Li species in electrolyte (~0 ppm), as well as provide insights into the evolution of the Li-metal microstructure during cycling (Fig. 2.2a). Here, ^{7}Li operando NMR measurements are performed using anode-less battery configuration of Cu||LiFePO$_4$ cells[36]. This plating and stripping process are shown in Fig. 2.2b, upon charging the Cu||LiFePO$_4$ cell, the Li metal resonance (~272 ppm) grows, reflecting the Li-metal deposition on the Cu current collector, and as expected it subsequently shrinks upon Li stripping during discharging. The pristine ^{7}Li spectra before charging, at the end of the first charge and after subsequent discharging extracted from the operando dataset are shown for each electrolyte concentration in Fig. S2.15 and Fig. 2.2a, which can be used for quantification. The Li-metal resonance in the spectra after charging shows highest intensity compared to the other state of charge, indicating the total Li metal plated on the current collector. At the end of discharge, Li-metal resonance decreased compared to the charged state but still visible compared to pristine spectra, which can be related to the amount of "dead" Li. This is also shown in their differential spectra that as the molarity of the Li salt in the electrolyte increases from 0.05 to 5.0 M, the amount of "dead" Li decreases (Fig. S2.16). Based on the NMR spectra and the CE, the amount of reversible Li metal, "dead" Li and Li in SEI species can be quantified with the method in Supplementary Note S2.1, and the results of which are shown in Fig. 2.2c and Table S2.2. The percentage of Li in the SEI and the "dead" Li both decrease with higher molarity, which consequently increases the capacity of the reversible Li metal. Only at 5.0 M the capacity loss is not dominated by the "dead" Li metal, suggesting favourable SEI properties for highly concentrated electrolytes.

The evolution of the ^{7}Li NMR resonance during charging and discharging can also provide insight into the evolution of the Li-metal microstructure, because the shift of the ^{7}Li metal peak is sensitive to the orientation and microstructure of the Li deposits due to the bulk magnetic susceptibility[31-33]. Generally, a pure Li-metal strip gives rise to a resonance signal at ~246 ppm when placed perpendicular to the fixed magnetic field B_0, which shifts to higher ppm values when the strip is parallel to B_0[31,33]. Therefore, mossy or whisker-like microstructures growing perpendicular to Cu, assuming the electrodes to be
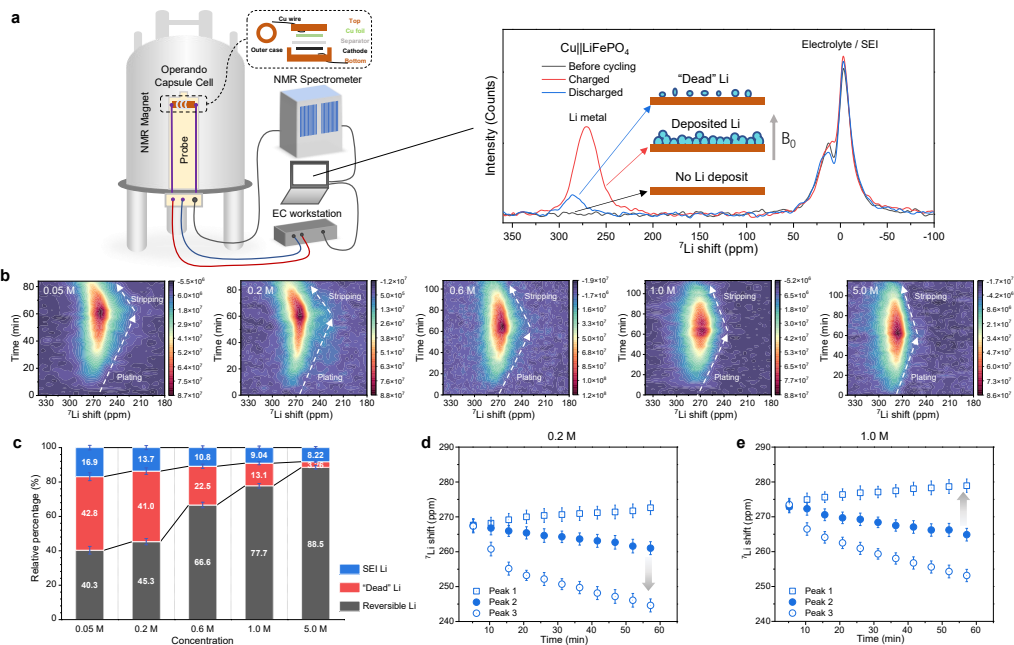
Fig. 2.2. Operando ^{7}Li NMR for quantification and microstructure evolution. a, The schematic of the operando NMR setup. The dashed box shows the operando capsule cell inserted in the NMR probe coil. The cell is connected to electrochemical workstation for galvanostatic charging/discharging. The figure on the right panel shows the spectra at different charge/discharge states, showing the resonance of the different Li special including the Li metal, SEI (after its formation) and Li species in the electrolyte. The intensity of Li metal resonance at fully charged and discharged state is linked to the amount of deposited Li metal and "dead" Li, respectively. The grey arrow indicates the magnetic field, B_0. **b**, Operando ^{7}Li NMR measurement during the first cycle of the Cu∥LiFePO$_4$ cells with different electrolyte concentrations at a current density of 1.0 mA cm^{-2}. **c**, Quantifying Li species after the first cycle, Li species in the SEI (blue bars), reversible Li metal (grey bars) and "dead" Li metal residual (red bars) species are derived from the Li metal integrated intensity ratio $I_{stripping}/I_{plating}$ and the CE (Supplementary Note S2.1). **d,e**, Evolution of the Li-metal resonances during charging in (**d**) 0.2 M LiFSI DME and (**e**) 1.0 M LiFSI DME electrolytes. Peak 1 and peak 3 stand for shoulder peaks on the left and right of the peak 2, respectively (Fig. S2.18). The grey arrow indicates the larger shift between the shoulder peak and the main peak.

perpendicular to B_0, have been associated with a chemical shift range centred at around 272 ppm, whereas mossy microstructures encompass broader spectral region covering a chemical shift range of approximate 250-290 ppm and more compact Li metal appears approaching ~246 ppm (Li-metal strip)[33]. Also, the vicinity of the deposits to the current

collector and the electrode, in combination with their bulk susceptibility, impact the shift. Electrodeposits near the Li-metal substrate result in a shift of ~260 ppm whereas whisker-like structures that extend further away from the surface appear at ~272 ppm. Due to the small diamagnetism of Cu, the Li-metal shift is hardly affected, however the paramagnetic $LiFePO_4$ can induce a +15 ppm shift approximately[36]. As shown in Fig. 2.2b, a distinct difference in distribution of chemical shifts is observed, broadening to smaller ppm values in low concentration electrolytes while broadening to high ppm values in high concentration electrolytes (Fig. S2.17). These distributions can be de-convoluted in three resonances, where peak 1 and peak 3 stand for shoulder peaks on the left (higher ppm) and right (lower ppm) of the peak 2, respectively (Figs. 2.2d, 2.2e and Fig. S2.18). In the 0.2 M electrolyte, peak 3 shifts significantly to lower ppm values along with peak 2 (Fig. 2.2d), suggesting the formation of relatively compact horizontal Li-metal microstructures at the end of plating, in line with the mushroom-like Li-metal morphology observed with SEM (Fig. 2.1f and Fig. S2.14). In the 1.0 M electrolyte, peak 2 and peak 3 also shift to smaller ppm values (Fig. 2.2e), but the shift is relatively small compared to that for the 0.2 M electrolyte. However, peak 1 shows a greater shift to higher ppm values compared to peak 3. This indicates that gradually more compact deposition of perpendicular Li-metal microstructure occurs, in line with the more columnar Li metal observed with SEM for this electrolyte concentration. The above results demonstrate that lower concentration (0.05-0.6 M) and higher concentration (1.0 M-5.0 M) LiFSI-DME electrolytes result in different Li-metal morphologies, which has profound impact on the evolution of the CE, "dead" Li and the SEI. In addition, [7]Li chemical shift at the very onset of Li plating tends to increase with increasing electrolyte molarity as shown in Fig. S2.17, which at this early stage is difficult to explain by a microstructural effect. A possible explanation is a difference in the coverage of the Li deposits on the Cu current collector[29,36], i.e., how much of the Cu current collector is covered by the Li-metal, suggesting that the coverage decreases with increasing electrolyte molarity. To gain insight in the role of the early-stage nucleation and coverage, two electrolyte concentrations, 0.2 M representing a lower concentration and 1.0 M representing an intermediate concentration, are studied in more

detail. The highly concentrated electrolyte is not selected because of its higher viscosity and cost, which makes it less attractive for future practical application.

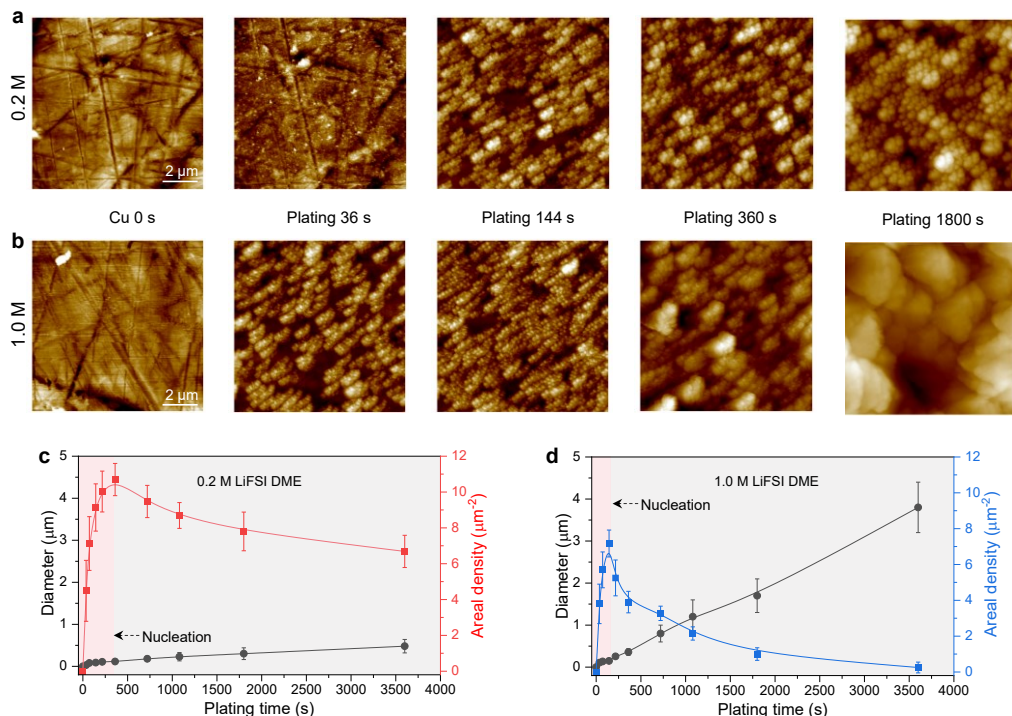## 2.4 Li nucleation and initial growth

Fig. 2.3. Li-metal nucleation and growth from in-situ AFM. Topography of the Cu substrate before and after Li plating at 0.5 mA cm^{-2} for 36 s (0.005 mAh cm^{-2}), 144 s (0.02 mAh cm^{-2}), 360 s (0.05 mAh cm^{-2}) and 1800 s (0.25 mAh cm^{-2}) in (**a**) 0.2 M LiFSI DME and (**b**) 1.0 M LiFSI DME electrolytes using in-situ electrochemical AFM measured on an area of 10 × 10 μm. Scale bar, 2 μm. Diameter of Li-metal deposits and the areal density evolution in (**c**) 0.2 M LiFSI DME and (**d**) 1.0 M LiFSI DME estimated from the AFM images, where the pink zone represents the nucleation process and the grey zone represents the following growth process.

To gain more insights into the nucleation and growth process, the initial Li deposition coverage and size of the Li-metal deposits on the Cu substrate are investigated by in-situ electrochemical atomic force microscopy (AFM). During these measurements there is no applied pressure due to the nature of the in-situ AFM setup (Fig. S2.19), and thus

represents different conditions from the morphologies shown in the SEM measurements (Figs. 2.1c and 2.1d), where the pressure of the separator on the Li-morphology can be expected to result in more compact plating. Figs. 2.3a and 2.3b show the AFM images before and after increasing the deposition time in the 0.2 M and 1.0 M LiFSI DME electrolytes. Before Li deposition (0 s deposition time in Figs. 2.3a and 2.3b) the grooves in Cu surface present due to polishing are clearly resolved. After 36 s (0.005 mAh cm^{-2}) a thin layer of nano-sized Li deposits can be observed for 0.2 M (Fig. 2.3a). In contrast, in 1.0 M electrolyte the coverage of the Cu substrate is around half of the detect area (Fig. 2.3b) with larger deposits of ~100 nm in diameter. During subsequent deposition to 360 s (0.05 mAh cm^{-2}), the number of Li-metal deposits in the 0.2 M electrolyte increases continuously (Fig. 2.3c). However, upon subsequent plating the size of the Li-metal deposits on top of this layer only marginally increases, to 300-500 nm after 3600 s (0.5 mAh cm^{-2}, Fig. S2.20), and its number remains high as summarized in Fig. 2.3c. In contrast, in the 1.0 M electrolyte the number of Li-metal deposits decreases sharply after 144s (0.02 mAh cm^{-2}) while the average size increases steadily (Fig. 2.3d), approaching several micrometres in diameter at 1800 s (0.25 mAh cm^{-2}) until a final diameter of around 4 μm is achieved (Fig. S2.21). The decrease in the number of Li-metal deposits appears to be a result of coalescence of smaller deposits, further supported by the cross-sectional SEM images shown in Fig S2.14. Based on the observation above, the increased coverage observed for the 0.2 M compared to the 1.0 M electrolyte therefore can be related to the lower shifts in 0.2 M than 1.0 M electrolyte as observed in ^{7}Li NMR spectra at the initial stage of plating (Fig. 2.2b). A higher coverage of Li-metal deposits, as observed for 0.2 M, can be considered favourable for dense Li-metal growth. Although the larger cylindrical deposits at 1.0 M resulted in denser plating as seen from the SEM study, some pores were left behind such that the Cu substrate was not fully covered. On the other hand, the continuous nucleation of Li-metal deposits in a longer time scale as observed for 0.2 M electrolyte can be expected to lead to higher final Li-metal coverage and thus a denser Li-metal film. However, this does not occur because the growth of the Li deposits is stalled in this dilute 0.2 M electrolyte to the final stages of deposition as indicated by operando ^{7}Li NMR results. While the depletion driven overpotential can qualitatively explain some

of these aspects, another decisive factor in the growth of Li deposits is the SEI formation, which is significantly influenced by the electrolyte concentration[37].

2.5 SEI structure and composition

Stabilized under the cryogenic conditions in the transmission electron microscope (TEM), the Li deposits and SEI structure are investigated with the 0.2 M and 1.0 M LiFSI DME electrolytes, and the results are shown in Figs. 2.4a-2.4d. In the low-magnification cryo-TEM images of the Li metal plated in 0.2 M LiFSI DME (Fig. 2.4a), whisker-like Li deposits are covered with an uneven SEI, resulting in a rougher surface (indicated by the light-dark variations in the SEI coating). Two areas were selected for higher magnification, marked with the solid box and dashed box. The thickness of the SEI for the 0.2 M electrolyte varies significantly. The region of the Fig. 2.4a (left) is measured to be approximately 26±2 nm, as shown by the high-resolution cryo-TEM images, where the interface between the deposited Li metal and the SEI is not well defined and irregular in shape. The SEI layer is dominated by amorphous components in which a small number of crystalline domains are randomly dispersed, forming a nanostructured mosaic SEI morphology[38]. Most likely the amorphous matrix represents organic species formed by DME solvent decomposition, whereas the crystalline grains represent the inorganic components of the SEI layer (Fig. 2.4c and Fig. S2.22). The latter are attributed to Li_2O and LiF from selected area electron diffraction (SAED) measurements (Fig. S2.23). From cryogenic scanning transmission electron microscopy (STEM) annular dark field (ADF) images combined with electron energy loss spectroscopy (EELS) mapping, it can be concluded that the SEI formed in the 0.2 M electrolyte is mainly organic, being rich in carbon and oxygen (Fig. S2.24). For the 1.0 M LiFSI DME electrolyte, the low magnification cryo-TEM image in Fig. 2.4b shows that the Li metal deposits have a larger diameter and the SEI is smoother and conformally covers the Li-metal deposits. In this case the SEI thickness is quite well defined with a thickness around 22-24 nm, exhibiting a multilayer nanostructure[39]. In the outer layer, the well-defined lattice fringes represent large crystalline grains (~10 nm), whereas the inner layer is largely amorphous (Fig. 2.4d and Fig. S2.22). The inorganic components in the outer layer are Li_2O and LiF, as

determined by SAED (Fig. S2.25). In the ADF and EELS mapping, a strong oxygen signal is present (Fig. S2.26), further confirmed by X-ray photoelectron spectroscopy (XPS) measurements (Fig. 2.4f).
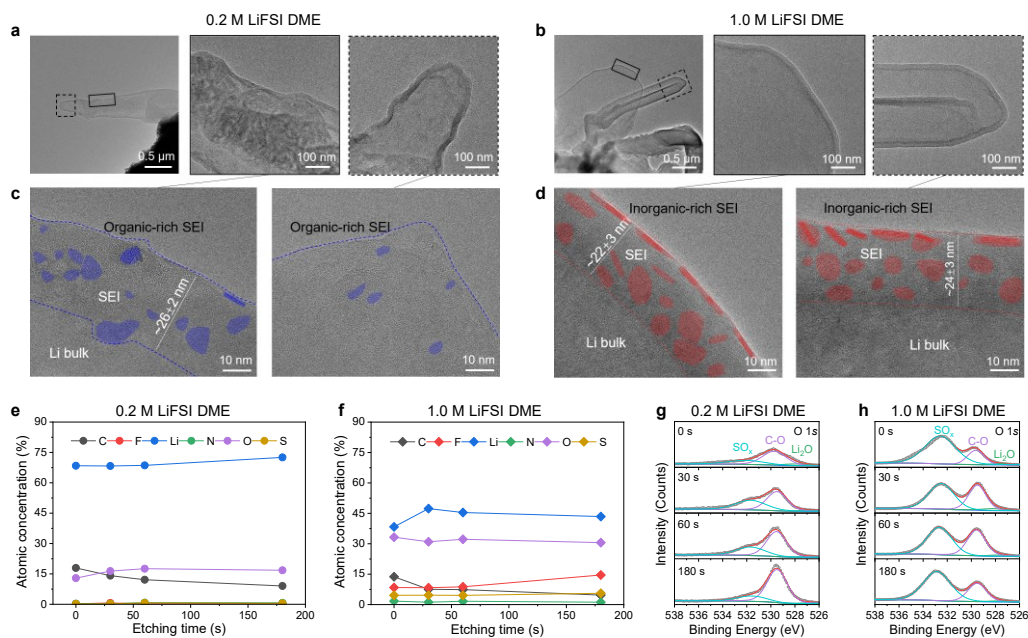

Fig. 2.4. Structural and chemical analysis of SEI from cryo-TEM and XPS. a, A bright-field cryo-TEM image showing the morphology of Li metal deposits using 0.2 M LiFSI DME electrolyte at a low magnification (left). The zoomed-in image of the region is marked by the black solid box (middle) and black dashed box (right). **b**, A bright-field cryo-TEM image showing the morphology of Li metal deposits using 1.0 M LiFSI DME electrolyte at a low magnification (left). The zoomed-in image of the region is marked by black solid box (middle) and black dashed box (right). **c,** High-resolution cryo-TEM images of the SEI layer on deposited Li metal in a 0.2 M LiFSI DME electrolyte corresponding to **a**, where the blue-colored area represents the inorganic components in SEI. **d**, High-resolution cryo-TEM images of the SEI layer on the deposited Li metal in a 1.0 M LiFSI DME electrolyte corresponding to **b**, where the red-colored area represents the inorganic components in the SEI. **e**, **f**, XPS depth profiles after cycling for both 0.2 and 1.0 M LiFSI DME electrolytes (Li||Cu cells, 20 cycles at 0.5 mA cm^{-2} for 1.0 mAh cm^{-2}) showing the SEI composition after different sputtering times on the deposited Li metal in (**e**) 0.2 M LiFSI DME and (**f**) 1.0 M LiFSI DME. **g**, **h**, Deconvoluted O 1*s* XPS depth profiles as a function of time of the SEI formed in (**g**) 0.2 M LiFSI DME and (**h**) 1.0 M LiFSI DME.

Since the organic components of the SEI are mainly decomposition products of the DME solvent, the carbon content in the SEI is expected to be higher. This appears to be

true for the organic-rich SEI (more organic components, such as C-O, C-C/C-H species from solvent decomposition) formed in the 0.2 M electrolyte based on the XPS measurements in Fig. 2.4e. In contrast, an inorganic-rich SEI (more inorganic components from anion decomposition) containing Li_2O and LiF is expected to have a higher ratio of O and F. This appears to apply to the SEI formed in the 1.0 M electrolyte based on the XPS measurements in Fig. 2.4f. The deconvoluted XPS depth profiles provide more detailed information on the impact of the electrolyte concentration on the SEI formation. In the 0.2 M electrolyte, the presence of a small fractions of SO_x and Li_2O indicates very limited salt decomposition, consistent with the low intensity of F, S, N containing compounds (Figs. S2.27-2.31). The large fraction of C containing species detected in the SEI formed in the 0.2 M electrolyte indicates that solvent decomposition dominates the SEI formation (Fig. 2.4g and Fig. S2.32), which is consistent with the large redox peak observed at ~0.5 V using cyclic voltammetry (Fig. S2.33). The higher salt concentration in the 1.0 M electrolyte results in more SO_x and Li_2O, suggesting that LiFSI decomposition dominates the SEI formation process (Fig. 2.4h), which is consistent with the higher LiF intensity in the Li 1s spectrum and the lower fraction of carbonate species (Figs. S2.31 and S2.32).

2.6 Joining the advantages of lower and higher concentration electrolytes

The higher nucleation coverage and longer nucleation periods in low concentration electrolytes, driven by the more severe Li-ion depletion, can be considered as a favourable starting point for dense Li-metal plating, and thus for more reversible cycling. However, the same ion depletion is responsible for a more organic-rich SEI through DME solvent decomposition, which promotes inhomogeneous Li plating/stripping and stalls the growth of large and dense Li-metal deposits. The larger surface area of the smaller deposits in dilute electrolytes causes more SEI growth, which leads to more irreversible capacity loss and electrolyte consumption during cycling. The benefit of a higher salt concentration is the thin, well defined multi-layer SEI that is rich in inorganic species, which guarantee a higher stability as well as a higher and more homogeneous Li-ion conductivity. This seems to be responsible for the continuous growth of large and dense Li-metal deposits, which

in turn suppresses the formation of "dead" Li metal, and the smaller surface area of these large deposits leads to a much smaller amount of SEI species, both these factors promoting the reversibility. The disadvantages are however that the lower nucleation density at higher electrolyte concentrations leaves parts of the Cu uncovered leading to a lower Li deposition coverage, and limiting the Li-metal density. This in addition to the known disadvantages of higher salt concentrations i.e. the increase in viscosity (lowering conductivity), reduction in wettability and increase in costs, have so far limited its practical application[40].
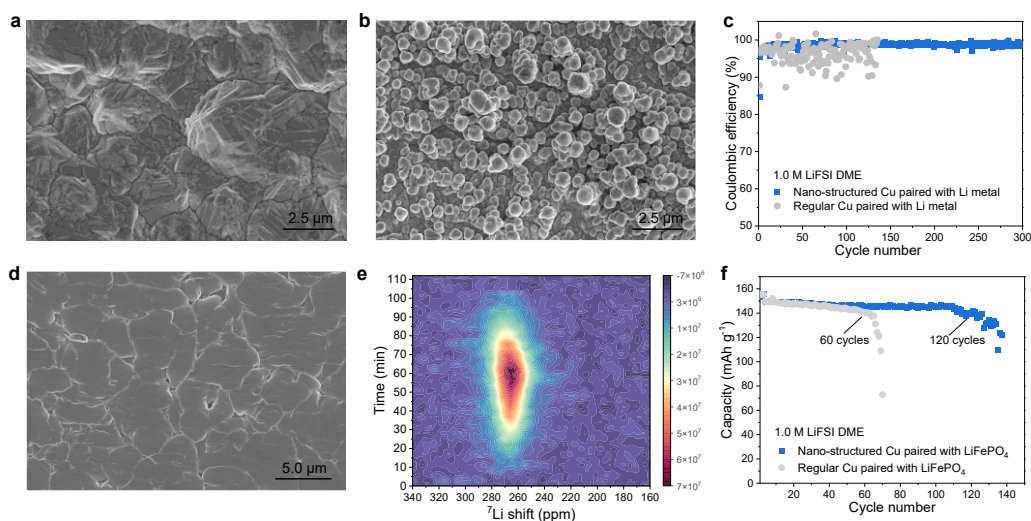

Fig. 2.5. Increasing the Li deposition coverage for the 1.0 M LiFSI DME electrolyte. a,b, Top-view SEM image of the (**a**) regular Cu foil and (**b**) nano-structured Cu foil. **c**, CE from Li‖Cu cells using the regular and nano-structured Cu in a 1.0 M LiFSI DME electrolyte cycled at a current density of 0.5 mA cm^{-2} to a capacity of 1.0 mAh cm^{-2}. **d**, Top-view SEM image of deposited Li metal on the nano-structured Cu in a 1.0 M LiFSI DME electrolyte cycled at a current density of 0.5 mA cm^{-2} to a capacity of 1.0 mAh cm^{-2}. **e**, Operando ^{7}Li NMR spectra acquired during the first cycle of Cu‖LiFePO$_4$ cells using the nano-structured Cu in a 1.0 M LiFSI DME electrolyte. **f**, Capacity retention of Cu‖ LiFePO$_4$ batteries cycled at C/3 in 1.0 M LiFSI DME electrolyte using different Cu foils with pre-deposit Li of 0.5 times the capacity of cathode electrodes. The areal capacity of LiFePO$_4$ cathode is 2.0 mAh cm^{-2}.

Therefore, the challenge is to combine the favourable properties of both high and low salt concentrations. With respect to the SEI composition, a stable SEI requires at least an intermediate, around 1.0 M, salt concentration (excluding the possibility of improving the

SEI with additives). Therefore, a rational strategy is to aim for increasing the density in nucleation sites at 1.0 M to achieve denser plating while keeping the favourable SEI morphology and composition. Several studies have demonstrated that initial nucleation pulses and can increase the density of Li-metal nucleation on the electrode surface[41-43]. However, the pulsed charging/discharging induces continuous consumption of both solvent and the Li from the cathode side which leads to more rapid degradation of the battery[44]. Instead, we propose to use the commercially available current collector covered by nano-sized Cu particles, to replace the regular Cu current collector (Fig. 2.5a), that acts as nucleation centres for Li-metal growth (Fig. 2.5b and Fig. S2.34 and S2.35) and study the deposition in combination with a 1.0 M LiFSI DME electrolyte.

Introducing the nano-structured Cu in Li‖Cu cells demonstrates a marked improvement in the average CE and in cycling stability as compared to the regular Cu (Fig. 2.5c). SEM images demonstrated that the nano-structured Cu results in more compact and smoother Li deposition as compared to the regular Cu (Fig. 2.5d and Fig. S2.36). Operando ^{7}Li NMR was performed to further verify the Li-metal microstructural evolution on the nano-structured Cu. Compared with using regular Cu, the Li-metal peak on nano-structured Cu results in a chemical shift at lower ppm values in the initial stages (Fig. 2.5e and Fig. S2.37), resembling the chemical shift observed in dilute electrolytes, indicating an increased Li deposition coverage. The nucleation on this nano-structured Cu was further studied by in-situ electrochemical AFM, where a larger nucleation size was achieved as expected for the1.0 M electrolyte (Fig. 2.3), but in this case in combination with a higher coverage (Fig. S2.38). In order to evaluate the potential application, Cu‖LiFePO$_4$ full cells were assembled to study the cycling stability of the nano-structured and the regular Cu. The results show stable cycling over 130 cycles for the nano-structured Cu, and the cell using regular Cu fails after around 60 cycles (Fig. 2.5f and Fig. S2.39), extending the cycling life more than two times.

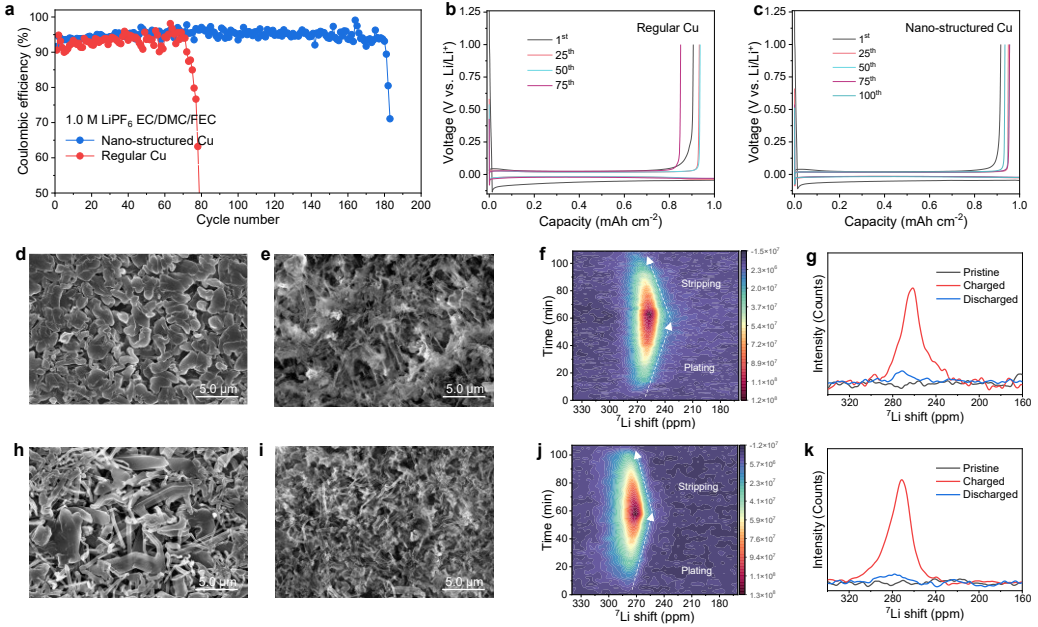## 2.7 Demonstration of the Li deposition coverage in commercial electrolyte

Fig. 2.6. Increasing the Li deposition coverage in ester electrolyte. a, CE of Li‖Cu cells using regular and nano-structured Cu, cycling at current density of 0.5 mA cm^{-2} to a capacity of 1.0 mAh cm^{-2}. **b**, **c**, Corresponding charge/discharge curves of Li-metal plating/stripping on (**b**) regular and (**c**) on the nano-structured Cu. **d**, **h**, Top-view SEM image of plated Li metal on (**d**) nano-structured and (**h**) on the regular Cu after three cycles then plating at 0.5 mA cm^{-2} to a capacity of 1.0 mAh cm^{-2}. **e**, **i**, Top-view SEM images of (**e**) the nano-structured and (**i**) regular Cu after Li stripping to 1.0 V vs. Li/Li^{+}. **f**, **j**, Operando ^{7}Li NMR spectra acquired during the first cycle of a Cu‖LiFePO$_4$ cell using the (**f**) nano-structured Cu and (**j**) regular Cu. **g**, **k**, ^{7}Li NMR spectra using the (**g**) nano-structured Cu and (**k**) regular Cu before (pristine), after Li plating (charged) and after Li stripping (discharged). The electrolyte for cells is 1.0 M LiPF$_6$ in EC: DMC (1:1 in weight) with 5% FEC.

Finally, the impact of increasing the Li deposition coverage and density via the nano-structure of the Cu substrate is investigated using a typical ester electrolyte. The standard carbonate electrolyte with 1.0 M LiPF$_6$ dissolved in ethylene carbonate and dimethyl carbonate (EC: DMC 1:1 in weight), including a 5% FEC additive which is known to improve the cycling stability of Li-metal anode. The electrochemical cycling of the Li‖Cu cells demonstrates that also in this case, the nano-structured Cu results in a higher CE (91.6% vs. 90.5%) and better cycling stability (Fig. 2.6a), as well as a lower overpotential (Fig. 2.6c), as compared to regular Cu under the same conditions (Fig. 2.6b). The Li-metal

deposits on the nano-structured Cu have a larger diameter (Fig. 2.6d) than those on the regular Cu, where the latter exhibits whisker-like microstructures (Fig. 2.6h). After Li stripping, the regular Cu shows more whisker-like Li residuals left on the surface (Fig. 2.6i), compared to that from the nano-structured Cu (Fig. 2.6e). Operando ^{7}Li NMR was carried out to gain insight in the Li-metal microstructure evolution during plating and stripping in the ester electrolyte, using the regular or nano-structured Cu in Cu||LiFePO$_4$ cells. Comparing the nano-structured and regular Cu shown in Fig. 2.6f and 2.6j, respectively, it is seen that the nano-structured Cu leads to lower ^{7}Li chemical shifts that can be associated with more compact plating and larger deposition coverage. In contrast the deposition on regular Cu results in higher shift for the ^{7}Li chemical shifts, indicating more whisker-like growth and less deposition coverage (Fig. 2.6g and 2.6k). Interestingly, based on the ^{7}Li NMR spectra after discharge, there is little difference in the amount of residual Li metal between the two Cu current collectors, which may be related to a similar SEI composition, also suggested by the similar CE. Even though the improvement in the CE upon cycling is small, the more compact plating on the nano-structured Cu enhances the cycling stability, extending the cycle life of the Li||Cu cells.

2.8 Comprehensive picture of Li-metal microstructure

Based on the above observations, the complex dependence of the deposition morphology on the concentration due to the different nucleation conditions as well as the different SEI growth conditions can be clarified. To achieve dense plating, not only requires large Li deposition diameters, such as achieved in higher concentrated electrolytes, but also requires a high deposition coverage. This is demonstrated by Li plating in 5.0 M LiFSI DME, where the larger Li deposits diameters are realized, but the low deposition coverage can be held responsible for leaving gaps between the deposits (Fig. 2.7a) which compromises the Li-metal density. In lower concentration electrolytes, such as 0.2 M LiFSI DME, the deposition coverage is high, but it results in a mosaic structured organic-rich SEI which does not support homogeneous plating or stripping of the Li metal (Fig. 2.7c), and consequentially results in porous Li-metal deposition and low reversibility. The favourable properties of both extremes can be combined in electrolytes with intermediate

concentrations, such as 0.6 M and 1.0 M, inducing a higher Li deposition coverage via the current collector surface structure (moving from Figs. 2.7b to 2.7d). The investigation of the Li-metal morphology and SEI structure as a function of electrolyte concentration demonstrates the importance of achieving high Li deposition coverage, in combination with the conditions to grow large deposits, promoting denser Li-metal deposition, a prerequisite to reversible Li-metal batteries.
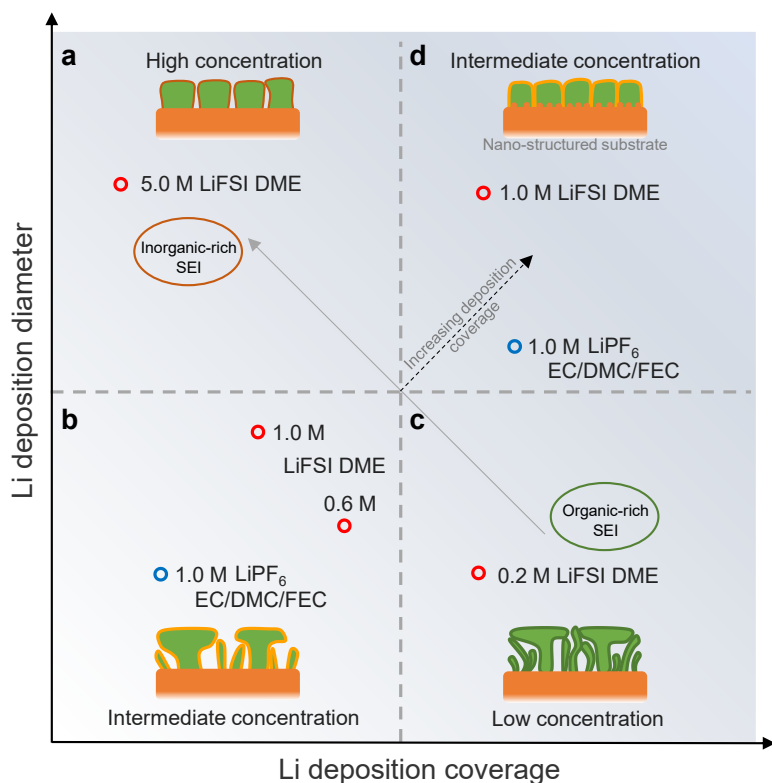

Fig. 2.7. Correlation between Li deposition coverage, Li deposition diameter and electrolytes. Four regions of Li-metal morphology can be distinguished that clarify the relationship. **a**, Highly concentrated electrolytes result in low deposition coverage and large Li deposition diameter. **b**, Intermediate concentration electrolytes result in small Li deposition coverage and small Li deposition diameter. **c**, Low concentration electrolytes result in high deposition coverage and small Li deposition diameter. **d**, Intermediate concentration electrolytes result in high deposition coverage when introducing a substrate with a high density of nucleation sites, resulting in large Li deposition diameter in combination with a high coverage.

2.9 Conclusions

In summary, Li microstructure was systematically investigated as a function of electrolyte concentration using a combination of operando, in-situ and ex situ experimental techniques that probe the Li-metal morphology and SEI on all length scales, formulating a comprehensive picture of the relationship between Li deposition coverage and microstructure in Li metal batteries. The higher deposition coverages can be formed in the dilute electrolytes, which provides a favourable starting point for dense Li-metal deposition. However, the formation of the organic-rich mosaic SEI, also a consequence of salt depletion at the Li-metal surface, prevents the growth of large Li deposits and dense Li-metal deposition. In contrast, higher concentrated electrolytes induce a thin and stable SEI, that induces the growth of large Li deposits. In this case, however, the relatively small deposition coverage limits the final density of the Li-metal deposition. These results imply the importance of deposition coverage in the microstructure of Li metal. Furthermore, the deposition coverage can be improved through the substrate surface structure, making it possible to combine the favourable aspects of low concentration electrolytes with those of highly concentrated electrolytes. For intermediate concentration electrolytes, the combination of the high deposition coverage with stable SEI driven from the functional additives or alternative salts/solvents provides a promising research direction for practical applications, which has been also demonstrated by the commercial carbonate electrolytes.

2.10 Methods

Materials

Li-metal foils (thickness of 250 μm) and Cu foils were purchased from MTI Corporation. All Li-metal foils were washed 3 times with DME solvent before use. Cu foils were immersed in diluted acetic acid for 3 min, subsequently washed with deionized water and acetone three times, separately, then they were quickly dried in the vacuum chamber of glove box at room temperature. The nano-structured Cu was purchased from Mingyu metal company. Battery-grade Dimethoxyethane (DME) and 4-Fluoroethylene carbonate (FEC) was purchased from Sigma-Aldrich, which was dehydrated with a 4 Å molecular

sieve (Sigma-Aldrich) to eliminate any trace water before use. Lithium bis(fluorosulfonyl)imide (LiFSI) was purchased from Sigma-Aldrich, which were dried at 100 °C under vacuum for 24 h before use.1.0 M $LiPF_6$ in EC: DMC (1:1, by weight) electrolyte was purchased from Sigma-Aldrich. All the electrolytes were prepared and stored in an Ar-filled glove box (H_2O < 0.1 ppm, O_2 < 0.1 ppm). $LiFePO_4$ was obtained from Leneng Technology for which the cathodes were prepared by mixing $LiFePO_4$ material, poly (vinylidene difluoride) (PVDF, MTI) binder and Super P (Alfa Aesar) conductive carbon in a weight ratio of 92:4:4. The resulting slurry was cast on the Al foil then dried at 60 °C for 6 h, followed by drying overnight at 120 °C in a vacuum oven.

Electrochemical measurements

For the electrochemical cycling tests, all batteries were assembled into CR2032 coin cells in an Ar-filled glove box (H_2O < 0.1 ppm, O_2 < 0.1 ppm) with Celgard 2500 separator. 70 µL electrolytes were injected into each coin cell for comparison. All coin cells were tested using multi-channel battery testing systems (Land CT2001A or Lanhe G340A) at room temperature. Symmetric Li‖Li cells were assembled to study the cycling stability under different current densities with different electrolytes, 15.6 mm diameter Li-metal foils with a 250 µm thickness were used as both the working and counter electrodes. For Li‖Cu cells, 14 mm diameter Li-metal foils were used as the reference, while 16 mm Cu foils was as a working electrode with the effective area for Li deposition of 1.54 cm^2. During cycles, capacity of 1 mAh cm^{-2} Li was deposited on Cu foils at various current densities and the cut-off voltage for stripping was set to 1.0 V vs. Li/Li^+.

The electrochemical cycling performance of Cu‖$LiFePO_4$ cells were tested in galvanostatic mode within a voltage range of 2.5–3.8 V. The cathodes had a diameter of 12 mm and loading of 2 mAh cm^{-2}. The Cu current collector was used after pre-deposition Li metal to 0.5 times the capacity of cathode electrodes. Cyclic voltammetry (CV) of Li‖Cu cells with various electrolytes was conducted at a scan rate of 0.8 mV s^{-1} from -0.1 to 2.5 V vs. Li/Li^+. Electrochemical impedance spectra (EIS) of the symmetric cells were collected on an Autolab (PGSTAT302N) in the frequency range of 0.1 Hz–1 MHz with a potential amplitude of 10 mV.

Li ion transference number (t_{Li}^+) of electrolytes was measured via the method of Abraham et al[29]. The polarization potential (ΔV) of 10 mV was used for symmetric Li‖Li cells with various kinds of electrolytes until the polarization currents reached a steady state, and the corresponding EIS measurements were collected both before and after the polarization. The t_{Li}^+ was calculated as following equation:

$$t_{Li^+} = \frac{I^{ss} R_b^{ss} (\Delta V - I^0 R_i^0)}{I^0 R_b^0 (\Delta V - I^{ss} R_i^{ss})} \tag{2.1}$$

where ΔV is the applied potential, I^0 is the initial current and I^{ss} is the steady-state current; R_b^0 and R_b^{ss} are the initial and steady-state values of the bulk resistances; R_i^0 and R_i^{ss} are the initial and steady-state values of the interfacial resistances, respectively, which were determined by impedance measurements before and after the potentiostatic polarization.

Ionic conductivity of electrolytes was measured using symmetric stainless steel‖stainless steel cells by collecting electrochemical impedance (R) at room temperature, and calculated using the following equation:

$$\sigma = \frac{L}{R \times S} \tag{2.2}$$

where σ is ionic conductivity, S is the effective area of electrode, L stands for the thickness between two stainless steel electrodes, respectively. Test cells were assembled with a Polytetrafluoroethylene (PTFE) ring between two stainless-steel electrodes. Hence, the effective area of electrode is calculated based on the inner diameter of the PTFE ring, and the thickness between two stainless steel electrodes is based on the thickness of the PTFE ring.

Materials characterization

Morphologies of electrodes were measured on a scanning electron microscope (SEM, HITACH SU8010). The obtained SEM images were analyzed with the PC-SEM (Hitachi SU8000 series) analysis software, and the particle size and number are further confirmed by the public domain software for processing and analyzing scientific images of Image J. Elemental composition on the surface of electrodes was analyzed by X-ray photoelectron spectroscopy (XPS, PHI 5000 VersaProbe II) using monochromatic Al Kα X-ray source. A sputter argon ion gun was equipped for depth profiling of the electrodes. Peaks were fitted using MultiPak software calibrated with respect to carbon (284.8 eV). The above

morphology and composition characterizations were performed with cells being disassembled after specific cycles in an Ar-filled glove box and rinsed with pure DME solvent three times to remove residual electrolyte, followed by drying in the glove box for several hours at room temperature to remove the residual solvent. Then electrodes were transferred into the vacuum transfer boxes to avoid air exposure. Powder X-ray diffraction (XRD) was performed using a Bruker D8 Advance diffractometer equipped with a Cu Kα radiation source (λ_1=1.54060 Å, λ_2=1.54439 Å at 40 kV and 40 mA) and a LynxEye_XE detector.

In-situ atomic force microscopy (AFM) characterization

In-situ electrochemical AFM measurements (Bruker Corp., Dimension Icon) were performed with a three-electrode cell powered by an electrochemical workstation (CHI760E). Cells were assembled in an argon-filled glove box (H_2O < 0.1 ppm, O_2 < 0.1 ppm) with Cu substrate as working electrode and Li strips (diameter of 1mm) as the counter and reference electrodes. Li was deposited at 0.5 mA cm^{-2}, and in-situ AFM observation was carried out under open-circuit conditions after a specific time of deposition. AFM topography images were collected with the peak force tapping mode and the ScanAsyst-Fluid tips ($k = 0.7$ N m^{-1}, Bruker Corporation) were used for their superior force control with a pN-level force between tip and electrode, diminishing the damage to sample surface in the liquid condition. The obtained AFM images were analyzed with the NanoScope Analysis software, and the particle size and number are further confirmed by Image J.

Cryo-transmission electron microscopy (Cryo-TEM) characterization

Cryo-(S)TEM experiments were performed on scanning transmission electron microscope (STEM) (JEM-ARM300F, JEOL Ltd.) operated at 300 kV with a cold field emission gun and double Cs correctors. The microscope was equipped with Gatan OneView and K2 cameras for images recording. During image acquisition, the corresponding electron dose flux (units of number of electrons per square Å per second, e^- $Å^{-2}$ s^{-1}) was recorded. Cryo-TEM images were obtained with an exposure time for each image of around 0.3 s with built-in drift correction function in GMS3 using the OneView and K2 camera. Cryo-TEM

images were taken with an electron dose rate of 50-500 e$^-$ Å^{-2} s^{-1}. Short-exposure single-frame shots were used to estimate the defocus and make it as close as possible to Scherzer defocus. The EELS spectrum images were recorded with a camera length of 20 mm, and a pixel dwell time of 10 ms. Energy drift during spectrum imaging was corrected by centering the zero-loss peak to 0 eV at each pixel. Elemental maps were computed through a two-window method in a pre-edge window fitted to a power-law background and a post-edge window of 50-200 eV on the core-loss signal. Analysis of the spectra has been performed in Digital Micrograph.

For cryo-TEM preparation of Li-metal anode, a lacey carbon TEM grid was put on Cu foils working electrode and assembled into Li‖Cu cells in an argon-filled glovebox. The cells were discharged at a constant current density of 1.0 mA cm^{-2} for 15 min, then TEM grid was taken out by disassembling the cells for measurement. TEM grid was carefully transferred into the cryo-TEM holder in glovebox with a specialized shutter to prevent air exposure and ice condensation onto the sample introducing any side reactions. Once the cryo-TEM holder was transferred into TEM column, the temperature was maintained at around -170 °C using liquid nitrogen. All cryo-TEM images were taken at around -170 °C to reduce beam damage.

Solid-state NMR characterization

Operando solid-state NMR measurements were conducted on a wide-bore Bruker Ascend 500 system equipped with a NEO console with a magnetic field strength of 11.7 T and a ^{7}Li resonance frequency being 194.37 MHz using a solenoidal Ag-coated Cu coil. Operando static ^{7}Li NMR measurements were performed using an automatic-tuning-and-matching probe (ATM VT X WB operando NMR probe, NMR Service) at room temperature which can allow for an automatic recalibration of the NMR radio-frequency (rf) circuit during an operando electrochemistry experiment. A highly shielded wire with low-pass filters was attached to the probe for electrochemical measurement, which could minimize the interferences between NMR and the electrochemistry circuit. Single-pulse with a π/2 pulse of 4 μs and recycle delay of 1.0 s was applied to acquire the 1D static spectrums. The electrochemical cell was simultaneously controlled by a Maccor battery testing system. A plastic capsule cell made out of polyether ether ketone (PEEK) was used

for operando NMR experiments. The cells were assembled using $LiFePO_4$ cathode (areal capacity is 2.0 mAh cm^{-2}) and Cu foils as working and counter electrodes with both a piece of Celgard and a piece of Glass fiber (Whatman GF/A) as separator. Before measurements, the assembled cells were rested for 2 h in glovebox. The operando capsule cell was aligned in an Ag-coated Cu coil with $LiFePO_4$ and Cu foil electrode were oriented perpendicular to B_0 and parallel with respect to the B_1 rf-field. During the static ^7Li NMR measurements the cells were cycled at current density of 1.0 mA cm^{-2}. During the charge and discharge process, NMR spectra were continuously acquired, each with a scan time of about three minutes. The chemical shift of ^7Li was referenced to 1.0 M aqueous solution of LiCl at 0 ppm. Bruker Topspin and Mestrenova software were used for data processing.

2

2.11 Supplementary information

Supplementary Notes

Supplementary Note S2.1

The quantification of the capacity loss is based on the method of Gunnarsdóttir et al[36]. The SEI formation capacity in the first cycle can be estimated from the dead Li by NMR and the Coulombic efficiency (*CE*) from the electrochemistry. The capacity loss (*CL*) in the first cycle is defined as:

$$CL = C_{\text{plating}} - C_{\text{stripping}} \tag{2.3}$$

The coulombic efficiency is calculated as follows:

$$CE = \frac{C_{\text{stripping}}}{C_{\text{plating}}} \tag{2.4}$$

where the C_{plating} is the full plating capacity (1mAh cm^{-2} in this work), assuming no side reactions.

Then the *CL* in the first cycle can be rewritten as:

$$CL = C_{\text{plating}} \times (1 - CE) \tag{2.5}$$

CL include the capacity loss from dead Li formation ($C_{\text{Dead Li}}$) and capacity loss from SEI formation (C_{SEI}) in electrochemical measurements as follows:

$$CL = C_{\text{Dead Li}} + C_{\text{SEI}} \tag{2.6}$$

$C_{\text{Dead Li}}$ is estimated by the following equation:

$$C_{\text{Dead Li}} = (C_{\text{Plating}} - C_{\text{SEI}}) \times \frac{I_{\text{stripping}}}{I_{\text{plating}}} \tag{2.7}$$

where $\frac{I_{\text{stripping}}}{I_{\text{plating}}}$ the ratio of the integrated intensity of the Li metal at the end of the 1$^{\text{st}}$ discharge to that measured at the end of the 1$^{\text{st}}$ charge. Therefore, *CL* can be calculated Equation 2.8, and the C_{SEI} and $C_{\text{Dead Li}}$ can be obtained.

$$CL = (C_{\text{Plating}} - C_{\text{SEI}}) \times \frac{I_{\text{stripping}}}{I_{\text{plating}}} + C_{\text{SEI}} \tag{2.8}$$

Supplementary Figures
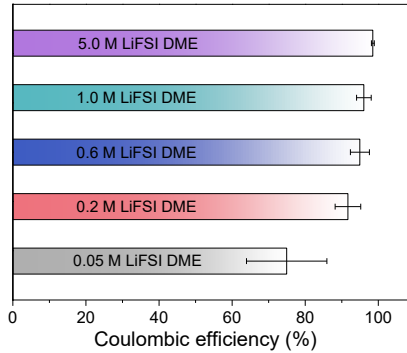
Fig. S2.1. **Average Coulombic efficiency (CE) of Li||Cu cells using different electrolytes for 100 cycles.** The cells were cycled at the current density of 0.5 mA cm^{-2} to an areal capacity of 1 mAh cm^{-2}.
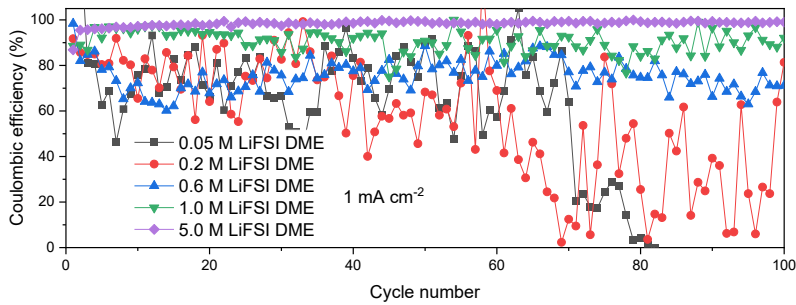
Fig. S2.2. **Cycling performance of Li||Cu cells with different electrolytes at a current density of 1 mA cm^{-2} to an areal capacity of 1 mAh cm^{-2}.**
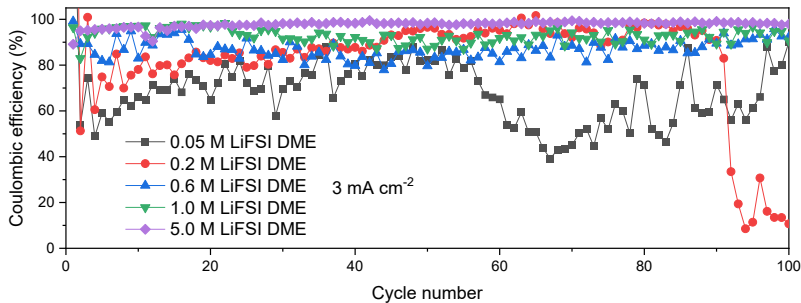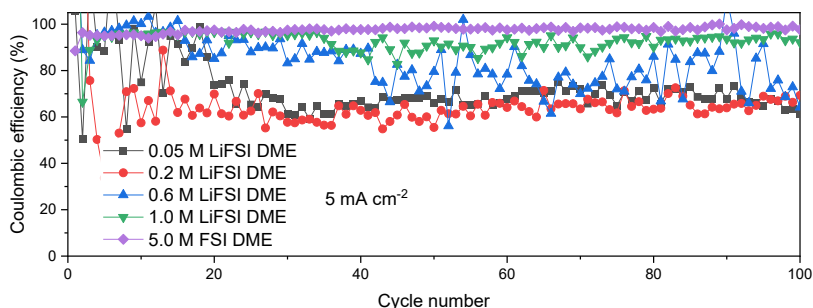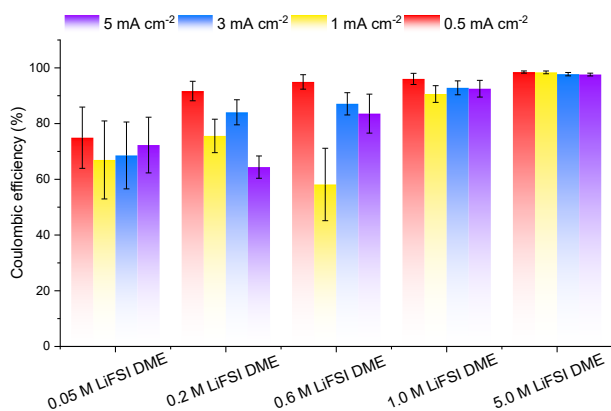

Fig. S2.3. **Cycling performance of Li||Cu cells with different electrolytes at a current density of 3 mA cm^{-2} to an areal capacity of 1 mAh cm^{-2}.**

Fig. S2.4. **Cycling performance of Li∥Cu cells with different electrolytes at a current density of 5 mA cm⁻² to an areal capacity of 1 mAh cm⁻².**

2

Fig. S2.5. **Average CE of Li∥Cu cells during 100 cycles under various current densities.** Li∥Cu cells using five different concentrations of LiFSI DME electrolytes were tested for 100 cycles at four cycling rates. In all cases, Li was plated on Cu current collector to a capacity of 1mAh cm⁻².
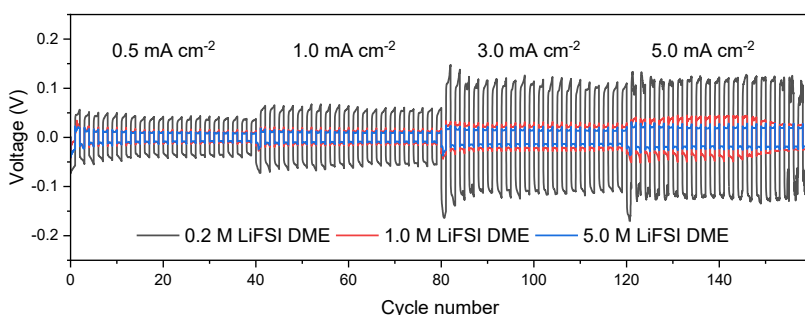
Fig. S2.6. **Voltage profile of Li∥Li symmetric cells at different current densities from 0.5 mA cm⁻² to 5 mA cm⁻².**
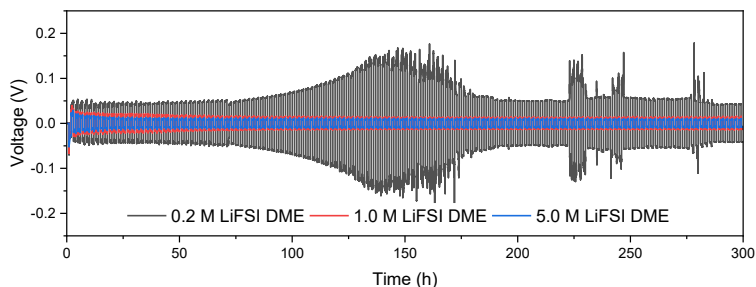
Fig. S2.7. **Galvanostatic cycling performance of Li||Li symmetrical cells at a current density of 1.0 mA cm^{-2} for 1 h.**
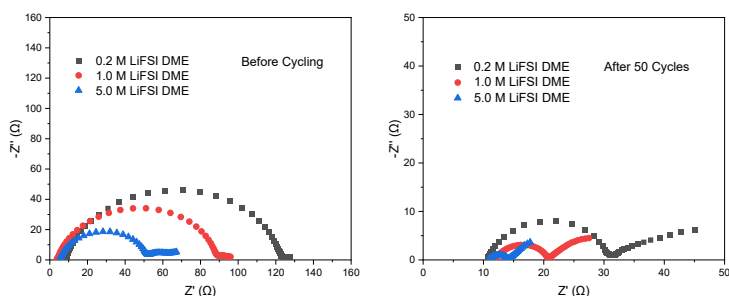
Fig. S2.8. **Electrochemical impedance spectroscopy (EIS) of Li||Li symmetric cells.** Nyquist plots are obtained from the Li||Li symmetric cells using different electrolytes before (left) and after 50 cycles at the current density of 1.0 mA cm^{-2} (right).
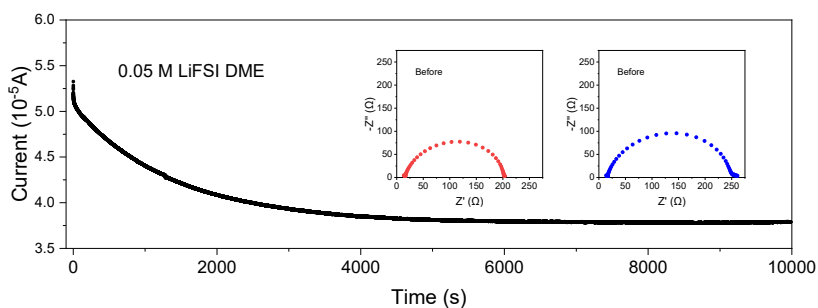
Fig. S2.9. **The chronoamperometry profile of a Li||Li symmetric cell using a 0.05 M LiFSI DME electrolyte under a polarization potential of 10 mV.** Inserts are the corresponding EIS plots before and after polarization, showing the initial and steady-state values of resistance, respectively.
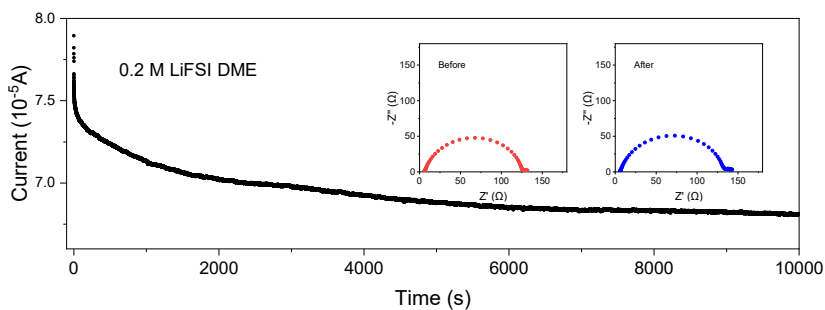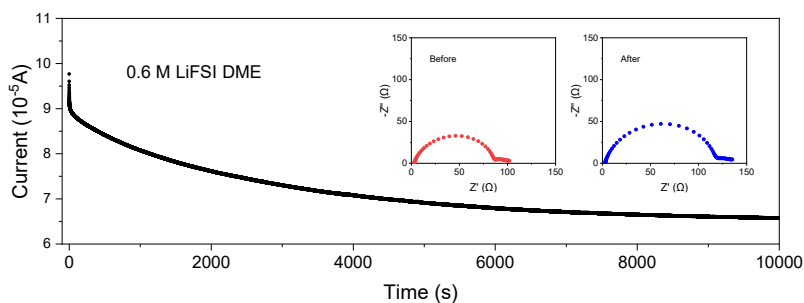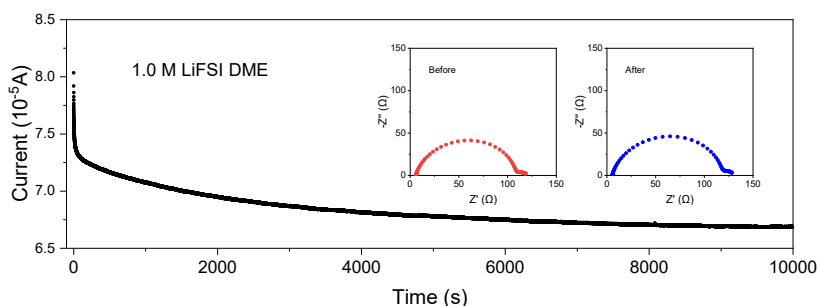
Fig. S2.10. **The chronoamperometry profile of a Li‖Li symmetric cell using a 0.2 M LiFSI DME electrolyte under a polarization potential of 10 mV.** Inserts are the corresponding EIS plots before and after polarization, showing the initial and steady-state values of resistance, respectively.

Fig. S2.11. **The chronoamperometry profile of a Li‖Li symmetric cell using a 0.6 M LiFSI DME electrolyte.** Inserts are the corresponding EIS plots before and after polarization, showing the initial and steady-state values of resistance, respectively.
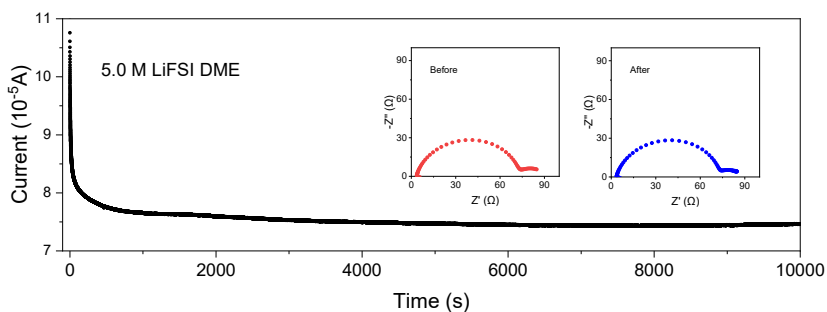

Fig. S2.12. **The chronoamperometry profile of a Li‖Li symmetric cell using a 1.0 M LiFSI DME electrolyte.** Inserts are the corresponding EIS plots before and after polarization, showing the initial and steady-state values of resistance, respectively.
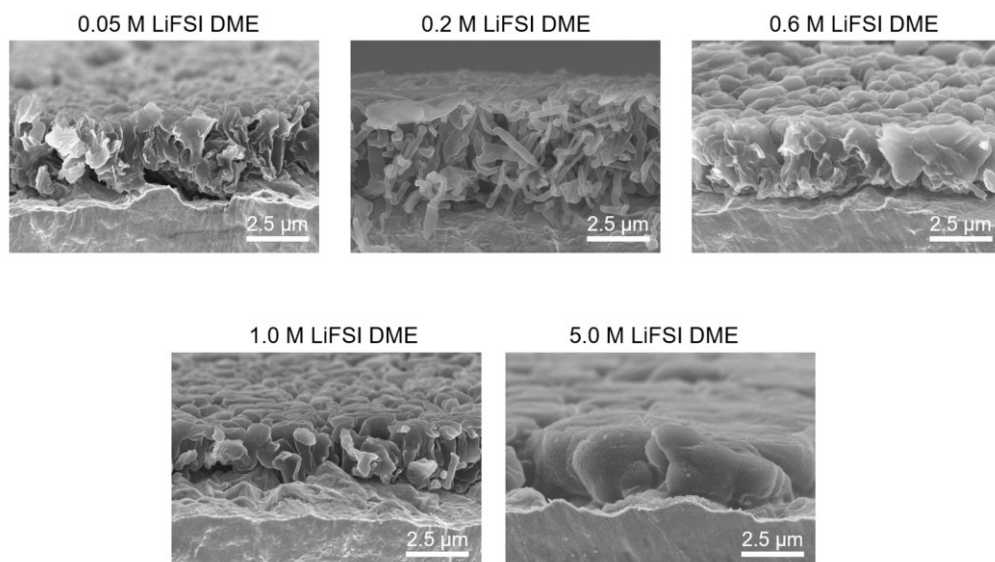
Fig. S2.13. **The chronoamperometry profile of a Li‖Li symmetric cell using a 5.0 M LiFSI DME electrolyte under a polarization potential of 10 mV.** Inserts are the corresponding EIS plots before and after polarization, showing the initial and steady-state values of resistance, respectively.

2

Fig. S2.14. **Cross-sectional SEM images of Li metal microstructures on Cu current collector.** The current density for Li plating is 0.5 mA cm^{-2} and the deposition capacity is 1 mAh cm^{-2}.
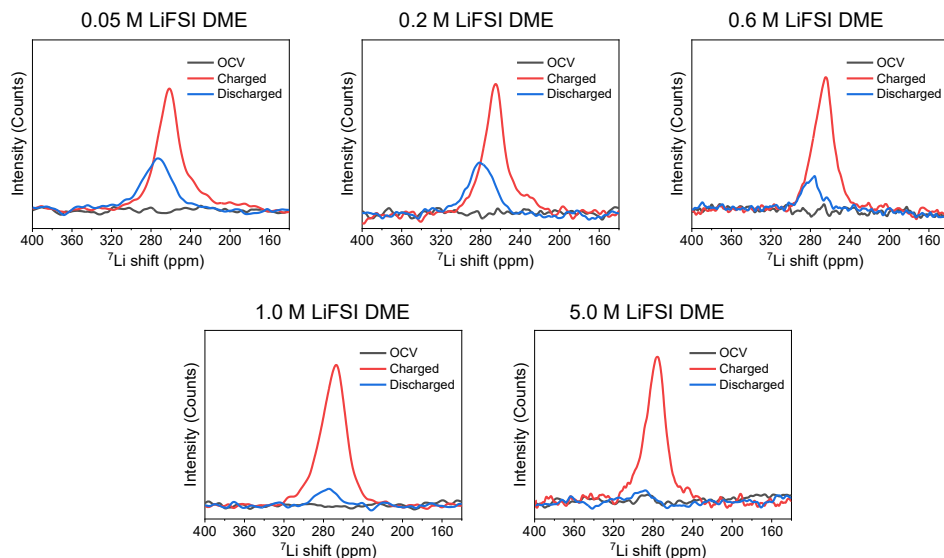
Fig. S2.15. **The spectra extracted from operando ^{7}Li NMR dataset.** Comparison of the Li-metal resonance in the ^{7}Li NMR spectra from the Cu‖LiFePO$_4$ cells before (pristine) and after Li plating (charged), and after Li stripping (discharged).
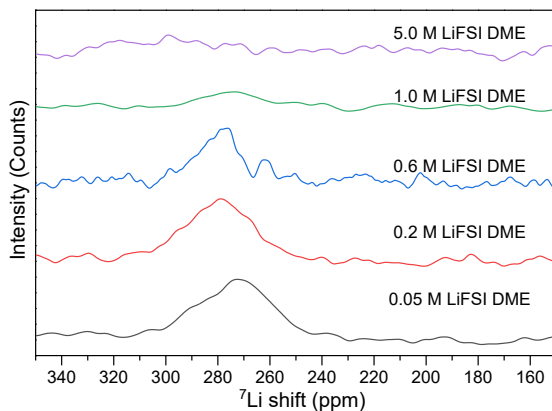

Fig. S2.16. **^{7}Li NMR spectra showing "dead" Li formed in different electrolytes.** The ^{7}Li NMR spectra showing the "dead" Li amount based on the difference between the discharged state and the pristine state in each concentration electrolyte.
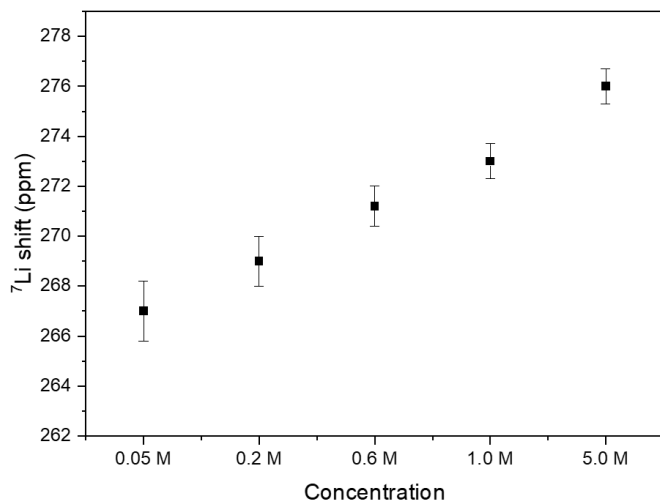
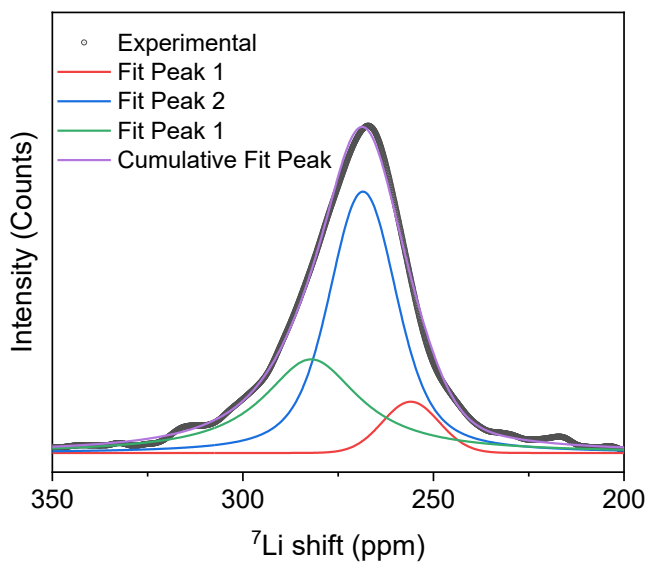**Fig. S2.17**. Initial ^{7}Li chemical shift as the function of electrolyte molarity.

Fig. S2.18. **The example of the fitted spectra of ^{7}Li NMR at the end of Li plating in the first cycle.** The peaks 1, 2 and 3 are indicated with different colors.
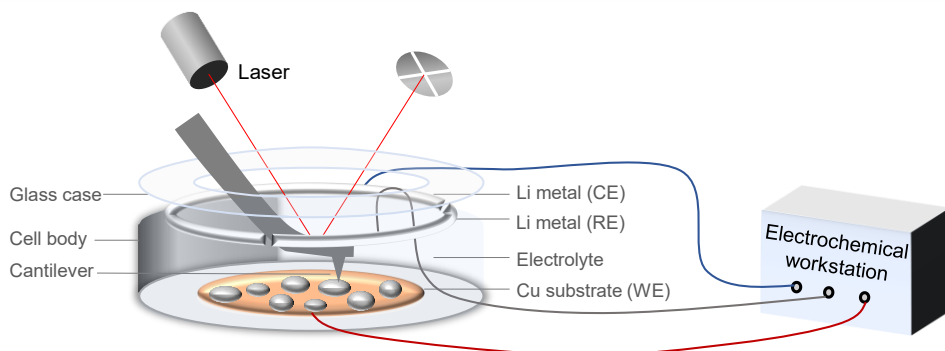
Fig. S2.19. **Schematic illustration of the setup for in-situ electrochemical AFM.** A three-electrode cell is assembled in an argon-filled glove box with a Cu foil as the working electrode (WE) and Li metal strips as both counter electrodes (CE) and reference electrodes (RE). The discharging (Li plating) process is controlled by an electrochemical workstation (CHI760E) outside of the glovebox.
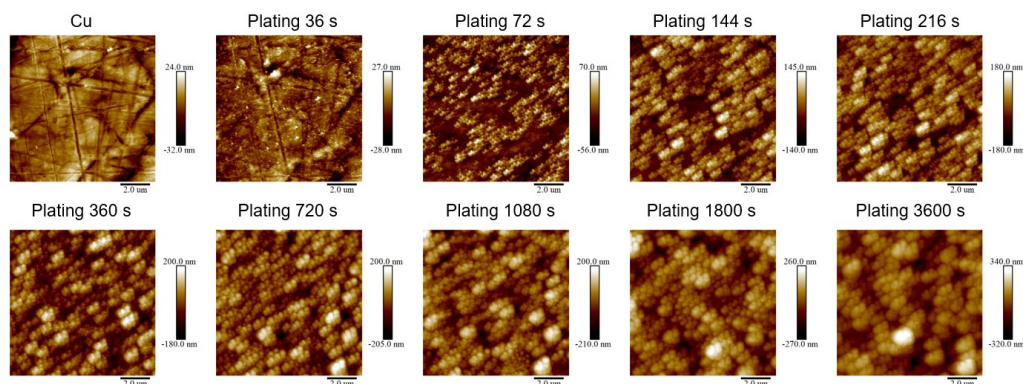

Fig. S2.20. **The in-situ electrochemical AFM images of Li metal deposited on Cu substrate in 0.2 M LiFSI DME electrolyte.**
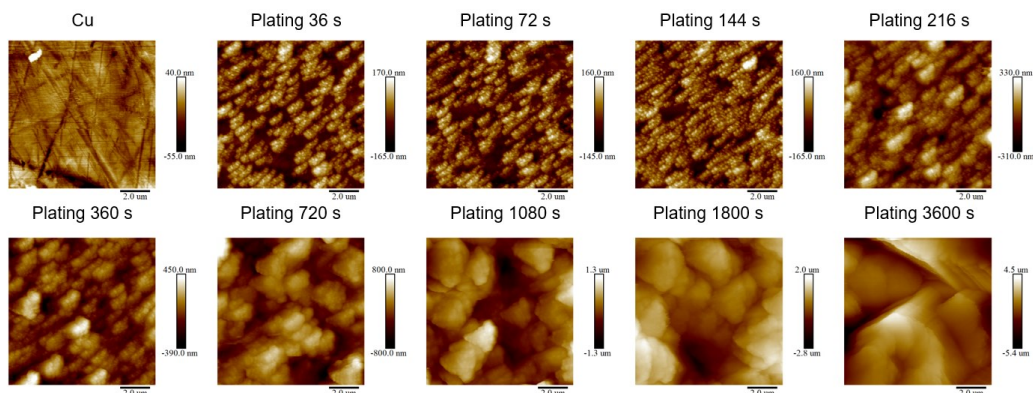
Fig. S2.21. **The in-situ electrochemical AFM images of Li metal deposited on Cu substrate in 1.0 M LiFSI DME electrolyte.**
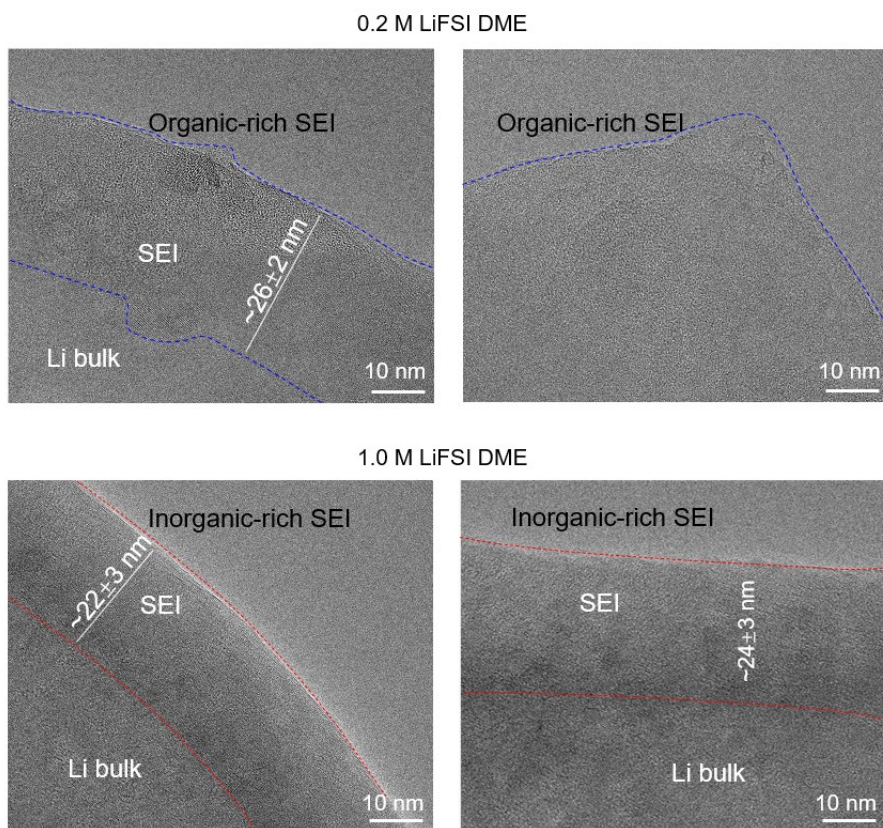
Fig. S2.22. **High-resolution cryo-TEM images of the SEI layer on deposited Li metal in 0.2 M LiFSI DME and 1.0 M LiFSI DME electrolyte.**
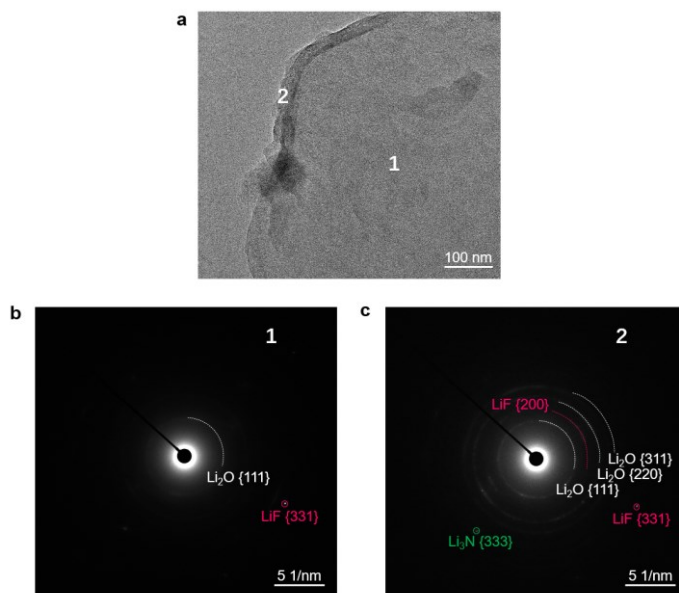
Fig. S2.23. **The selected-area electron diffraction (SAED) patterns of plated Li metal in 0.2 M LiFSI DME electrolyte. a,** High-resolution cryo-TEM image of the SEI layer on plated Li metal. **b**,**c**, The corresponding SAED patterns of (**b**) the bulk Li and (**c**) the solid electrolyte interface (SEI) as marked in **a**.

Fig. S2.24. Electron energy loss spectroscopy (EELS) mapping showing the elemental distribution on plated Li metal in a 0.2 M LiFSI DME electrolyte. Representative cryo-STEM ADF image of plated Li metal (top left panel) and corresponding EELS mapping collected on the *K*-edge reveals carbon, oxygen, nitrogen, fluorine and sulfur components.
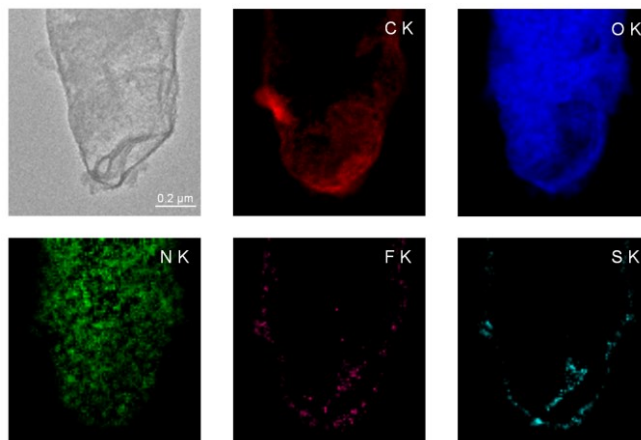
Fig. S2.25. The SAED pattern of plated Li metal in 1.0 M LiFSI DME electrolyte. a, High-resolution cryo-TEM image of the SEI layer on plated Li metal. **b,c**, The corresponding SAED pattern of (**b**) the bulk Li and (**c**) the SEI as marked in **a**.
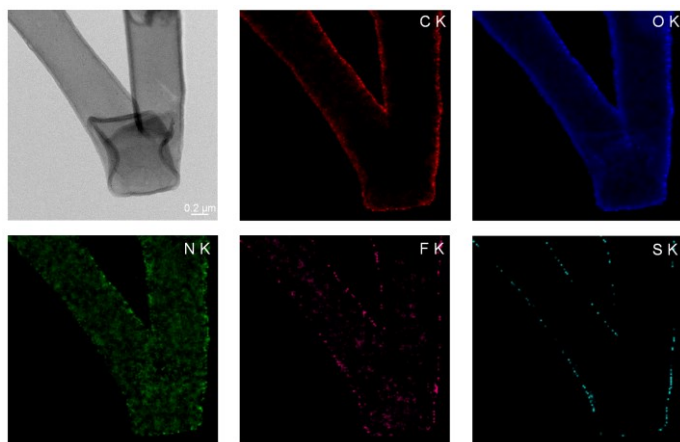
Fig. S2.26. EELS mapping showing the elemental distribution on plated Li metal in a 1.0 M LiFSI DME electrolyte. Representative cryo-STEM ADF image of the deposited Li metal (top left) and corresponding EELS mapping on the *K*-edge reveals carbon, oxygen, nitrogen, fluorine and sulfur components.

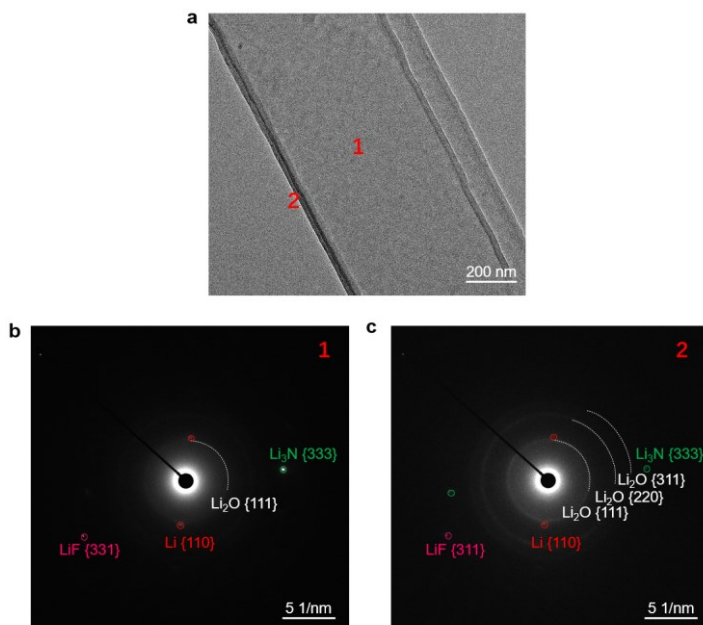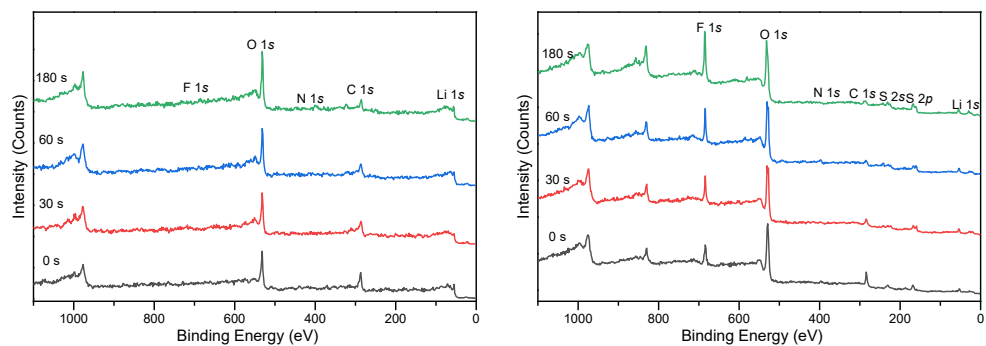**Fig. S2.27. The survey spectra of XPS depth profiles in 0.2 M LiFSI DME (left) and 1.0 M LiFSI DME (right) electrolytes.**
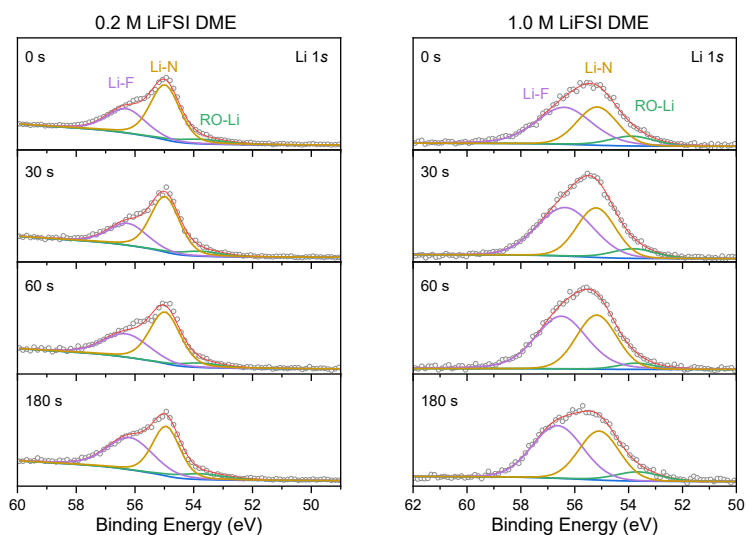
Fig. S2.28. Li 1s XPS depth profiles of the SEI formed in a 0.2 M LiFSI DME (left) and a 1.0 M LiFSI DME (right) electrolyte.
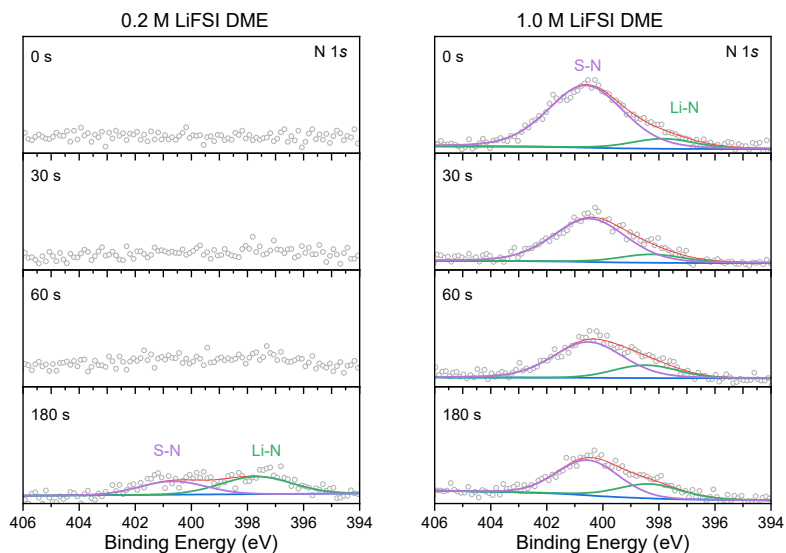
Fig. S2.29. N 1*s* XPS depth profiles of the SEI formed in a 0.2 M LiFSI DME (left) and a 1.0 M LiFSI DME (right) electrolyte.
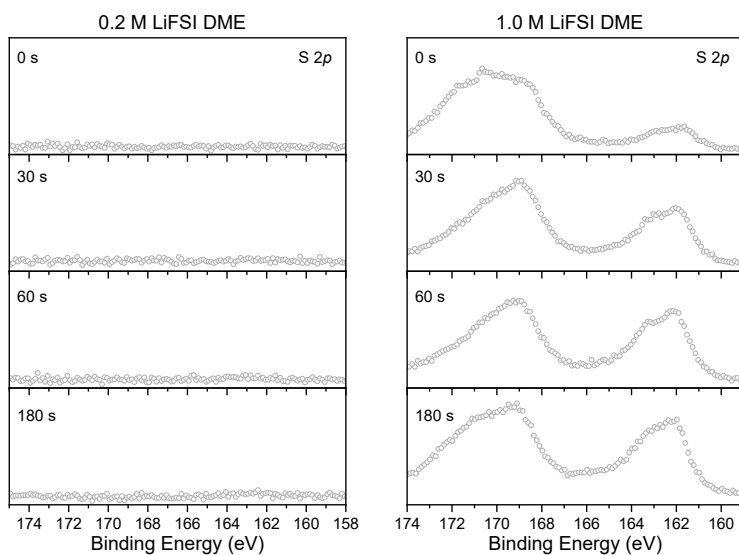
Fig. S2.30. S 2*p* XPS depth profiles of the SEI formed in a 0.2 M LiFSI DME (left) and a 1.0 M LiFSI DME (right) electrolyte.
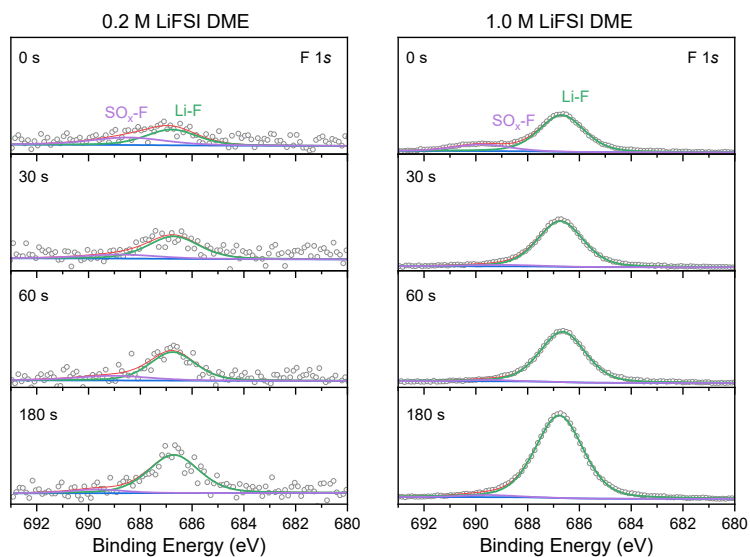
Fig. S2.31. F 1*s* XPS depth profiles of the SEI formed in a 0.2 M LiFSI DME (left) and a 1.0 M LiFSI DME (right) electrolyte.
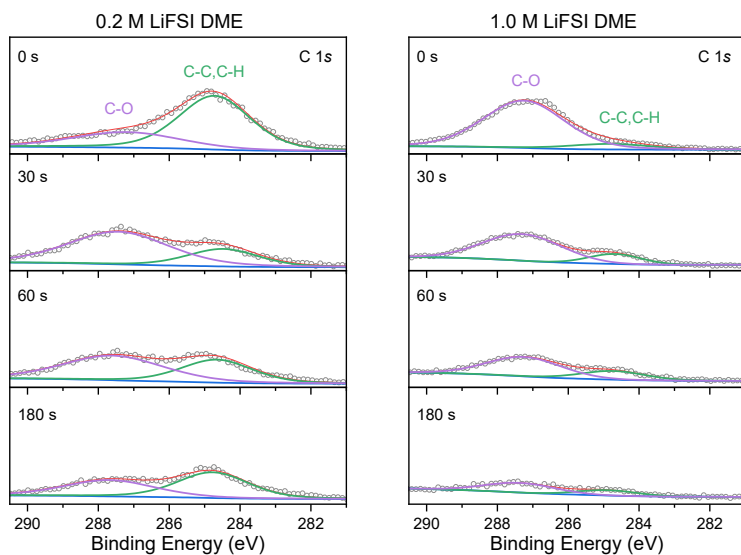
Fig. S2.32. C 1*s* XPS depth profiles of the SEI formed in a 0.2 M LiFSI DME (left) and a 1.0 M LiFSI DME (right) electrolyte.
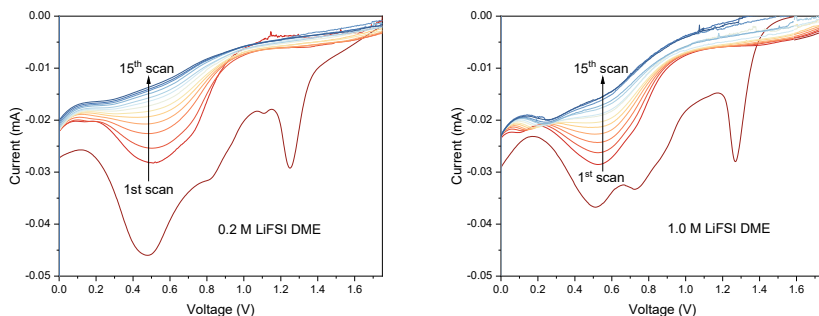
Fig. S2.33. Zoomed-in CV plot of Li plating/stripping in different electrolytes for fifteen cycles with a scan rate of 0.8 mV s⁻¹.
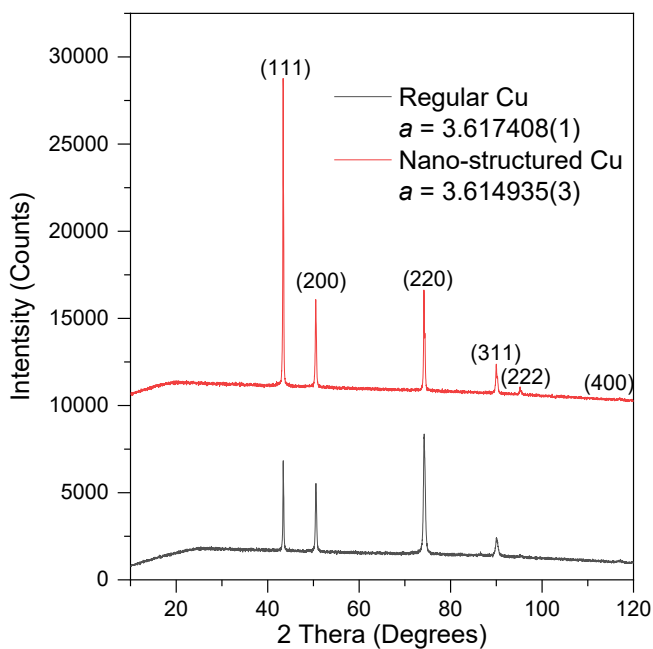
Fig. S2.34. X-ray diffraction patterns of two kinds of Cu foil used in this work. The peaks observed were compared with the standard powder diffraction file of No. 04-0838. Both patterns are indexed in the cubic structure, where the lattice parameters of the Cu foils are almost consistent, but the (111) peak of the nano-structured Cu shows increased intensity.
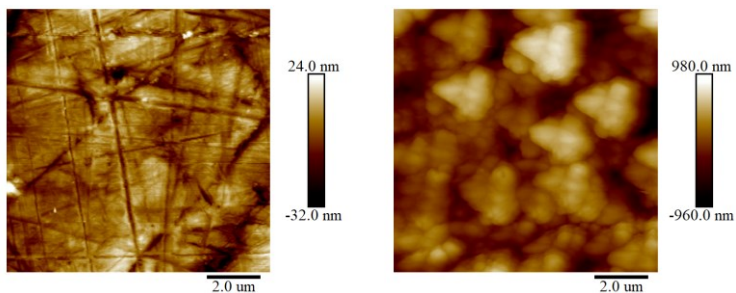
Fig. S2.35. AFM images of the topography of the regular Cu (left) and nano-structured Cu (right) in an area of 10 × 10 μm.
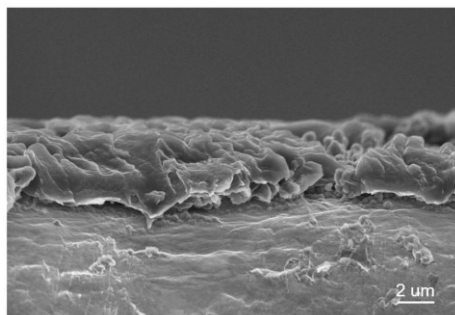
Fig. S2.36. Cross-sectional SEM image of Li deposition on nano-structured Cu foil in a 1.0 M LiFSI DME electrolyte at the current density of 0.5 mA cm^{-2} to an areal capacity of 1 mAh cm^{-2}.
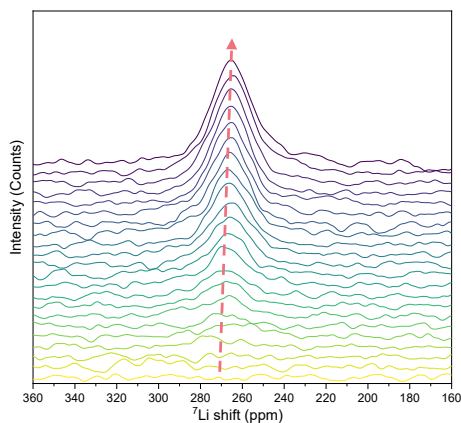
Fig. S2.37. Stacking plot of operando ^{7}Li NMR spectra during charging of a Cu|| LiFePO$_4$ cell with nano-structured Cu foil in a 1.0 M LiFSI DME electrolyte.
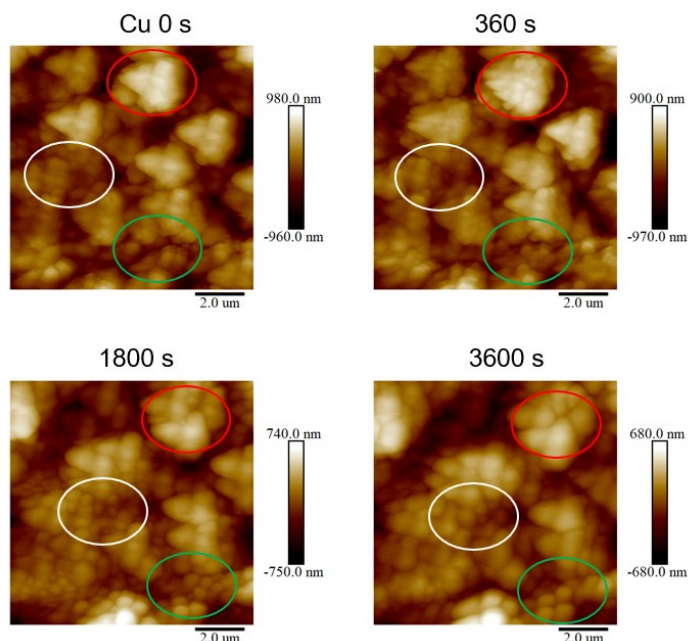
Fig. S2.38. The in-situ electrochemical AFM images of the Cu substrate topography before and after Li plating at 0.5 mA cm^{-2} for 360 s (0.05 mAh cm^{-2}), 1800 s (0.25 mAh cm^{-2}) and 1800 s (0.5 mAh cm^{-2}) on nano-structured Cu foil in 1.0 M LiFSI DME electrolyte. The colored circles with the same size indicate the tomography evolution with different amount of Li metal plating compared to the bare Cu. After plating 360 s, new particles can be observed compared with the bare Cu, which is ascribed to the Li deposits. With the capacity of deposited Li increases, some particle coalesced and grow larger.
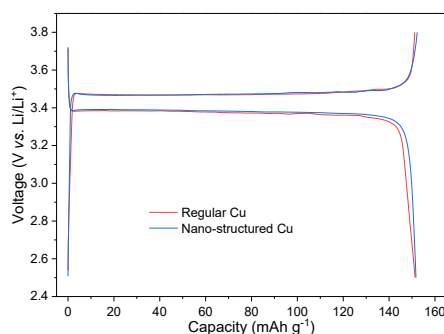
Fig. S2.39. Charge and discharge curves of Cu‖LiFePO$_4$ batteries cycled at 1/3C in a 1.0 M LiFSI DME electrolyte with different Cu foils. The areal capacity of LiFePO$_4$ cathode is 2 mAh cm^{-2}. The regular or nano-structured Cu current collector were used to assemble Cu‖LiFePO$_4$ after pre-deposit Li of 0.5 times the capacity of cathode electrodes.

Supplementary Tables

Table S2.1. Electrochemical and physical properties for LiFSI-DME electrolytes at room temperature.

Molarity of LiFSI in DME (mol L^{-1})	Conductivity (mS cm^{-1})	t_{Li^+}	Viscosity (mPa·s)
0.05	~1.6	0.08±0.03	0.42
0.2	~3.2	0.27±0.05	0.57
0.6	~9.6	0.39±0.03	0.89
1.0	~16.1	0.57±0.04	1.36
5.0	~1.9	0.31±0.05	20.24

2

Table S2.2. Coulombic efficiency, SEI and "dead" Li portion in the first cycle determined by the combination of electrochemical test and operando NMR.

Molarity of LiFSI in DME (mol L^{-1})	Coulombic efficiency (%)	SEI formation capacity (%)	"Dead" Li capacity (%)
0.05	40.3±2.2	16.9±1.3	42.8±2.3
0.2	45.3±1.8	13.7±1.1	41.0±1.9
0.6	66.6±1.6	10.8±1.0	22.5±1.2
1.0	77.7±1.3	9.0±0.9	13.1±0.9
5.0	88.5±1	8.2±0.5	3.3±0.3

References

1   J. M. Tarascon & M. Armand. Issues and challenges facing rechargeable lithium batteries. *Nature* **414**, 359-367, (2001).

2   M. S. Whittingham. Lithium Batteries and Cathode Materials. *Chemical Reviews* **104**, 4271-4302, (2004).

3   D. Lin, Y. Liu & Y. Cui. Reviving the lithium metal anode for high-energy batteries. *Nature Nanotechnology* **12**, 194-206, (2017).

4   M. Armand & J. M. Tarascon. Building better batteries. *Nature* **451**, 652-657, (2008).

5   I. Yoshimatsu, T. Hirai & J. i. Yamaki. Lithium Electrode Morphology during Cycling in Lithium Cells. *Journal of The Electrochemical Society* **135**, 2422-2427, (1988).

6   P. G. Bruce, L. J. Hardwick & K. M. Abraham. Lithium-air and lithium-sulfur batteries. *MRS Bulletin* **36**, 506-512, (2011).

7   J. Liu, Z. Bao, Y. Cui, E. J. Dufek, J. B. Goodenough, P. Khalifah, Q. Li, B. Y. Liaw, P. Liu, A. Manthiram, Y. S. Meng, V. R. Subramanian, M. F. Toney, V. V. Viswanathan, M. S. Whittingham, J. Xiao, W. Xu, J. Yang, X.-Q. Yang & J.-G. Zhang. Pathways for practical high-energy long-cycling lithium metal batteries. *Nature Energy* **4**, 180-186, (2019).

8   X. B. Cheng, R. Zhang, C. Z. Zhao, F. Wei, J. G. Zhang & Q. Zhang. A review of solid electrolyte interphases on lithium metal anode. *Advanced science* **3**, 1500213, (2016).

9   X.-B. Cheng, R. Zhang, C.-Z. Zhao & Q. Zhang. Toward Safe Lithium Metal Anode in Rechargeable Batteries: A Review. *Chemical Reviews* **117**, 10403-10473, (2017).

10 N. R. Geise, R. M. Kasse, J. Nelson Weker, H.-G. Steinrück & M. F. Toney. Quantification of Efficiency in Lithium Metal Negative Electrodes via Operando X-ray Diffraction. *Chemistry of Materials* **33**, 7537-7545, (2021).

11 A. J. Louli, M. Genovese, R. Weber, S. Hames, E. Logan & J. Dahn. Exploring the impact of mechanical pressure on the performance of anode-free lithium metal cells. *Journal of The Electrochemical Society* **166**, A1291, (2019).

12 R. Weber, M. Genovese, A. J. Louli, S. Hames, C. Martin, I. G. Hill & J. R. Dahn. Long cycle life and dendrite-free lithium morphology in anode-free lithium pouch cells enabled by a dual-salt liquid electrolyte. *Nature Energy* **4**, 683-689, (2019).

13 C. Fang, B. Lu, G. Pawar, M. Zhang, D. Cheng, S. Chen, M. Ceja, J.-M. Doux, H. Musrock, M. Cai, B. Liaw & Y. S. Meng. Pressure-tailored lithium deposition and dissolution in lithium metal batteries. *Nature Energy* **6**, 987-994, (2021).

2

14   R. M. Kasse, N. R. Geise, E. Sebti, K. Lim, C. J. Takacs, C. Cao, H.-G. Steinrück & M. F. Toney. Combined Effects of Uniform Applied Pressure and Electrolyte Additives in Lithium-Metal Batteries. *ACS Applied Energy Materials* **5**, 8273-8281, (2022).

15   J. Wang, W. Huang, A. Pei, Y. Li, F. Shi, X. Yu & Y. Cui. Improving cyclability of Li metal batteries at elevated temperatures and its origin revealed by cryo-electron microscopy. *Nature Energy* **4**, 664-670, (2019).

16   Q. Shi, Y. Zhong, M. Wu, H. Wang & H. Wang. High-capacity rechargeable batteries based on deeply cyclable lithium metal anodes. *Proceedings of the National Academy of Sciences* **115**, 5676-5680, (2018).

17   R. Mogi, M. Inaba, Y. Iriyama, T. Abe & Z. Ogumi. In Situ Atomic Force Microscopy Study on Lithium Deposition on Nickel Substrates at Elevated Temperatures. *Journal of The Electrochemical Society* **149**, A385, (2002).

18   Y. Guo, D. Li, R. Xiong & H. Li. Investigation of the temperature-dependent behaviours of Li metal anode. *Chemical Communications* **55**, 9773-9776, (2019).

19   K. Xu. Electrolytes and Interphases in Li-Ion Batteries and Beyond. *Chemical Reviews* **114**, 11503-11618, (2014).

20   Z. Huang, G. Zhou, W. Lv, Y. Deng, Y. Zhang, C. Zhang, F. Kang & Q.-H. Yang. Seeding lithium seeds towards uniform lithium deposition for stable lithium metal anodes. *Nano Energy* **61**, 47-53, (2019).

21   J. Qian, W. A. Henderson, W. Xu, P. Bhattacharya, M. Engelhard, O. Borodin & J.-G. Zhang. High rate and stable cycling of lithium metal anode. *Nature Communications* **6**, 6362, (2015).

22   Z. Zeng, V. Murugesan, K. S. Han, X. Jiang, Y. Cao, L. Xiao, X. Ai, H. Yang, J.-G. Zhang, M. L. Sushko & J. Liu. Non-flammable electrolytes with high salt-to-solvent ratios for Li-ion and Li-metal batteries. *Nature Energy* **3**, 674-681, (2018).

23   L. Suo, W. Xue, M. Gobet, S. G. Greenbaum, C. Wang, Y. Chen, W. Yang, Y. Li & J. Li. Fluorine-donating electrolytes enable highly reversible 5-V-class Li metal batteries. *Proceedings of the National Academy of Sciences* **115**, 1156, (2018).

24   Q. Pang, A. Shyamsunder, B. Narayanan, C. Y. Kwok, L. A. Curtiss & L. F. Nazar. Tuning the electrolyte network structure to invoke quasi-solid state sulfur conversion and suppress lithium dendrite formation in Li–S batteries. *Nature Energy* **3**, 783-791, (2018).

25   Z. Yu, H. Wang, X. Kong, W. Huang, Y. Tsao, D. G. Mackanic, K. Wang, X. Wang, W. Huang, S. Choudhury, Y. Zheng, C. V. Amanchukwu, S. T. Hung, Y. Ma, E. G. Lomeli, J. Qin, Y. Cui

2

& Z. Bao. Molecular design for electrolyte solvents enabling energy-dense and long-cycling lithium metal batteries. *Nature Energy* **5**, 526-533, (2020).

26 X. Fan, L. Chen, O. Borodin, X. Ji, J. Chen, S. Hou, T. Deng, J. Zheng, C. Yang, S.-C. Liou, K. Amine, K. Xu & C. Wang. Non-flammable electrolyte enables Li-metal batteries with aggressive cathode chemistries. *Nature Nanotechnology* **13**, 715-722, (2018).

27 R. M. Kasse, N. R. Geise, J. S. Ko, J. Nelson Weker, H.-G. Steinrück & M. F. Toney. Understanding additive controlled lithium morphology in lithium metal batteries. *Journal of Materials Chemistry A* **8**, 16960-16972, (2020).

28 D. Hong, Y. Choi, J. Ryu, J. Mun, W. Choi, M. Park, Y. Lee, N.-S. Choi, G. Lee, B.-S. Kim & S. Park. Homogeneous Li deposition through the control of carbon dot-assisted Li-dendrite morphology for high-performance Li-metal batteries. *Journal of Materials Chemistry A* **7**, 20325-20334, (2019).

29 K. M. Abraham, Z. Jiang & B. Carroll. Highly Conductive PEO-like Polymer Electrolytes. *Chemistry of Materials* **9**, 1978-1988, (1997).

30 H. J. Chang, A. J. Ilott, N. M. Trease, M. Mohammadi, A. Jerschow & C. P. Grey. Correlating Microstructural Lithium Metal Growth with Electrolyte Salt Depletion in Lithium Batteries Using 7Li MRI. *Journal of the American Chemical Society* **137**, 15209-15216, (2015).

31 R. Bhattacharyya, B. Key, H. Chen, A. S. Best, A. F. Hollenkamp & C. P. Grey. In situ NMR observation of the formation of metallic lithium microstructures in lithium batteries. *Nature Materials* **9**, 504-510, (2010).

32 H. J. Chang, N. M. Trease, A. J. Ilott, D. Zeng, L.-S. Du, A. Jerschow & C. P. Grey. Investigating Li Microstructure Formation on Li Anodes for Lithium Batteries by in Situ 6Li/7Li NMR and SEM. *The Journal of Physical Chemistry C* **119**, 16443-16451, (2015).

33 S. Chandrashekar, N. M. Trease, H. J. Chang, L.-S. Du, C. P. Grey & A. Jerschow. 7Li MRI of Li batteries reveals location of microstructural lithium. *Nature Materials* **11**, 311-315, (2012).

34 O. Pecher, P. M. Bayley, H. Liu, Z. Liu, N. M. Trease & C. P. Grey. Automatic Tuning Matching Cycler (ATMC) in situ NMR spectroscopy as a novel approach for real-time investigations of Li- and Na-ion batteries. *Journal of Magnetic Resonance* **265**, 200-209, (2016).

35 Y. Xiang, M. Tao, G. Zhong, Z. Liang, G. Zheng, X. Huang, X. Liu, Y. Jin, N. Xu, M. Armand, J.-G. Zhang, K. Xu, R. Fu & Y. Yang. Quantitatively analyzing the failure processes of rechargeable Li metal batteries. *Science advances* **7**, eabj3423, (2021).

2

36 A. B. Gunnarsdóttir, C. V. Amanchukwu, S. Menkin & C. P. Grey. Noninvasive In Situ NMR Study of "Dead Lithium" Formation and Lithium Corrosion in Full-Cell Lithium Metal Batteries. *Journal of the American Chemical Society* **142**, 20814-20827, (2020).

37 J. Xiao. How lithium dendrites form in liquid batteries. *Science* **366**, 426-427, (2019).

38 E. Peled, D. Golodnitsky & G. Ardel. Advanced model for solid electrolyte interphase electrodes in liquid and polymer electrolytes. *Journal of the Electrochemical Society* **144**, L208, (1997).

39 Y. Li, Y. Li, A. Pei, K. Yan, Y. Sun, C.-L. Wu, L.-M. Joubert, R. Chin, A. L. Koh, Y. Yu, J. Perrino, B. Butz, S. Chu & Y. Cui. Atomic structure of sensitive battery materials and interfaces revealed by cryo–electron microscopy. *Science* **358**, 506-510, (2017).

40 Y. Yamada, J. Wang, S. Ko, E. Watanabe & A. Yamada. Advances and issues in developing salt-concentrated battery electrolytes. *Nature Energy* **4**, 269-280, (2019).

41 D. Rehnlund, C. Ihrfors, J. Maibach & L. Nyholm. Dendrite-free lithium electrode cycling via controlled nucleation in low LiPF6 concentration electrolytes. *Materials Today* **21**, 1010-1018, (2018).

42 H. Yang, E. O. Fey, B. D. Trimm, N. Dimitrov & M. S. Whittingham. Effects of pulse plating on lithium electrodeposition, morphology and cycling efficiency. *Journal of Power Sources* **272**, 900-908, (2014).

43 Y. Liu, B. Li, J. Liu, S. Li & S. Yang. Pre-planted nucleation seeds for rechargeable metallic lithium anodes. *Journal of Materials Chemistry A* **5**, 18862-18869, (2017).

44 A. B. Gunnarsdóttir, S. Vema, S. Menkin, L. E. Marbella & C. P. Grey. Investigating the effect of a fluoroethylene carbonate additive on lithium deposition and the solid electrolyte interphase in lithium metal batteries using in situ NMR spectroscopy. *Journal of Materials Chemistry A* **8**, 14975-14992, (2020).

2

3. High entropy liquid electrolytes for lithium batteries

Abstract

High-entropy alloys/compounds have large configurational entropy by introducing multiple components, showing improved functional properties that exceed those of conventional materials. However, how increasing entropy impacts the thermodynamic/kinetic properties in liquids that are ambiguous. Here we show this strategy in liquid electrolytes for rechargeable lithium (Li) batteries, demonstrating the substantial impact of raising the entropy of electrolytes by introducing multiple salts. Unlike all liquid electrolytes so far reported, the participation of several anionic groups in this electrolyte induces a larger diversity in solvation structures, unexpectedly decreasing solvation strengths between Li ions and solvents/anions, facilitating Li-ion diffusivity and the formation of stable interphase passivation layers. In comparison to the single-salt electrolytes, a low-concentration dimethyl ether electrolyte with four salts shows an enhanced cycling stability and rate capability. These findings, rationalized by the fundamental relationship between entropy-dominated solvation structures and ion transport, brings forward high-entropy electrolytes as a composition-rich and unexplored materials for Li batteries and beyond.

3

3.1 Introduction

High-entropy (HE) alloys have attracted significant attention in the fields of materials science and engineering since the introduction from 2004[1,2], because of their potentially desirable properties[3-6]. Several structural, thermodynamic and dynamic principles have been proposed to demonstrate the special nature of such materials. Firstly, the presence of several principal elements, typically more than five, can promote the formation of solid-solution phases. On the other hand, the distortion of the local lattice due to the configurational disorder can lead to improved mechanical properties[4]. Another contributor to the improved functional properties of HE alloys is suggested to be the different diffusion kinetics[7], which however is subject to debate, as experimental studies are rare and complex, and the state of knowledge is still far from complete[8,9].

A new research direction within the class of HE materials is liquid electrolyte solutions, which function as an ion conducting membrane between battery electrodes[10,11]. However, the basic properties of HE electrolytes are unexplored to date. This motivates investigation as to how the main electrolyte functional properties are impacted, including redox stability, ion conductivity, charge transfer and solid electrolyte interphase (SEI) formation. An important aspect herein is to determine whether the changes in electrolyte behaviour can be ascribed to the larger entropy associated with the presence of multiple principal components, or to the properties of the principle chemical components themselves. By combining multiple salts with a single solvent or/and a single salt with multiple solvents, a more complex and diverse solvation structure is expected to form, which is due to the diversity of local interactions between solvents, Li-ion and anionic groups[10]. Such complex solvation structure could influence redox stability, charge transfer and the SEI composition and structure (Fig. 3.1a). These properties determine to a large extent the battery performance parameters such as cycle life and rate performance[12,13]. How entropy impacts the dynamic properties such as diffusivity and conductivity is an intriguing aspect, as entropy is only formally related to the thermodynamic properties. However, for liquids, excess entropy scaling has been proposed and empirically demonstrated to be the relationship between the entropy of the system and its kinetic behaviour, suggesting that increasing the entropy can result in improved diffusivity[14,15],

which has never been explored for electrolytes. Due to the potential to be able to tune electrolyte properties through the entropy, and the lack of knowledge thereof, we embark on a systematic study of the properties of HE electrolytes and their impact on the relevant processes in Li batteries.

Differing from mixing solvents that is a common strategy to compensate deficiencies of the individual solvents, where extra functional solvents are introduced as additives to the corresponding functional properties[16-20]. In this work, we show a prototype HE electrolyte through combining 0.15 mol/L (M) lithium bis(fluorosulfonyl)imide (LiFSI), 0.15 M lithium bis(trifluoromethanesulfonyl)imide (LiTFSI), 0.15 M lithium difluoro(oxalato)borate (LiDFOB) and 0.15 M lithium nitrate (LiNO$_3$) in a single solvent of dimethoxyethane (DME) (Supplementary Note S3.1 and Fig. S3.1). This results in a 0.6 M HE-DME electrolyte, which is compared to each of the single salt electrolytes with the same 0.6 M concentration. Results show that more anionic groups can participate in the solvation structures (similar to highly concentrated electrolytes) in the low salt concentration electrolyte, however, the interactions of Li ions with both solvent and anionic groups are much weaker in this HE electrolyte, a direct result from the higher disorder, which is never found in any liquid electrolytes. The consequence is the formation of inorganic-rich and stable interphase layers on the electrodes, responsible for more stable cycling of high-voltage Li batteries. Additionally, the weaker solvation strength facilitates Li-ion mobility, resulting in substantial improvement in rate capability. This suggests that raising the entropy of mixing through introducing multiple salts in solvent provides a general strategy to tailor the functional properties for the development of electrolytes.

3.2 Characterization of the electrolytes and compatibility with anodes

The Li-ion solvation environment of the electrolytes is studied using nuclear magnetic resonance (NMR) spectroscopy (Fig. 3.1b, Figs. S3.2 and S3.3), where the chemical shift reflects the shielding of the Li-ions as a result of the solvation environment. The 0.6 M LiTFSI-DME, 0.6 M LiFSI-DME and 0.6 M LiDFOB-DME single-salt electrolytes result in more negative shifts of -1.19, -1.17 and -0.73 ppm, respectively. In this case the Li-ions thus experience relatively strong shielding due to a high electron density, indicating a

stronger solvation interaction with both solvent and anions. In contrast, a downfield shift for the 0.6 M HE-DME electrolyte is observed, at -0.68 ppm, demonstrating a relatively lower shielding of the Li-ions, which may promote Li-ion diffusivity based on a weaker solvation interaction[21].
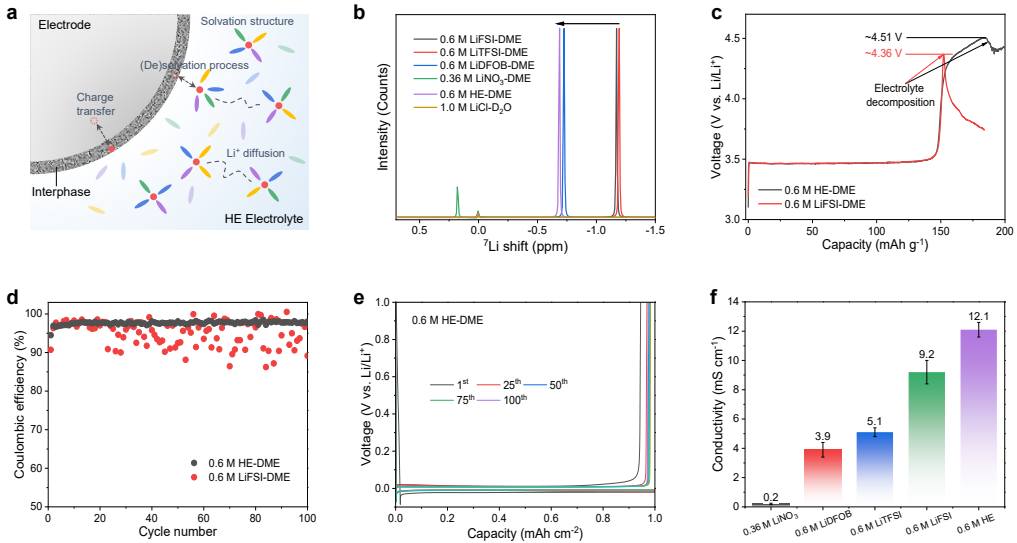

Fig. 3.1 Properties of the HE liquid electrolyte. a, Schematic of the HE electrolyte battery system. **b**, ^{7}Li NMR spectra of single-salt electrolytes and the as-prepared HE electrolyte. Due to the relatively low salt solubility of LiNO$_3$ in DME, a 0.36 M LiNO$_3$-DME electrolyte was prepared for comparison. **c**, Galvanostatic charge profiles of Li‖LiFePO$_4$ cells with different electrolytes at a current density of 0.02C. **d**, Li plating/stripping CE in Li‖Cu cells using 0.6 M LiFSI-DME and 0.6 M HE-DME electrolytes. **e**, Galvanostatic Li plating/stripping profiles of 0.6 M HE-DME electrolyte. **f**, Comparison of the Li-ion conductivity of different electrolytes.

The oxidation and reduction stability of the electrolytes with single salt and different salt combinations are evaluated (Figs. S3.4-S3.9 and Supplementary Note S3.2). Among the single-salt electrolytes, 0.6 M LiFSI-DME shows the best overall stability, therefore it is selected as the control group in the detailed study of the 0.6 M HE-DME electrolyte. The oxidative stability limit is evaluated using Li‖LiFePO$_4$ cells with a cut-off voltage of 5.0 V, making use of the absence of an oxidation reaction of LiFePO$_4$ above ~3.8 V (Fig. 3.1c). The 0.6 M HE-DME shows an oxidation stable potential up to ~4.51 V, higher than the single salt (4.36 V for 0.6 M LiFSI-DME), where the subsequent capacity increase is suggested to be from the formation of a cathode electrolyte interphase (CEI) on the surface

of the cathode. Under a polarization potential of 4.2 V vs. Li/Li$^+$, the 0.6 M HE-DME electrolyte presents a stable anodic current due to the suppressed corrosion of the aluminium foil, in contrast to the 0.6 M LiFSI-DME, which suffers from a rapid dissolution of the aluminium foil (Fig. S3.10). Also, the stability against reduction by Li-metal anode appears to be improved as Li‖Cu cells with the 0.6 M HE-DME exhibits stable Li metal plating/stripping voltage profiles with a Coulombic efficiency (CE) up to 98.6%, considerably higher than that of 0.6 M LiFSI-DME (Figs. 3.1d, 3.1e and Fig. S3.5). Symmetric Li‖Li cells, electrochemical impedance (EIS) and cyclic voltammetry (CV) measurements are performed (Figs. S3.11-S3.19 and Supplementary Note S3.3), all indicating the improved stability of the 0.6 M HE-DME electrolyte against the Li anode.

Measurement of the Li-ion transference number and conductivity of the 0.6 M HE-DME electrolyte (Fig. 3.1f, Fig. S3.20 and Table S3.1), result in 0.46 and ~12.1 mS cm^{-1}, respectively. This is higher than that measured for the 0.6 M LiFSI-DME electrolyte (0.39 and 9.6 mS cm^{-1}, respectively)[22]. The rate capability of the 0.6 M HE-DME electrolyte is investigated in Li‖Li$_4$Ti$_5$O$_{12}$ cells (Figs. S3.21 and S3.22), making use of the excellent Li$_4$Ti$_5$O$_{12}$ rate performance and medium working potential. When the rate is increased to 5.0C, the capacity retention of the 0.6 M LiFSI-DME electrolyte decreases to ~40 mAh g^{-1}, much lower than that of ~115 mAh g^{-1} in 0.6 M HE-DME electrolyte (Fig. S3.21). This improved rate performance can directly be related to the higher transference number and conductivity of the 0.6 M HE-DME electrolyte. It should be emphasized that the conductivity of the 0.6 M HE-DME electrolyte is higher than that of the electrolytes with individual salts, showing that the combination of salts results in a higher diffusivity.

3.3 Compatibility with cathodes

The oxidation stability of the 0.6 M HE-DME electrolyte is investigated in Li‖LiNi$_{0.8}$Co$_{0.1}$Mn$_{0.1}$O$_2$ (NCM811) cells (Fig. S3.23) in the voltage range of 2.8-4.3 V vs. Li/Li$^+$ with a cathode areal capacity of 2.0 mAh cm^{-2}. The upper cut-off voltage is challenging for the DME solvent because its relatively low oxidation stability. In combination with the 0.6 M LiFSI-DME electrolyte, Li‖NCM811 cells are not able to reach the cut-off voltage of 4.3 V at a current density of 0.1C (Fig. 3.2a), presumably

because the cathode results in undesired oxidation of the electrolyte, catalysed by the formed high-valence Ni species upon de-lithiation (charging)[23]. In comparison, the 0.6 M HE-DME electrolyte shows significantly improved reversible cycling when charged to 4.3 V, where two reproducible cells deliver similar charge/discharge profiles with a specific capacity of 182 mAh g^{-1} (Fig. 3.2b and Fig. S3.24). Li‖NCM811 cells with 0.6 M LiDFOB-DME, 0.6 M LiTFSI-DME and 0.36 M LiNO$_3$-DME electrolytes are also evaluated (Figs. S3.25-3.28). Cells with 0.6 M LiDFOB-DME electrolyte can charge to 4.3 V, resulting in approximately 20 cycles, followed by a rapid decay to ~30% of the initial capacity after 50 cycles (Figs. S3.25 and S3.28), similarly due to the continuous electrolyte and Li consumption[24] as observed in Li‖Cu cells. The 0.36 M LiNO$_3$-DME electrolyte does not support cycling at all (Fig. S3.27). The above results indicate that the 0.6 M HE-DME electrolyte improves the oxidation stability of the NCM811 cathode significantly.

3

The rate performance is evaluated in Li‖NCM811 cells (Figs. 3.2c, 3.2d and Fig. S3.29). When charged at 6.0C (1,080 mA g^{-1}), more than 60% capacity retention is achieved (Fig. 3.2d) while the corresponding charge/discharge curves remain comparable, reflecting stable cycling. Cycling performance tests of the 0.6 M HE-DME electrolyte in Li‖NCM811 cells are performed at 0.333C (Fig. 3.2e, Figs. S3.30 and S3.31), resulting in a capacity retention of over 82% after 100 cycles charged to 4.3 V. When the charged cut-off voltage is lowered to 4.2 V, an enhanced capacity retention of more than 90% is obtained, showing reduced reactions with DME. This is further demonstrated by the LiFePO$_4$ cathodes cycled at 2.5-3.8 V, resulting in a capacity retention of more than 95% after 500 cycles, which implies that a more stable interphase is formed with the 0.6 M HE-DME electrolyte compared to the 0.6 M LiFSI-DME electrolyte in the suitable voltage range (Fig. 3.2f and Fig. S3.32).

As an ultimate test of the power density and cycle life, long-term cycling of the 0.6 M HE-DME electrolyte at an aggressive rate of 6.0C in Li‖NCM811 cells was conducted (Fig. 3.2g, Figs. S3.29 and S3.33). A capacity retention of approximately 85% and 80% is achieved after 500 and 600 cycles, respectively. Increasing the cycling rate from 0.333C to 6.0C increases the CE from 99.3% to 99.8%, indicating that shorter exposure to the

high potentials reduces the interfacial reactions of DME to some extent. After long-term cycling at 6.0C for 1000 cycles, a capacity of more than 155.0 mAh g^{-1} can be recovered at a rate of 0.5C (Fig. S3.33). These results further support the DME is responsible for the capacity decay for high-voltage cathodes, but mixing of several salts in this HE electrolyte demonstrates substantial improvements and possible potential application.
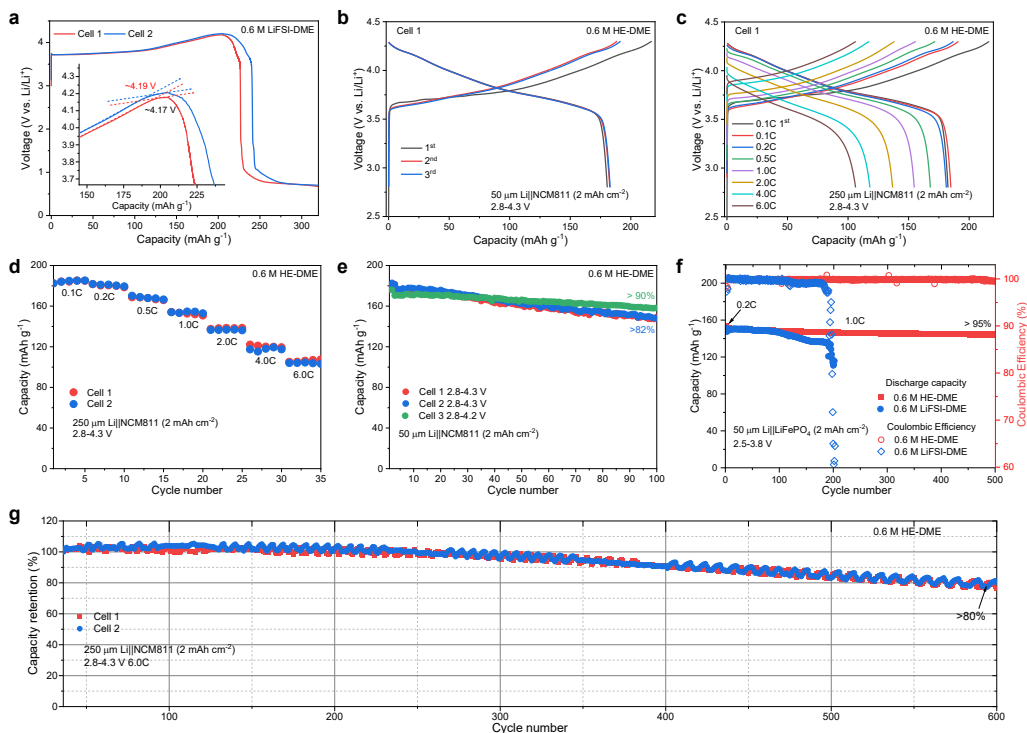
Fig. 3.2 Electrochemical performance. a,b, Galvanostatic charge/discharge curves of LiNi$_{0.8}$Co$_{0.1}$Mn$_{0.1}$O$_2$(NCM811) cells in (**a**) 0.6 M LiFSI-DME, (**b**) 0.6 M HE-DME electrolytes within the voltage range of 2.8-4.3 V at a rate of 0.1C. Cells were tested with a capacity of 2 mAh cm^{-2} for NCM811 and 50 μm Li metal foils, resulting in a negative/positive capacity ratio (N/P) of 5. **c**, Galvanostatic charge/discharge curves of NCM811 cells in the 0.6 M HE-DME electrolyte at different rates. **d**, Electrochemical rate capability of NCM811 in the 0.6 M HE-DME electrolyte. **e**, Cycling performance of NCM811 in the 0.6 M HE-DME electrolyte cycled at a 0.1C rate for three cycles before cycling at a 0.333C rate at different voltage ranges. **f**, Cycling performance of LiFePO$_4$ (LFP) cells cycled at a 0.2C rate for three cycles before cycling at a 1.0C rate. **g**, Long-term cycling capacity retention of NCM811 cells in the 0.6 M HE-DME electrolyte cycled at a rate of 6.0C.

3.4 Li-metal deposits morphology and microstructure
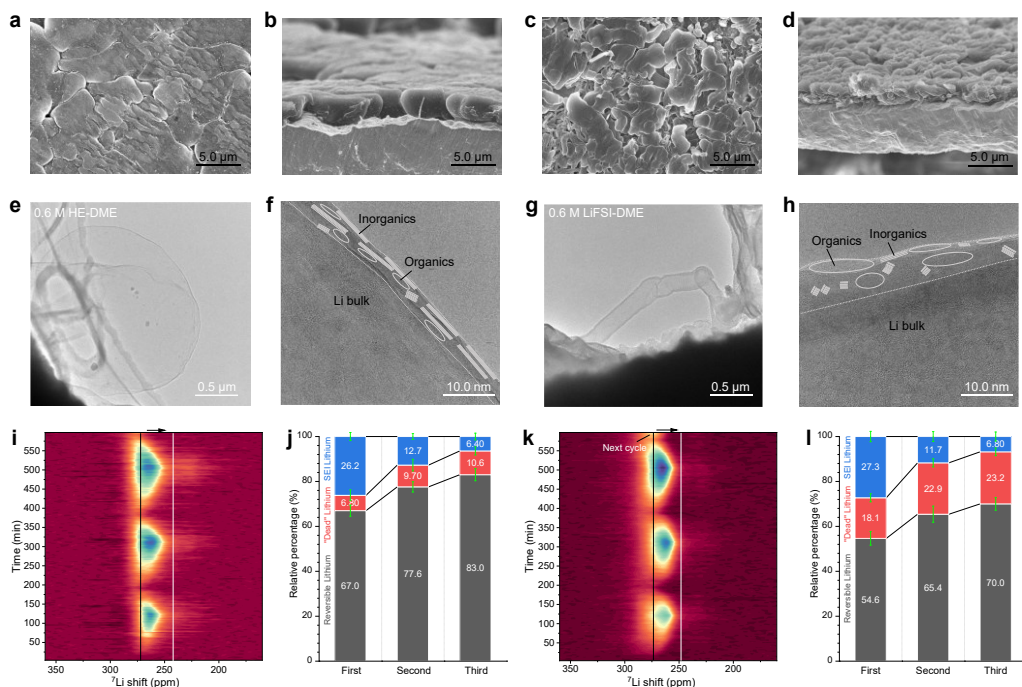

Fig. 3.3 Morphology and microstructure of the Li deposits. Li-metal morphology after plating **a**, **b**, for the 0.6 M HE-DME electrolyte; **c**, **d**, for the 0.6 M LiFSI-DME electrolyte. (**a**) and (**c**) top view; (**b**) and (**d**) cross-sectional view. Microstructure of deposited Li-metal and interfacial phase from cryo-TEM images **e**, **f**, for the 0.6 M HE-DME electrolyte; **g**, **h**, for the 0.6 M LiFSI-DME electrolyte. The enlarged images of (**f**) and (**h**) are shown in the Fig. S3.46 and S3.47. Operando ^{7}Li solid-state NMR spectra and quantification of the Li species, **i**, **j**, for the 0.6 M HE-DME electrolyte; **k**, **l**, for the 0.6 M LiFSI-DME electrolyte. Li species in the SEI (blue bars), reversible Li metal (gray bars), and "dead" Li metal residual (red bars) species are derived from the Li metal integrated intensity ratio I(stripping)/I(plating) and the CE. Error bars are obtained by different tests. The corresponding galvanostatic charge/discharge curves of Cu‖LiFePO$_4$ cells at different electrolytes are shown in Fig. S3.60.

To determine the origin of the improved electrochemical performance of HE-DME in combination with Li-metal anode, the morphology of Li metal plated on bare Cu foil is investigated with scanning electron microscopy (SEM) (Figs. 3.3a-3.3d and Figs. S3.34-S3.38). The deposited Li-metal in the 0.6 M HE-DME electrolyte is compact and well connected to the Cu substrate with particle sizes in the order of 10 μm (Figs. 3.3a, 3.3b and Fig. S3.34). In contrast, for the 0.6 M LiFSI-DME electrolyte, porous and dendritic

Li deposits are observed that are less well connected to the Cu substrate (Figs. 3.3c, 3.3d and Fig. S3.35) which is responsible for the residual dendritic Li after stripping (Fig. S3.36). For the 0.6 M HE-DME electrolyte, the Cu substrate after stripping shows less residual Li metal (Figs. S3.37, S3.38 and Supplementary Note S3.4). The Li-metal deposition process is further investigated with in-situ electrochemical atomic force microscopy (AFM) (Figs. S3.39-S3.41 and Supplementary Note S3.5), where the deposited Li metal particles in the 0.6 M HE-DME electrolyte grow comparatively larger into a more compact morphology.

Cryo-transmission electron microscopy (cryo-TEM) is used to evaluate the Li metal and SEI structure[25] in both the 0.6 M HE-DME and LiFSI-DME electrolytes (Figs. 3.3e-3.3h). In the 0.6 M HE-DME electrolyte, large Li metal particles with thin SEI (approximately 6 nm thick) are observed (Figs. 3.3e, 3.3f and Figs. S3.42-S3.44), which is different from the whisker and needle-like Li metal deposits with thicker and non-uniform SEI layer in 0.6 M LiFSI-DME electrolyte (Figs. 3.3g, 3.3h and Figs. S3.43 and S3.45). Being inorganic-dominant, this indicates that more anionic groups participate in the SEI formation for the 0.6 M HE-DME electrolyte (Fig. 3.3f and Fig. S3.46). Whereas for the 0.6 M LiFSI-DME electrolyte, a mosaic structured SEI is formed, which is dominated by DME solvent decomposition (Fig. 3.3h and Fig. S3.47). Selected area electron diffraction (SAED) and high-resolution TEM imaging (Fig. S3.48) reveal that Li-metal growth is different in these electrolytes. In the 0.6 HE-DME electrolyte, large spherical crystallites are observed, with the (110) planes parallel to Cu substrate (Figs. S3.48a and S3.48c). This is consistent with a previous study which indicates that this crystalline texturing is beneficial to increase the homogeneity of Li growth[26]. It signifies that after nucleation, Li-ion transport facilitates the regular and homogeneous Li-metal growth in the 0.6 HE-DME electrolyte. This does not apply in the 0.6 M LiFSI-DME electrolyte where the particles are polycrystalline in nature (Figs. S3.48b and S3.48d). Cryo-scanning transmission electron microscopy (STEM) electron energy loss spectroscopy (EELS) mapping also reveals a very different elemental distribution in the SEIs (Figs. S3.49 and S3.50). In the 0.6 M HE-DME electrolyte, the outer surface is rich in O, while F, S, N and B are uniformly distributed over the surface of the particles (Figs.

S3.49 and S3.50). However, for the 0.6 M LiFSI-DME electrolyte, part of the outer surface is rich in C and O, and overall C is much more abundantly present. The SEI composition is further studied using X-ray photoelectron spectroscopy (XPS) (Figs. S3.51-S3.59 and Supplementary Note S3.6), where O $1s$, F $1s$, and N $1s$ spectra confirm that the inorganic Li-F, Li-N, B-F, Li-O and B-O species dominate the SEI in the 0.6 M HE-DME electrolyte. The presence of these species could be responsible for a more facile and homogeneous Li-ion supply, supporting dense Li-metal growth[27], and less decomposition of solvent species in 0.6 M LiFSI-DME electrolyte.

Operando solid-state ^{7}Li NMR is used to determine the origin of Li loss during plating/stripping in both electrolytes[28] (Supplementary Note S3.7). To enable quantification, an anode-less Cu||LiFePO$_4$ full cell configuration is employed[29,30]. As expected, the ^{7}Li metal resonance is absent before cycling and appears upon plating at approximately 260-270 ppm (Figs. 3.3i and 3.3k) reaching the highest integrated intensity after charging. Subsequently, the intensity decreases during discharging (Li stripping), leaving some intensity, which represents the "dead" or inactive Li metal. From the operando ^{7}Li NMR spectra and the CE, the fraction of reversible Li metal, dead Li-metal and Li in the SEI is calculated for the first three cycles[31] and shown in Figs. 3.3j and 3.3l. During the first cycle, both electrolytes have similar Li loss into SEI formation, however, the "dead" Li-metal fraction is smaller in the 0.6 M HE-DME electrolyte, which contributes to the higher CE observed for this electrolyte (Figs. 3.3i and 3.3j). During the second and third cycles, the fraction of "dead" Li metal grows in both electrolytes (Fig. S3.61), being higher in the 0.6 M LiFSI-DME electrolyte, which results in a 2.4-times larger fraction of dead Li-metal. At the end of each plating process, the ^{7}Li metal resonance in the 0.6 M HE-DME electrolyte moves to lower ppm values as compared to that in 0.6 M LiFSI-DME electrolyte. It reaches values close to that of Li metal foil at ~246 ppm[30], demonstrating that the 0.6 M HE-DME electrolyte results in a more dense Li metal morphology[31,32], consistent with SEM observations above.

3

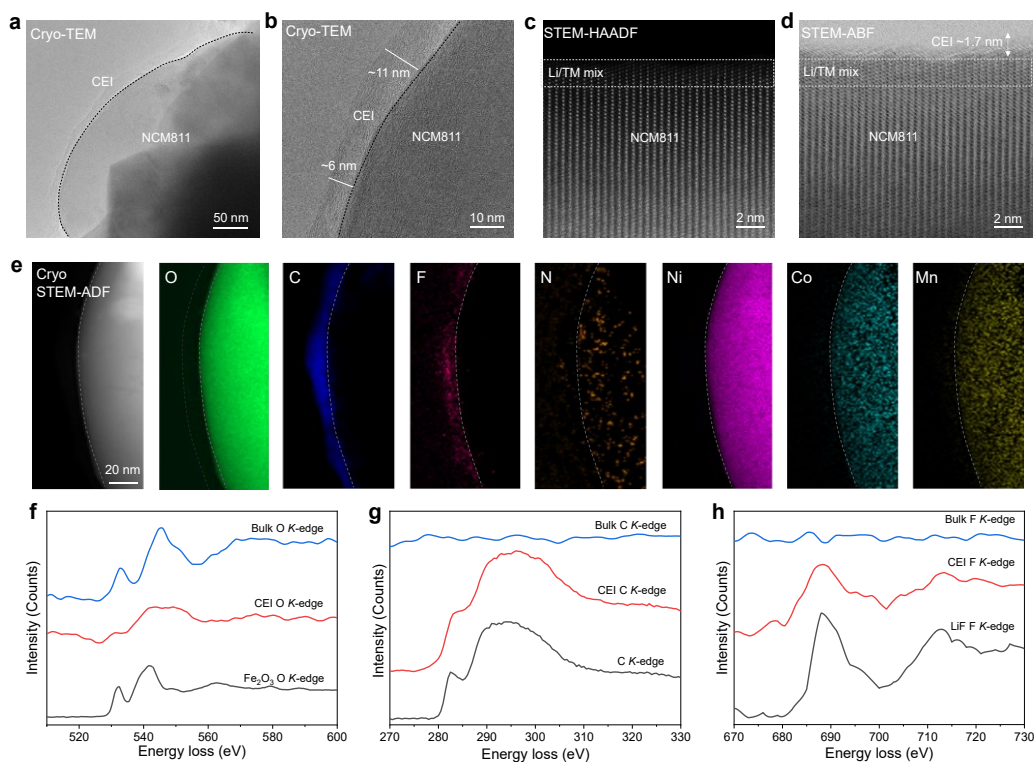## 3.5 Morphology, microstructure and composition of cathode interphase

Fig. 3.4 Morphology, microstructure and composition of the CEI. a, **b**, Cryo-TEM images of the CEI after cycling in the 0.6 M HE-DME electrolyte. **c,** Atomic-resolution HAADF and **d**, ABF-STEM images collected at room temperature. A Li/TM (TM: transition metal) mixed layer was observed near the surface of the particle with a thickness of around 2 nm in both the HAADF and ABF images, in addition, a layer around 1.7 nm was found on the ABF image using its ability to detect light elements. **e**, Cryo-STEM EELS mapping of the NCM811 CEI including a cryo-STEM ADF image, and O, C, F, N, Ni, Co and Mn elemental maps. Scale bar is 20 nm. EELS fine structure of **f**, O K-edge in the bulk and CEI with Fe_2O_3 included as a reference; **g**, C K-edge in the bulk and CEI with carbon as a reference; **h**, F K-edge in the bulk and CEI with LiF as a reference.

To understand the stable cycling of the NCM811 cathode in the 0.6 M HE-DME electrolyte, the morphology, microstructure and composition of the CEI is investigated. After cycling, the morphology of the cathode particles, where the secondary particles consist of densely packed primary sub-micron sized particles, is preserved in the 0.6 M HE-DME electrolyte when comparing SEM images taken before and after cycling (Fig. S3.62). Cryo-TEM at -170 °C is performed to study the nanostructure and chemical

composition of the air-sensitive CEI formed on the surface of the particles. Compared to the pristine material (Fig. S3.63) a conformal CEI layer is formed after cycling with a thickness in the range of ~6-11 nm (Figs. 3.4a, 3.4b, and Fig. S3.64). The corresponding fast Fourier transform (FFT) patterns of the near-surface region in the NCM811 particles indicates that the original layered structure is largely preserved (Fig. S3.64). Atomic-resolution high-angle annular dark field (HAADF) and annular bright field (ABF)-STEM images are collected from the cycled NCM811 electrodes at room temperature. A mixed Li/TM (TM: transition metal) layer of approximately 2 nm is observed at the surface of the NCM811 particle, in both HAADF and ABF images (Figs. 3.4c and 3.4d), which indicates that the detrimental phase transition to the rock-salt phase, which is observed for carbonate electrolytes[33], has not occurred up to 50 cycles in the 0.6 HE-DME electrolyte. Cryo-STEM EELS mappings are recorded to study the elemental distribution in the CEI layer and the near-surface structure of the cycled cathode (Fig. 3.4e and Fig. S3.65). The results indicate the presence of O-, C-, F- and N- containing components in the conformal CEI layer, where O, C and F are the main components participating in the CEI formation and N uniformly distributes on the surface of particle (Fig. 3.4e and Supplementary Note S3.8).

The EELS fine structure at O K-edge, C K-edge and F K-edge provides further insights in the CEI and bulk NCM811 composition (Figs. 3.4f-3.4h). The O ($2p$)-TM ($3d$) hybridized peaks at around 533 and 544 eV in the cathode bulk are relatively higher compared to the referenced O K-edge of Fe_2O_3. O in the CEI layer shows a bonding that is similar to organic polymer carbonate compositions[34] (Fig. 3.4f), which is most likely the result of DFOB$^-$ decomposition[35]. With a peak around 290 eV in C K-edge EELS spectra, the formation of carbonate bonds in the CEI layer is further supported (Fig. 3.4g). Finally, F K-edge EELS indicates the presence of LiF in CEI layer (Fig. 3.4h). The XPS depth profiling analysis further confirmed these observations of the element distribution, showing that O and F are the dominant species in CEI layer formed in 0.6 M HE-DME electrolyte (Figs. S3.66-S3.73 and Supplementary Note S3.9). This compositional analysis indicates that the CEI that formed in 0.6 M HE-DME electrolyte consists of components that supports a high stability, in combination with a high conductivity.

3.6 Solvation structure in HE electrolyte

The solvation structure of the single-salt and HE-DME electrolytes is investigated with Raman spectroscopy (Fig. 3.5a and Figs. S3.74-S3.76). The HE-DME electrolyte shows a weaker solvation interaction between Li ions and the DME solvent, indicated by the decreased peak intensity at ~2.22 eV[36,37], compared with the single-salt electrolytes (Fig. S3.76). In the 0.36 M LiNO$_3$-DME electrolyte, this peak also appears weaker, which in this case should be attributed to the poor solubility of LiNO$_3$ in DME[38], where the strong Li$^+$-NO$_3^-$ interaction results in a lower conductivity compared to the HE-DME electrolyte (Table S3.1). In comparison with the different concentrations of the LiFSI-DME electrolyte (Fig. 3.5b, Figs. S3.75 and S3.76), solvation in the 0.6 M HE-DME electrolyte is most similar to that of the dilute electrolytes (0.2 M and 0.05 M). This is also very different from the strong interactions between anions and Li ions in the concentrated electrolytes (5.0 M) [39,40]. In line with this, the ^{7}Li chemical shift of the 0.6 M HE-DME electrolyte indicates weaker shielding and therefore weak solvation; even weaker than a dilute 0.05 M LiFSI-DME electrolyte (Fig. 3.5c).

The HE electrolyte introduces a diversity in anion species, which in turn are expected to result in a larger variety of solvation structures, weakening the interaction between Li ions and DME/anions as inferred above from NMR. To gain more insights into the solvation structure, density functional theory (DFT) and molecular dynamics (MD) simulations were carried out (Fig. S3.77, Tables S3.2 and S3.3). The various principal anion species in the 0.6 M HE-DME electrolyte result in a rich diversity of more than 30 types of Li-ion solvation environments, much more than what is predicted for the 0.6 M LiFSI-DME electrolyte (Figs. 3.5d, 3.5e and Figs. S3.78 and S3.79). The simulated self-diffusion coefficient of 2.3×10^{-6} cm^2 s^{-1} is larger than that of the 0.6 M LiFSI-DME electrolyte (Fig. 3.5f), indicating improved Li-ion mobility in agreement with the measured conductivity (Fig. 3.1f and Table S3.1).
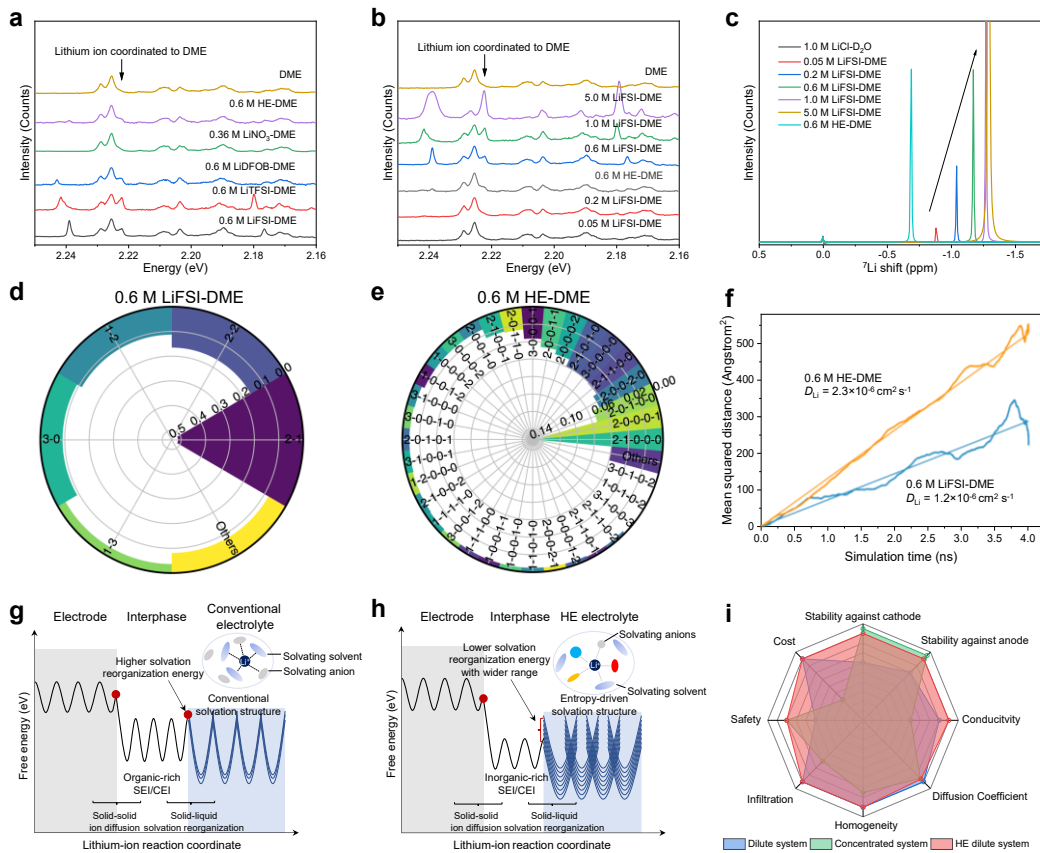
3.7 Discussion

Fig. 3.5 Solvation structure of the HE electrolytes. a, Raman spectra of the single and HE electrolytes. **b**, Raman spectra of different LiFSI concentration DME electrolytes. **c,** ^{7}Li NMR spectra of the HE-DME electrolyte and the LiFSI in DME electrolytes, referenced to a 1 M LiCl in D$_2$O solution. Li-ion coordination environments of **d,** the 0.6 M LiFSI-DME electrolyte and **e,** of the 0.6 M HE-DME electrolyte determined from MD simulations (detailed description in the Table S3.2 and S3.3). **f**, The Li-ion self-diffusion coefficient (D_{Li}) from the MD simulated mean squared displacement for the 0.6 M LiFSI-DME electrolyte (orange line) and the 0.6 M HE-DME electrolyte (blue line). **g**, **h**, Schematic diagram illustrating the ion transport between electrode and electrolyte in a (**g**) conventional electrolyte and (**h**) 0.6 M HE electrolyte. **i**, Performance of the HE electrolyte compared with conventional dilute electrolytes and high-concentration electrolytes.

The MD simulations demonstrate that the introduction of several salts into the HE electrolyte leads to a much larger diversity in solvation structures, expressing the increasing entropy, and to a higher Li-ion mobility, as compared to single salt electrolytes

with the same salt concentration. A way of defining the relationship between the entropy and the dynamic properties of liquids was introduced by Rosenfeld[14] in 1977, which became known as excess entropy scaling, an approximate semi-quantitative relationship that is currently widely employed to estimate dynamic properties of liquids, such as diffusion constants and heat conductivities[15]. In general, excess entropy scaling indicates that the diffusivity increases with the entropy of the system. It can provide a qualitative argument for the present observation, where increasing the entropy by introducing multiple salts (resulting in a richer variation in solvation structures), has resulted in an increase of the diffusivity and conductivity, while keeping the total salt molarity the same. An intuitive explanation is that increasing the number of principle components in an electrolyte will lead to a wider distribution in diffusional barriers based on a wider diversity in solvation structures. Early studies have shown that in regular lattices, random distributions in energy barriers for diffusion typically enhances three-dimensional diffusion, as compared to a uniform energy barrier, which can simply be explained by the availability of a percolation network with lower-than-average energy barriers[41].

The solvation structure of the liquid electrolyte plays a dominant role in the charge transfer between electrolyte and the electrode as well as in the SEI formation, where the resulting SEI morphology and composition determine the Li-ion transport through the SEI. According to the radial distribution function (RDF) of the 0.6 M LiFSI-DME electrolyte obtained from the MD simulations (Fig. S3.80), O shows a strong tendency to coordinate with the Li-ion in comparison to the other elements, indicating a relatively strong interaction between Li ions and solvent molecules. However, in the HE-DME electrolyte, F and N also coordinate with Li ions, indicating more anion-rich solvation structures. This rationalizes the observation that for the HE electrolyte, both the SEI on anode and the CEI on the cathode are rich in the decomposed salt anions. These salt anions, responsible for the higher electrochemical stability, facilitate Li-ion transfer between the electrolyte and SEI/CEI[42,43] and most likely also a higher Li-ion conductivity in both the SEI and CEI. As for the SEI-electrolyte interface, the large diversity in solvation structures in the HE electrolyte leads to a wider range of solvation energies, as indicated by DFT (Fig. S3.81). This diversity results in lower solvation reorganization energies that facilitate Li-ion

diffusion as well as charge transfer towards the interphase as schematically illustrated in Figs. 3.5g and 3.5h. The de-solvation processes in the entropy-dominated and conventional dilute electrolyte are further illustrated in Fig. S3.82. In the HE electrolyte, the inorganic rich SEI/CEI and improved Li-ion kinetics are attributed to the increasing entropy of mixing, resulting in more dense Li metal growth, despite the low concentration of HE electrolyte. Based on the above results, the characteristics of conventional dilute electrolytes, high salt concentration electrolytes and HE electrolytes are compared in Fig. 3.5i. From this comparison, the HE demonstrates promising assets, especially realizing that it enables improved stability against the anode/cathode in low salt concentration liquid electrolytes, which typically can be achieved in highly concentrated electrolytes (Fig. S3.83).

3.8 Conclusions

In summary, we present liquid electrolytes with multiple salts and investigated the role and impact of entropy in this class of materials. Via introducing multiple salts (e.g., LiFSI, LiTFSI, LiDFOB and LiNO$_3$) in an ether solvent, a HE electrolyte has been prepared for the proof of concept, which exhibits a higher reversibility for Li metal plating/stripping and a higher oxidation stability for Ni-rich cathode charging to a high cut-off voltage and results in improved rate performance. Despite the low salt concentration (0.6 M) and the poor oxidation stability of DME, the high entropy endows the solution with the demonstrated promising electrolyte properties. The results show that more salt anions participate in the solvation structures of the low-concentration HE electrolyte, resulting in a thinner and inorganic-rich SEI compared to the single salt electrolyte. The improved interphase properties enhance anodic and cathodic electrochemical stability (Fig. S3.84), and results in more compact Li metal plating and higher oxidative stability of ether-based solvents for 4 V-class Li batteries. This rationalizes the improved reversibility of the charge/discharge cycles and improved rate performance that exceeds these of conventional electrolytes. Moreover, the observed weaker solvation strengths between Li ions and the solvents/anions, as compared to the commonly single-salt low- and high-concentration electrolytes, is held responsible for the enhanced charge transfer and the

improved electrolyte conductivity. This is the consequence of the increased entropy of mixing leading to more diverse and more facile solvation rearrangements in the HE electrolyte (Figs. S3.82 and S3.83).

The compositional landscape of HE materials is huge, as the chemistry and relative amounts of both solvents and salts can be varied. The present investigation suggests that raising the entropy by introducing multiple salts can be used to improve its functional properties through the solvation structure, where the choice of specific salts and solvents should be guided by their interactions with the specific anode and cathode chemistry. This is further supported by preparing a five-component salt HE electrolyte supporting even longer stable cycling (Figs. S3.85-S3.87 and Supplementary Note S3.10). This exploration motivates more fundamental and systematic research, which is of general scientific importance and will guide the development of better electrolyte systems and beyond.

3.9 Methods

Materials

Li-metal foils (thickness of 250 μm), Cu foils and Al foils were purchased from MTI Corporation, and Li metal foils (50 μm) were purchased from China Energy Lithium Co., Ltd. All Li-metal foils were washed 3 times with dimethoxyethane (DME) solvent before use. Cu foils were immersed in diluted acetic acid for several minutes, subsequently washed by deionized water and acetone three times, separately, then they were quickly dried in the vacuum oven of glove box at room temperature. DME solvent was purchased from Sigma-Aldrich, which was dehydrated with a 4 Å molecular sieve (Sigma-Aldrich) to eliminate the possible trace water. Lithium bis(fluorosulfonyl)imide (LiFSI), lithium bis(trifluoromethanesulfonyl) imide (LiTFSI), Lithium Difluoro(oxalato)borate (LiDFOB) were obtained from Sigma-Aldrich, and Lithium bis(pentafluoroethanesulfonyl)imide (LiBETI) were obtained from 3M company, which were dried under vacuum condition at 80 °C for 24 h after purchased. Lithium nitrate (LiNO$_3$, >99.9%) was purchased from Shenzhen Capchem Technology Co., Ltd and used as-received. All the electrolytes were prepared by dissolving the specific amount of different Li salts in DME solvent in an Ar-

filled glove box (H_2O < 0.1 ppm, O_2 < 0.1 ppm). 0.6 mol L^{-1} (M) LiFSI-DME, 0.6 M LiTFSI-DME, 0.6 M LiDFOB-DME and 0.36 M $LiNO_3$-DME electrolytes denote that the corresponding concentration of different salts are dissolved in DME, where 0.6 M $LiNO_3$-DME electrolyte can't be prepared because of the relatively low salt solubility. HE-DME electrolyte was prepared by dissolving 0.15 M LiFSI, 0.15 M LiTFSI, 0.15 M LiDFOB and 0.15 M $LiNO_3$ into DME solvent with the total concentration of Li to be 0.6 M. 5-component 0.6 M HE-DME electrolyte was prepared by dissolving 0.15 M LiFSI, 0.10 M LiTFSI, 0.10 M LiBFTI, 0.10 M LiDFOB and 0.15 M $LiNO_3$ into DME solvent with the total concentration of Li to be 0.6 M.

$LiFePO_4$ was obtained from Leneng Technology for which the cathodes were prepared by mixing $LiFePO_4$ material, poly(vinylidene difluoride) (PVDF, MTI) binder and Super P (Alfa Aesar) conductive carbon in a weight ratio of 92:4:4. The resulting slurry was cast on the Al foil then dried at 60 °C for 6 h, followed by drying overnight at 120 °C in a vacuum oven. $Li_4Ti_5O_{12}$ anode was purchased from MTI Corporation as received. $LiNi_{0.8}Co_{0.1}Mn_{0.1}O_2$ (NCM811) was synthesized using coprecipitation method. The certain amount of alkaline aqueous solution (NH_4OH and NaOH) was poured into deionized water (1.5 L) to form the base solution in a tank reactor under continuous stirring. Then, a 2 M solution of $NiSO_4 \cdot 6H_2O$, $CoSO_4 \cdot 7H_2O$ and $MnSO_4 \cdot H_2O$ with a molar ratio of 8:1:1 and an aqueous solution of 5 M NH_4OH and 10 M NaOH were added into the base solution in the tank reactor with a steady rate of 8 mL min^{-1}. The coprecipitation temperature was controlled at 50 °C, and pH value was maintained at around 11 by NH_4OH with stirring speed of 500 rpm under nitrogen atmosphere. The coprecipitated $Ni_{0.8}Co_{0.1}Mn_{0.1}(OH)_2$ precursor was prepared, which was subsequently washed by deionized water and ethanol for four times and dried in a vacuum at 120 °C for 24 h. The apparent and tap density of $Ni_{0.8}Co_{0.1}Mn_{0.1}(OH)_2$ precursor are 1.88 g cm^{-3} and 2.06 g cm^{-3}, respectively. For preparation of NCM 811 materials, the as-obtained precursor was mixed with $LiOH \cdot H_2O$ at a molar ratio of 1:1.03; then firstly heated at 500 °C for 5 h and subsequently calcined at 780 °C for 12 h in oxygen atmosphere. After cooling naturally, the obtained material was directly put into an Ar-filled glovebox to prevent any moisture exposition. The NCM811 electrodes were prepared by mixing active material, Super P

and PVDF binder in the mass ratio of 90: 5: 5 in N-methyl-2-pyrrolidone (NMP) solvent and cast on Al foil and then dried at 60 °C for 6 h, followed by drying in a vacuum oven at 120 °C overnight. X-ray diffraction pattern demonstrates the pure phase of this prepared NCM811 material.

Electrochemical measurements

Electrochemical cycling tests of all batteries were based on CR2032 coin cells assembled in an Ar-filled glove box (H_2O < 0.1 ppm, O_2 < 0.1 ppm) with Celgard 2500 separator and tested at room temperature, unless stated otherwise. 70 μL electrolytes were injected into each coin cell for comparison. All coin cells were tested using multi-channel battery testing systems (Land CT2001A or Lanhe G340A) at room temperature. Symmetric Li||Li cells were assembled to study the cycling stability under different current densities with various electrolytes. 15.6 mm diameter Li-metal foils with 250 μm thickness were used as both the working and counter electrodes. For Li||Cu cells, 14 mm diameter Li metal foils were used as the reference, while 16 mm Cu foils was used as a working electrode with the effective area for Li deposition of 1.54 cm^2. During cycles, capacity of 1 mAh cm^{-2} Li was deposited on Cu foils at a current density of 0.5 mA cm^{-2} and then stripped to a cut-off voltage of 1.0 V vs. Li/Li$^+$.

Electrochemical cycling performance of $LiFePO_4$ and NCM811 electrodes (12 mm diameter) are all with an areal capacity of 2 mAh cm^{-2} tested with Li-metal foils with a thickness of 50 μm as counter electrode. Li||NCM811 cells were electrochemically cycled between 2.8-4.3 V under a 0.1C rate for three cycles before cycling at 0.333C rate (1C=180 mA g^{-1}). Li||$LiFePO_4$ cells were cycled in the galvanostatic mode, whereas a voltage range of 2.5–5.0 V was used to gauge the oxidation stabilities of the different electrolytes for which $LiFePO_4$ cathode doesn't show the extra redox reaction from Fe^{2+} to Fe^{3+} above ~3.8 V. For electrochemical rate capabilities of Li||$Li_4Ti_5O_{12}$ and Li||NCM811 cells, the areal capacity of 2 mAh cm^{-2} for $Li_4Ti_5O_{12}$ (12 mm diameter) and capacity of 2 mAh cm^{-2} for NCM811 were used with Li metal foils having a thickness of 250 μm as counter electrode. Cyclic voltammetry (CV) of Li||Cu cells with various electrolytes were conducted at a scan rate of 0.8 mV s^{-1} from -0.1 to 2.5 V vs. Li/Li$^+$.

Electrochemical impedance spectra (EIS) of the symmetric cells were collected on an Autolab (PGSTAT302N) in the frequency range of 0.1 Hz–1 MHz with a potential amplitude of 10 mV.

The Li ion transference number (t_{Li}^+) of the electrolytes was measured via the method from Abraham *et al.*[7] The polarization potential (ΔV) of 10 mV was used for symmetric Li||Li cells using the HE-DME electrolyte until the polarization currents reached a steady state The corresponding EIS measurements were collected before and after the polarization. The t_{Li}^+ was calculated using the following equation (3.1):

$$t_{Li^+} = \frac{I^{ss}R_b^{ss}(\Delta V - I^0 R_i^0)}{I^0 R_b^0(\Delta V - I^{ss} R_i^{ss})} \tag{3.1}$$

where ΔV is the applied potential, I^0 is the initial current and I^{ss} is the steady-state current; R_b^0 and R_b^{ss} are the initial and steady-state values of the bulk resistances and R_i^0 and R_i^{ss} are initial and steady-state values of the interfacial resistances, respectively, which were examined by impedance measurements before and after the potentiostatic polarization.

Ionic conductivity of electrolytes was measured using symmetric stainless steel||stainless steel cells by collecting the electrochemical impedance (R) at room temperature, and calculated using the equation (3.2):

$$\sigma = \frac{L}{R \times S} \tag{3.2}$$

where σ is ionic conductivity, S is the effective area of electrode, L stands for the thickness between two stainless-steel electrodes, respectively. Test cells were assembled with a Polytetrafluoroethylene (PTFE) ring between two electrodes. Hence, the effective area of electrode is calculated based on the inner diameter PTFE ring, and the thickness two stainless-steel electrodes is based on total thickness of PTFE ring.

For the evaluation of Al foil corrosion, Al||Li cells were assembled with a 250 μm thick Li metal foil with 70 μL of different kinds of electrolytes. The cells were tested with the potentiostatic mode at 4.2 V vs. Li/Li$^+$ for 24 h.

Materials characterization

Morphologies of electrodes were measured on a cold field scanning electron microscope (SEM, HITACH-S4800, SU8010). Elemental composition on the surface of the electrodes was analyzed by X-ray photoelectron spectroscopy (XPS, PHI 5000 VersaProbe II) using

3

a monochromatic Al Kα X-ray source with X-ray settings being 100 μm 25 W 15 kV. Peaks were fitted using MultiPak software calibrated with respect to carbon (284.8 eV). The above morphology and composition characterization were performed with cells being disassembled after specific cycles in an Ar-filled glove box and rinsed with pure DME solvent three times to remove residual electrolyte, followed by drying in a glove box for several hours at room temperature to remove the residual solvent. Then these electrodes were transferred into the vacuum transfer boxes for measurements to avoid air exposure. Raman spectroscopy was measured by Micro-laser confocal Raman spectrometer (Horiba LabRAM HR800 spectrometer) equipped with an Olympus BX microscope and an argon ion laser (532 nm) at room temperature. All the electrolytes were hermetically sealed in quartz cuvettes in a glovebox before measurement. Powder X-ray diffraction (XRD) was performed using a Bruker D8 Advance diffractometer equipped with a Cu Kα radiation source (λ_1=1.54060 Å, λ_2=1.54439 Å at 40 kV and 40 mA) and a LynxEye_XE detector.

Cryo-transmission electron microscopy (cryo-TEM) characterization

Conventional and cryo-(S)TEM experiments were performed on a scanning transmission electron microscope (STEM) (JEM-ARM300F, JEOL Ltd.) operated at 300 kV with a cold field emission gun and double Cs correctors. During image acquisition, the corresponding electron dose flux (units of number of electrons per square Å per second, e^- Å^{-2} s^{-1}) was recorded. Conventional STEM images were taken with a dose rate of over 1000 e^- Å^{-2} s^{-1} with an exposure time for each image of several seconds. Cryo-TEM images were obtained with an exposure time for each image of around 0.3 s with built-in drift correction function using the OneView and K2 cameras. Cryo-TEM images were taken with an electron dose rate of 50-500 e^- Å^{-2} s^{-1}. Short-exposure single-frame shots were used to estimate the defocus and make it as close as possible to Scherzer defocus. EELS spectra were acquired on a GIF Quantum camera with a dispersion of 1 eV/channel, utilizing the Dual EELS capability to correct for drift in the low-loss centered on the zero-loss peak and core-loss centered on the *C K*-edge. The EELS spectrum images were carried out with a camera length of 20 mm, and a pixel dwell time of 10 ms. Energy drift during spectrum imaging was corrected by centering the zero-loss peak to 0 eV at each pixel. Elemental maps were computed through a two-window method in a pre-edge

window fitted to a power-law background and a post-edge window of 50-200 eV on the core-loss signal. Analysis of the spectra has been performed in Gatan microscopy suite software. For cryo-TEM sample preparation and transfer, cells were disassembled immediately in an argon-filled glovebox after cycling and then both Li metal anodes and NCM811 cathodes were rinsed with pure DME three times to remove Li salts, followed by drying in the glove box for one hour at room temperature to remove the residual solvent. During the washing procedure, approximately 10 mL DME was carefully dropped onto each of the electrodes one time to reduce additional artifacts on the electrodes.

For cryo-TEM preparation of Li-metal anode, a carbon TEM grid was put on Cu foil working electrode and assembled into Li||Cu cells in an argon-filled glovebox. The cells were discharged at a constant current density of 1.0 mA cm^{-2} for 15 min, after which the TEM grid was taken out by disassembling the cells for measurement. The TEM grid was carefully transferred into the cryo-TEM holder in glovebox with a specialized shutter to prevent air exposure and ice condensation onto the sample introducing any side reactions. Once the cryo-TEM holder was transferred into TEM column, the temperature was maintained at around -170 $^{\circ}$C using liquid nitrogen. For cryo-TEM preparation of NCM811 cathodes, conventional Li||NCM811 cells were cycled at 0.333C for 50 cycles in the voltage range of 2.8-4.3 V and then disassembled in glovebox. After rinsing the cathode, a small piece of cathode was sealed in an airtight container with pure DME inside. Then the sealed airtight container was taken out from glovebox and the sample was dispersed for three minutes by ultrasonic method. After that, the dispersed cathode was dropped on the TEM grids in glovebox and loaded into the cryo-TEM holder for further measurement. The same specialized shutter was also used to prevent air exposure. All cryo-TEM images are taken at around -170 $^{\circ}$C to reduce beam damage. For the conventional STEM experiments, the above dispersed sample was dropped on a copper grid, dried for three hours in a vacuum and loaded into the double-tilt holder. The STEM-HAADF and ABF images were recorded at room temperature.

In-situ atomic force microscopy (AFM) characterization

In-situ electrochemical AFM measurement (Bruker Corporation) was performed with a three-electrode cell powered by an electrochemical workstation (CHI760E) in an argon-

filled glove box ($H_2O < 0.1$ ppm, $O_2 < 0.1$ ppm). Cells were assembled with Cu substrate as working electrode and Li metal stripe as the counter and reference electrodes. During the electrochemical measurement, cells were discharged at a constant current density of 0.5 mA cm^{-2} in which the images of Li plating process were collected at different times. AFM topography images were collected with the peak force tapping mode and the ScanAsyst-Fluid tips ($k = 0.7$ N m^{-1},) were used for their superior force control with a pN-level force between tip and electrode, diminishing the damage to sample surface in the liquid condition. The obtained AFM images were analyzed with NanoScope Analysis software.

Liquid nuclear magnetic resonance (NMR) characterization

Liquid NMR spectra were recorded with an Agilent 400 MHz DD2 NMR spectrometer with 5 mm ONE NMR Probe at room temperature, which worked at 155.5 MHz on ^{7}Li, 100.6 MHz on ^{13}C, and 376.49 MHz on ^{19}F, respectively. The chemical shift values are given in ppm. ^{7}Li chemical shift was referenced to the standard solution: 1 M LiCl in D_2O for ^{7}Li (0 ppm). The external standard solutions were sealed into WILMAD coaxial insert tubes, and inserted into the 5-mm KONTES tubes with electrolytes and sealed with PTFE caps. Mestrelab Research Mnova software was used for data processing.

Solid-state NMR characterization

Operando solid-state NMR measurements were conducted on a wide-bore Bruker Ascend 500 system equipped with a NEO console in a magnetic field strength of 11.7T and a ^{7}Li resonance frequency being 194.37 MHz using a solenoidal Ag-coated Cu coil. Operando static ^{7}Li NMR measurements were performed using an automatic-tuning-and-matching probe (ATM VT X operando WB NMR probe, NMR Service) at room temperature which can allow for an automatic recalibration of the NMR radio-frequency (rf) circuit during an operando electrochemistry experiment. A highly shielded wire with low-pass filters was attached to the probe for electrochemical measurement, which could minimize the interferences between NMR and the electrochemistry circuit. Single-pulse with a $\pi/2$ pulse of 4 µs and recycle delay of 1.0 s was applied to acquire the 1D static spectrums. A recycle delay of three times of T_1 was used each time, where T_1 was determined using saturation

recovery experiments. The electrochemical cell was simultaneously controlled by a Maccor battery testing system. A plastic capsule cell made out of polyether ether ketone (PEEK) was used for the operando NMR experiments. The cells were assembled using LiFePO$_4$ cathode (areal capacity is 2.0 mAh cm^{-2}) and Cu foils as working and counter electrodes with both a piece of Celgard and a piece of Glass fiber (Whatman GF/A) as separator. Before measurements, the assembled cells were rested for 2 h in glovebox. The operando capsule cell was aligned in an Ag-coated Cu coil with LiFePO$_4$ and Cu foil electrode oriented perpendicular to B_0 and parallel with respect to the B_1 rf-field. During charge-discharge process, NMR spectra were continuously acquired. The chemical shift of ^{7}Li was referenced to 1 M aqueous solution of LiCl at 0 ppm. The spectra were processed in the Bruker Topspin software, using the automatic phase and baseline correction. Mestrelab Research Mnova software was used for data processing and analysis.

Molecular dynamics (MD) simulations

MD simulations were conducted on single and HE electrolyte systems with different Li salts and concentrations using the LAMMPS package[44]. Molecules and ions were described by the optimized potentials for a liquid simulations all-atom (OPLS-AA) force field[45]. Partial charges were computed by fitting the molecular electrostatic potential at the atomic centers with the Møller–Plesset second-order perturbation method with the correlation-consistent polarized valence cc-pVTZ(-f) basis set[46]. In order to create a certain concentration of salt within DME, a 1:10 salt/solvent ratio is required. Simulation boxes with dimensions of 60×60×60 Å were randomly packed with 1200 molecules of DME and 120 salt molecules using the software Packmol[47]. A cut-off distance of 1.1 nm was chosen for the Lennard-Jones interactions. A conjugate-gradient energy minimization was first performed on both simulation boxes. A time-step of 0.5 fs was chosen for the MD simulations performed after this point. Isothermal-isobaric ensemble simulations at 300 K was first performed for 5 ns in order to obtain the correct volumes of both systems. Subsequently, both systems were equilibrated at room temperature using canonical ensemble simulations for another 6 ns. The canonical ensemble simulations were continued for another 10 ns, and snapshots of the simulation were obtained every 0.5 ps. The solvation structures of the simulation were analyzed using the Python Materials

3

Genomics (pymatgen) package[48]. The radial density functions and the diffusivities of the Li ions were computed using the MDAnalysis package[49].

DFT Calculations

Quantum chemical calculations were conducted using density functional theory (DFT) method with Becke's three parameters (B3) exchange functional in Lee-Yang-Parr (LYP) nonlocal correlation functional (B3LYP)[50,51]. All the geometry optimizations were performed with the B3LYP/6-31+G(d,p) level. The energy calculations were performed at B3LYP/6-311+ +G(3df,3dp) level for more accurate calculation. All DFT calculations were performed by using the Gaussian 09 program package[52]. The solvation structure formation energy was calculated as following equation (3.3):

$$E_{Form} = E_{cluster} - \sum E_{molecule} \qquad (3.3)$$

where $E_{cluster}$ is the energy of the solvation structure and $E_{molecule}$ is the energy summation of all molecules forming the solvation structure.

3

3.10 Supplementary information

Supplementary Notes

Supplementary Note S3.1

To study the effect of HE electrolytes, several criteria have been taken into consideration while selecting the principal components. DME is selected as solvent because it strongly dissociates from various alkali metal salts, due to its high donor number. The salt concentration is chosen to be 0.6 M for two main reasons. First, because this is commercially compatible (higher concentrations increase the cost of batteries considerably, Fig. S3.1). Second, because it offers a more challenging condition for the stability of the electrode/electrolyte interface. The selection criteria of the salts are their solubility in the DME solvent, commercial availability and the presence of oxygen containing anionic groups, aiming to balance the interaction between Li-ions and DME. Based on these criteria, LiFSI, LiTFSI, LiDFOB and $LiNO_3$ were selected to prepare the 0.6 M HE electrolyte, resulting in a uniform and stable solution.

Supplementary Note S3.2

The oxidation stability of single salt electrolytes is evaluated using Li‖LiFePO$_4$ cells at a low current density of 0.02C (1C=150 mAh g^{-1}). A charge cut-off voltage of 5.0 V is set to study the oxidation stability of the electrolytes, making use of the absence of a redox reaction of LiFePO$_4$ above ~3.8 V (Fig. S3.4). This results in the onset of oxidation at ~4.81, 4.62, 4.36, and 4.19 V vs Li/Li$^+$ for 0.6 M LiDFOB-DME, 0.6 M LiTFSI-DME 0.6 M LiFSI-DME and 0.36 M $LiNO_3$-DME respectively. The reduction stability of single salt electrolytes is evaluated in Li‖Cu cells (Figs. S3.5-S3.8), where the 0.6 M LiFSI-DME electrolyte shows the most reversible cycling with a Coulombic efficiency (CE) > 97.0% after 50 cycles. The other single salt electrolytes result in a CE < 50.0% after 50 cycles, and 0.36 M $LiNO_3$-DME is not able to cycle at all showing large overpotentials of approximately ~400 mV, and large stripping capacities due to electrolyte decomposition (Fig. S3.8). These results are qualitatively summarized in Fig. 3.1c, where 0.6 M LiFSI-DME is concluded to show the best overall stability in single salt electrolytes, and is selected as the control group in the detailed study of the 0.6 M HE-DME electrolyte. The

different combination of salts in the electrolyte are also tested (Fig. S3.9). From the comparisons it is clear that the HE electrolyte stands out in its performance.

Supplementary Note S3.3

Symmetric Li‖Li cells are used to test the cycling stability and overpotential in both electrolytes, where the 0.6 M HE-DME electrolyte exhibits overpotentials of ~18 mV, ~10 mV and ~8 mV after the 1st, 50th and 200th cycle respectively at a current density of 1 mA cm^{-2}, outperforming the single salt electrolytes (Figs. S3.11 and S3.12), corresponding to a lower electrochemical impedance (Fig. S3.12). Furthermore, the cycling stability at current densities of 0.5, 1.0, 3.0 and 5.0 mA cm^{-2} are evaluated, demonstrating the competitive conductivity of this 0.6 M HE-DME electrolyte (Fig. S3.13). In contrast, the 0.6 M LiFSI-DME electrolyte is not able to cycle at high current densities in symmetric Li‖Li cells. This can be attributed to its limited conductivity and SEI layer that results in concentration polarization at the surface of the electrodes[53]. The 0.6 M HE-DME electrolyte has a slightly higher reduction potential for the decomposition of anionic groups at ~1.32 V, and the current density is relatively small according to the cyclic voltammetry (CV) measurements of the Li‖Cu cells (Figs. S3.14-S3.19). After the initial cycles, the reduction peak disappears (Fig. S3.15), indicating that an SEI has been formed during the initial cycles[18].

Supplementary Note S3.4

The denser and better connected Li metal deposits formed in the 0.6 M HE-DME electrolyte is beneficial for electron transport, allowing efficient Li metal stripping and suppressing the formation of "dead"/inactive Li metal[54]. At the same time it minimizes the exposed surface area resulting in less electrolyte decomposition, suppressing the formation of porous and dendritic Li on subsequent Li metal deposition[55].

Supplementary Note S3.5

The process of Li metal deposition on the Cu current collector is also investigated with in-situ electrochemical atomic force microscopy (AFM), where in contrast to a regular cell, there is no pressure exerted by the separator on the Li metal. At the early stage of plating of 36 s (0.005 mAh cm^{-2}), for both electrolytes, the Cu electrodes are covered by Li

nanoparticles, the density of which appears slightly higher in the 0.6 M HE-DME electrolyte (Figs. S3.39 and S3.40). After plating for 72 s (0.01 mAh cm^{-2}), a distinct difference in plating emerges between the two electrolytes as larger particle sizes are observed in the 0.6 M HE-DME electrolyte. For the 0.6 M LiFSI-DME electrolyte, even more nanoparticles are observed as compared to 36 s of deposition, which continues up to at least 144s (0.02 mAh cm^{-2}) (Fig. S3.39). From 216 to 1080 s, part of these nanoparticles gradually grows in size resulting in a porous morphology. In comparison, the deposited Li-metal particles in 0.6 M HE-DME electrolyte grow larger into a more compact morphology (Fig. S3.40). At 2520 s (0.35 mAh cm^{-2}) the difference in particle size becomes even larger, being in the range of 10-500 nm in the 0.6 M LiFSI-DME electrolyte and in the range of 2-5 μm in the 0.6 M HE-DME electrolyte (Figs. S3.39-S3.41). The continuous nucleation of Li-metal deposits may be related to the much higher overpotential during Li metal deposition in the 0.6 M LFSI-DME electrolyte which can be related to the lower conductivity of the electrolyte and the SEI[56,57].

Supplementary Note S3.6

The SEI composition is further studied by X-ray photoelectron spectroscopy (XPS) (Figs. S3.51-S3.59). Based on the survey spectra (Fig. S3.51), F, C and O elements dominate the SEI formed in the 0.6 M HE-DME electrolyte, and much less F is present in the SEI formed in the 0.6 M LiFSI-DME electrolyte, even with different sputtering depths. With increasing sputtering depth, looking deeper in the SEI formed in the 0.6 M HE-DME electrolyte, the F and O content increases and the C content decreases, indicating the initial decomposition products on the Cu substrate result from the anionic groups in the 0.6 M HE-DME electrolyte. At the largest sputtering depth, B appears originating from the DFOB^{-} anion (Fig. S3.59), consistent with its high reduction potential (Fig. S3.14). In addition, high-resolution O 1s, F 1s, and N 1s spectra confirm that the inorganic Li-F, Li-N, B-F, Li-O and B-O species dominate the SEI in the 0.6 M HE-DME electrolyte. In the 0.6 M LiFSI-DME electrolyte, the similar amount of S content before and after sputtering indicates continuous decomposition of the FSI^{-} group. These observations indicate that in comparison to the 0.6 M LiFSI-DME electrolyte, the 0.6 M HE-DME electrolyte results in larger, crystalline Li metal particles, with a thinner and inorganic rich layered SEI. The

3

latter can be held responsible for more facile and homogeneous Li-ion supply, supporting dense Li metal growth, and less decomposition of electrolyte species, both of which explain the better reversibility of the Li metal anode in combination with the 0.6 M HE-DME electrolyte.

Supplementary Note S3.7

Via the Knight shift, Li metal can be distinguished from the diamagnetic Li species in the SEI, and the amount can be quantified under the condition that the deposits are significantly smaller than the skin depth, the penetration depth, of the radiofrequency field (11 μm for the present measurements)[30]. As a result, these measurements allow the quantification of the amount of "dead" Li metal after stripping, representing Li metal deposits that are electronically disconnected from the Cu current collector[30]. Combining this with the CE from the electrochemical measurement, the amount of Li in the SEI can be quantified[31]. Additionally, operando solid-state ^{7}Li NMR provides information on the evolution of the Li metal morphology based on the characteristic chemical shifts of mossy structures and dendritic Li [29,32,58]. In this work, Li corrosion is not taken into account based on the relatively low corrosion current compared to the plating/stripping current[31].

Supplementary Note S3.8

The CEI in the 0.6 M HE-DME electrolyte is rich in O, with a lower concentration as compared to the bulk cathode material, and in contrast the TM elements (Ni, Co and Mn) are only observed in the bulk cathode material indicating the CEI inhibits dissolution of TM ions. Generally, TM ion dissolution plays an important role in these systems, where DME oxidation generates acidic species that degrade the surface structure of the cathode[59]. The STEM-ABF image further demonstrates that TM ions do not participate in the formation of the CEI where a layer around 1.7 nm is only found in the ABF image (Fig. 3.4d) due to its ability to observe light elements, and not in the HAADF image which is sensitive to the heavier elements. This is thinner than observed with cryo-TEM, most likely because of the air and beam exposure of the CEI component.

Supplementary Note S3.9

To further investigate the elemental distribution on the surface of the NCM811 (after cycling), XPS depth profiling analysis is carried out after cycling in the 0.6 M HE-DME electrolyte (Figs. S3.66-S3.73). The survey spectra (Fig. S3.66) and atomic ratio's (Figs. S3.67) show that C, O and F are the dominant species in the CEI layer, consistent with the cryo-STEM EELS mapping results. The C 1s, O 1s, N 1s and S 2p spectra (Figs. S3.68-S3.71), indicate the presence of C–O, C=O, –CF$_x$, N–O, S–N and –SO$_x$, suggesting that the various anionic groups of the HE-DME electrolyte are involved in the formation of the CEI layer. Based on the F 1s and Li 1s spectra, the CEI formed in the 0.6 M HE-DME electrolyte is rich in LiF, the concentration of which increases with the depth in the CEI (Figs. S3.72 and S3.73), which can be held responsible for the high-voltage stability of the CEI layer[60,61].

Supplementary Note S3.10

Based on the favourable properties of the studied four-component 0.6 M HE electrolyte, a five-component 0.6 M HE electrolyte is prepared to further increase the entropy aims to improve functional properties. Li bis(pentafluoroethanesulfonyl)imide (LiBETI) is introduced as the fifth component to replace parts of the LiTFSI and LiDFOB salts. It was selected because of its larger complexity, further contributing to a larger entropy of mixing and additionally because of its higher oxidation stability[62]. This results in an electrolyte composition of 0.15 M LiFSI, 0.1 M LiTFSI, 0.1 M LiDFOB, 0.1 M LiBETI and 0.15 M LiNO$_3$ with DME as the solvent, which is referred to as five-component 0.6M HE electrolyte. The stability towards Li metal is investigated using Li‖Cu cells (Figs. S3.85a and S3.85b), demonstrating in direct comparison with the four-component 0.6M HE electrolyte a higher reversibility with CE exceeds 99.0%, which is related to the even more compact Li metal deposition (Fig. S3.85c). Furthermore, the oxidation stability of the five-component 0.6 M HE electrolyte is also improved, up to 4.61 V, after which the oxidation quickly passivates (Fig. S3.85d). On comparing the four- and five- component HE electrolytes in rate capability and cycling performance tests in Li‖NCM811 cells, it is found that the latter has a slightly higher capacity retention when charged/discharged at 6.0C (Figs. S3.85e and S3.86) as well as a slightly better capacity retention at a charge/discharge rate of 0.333C (Figs. S3.85f and S3.87). Thereby, a second example is

3

provided of a multi component salt electrolyte, where we propose that the wider diversity in solvation structures leads to weaker DME solvation, finally resulting in an inorganic rich and more stable SEI as well as in a higher Li-ion conductivity, responsible for its improved performance.

3

Supplementary Figures
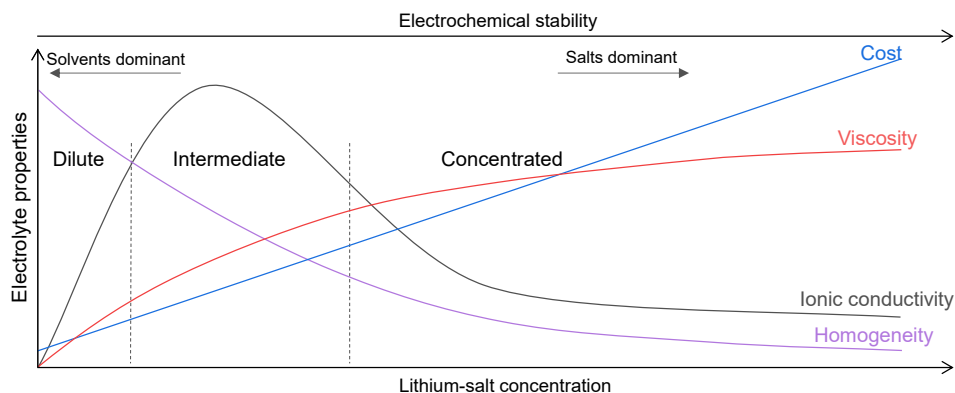
Fig. S3.1. Illustration of electrolyte properties vs. Li-salt concentration vs. Electrochemical stability in liquid electrolytes. Three parts of dilute, intermediate and concentrated solutions are shown, where in general electrochemical stability against anode/cathode are dominated by solvents for dilute systems and dominated by salts for concentrated systems.

3
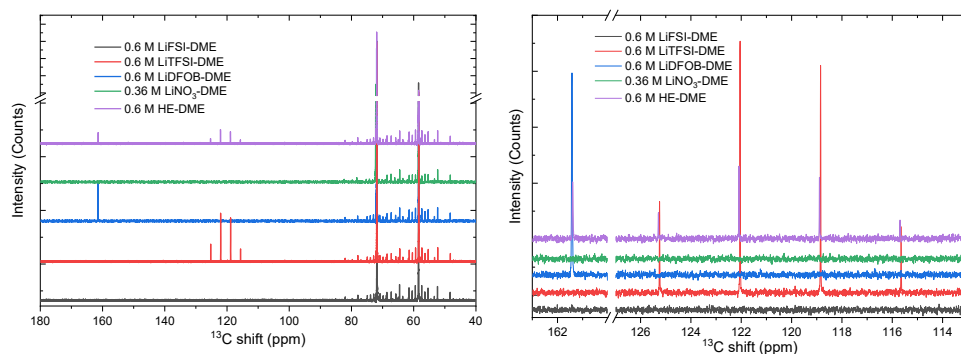
Fig. S3.2. Liquid ^{13}C nuclear magnetic resonance (NMR) spectra of single salt electrolytes and the as-prepared HE-DME electrolyte. The top figure is the complete ^{13}C chemical shift range; and the bottom shows sections of the spectra corresponding to the salt part. Compared with the ^{13}C peaks at around 115.7, 118.9, 122 and 125.5 ppm assigned to TFSI$^-$ group, these peaks showed a shift in HE-DME electrolyte, but compared with ^{13}C peak at around 161.5 ppm assigned to the DFOB$^-$ group, the peak moved in the HE-DME electrolyte.
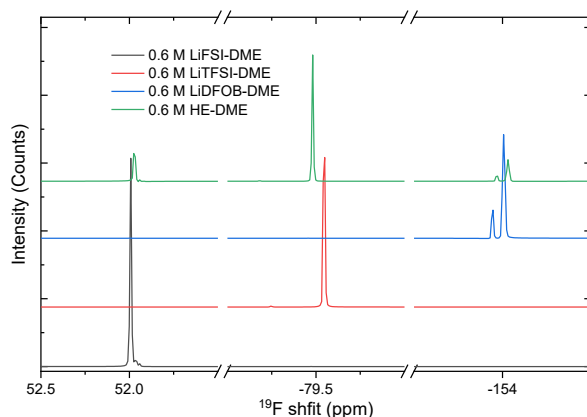
Fig. S3.3. Liquid ^{19}F NMR spectra of single salt electrolytes and the as-prepared HE-DME electrolyte. The ^{19}F NMR spectra in the HE-DME electrolyte include three parts, the peak around 52.0 ppm from FSI^- group, the peak around -80.0 ppm from $TFSI^-$ group and the peak around -154.0 ppm from $DFOB^-$ group. Compared with the peak in single salt electrolytes, the peaks at around 52.0 ppm and -154.0 ppm move downfield, yet the peak around -80.0 ppm moves the up-field, indicating that different solvation structures of salt anion groups exist in the HE-DME electrolyte.
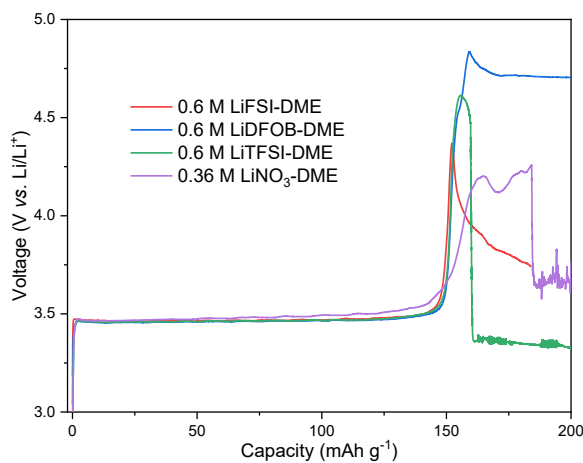
Fig. S3.4. The oxidation and reduction stability of the single salt electrolytes. Galvanostatic charge profiles of Li||LiFePO$_4$ cells with different electrolytes at a current density of 0.02C. A charge cut-off voltage of 5.0 V was set to study the oxidation stability of electrolytes. LiFePO$_4$ cathode was chosen as it does not show the extra redox reaction from Fe^{2+} to Fe^{3+} on being charged to above ~3.8 V.
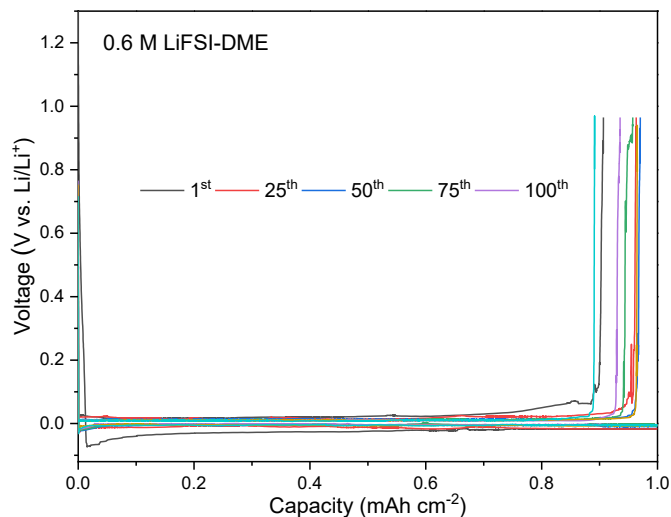
Fig. S3.5. Galvanostatic Li plating/stripping profiles of Li‖Cu cell with 0.6 M LiFSI-DME electrolyte. The cells were plated for 2 h at 0.5 mA cm^{-2} followed by stripping to a cut-off voltage of 1.0 V vs. Li/Li$^+$.

3
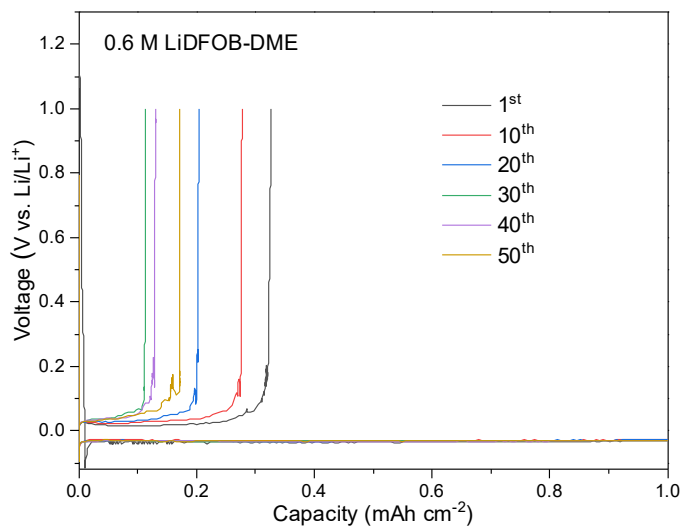
Fig. S3.6. Galvanostatic Li plating/stripping profiles of Li‖Cu cell with 0.6 M LiDFOB-DME electrolyte. The cells were plated for 2 h at 0.5 mA cm^{-2} followed by stripping to a cut-off voltage of 1.0 V vs. Li/Li$^+$.
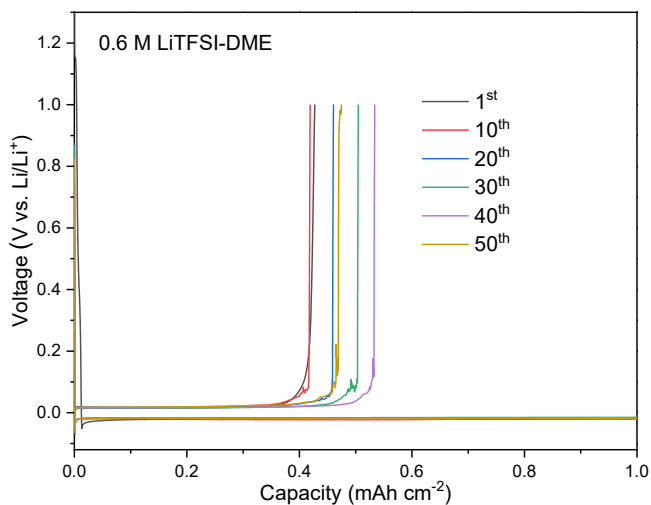
Fig. S3.7. Galvanostatic Li plating/stripping profiles of Li||Cu cell with 0.6 M LiTFSI-DME electrolyte. The cells were plated for 2 h at 0.5 mA cm^{-2} followed by stripping to a cut-off voltage of 1.0 V vs. Li/Li$^+$.
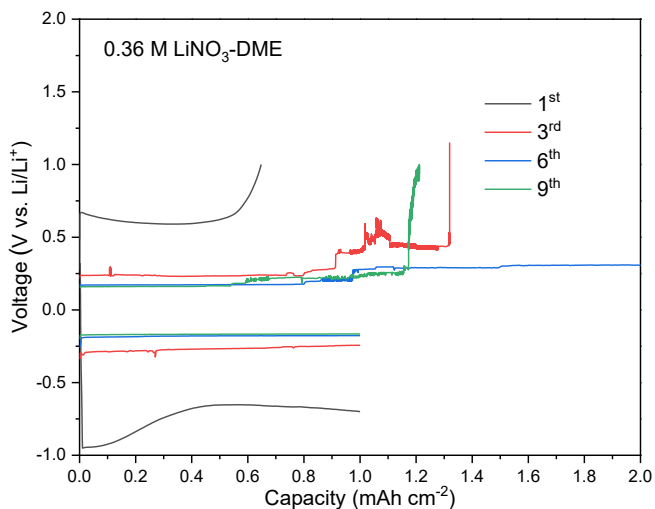
Fig. S3.8. Galvanostatic Li plating/stripping profiles of Li||Cu cell with 0.36 M LiNO$_3$-DME electrolyte. The cells were plated for 2 h at 0.5 mA cm^{-2} followed by stripping to a cut-off voltage of 1.0 V vs. Li/Li$^+$.
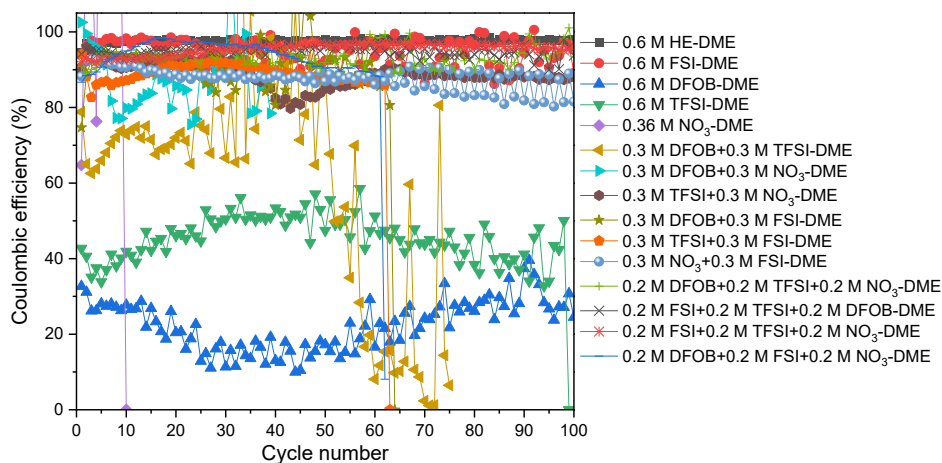
Fig. S3.9. Li plating/stripping Coulombic efficiency (CE) in Li||Cu cells using various electrolytes. Li was electrodeposited at 0.5 mA cm^{-2} to a total capacity of 1 mAh cm^{-2}.

3
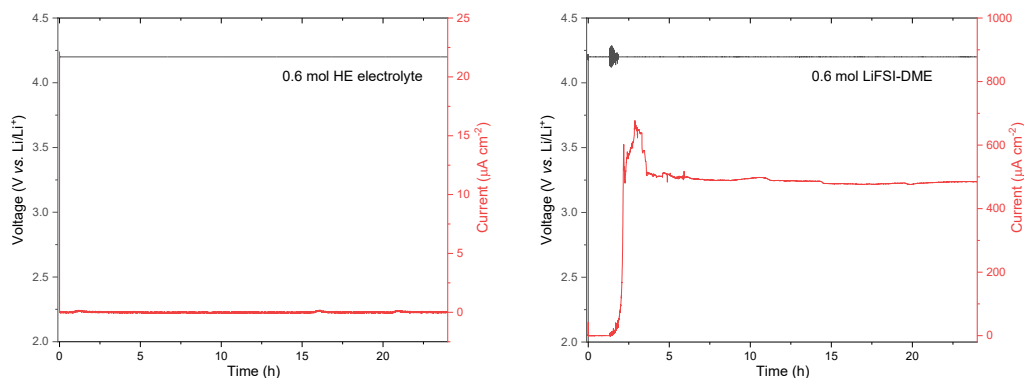
Fig. S3.10. Potentiostatic charge profiles of as-prepared 0.6 M HE-DME electrolyte and 0.6 M LiFSI-DME electrolytes. Li||Al cells were used to study the corrosion current of Al foil in different electrolytes at the polarization potential of 4.2 V vs. Li/Li$^+$ for 24 h. In the 0.6 M LiFSI-DME electrolyte, the anodic current dramatically increased after a short time of about 2 h, suggesting a rapid dissolution of Al at high potential, whereas the HE-DME electrolyte showed a stable anodic current under the same condition.
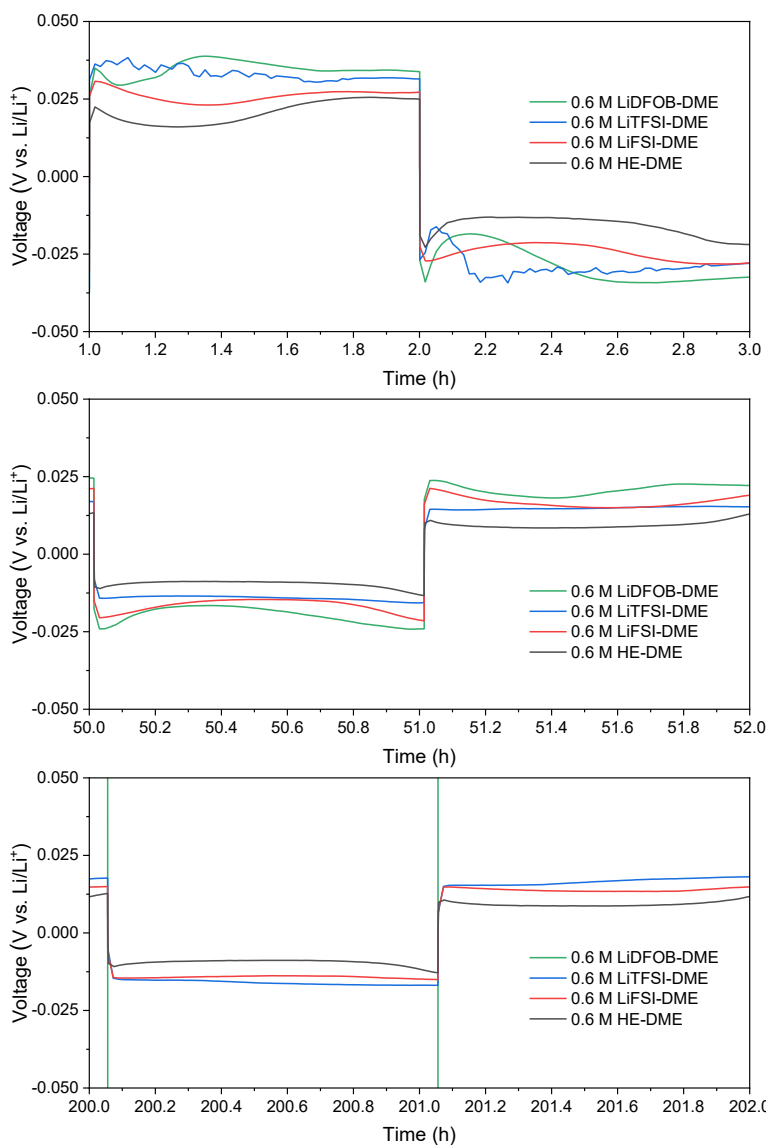
Fig. S3.11. Enlarged voltage profiles of symmetric Li||Li cells cycled in different electrolytes. The Li||Li symmetric were cycled under a current density of 1 mA cm^{-2} with each plating/stripping time of 1 h.
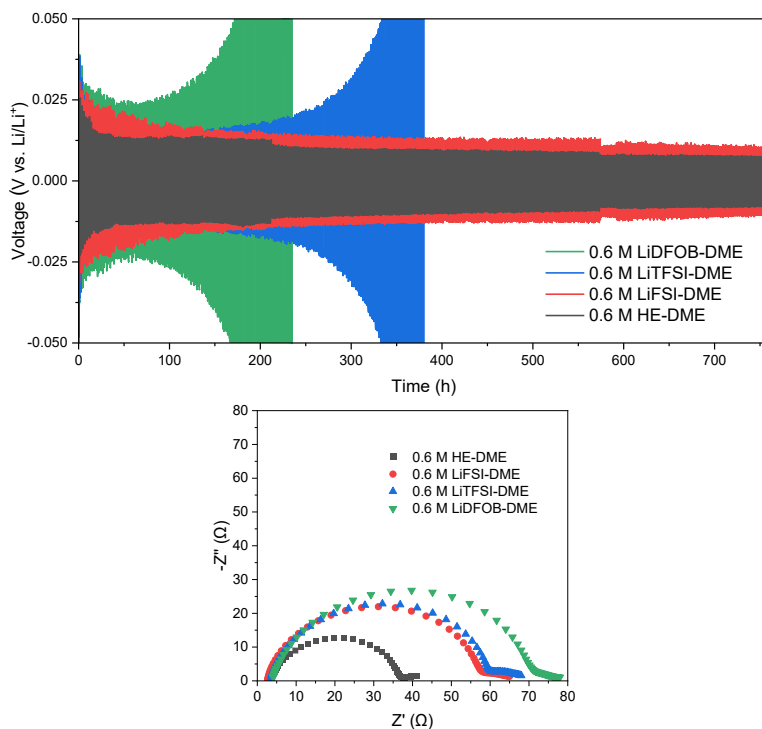
Fig. S3.12. Evolution of voltage profiles of symmetric Li‖Li cells and electrochemical impedance spectra (EIS) in different electrolytes. The Li‖Li symmetric cells were cycled under a current density of 1 mA cm^{-2} with each plating/stripping time of 1 h.
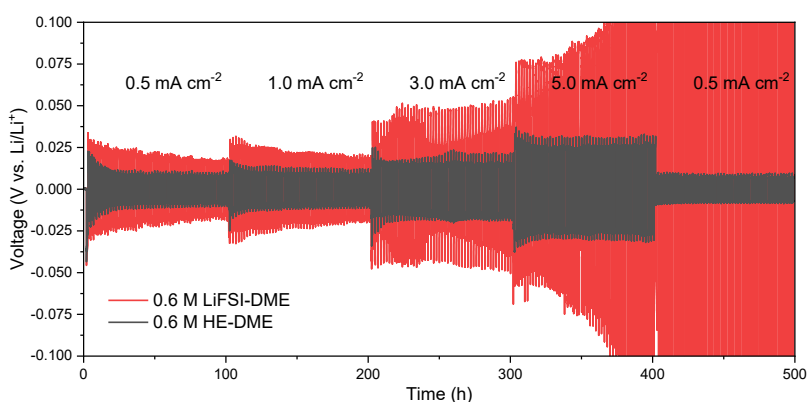
Fig. S3.13. Rate profile for symmetric cells with different electrolytes. Li‖Li cells at current density from 0.5 to 5 mA cm^{-2} with each plating/stripping time of 1 h.
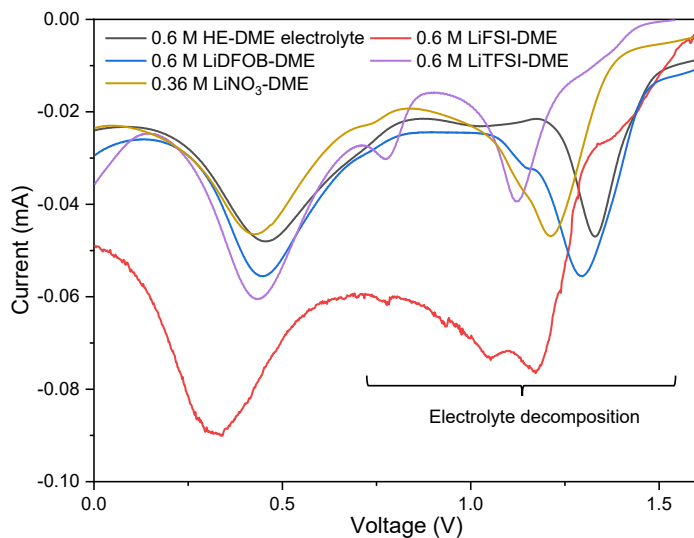
Fig. S3.14. Cyclic voltammetry (CV) curves of Li||Cu cells. Cells were tested at a scan rate of 0.8 mV s^{-1} from -0.1 to 2.5 V vs. Li/Li^{+}.
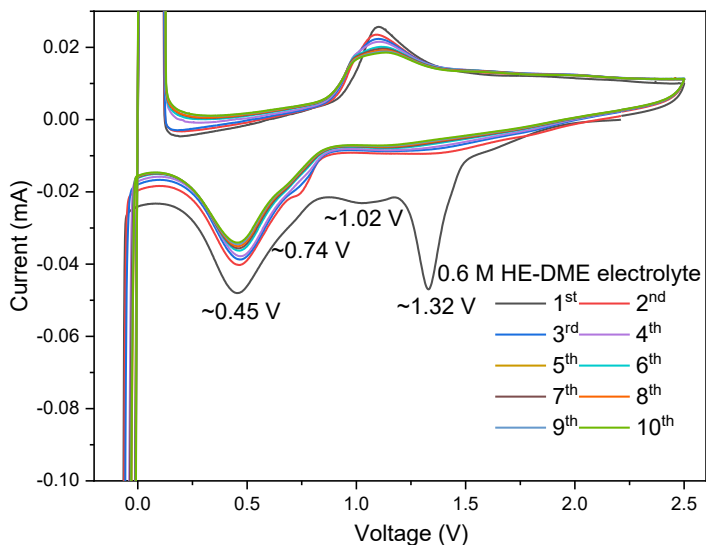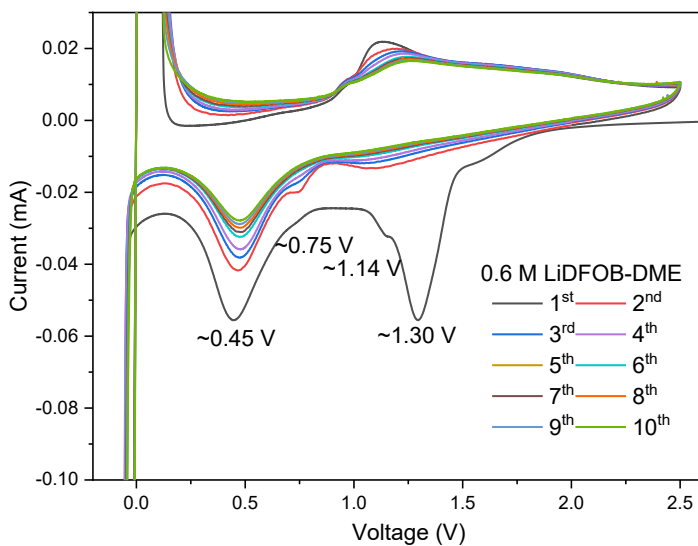

Fig. S3.15. CV curves of Li||Cu cell in 0.6 M HE-DME electrolyte. A scan rate of 0.8 mV s^{-1} was applied with a voltage range from -0.1 to 2.5 V vs. Li/Li^{+}.
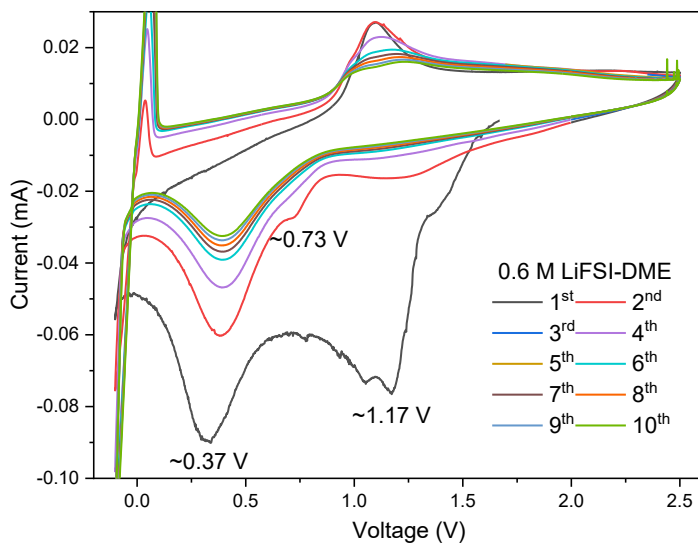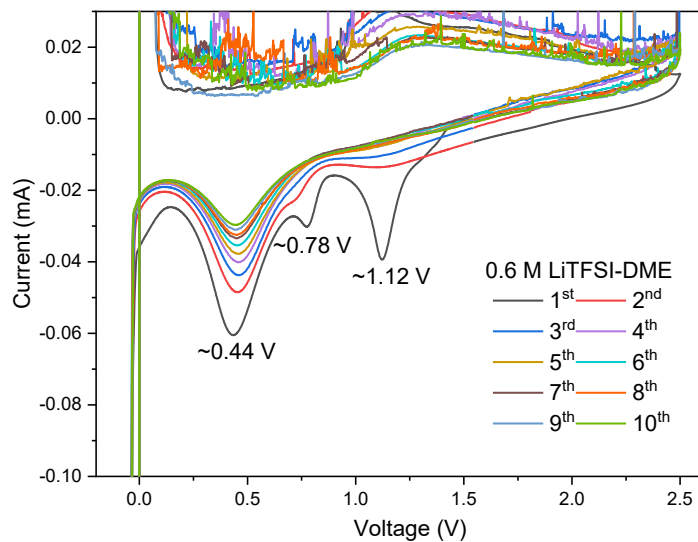
Fig. S3.16. CV curves of Li||Cu cell in 0.6 M LiFSI-DME electrolyte. A scan rate of 0.8 mV s^{-1} was applied with a voltage range from -0.1 to 2.5 V vs. Li/Li$^+$.
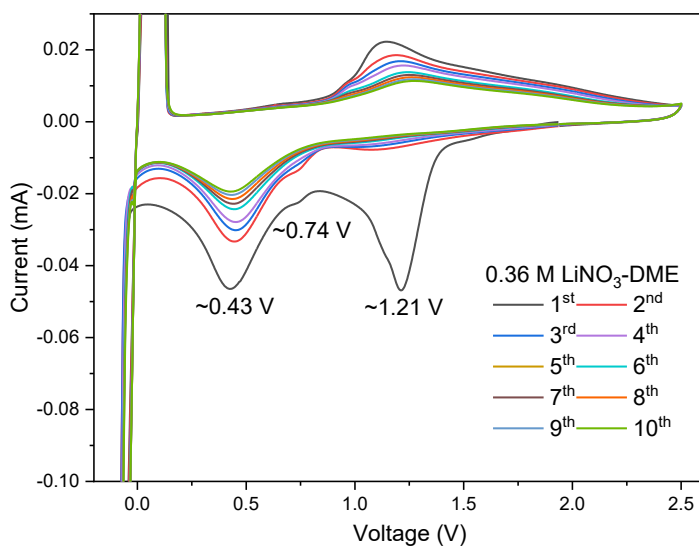

Fig. S3.17. CV curves of Li||Cu cell in 0.6 M LiDFOB-DME electrolyte. A scan rate of 0.8 mV s^{-1} was applied with a voltage range from -0.1 to 2.5 V vs. Li/Li$^+$.
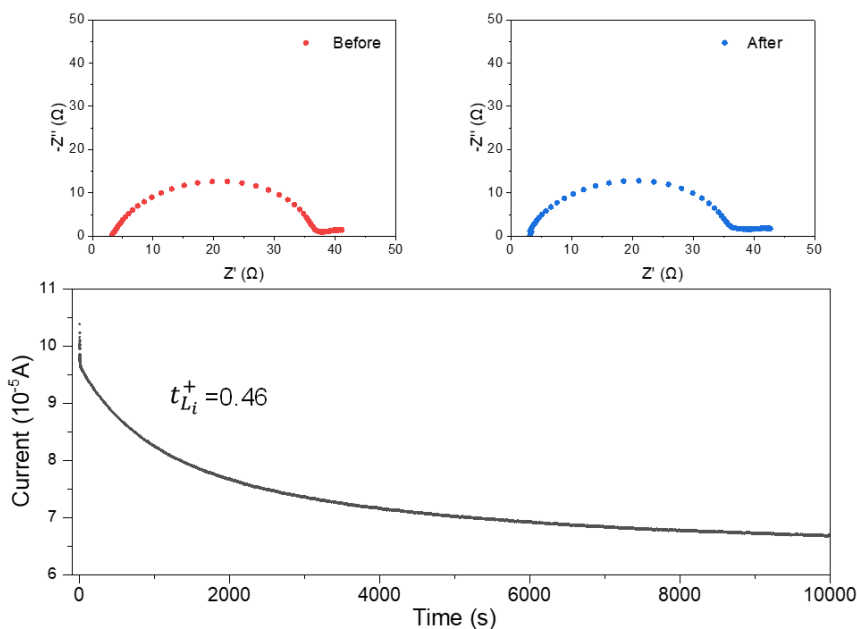
Fig. S3.18. CV curves of Li||Cu cell in 0.6 M LiTFSI-DME electrolyte. A scan rate of 0.8 mV s^{-1} was applied with a voltage range from -0.1 to 2.5 V vs. Li/Li^{+}.

Fig. S3.19. CV curves of Li||Cu cell in 0.36 M LiNO₃-DME electrolyte. A scan rate of 0.8 mV s^{-1} was applied with a voltage range from -0.1 to 2.5 V vs. Li/Li^{+}.

Fig. S3.20. Chronoamperometry profile of symmetric Li||Li cells in HE-DME electrolyte under a polarization voltage of 10 mV. Insets showed the EIS before and after polarization.
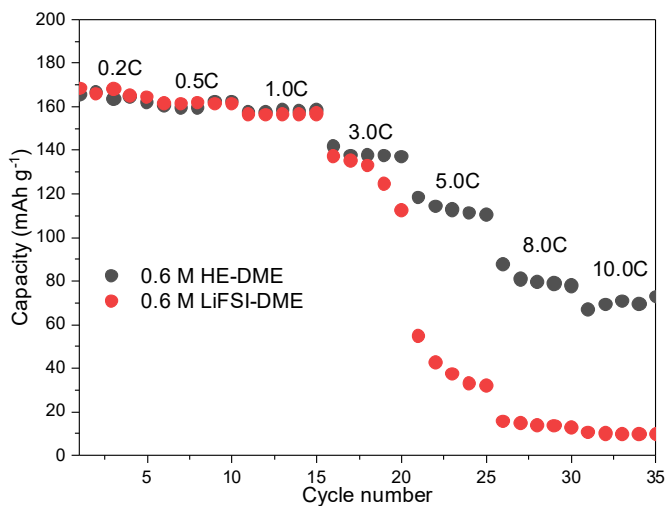

Fig. S3.21. Rate performance of Li||Li$_4$Ti$_5$O$_{12}$ cells. Cells were evaluated by increasing the charging/discharging rate from 0.2 to 10.0C in different electrolytes within a voltage window of 1.0-2.5 V vs. Li/Li$^+$ (1C = 165 mA g^{-1}).
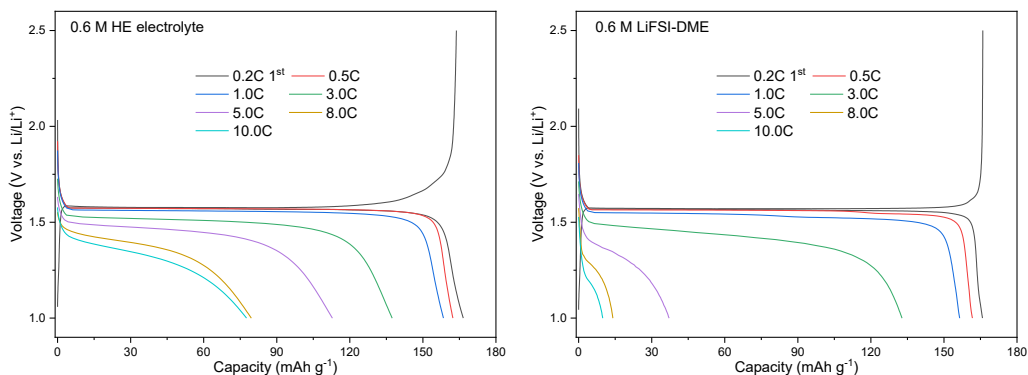
Fig. S3.22. Galvanostatic charge/discharge curves of Li∥Li$_4$Ti$_5$O$_{12}$ cells. Cells were evaluated by increasing the charging/discharging rate from 0.2 to 10.0 C in the 0.6 M HE-DME and 0.6 M LiFSI-DME electrolytes within a voltage window of 1.0-2.5 V vs. Li/Li$^+$.
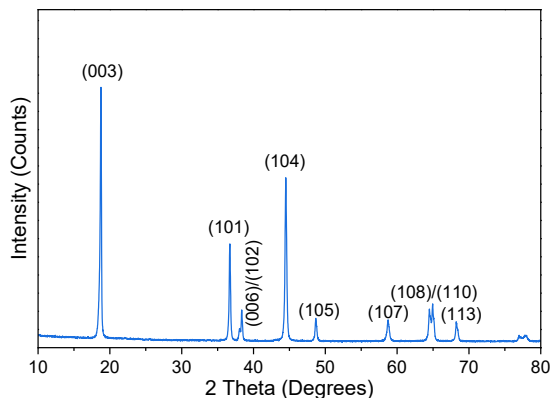

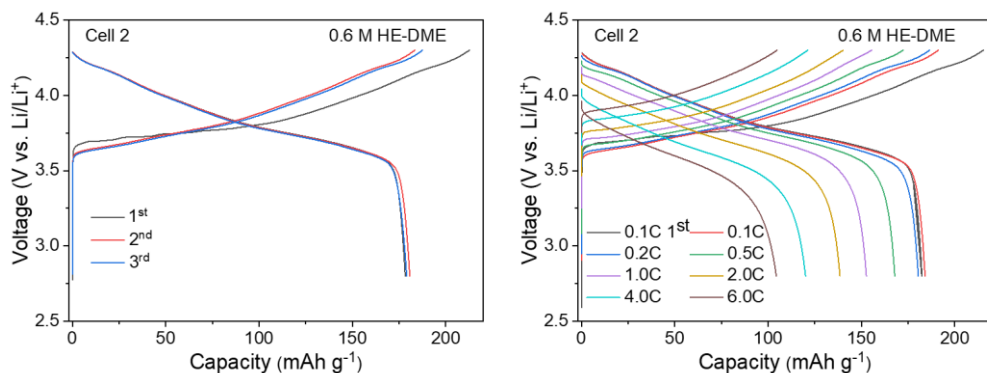**Fig. S3.23. X-ray diffraction pattern of the prepared NCM811 oxide.**

Fig. S3.24. Galvanostatic charge/discharge curves of Li∥NCM811 cells of 0.6 M HE-DME electrolyte. Cells were cycled at a rate of 0.1C (left) and different rates (right) in the voltage range of 2.8-4.3 V.
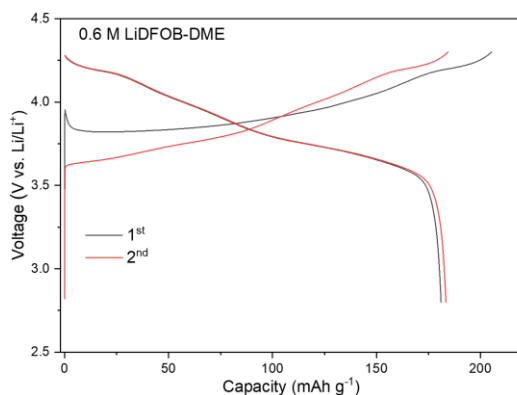
Fig. S3.25. Galvanostatic charge/discharge curves of Li‖NCM811 cells in 0.6 M LiDFOB-DME electrolyte. Cells were cycled within the voltage range of 2.8-4.3 V at a rate of 0.1C.

Fig. S3.26. Galvanostatic charge/discharge curves of Li‖NCM811 cells in 0.6 M LiTFSI-DME electrolyte. Cells were cycled within the voltage range of 2.8-4.3 V at a rate of 0.1C.
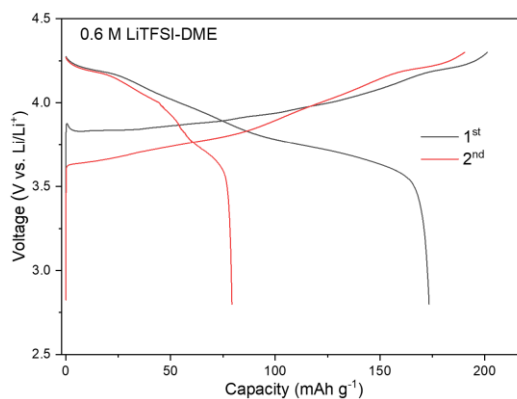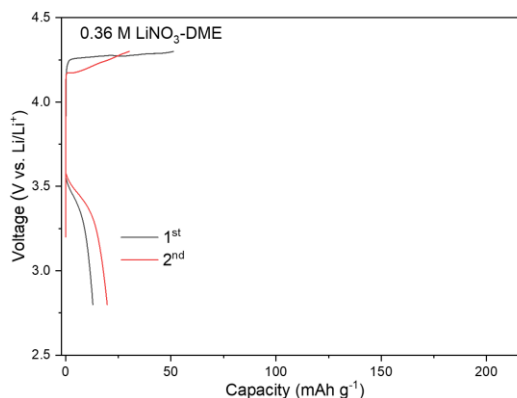

Fig. S3.27. Galvanostatic charge/discharge curves of Li‖NCM811 cells in 0.36 M LiNO₃-DME electrolyte. Cells were cycled within the voltage range of 2.8-4.3 V at a rate of 0.1C.
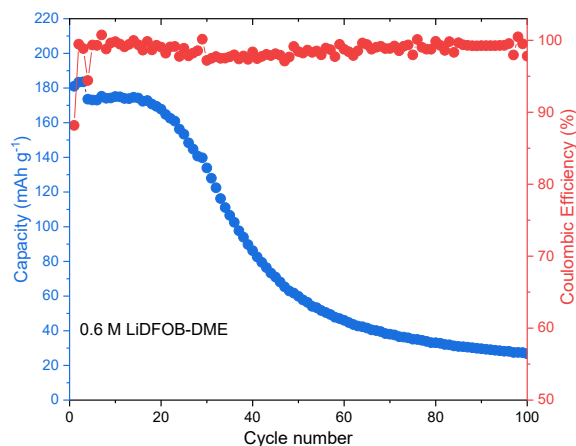
Fig. S3.28. Cycling performance of Li||NCM811 cells with 0.6 M LiDFOB-DME electrolyte. Cells were cycled between 2.8 and 4.3 V at a 0.1C rate for three cycles before cycling at a 0.333C rate.
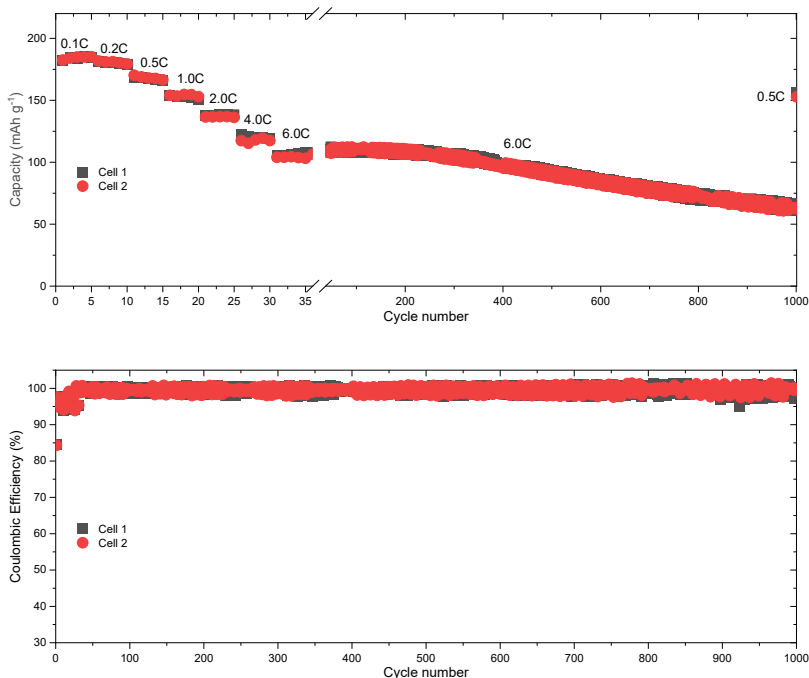
Fig. S3.29. Electrochemical rate capabilities and CE of Li||NCM811 cells in the 0.6 M HE-DME electrolyte. Cells were cycled between 2.8 and 4.3 V from 0.1 to 6.0C, after which long-term cycling at 6.0C was performed up to 1000 cycles, and then a recovery cycle of 0.5C was set.

Fig. S3.30. CE of Li‖NCM811 cells in the 0.6 M HE-DME electrolyte. Two representative cells are shown.

Fig. S3.31. EIS of Li‖NCM811 cells in 0.6 M HE-DME electrolyte before and after cycling.
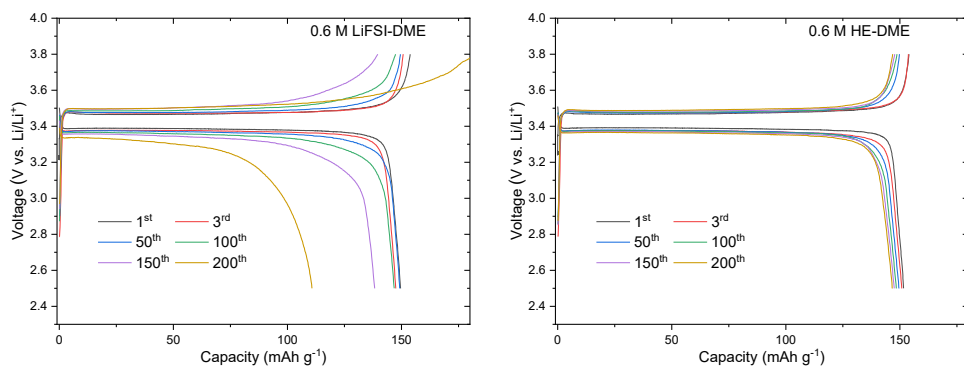
Fig. S3.32. Galvanostatic charge/discharge curves of Li‖LiFePO$_4$ cells in electrolytes. Cells were cycled within the voltage range of 2.5-3.8 V at a rate of 0.2C for three cycles before cycling at a 1.0C rate.
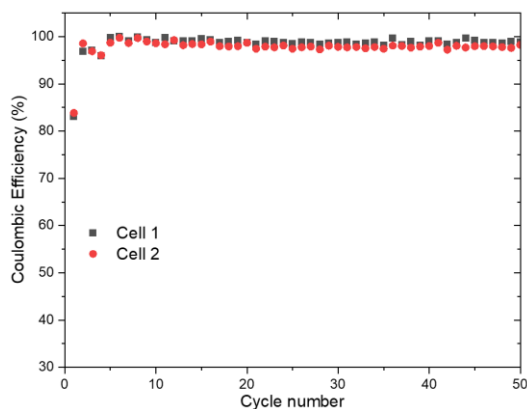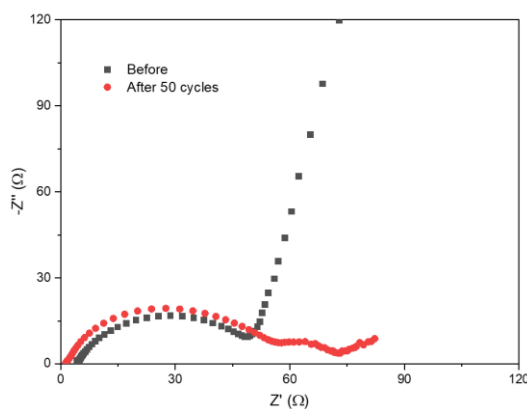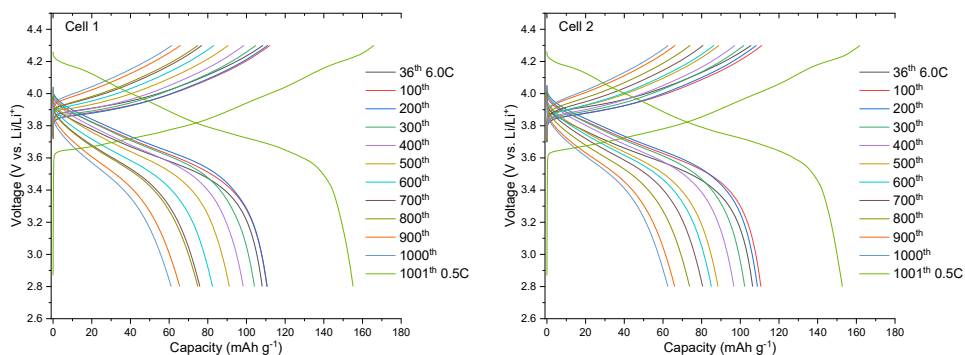
Fig. S3.33. Galvanostatic charge/discharge curves of the Li||NCM811 cells in the 0.6 M HE-DME electrolyte at a rate of 6.0C. The 1001th cycle was a recovery cycle performed at 0.5C.
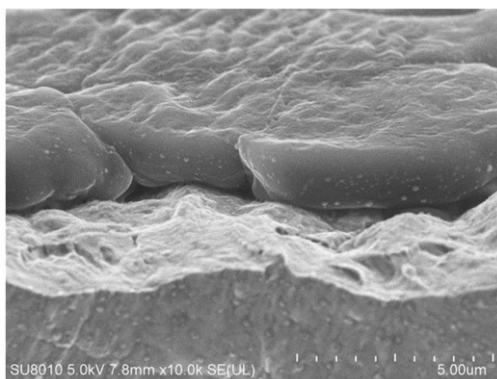
Fig. S3.34. Scanning electron microscopy (SEM) image of deposited Li metal in the 0.6 M HE-DME electrolyte from a cross-sectional view. Cells were cycled at a current density of 0.5 mA cm^{-2} to the capacity of 1 mAh cm^{-2} on Cu foils.
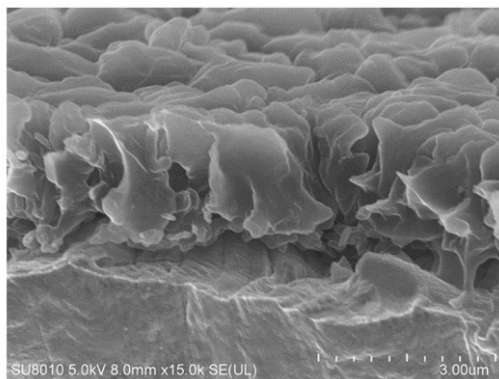
Fig. S3.35. SEM image of deposited Li metal in 0.6 M LiFSI-DME electrolyte from a cross-sectional view. Cells were cycled at a current density of 0.5 mA cm^{-2} to a capacity of 1 mAh cm^{-2} on Cu foils.
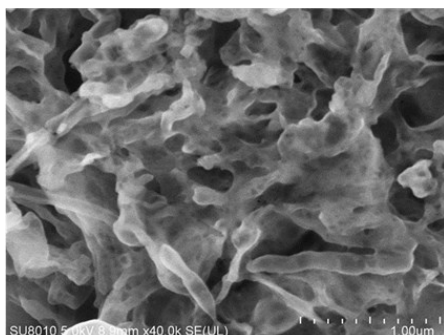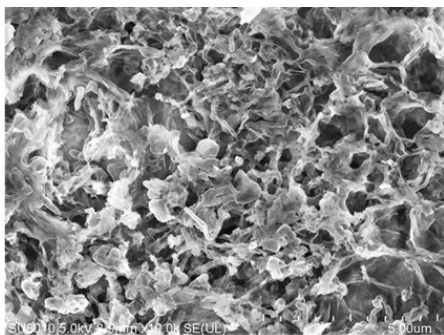
Fig. S3.36. SEM images of stripped Li metal in 0.6 M LiFSI-DME electrolyte from a top view. Cells were cycled at a current density of 0.5 mA cm^{-2} with plating for 2 h followed by stripping to a cut-off voltage of 1.0 V vs. Li/Li$^+$.
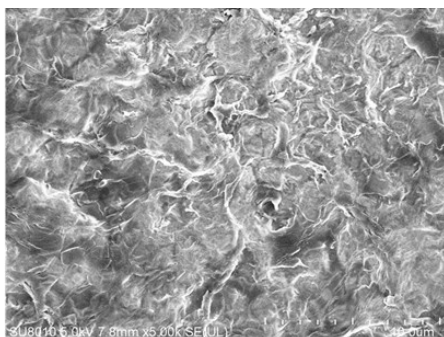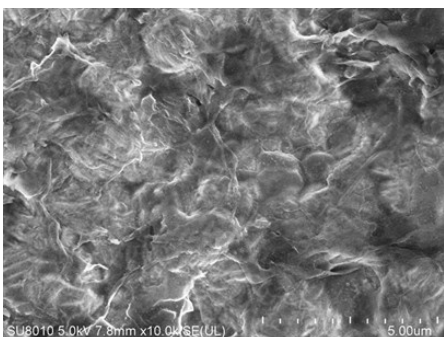
Fig. S3.37. SEM images of stripped Li metal in 0.6 M HE-DME electrolyte from a top view. Cells were cycled at a current density of 0.5 mA cm^{-2} with plating for 2 h followed by stripping to a cut-off voltage of 1.0 V vs. Li/Li$^+$.
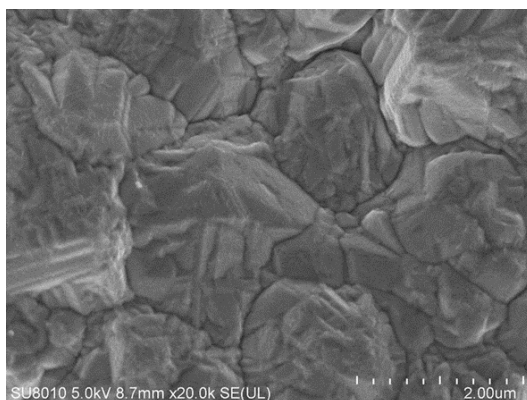
Fig. S3.38. SEM image of Cu foil. Top view image of bare Cu foil used for current collector.

Cu

Plating 36s

Plating 72s

77.0 nm

-110.0 nm

2.0 um

160.0 nm

-160.0 nm

2.0 um

190.0 nm

-210.0 nm

2.0 um

Plating 144s

Plating 216s

Plating 360s

210.0 nm

-240.0 nm

2.0 um

260.0 nm

-275.0 nm

2.0 um

350.0 nm

-310.0 nm

2.0 um

Plating 720s

Plating 1080s

Plating 1800s

460.0 nm

-430.0 nm

2.0 um

540.0 nm

-520.0 nm

2.0 um

560.0 nm

-555.0 nm

2.0 um

Plating 2520s

580.0 nm

-610.0 nm

2.0 um
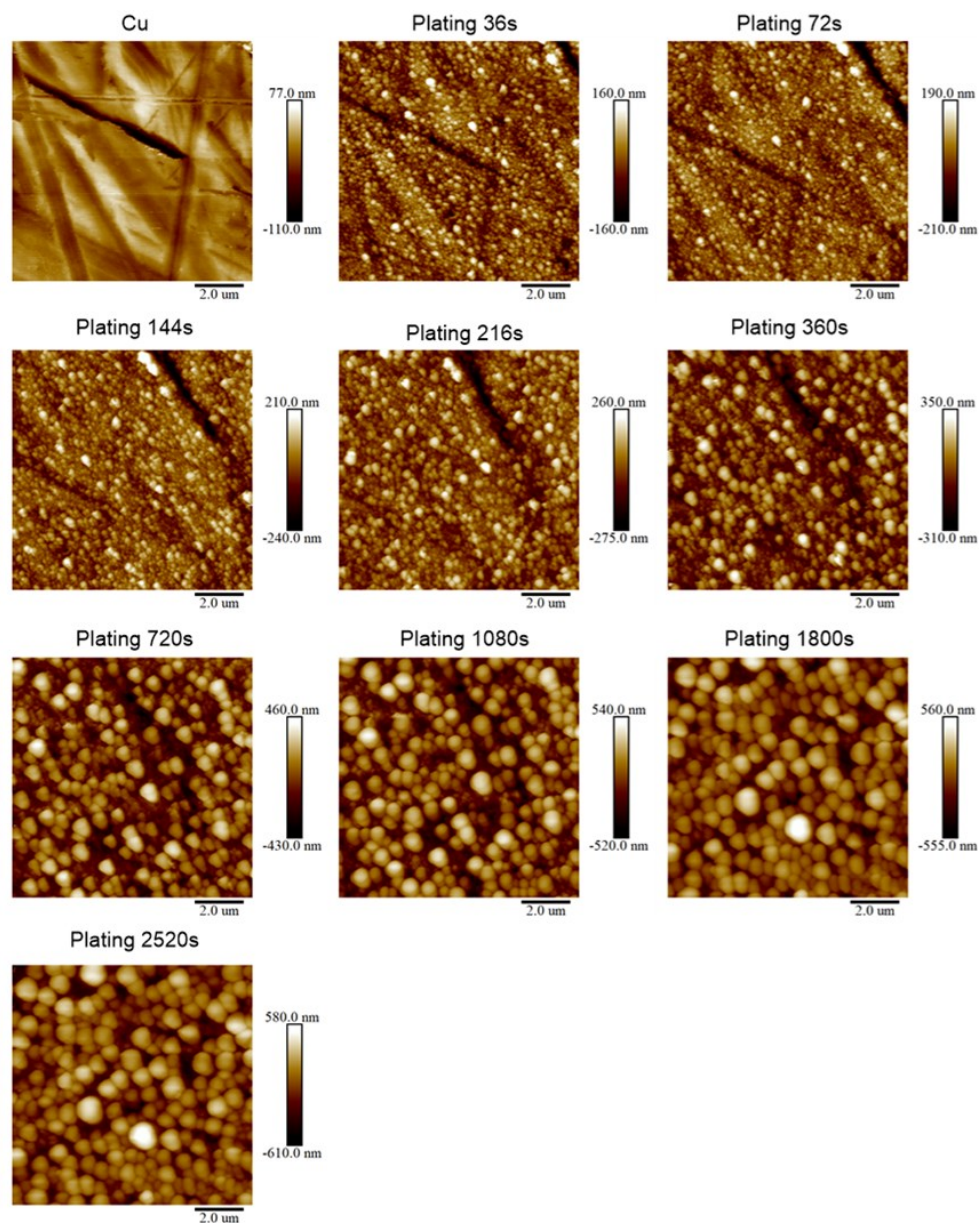
Fig. S3.39. In-situ electrochemical atomic force microscopy (AFM) images of deposited Li metal in 0.6 M LiFSI-DME electrolyte. During the electrochemical measurement, cells were discharged at a constant current density of 0.5 mA cm^{-2} in which the images of the Li plating process were collected at different times.
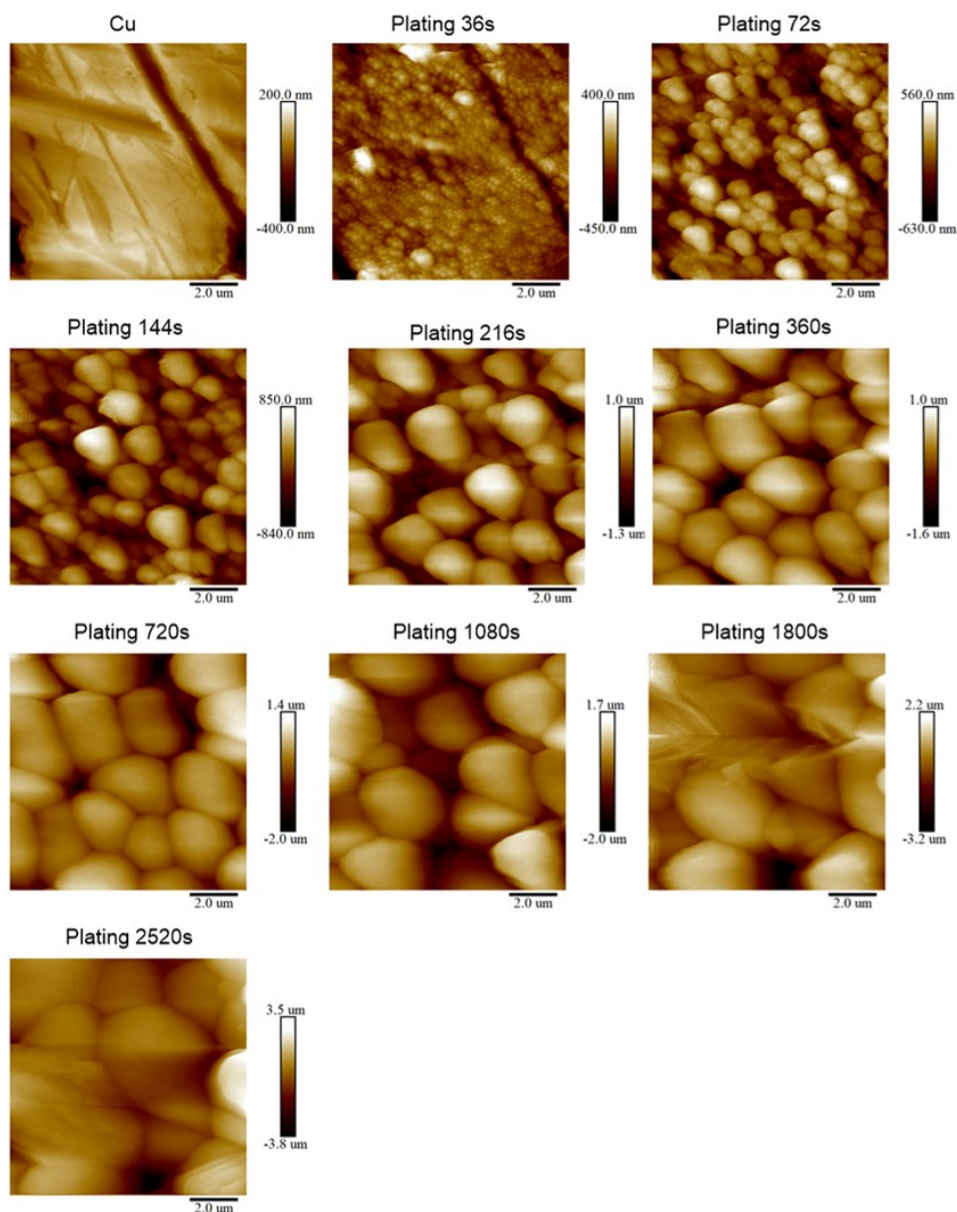
Fig. S3.40. In-situ electrochemical AFM images of deposited Li metal in 0.6 M HE-DME electrolyte. During the electrochemical measurement, cells were discharged at a constant current density of 0.5 mA cm^{-2} in which the images of the Li plating process were collected at different times.

Plating 5400 s

3.4 um

-3.7 um

2.0 um
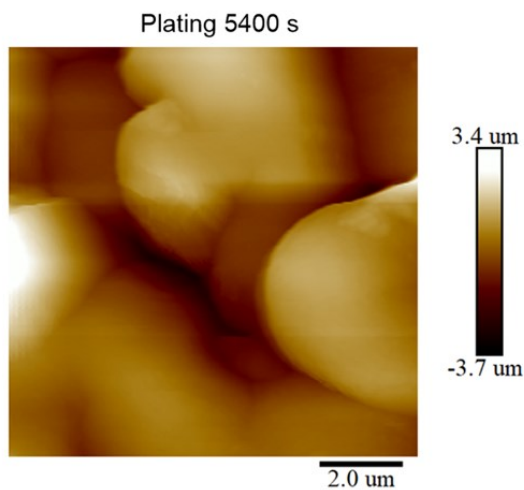
Fig. S3.41. In-situ electrochemical AFM image of deposited Li metal in 0.6 M HE-DME electrolyte. Image of deposited Li metal was collected after 5400 s of deposition.

0.5 µm

0.5 µm
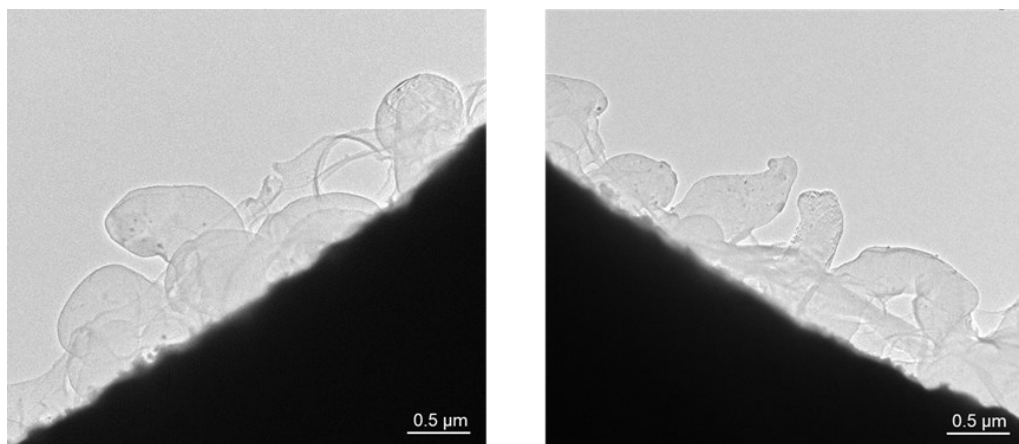
Fig. S3.42. Microstructure of deposited Li metal from cryo-transmission electron microscopy (Cryo-TEM) using the 0.6 M HE-DME electrolyte.
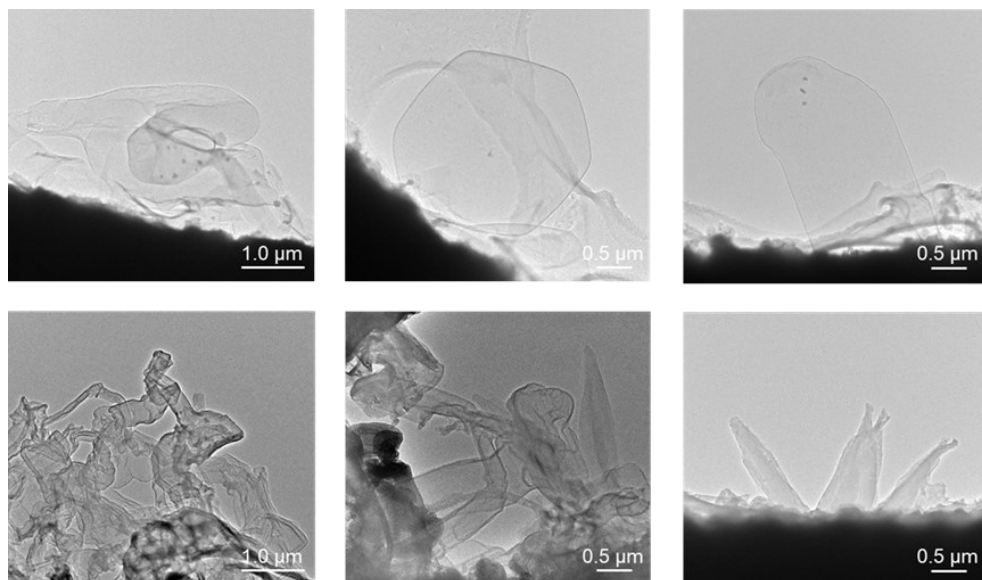
Fig. S3.43. Microstructure of deposited Li metal from cryo-TEM images recorded from different sites. The top images were from the 0.6 M HE-DME electrolyte and the bottom were from the 0.6 M LiFSI-DME electrolyte.
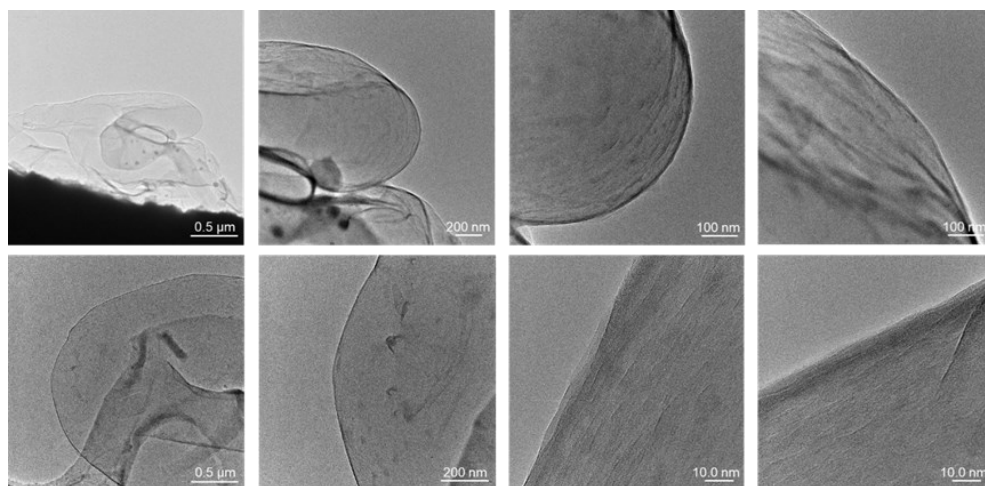
Fig. S3.44. Microstructure of deposited Li metal from cryo-TEM images recorded from different sites. Images were recorded on Li metal deposited in the 0.6 M HE-DME electrolyte.
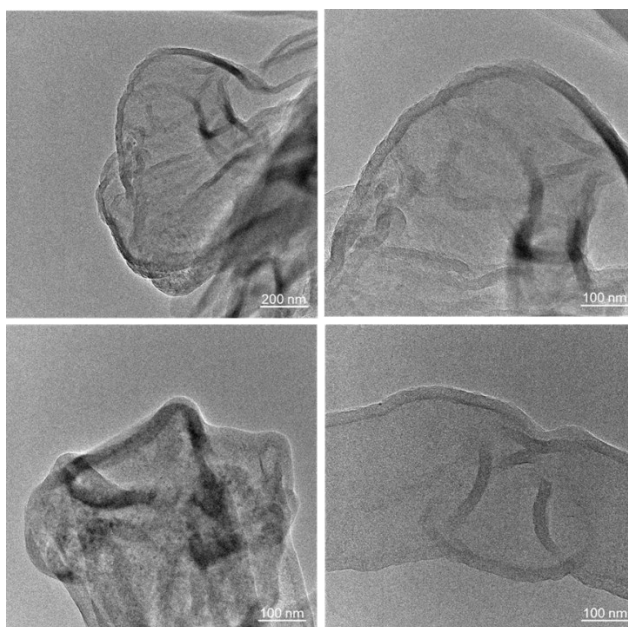
Fig. S3.45. Microstructure of deposited Li metal from cryo-TEM images recorded from different sites. Images were recorded on using the 0.6 M LiFSI-DME electrolyte.
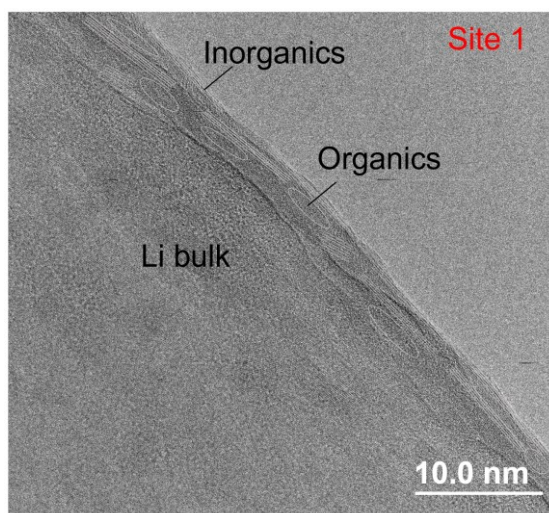
Fig. S3.46. Microstructure of deposited Li metal and interfacial phase from cryo-TEM images on using the 0.6 M HE-DME electrolyte. It shows the distribution of inorganics and organics in the SEI. Site 1 is shown in Fig. 3.2f.
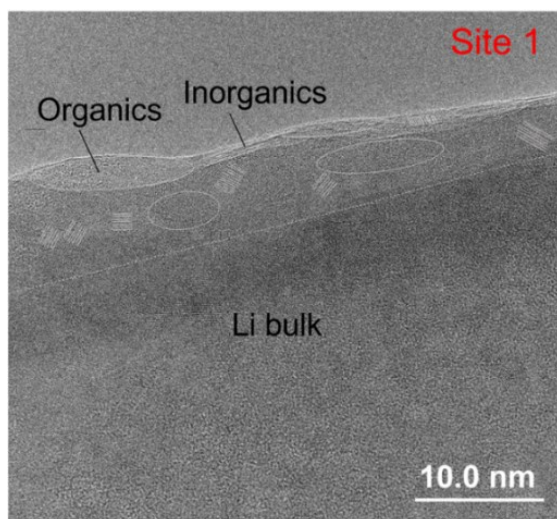
Fig. S3.47. Microstructure of deposited Li metal and interfacial phase from cryo-TEM images on using a 0.6 M LiFSI-DME electrolyte. It shows the distribution of inorganics and organics in the SEI. Site 1 is shown in Fig. 3.2h.

3
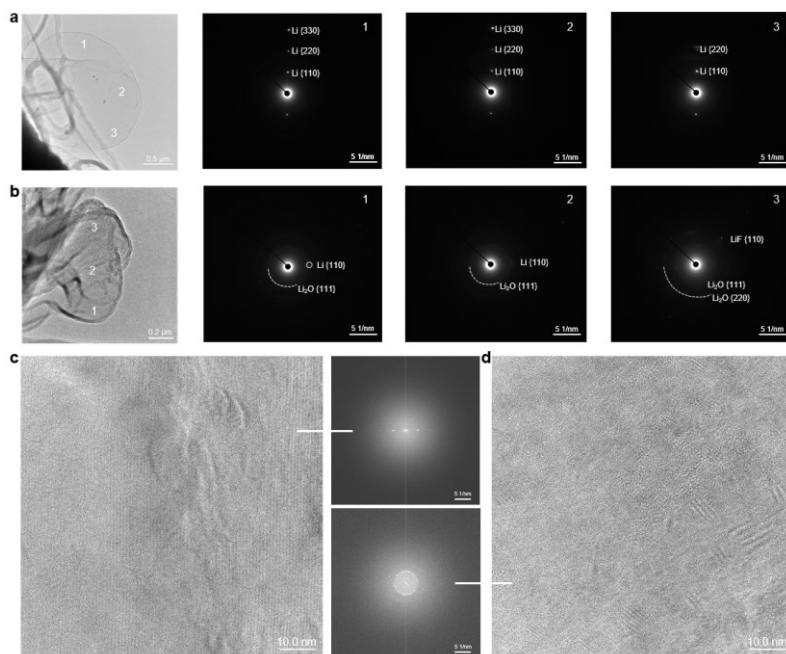
Fig. S3.48. Structures of deposited Li metal from cryo-TEM images. a, Images of deposited Li metal from 0.6 M HE-DME electrolyte and its selected area electron diffraction (SAED) at different sites. **b,** Images of deposited Li metal from 0.6 M LiFSI-DME electrolyte and its SAED at different sites. High-resolution TEM images of deposited Li metal in **c,** 0.6 M HE-DME electrolyte and **d,** 0.6 M LiFSI-DME electrolyte and the corresponding SAED.
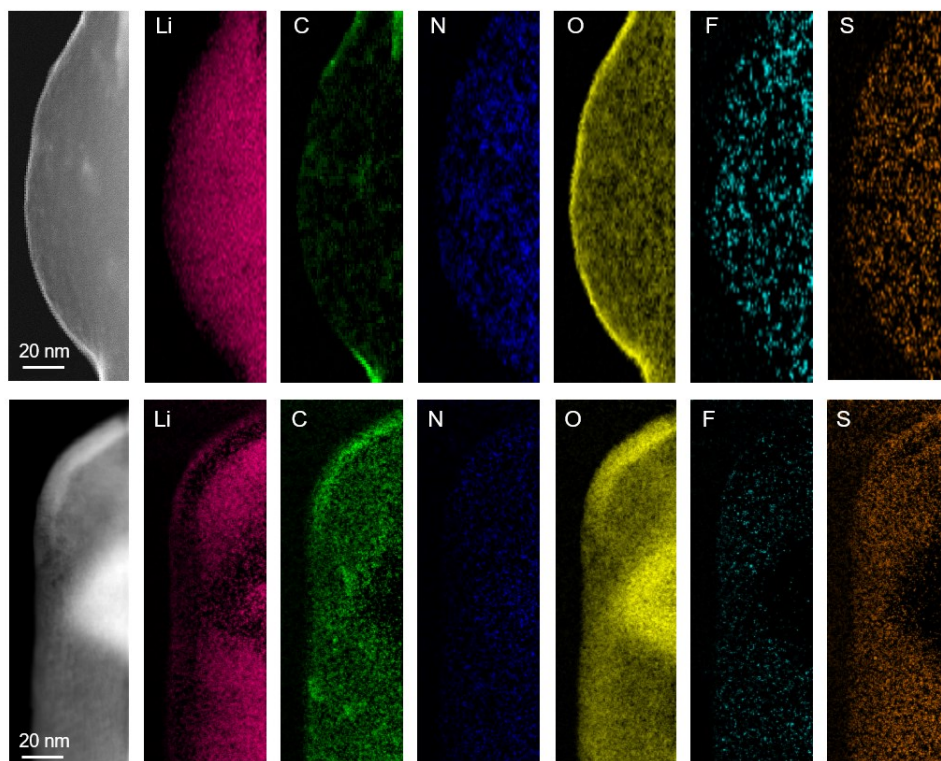
Fig. S3.49. Electron energy loss spectroscopy (EELS) mapping of deposited Li metal. Top panels are from the 0.6 M HE-DME electrolyte and the bottom are from the 0.6 M LiFSI-DME electrolyte.
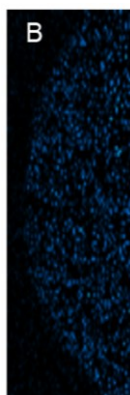
Fig. S3.50. Cryo-STEM EELS mapping of deposited Li metal. Image of B from LiDFOB salt in 0.6 M HE-DME electrolyte.
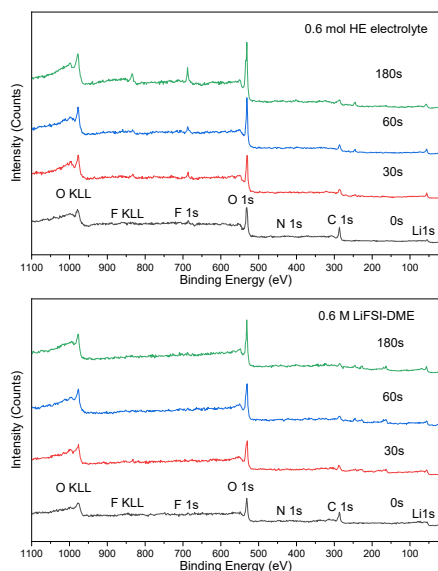
Fig. S3.51. Surveys of X-ray photoelectron spectroscopy (XPS) spectra of Li metal electrodes in 0.6 M HE-DME and 0.6 M LiFSI-DME electrolytes. Spectra were recorded after cycles from the surface of Cu electrodes at different depths.
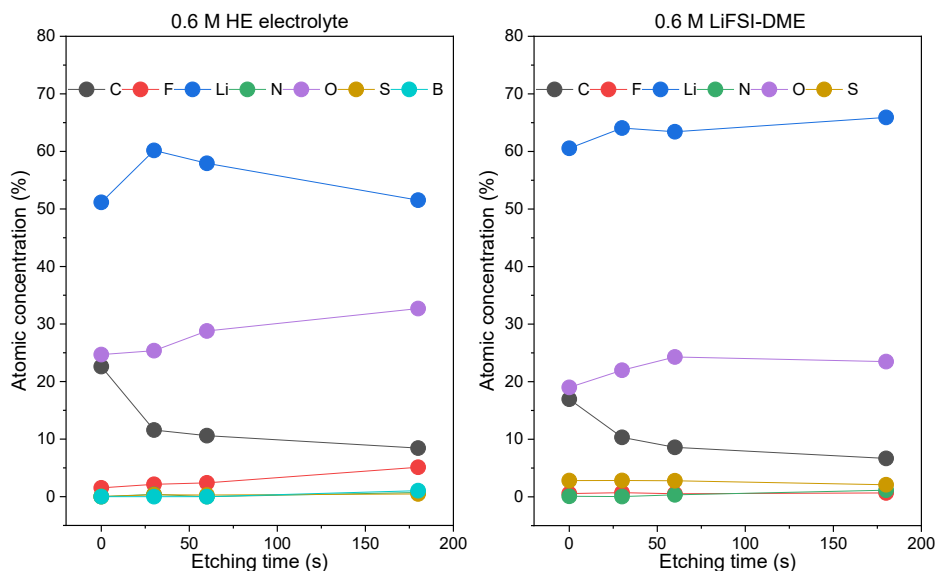
Fig. S3.52. Elemental composition on Cu electrodes from XPS spectra. The left panel is from the 0.6 M HE-DME electrolyte and the right panel is from the 0.6 M LiFSI-DME electrolyte.
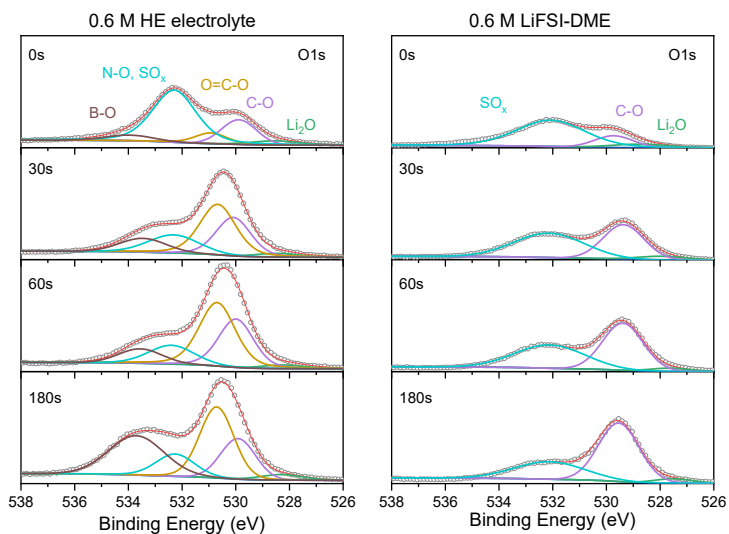
Fig. S3.53. O 1s spectra on the surface of the Cu electrodes. The left panel is from the 0.6 M HE-DME electrolyte and the right panel is from the 0.6 M LiFSI-DME electrolyte.
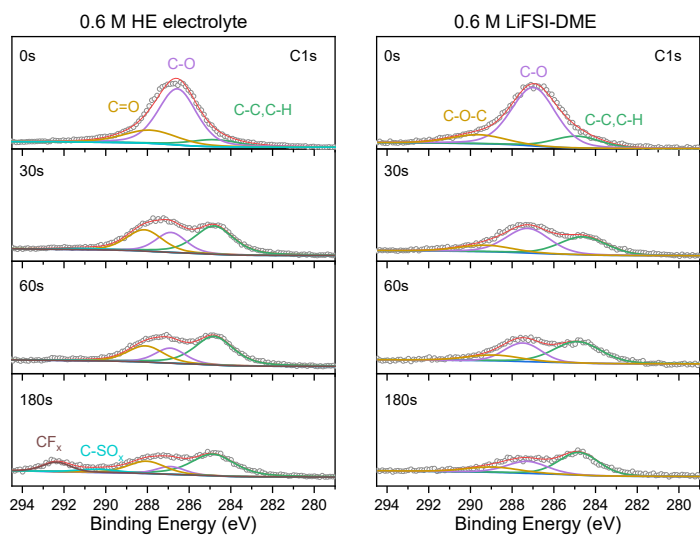
Fig. S3.54. C 1s spectra on the surface of the Cu electrodes. The left panel is from the 0.6 M HE-DME electrolyte and the right panel is from the 0.6 M LiFSI-DME electrolyte.
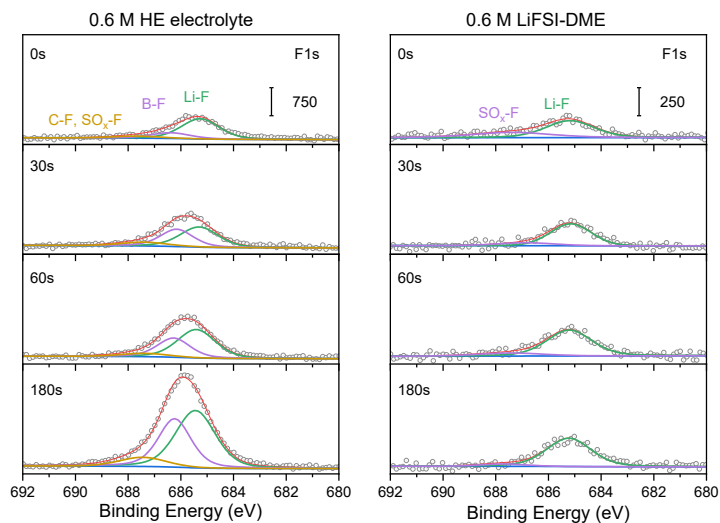
Fig. S3.55. F 1s spectra on the surface of the Cu electrodes. The left panel is from the 0.6 M HE-DME electrolyte and the right panel is from the 0.6 M LiFSI-DME electrolyte.
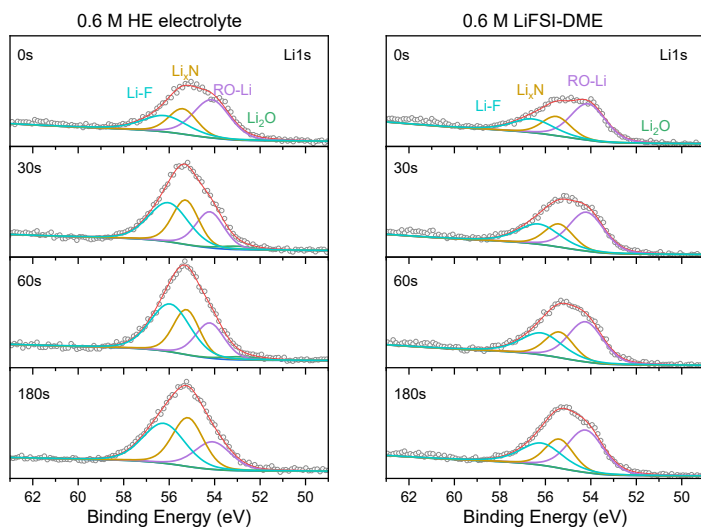
Fig. S3.56. Li 1s spectra on the surface of the Cu electrodes. The left panel is from the 0.6 M HE-DME electrolyte and the right panel is from the 0.6 M LiFSI-DME electrolyte.
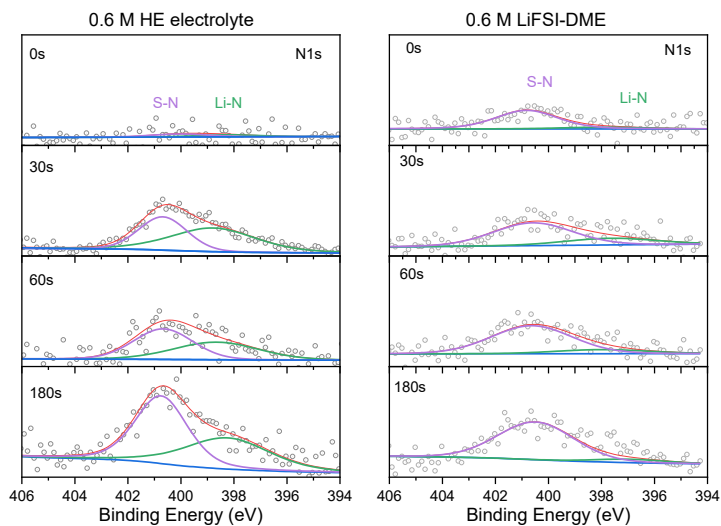
Fig. S3.57. N 1*s* spectra on the surface of the Cu electrodes. The left panel is from the 0.6 M HE-DME electrolyte and the right panel is from the 0.6 M LiFSI-DME electrolyte.
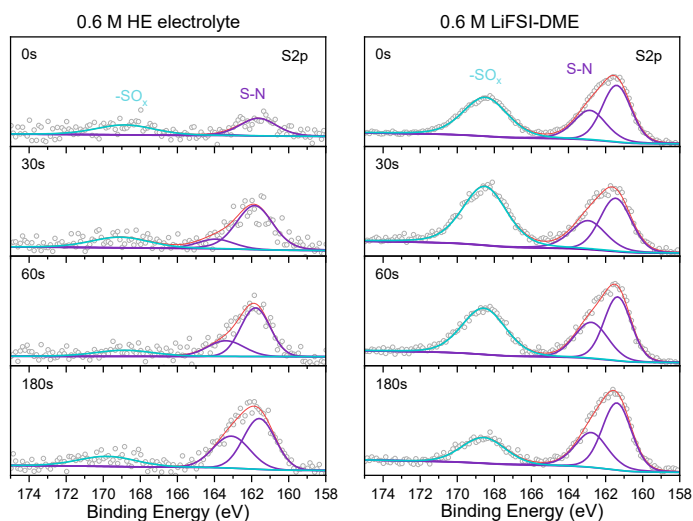
Fig. S3.58. S 2*p* spectra on the surface of the Cu electrodes. The left panel is from the 0.6 M HE-DME electrolyte and the right panel is from the 0.6 M LiFSI-DME electrolyte.
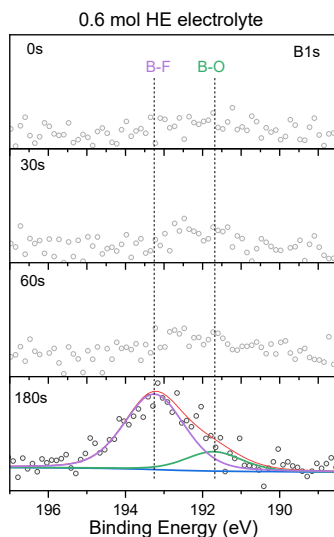
Fig. S3.59. B 1s spectra on the surface of the Cu electrode from the 0.6 M HE-DME electrolyte.
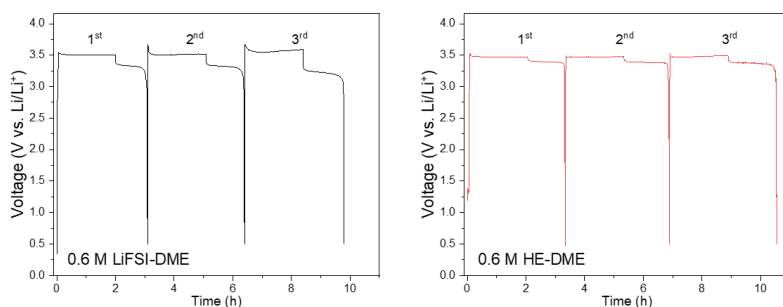
Fig. S3.60. Galvanostatic charge/discharge curves of Cu‖LiFePO₄ cells using 0.6 M LiFSI-DME and 0.6 M HE-DME electrolytes for the operando NMR tests.
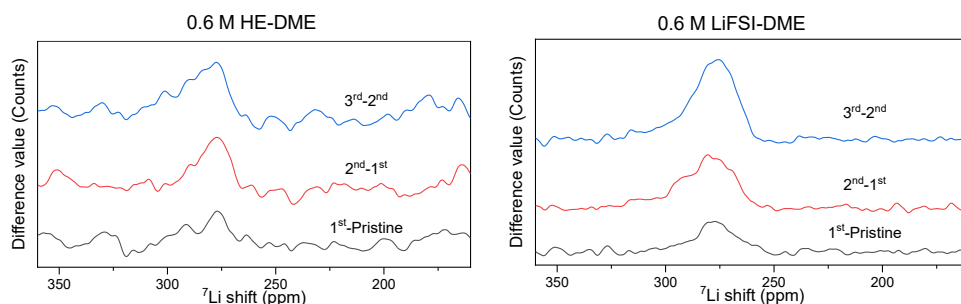
Fig. S3.61. ⁷Li solid-state NMR spectra after different cycles from 0.6 M HE-DME and 0.6 M LiFSI-DME electrolytes. These one-dimensional spectra are the difference from the stripped states for the first, second and third cycles.
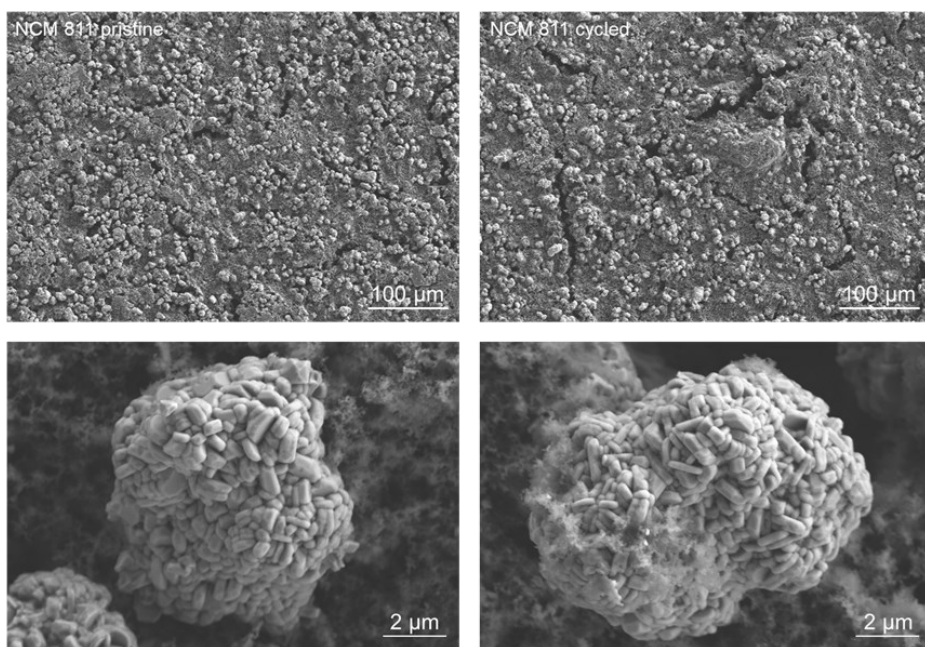
Fig. S3.62. SEM images of NCM811 cathode at different magnifications. The left panels are the pristine electrodes before cycling, and the right panels are the cycled electrodes. It is shown that secondary micron sized particles both uncycled and cycled consisted of densely packed primary sub-micron sized particles with a clean surface.
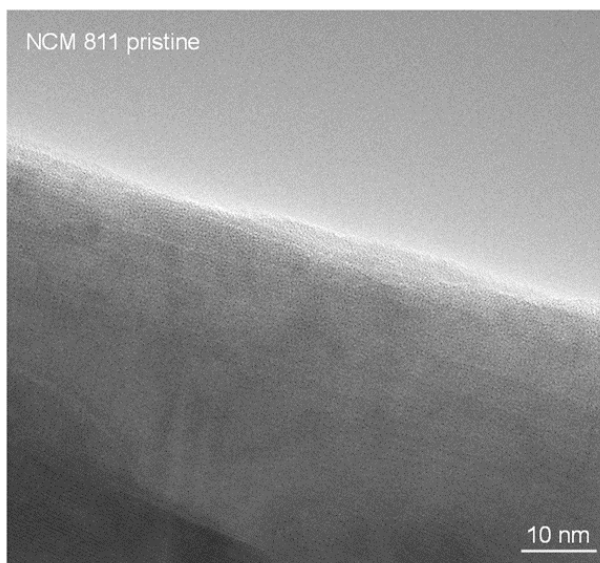
Fig. S3.63. TEM image of pristine NCM811 cathode. No interphase layer could be observed along the surface of the particle.
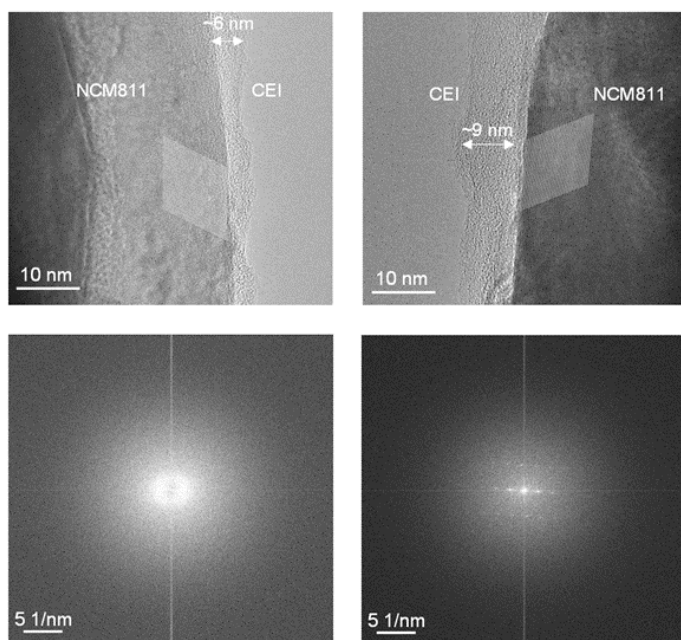
Fig. S3.64. Morphology, microstructure and composition of cathode electrolyte interphase. Cryo-TEM images of the cathode electrolyte interphase (CEI) from different NCM811 cathode particles. A clear CEI layer was observed along the surface of the particle with the thickness between 6 and 9 nm. The bottom panels show the fast Fourier transform images from the CEI area and the bulk area of the NCM811 cathode.
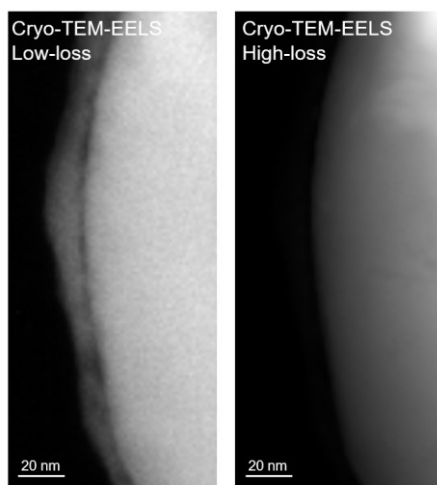
Fig. S3.65. Cryo-STEM EELS images of NCM811 cathode after 50 cycles. The left panel is from the low-loss area with high recognition of light elements and the right panel is from the high-loss area.
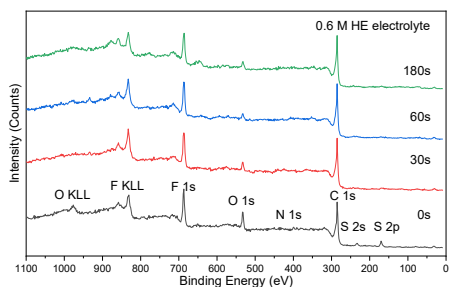
Fig. S3.66. Surveys of XPS spectra of the NCM811 electrode in the 0.6 M HE-DME electrolyte. Spectra were recorded at different depths.
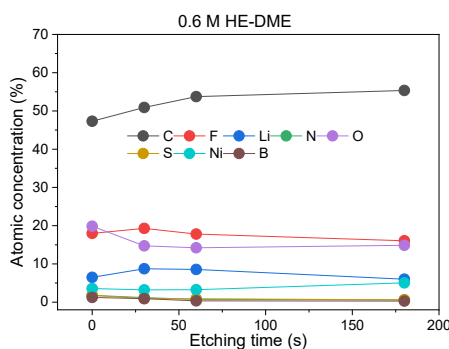
Fig. S3.67. Elemental composition on the surface of the NCM811 electrode from XPS spectra.
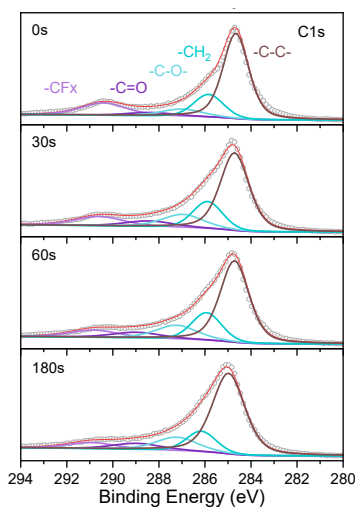
Fig. S3.68. C 1*s* spectra on the surface of the NCM811 cathode in the 0.6 M HE-DME electrolyte.
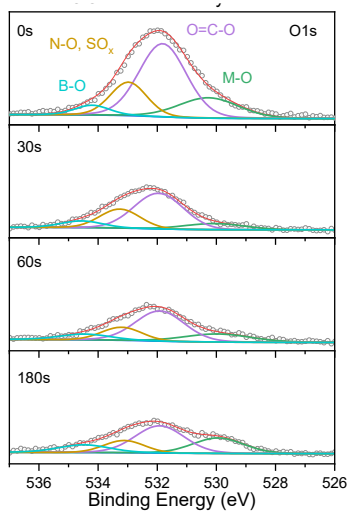
Fig. S3.69. O 1s spectra on the surface of the NCM811 cathode in the 0.6 M HE-DME electrolyte.
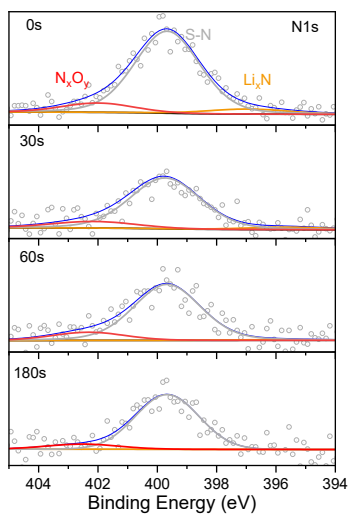
Fig. S3.70. N 1s spectra on the surface of the NCM811 cathode in the 0.6 M HE-DME electrolyte.
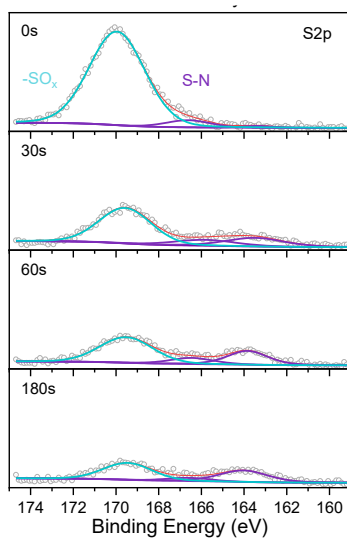
Fig. S3.71. S 2*p* spectra on the surface of the NCM811 cathode in the 0.6 M HE-DME electrolyte.

3
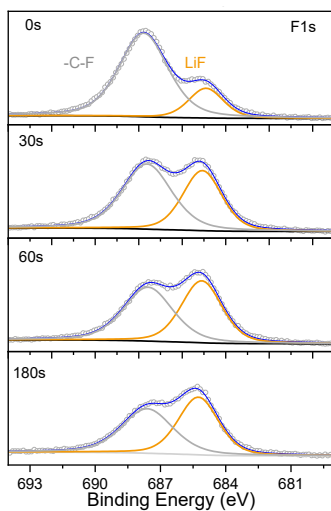
Fig. S3.72. F 1*s* spectra on the surface of the NCM811 cathode in the 0.6 M HE-DME electrolyte.
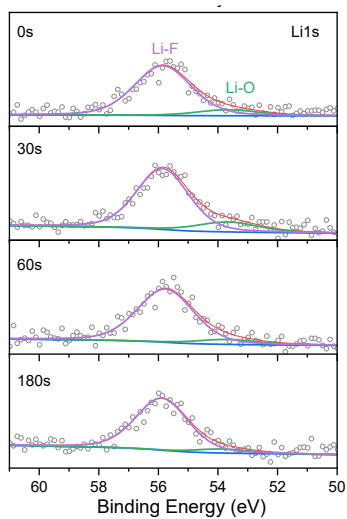
Fig. S3.73. Li 1*s* spectra on the surface of the NCM811 cathode in the 0.6 M HE-DME electrolyte.
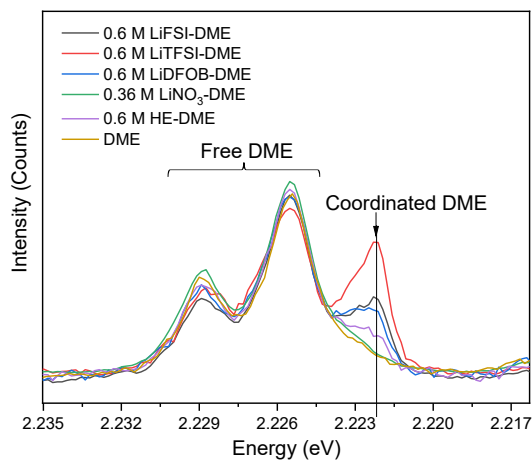
Fig. S3.74. Solvation structure from Raman spectra of 0.6 M HE-DME electrolyte and 0.6 M LiFSI-DME, 0.6 M LiTFSI-DME, 0.6 M LiDFOB-DME and 0.36 M LiNO₃-DME electrolytes.
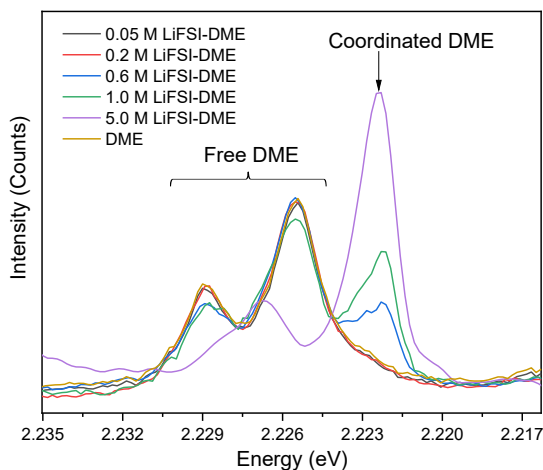
Fig. S3.75. Solvation structure from Raman spectra of 0.05 M, 0.2 M, 0.6 M, 1.0 M and 5.0 M LiFSI-DME electrolytes.
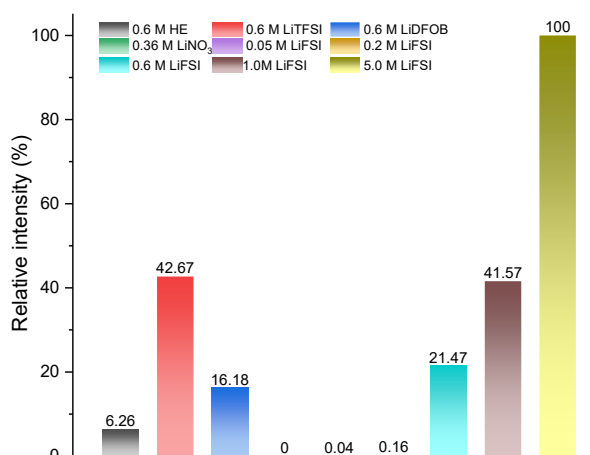
Fig. S3.76. Solvation structure from Raman spectra of different electrolytes. Compared with the other electrolytes, the 0.6 M HE-DME electrolyte shows relatively weak DME solvent coordination (the intensity of the peak at 2.23 eV), very similar to the lower salt concentration 0.05 M and 0.2 M LiFSI-DME electrolytes, which can be related to various solvation structures co-existing in this HE-DME electrolyte.
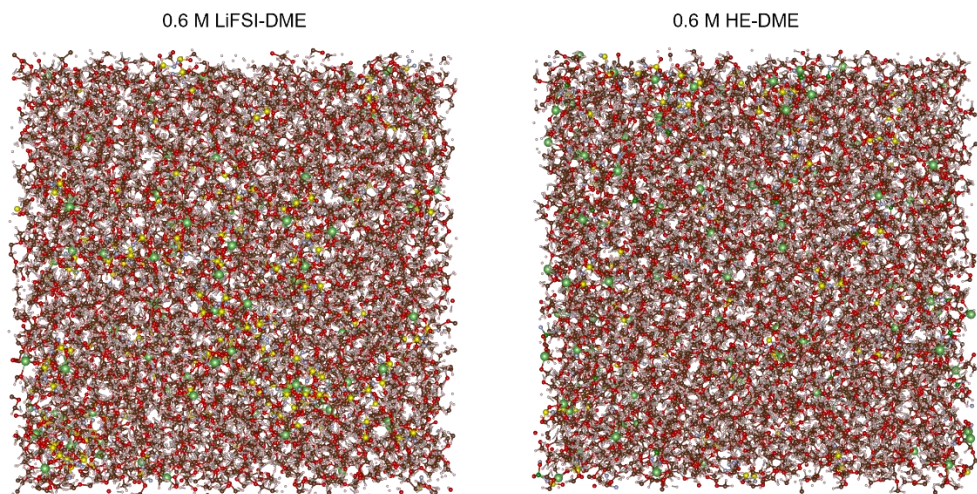
Fig. S3.77. Simulation structure for 0.6 M LiFSI-DME and 0.6 M HE-DME electrolytes. See the method for details.
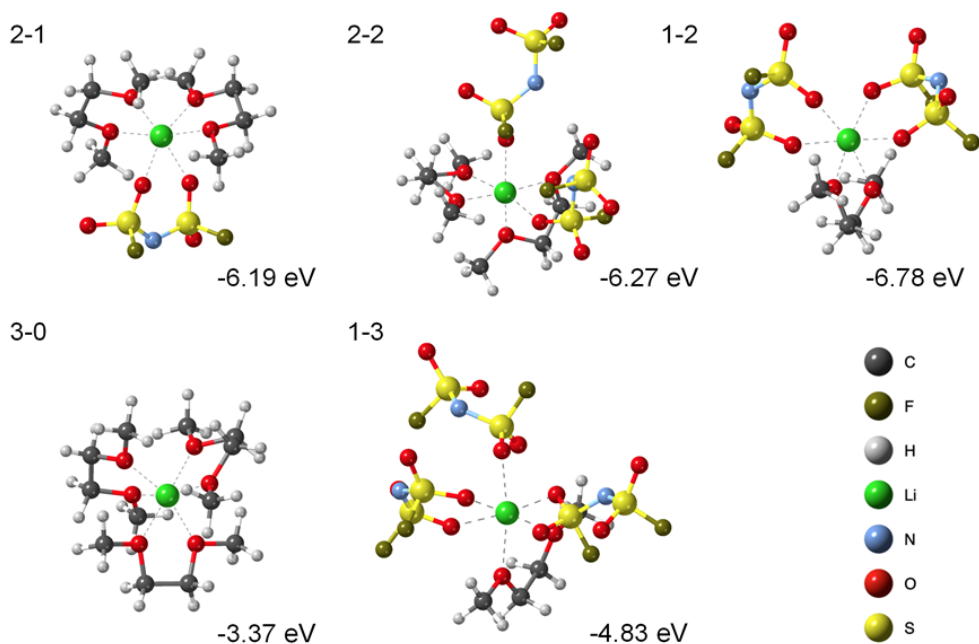
Fig. S3.78. The representative solvation structures and energies in the 0.6 M LiFSI-DME electrolyte. The detailed structures are shown in Table S3.2.
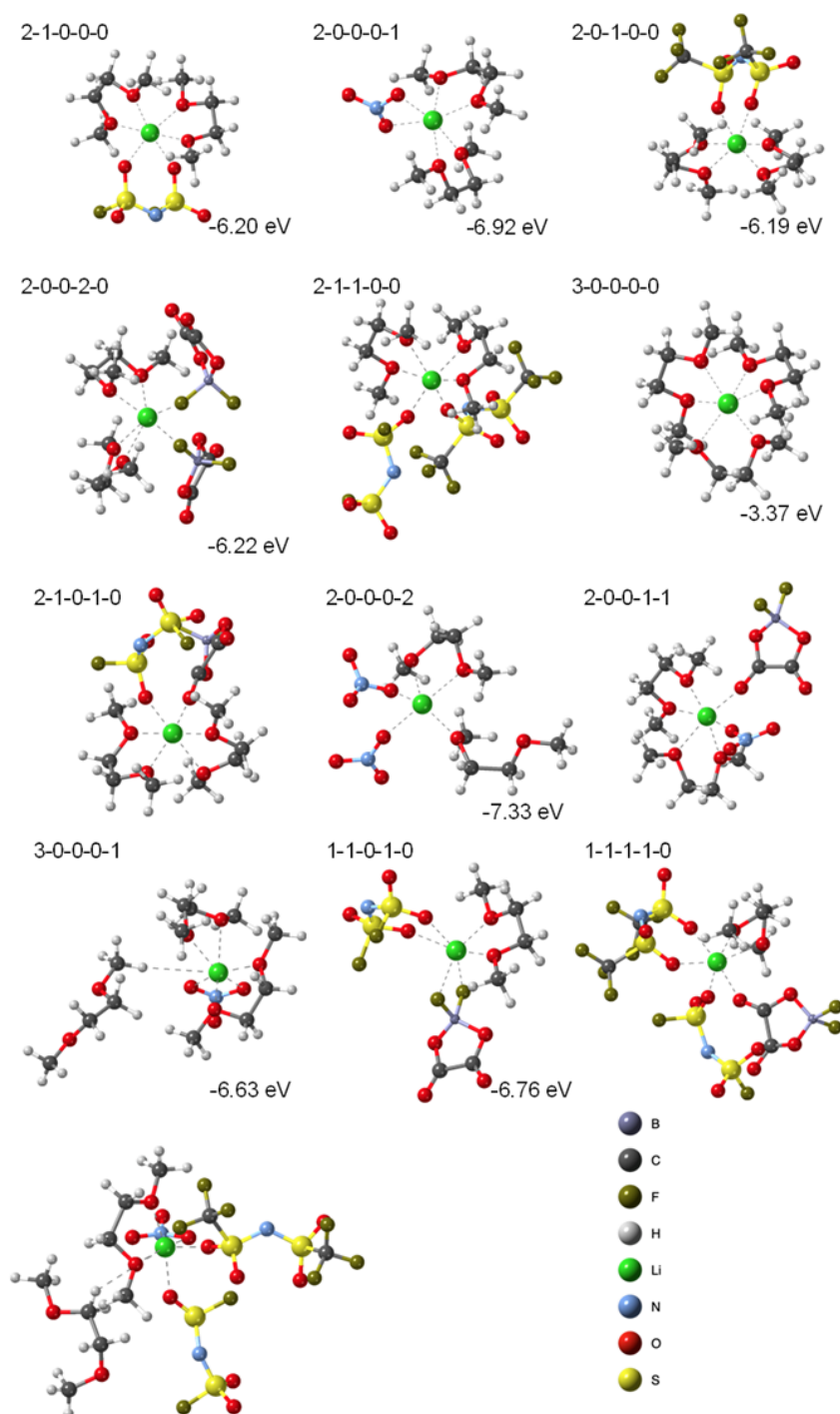
Fig. S3.79. The representative solvation structures and energies in the 0.6 M HE-DME electrolyte. The detailed structures are shown in Table S3.3.
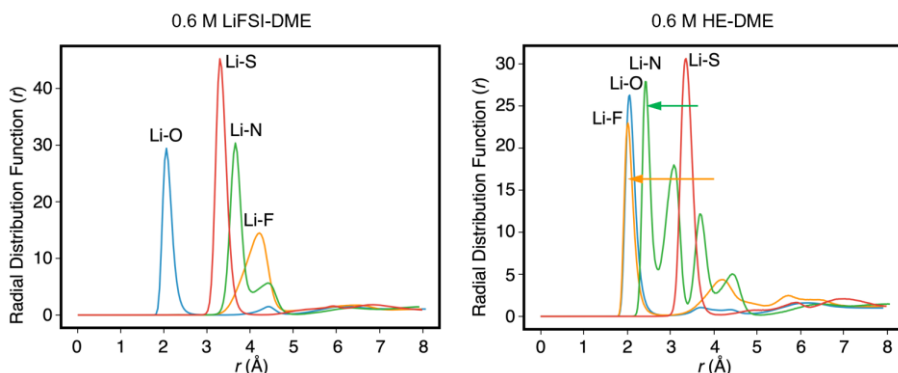
Fig. S3.80. Simulation of the radial distribution function (RDF) of Li–O, Li–F, Li–N and Li–S in 0.6 M LiFSI-DME and 0.6 M HE-DME electrolytes, respectively. According to the RDF results of the 0.6 M LiFSI-DME electrolyte obtained from the MD simulations, oxygen shows a strong tendency to coordinate with the Li-ion in comparison to the other elements, indicating a relatively strong interaction between Li ions and solvent molecules. However, in the HE-DME electrolyte, fluorine and nitrogen also coordinate with Li ions, indicating more anion rich solvation structures. This rationalizes the observation that for the HE electrolyte, both the SEI on anode and the CEI on the cathode are rich in decomposed salt anions.

3
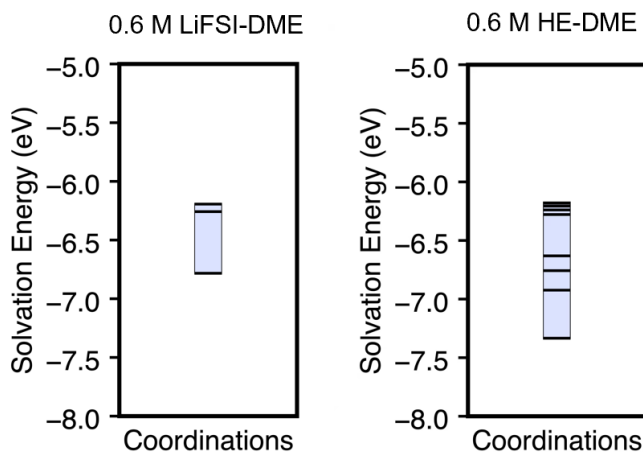
Fig. S3.81. The energies of the representative solvation structures in 0.6 M LiFSI-DME and 0.6 M HE-DME electrolytes. The detailed structures are shown in Table S3.3.
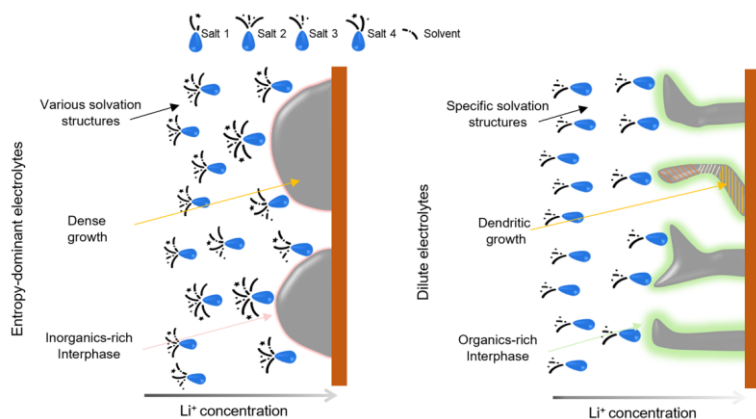
Fig. S3.82. The illustration of de-solvation processes in entropy-dominated electrolytes and conventional dilute electrolytes. This diversity results in lower solvation reorganization energies that facilitate Li-ion diffusion as well as charge transfer towards the interphase. The de-solvation processes in the entropy-dominated and conventional dilute electrolyte are further illustrated where in the HE electrolyte, the inorganic rich SEI/CEI and improved Li-ion kinetics are attributed to the increasing entropy, resulting in more dense Li metal growth, despite the low concentration of HE electrolyte.
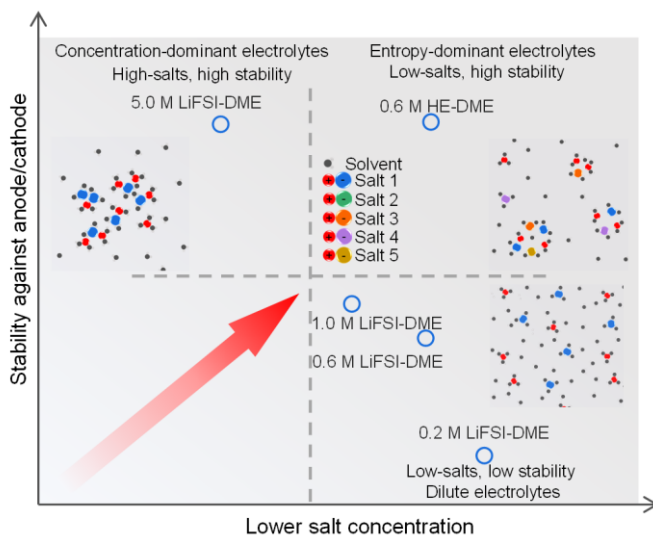
Fig. S3.83. Relationship between the salt concentration and stability against anode/cathode in liquid electrolytes. Based on the above results, the characteristics of conventional dilute electrolytes, high salt concentration electrolytes and HE electrolytes are compared. From this comparison, the HE demonstrates promising assets, especially realizing improved stability against the anode/cathode in low salt concentration liquid electrolytes, typically achieved only with highly concentrated electrolytes.
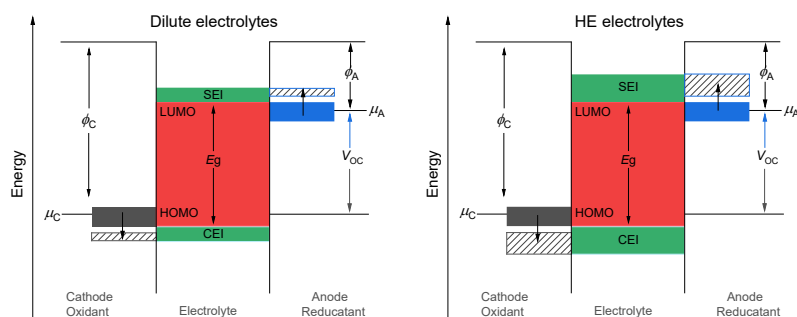
Fig. S3.84. Schematic diagram about formation of the SEI/CEI layer between electrodes and the liquid electrolyte in cells. The anode with an electrochemical potential μ_A above the lowest unoccupied molecular orbital (LUMO) could reduce the electrolyte but the SEI formation could prevent electron transfer to electrolyte LUMO; cathode with electrochemical potential μ_C below the highest occupied molecular orbital (HOMO) could also oxidize the electrolyte but the CEI formation limits the electron transfer to the cathode from the electrolyte HOMO. Compared to the dilute electrolytes, the HE electrolyte with various kinds of salts could enhance the stabilities of both SEI and CEI layers, enlarging the voltage window of electrolytes.

3
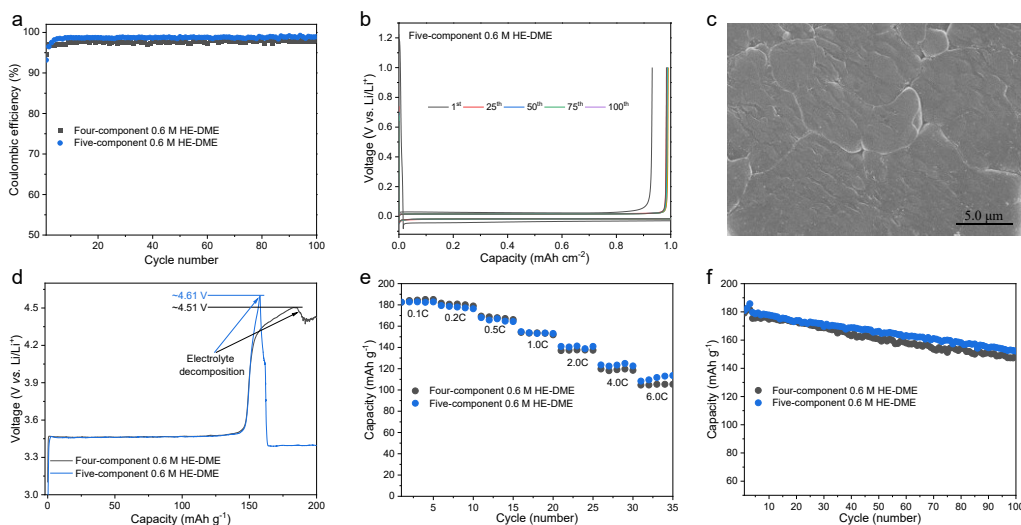
Fig. S3.85. Optimization of a five-component 0.6 M HE electrolyte. a, Li plating/stripping CE in Li‖Cu cells using the four-component 0.6 M HE and the five-component 0.6 M HE electrolytes at 0.5 mA cm^{-2} (dis)charging each time to a capacity of 1 mAh cm^{-2}. The five-component 0.6 M HE electrolyte, including 0.15 M LiFSI, 0.1 M LiTFSI, 0.1 M LiDFOB, 0.1 M LiBETI and 0.15 M LiNO$_3$ in DME, was prepared to explore its performance in comparison with the four-component 0.6 M HE electrolyte. **b,** Galvanostatic Li plating/stripping profiles of a Li‖Cu cell for the five-component 0.6 M HE electrolyte at different cycles. **c,** Morphology of the deposited Li metal from top-view SEM for the five-component 0.6 M HE electrolyte at a current density of 0.5 mA cm^{-2}, charged to a capacity of 1 mAh cm^{-2} on Cu foil. **d,** Galvanostatic charge profiles of Li‖LiFePO$_4$ cells of the four and five component 0.6 M HE electrolytes at a current density of 0.02 C to study the oxidation stability of the electrolytes. **e,** Electrochemical rate capabilities and **f,** cycling performance of Li‖NCM811 cells cycled in the voltage window from 2.8 to 4.3 V using the four and five component 0.6 M HE electrolytes.
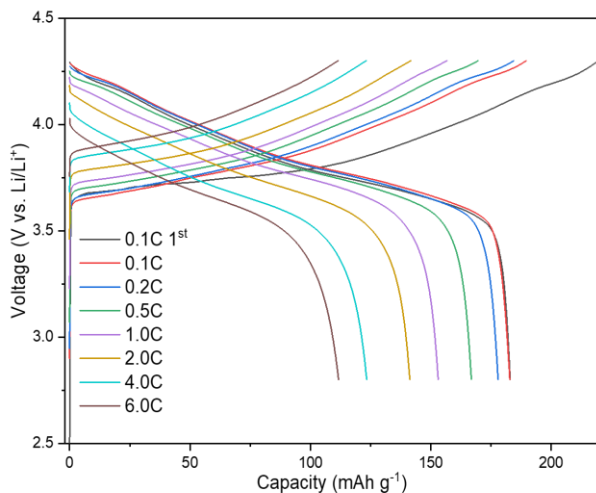
Fig. S3.86. Galvanostatic charge/discharge curves of Li‖NCM811 cell in five-component 0.6 M HE-DME electrolyte at different rates. The cells were cycled at 2.8-4.3 V.
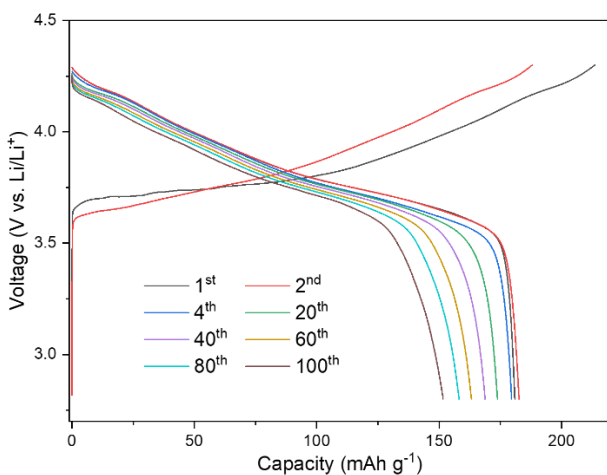
Fig. S3.87. Galvanostatic charge/discharge curves of Li‖NCM811 cell in five-component 0.6 M HE-DME electrolyte at different cycles. Cells were cycled at the voltage range of 2.8-4.3 V under a rate of 0.1C for three cycles before cycling at 0.333C rate.

Supplementary Tables

Table S3.1. Properties for 0.6 M LiFSI-DME, 5.0 M LiFSI-DME and 0.6 M HE-DME electrolytes at room temperature.

	T_{Li}^+	Conductivity (mS cm^{-1})	D_s (10^{-5} cm^2 s^{-1})
0.6 M LiFSI-DME	~0.39	~9.6	1.62
5.0 M LiFSI-DME	~0.31	~1.9	0.28
0.6 M HE-DME	~0.46	~10.2	1.96

Table S3.2. The types of solvation structures and their corresponding proportion in the 0.6 M LiFSI-DME electrolyte.

DME-LiFSI	Proportion
2-1	0.51295
2-2	0.165241667
1-2	0.11296875
3-0	0.091239583
1-3	0.036404167
Others	0.081196

Table S3.3. The types of solvation structures and their corresponding proportion in the 0.6 M HE-DME electrolyte.

DME-LiFSI-LiTFSI-LiDFOB-LiNO$_3$	Proportion	DME	LiFSI	LiTFSI	LiDFOB	LiNO$_3$
2-1-0-0-0	0.144806	2	1	0	0	0
2-0-0-0-1	0.139000	2	0	0	0	1
2-0-1-0-0	0.074173	2	0	1	0	0
2-0-0-2-0	0.065970	2	0	0	2	0
2-1-1-0-0	0.061083	2	1	1	0	0
3-0-0-0-0	0.060497	3	0	0	0	0
2-1-0-1-0	0.060212	2	1	0	1	0
2-0-0-0-2	0.051047	2	0	0	0	2
2-0-0-1-1	0.045853	2	0	0	1	1
3-0-0-0-1	0.036520	3	0	0	0	1
2-0-1-1-0	0.025692	2	0	1	1	0
2-1-0-0-1	0.024130	2	1	0	0	1
2-0-0-1-0	0.013062	2	0	0	1	0
2-0-0-0-0	0.013018	2	0	0	0	0

3

3-0-0-0-2	0.012802	3	0	0	0	2
1-0-0-0-2	0.012680	1	0	0	0	2
2-0-0-1-2	0.009469	2	0	0	1	2
1-1-0-0-1	0.008780	1	1	0	0	1
1-0-0-1-2	0.008232	1	0	0	1	2
3-1-0-0-0	0.008113	3	1	0	0	0
2-0-2-0-0	0.007466	2	0	2	0	0
3-0-0-1-0	0.007105	3	0	0	1	0
3-0-0-1-1	0.006357	3	0	0	1	1
2-0-1-0-1	0.005442	2	0	1	0	1
1-0-1-2-0	0.005358	1	0	1	2	0
1-0-0-0-1	0.005228	1	0	0	0	1
3-1-0-0-1	0.005087	3	1	0	0	1
1-2-0-0-0	0.005020	1	2	0	0	0
1-1-0-0-2	0.004825	1	1	0	0	2
3-0-1-0-0	0.004722	3	0	1	0	0
2-1-0-0-2	0.003660	2	1	0	0	2
1-1-1-1-0	0.003588	1	1	1	1	0
2-1-0-1-1	0.000679	2	1	0	1	1
2-1-1-0-1	0.000010	2	1	1	0	1
2-0-1-1-1	0.000001	2	0	1	1	1
Others	0.06					

3

References

1 J. W. Yeh, S. K. Chen, S. J. Lin, J. Y. Gan, T. S. Chin, T. T. Shun, C. H. Tsau & S. Y. Chang. Nanostructured High-Entropy Alloys with Multiple Principal Elements: Novel Alloy Design Concepts and Outcomes. *Advanced Engineering Materials* **6**, 299-303, (2004).

2 B. Cantor, I. T. H. Chang, P. Knight & A. J. B. Vincent. Microstructural development in equiatomic multicomponent alloys. *Materials Science and Engineering: A* **375-377**, 213-218, (2004).

3 E. P. George, D. Raabe & R. O. Ritchie. High-entropy alloys. *Nature Reviews Materials* **4**, 515-534, (2019).

4 B. E. MacDonald, Z. Fu, B. Zheng, W. Chen, Y. Lin, F. Chen, L. Zhang, J. Ivanisenko, Y. Zhou, H. Hahn & E. J. Lavernia. Recent Progress in High Entropy Alloy Research. *JOM* **69**, 2024-2031, (2017).

5 L. R. Owen & N. G. Jones. Lattice distortions in high-entropy alloys. *Journal of Materials Research* **33**, 2954-2969, (2018).

6 D. B. Miracle & O. N. Senkov. A critical review of high entropy alloys and related concepts. *Acta Materialia* **122**, 448-511, (2017).

7 K. M. Abraham, Z. Jiang & B. Carroll. Highly Conductive PEO-like Polymer Electrolytes. *Chemistry of Materials* **9**, 1978-1988, (1997).

8 S. V. Divinski, A. V. Pokoev, N. Esakkiraja & A. Paul. A Mystery of "Sluggish Diffusion" in High-Entropy Alloys: The Truth or a Myth? *Diffusion Foundations* **17**, 69-104, (2018).

9 K. Y. Tsai, M. H. Tsai & J. W. Yeh. Sluggish diffusion in Co–Cr–Fe–Mn–Ni high-entropy alloys. *Acta Materialia* **61**, 4887-4897, (2013).

10 K. Xu. Electrolytes and Interphases in Li-Ion Batteries and Beyond. *Chemical Reviews* **114**, 11503-11618, (2014).

11 B. Dunn, H. Kamath & J.-M. Tarascon. Electrical Energy Storage for the Grid: A Battery of Choices. *Science* **334**, 928-935, (2011).

12 H. Zhang, G. G. Eshetu, X. Judez, C. Li, L. M. Rodriguez-Martínez & M. Armand. Electrolyte Additives for Lithium Metal Anodes and Rechargeable Lithium Metal Batteries: Progress and Perspectives. *Angewandte Chemie International Edition* **57**, 15002-15027, (2018).

13 X.-B. Cheng, R. Zhang, C.-Z. Zhao & Q. Zhang. Toward Safe Lithium Metal Anode in Rechargeable Batteries: A Review. *Chemical Reviews* **117**, 10403-10473, (2017).

14 Y. Rosenfeld. Relation between the transport coefficients and the internal entropy of simple systems. *Physical Review A* **15**, 2545-2549, (1977).

3

15 J. C. Dyre. Perspective: Excess-entropy scaling. *The Journal of Chemical Physics* **149**, 210901, (2018).

16 X. Dong, Y. Lin, P. Li, Y. Ma, J. Huang, D. Bin, Y. Wang, Y. Qi & Y. Xia. High-Energy Rechargeable Metallic Lithium Battery at −70 °C Enabled by a Cosolvent Electrolyte. *Angewandte Chemie International Edition* **58**, 5623-5627, (2019).

17 W. Zhang, H. Xia, Z. Zhu, Z. Lv, S. Cao, J. Wei, Y. Luo, Y. Xiao, L. Liu & X. Chen. Decimal Solvent-Based High-Entropy Electrolyte Enabling the Extended Survival Temperature of Lithium-Ion Batteries to −130 °C. *CCS Chemistry* **3**, 1245-1255.

18 Q. Wang, Z. Yao, C. Zhao, T. Verhallen, D. P. Tabor, M. Liu, F. Ooms, F. Kang, A. Aspuru-Guzik, Y.-S. Hu, M. Wagemaker & B. Li. Interface chemistry of an amide electrolyte for highly reversible lithium metal batteries. *Nature Communications* **11**, 4188, (2020).

19 X. Wang, C. Yamada, H. Naito, G. Segami & K. Kibe. High-Concentration Trimethyl Phosphate-Based Nonflammable Electrolytes with Improved Charge–Discharge Performance of a Graphite Anode for Lithium-Ion Cells. *Journal of The Electrochemical Society* **153**, A135, (2006).

20 E. J. Plichta, M. Hendrickson, R. Thompson, G. Au, W. K. Behl, M. C. Smart, B. V. Ratnakumar & S. Surampudi. Development of low temperature Li-ion electrolytes for NASA and DoD applications. *Journal of Power Sources* **94**, 160-162, (2001).

21 B. Qiao, G. M. Leverick, W. Zhao, A. H. Flood, J. A. Johnson & Y. Shao-Horn. Supramolecular Regulation of Anions Enhances Conductivity and Transference Number of Lithium in Liquid Electrolytes. *Journal of the American Chemical Society* **140**, 10932-10936, (2018).

22 Q. Wang, C. Zhao, S. Wang, J. Wang, M. Liu, S. Ganapathy, X. Bai, B. Li & M. Wagemaker. Clarifying the Relationship between the Lithium Deposition Coverage and Microstructure in Lithium Metal Batteries. *Journal of the American Chemical Society* **144**, 21961-21971, (2022).

23 Y.-K. Sun, S.-T. Myung, B.-C. Park, J. Prakash, I. Belharouak & K. Amine. High-energy cathode material for long-life and safe lithium batteries. *Nature Materials* **8**, 320-324, (2009).

24 S. Jiao, X. Ren, R. Cao, M. H. Engelhard, Y. Liu, D. Hu, D. Mei, J. Zheng, W. Zhao, Q. Li, N. Liu, B. D. Adams, C. Ma, J. Liu, J.-G. Zhang & W. Xu. Stable cycling of high-voltage lithium metal batteries in ether electrolytes. *Nature Energy* **3**, 739-746, (2018).

25 M. J. Zachman, Z. Tu, S. Choudhury, L. A. Archer & L. F. Kourkoutis. Cryo-STEM mapping of solid–liquid interfaces and dendrites in lithium-metal batteries. *Nature* **560**, 345-349, (2018).

3

26 F. Shi, A. Pei, A. Vailionis, J. Xie, B. Liu, J. Zhao, Y. Gong & Y. Cui. Strong texturing of lithium metal in batteries. *Proceedings of the National Academy of Sciences* **114**, 12138, (2017).

27 Z. Zhang, Y. Li, R. Xu, W. Zhou, Y. Li, T. Oyakhire Solomon, Y. Wu, J. Xu, H. Wang, Z. Yu, T. Boyle David, W. Huang, Y. Ye, H. Chen, J. Wan, Z. Bao, W. Chiu & Y. Cui. Capturing the swelling of solid-electrolyte interphase in lithium metal batteries. *Science* **375**, 66-70, (2022).

28 Y. Xiang, M. Tao, G. Zhong, Z. Liang, G. Zheng, X. Huang, X. Liu, Y. Jin, N. Xu, M. Armand, J.-G. Zhang, K. Xu, R. Fu & Y. Yang. Quantitatively analyzing the failure processes of rechargeable Li metal batteries. *Science Advances* **7**, eabj3423.

29 S. Chandrashekar, N. M. Trease, H. J. Chang, L.-S. Du, C. P. Grey & A. Jerschow. 7Li MRI of Li batteries reveals location of microstructural lithium. *Nature Materials* **11**, 311-315, (2012).

30 R. Bhattacharyya, B. Key, H. Chen, A. S. Best, A. F. Hollenkamp & C. P. Grey. In situ NMR observation of the formation of metallic lithium microstructures in lithium batteries. *Nature Materials* **9**, 504-510, (2010).

31 A. B. Gunnarsdóttir, C. V. Amanchukwu, S. Menkin & C. P. Grey. Noninvasive In Situ NMR Study of "Dead Lithium" Formation and Lithium Corrosion in Full-Cell Lithium Metal Batteries. *Journal of the American Chemical Society* **142**, 20814-20827, (2020).

32 H. J. Chang, N. M. Trease, A. J. Ilott, D. Zeng, L.-S. Du, A. Jerschow & C. P. Grey. Investigating Li Microstructure Formation on Li Anodes for Lithium Batteries by in Situ 6Li/7Li NMR and SEM. *The Journal of Physical Chemistry C* **119**, 16443-16451, (2015).

33 C. Xu, K. Märker, J. Lee, A. Mahadevegowda, P. J. Reeves, S. J. Day, M. F. Groh, S. P. Emge, C. Ducati, B. Layla Mehdi, C. C. Tang & C. P. Grey. Bulk fatigue induced by surface reconstruction in layered Ni-rich cathodes for Li-ion batteries. *Nature Materials* **20**, 84-92, (2021).

34 Z. Zhang, J. Yang, W. Huang, H. Wang, W. Zhou, Y. Li, Y. Li, J. Xu, W. Huang, W. Chiu & Y. Cui. Cathode-Electrolyte Interphase in Lithium Batteries Revealed by Cryogenic Electron Microscopy. *Matter* **4**, 302-312, (2021).

35 M. H. Fu, K. L. Huang, S. Q. Liu, J. S. Liu & Y. K. Li. Lithium difluoro(oxalato)borate/ethylene carbonate+propylene carbonate+ethyl(methyl) carbonate electrolyte for LiMn2O4 cathode. *Journal of Power Sources* **195**, 862-866, (2010).

3

36 B. L. Papke, M. A. Ratner & D. F. Shriver. Vibrational Spectroscopic Determination of Structure and Ion Pairing in Complexes of Poly(ethylene oxide) with Lithium Salts. *Journal of The Electrochemical Society* **129**, 1434-1438, (1982).

37 W. A. Henderson. Glyme−Lithium Salt Phase Behavior. *The Journal of Physical Chemistry B* **110**, 13177-13183, (2006).

38 C. M. Burke, V. Pande, A. Khetan, V. Viswanathan & B. D. McCloskey. Enhancing electrochemical intermediate solvation through electrolyte anion selection to increase nonaqueous Li–O2; battery capacity. *Proceedings of the National Academy of Sciences* **112**, 9293, (2015).

39 Y. Yamada, M. Yaegashi, T. Abe & A. Yamada. A superconcentrated ether electrolyte for fast-charging Li-ion batteries. *Chemical Communications* **49**, 11194-11196, (2013).

40 D. C. Wallace. Statistical theory for the entropy of a liquid. *Physical Review A* **39**, 4843-4847, (1989).

41 P. Argyrakis, A. Milchev, V. Pereyra & K. W. Kehr. Dependence of the diffusion coefficient on the energy distribution of random barriers. *Physical Review E* **52**, 3623-3631, (1995).

42 K. Xu. Nonaqueous Liquid Electrolytes for Lithium-Based Rechargeable Batteries. *Chemical Reviews* **104**, 4303-4418, (2004).

43 K. Hayashi, Y. Nemoto, S. Tobishima & J. Yamaki. Mixed solvent electrolyte for high voltage lithium metal secondary cells. *Electrochimica Acta* **44**, 2337-2344, (1999).

44 S. Plimpton. Fast parallel algorithms for short-range molecular dynamics. **117**, 1-19, (1995).

45 W. L. Jorgensen, D. S. Maxwell & J. Tirado-Rives. Development and testing of the OPLS all-atom force field on conformational energetics and properties of organic liquids. **118**, 11225-11236, (1996).

46 S. V. Sambasivarao, O. Acevedo & computation. Development of OPLS-AA force field parameters for 68 unique ionic liquids. **5**, 1038-1050, (2009).

47 L. Martínez, R. Andrade, E. G. Birgin & J. Martínez. PACKMOL: a package for building initial configurations for molecular dynamics simulations. **30**, 2157-2164, (2009).

48 S. P. Ong, W. D. Richards, A. Jain, G. Hautier, M. Kocher, S. Cholia, D. Gunter, V. L. Chevrier, K. A. Persson & G. J. C. M. S. Ceder. Python Materials Genomics (pymatgen): A robust, open-source python library for materials analysis. **68**, 314-319, (2013).

49 R. J. Gowers, M. Linke, J. Barnoud, T. J. E. Reddy, M. N. Melo, S. L. Seyler, J. Domanski, D. L. Dotson, S. Buchoux & I. M. Kenney. MDAnalysis: a Python package

3

for the rapid analysis of molecular dynamics simulations. Report No. 2575-9752, (Los Alamos National Lab.(LANL), Los Alamos, NM (United States), 2019).

50   C. Lee, W. Yang & R. G. Parr. Development of the Colle-Salvetti correlation-energy formula into a functional of the electron density. *Physical Review B* **37**, 785-789, (1988).

51   S. F. Boys & F. Bernardi. The calculation of small molecular interactions by the differences of separate total energies. Some procedures with reduced errors. *Molecular Physics* **100**, 65-73, (2002).

52   M. Frisch, G. Trucks, H. B. Schlegel, G. E. Scuseria, M. A. Robb, J. R. Cheeseman, G. Scalmani, V. Barone, B. Mennucci & G. J. I. Petersson, Wallingford CT. gaussian 09, Revision d. 01, Gaussian. **201**, (2009).

53   J. Maier. Concentration Polarization of Salt-Containing Liquid Electrolytes. *Advanced Functional Materials* **21**, 1448-1455, (2011).

54   R. Weber, M. Genovese, A. J. Louli, S. Hames, C. Martin, I. G. Hill & J. R. Dahn. Long cycle life and dendrite-free lithium morphology in anode-free lithium pouch cells enabled by a dual-salt liquid electrolyte. *Nature Energy* **4**, 683-689, (2019).

55   C. Fang, B. Lu, G. Pawar, M. Zhang, D. Cheng, S. Chen, M. Ceja, J.-M. Doux, H. Musrock, M. Cai, B. Liaw & Y. S. Meng. Pressure-tailored lithium deposition and dissolution in lithium metal batteries. *Nature Energy* **6**, 987-994, (2021).

56   D. Rehnlund, C. Ihrfors, J. Maibach & L. Nyholm. Dendrite-free lithium electrode cycling via controlled nucleation in low LiPF6 concentration electrolytes. *Materials Today* **21**, 1010-1018, (2018).

57   A. Pei, G. Zheng, F. Shi, Y. Li & Y. Cui. Nanoscale Nucleation and Growth of Electrodeposited Lithium Metal. *Nano Letters* **17**, 1132-1139, (2017).

58   V. Küpers, M. Kolek, P. Bieker, M. Winter & G. Brunklaus. In situ 7Li-NMR analysis of lithium metal surface deposits with varying electrolyte compositions and concentrations. *Physical Chemistry Chemical Physics* **21**, 26084-26094, (2019).

59   D. H. Jang & S. M. Oh. Electrolyte Effects on Spinel Dissolution and Cathodic Capacity Losses in 4 V Li / LixMn2O4 Rechargeable Cells. *Journal of The Electrochemical Society* **144**, 3342-3348, (1997).

60   L. Suo, W. Xue, M. Gobet, S. G. Greenbaum, C. Wang, Y. Chen, W. Yang, Y. Li & J. Li. Fluorine-donating electrolytes enable highly reversible 5-V-class Li metal batteries. *Proceedings of the National Academy of Sciences* **115**, 1156, (2018).

3

61 C. Wang, Y. S. Meng & K. Xu. Perspective—Fluorinating Interphases. *Journal of The Electrochemical Society* **166**, A5184-A5186, (2018).

62 L. J. Krause, W. Lamanna, J. Summerfield, M. Engle, G. Korba, R. Loch & R. Atanasoski. Corrosion of aluminum at high voltages in non-aqueous electrolytes containing perfluoroalkylsulfonyl imides; new lithium salts for lithium-ion cells. *Journal of Power Sources* **68**, 320-325, (1997).

3

4. Entropy-driven liquid electrolytes for lithium batteries

Abstract

Developing liquid electrolytes with higher kinetics and enhanced interphase stability is one of the key challenges for lithium (Li) batteries. However, the poor solubility of Li salts in solvents sets constraints that compromises the electrolyte properties. Here we show that introducing multiple salts to form a high-entropy (HE) solution, alters the solvation structure, which can be used to raise the solubility of specific salts and stabilize electrode-electrolyte interphases. The prepared HE electrolytes significantly enhance the cycling and rate performance of Li batteries. For Li-metal anodes the reversibility exceeds 99%, which extends the cycle life of batteries even under aggressive cycling conditions. For commercial batteries, combining a graphite anode with a $LiNi_{0.8}Co_{0.1}Mn_{0.1}O_2$ cathode, more than 1000 charge-discharge cycles are achieved while maintaining a capacity retention of more than 90%. These performance improvements with respect to regular electrolytes are rationalized by the unique features of the solvation structure in HE electrolytes. The weaker solvation interaction induced by the higher disorder results in improved Li-ion kinetics, and the altered solvation composition leads to stabilized interphases. Finally, the increased entropy, induced by the presence of multiple salts, enables a decrease in melting temperature of the electrolytes and thus enables lower battery operation temperatures without changing the solvents.

4

4.1 Introduction

Synthesizing new materials through increasing their configurational entropy is an emerging concept in materials science. High-entropy (HE) alloys[1,2], typically consisting of five or more principal elements, facilitate the formation of solid-solution phases with simple structures[3]. This has been extended to entropy-stabilized functional oxides and fluorites and other solid chemistries[4,5]. For a given system, the configurational entropy will increase with the number of principle components introduced, which will lower the Gibbs free energy, manifesting itself in extended solubility limits through the entropy-driven structural stabilization[6]. Thereby, increasing the entropy to stabilize phases provides opportunities to design functional materials for various fields, including catalysis[7], dielectrics[8] and energy storage [9], making it possible to resolve challenging issues in traditional systems.

Compared to solids, liquids naturally exhibit a larger entropy because of their more dynamic and disordered nature. Dissolving solutes in solvents to form a uniform solution is thermodynamically similar to the formation of single-phase solid compounds. Solutes and solvents exhibit different compatibilities, as expressed by their free energy of solvation (mixing) (ΔG_{mix}), which is build up by the enthalpy of mixing (ΔH_{mix}) and the entropy of mixing (ΔS_{mix}) through the combination of the 1st and 2nd laws of thermodynamics:

$$\Delta G_{mix} = \Delta H_{mix} - T\Delta S_{mix} \qquad (4.1)$$

ΔS_{mix} can be expressed in terms of the composition as follows:

$$\Delta S_{mix} = -nR \sum_i x_i ln x_i \qquad (4.2)$$

where R is the gas constant, n the total number of moles and x_i the mole fraction of component i. In a conventional electrolyte with few components, the solubility of the solutes is determined by the competition between ΔH_{mix} (a more positive value leads to a lower solubility) and ΔS_{mix} (a larger value increases the solubility). When the solubility limit is exceeded at specific conditions (i.e., temperature and pressure), the solute will precipitate, forming a heterogeneous system, which is conceptually similar to spinodal decomposition in solids (Fig. 4.1a). Therefore, introducing multiple components to increase the entropy of mixing (ΔS_{mix}), in principle, represents a strategy to promote the

formation of homogeneous solutions of liquids (Fig. 4.1b), which can be relevant for a wide number of applications.

This is especially relevant for batteries, e.g., lithium (Li) -ion battery, where adding salt and solvent additives in liquid electrolytes plays a crucial role in achieving a long cycle life, through the formation of stable interphases, and improving Li-ion transport to lower the internal resistance[10-13]. However, one of the main challenges is the compatibility of salts and solvents to form uniform solutions, which imposes restrictions in developing high-performance electrolytes. An exponent of this is $LiNO_3$, a widely used additive in ether-based electrolytes to increase the interphase stability with electrodes[14]. However, it is considered to be incompatible with commercial high-voltage carbonate solvents[15,16], such as ethylene carbonate (EC)/dimethyl carbonate (DMC) (Supplementary Note S4.1). Therefore, increasing the $LiNO_3$ solubility in carbonates through other routes has attracted wide attention. Introducing Lewis acid salts[17,18] or cosolvents[19-21] has recently been reported to weaken the Coulombic interaction between NO^{3-} and Li^+ and thus improve its solubility. However, the corresponding concerns is that these extra additives compromise the electrolyte properties and degrade the interphase stability due to their intrinsic reactivity during (dis)charge[19,20,22-24]. Therefore, new strategies to improve the solubility of specific salts, especially in commercially available electrolytes (e.g., EC/DMC) are desirable.

Here, we show that introducing multiple, commonly used Li salts in commercial carbonate solvents enhances the solubility of specific salts by raising the entropy of mixing, using $LiNO_3$ as a proof of concept. The resulting high entropy (HE) liquid electrolytes are shown to have a much more diverse solvation structure, where more salt anion groups interact with the Li ions. A consequence of the higher disorder weakens the interaction between Li ions with both salts and solvents. This results in the formation of uniform liquid electrolytes, that can achieve more stable electrode/electrolyte interphases and higher Li-ion mobility, responsible for substantial improvements in Li battery performances. It should be noted this is essentially different from the mixing of several solvents with 1 up to 3 salts to form the so-called "mixing electrolytes", where the functional properties of entropy stabilization on the system are not relevant[25].

4.2 Formation and solvation structures of the entropy-driven electrolyte
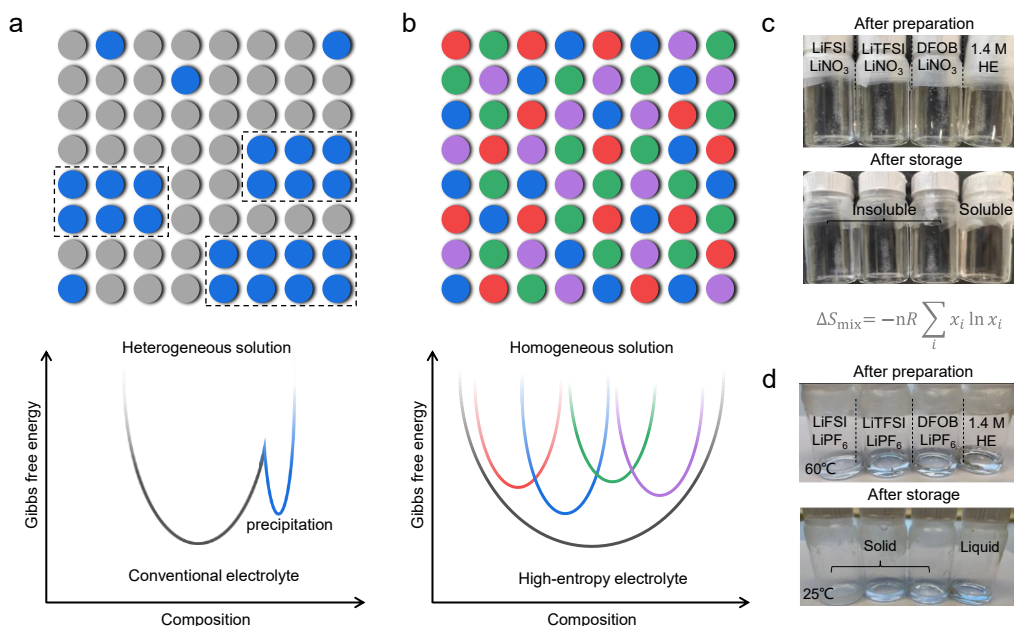
Fig. 4.1. Improving the stability of liquid electrolytes through increasing entropy of mixing. a, **b**, Schematic diagram of compositional structure and energy in heterogeneous solution with precipitation of a component and a homogeneous solution by increasing the entropy of mixing. **c**, Solubility of different salts in EC/DMC (1:1 by weight) with 5% FEC: from left to right 0.1 M LiFSI/0.1 M LiNO$_3$/1.0 M LiPF$_6$, 0.1 M LiTFSI/0.1 M LiNO$_3$/1.0 M LiPF$_6$, 0.1 M LiDFOB/0.1 M LiNO$_3$/1.0 M LiPF$_6$, and 0.1 M LiFSI/0.1 M LiTFSI/0.1 M LiDFOB/0.1 M LiNO$_3$/1.0 M LiPF$_6$ (1.4 M HE). The white precipitation in the electrolytes is LiNO$_3$-related compounds. **d**, Liquid to solid phase transition behavior of different salts in the EC solvent: from left to right 0.4 M LiFSI/1.0 M LiPF$_6$, 0.4 M LiTFSI/1.0 M LiPF$_6$, 0.4 M LiDFOB/1.0 M LiPF$_6$, 1.4 M HE. The EC-based electrolytes are prepared at around 60°C and stored at room temperature.

The commercial 1.0 M LiPF$_6$ in EC/DMC carbonate electrolyte (1:1 by weight) with 5% fluoroethylene carbonate (FEC) is selected as baseline electrolyte, which has negligible solubility for LiNO$_3$ ($\leq$ 1000 ppm)[15,16]. The commercially available salts LiFSI, LiTFSI and LiDFOB are introduced based on their relative innocuousness and good solubility in carbonates, and combined to raise the entropy of the electrolyte. The presence of these multiple salt components increases the solubility of LiNO$_3$ up to 0.1 M (Fig. S4.1), leading to the obtained HE electrolyte composition of 0.1 M LiFSI/0.1 M LiTFSI/0.1 M

LiDFOB/0.1 M LiNO$_3$/1.0 M LiPF$_6$ in EC/DMC (1:1 by weight) with 5% FEC, henceforth referred to as 1.4 M HE-EDF. To investigate the influence of the individual salts on promoting LiNO$_3$ dissolution, electrolytes were prepared with each salt, all combined with 0.1 M LiNO$_3$ into 1.0 M LiPF$_6$ in EC/DMC with 5% FEC (Fig. 4.1c). None of the individual salt is able to promote LiNO$_3$ dissolution, where insoluble LiNO$_3$ is clearly observed, and thus the combination of multiple salts is held responsible for the increased LiNO$_3$ solubility. The same strategy is further examined in an ether-based system (Fig. S4.2 and Supplementary Note S4.2), also resulting in a significant improvement of the LiNO$_3$ solubility by raising the entropy of mixing through introducing multiple salts. In the HE electrolyte, the larger variety of solvation interactions are anticipated to be responsible for the larger entropy of mixing, thereby decreasing the Gibbs Free energy and thus increasing the solubility. In addition, this can be expected to influence the temperature-dependent properties of the electrolytes due to its diverse solvation structure. To demonstrate this, the pure EC solvent that is solid at room temperature (melting point ~36.4 °C), is mixed with each single salt as well as with the combination of multiple salts to form a HE system. After preparation at 60°C, all electrolytes are clear, representing uniform solutions. However, during cooling to room temperature, the electrolytes with the single extra salt turn into semi-solid or solid, except for the HE electrolyte, which maintains liquid for a longer period of several hours (Fig. 4.1d). This suggests that raising the entropy can also be an effective strategy to improve the electrolyte properties for lower temperature applications as was also suggested for introducing specific solvents, in which case however the melting point of the solvents plays a dominant role[25,26].

The very small solubility of LiNO$_3$ in 1.0 M LiPF$_6$-EDF ($\leq$ 1000 ppm)[15,16] increases several orders of magnitude in the HE electrolyte (Fig. S4.3), suggesting that the solvation structure in the HE electrolyte is different compared to that in the single salt electrolytes. Raman spectroscopy demonstrates that the 1.4 M HE-EDF electrolyte has a weaker solvation interaction between the Li-ions and EDF solvents, as compared to the single-salt 1.4 M LiPF$_6$-EDF electrolyte and the other control electrolytes, reflected by the weaker coordinated peak (Fig. 4.2a, Figs. S4.4, S4.5 and Supplementary Note S4.3). Consistently, a downfield shift in the ^{7}Li NMR spectra is observed for the 1.4 M HE-EDF electrolyte

(Fig. 4.2b, Fig. S4.6 and Supplementary Note S4.4) indicating weaker interactions of Li ions with both solvents and anion groups. This can be attributed to the HE composition, which effectively increases the disorder of the system, presenting a conceptually different mechanism compared to the reported increase in the $LiNO_3$ solubility [17-21,27], and in high-salt concentration electrolytes[28]. In general, the decreased solvation interaction of Li ions with solvents will result in the relatively increased interaction with anion groups from salts and vice versa, however, the average solvation strength is found to decrease, improving the Li-ion transport[17-21,27,28]. Therefore, benefiting from the altered solvation structure and interactions, a higher conductivity and lower viscosity of (1.76 mPa·s vs. 2.62 mPa·s) is achieved in the 1.4 M HE-EDF compared with the control electrolytes (the inset of Fig. 4.2b).

Molecular dynamics (MD) simulations indicate that the various anion species in 1.4 M HE-EDF electrolyte result in a rich diversity of over 100 types of Li-ion solvation environments, much more than what is obtained from the 1.4 M $LiPF_6$-EDF electrolyte (Figs. S4.7-S4.11 and Table S4.1 and S4.2). Based on the radial distribution function (RDF), the Li-F interaction, between PF_6^- and Li ions, is decreased in the 1.4 M HE-EDF electrolyte as compared to the 1.4 M $LiPF_6$-EDF electrolyte. In contrast the Li-O, Li-N, Li-S interactions from the various anion groups are enhanced, which is anticipated to promote the formation of an anion-dominated and inorganic-rich SEI composition that will increase the interphase stability as will be discussed below (Fig. S4.12). The simulated self-diffusion coefficient of the 1.4 M HE-EDF electrolyte (1.9×10^{-6} cm^2 s^{-1}) is larger than that of the 1.4 M $LiPF_6$-EDF electrolyte (1.2×10^{-6} cm^2 s^{-1}) (Fig. S4.13), in agreement with the measured improvement in the conductivity. The higher Li-ion mobility in the 1.4 M HE-EDF electrolyte is also confirmed by the larger Li transference number (Fig. S4.14) and higher exchange current density (Fig. S4.15). This entropy induced improved ion transport can be explained by excess entropy scaling in liquid systems[29,30], where the increasing number of components leads to a wider distribution in diffusional barriers from the diverse solvation structures, enhancing diffusional channels via the available percolation network[31]. In addition, the 1.4 M HE-EDF electrolyte has a slightly higher reduction potential for the decomposition of salts at around 1.23 V (Fig. S4.16). After the

4

initial cycles, the reduction peak intensity decreases in the 1.4 M HE-EDF electrolyte and stabilizes during subsequent cycles, indicating that a stable SEI has formed during the initial cycle[32].

4.3 Anode interphase stability
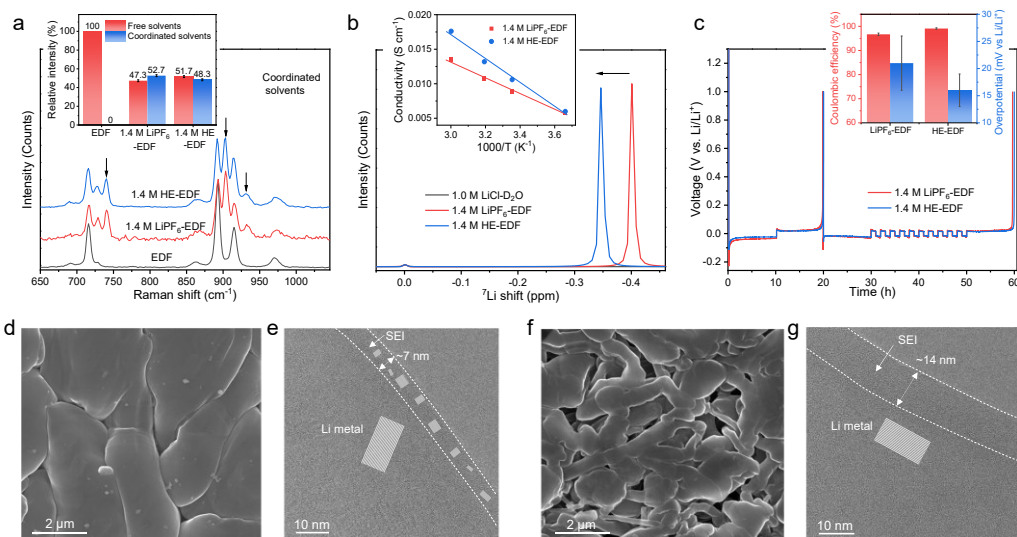
Fig. 4.2. Solvation structure and compatibility of HE electrolyte with Li metal anode. a, Raman spectra of the EDF solvent, 1.4 M LiPF₆-EDF, and 1.4 M HE-EDF. The black arrows mark the peaks that represent Li ions coordinated to solvents. The insert shows the distribution of free solvent and coordinated solvent (Li⁺-EDF) from the peak fitting results (Fig. S4.5). **b**, Liquid ⁷Li NMR spectra of 1.4 M LiPF₆-EDF and 1.4 M HE-EDF electrolytes. The inset shows the Li ionic conductivity of the 1.4 M LiPF₆-EDF and 1.4 M HE-EDF electrolytes at various temperatures. **c**, Li metal CE in Li∥Cu cells using different electrolytes. **d, f**, SEM images of deposited Li metal on Cu foil at a current density of 0.5 mA cm⁻² to 1 mAh cm⁻² in (**d**) 1.4 M HE-EDF electrolyte and (**f**) 1.4 M LiPF₆-EDF electrolyte. **e, g**, Cryo-TEM images showing microstructure of deposited Li metal and interphase with I 1.4 M HE-EDF electrolyte and (**g**) 1.4 M LiPF₆-EDF electrolyte.

The compatibility with Li-metal anodes is evaluated by Coulombic efficiency (CE) measurements[33,34]. The 1.4 M HE-EDF electrolyte shows a higher average CE, exceeding 99%, and a lower overpotential compared to the single-salt 1.4 M LiPF₆-EDF electrolyte (Fig. 4.2c), further confirmed by the galvanostatic cycling of Li∥Cu and Li∥Li cells (Figs. S4.17-S4.19). To determine the origin of the improved performance of the 1.4 M HE-EDF

electrolyte in combination with a Li-metal anode, the plating/stripping morphology of Li metal is investigated using scanning electron microscopy (SEM). The deposited Li metal in the 1.4 M HE-EDF electrolyte is compact and well connected to the Cu substrate with particle sizes around several micrometres (Fig. 4.2d, Figs. S4.20 and S4.21). In contrast, the 1.4 M LiPF$_6$-EDF electrolyte results in porous and whisker-like dendritic Li deposits that are less-well connected to the Cu (Fig. 4.2f and Fig. S4.21). After stripping, a porous morphology with some residual dendritic Li is observed for 1.4 M LiPF$_6$-EDF electrolyte (Fig. S4.22) whereas much less residual Li metal is left behind for 1.4 M HE-EDF electrolyte, indicating more complete and homogenous stripping (Figs. S4.22 and S4.23). The denser and better-connected Li-metal deposits formed in the 1.4 M HE-EDF electrolyte are beneficial for electron transport, allowing efficient stripping and suppressing the formation of inactive Li[32]. At the same time, the compact deposits minimize the exposed surface area resulting in less electrolyte decomposition, which in turn suppresses the formation of porous Li on subsequent cycling. To the best of our knowledge, this represents important improvement for the commercial carbonate electrolytes under typical cycling conditions. To further investigate the Li-metal morphology and SEI properties, cryogenic transmission electron microscopy (cryo-TEM) is conducted at -170 °C [35]. In the 1.4 M HE-EDF electrolyte, large Li-metal deposits are observed, but with a thin SEI layer (Figs. 4.2e and Fig. S4.24). In sharp contrast, the 1.4 M LiPF$_6$-EDF electrolyte shows whisker and needle-like deposits (Figs. S4.25 and S4.26) and a thicker SEI (Fig. 4.2g). The SEI composition and structures are also different, being inorganic dominated for the 1.4 M HE-EDF electrolyte (Fig. 4.2e and Fig. S4.24), implying that more anion groups participate in the SEI formation[36]. Whereas, for the 1.4 M LiPF$_6$-EDF electrolyte a carbon-rich amorphous structure is observed, driven by decomposition of the solvents (Fig. S4.26). The SEI composition is further studied using X-ray photoelectron spectroscopy (XPS) (Figs. S4.27-S4.35 and Supplementary Note S4.5), where O 1s, F 1s, and N 1s spectra confirm that the inorganic Li-F, Li-N, B-F, Li-O and B-O species dominate the SEI in the 1.4 M HE-EDF electrolyte. The presence of these species suggests a more facile and homogeneous Li-ion supply, supporting dense Li metal growth. This explains the better reversibility of the Li-metal anode in 1.4 M HE-

4

EDF compared with 1.4 M LiPF$_6$-EDF electrolyte. To study the Li loss during cycling, operando solid-state ^{7}Li NMR[37,38] is conducted in anode-less Cu||LiFePO$_4$ cells (Supplementary Note S4.6). Upon charging, Li deposition occurs on the Cu electrode and the Li metal resonance appears. At the end of discharge, the Li-metal peak remains, indicating the formation of "dead" Li (Figs. S4.36 and S37). In both electrolytes, the integrated intensity of the Li-metal peak grows linearly during charging (Fig. S4.38), but less "dead" Li is observed in the 1.4 M HE-EDF electrolyte after discharging, and the accumulated "dead" Li during the following cycles is strongly reduced, which is consistent with the better cycling stability observed for the HE electrolyte.

4.4 Cathode interphase stability

The oxidation stability of 1.4 M HE-EDF is evaluated by linear sweep voltammetry (LSV) in a Li||Al/C cell (Fig. S4.39), where the voltage of initial decomposition is around 4.7 V vs. Li/Li$^+$, higher than that of the 1.4 M LiPF$_6$-EDF electrolyte, which is promising for application in nickel-rich cathodes. Thus, the electrolytes are evaluated in combination with LiNi$_{0.8}$Co$_{0.1}$Mn$_{0.1}$O$_2$ (NCM811) cathodes into Li||NCM811 cells. The cells were cycled in the voltage range of 2.8-4.3 V vs. Li/Li$^+$ with an NCM811 areal capacity of 2.0 mAh cm^{-2} and a thickness of Li metal in 50 μm. During the initial cycles at 0.1C, the cells with the different electrolytes show a similar discharge capacity around 180 mAh g^{-1} (Figs. S4.40 and S4.41), but the long-term cycling stability of 1.4 M HE-EDF electrolyte is significantly improved over the 1.4 M LiPF$_6$-EDF electrolyte, resulting in a capacity retention of over 82% after 400 cycles at 0.5C (Fig. 4.3a). The influence of LiNO$_3$ was also investigated by comparison with the 1.3 M HE-EDF electrolyte without LiNO$_3$. Even though not as good as 1.4 M HE-EDF, the cell with the 1.3 M HE-EDF electrolyte exhibits an-improved cycling stability compared to the 1.4 M LiPF$_6$-EDF (Figs. S4.42-S4.44). When increasing the current rate to 9.0C (1,620 mA g^{-1}), the cells using 1.4 M HE-EDF electrolyte achieve more than 60% capacity retention (Fig. 4.3b), much higher than that of the cells using 1.4 M HE-EDF electrolyte (Fig. S4.45), in line with the improved Li-
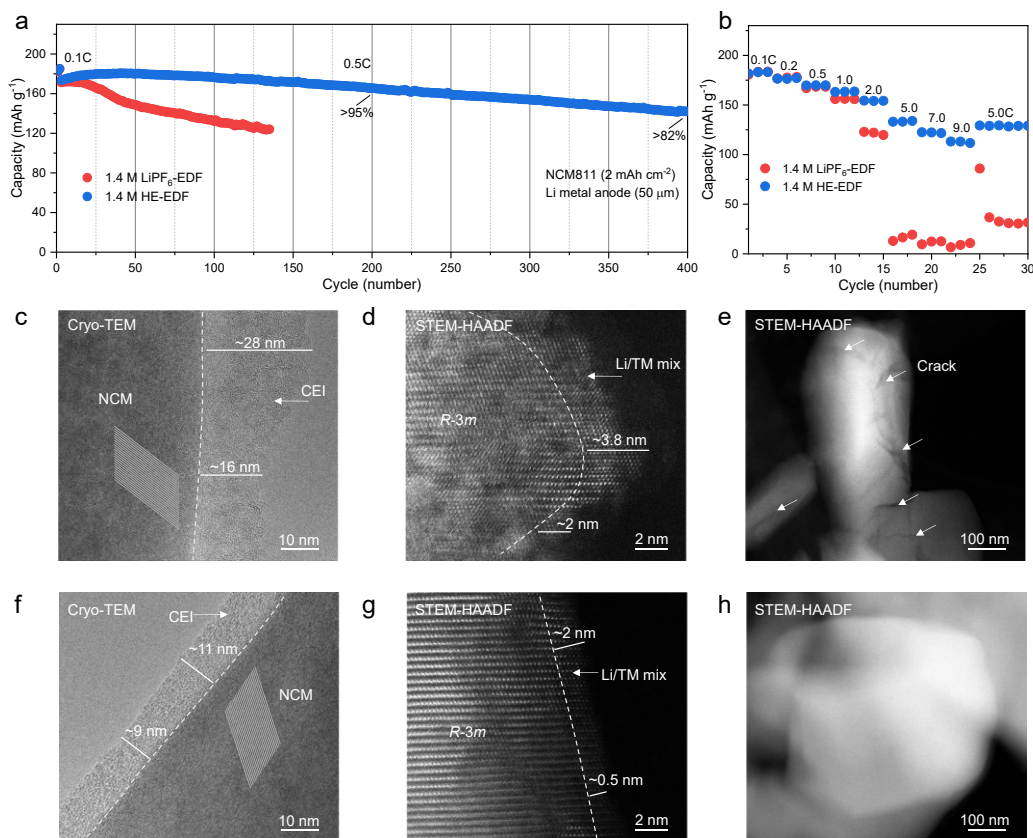
Fig. 4.3. Electrochemical performance and cathode interphase stability of HE electrolyte. a, Capacity retention of Li∥NCM811 cells with 1.4 M LiPF$_6$-EDF or 1.4 M HE-EDF electrolytes cycled between 2.8-4.3 V with 0.1C for three cycles and 0.5C for the following cycles. The areal capacity of NCM811 electrode is 2 mAh cm^{-2} and the Li metal anode is 50 μm. **b**, Rate performance of Li∥NCM811 cells cycled between 2.8-4.3 V under various current densities in different electrolytes. **c**, **f**, Cryo-TEM images of NCM811 cathode electrolyte interphase after cycling in (**c**) 1.4 M LiPF$_6$-EDF and (**f**) 1.4 M HE-EDF electrolytes. **d**, **g**, High resolution STEM-HAADF images of NCM811 cathode after cycling in (**d**) 1.4 M LiPF$_6$-EDF, and (**g**) 1.4 M HE-EDF electrolytes. **e**, **h**, Low-magnification STEM-HAADF images of primary NCM811 particle morphology after cycling in (**e**) 1.4 M LiPF$_6$-EDF and (**h**) 1.4 M HE-EDF electrolytes.

ion mobility discussed above and the smaller impedance originating from the more stable interphase (Fig. S4.46). After cycling, the morphology of the cathodes is investigated by SEM. The secondary cathode particles in the 1.4 M HE-EDF electrolyte are well preserved, while cracks and pulverization of the secondary particles are observed for the 1.4 M LiPF$_6$-EDF electrolyte (Fig. S4.47). Despite the presence of multiple salts, the 1.4 M HE-EDF

electrolyte does not show Al foil corrosion, as demonstrated by a stable anodic current at a polarization potential of 4.2 V vs. Li/Li$^+$ for 20 h (Fig. S4.48).

The structure and chemical composition of the air-sensitive CEI layers are studied by cryo-TEM. Compared to the pristine materials (Fig. S4.49), an amorphous CEI layer is formed at the surface of the particles with a thickness from 16 to 28 nm in the 1.4 M LiPF$_6$-EDF electrolyte (Fig. 4.3c), which is thicker in the 1.4 M HE-EDF electrolyte (Fig. 4.3f). Atomic-resolution high-angle annular dark field (HAADF) scanning transmission electron microscopy (STEM) images collected at room temperature reveal a mixed Li/TM (TM: transition metal) layer at the surface of the cathode particles with a thickness from around 2 nm to 3.8 nm in 1.4 M LiPF$_6$-EDF electrolyte after cycling, along with lattice distortions (Fig. 4.3d). However, for the 1.4 M HE-EDF electrolyte, the mixing layer is much thinner and the layered structure is well preserved (Fig. 4.3g), indicating that microstructural degradation and side reactions are effectively suppressed. In addition, the low-magnification STEM-HAADF images show cracks formed on the primary cathode particles after cycling in the 1.4 M LiPF$_6$-EDF electrolyte (Fig. 4.3e and Fig. S4.50), whereas no obvious cracks are observed in 1.4 M LiPF$_6$-EDF electrolyte (Fig. 4.3h), indicating the improved structural stability of the cathodes. The CEI compositions are studied by electron energy loss spectroscopy (EELS) (Figs. S4.51 and S4.52), in which the CEI formed in 1.4 M HE-EDF electrolyte shows more O-, F-, and N-containing components, compared with that in 1.4 M LiPF$_6$-EDF electrolyte, which is confirmed with XPS depth profiling analysis (Figs. S4.53-S4.57 and Supplementary Note S4.7). This compositional distribution demonstrates that the CEI in the 1.4 M HE-EDF electrolyte is more stable due to its inorganic-rich species. Further, graphite‖NCM811 full cells using the 1.4 M HE-EDF electrolyte are also tested (Fig. S4.58), resulting in approximately 90% capacity retention after 1000 cycles at 2.0C cycling rate, demonstrating this HE electrolyte has excellent potential for the use in practical Li-ion batteries.

4.5 Temperature-dependent properties

Crystallization (freezing) upon cooling of electrolytes presents a bottleneck for low-temperature application of Li batteries[39]. When the temperature decreases below the

melting point, a phase transition from liquid to solid will occur, which considerably lowers the conductivity of the remaining liquid phase and may even block electrode pores, temporarily isolating sections of the active material and thus causing capacity loss. Thermodynamically, the melting temperature of electrolytes is determined by the Gibbs free energy, and decreasing this by increasing the entropy of mixing (S_{mix}) (Fig. 4.4a) can be a promising strategy to lower the freezing point of the electrolyte[40]. Here, we show that introducing multiple salts to form the HE composition lowers the freezing point, improving the low-temperature electrolyte properties. In line with the observations for the pure EC solvent in Fig. 4.1d, the freezing point of the 1.4 M HE-EDF electrolyte is lower compared to the 1.4 M LiPF$_6$-EDF electrolyte (Fig. S4.59). However, the nature of the solvents has a larger impact on the freezing point, which remains the limitation of EC/DMC solvents. Generally, introducing solvents having lower melting points is the established route to achieve low-temperature battery performance[25,26]. To investigate if the present multicomponent salt strategy can lower the melting point of low-temperature solvents even further, a combination of propylene carbonate (PC) and diethyl carbonate (DEC) solvents is investigated[10,11]. A HE electrolyte consisting of five components with equal molar fractions salt of 0.15 M LiPF$_6$/0.15 M LiFSI/0.15 M LiTFSI/0.15 M LiDFOB/0.15 M LiNO$_3$ in PC/DEC (1:1) with 5% FEC (referred to as 0.75 M HE-PDF) is prepared (see the methods), where 0.15 M LiNO$_3$ can be dissolved in this mixed solvent. For comparison, a single salt electrolyte with the same molarity and solvents of 0.75 M LiPF$_6$ in PC/DEC with 5% FEC (referred to as 0.75 M LiPF$_6$-PDF) is prepared. The solvation structure of the HE electrolyte is studied at different temperatures using variable-temperature (VT) ^{7}Li NMR experiments (Figs. 4.4b and 4.4c). As temperature decreases, the ^{7}Li resonance of the 0.75 M HE-PDF shows a smaller shift compared to the 0.75 M LiPF$_6$-PDF electrolyte, which demonstrates that introducing multiple salts stabilizes the solution when the temperature changes. The downfield shift of 0.75M HE-PDF compared to 0.75 M LiPF$_6$-PDF at each temperature indicates a weaker solvation strength for the HE electrolyte, that can be expected to promote the Li-ion kinetics.

4
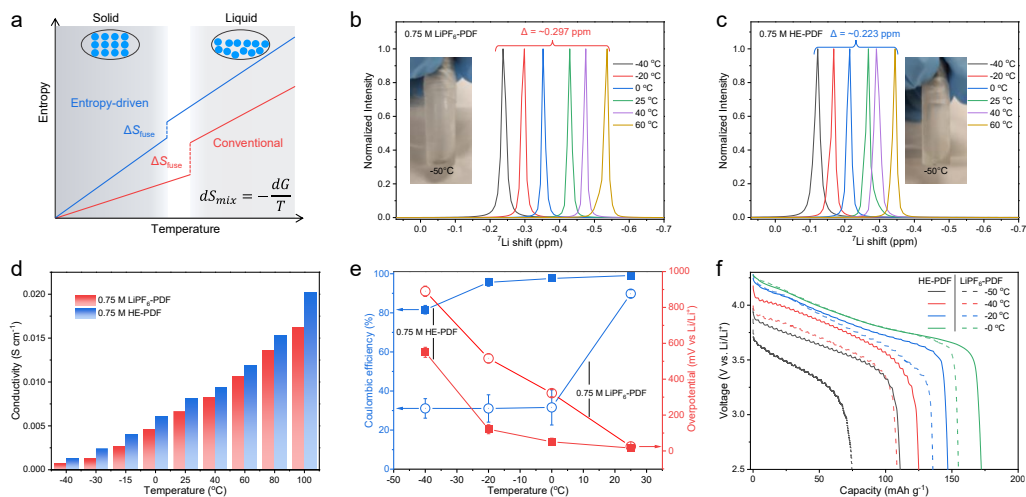
Fig. 4.4. Temperature-dependent properties of HE electrolytes. a, Schematic diagram of the entropy evolution during phase changes as the function of temperature, where the blue line indicates the evolution trend of the HE electrolyte and the red line indicates the trend of a conventional electrolyte. **b**, **c**, Variable temperature liquid ^{7}Li NMR spectra of (**b**) 0.75 M LiPF$_6$ in PC/DEC with 5% FEC (0.75 M LiPF$_6$-PDF) and (**c**) 0.15 M LiPF$_6$/0.15 M LiFSI/0.15 M LiTFSI/0.15 M LiDFOB/0.15 M LiNO$_3$ in PC/DEC with 5% FEC (0.75 M HE-PDF). **d**, Ionic conductivity of the 0.75 M LiPF$_6$-PDF and 0.75 M HE-PDF electrolytes at various temperatures. **e**, CE and overpotential of Li∥Cu cells at different temperatures with 0.75 M LiPF$_6$-PDF or 0.75 M HE-PDF electrolyte. **f**, Discharge curves of Li∥NCM811 cells cycling at 0.1C in 0.75 M LiPF$_6$-PDF and 0.75 M HE-PDF electrolytes at different temperatures within the voltage range of 2.5-4.3 V at lower temperatures.

Indeed, the HE-PDF electrolyte shows a higher conductivity (Fig. 4.4d) and Li transference number (0.456 vs. 0.401 of the HE-PDF and LiPF$_6$-PDF electrolytes, respectively) as well as a higher exchange current density, confirming the improved bulk kinetics and charge transfer upon increasing the entropy (Figs. S4.60-S4.62). These properties are held responsible for the improved electrochemical performance reflected by the lower overpotential and higher average CE at different temperatures (Figs. S4.63 and S4.64). When cycled at -40 °C, the CE maintains larger than 80%, outperforming the 0.75 M LiPF$_6$-PDF with a CE around 30% (Fig. 4.4e and Fig. S4.65).

In addition, the 0.75 M HE-PDF electrolyte shows a higher oxidation stability (Fig. S4.66), which can be applied to high-voltage cathode. The Li∥NCM811 cells employing

the different electrolytes are firstly evaluated at room temperature, both delivering similar initial charge and discharge voltage profiles with a specific capacity of around 180 mAh g^{-1} (Fig. S4.67). Upon subsequent cycling, the cells with the 0.75 M HE-PDF electrolyte present much better cycling stability, retaining over 92% of its initial capacity after 300 cycles (Fig. S4.68). In comparison, the battery with the 0.75 M LiPF$_6$-PDF electrolyte rapidly decays after 85 cycles. The battery performance is additionally evaluated at different temperatures (Fig. 4.4f), where the 0.75 M HE-PDF electrolyte shows higher capacity retention at each temperature, also in these cases showing improved low-temperature performance compared to the 0.75 M LiPF$_6$-PDF electrolyte. The low-temperature cycling stability of Li‖NCM811 cells is measured at -20 °C, where the cells with 0.75 M HE-PDF electrolyte exhibit the higher capacity retention of around 99% after cycles (Figs. S4.69 and S4.70). This is in line with the improved kinetics and enhanced interphase stability of this HE-PDF electrolytes as observed above.

4.6 Conclusions

The present work shows that increasing the entropy of mixing, by introducing multiple solutes, can be used to increase the stability of solvent-solute combinations, offering an attractive strategy to develop advanced electrolytes for (non)aqueous batteries. The resulting electrolytes show improved Li-ion kinetics and strongly altered solvation interactions due to the disordered solvation structure, a result of mixing several salts. This leads to the formation of more stable and inorganic-rich interphases on the electrodes, strongly improving the electrochemical performance of batteries with practical applicability. Another aspect of the higher solvation-structure entropy is the lowering of the electrolyte melting point to some extent, thereby improving low-temperature performance.

This study using commercial carbonate electrolytes (i.e., LiPF$_6$-EC/DMC) as starting point, should be considered a prototype study towards the general impact of increasing entropy induced by multiple salts, where strategies using advanced salts[41] and/or solvents[32] in combination with fluorine-rich[42] or salt-concentrated[28] can be expected to provide opportunities to further improve these electrolytes. Conceptually different to

change the chemical and physical properties by introducing additional salts in electrolyte, the present work demonstrates that raising the entropy by adding multiple salts, induces a general and fundamental change in solvation interaction and structure, that (along with the specific salt chemistry) can be used to improve electrolyte properties. As liquids are widely utilized as reaction media in the synthesis of functional materials and drugs, introducing multiple components forming the HE solutions, can be considered an interesting route to alter the inter molecular interactions such that it can impact mass transfer processes relevant for preparation processes.

4.7 Methods

Materials

Solvents of ethylene carbonate (EC), dimethyl carbonate (DMC), fluoroethylene carbonate (FEC), propylene carbonate (PC), diethyl carbonate (DEC) and Dimethoxyethane (DME) were purchased from E-Lyte innovations with battery-grade purity, which was dehydrated with a 4 Å molecular sieve (Sigma-Aldrich) to eliminate the trace water. Lithium hexafluorophosphate (LiPF$_6$), lithium bis(fluorosulfonyl)imide (LiFSI), lithium bis(trifluoromethanesulfonyl) imide (LiTFSI), lithium difluoro(oxalato)borate (LiDFOB) were obtained from E-Lyte innovations, and they were dried in the vacuum oven of glove box 80 °C overnight. Lithium nitrate (LiNO$_3$, >99.9%) was purchased from Shenzhen Capchem Technology Co., Ltd and used as-received. All the electrolytes were prepared by dissolving the specific amount of different Li salts in solvents in an Ar-filled glove box (H$_2$O < 0.1 ppm, O$_2$ < 0.1 ppm). Li metal foils (50 µm) were purchased from China Energy Lithium Co., Ltd; Li metal foils (thickness of 250 µm), Cu foils and Al foils were purchased from MTI Corporation. All Li metal foils were washed 3 times with DMC solvent before use. Cu foils were immersed in diluted acetic acid for several minutes, subsequently washed by deionized water and acetone three times, separately, then they were quickly dried in the vacuum oven of glove box at room temperature.

LiNi$_{0.8}$Co$_{0.1}$Mn$_{0.1}$O$_2$ (NCM811) was synthesized using coprecipitation method. The certain amount of alkaline aqueous solution (NH$_4$OH and NaOH) was poured into deionized water (1.5 L) to form the base solution in a tank reactor under continuous stirring. Then, a 2 M solution of NiSO$_4$·6H$_2$O, CoSO$_4$·7H$_2$O and MnSO$_4$·H$_2$O with a molar ratio of 8:1:1 and an aqueous solution of 5 M NH$_4$OH and 10 M NaOH were added into the base solution in the tank reactor with a steady rate of 8 mL min^{-1}. The coprecipitation temperature was controlled at 50 ^{o}C, and pH value was maintained at around 11 by NH$_4$OH with stirring speed of 500 rpm under nitrogen atmosphere. The coprecipitated Ni$_{0.8}$Co$_{0.1}$Mn$_{0.1}$(OH)$_2$ precursor was prepared, which was subsequently washed by deionized water and ethanol for four times and dried in a vacuum at 120 ^{o}C for 24 h. The apparent and tap density of Ni$_{0.8}$Co$_{0.1}$Mn$_{0.1}$(OH)$_2$ precursor are 1.88 g cm^{-3} and 2.06 g cm^{-3}, respectively. For preparation of NCM 811 materials, the as-obtained precursor was mixed with LiOH·H$_2$O at a molar ratio of 1:1.03; then heated at 500 ^{o}C for 5 h and subsequently calcined at 780 ^{o}C for 12 h in oxygen atmosphere. After cooling naturally, the obtained material was directly put into an Ar-filled glovebox to prevent any moisture exposition. The NCM811 electrodes were prepared by mixing active material, Super P and PVDF binder in the mass ratio of 90: 5: 5 in N-methyl-2-pyrrolidone (NMP) solvent and cast on Al foil and then dried at 60 °C for 6 h, followed by drying in a vacuum oven at 120 °C overnight. LiFePO$_4$ was obtained from Leneng Technology for which the cathodes were prepared by mixing LiFePO$_4$ material, poly(vinylidene difluoride) (PVDF, MTI) binder and Super P (Alfa Aesar) conductive carbon in a weight ratio of 92:4:4. The resulting slurry was cast on the Al foil then dried at 60 °C for 6 h, followed by drying overnight at 120 °C in a vacuum oven overnight. Graphite was obtained from BTR New Material Group Co., Ltd. The anode was prepared by mixing active material, conductive carbon (Super P), and PVDF conductive carbon in a weight ratio of 94:3:3. The resulting slurry was cast on the Cu foil then dried at 60 °C for 6 h, followed by drying overnight at 100 °C in a vacuum oven.

Preparation of electrolytes

The 1.4 mol L^{-1} (M) LiPF$_6$-EDF is prepared by dissolving 0.4 M LiPF$_6$ in the commercial 1.0 LiPF$_6$ EC/DMC (1:1 in volume) electrolyte with 5% FEC. The 1.4 M HE-EDF was

prepared by dissolving 0.1 M LiFSI, 0.1 M LiDFOB, 0.1 M LiTFSI, 0.1 M $LiNO_3$ in the same commercial electrolyte. The prepared electrolyte was stored for a period (around 2 weeks) to get a uniform solution under the assistance of a touch mixer machine, and intermittently heated at around 60~80 ^{o}C. The others EC-based control electrolytes are also prepared using the same method but with the different salts. The 0.75 M HE-PDF was prepared by first dissolving equal molar salt in the order of 0.15 M $LiNO_3$, 0.15 M $LiPF_6$, 0.15 M LiTFSI, 0.15 M LiFSI, and 0.15 M LiDFOB in PC under around 60~80 ^{o}C with the assistance of a touch mixer machine and then add the DEC and 5% FEC. 0.75 M $LiPF_6$-PDF is prepared by dissolve 0.75 M $LiPF_6$ in PC and DEC (1:1 in volume) with 5% FEC.

Electrochemical measurements

Electrochemical cycling tests of all batteries were based on CR2032 coin cells assembled in an Ar-filled glove box (H_2O < 0.1 ppm, O_2 < 0.1 ppm) with Celgard 2500 separator, unless stated otherwise. 70 μL electrolytes were injected into each coin cell for comparison. All coin cells were tested using multi-channel battery testing systems (Land CT2001A or Lanhe G340A). Symmetric Li||Li cells were assembled to study the cycling stability with different electrolytes, where 15.6 mm diameter Li metal foils with 250 μm thickness were used. For Li||Cu cells, 14 mm diameter Li metal foils and 16 mm Cu foils were used, with the effective area for Li deposition of 1.54 cm^2. During cycles, capacity of 1 mAh cm^{-2} Li was deposited on Cu foils at a current density of 0.5 mA cm^{-2} and then stripped until a cut-off voltage of 1.0 V vs. Li/Li$^+$.

Electrochemical cycling performance of NCM811 electrodes are with an areal capacity of 2 mAh cm^{-2} tested with Li metal foils (50 μm) as counter electrode. Li||NCM811 cells were electrochemically cycled between 2.8-4.3 V under a 0.1C rate for three cycles before cycling at 0.5C rate (1C=~180 mA g^{-1}) under room temperature. The low temperature cycling of Li||NCM811 cells is carried out in a freezer under -20°C with a voltage range between 2.5-4.3V. Graphite||NCM811 cells are cycled between 3.0 and 4.2 V at a 0.1C rate for the first three cycles and 2.0C for following cycling. The negative/positive ratio is around 1.05-1.10.

Cyclic voltammetry (CV) of Li||Cu cells with various electrolytes were conducted at a scan rate of 0.8 mV s^{-1} from -0.1 to 2.5 V vs. Li/Li$^+$. Electrochemical impedance spectra

(EIS) of the symmetric cells were collected on an Autolab (PGSTAT302N) in the frequency range of 0.1 Hz–1 MHz with a potential amplitude of 10 mV. Tafel plots were collected on an Autolab (PGSTAT302N), and they were measured at a voltage range from -0.2 to 0.2 V vs. Li/Li$^+$ in Li symmetric cells with a scan rate of 0.5 mV s^{-1}. Exchange current density, i_0, is determined by fitting the linear portion of the Tafel plot. The Al foil corrosion is studied in Li||Al/C coin cells in different electrolytes at the polarization potential of 4.2 V vs. Li/Li$^+$ for 20 h.

The Li ion transference number ($t_{Li}{}^+$) of the electrolytes was measured via the method from Abraham et al.[43] The polarization potential (ΔV) of 10 mV was used for symmetric Li||Li cells using different electrolyte until the polarization currents reached a steady state. The corresponding EIS measurements were collected before and after the polarization. The $t_{Li}{}^+$ was calculated using the following equation (4.3):

$$t_{Li^+} = \frac{I^{ss}R_b^{ss}(\Delta V - I^0 R_i^0)}{I^0 R_b^0(\Delta V - I^{ss}R_i^{ss})} \tag{4.3}$$

where ΔV is the applied potential, I^0 is the initial current and I^{ss} is the steady-state current; R_b^0 and R_b^{ss} are the initial and steady-state values of the bulk resistances and R_i^0 and R_i^{ss} are initial and steady-state values of the interfacial resistances, respectively, which were examined by impedance measurements before and after the potentiostatic polarization.

4

Ionic conductivity of electrolytes was measured using symmetric stainless steel||stainless steel cells by collecting the electrochemical impedance (R) at room temperature, and calculated using the equation (4.4):

$$\sigma = \frac{L}{R \times S} \tag{4.4}$$

where σ is ionic conductivity, S is the effective area of electrode, L stands for the thickness between two stainless-steel electrodes, respectively. Test cells were assembled with a Polytetrafluoroethylene (PTFE) ring between two electrodes. Hence, the effective area of electrode is calculated based on the inner diameter PTFE ring, and the thickness two stainless-steel electrodes is based on total thickness of PTFE ring.

For the evaluation of Al foil corrosion, Li||Al/C cells were assembled with a 250 μm thick Li metal foil with 70 μL of different electrolytes. The cells were tested with the potentiostatic mode at 4.2 V vs. Li/Li$^+$ for 20 h.

Materials characterizations

Morphologies of electrodes were measured on a cold field scanning electron microscope (SEM, HITACH-S4800, SU8010). Elemental composition on the surface of the electrodes was analyzed by X-ray photoelectron spectroscopy (XPS, PHI 5000 VersaProbe II) using a monochromatic Al Kα X-ray source. For depth profiling of the electrodes, a sputter argon ion gun was used. Peaks were fitted using MultiPak software calibrated with respect to carbon (284.8 eV). The above morphology and composition characterization were performed with cells being disassembled after specific cycles in an Ar-filled glove box and rinsed with pure DMC solvent three times to remove residual electrolyte, followed by drying in a glove box for several hours at room temperature to remove the residual solvent. Then these electrodes were transferred into the vacuum transfer boxes for measurements to avoid air exposure. Raman spectroscopy was measured by Micro-laser confocal Raman spectrometer (Horiba LabRAM HR800 spectrometer) equipped with an Olympus BX microscope and an argon ion laser (532 nm) at room temperature. All the electrolytes were hermetically sealed in quartz cuvettes in a glovebox before measurement.

Cryo-transmission electron microscopy (cryo-TEM) characterization

Conventional and cryo-TEM experiments were performed on a scanning transmission electron microscope (STEM) (JEM-ARM300F, JEOL Ltd.) operated at 300 kV with a cold field emission gun and double Cs correctors. The microscope was equipped with Gatan OneView and K2 cameras for images recording. During image acquisition, the corresponding electron dose flux (units of number of electrons per square Å per second, $e^- Å^{-2} s^{-1}$) was recorded. Conventional STEM images were taken with a dose rate of over $1000\ e^-\ Å^{-2}\ s^{-1}$ with an exposure time for each image of several seconds. Cryo-TEM images were obtained with an exposure time for each image of around 0.3 s with built-in drift correction function in GMS3 using the OneView and K2 camera. Cryo-TEM images were taken with an electron dose rate of 50-500 $e^-\ Å^{-2}\ s^{-1}$. Short-exposure single-frame shots were used to estimate the defocus and make it as close as possible to Scherzer defocus. The EELS spectrum images were carried out with a camera length of 20 mm, and a pixel dwell time of 10 ms. Energy drift during spectrum imaging was corrected by centering the zero-loss peak to 0 eV at each pixel. Elemental maps were computed through a two-

window method in a pre-edge window fitted to a power-law background and a post-edge window of 50-200 eV on the core-loss signal.

For cryo-TEM preparation of Li metal anode, a lacey carbon TEM grid was put on Cu foil working electrode and assembled into Li||Cu cells in an argon-filled glovebox. The cells were discharged at a constant current density of 1.0 mA cm^{-2} for 15 min, after which the TEM grid was taken out by disassembling the cells for measurement. The TEM grid was carefully transferred into the cryo-TEM holder in glovebox with a specialized shutter to prevent air exposure and ice condensation onto the sample introducing any side reactions. Once the cryo-TEM holder was transferred into TEM column, the temperature was maintained at around -170 ℃ using liquid nitrogen. For cryo-TEM preparation of NCM811 cathodes, Li||NCM811 cells were cycled at 0.5C for 50 cycles in the voltage range of 2.8-4.3 V and then disassembled in glovebox. After rinsing the cathode, a small piece of cathode was sealed in an airtight container with pure DMC inside. Then the sealed airtight container was taken out from glovebox and the sample was dispersed for three minutes by ultrasonic method. After that, the dispersed cathode was dropped on the TEM grids in glovebox and loaded into the cryo-TEM holder for further measurement. The same specialized shutter was also used to prevent air exposure. All cryo-TEM images are taken at around -170 ℃ to reduce beam damage. For the conventional STEM experiments, the above dispersed sample was dropped on a copper grid, dried for three hours in a vacuum and loaded into the double-tilt holder.

Liquid nuclear magnetic resonance (NMR) characterization

Liquid NMR spectra were recorded with an Agilent 400 MHz DD2 NMR spectrometer with 5 mm ONE NMR Probe at room temperature, which worked at 155.5 MHz on ^{7}Li. The chemical shift values are given in ppm. ^{7}Li chemical shift was referenced to the standard solution: 1 M LiCl in D_2O for ^{7}Li (0 ppm). All referenced solutions are measured in the enclosed internal capillary in D_2O. During measurement, all electrolytes were sealed into 5-mm Pyrex capillary tubes with PTFE caps, and then was inserted into an NMR tube containing the external standard solutions. Mestrelab Research Mnova was used for data processing. The variable temperature NMR experiments were carried out with a temperature range from -40℃ to 60℃.

Solid-state NMR characterization

Operando solid-state NMR measurements were conducted on a wide-bore Bruker Ascend 500 system equipped with a NEO console with a magnetic field strength of 11.7T and a ^{7}Li resonance frequency being 194.37 MHz using a solenoidal Ag-coated Cu coil. Operando static ^{7}Li NMR measurements were performed using an automatic-tuning-and-matching probe (ATM VT X operando WB NMR probe, NMR Service) at room temperature which can allow for an automatic recalibration of the NMR radio-frequency (rf) circuit during an operando electrochemistry experiment. A highly shielded wire with low-pass filters was attached to the probe for electrochemical measurement, which could minimize the interferences between NMR and the electrochemistry circuit. Single-pulse with a $\pi/2$ pulse of 4 μs and recycle delay of 1.0 s was applied to acquire the 1D static spectrums. A recycle delay of three times of T_1 was used each time, where T_1 was determined using saturation recovery experiments. The electrochemical cell was simultaneously controlled by a Maccor battery testing system. A plastic capsule cell made out of polyether ether ketone (PEEK) was used for the operando NMR experiments. The cells were assembled using LiFePO$_4$ cathode (areal capacity is 2.0 mAh cm^{-2}) and Cu foils as working and counter electrodes with both a piece of Celgard and a piece of Glass fiber (Whatman GF/A) as separator. Before measurements, the assembled cells were rested for 2 hours in glovebox. The operando capsule cell was aligned in an Ag-coated Cu coil with LiFePO$_4$ and Cu foil electrode oriented perpendicular to B_0 and parallel with respect to the B_1 rf-field. During the static ^{7}Li NMR measurements, the cells were charged to the capacity of 1 mAh cm^{-2} at current density of 0.5 mA cm^{-2}. During charge and discharge process, NMR spectra were continuously acquired, with each scan time of about three minutes. The chemical shift of ^{7}Li was referenced to 1 M aqueous solution of LiCl at 0 ppm. The spectra were processed in the Bruker Topspin software, using the automatic phase and baseline correction. Mestrenova were used for data processing and analysis.

Molecular dynamics (MD) simulations

Classical MD simulations were conducted on single and high-entropy electrolyte systems with different Li salts and concentrations using the LAMMPS package[44]. Molecules and

ions were described by the optimized potentials for a liquid simulations all-atom (OPLS-AA) force field[45]. Partial charges were computed by fitting the molecular ESP at the atomic centers with the Møller–Plesset second-order perturbation method with the correlation-consistent polarized valence cc-pVTZ(-f) basis set[46]. The single salt system contains a 1 M LiPF$_6$ dissolved in EC/FEC/DMC solvent, while the multiple salts system contains a 1 M mixture of LiPF$_6$ and 0.1 M LiFSI, 0.1 M LiTFSI, 0.1 M LiDFOB and 0.1 M LiNO$_3$, respectively, dissolved within EC/FEC/DMC solvent with the ratio of 19:19:2. In order to create a certain concentration of salt within EC/FEC/DMC, a 1:10 salt/solvent ratio is required. Simulation boxes with dimensions of 60×60×60 Å were randomly packed with 1000 molecules of EC/FEC/DMC and 100 salt molecules using the software Packmol[47]. A cutoff distance of 1.1 nm was chosen for the Lennard-Jones interactions. A conjugate-gradient energy minimization was first performed on both simulation boxes. A time-step of 0.5 fs was chosen for the MD simulations performed after this point. Isothermal-isobaric ensemble simulations at 300 K was first performed for 5 ns in order to obtain the correct volumes of both systems. Subsequently, both systems were equilibrated at room temperature using canonical ensemble simulations for another 6 ns. The canonical ensemble simulations were continued for another 4 ns, and snapshots of the simulation were obtained every 0.5 ps. The solvation structures of the simulation were analyzed using the Python Materials Genomics (pymatgen) package[48]. The radial density functions and the Li-ion diffusivities were computed using the MDAnalysis package[49].

DFT Calculations

Quantum chemical calculations were conducted using density functional theory (DFT) method with Becke's three parameters (B3) exchange functional in Lee-Yang-Parr (LYP) nonlocal correlation functional (B3LYP)[50,51]. All the geometry optimizations were performed with the B3LYP/6-31+G(d,p) level. The energy calculations were performed at B3LYP/6-311++G(3df,3dp) level for more accurate calculation. All DFT calculations were performed by using the Gaussian 09 program package60[52].

4

4.8 Supplementary information

Supplementary Notes

Supplementary Note S4.1

Compatibility of LiNO$_3$ with carbonate solvents. Generally, the dielectric constant and Gutmann donor number (DN) are used to evaluate the ability of a solvent to dissolve salts. EC has a dielectric constant around 90, which exceeds that of the ether solvent DME (7.2), suggesting that EC solvent can dissociate LiNO$_3$. However, EC is a solid at room temperature and needs to be used in combination with a less viscous solvent, which comes along with a low dielectric constant, for instance of a linear carbonate solvent of DMC (dielectric constant around 3.1). However, the mixture of them results in the very negligible solubility of LiNO$_3$. Salt dissociation is also related to the DN of the solvents, a parameter measuring the Lewis basicity[53], where the DN of cyclic carbonates (~15) is lower than that of LiNO$_3$ (~22) and DME (~20), rationalizing the low solubility of LiNO$_3$ in carbonates.

Supplementary Note S4.2

The increased solubility in ether solvent with mixing more salts. Compared with carbonate solvents, the ether solvents have the enhanced solubility of LiNO$_3$, for example of which can form the ~0.4 M LiNO$_3$ in DME electrolyte, but further increasing LiNO$_3$ up to 1.0 M makes the solution supersaturated with a large amount of precipitate in the bottle (Fig. S4.2a). Interestingly, this supersaturated solution is found to change into a uniform solution after adding 0.5 M LiFSI, 0.5 M LiTFSI and 0.5 M LiDFOB (Fig. S4.2b) together, and this obtained solution can still dissolve another 0.2 M LiNO$_3$ (Fig. S4.2c). As further adding 0.2 M LiNO$_3$ in this solution, a little bit of precipitate of LiNO$_3$ is observed in the bottle (Fig. S4.2d) forming 0.5 M LiFSI, 0.5 M LiTFSI, 0.5 M LiDFOB and about 1.3 M LiNO$_3$ DME electrolyte, which further indicates the increasing entropy is able to increase solubility of LiNO$_3$ in DME solvent.

Supplementary Note S4.3

Solvation structures of different electrolytes from Raman spectra. The interaction between Li ions and solvents in different electrolytes were characterized using Raman

spectroscopy. After adding 1.0 M LiPF$_6$ into EDF solvent, extra peaks appear as indicated by the black arrows, which is corresponding to the Li ion coordinated to solvents (Fig. S4.4a). As the salt concentration increased to 1.4 M, the intensity of the coordinate peaks increases, indicating that more solvent molecules can be coordinated with Li ions due to the increased Li molarity. However, when add 0.1 M LiNO$_3$ to the 1.0 M LiPF$_6$-EDF, the intensity of the coordinated peaks does not increase (Fig. S4.4b), which can be explained by the neglective solubility of the LiNO$_3$ in the conventional carbonate-based electrolyte as shown in Fig. S4.3. Then 0.1 M LiTFSI, 0.1 M LiFSI, 0.1 M LiDFOB were added into the 1.0 M LiPF$_6$-EDF to prepare 1.3 M HE-EDF electrolyte, where the intensity of the coordinated peaks increase compared with the baseline electrolyte but still lower than those of 1.4 M LiPF$_6$-EDF due to lower Li-ion molarity. Finally, 1.4 M HE-EDF electrolyte was obtained by adding 0.1 M LiNO$_3$ to 1.3 M HE-EDF. Compared to the 1.4 M LiPF$_6$-EDF, the intensity of the coordinated peaks in 1.4 M HE-EDF electrolyte are lower (Fig. S4.4c), which indicates that less solvents are coordinated with Li ion. This is further confirmed by lower fraction of coordinated solvents calculated according to the peak fitting of the Raman spectra as shown in Fig. 4.2a and Fig. S4.5.

Supplementary Note S4.4

Solvation structures of different electrolytes from NMR spectra. The different peak shifting in ^{7}Li NMR describes the different solvation structure around Li ion. The upfield shifting (to lower ppm value) or downfield shifting (to higher ppm value) represent increased and decreased electron density around the nuclei of dissociated Li ion, respectively. In Fig. S4.6, the peak of 1.4 M LiPF$_6$-EDF electrolyte shifts to the upfield direction as compared with the peak of 1.0 M LiPF$_6$-EDF electrolyte, indicating increased electron density around solvated Li ion resulted from the increased salt concentration. Similar trend can be observed when 0.1 M LiTFSI, 0.1 M LiFSI, 0.1 M LiDFOB were added into the 1.0 M LiPF$_6$-EDF to prepare 1.3 M HE-EDF electrolyte, where the peak of 1.3 M HE-EDF shifts to upfield but with higher ppm value than 1.4 M LiPF$_6$-EDF. When 0.1 M LiNO$_3$ was added into 1.0 M LiPF$_6$-EDF, no peak shifting was observed for the obtained electrolyte compared with the baseline 1.0 M LiPF$_6$-EDF electrolyte due to the poor solubility of LiNO$_3$. However, after adding 0.1 M LiNO$_3$ to 1.3 M HE-EDF, the peak

4

of the obtained 1.4 M HE-EDF electrolyte unexpectedly shift to downfield, indicating a decreased electron density around solvated Li ions. This weaker solvation in 1.4 M HE-EDF electrolyte present a unique solvation structure where the interactions of Li ion with both anionic group and solvents are decreased.

Supplementary Note S4.5

XPS analysis of SEI on Li metal anode. XPS has been conducted to characterize composition of SEI layers formed on the electrodeposited Li metal anode in 1.4 M $LiPF_6$-EDF and 1.4 M HE-EDF electrolytes. The SEI derived from 1.4 M $LiPF_6$-EDF contains high concentrations of Li and O elements, compare to that in the 1.4 M HE-EDF electrolyte. In addition, a higher content of F, B, N and S4. Elements can be found in HE-derived SEI, suggesting the decomposition of the anionic group at the Li metal anode. The detail spectrum in the C1s region contains four peaks. The first peak at 284.8 eV can be attribute to C-C/C-H species from the decomposition of EC, DME and FEC, where the 1.4 M $LiPF_6$-EDF shows higher intensity of the C-C/C-H peak especially on the surface as compared with that of 1.4 M HE-EDF electrolytes, indicating solvent dominated SEI formation. The second peak at around 286.3 eV comprises C-O species. In the 1.4 M $LiPF_6$-EDF, the C-O species comes from the decomposition of solvents, while in the 1.4 M HE-EDF electrolyte, except for the solvents, salt like LiDFOB is also able to form C-O species. More C-O species observed in the 1.4 M HE-EDF is therefore attributed to the decomposition of $DFOB^-$ anionic group since the lower C-C/C-H reflect less solvent decomposition. The third peak at around 288.3 eV (assigned to CO_3^{2-}) and the forth peak at around 290.2 eV (assigned to $Poly(CO_3^{2-})$) are from $ROCO_2Li$ formed by the decomposition of DMC and the polyethylene oxide species formed by EC polymerization respectively, where the higher peak intensity of these two peaks in 1.4 M $LiPF_6$-EDF is in agreement with more solvent decomposition as compared with 1.4 M HE-EDF electrolyte. Matching the C 1s features, signals due to O=C-O (~532.3 eV) and C-O (~529.5 eV) species are also observed in the O 1s spectra, where 1.4 M $LiPF_6$-EDF shows higher content of these species than 1.4 M HE-EDF electrolyte. In addition, extra peaks attributed to B-O, N-O, SO_x in 1.4 M HE-EDF electrolyte are observed due to the decomposition of multiple salts. In the F 1s spectra, peaks due to Li-F (~685.5 eV) and P-F (~688.4 eV)

species in both electrolytes are detected due to the decomposition of LiPF$_6$, while in 1.4 M HE-EDF electrolyte the C-F species contributed from other anionic group is also observed together with a decreased content of P-F species. Li-F content in both electrolytes accounted for a large proportion of the F-containing species, which is confirmed in Li-F peak (~56.5 eV) the Li 1s spectra. In addition, less the RO-Li species that derived from the solvent can be found in the SEI formed in 1.4 M HE-EDF electrolyte, which is in agreement with that observed in C 1s and O 1s spectra. Overall, more inorganic-rich surface features can be obtained with 1.4 M HE-EDF than that of 1.4 M LiPF$_6$-EDF.

Supplementary Note S4.6

Operando ^{7}Li NMR. To gain insight into the evolution of the Li metal during cycling in different electrolyte, operando ^{7}Li solid-state NMR was conducted using Cu||LiFePO$_4$ operando cell. ^{7}Li solid-state NMR selectively measures the nuclear magnetic resonance frequency of the Li species, where the development of operando probes allows to monitor processes while the battery is cycling[54]. The Li metal species have a chemical shift in the range of 240 to 290 ppm, which is due to the Knight shift quantifying the augmentation of the local magnetic field by the conduction electrons. Therefore, Li metal can be distinguished from the diamagnetic Li species in the electrolyte and SEI[38]. As a result, these measurements allow the quantification of the amount of "dead" Li metal after stripping, representing Li metal deposits that are electronically disconnected from the Cu current collector.[38] In this work, Li corrosion is not taken into account based on the relatively low corrosion current compared to the plating/stripping current[55].

Supplementary Note S4.7

XPS analysis of CEI on NCM811. The XPS was performed on the CEI on the NCM811 cathodes after cycling. The CEI formed in 1.4 M LiPF$_6$-EDF shows average elements concentration distribution within different depth and a higher C content as compared with 1.4 M HE-EDF electrolyte. By contrast, CEI formed in 1.4 M HE-EDF shows increased F and decreased C content. In the F 1*s* spectra peaks attributed to Li-F and P-F species in both electrolytes are detected, and the C-F species from anionic group can be detected in 1.4 M HE-EDF electrolyte. In the O 1*s* spectra, more Ploy(CO$_3$$^{2-}$), C=O and C-O species

indicate that more solvent participate in the CEI formation in 1.4 M $LiPF_6$-EDF as compared to the 1.4 M HE-EDF electrolyte. Less M-O species in the cathode material can be detected for the CEI formed in 1.4 M HE-EDF electrolyte, which signifies a thinner CEI layer as compared with the CEI formed in 1.4 M $LiPF_6$-EDF.
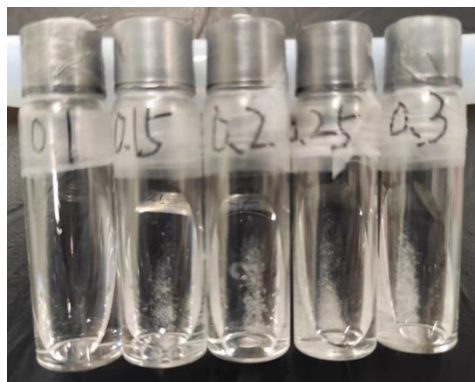
4

Fig. S4.1. Optical images of electrolytes. 1.0 M $LiPF_6$/0.1 M LiFSI/0.1 M LiTFSI/0.1 M LiDFOB in EC/DMC (1:1 by weight) with 5%FEC (refer to as 1.3M HE-EDF) with different concentrations of $LiNO_3$ after storage. The concentration of $LiNO_3$ from left to right is 0.1 M, 0.15 M, 0.2 M, 0.25 M, or 0.3 M, respectively.
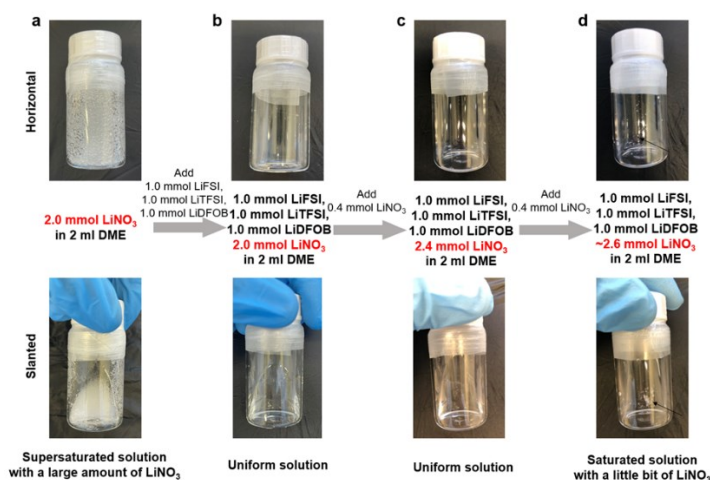
Fig. S4.2. The increasing solubility of $LiNO_3$ in HE-ether electrolyte. a, A supersaturated solution of 2.0 mmol $LiNO_3$ in 2 ml DME solvent with a large amount of $LiNO_3$ particles. **b,** A uniform solution after adding 1.0 mmol LiFSI, 1.0 mmol LiTFSI and 1.0 mmol LiDFOB in the supersaturated solution of **a**. **c,** A uniform solution after adding more 0.4 mmol $LiNO_3$ in the solution of **b**, **d,** A saturated solution after adding more 0.4 mmol $LiNO_3$ in the solution of **c** with a little bit of $LiNO_3$ particles. The bottles in top panel are in horizontal position, and in bottom panel are slanted.
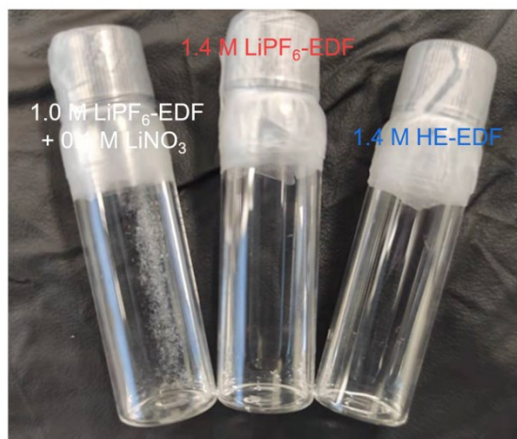
Fig. S4.3. Image of the electrolytes after preparation. 1.0 M LiPF$_6$/0.1 M LiNO$_3$, 1.4 M LiPF$_6$, and 1.4 M HE in EDF are shown. The insoluble component observed bottle is LiNO$_3$.
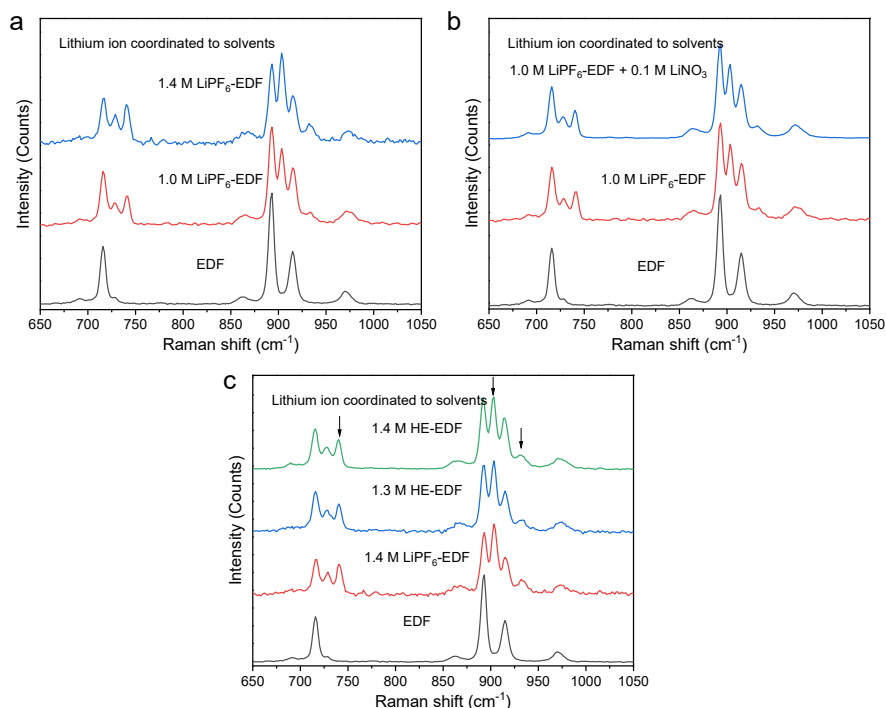
Fig. S4.4. Raman spectra of different electrolytes. a, Raman spectra of EC/DMC/5%FEC solvent (EDF), 1.0 M LiPF$_6$-EDF, and 1.4 M LiPF$_6$-EDF. **b,** Raman spectra of EDF, 1.0 M LiPF$_6$-EDF, and 1.0 M LiPF$_6$-EDF with 0.1 M LiNO$_3$. **c,** Raman spectra of EDF, 1.4 M LiPF$_6$-EDF, 1.3 M HE-EDF (0.1 M LiFSI, 0.1 M LiTFSI, 0.1 M LiDFOB and 1.0 M LiPF$_6$ in EC/DMC with 5% FEC), and 1.4 M HE-EDF. The black arrows indicate the Li ion coordinated to solvents.
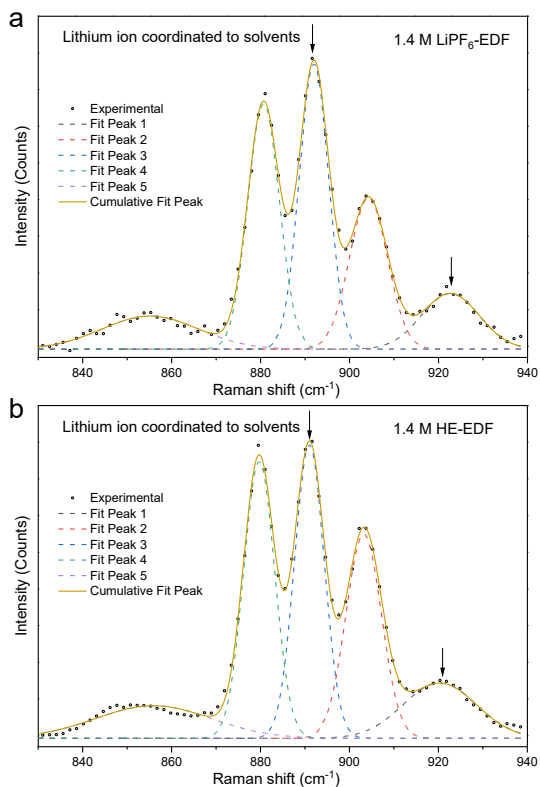
Fig. S4.5. Raman spectra for different electrolytes. The deconvoluted peaks for **a,** 1.4 M $LiPF_6$-EDF and **b,** 1.4 M HE-EDF.
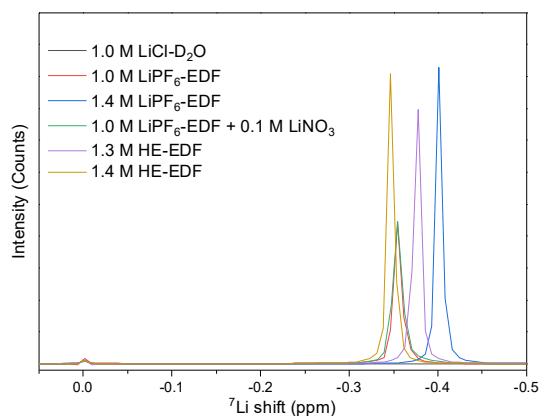
Fig. S4.6. ^7Li NMR spectra of different electrolytes. The chemical shifts are referenced to 1.0 M LiCl in D_2O at 0 ppm.
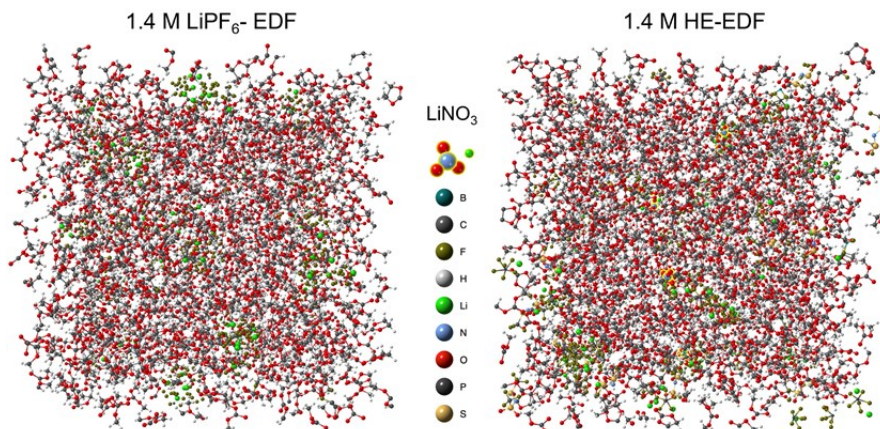
Fig. S4.7. Model packages for MD Simulation. The left panel is 1.4 M LiPF$_6$-EDF and the right panel is 1.4 M HE-EDF electrolyte.

Fig. S4.8. Li-ion coordination environments determined from MD simulations. The main solvation and corresponding ratio in 1.4 M LiPF$_6$-EDF electrolyte is presented.
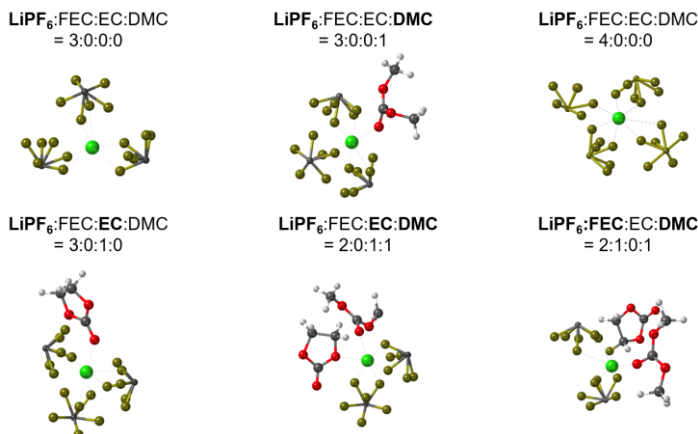
Fig. S4.9. The representative solvation structures from MD simulations for the 1.4 M LiPF$_6$-EDF electrolyte. The green atom in the centre represents Li ion and the surrounding molecules are the solvents and anions.
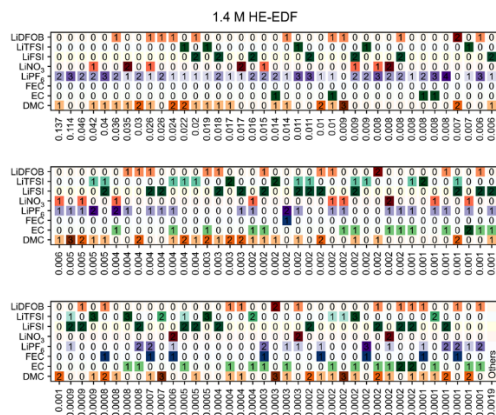
Fig. S4.10. Li-ion coordination environments determined from MD simulations. The main solvation and corresponding ratio in 1.4 M HE-EDF electrolyte is presented.
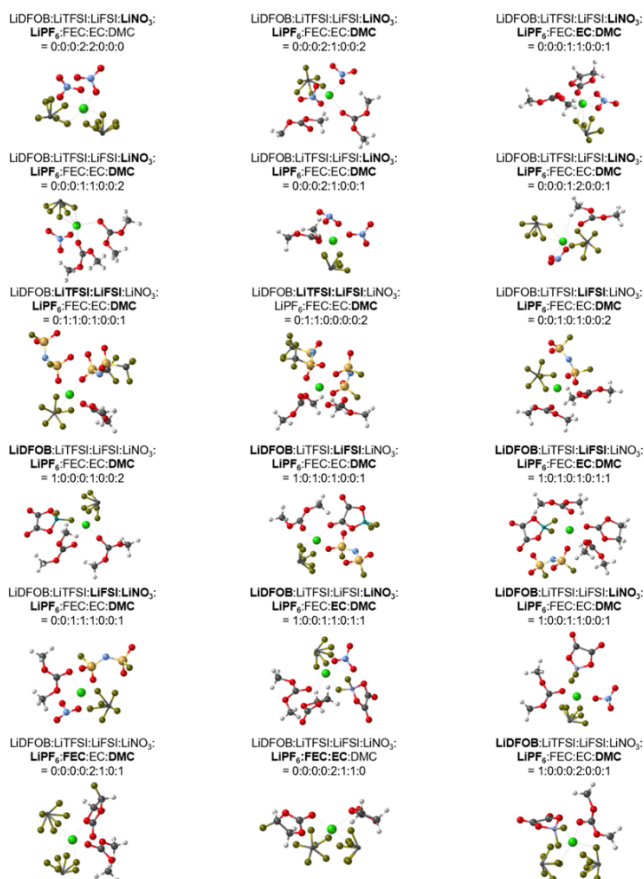
Fig. S4.11. The representative solvation structures from MD simulations for the 1.4 M HE-EDF electrolyte. The green atom in the centre represents Li ion and the surrounding molecules are the solvents and anions.
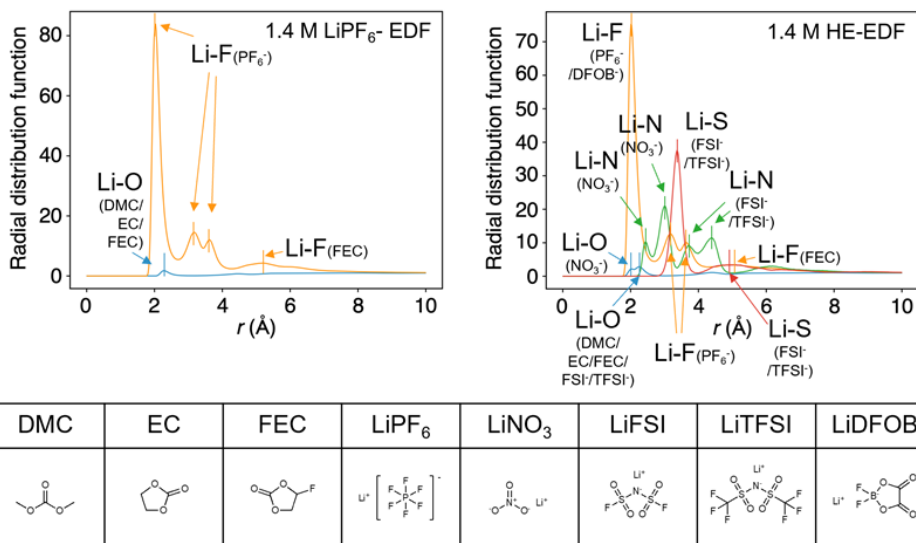
Fig. S4.12. Radial distribution function from MD simulations for 1.4 M LiPF₆-EDF and 1.4 M HE-EDF electrolytes. The table at the bottom shows the structure of the related salts and solvents.

4
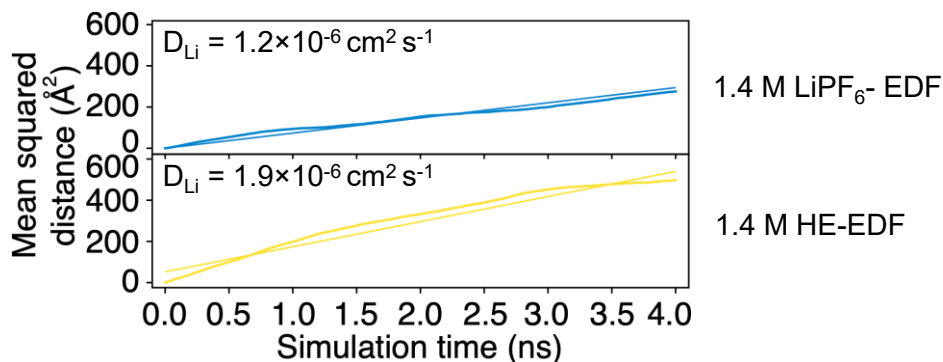
Fig. S4.13. The Li-ion self-diffusion coefficient (D_{Li}). They are obtained from the MD simulated mean squared displacement for the 1.4 M HE-EDF electrolyte (bottom) and the 1.4 M LiPF₆-EDF electrolyte (top).
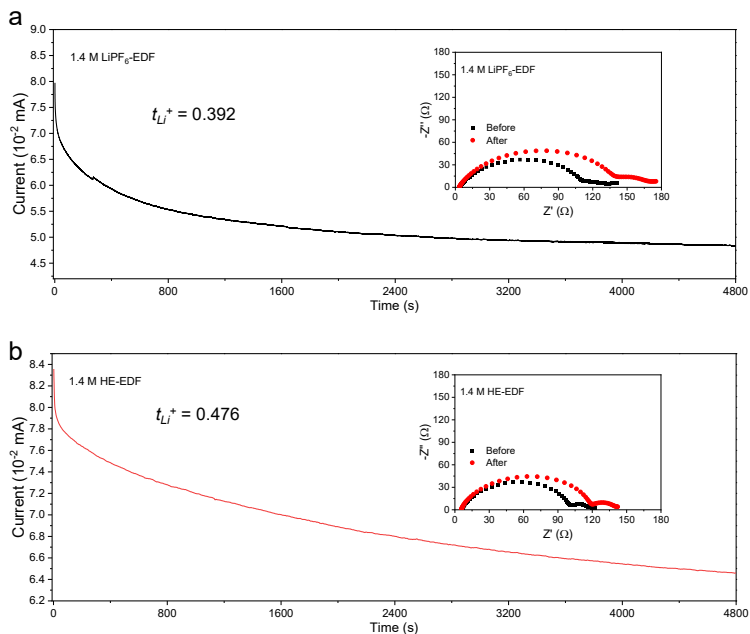
Fig. S4.14. Li transference number. Chronoamperometry profile under a polarization voltage of 10 mV for **a,** 1.4 M LiPF$_6$-EDF and **b,** 1.4 M HE-EDF electrolyte in Li∥Li cells. The corresponding electrochemical impedance spectroscopy (EIS) before and after polarization of the initial and steady-state values of resistances respectively are shown inside.
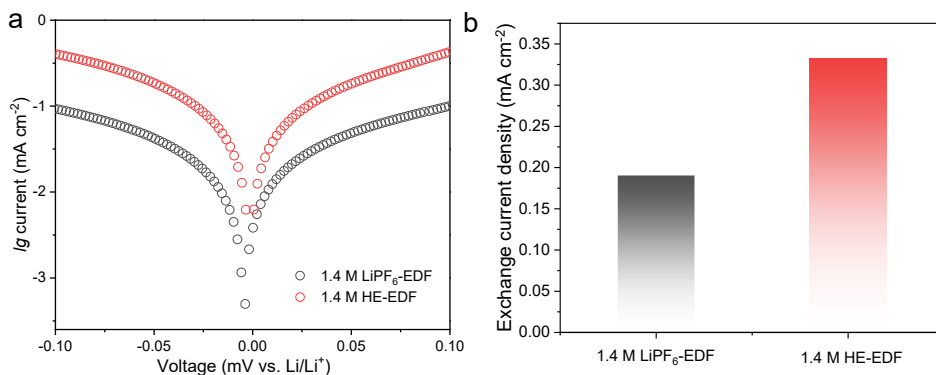
Fig. S4.15. Exchange current density from Tafel plots. a, Galvanostatic Li plating/stripping using Li∥Li cells in 1.4 M LiPF$_6$-EDF and 1.4 M HE-EDF electrolytes. **b,** Exchange current density from linear fitting of the Tafel curve.
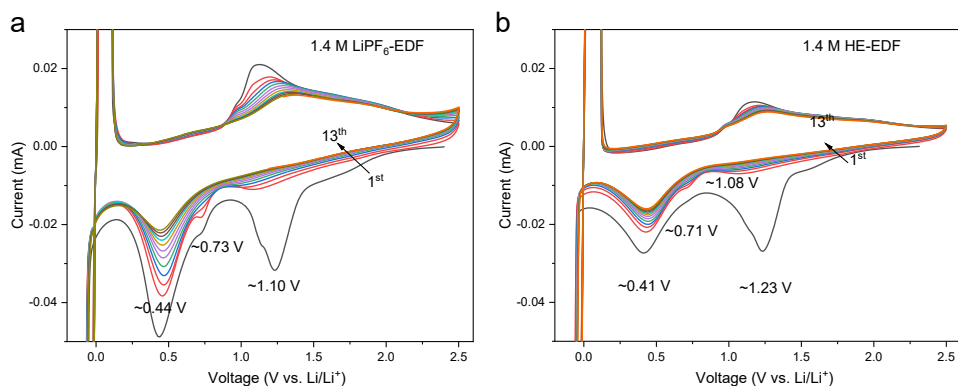
Fig. S4.16. Cyclic voltammetry (CV) curves of Li‖Cu cell. The measurements were carried out at a scan rate of 0.8 mV s^{-1} from -0.1 to 2.5 V vs. Li/Li$^+$ for **a,** 1.4 M LiPF$_6$-EDF and **b,** 1.4 M HE-EDF electrolytes.

4
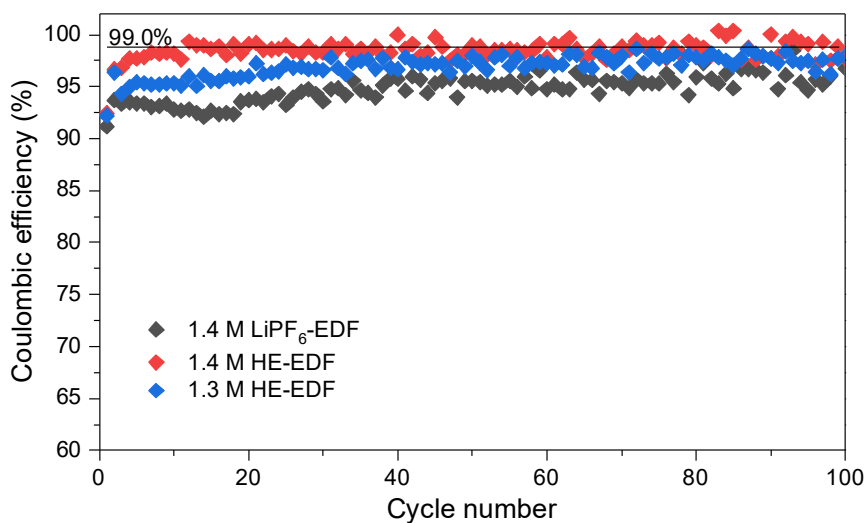
Fig. S4.17. Galvanostatic Li plating/stripping Coulombic efficiency (CE) in Li‖Cu cells using different electrolytes. Li was electrodeposited at 0.5 mA cm^{-2} to a capacity of 1 mAh cm^{-2}.
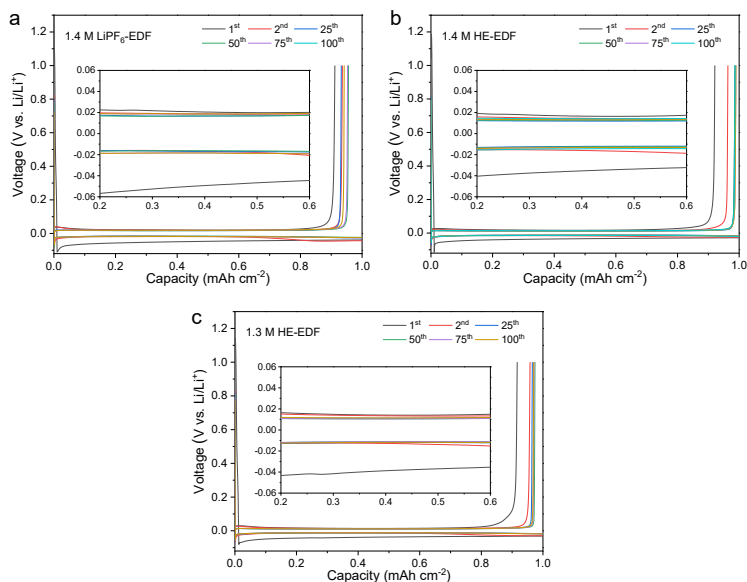
Fig. S4.18. Galvanostatic Li plating/stripping profiles of Li‖Cu cells. **a,** 1.4 M LiPF$_6$-EDF and **b,** 1.4 M HE-EDF and **c** 1.3 M HE-EDF electrolyte of selected cycles at 0.5 mA cm^{-2} and 1 mAh cm^{-2}. The inserts show the zoomed-in voltage curves of selected cycles.
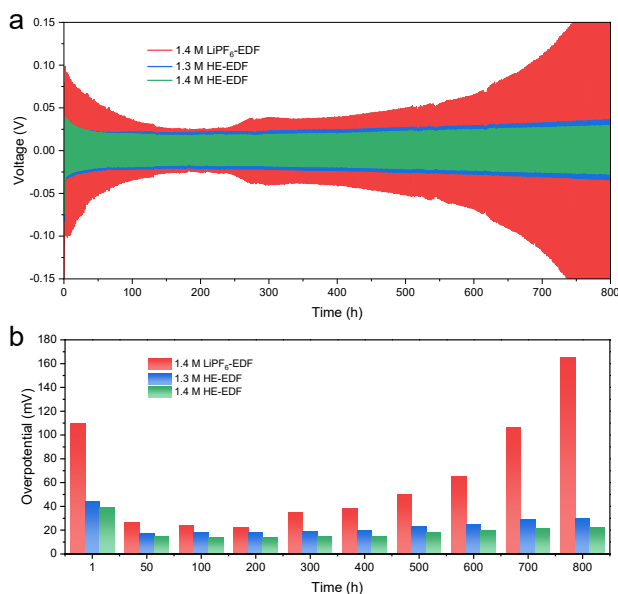
Fig. S4.19. Galvanostatic Li plating/stripping in Li‖Li cells. a, Long-term cycling of Li‖Li cells in different electrolyte at 0.5 mA cm^{-2} to a capacity of 0.5 mAh cm^{-2}. **b,** The overpotential of Li‖Li cells from the voltage curves at different stage of cycling.
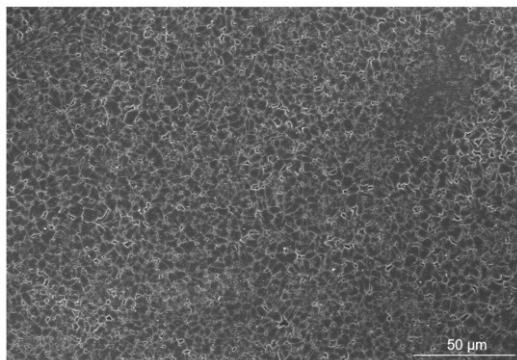
Fig. S4.20. SEM image showing Li metal morphology at low magnification. The Li metal is plated on Cu current collector in 1.4 M HE-EDF electrolyte.
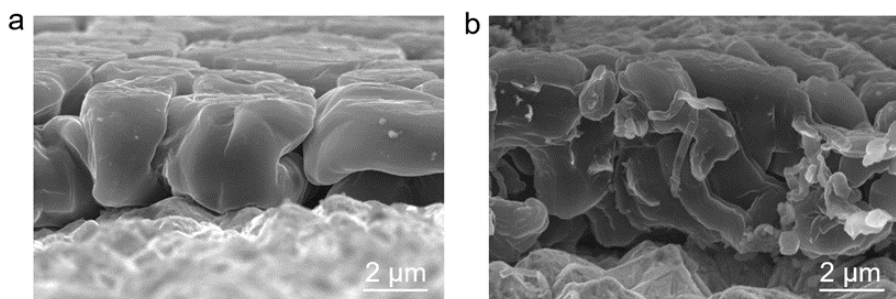
Fig. S4.21. Cross-section SEM images of Li metal plated in different electrolytes. Li metal after first cycle plating using **a,** 1.4 M HE-EDF and **b,** 1.4 M LiPF$_6$-EDF electrolytes in Li‖Cu cells at 0.5 mA cm^{-2} to a capacity of 1.0 mAh cm^{-2}.
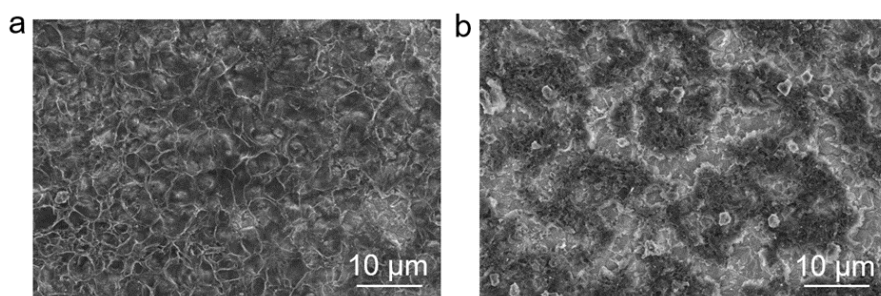
Fig. S4.22. SEM images of Cu foil after stripping in different electrolyte. The stripped Li metal on Cu current collector in **a,** 1.4 M HE-EDF and **b,** 1.4 M LiPF$_6$-EDF electrolytes from top view. Cells were cycled at a current density of 0.5 mA cm^{-2} to a capacity of 1.0 mAh cm^{-2} followed by stripping to a cut-off voltage of 1.0 V vs. Li/Li$^+$.
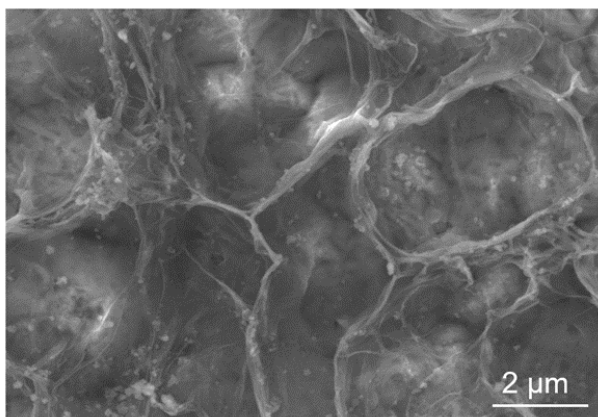
Fig. S4.23. SEM image of Cu foil after stripping at high magnification. It shows the Cu collector after Li metal stripping in 1.4 M HE-EDF electrolyte with a scale of 2 μm.
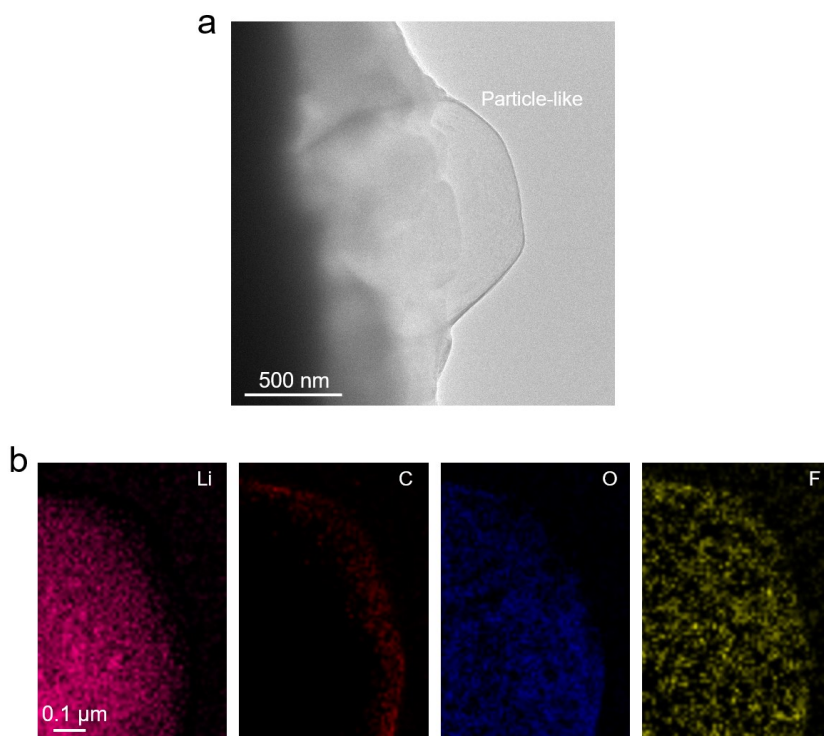
Fig. S4.24. Microstructure of plated Li metal and component of SEI. a, Cryo-TEM image of plated Li metal on a Cu grid in 1.4 M HE-EDF. **b,** Cryo-STEM EELS elemental mapping of plated Li metal and SEI.
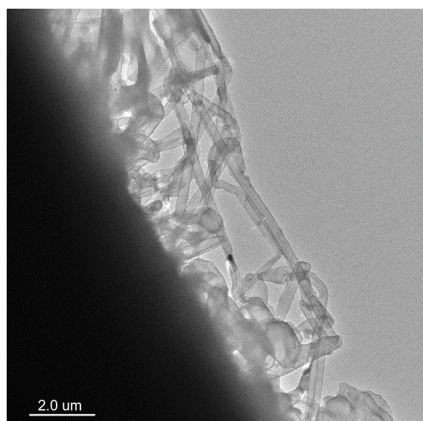
Fig. S4.25. Cryo-TEM image at low magnification. The plated Li on a Cu grid is collected in 1.4 M LiPF$_6$-EDF.
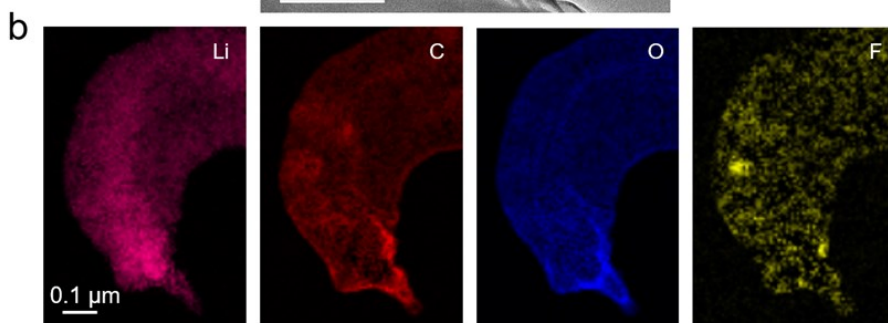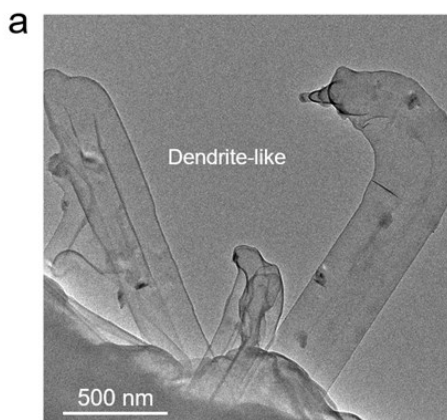
Fig. S4.26. Microstructure of plated Li metal and component of SEI in 1.4 M LiPF$_6$-EDF. a, Cryo-TEM image of plated Li metal on a Cu grid in 1.4 M LiPF$_6$-EDF. **b,** Cryo-STEM EELS elemental mapping of plated Li metal and SEI.
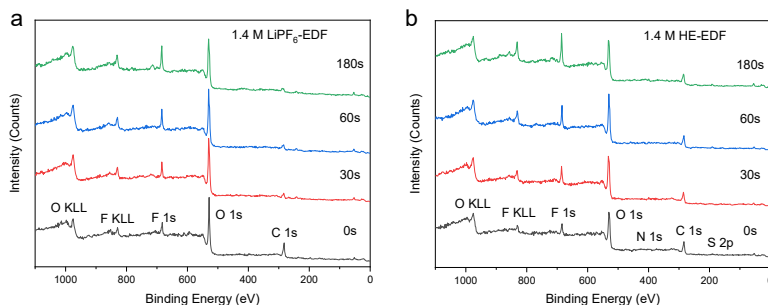
Fig. S4.27. Surveys of X-ray photoelectron spectroscopy (XPS) spectra of Li metal electrodes. **a,** 1.4 M LiPF$_6$-EDF and **b,** 1.4 M HE-EDF electrolytes. Spectra were collected after 20 cycles from the surface of Cu electrodes in Li‖Cu cells at different depths.
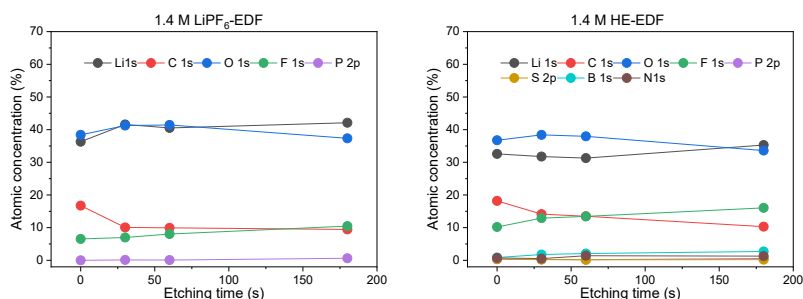
Fig. S4.28. XPS depth profiles of Li plated on Cu current collector. The left panel is from using the 1.4 M LiPF$_6$-EDF electrolyte and the right panel is the 1.4 M HE-EDF electrolyte.
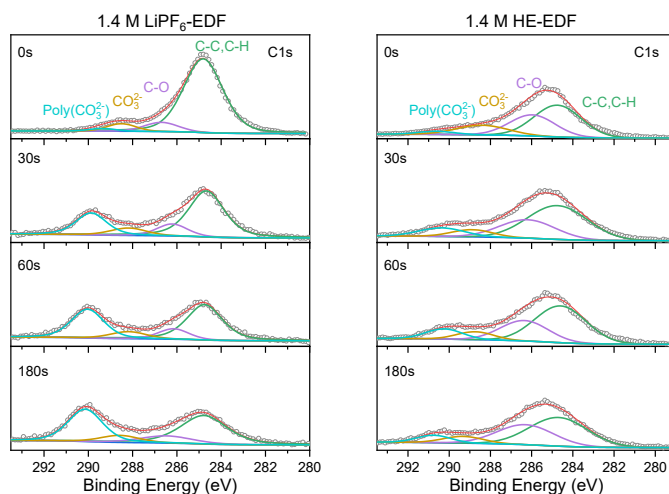
Fig. S4.29. C 1*s* spectra on the surface of the Cu current collector after Li metal stripping. They are in 1.4 M LiPF$_6$-EDF and 1.4 M HE-EDF electrolyte in different depth by applying different etching time from 0 s to 180 s.
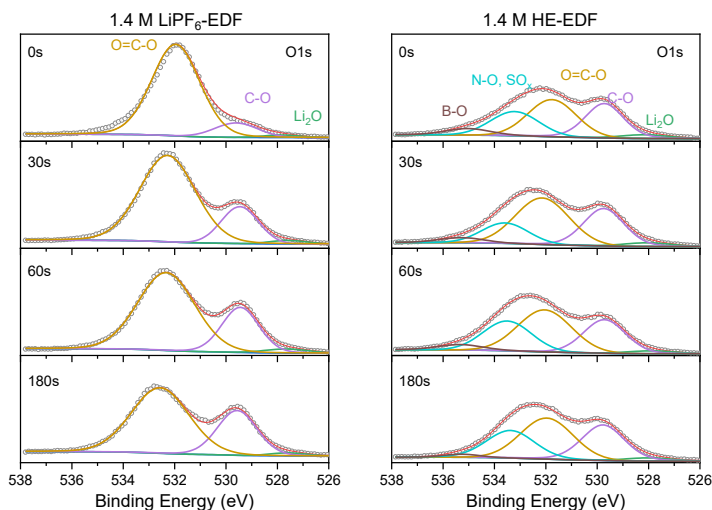
Fig. S4.30. O 1*s* spectra on the surface of the Cu current collector after Li metal stripping. They are in 1.4 M LiPF$_6$-EDF and 1.4 M HE-EDF electrolyte in different depth by applying different etching time from 0 s to 180 s.

4
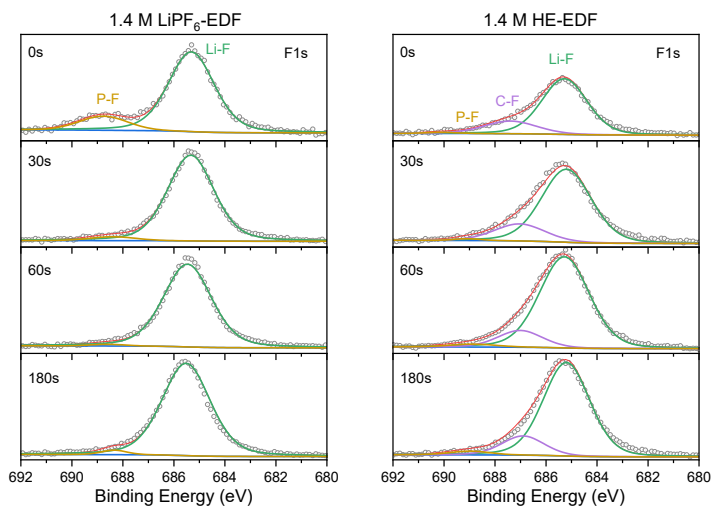
Fig. S4.31. F 1*s* spectra on the surface of the Cu current collector after Li metal stripping. They are in 1.4 M LiPF$_6$-EDF and 1.4 M HE-EDF electrolyte in different depth by applying different etching time from 0 s to 180 s.
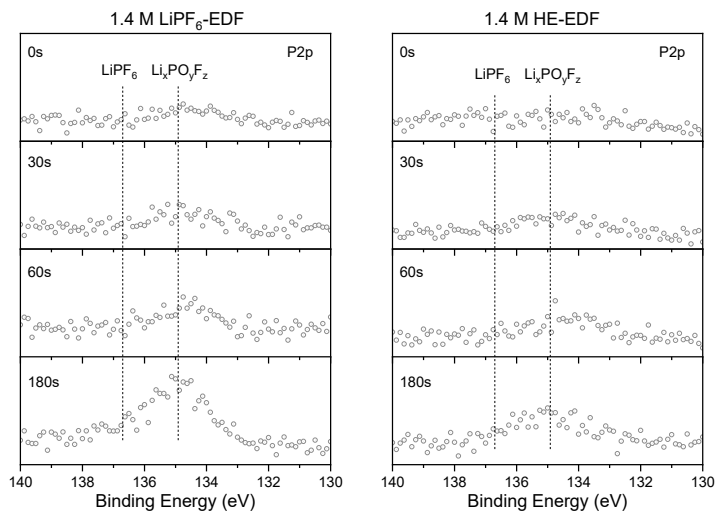
Fig. S4.32. P 2*p* spectra on the surface of the Cu current collector after Li metal stripping. They are in 1.4 M LiPF$_6$-EDF and 1.4 M HE-EDF electrolyte in different depth by applying different etching time from 0 s to 180 s.
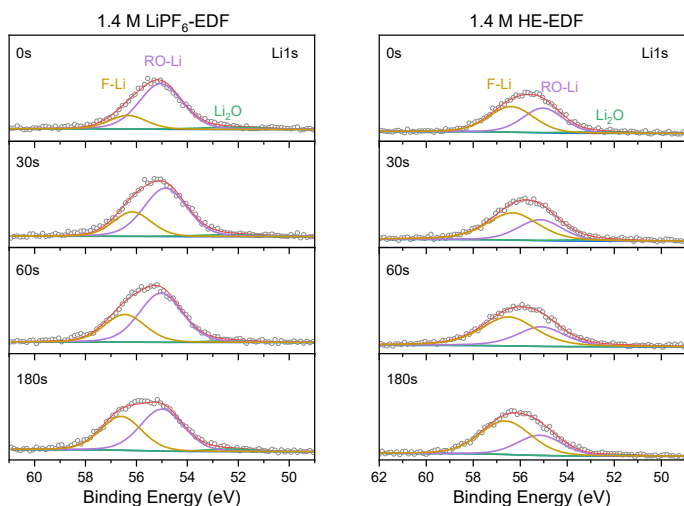
Fig. S4.33. Li 1s spectra on the surface of the Cu current collector after Li metal stripping. They are in 1.4 M LiPF$_6$-EDF and 1.4 M HE-EDF electrolyte in different depth by applying different etching time from 0 s to 180 s.
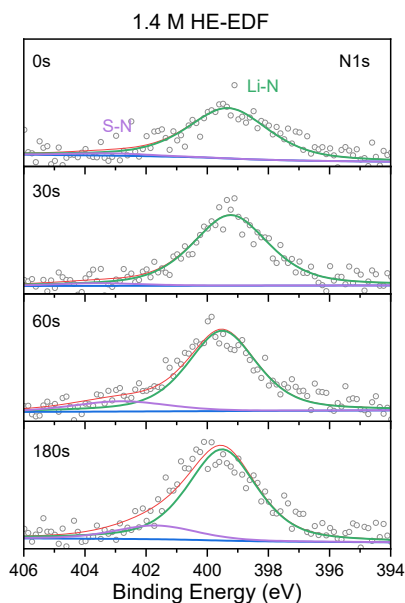
Fig. S4.34. N 1*s* spectra on the surface of the Cu current collector after Li metal stripping. They are in 1.4 M HE-EDF electrolyte in different depth by applying different etching time from 0 s to 180 s.

4
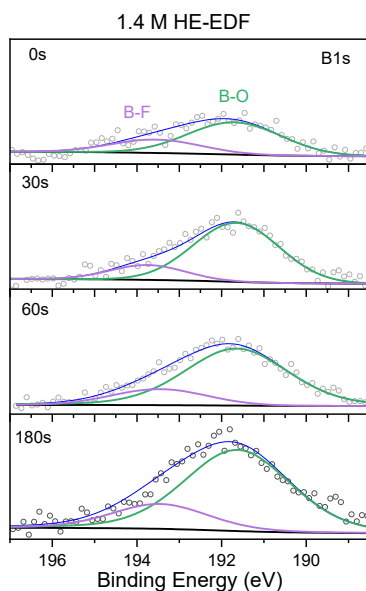
Fig. S4.35. B 1*s* spectra on the surface of the Cu current collector after Li metal stripping. They are in 1.4 M HE-EDF electrolyte in different depth by applying different etching time from 0 s to 180 s.
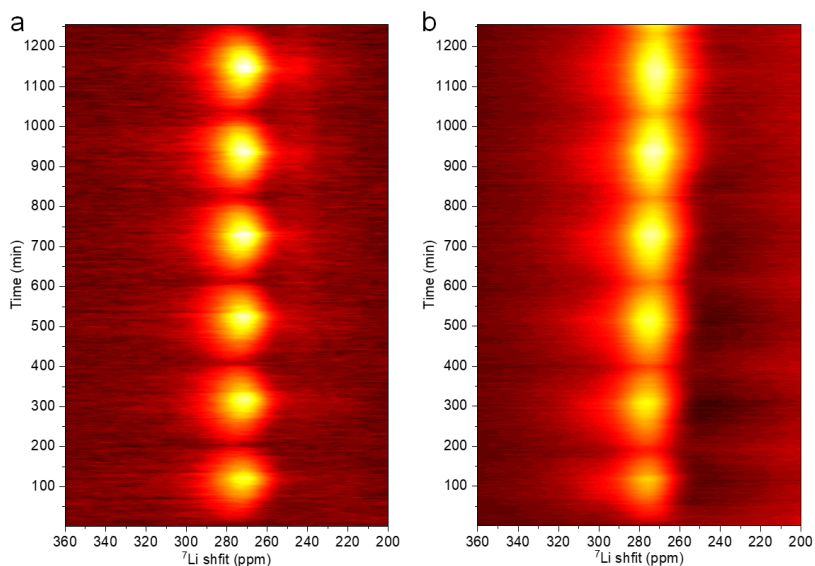
Fig. S4.36. Operando ⁷Li NMR measurement of Cu∥LiFePO₄ cells using different electrolytes.
a, The ⁷Li NMR spectra acquired during the plating and stripping of Li metal in 1.4 M HE-EDF
for 6 cycles. **b,** The ⁷Li NMR spectra acquired during the plating and stripping of Li metal in 1.4
M LiPF₆-EDF for 6 cycles.
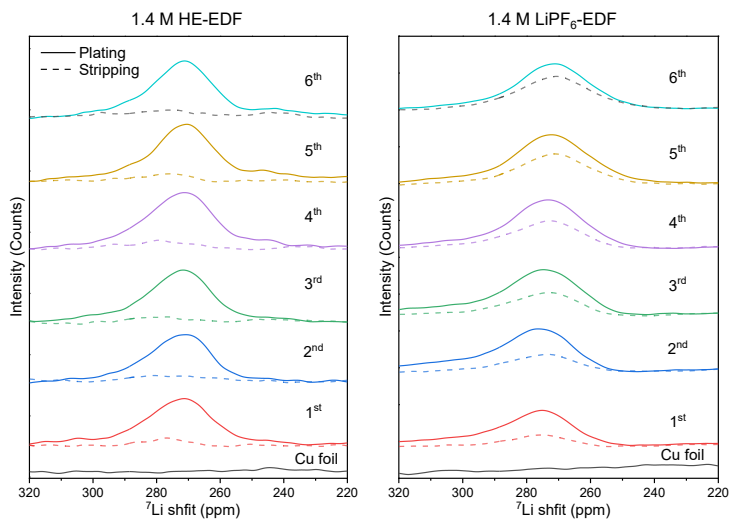
Fig. S4.37. The selected ⁷Li NMR spectra from operando ⁷Li NMR. They show the resonance
of the Li metal peaks before and after Li plating/stripping in Cu∥LiFePO₄ cells in different
electrolytes. Charging the cell results in Li metal plating, as shown in the plating ⁷Li NMR spectrum.
At the end of Li metal stripping (discharging the cell), the Li metal signal can still be observed,
which is attributed to "dead" Li. During the following cycles of the operando cell an accumulation
of "dead" Li can be observed, the intensity of the Li metal signal increasing at the end of stripping
in each cycle.
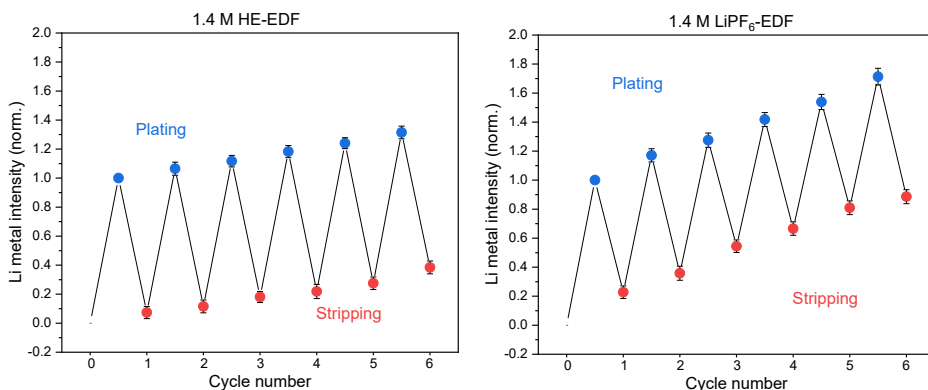
Fig. S4.38. Integrated intensity of the Li metal peak in operando ^{7}Li NMR for different electrolytes. It is normalized to the intensity at the end of plating in the first plating.
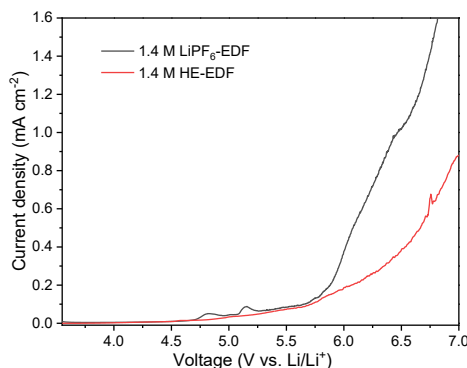
Fig. S4.39. Linear sweep voltammetry (LSV) of Al/C‖Li cells to show oxidation stability of different electrolytes. Each cell was scanned from open circuit voltage to 7 V (vs. Li/Li$^+$).
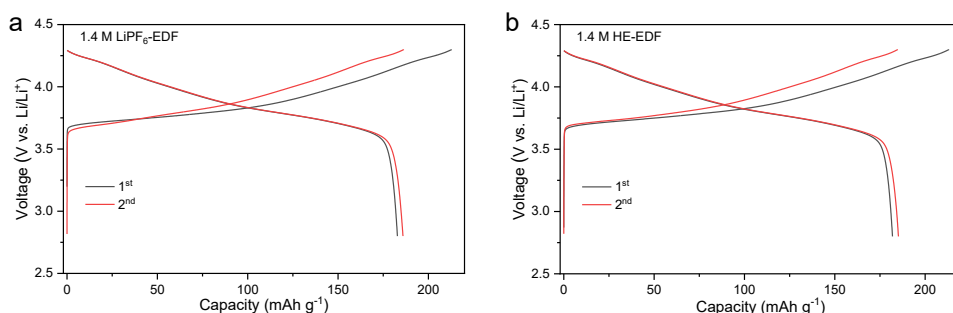
Fig. S4.40. Galvanostatic charge/discharge curves of Li‖NCM811 cells for initial cycles. **a,** 1.4 M LiPF$_6$-EDF and **b,** 1.4 M HE-EDF electrolyte for first two cycles. Cells were cycled at the voltage range of 2.8-4.3 V under a rate of 0.1C.
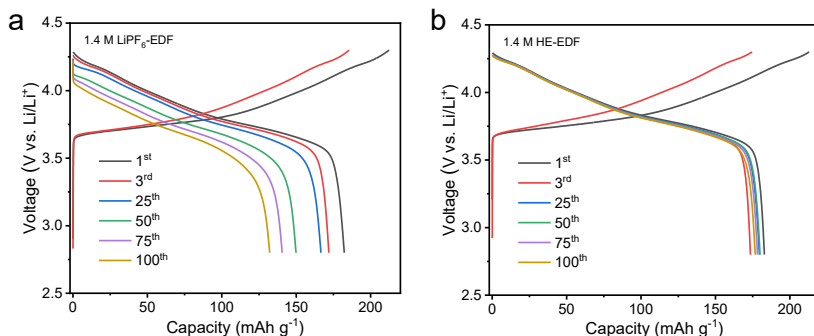
Fig. S4.41. Galvanostatic charge/discharge curves of Li‖NCM811 cells at selected cycles. a, 1.4 M LiPF$_6$-EDF and **b,** 1.4 M HE-EDF electrolyte at the voltage range of 2.8-4.3 V at a rate of 0.1C for three cycles before cycling at 0.5C.
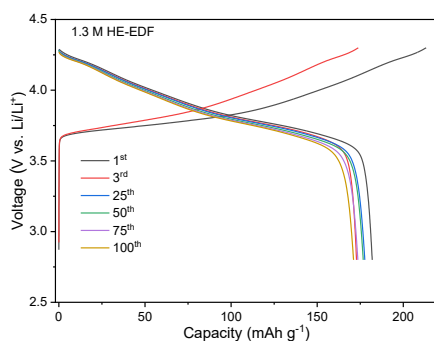
Fig. S4.42. Galvanostatic charge/discharge curves of Li‖NCM811 cells with 1.3 M HE-EDF electrolyte. The voltage range is 2.8-4.3 V with a rate of 0.1C for three cycles and 0.5C for the following cycles.

4
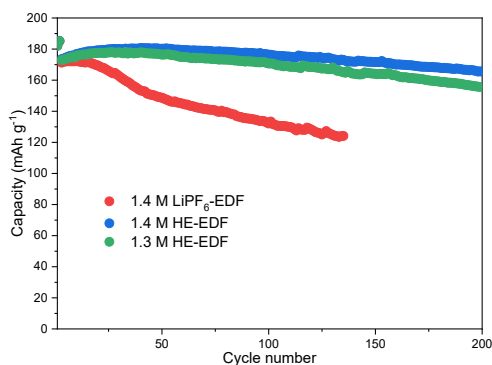
Fig. S4.43. Cycling capacity retention of Li‖NCM811 cells. 1.4 M LiPF$_6$-EDF, 1.4 M HE-EDF and 1.3 M HE-EDF electrolytes are used and cycled between 2.8 and 4.3 V at a 0.1C rate for three cycles before cycling at a 0.5C rate.
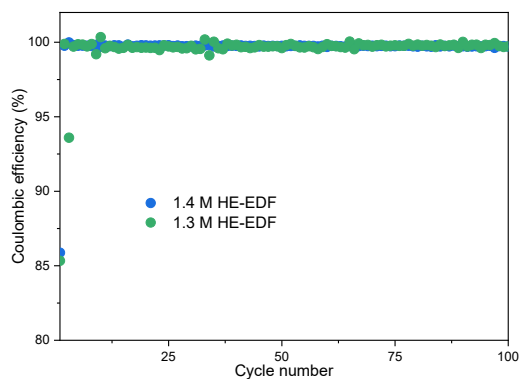
Fig. S4.44. CE of Li‖NCM811 cells with different electrolyte. The first 100 cycles are shown using 1.4 M HE-EDF and 1.3 M HE-EDF electrolytes.
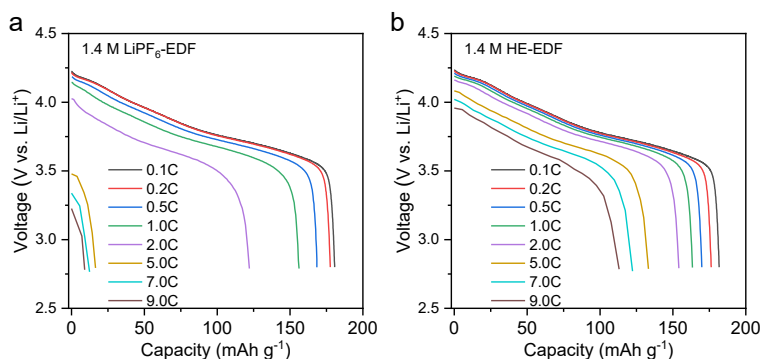
Fig. S4.45. Galvanostatic discharge curves of the Li‖NCM811 cells at different rates. a, 1.4 M LiPF$_6$-EDF and **b,**1.4 M HE-EDF electrolyte.
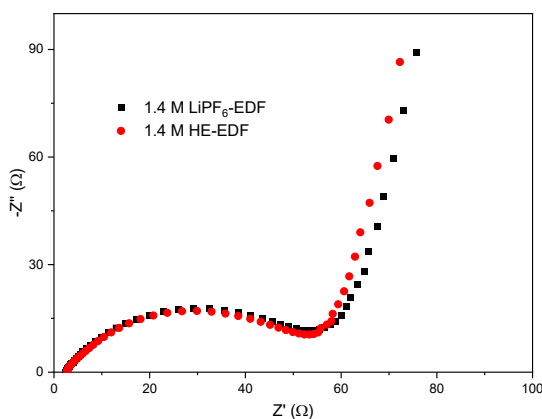
Fig. S4.46. EIS of Li‖NCM811 cells before cycling. 1.4 M LiPF$_6$-EDF and 1.4 M HE-EDF electrolytes are used.
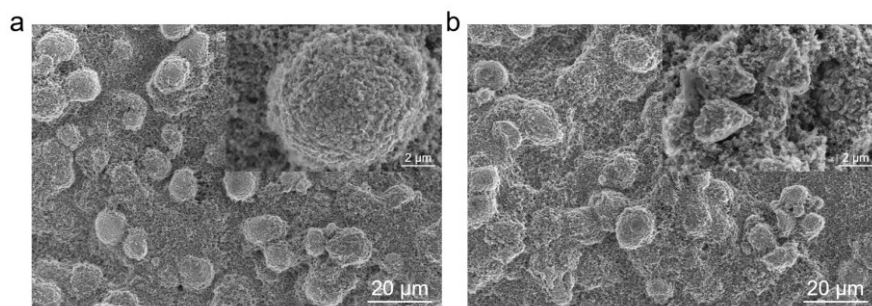
Fig. S4.47. SEM images of NCM811 electrode in different electrolytes after rate cycling. a, Cycled electrode in 1.4 M HE-EDF electrolyte. It is shown that secondary micron sized particles consist of densely packed primary sub-micron sized particles with a clean surface. **b,** Cycled electrode in 1.4 M LiPF$_6$-EDF. It can be observed that the secondary particles are damaged during cycling.
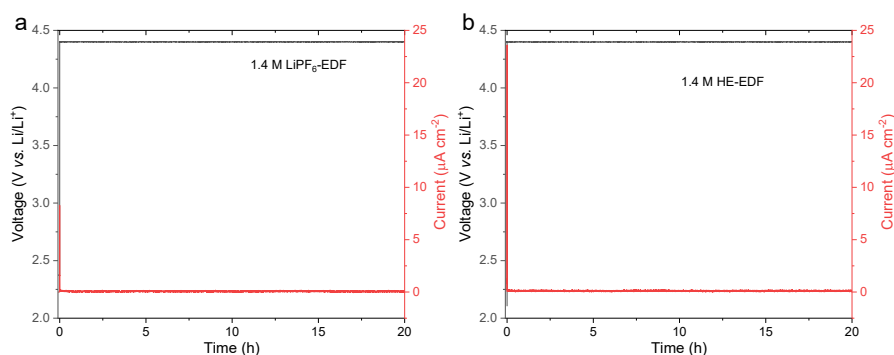
Fig. S4.48. Potentiostatic charge profiles. **a,** 1.4 M LiPF$_6$-EDF and **b,** 1.4 M HE-EDF electrolytes. Li‖Al/C coin cells were used to study the corrosion current in different electrolytes at the polarization potential of 4.2 V vs. Li/Li$^+$ for 20 h, where both electrolytes show a stable anodic current under the same conditions.
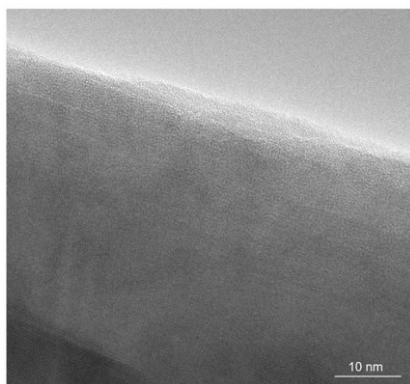
Fig. S4.49. TEM image of pristine NCM811 cathode. No interphase layer can be observed along the surface of the particle.
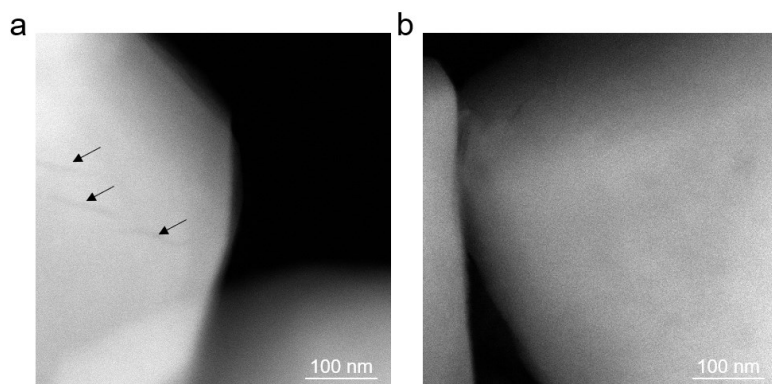
Fig. S4.50. NCM811 particle surface morphology after cycling. a, 1.4 M LiPF$_6$-EDF and **b,** 1.4 M HE-EDF electrolytes by STEM-HAADF images.
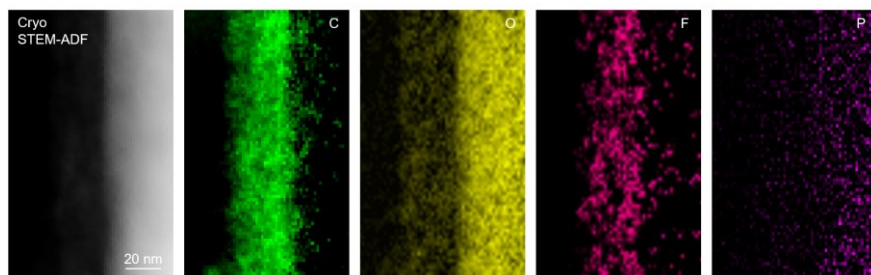
Fig. S4.51. Cryo-STEM electron energy loss spectroscopy (EELS) mapping of CEI on NCM811 cathode after cycling. The battery is cycled in 1.4 M LiPF$_6$-EDF.
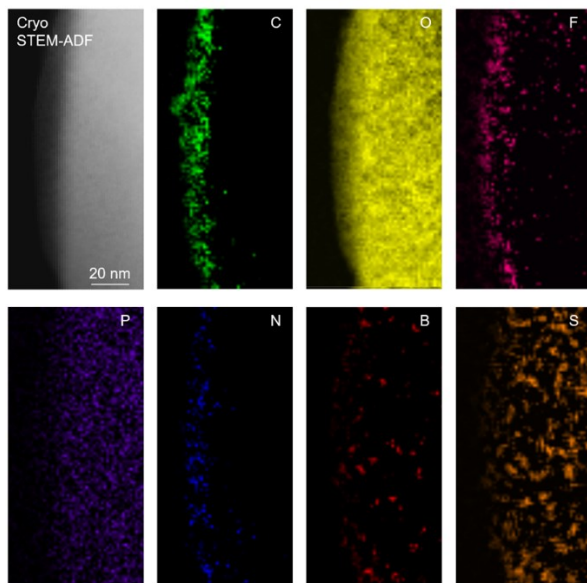
Fig. S4.52. CEI morphology and composition in 1.4 M HE-EDF. Cryo-STEM EELS mapping of CEI on NCM811 after cycling in 1.4 M HE-EDF electrolyte.
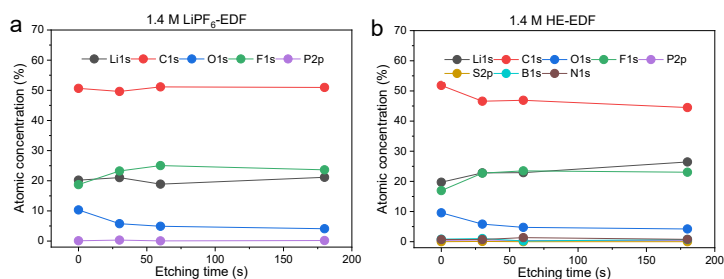
Fig. S4.53. Elemental composition on the surface of the NCM811 electrode from XPS spectra after 20 cycles. a, 1.4 M LiPF$_6$-EDF and **b,** 1.4 M HE-EDF.
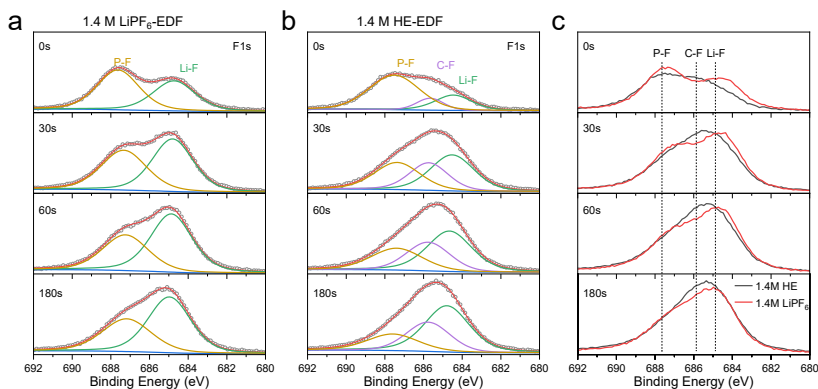
Fig. S4.54. F 1s spectra on the surface of the NCM811 cathode after cycling. a, 1.4 M LiPF$_6$-EDF and **b,** 1.4 M HE-EDF at different depth by applying different etching time. **c,** the overlay plot of the experimental curves of both electrolytes, where the content of P-F species is similar in both electrolyte while more C-F species can be observed in the 1.4 M HE-EDF electrolyte.
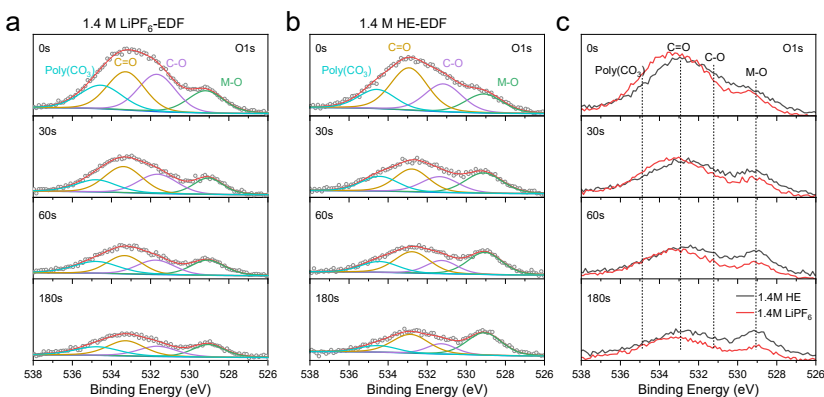
Fig. S4.55. O 1s spectra on the surface of the NCM811 cathode after cycling. a, 1.4 M LiPF$_6$-EDF and **b,** 1.4 M HE-EDF at different depth by applying different etching time. **c,** the overlay plot of the experimental curves of both electrolytes, where more M-O species in 1.4 M HE-EDF indicates a thinner CEI layer.
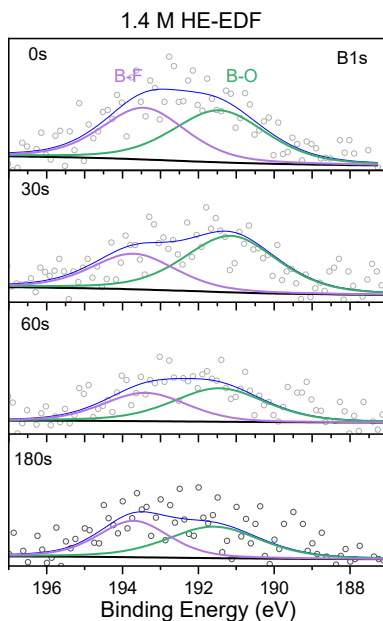
Fig. S4.56. B 1s spectra on the surface of the NCM811 cathode after cycling. They are obtained in 1.4 M HE-EDF at different depth by applying different etching time.

4
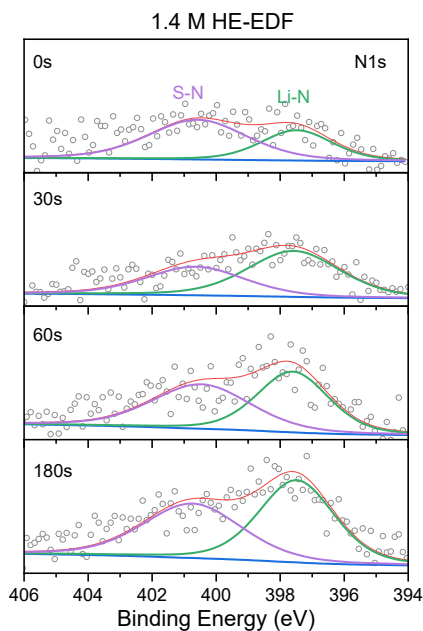
Fig. S4.57. N 1s spectra on the surface of the NCM811 cathode after cycling. They are obtained in 1.4 M HE-EDF at different depth by applying different etching time.
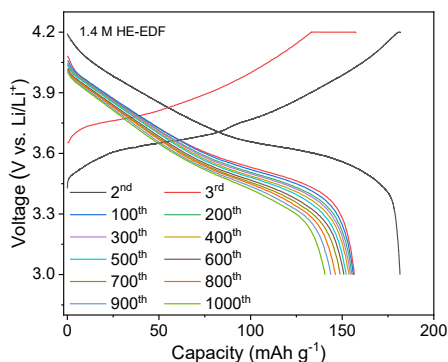
Fig. S4.58. Galvanostatic charge/discharge curves of graphite||NCM811 cells. The battery works in 1.4 M HE-EDF electrolyte under 25 °C.
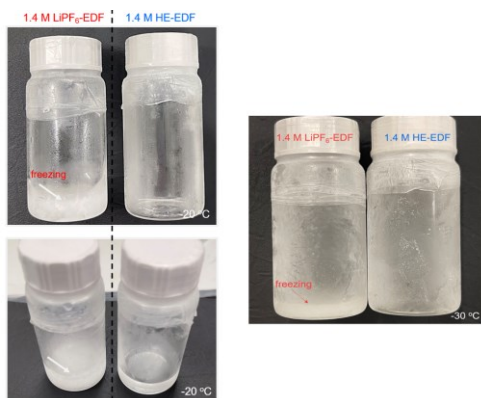
Fig. S4.59. Optical images of 1.4 M LiPF₆-EDF and 1.4 M HE-EDF electrolytes stored at -20 °C for two days. The 1.4 M LiPF₆-EDF electrolyte is frozen but the 1.4 M HE-EDF electrolyte is still liquid. When the temperature decreases to -30 °C for around 0.5 h, the 1.4 M LiPF₆-EDF electrolyte is found to be totally frozen in a solid state on the bottom of the bottle while part of the 1.4 M HE-EDF electrolyte tends to be frozen with the smaller ice crystal formation.
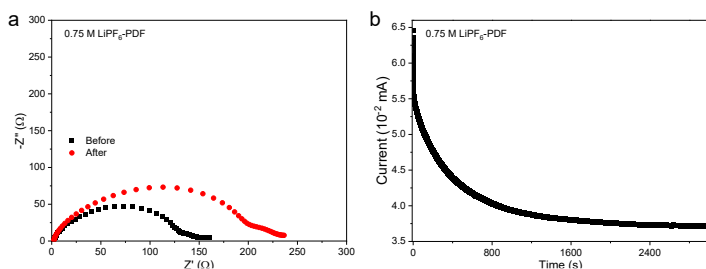
Fig. S4.60. Li transference number of 0.75 M LiPF₆-PDF electrolyte in symmetric Li||Li cells. a, Chronoamperometry profile under a polarization voltage of 10 mV. **b,** The corresponding EIS before and after polarization showing the initial and steady-state values of resistances respectively.
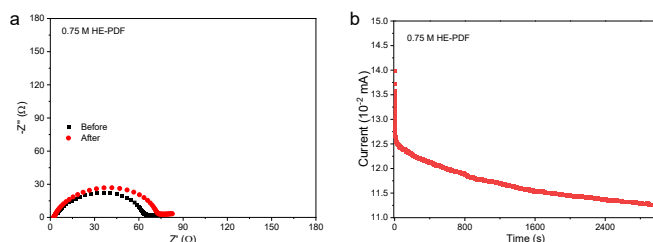
Fig. S4.61. Li transference number of 0.75 M HE-PDF electrolyte in symmetric Li‖Li cells. a, Chronoamperometry profile under a polarization voltage of 10 mV. **b,** The corresponding EIS before and after polarization showing the initial and steady-state values of resistances respectively.
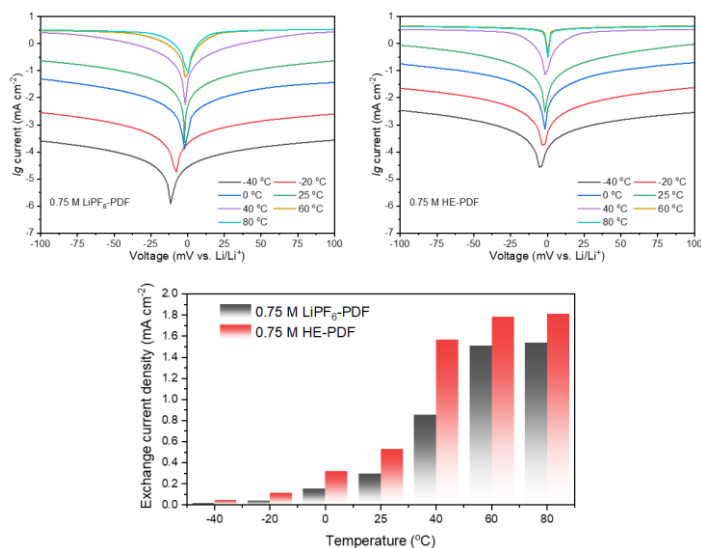
Fig. S4.62. Tafel plots and the exchange current density for different electrolytes. 0.75 M LiPF$_6$-PDF and 0.75 M HE-PDF electrolytes are used in Li‖Li cells to obtained Tafel plots under different temperatures, and the exchange current density is obtained from linear fitting of Tafel plots.
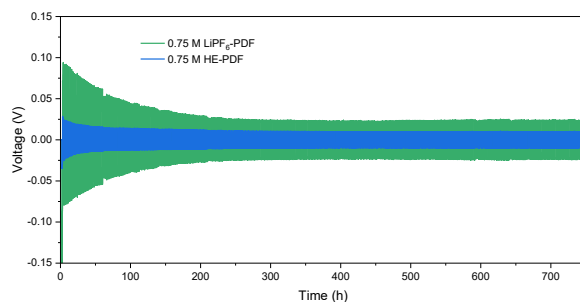
Fig. S4.63. Evolution of voltage profiles of symmetric Li‖Li cells using 0.75 M LiPF$_6$-PDF and 0.75 M HE-PDF electrolytes. The Li‖Li symmetric cells were cycled under a current density of 0.5 mA cm^{-2} with the plating/stripping time of 1 h under 25 °C.
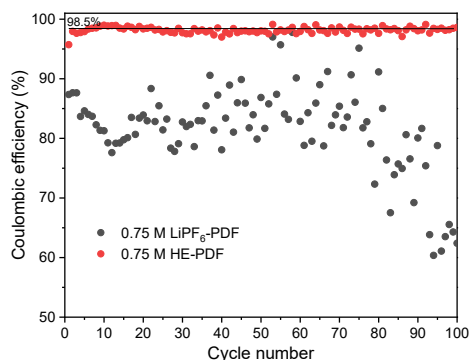
Fig. S4.64. Galvanostatic Li plating/stripping CE in Li‖Cu cells using 0.75 M LiPF$_6$-PDF and 0.75 M HE-PDF electrolytes. Li was electrodeposited at 0.5 mA cm^{-2} to a capacity of 1 mAh cm^{-2} under 25 ºC.
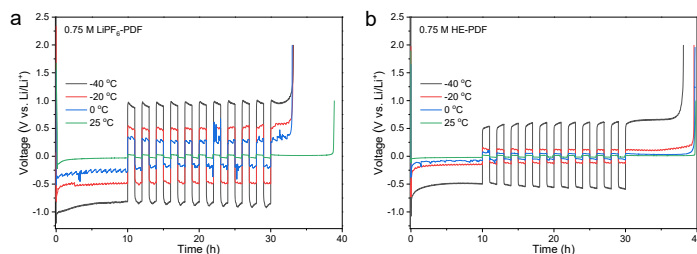
Fig. S4.65. Measurement of Li metal CE in Li‖Cu cells. Cells with **a,** 0.75 M LiPF$_6$-PDF and **b,** 0.75 M HE-PDF electrolyte were tested under different temperatures.

4
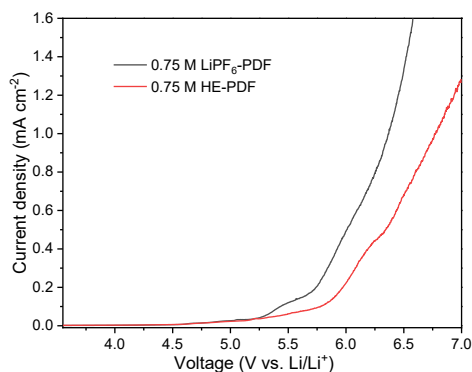
Fig. S4.66. LSV test with carbon coated Al foil as the working electrode and Li metal as the counter and reference electrodes. The data are obtained at a scan rate of 0.5 mV s^{-1} in the range from open circuit voltage to 7.0 V vs. Li/Li$^+$.
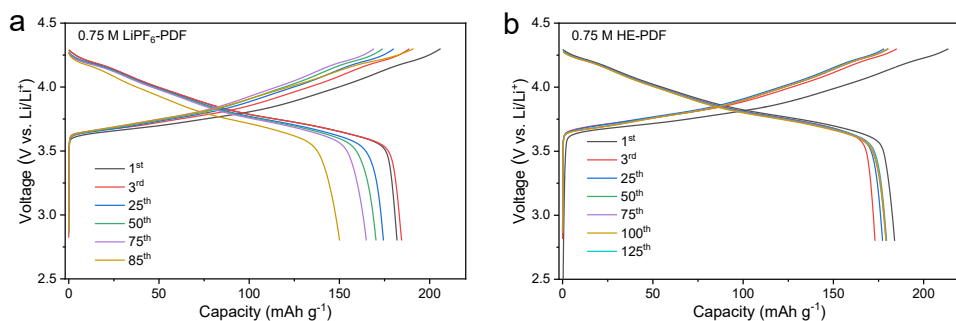
Fig. S4.67. Galvanostatic charge/discharge curves of selected cycles of Li||NCM811 cells at room temperature. a, 0.75 M LiPF$_6$-PDF and **b,** 0.75 M HE-PDF electrolyte cycling under 25 °C. The cells are cycled between the voltage range from 2.8 to 4.3 V at 0.1C rate for two cycles and 0.5C rate for the following cycles.
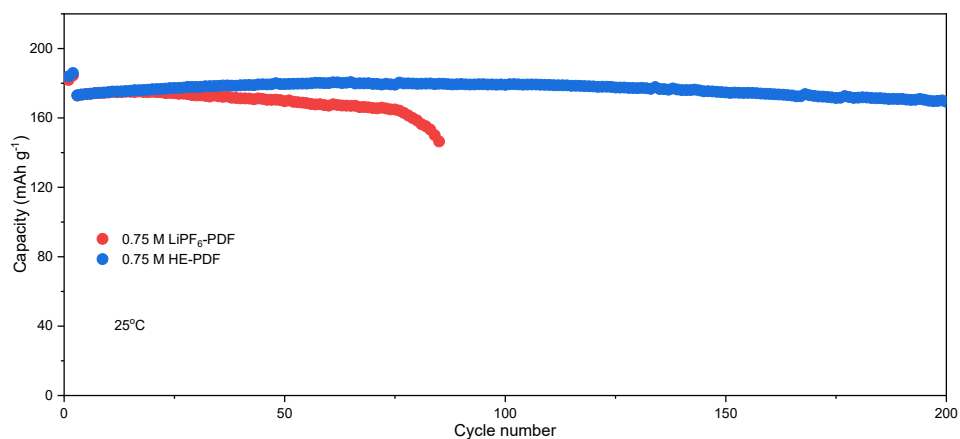
Fig. S4.68. Cycling performance at room temperature. Li||NCM811 cells work with 0.75 M LiPF$_6$-PDF or 0.75 M HE-PDF electrolyte cycled between 2.8 and 4.3 V at 0.1C rate for two cycles and 0.5C rate for the following cycles under 25 °C.
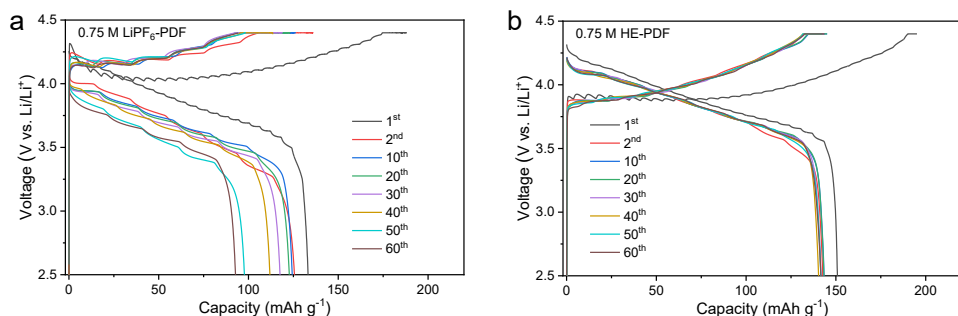
Fig. S4.69. Galvanostatic charge/discharge curves of Li‖NCM811 cells at low temperature. Voltage curves for the selected cycles of Li‖NCM811 cells using **a,** 0.75 M LiPF$_6$-PDF and **b,** 0.75 M HE-PDF electrolyte cycling under -20 °C. The cells are cycled between 2.8 and 4.3 V at 0.1C rate for the first cycle and 0.5C rate for the following cycles.
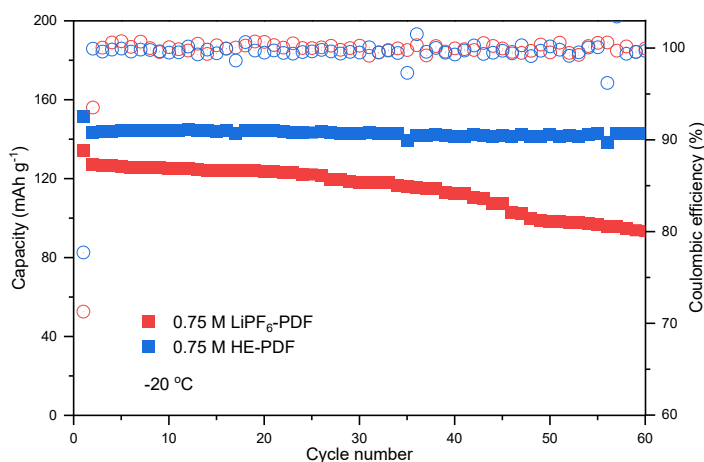
Fig. S4.70. Cycling performance at low temperature. Li‖NCM811 cells with 0.75 M LiPF$_6$-PDF and 0.75 M HE-PDF electrolytes cycled between 2.8 and 4.3 V at 0.1C rate for the first cycle and 0.5C rate for the following cycles under -20 °C.

Supplementary Tables

Table S4.1. The types of solvation structures and their corresponding proportion in the 1.4 M LiPF$_6$-EDF electrolyte.

1.4 M LiPF$_6$-EDF	DMC	EC	FEC	LiPF$_6$	Ratio
0_0_0_3	0	0	0	3	0.29
1_0_0_2	1	0	0	2	0.23
0_0_0_4	0	0	0	4	0.1
0_0_0_2	0	0	0	2	0.1
1_0_0_3	1	0	0	3	0.05
0_0_0_1	0	0	0	1	0.04
0_1_0_2	0	1	0	2	0.03
2_0_0_2	2	0	0	2	0.03
1_1_0_2	1	1	0	2	0.03
0_1_0_3	0	1	0	3	0.03
2_0_0_1	2	0	0	1	0.02
2_0_0_0	2	0	0	0	0.01
2_1_0_1	2	1	0	1	0.01
1_0_0_1	1	0	0	1	0.01
3_0_0_1	3	0	0	1	0.01
0_2_0_2	0	2	0	2	0.01
1_0_1_2	1	0	1	2	0.005997

Table S4.2. The types of solvation structures and their corresponding proportion in the 1.4 M HE-EDF electrolyte.

1.4 M HE-EDF	DMC	EC	FEC	LiPF$_6$	LiNO$_3$	LiFSI	LiTFSI	LiDFOB	Ratio
1_0_0_2_0_0_0_0	1	0	0	2	0	0	0	0	0.1373
0_0_0_3_0_0_0_0	0	0	0	3	0	0	0	0	0.1140
0_0_0_2_0_0_0_0	0	0	0	2	0	0	0	0	0.0461
1_0_0_2_1_0_0_0	1	0	0	2	1	0	0	0	0.0415
1_0_0_3_0_0_0_0	1	0	0	3	0	0	0	0	0.0404
1_0_0_2_0_0_0_1	1	0	0	2	0	0	0	1	0.0361
1_0_0_1_2_0_0_0	1	0	0	1	2	0	0	0	0.0346
2_0_0_2_0_0_0_0	2	0	0	2	0	0	0	0	0.0296
1_0_0_1_1_0_0_1	1	0	0	1	1	0	0	1	0.0259
0_0_0_2_0_0_0_1	0	0	0	2	0	0	0	1	0.0255
2_0_0_1_0_0_0_1	2	0	0	1	0	0	0	1	0.0245
2_0_0_1_0_0_1_0	2	0	0	1	0	0	1	0	0.0215
1_0_0_1_0_2_0_1	1	0	0	1	0	2	0	1	0.0204
1_0_0_1_0_0_1_0	1	0	0	1	0	0	1	0	0.0185
1_0_0_2_0_2_0_0	1	0	0	2	0	2	0	0	0.0185
1_0_0_1_0_0_0_0	1	0	0	1	0	0	0	0	0.0173
0_0_0_1_2_0_0_0	0	0	0	1	2	0	0	0	0.0165
0_0_0_2_0_2_0_0	0	0	0	2	0	2	0	0	0.0155
0_0_0_2_1_0_0_0	0	0	0	2	1	0	0	0	0.0152
1_1_0_2_0_0_0_0	1	1	0	2	0	0	0	0	0.0139
1_0_0_1_0_0_0_1	1	0	0	1	0	0	0	1	0.0136

0_0_0_3_0_0_1_0	0	0	0	3	0	0	1	0	0.0108
0_0_0_3_0_2_0_0	0	0	0	3	0	2	0	0	0.0107
2_0_0_1_0_0_0_0	2	0	0	1	0	0	0	0	0.0097
1_1_0_1_0_0_0_1	1	1	0	1	0	0	0	1	0.0095
3_0_0_0_0_0_0_1	3	0	0	0	0	0	0	1	0.0093
0_0_0_2_1_2_0_0	0	0	0	2	1	2	0	0	0.0093
0_0_0_2_0_0_1_0	0	0	0	2	0	0	1	0	0.0086
0_0_0_3_1_0_0_0	0	0	0	3	1	0	0	0	0.0082
0_0_0_2_2_0_0_0	0	0	0	2	2	0	0	0	0.0080
0_0_0_2_0_2_0_1	0	0	0	2	0	2	0	1	0.0080
0_0_0_1_0_0_0_0	0	0	0	1	0	0	0	0	0.0079
0_1_0_2_0_0_0_0	0	1	0	2	0	0	0	0	0.0078
0_1_0_3_0_0_0_0	0	1	0	3	0	0	0	0	0.0077
0_0_0_4_0_0_0_0	0	0	0	4	0	0	0	0	0.0076
2_0_0_0_0_0_0_2	2	0	0	0	0	0	0	2	0.0073
0_0_0_1_0_0_1_0	0	0	0	1	0	0	1	0	0.0070
0_0_0_3_0_0_0_1	0	0	0	3	0	0	0	1	0.0057
1_0_0_1_0_2_0_0	1	0	0	1	0	2	0	0	0.0057
1_0_0_1_1_0_0_0	1	0	0	1	1	0	0	0	0.0056
3_0_0_1_0_0_0_0	3	0	0	1	0	0	0	0	0.0046
2_0_0_1_1_0_0_0	2	0	0	1	1	0	0	0	0.0046
1_0_0_2_0_0_1_0	1	0	0	2	0	0	1	0	0.0046
1_0_0_0_0_2_1_0	1	0	0	0	0	2	1	0	0.0045
0_1_0_2_1_0_0_0	0	1	0	2	1	0	0	0	0.0043
0_0_0_1_0_0_0_1	0	0	0	1	0	0	0	1	0.0041
2_0_0_0_0_0_0_1	2	0	0	0	0	0	0	1	0.0041
0_0_0_1_0_2_0_1	0	0	0	1	0	2	0	1	0.0040
0_0_0_1_0_2_0_0	0	0	0	1	0	2	0	0	0.0039
1_1_0_1_0_0_1_0	1	1	0	1	0	0	1	0	0.0039
2_0_0_0_0_0_1_0	2	0	0	0	0	0	1	0	0.0039
1_0_0_0_0_0_1_0	1	0	0	0	0	0	1	0	0.0037
2_1_0_0_0_0_0_1	2	1	0	0	0	0	0	1	0.0034
1_0_0_0_0_2_0_1	1	0	0	0	0	2	0	1	0.0034
2_0_0_0_0_0_2_0	2	0	0	0	0	0	2	0	0.0034
2_0_0_1_0_2_0_0	2	0	0	1	0	2	0	0	0.0030
1_1_0_1_1_0_0_0	1	1	0	1	1	0	0	0	0.0024
1_1_0_0_0_2_0_1	1	1	0	0	0	2	0	1	0.0024
1_0_0_0_0_0_2_0	1	0	0	0	0	0	2	0	0.0024
0_0_1_2_0_0_0_0	0	0	1	2	0	0	0	0	0.0024
1_0_0_1_0_2_1_0	1	0	0	1	0	2	1	0	0.0023
0_0_0_0_0_2_1_0	0	0	0	0	0	2	1	0	0.0022
2_0_0_0_0_2_0_1	2	0	0	0	0	2	0	1	0.0020
0_0_0_1_1_0_0_1	0	0	0	1	1	0	0	1	0.0020
0_1_0_1_1_0_0_0	0	1	0	1	1	0	0	0	0.0019
1_1_0_0_0_2_1_0	1	1	0	0	0	2	1	0	0.0018
0_0_0_0_0_0_1_0	0	0	0	0	0	0	1	0	0.0018
1_0_0_0_0_0_0_2	1	0	0	0	0	0	0	2	0.0016
0_1_0_1_2_0_0_0	0	1	0	1	2	0	0	0	0.0016
0_1_0_1_0_0_0_0	0	1	0	1	0	0	0	0	0.0015
0_1_0_1_0_0_1_0	0	1	0	1	0	0	1	0	0.0015
0_0_0_0_0_0_2_0	0	0	0	0	0	0	2	0	0.0013

4

0_0_0_1_1_0_0_0	0	0	0	1	1	0	0	0	0.0013
0_1_0_1_0_0_0_1	0	1	0	1	0	0	0	1	0.0011
2_0_0_0_0_2_1_0	2	0	0	0	0	2	1	0	0.0011
0_2_0_1_1_0_0_0	0	2	0	1	1	0	0	0	0.0011
0_1_0_0_0_2_0_1	0	1	0	0	0	2	0	1	0.0011
1_1_0_1_0_2_0_0	1	1	0	1	0	2	0	0	0.0010
2_0_0_0_0_0_0_0	2	0	0	0	0	0	0	0	0.0010
0_0_0_1_0_2_1_0	0	0	0	1	0	2	1	0	0.0009
0_0_0_0_0_2_0_1	0	0	0	0	0	2	0	1	0.0009
1_0_0_0_0_0_3_0	1	0	0	0	0	0	3	0	0.0009
2_0_1_0_0_0_0_1	2	0	1	0	0	0	0	1	0.0008
1_0_0_0_0_0_0_0	1	0	0	0	0	0	0	0	0.0008
0_1_0_0_0_0_3_0	0	1	0	0	0	0	3	0	0.0008
0_1_0_2_0_2_0_0	0	1	0	2	0	2	0	0	0.0008
1_0_1_2_0_0_0_0	1	0	1	2	0	0	0	0	0.0007
3_0_0_0_0_0_2_0	3	0	0	0	0	0	2	0	0.0007
0_0_1_1_2_0_0_0	0	0	1	1	2	0	0	0	0.0006
0_1_0_0_0_2_1_0	0	1	0	0	0	2	1	0	0.0005
1_0_0_0_0_2_0_0	1	0	0	0	0	2	0	0	0.0005
0_0_0_0_0_0_3_0	0	0	0	0	0	0	3	0	0.0005
0_0_0_0_0_2_0_0	0	0	0	0	0	2	0	0	0.0004
1_1_0_0_0_0_0_1	1	1	0	0	0	0	0	1	0.0004
1_0_0_0_0_0_0_1	1	0	0	0	0	0	0	1	0.0004
0_1_0_0_0_0_2_0	0	1	0	0	0	0	2	0	0.0004
0_1_1_2_0_0_0_0	0	1	1	2	0	0	0	0	0.0003
3_0_0_0_0_0_0_2	3	0	0	0	0	0	0	2	0.0003
1_1_0_1_0_0_0_0	1	1	0	1	0	0	0	0	0.0003
0_0_0_1_2_0_0_1	0	0	0	1	2	0	0	1	0.0003
2_0_0_0_0_2_0_0	2	0	0	0	0	2	0	0	0.0002
1_0_1_1_0_0_0_0	1	0	1	1	0	0	0	0	0.0002
1_1_0_0_0_0_1_0	1	1	0	0	0	0	1	0	0.0002
3_0_0_0_0_0_1_0	3	0	0	0	0	0	1	0	0.0002
1_1_0_0_0_0_3_0	1	1	0	0	0	0	3	0	0.0002
0_0_1_3_0_0_0_0	0	0	1	3	0	0	0	0	0.0002
2_1_0_0_0_2_0_1	2	1	0	0	0	2	0	1	0.0002
1_1_0_1_2_0_0_0	1	1	0	1	2	0	0	0	0.0002
0_2_0_0_0_2_0_1	0	2	0	0	0	2	0	1	0.0002
1_2_0_0_0_2_0_1	1	2	0	0	0	2	0	1	0.0002
1_0_1_1_0_0_0_1	1	0	1	1	0	0	0	1	0.0002
1_1_0_0_0_0_2_0	1	1	0	0	0	0	2	0	0.0001
2_0_0_2_0_2_0_0	2	0	0	2	0	2	0	0	0.0001
0_0_1_2_0_0_0_1	0	0	1	2	0	0	0	1	0.0001
2_1_0_1_0_0_0_0	2	1	0	1	0	0	0	0	0.0001
0_1_0_2_0_0_0_1	0	1	0	2	0	0	0	1	0.0001
Others	0	0	0	0	0	0	0	0	0.0019

4

References

1   J. W. Yeh, S. K. Chen, S. J. Lin, J. Y. Gan, T. S. Chin, T. T. Shun, C. H. Tsau & S. Y. Chang. Nanostructured High-Entropy Alloys with Multiple Principal Elements: Novel Alloy Design Concepts and Outcomes. *Advanced Engineering Materials* **6**, 299-303, (2004).

2   B. Cantor, I. T. H. Chang, P. Knight & A. J. B. Vincent. Microstructural development in equiatomic multicomponent alloys. *Materials Science and Engineering: A* **375-377**, 213-218, (2004).

3   E. P. George, D. Raabe & R. O. Ritchie. High-entropy alloys. *Nature Reviews Materials* **4**, 515-534, (2019).

4   C. M. Rost, E. Sachet, T. Borman, A. Moballegh, E. C. Dickey, D. Hou, J. L. Jones, S. Curtarolo & J.-P. Maria. Entropy-stabilized oxides. *Nature Communications* **6**, 8485, (2015).

5   N. Dragoe & D. Bérardan. Order emerging from disorder. *Science* **366**, 573-574, (2019).

6   A. Sarkar, Q. Wang, A. Schiele, M. R. Chellali, S. S. Bhattacharya, D. Wang, T. Brezesinski, H. Hahn, L. Velasco & B. Breitung. High-Entropy Oxides: Fundamental Aspects and Electrochemical Properties. *Advanced Materials* **31**, 1806236, (2019).

7   Y. Sun & S. Dai. High-entropy materials for catalysis: A new frontier. *Science Advances* **7**, eabg1600.

8   D. Bérardan, S. Franger, D. Dragoe, A. K. Meena & N. Dragoe. Colossal dielectric constant in high entropy oxides. *Physica Status Solidi-Rapid Research Letters* **10**, 328-333, (2016).

9   C. Zhao, F. Ding, Y. Lu, L. Chen & Y. S. Hu. High-entropy layered oxide cathodes for sodium-ion batteries. *Angewandte Chemie International Edition* **59**, 264-269, (2020).

10 K. Xu. Electrolytes and Interphases in Li-Ion Batteries and Beyond. *Chemical Reviews* **114**, 11503-11618, (2014).

11 B. Dunn, H. Kamath & J.-M. Tarascon. Electrical Energy Storage for the Grid: A Battery of Choices. *Science* **334**, 928-935, (2011).

12 K. Xu. Nonaqueous Liquid Electrolytes for Lithium-Based Rechargeable Batteries. *Chemical Reviews* **104**, 4303-4418, (2004).

13 Q. Wang, C. Zhao, S. Wang, J. Wang, M. Liu, S. Ganapathy, X. Bai, B. Li & M. Wagemaker. Clarifying the Relationship between the Lithium Deposition Coverage and Microstructure in Lithium Metal Batteries. *Journal of the American Chemical Society* **144**, 21961-21971, (2022).

14 D. Aurbach, E. Pollak, R. Elazari, G. Salitra, C. S. Kelley & J. Affinito. On the Surface Chemical Aspects of Very High Energy Density, Rechargeable Li–Sulfur Batteries. *Journal of The Electrochemical Society* **156**, A694, (2009).

4

15 Y. Liu, D. Lin, Y. Li, G. Chen, A. Pei, Y. Li & Y. Cui. Solubility-mediated sustained release enabling nitrate additive in carbonate electrolytes for stable lithium metal anode. *Nature Communications* **9**, 3656, (2018).

16 Q. Shi, Y. Zhong, M. Wu, H. Wang & H. Wang. High-capacity rechargeable batteries based on deeply cyclable lithium metal anodes. *Proceedings of the National Academy of Sciences* **115**, 5676-5680, (2018).

17 W. Zhang, Q. Wu, J. Huang, L. Fan, Z. Shen, Y. He, Q. Feng, G. Zhu & Y. Lu. Colossal Granular Lithium Deposits Enabled by the Grain-Coarsening Effect for High-Efficiency Lithium Metal Full Batteries. *Advanced Materials* **32**, 2001740, (2020).

18 C. Yan, Y.-X. Yao, X. Chen, X.-B. Cheng, X.-Q. Zhang, J.-Q. Huang & Q. Zhang. Lithium Nitrate Solvation Chemistry in Carbonate Electrolyte Sustains High-Voltage Lithium Metal Batteries. *Angewandte Chemie International Edition* **57**, 14055-14059, (2018).

19 Y. Jie, X. Liu, Z. Lei, S. Wang, Y. Chen, F. Huang, R. Cao, G. Zhang & S. Jiao. Enabling High-Voltage Lithium Metal Batteries by Manipulating Solvation Structure in Ester Electrolyte. *Angewandte Chemie International Edition* **59**, 3505-3510, (2020).

20 X. Wang, S. Wang, H. Wang, W. Tu, Y. Zhao, S. Li, Q. Liu, J. Wu, Y. Fu, C. Han, F. Kang & B. Li. Hybrid Electrolyte with Dual-Anion-Aggregated Solvation Sheath for Stabilizing High-Voltage Lithium-Metal Batteries. *Advanced Materials* **33**, 2007945, (2021).

21 S. Chen, J. Zheng, L. Yu, X. Ren, M. H. Engelhard, C. Niu, H. Lee, W. Xu, J. Xiao, J. Liu & J.-G. Zhang. High-Efficiency Lithium Metal Batteries with Fire-Retardant Electrolytes. *Joule* **2**, 1548-1558, (2018).

22 P. Arora, R. E. White & M. Doyle. Capacity Fade Mechanisms and Side Reactions in Lithium-Ion Batteries. *Journal of The Electrochemical Society* **145**, 3647-3667, (1998).

23 H. Yang, X. Chen, N. Yao, N. Piao, Z. Wang, K. He, H.-M. Cheng & F. Li. Dissolution–Precipitation Dynamics in Ester Electrolyte for High-Stability Lithium Metal Batteries. *ACS Energy Letters* **6**, 1413-1421, (2021).

24 S. C. Kim, X. Kong, R. A. Vilá, W. Huang, Y. Chen, D. T. Boyle, Z. Yu, H. Wang, Z. Bao, J. Qin & Y. Cui. Potentiometric Measurement to Probe Solvation Energy and Its Correlation to Lithium Battery Cyclability. *Journal of the American Chemical Society* **143**, 10301-10308, (2021).

25 W. Zhang, H. Xia, Z. Zhu, Z. Lv, S. Cao, J. Wei, Y. Luo, Y. Xiao, L. Liu & X. Chen. Decimal Solvent-Based High-Entropy Electrolyte Enabling the Extended Survival Temperature of Lithium-Ion Batteries to −130 °C. *CCS Chemistry* **3**, 1245-1255.

4

26 X. Dong, Y. Lin, P. Li, Y. Ma, J. Huang, D. Bin, Y. Wang, Y. Qi & Y. Xia. High-Energy Rechargeable Metallic Lithium Battery at −70 °C Enabled by a Cosolvent Electrolyte. *Angewandte Chemie International Edition* **58**, 5623-5627, (2019).

27 S. Li, W. Zhang, Q. Wu, L. Fan, X. Wang, X. Wang, Z. Shen, Y. He & Y. Lu. Synergistic Dual-Additive Electrolyte Enables Practical Lithium-Metal Batteries. *Angewandte Chemie International Edition* **59**, 14935-14941, (2020).

28 Y. Yamada, J. Wang, S. Ko, E. Watanabe & A. Yamada. Advances and issues in developing salt-concentrated battery electrolytes. *Nature Energy* **4**, 269-280, (2019).

29 Y. Rosenfeld. Relation between the transport coefficients and the internal entropy of simple systems. *Physical Review A* **15**, 2545-2549, (1977).

30 J. C. Dyre. Perspective: Excess-entropy scaling. *The Journal of Chemical Physics* **149**, 210901, (2018).

31 P. Argyrakis, A. Milchev, V. Pereyra & K. W. Kehr. Dependence of the diffusion coefficient on the energy distribution of random barriers. *Physical Review E* **52**, 3623-3631, (1995).

32 Q. Wang, Z. Yao, C. Zhao, T. Verhallen, D. P. Tabor, M. Liu, F. Ooms, F. Kang, A. Aspuru-Guzik, Y.-S. Hu, M. Wagemaker & B. Li. Interface chemistry of an amide electrolyte for highly reversible lithium metal batteries. *Nature Communications* **11**, 4188, (2020).

33 B. D. Adams, J. Zheng, X. Ren, W. Xu & J.-G. Zhang. Accurate Determination of Coulombic Efficiency for Lithium Metal Anodes and Lithium Metal Batteries. *Advanced Energy Materials* **8**, 1702097, (2018).

34 D. Aurbach, Y. Gofer & J. Langzam. The Correlation Between Surface Chemistry, Surface Morphology, and Cycling Efficiency of Lithium Electrodes in a Few Polar Aprotic Systems. *Journal of The Electrochemical Society* **136**, 3198-3205, (1989).

35 M. J. Zachman, Z. Tu, S. Choudhury, L. A. Archer & L. F. Kourkoutis. Cryo-STEM mapping of solid–liquid interfaces and dendrites in lithium-metal batteries. *Nature* **560**, 345-349, (2018).

36 Z. Zhang, Y. Li, R. Xu, W. Zhou, Y. Li, T. Oyakhire Solomon, Y. Wu, J. Xu, H. Wang, Z. Yu, T. Boyle David, W. Huang, Y. Ye, H. Chen, J. Wan, Z. Bao, W. Chiu & Y. Cui. Capturing the swelling of solid-electrolyte interphase in lithium metal batteries. *Science* **375**, 66-70, (2022).

37 S. Chandrashekar, N. M. Trease, H. J. Chang, L.-S. Du, C. P. Grey & A. Jerschow. 7Li MRI of Li batteries reveals location of microstructural lithium. *Nature Materials* **11**, 311-315, (2012).

4

38 R. Bhattacharyya, B. Key, H. Chen, A. S. Best, A. F. Hollenkamp & C. P. Grey. In situ NMR observation of the formation of metallic lithium microstructures in lithium batteries. *Nature Materials* **9**, 504-510, (2010).

39 D. Hubble, D. E. Brown, Y. Zhao, C. Fang, J. Lau, B. D. McCloskey & G. Liu. Liquid electrolyte development for low-temperature lithium-ion batteries. *Energy & Environmental Science* **15**, 550-578, (2022).

40 Y. Ugata, Y. Chen, S. Sasagawa, K. Ueno, M. Watanabe, H. Mita, J. Shimura, M. Nagamine & K. Dokko. Eutectic Electrolytes Composed of LiN(SO2F)2 and Sulfones for Li-Ion Batteries. *The Journal of Physical Chemistry C* **126**, 10024-10034, (2022).

41 G. G. Eshetu, X. Judez, C. Li, M. Martinez-Ibañez, I. Gracia, O. Bondarchuk, J. Carrasco, L. M. Rodriguez-Martinez, H. Zhang & M. Armand. Ultrahigh Performance All Solid-State Lithium Sulfur Batteries: Salt Anion's Chemistry-Induced Anomalous Synergistic Effect. *Journal of the American Chemical Society* **140**, 9921-9933, (2018).

42 C. Wang, Y. S. Meng & K. Xu. Perspective—Fluorinating Interphases. *Journal of The Electrochemical Society* **166**, A5184-A5186, (2018).

43 K. M. Abraham, Z. Jiang & B. Carroll. Highly Conductive PEO-like Polymer Electrolytes. *Chemistry of Materials* **9**, 1978-1988, (1997).

44 S. Plimpton. Fast Parallel Algorithms for Short-Range Molecular Dynamics. *Journal of Computational Physics* **117**, 1-19, (1995).

45 W. L. Jorgensen, D. S. Maxwell & J. Tirado-Rives. Development and Testing of the OPLS All-Atom Force Field on Conformational Energetics and Properties of Organic Liquids. *Journal of the American Chemical Society* **118**, 11225-11236, (1996).

46 S. V. Sambasivarao & O. Acevedo. Development of OPLS-AA Force Field Parameters for 68 Unique Ionic Liquids. *Journal of Chemical Theory and Computation* **5**, 1038-1050, (2009).

47 L. Martínez, R. Andrade, E. G. Birgin & J. M. Martínez. PACKMOL: A package for building initial configurations for molecular dynamics simulations. *Journal of Computational Chemistry* **30**, 2157-2164, (2009).

48 S. P. Ong, W. D. Richards, A. Jain, G. Hautier, M. Kocher, S. Cholia, D. Gunter, V. L. Chevrier, K. A. Persson & G. Ceder. Python Materials Genomics (pymatgen): A robust, open-source python library for materials analysis. *Computational Materials Science* **68**, 314-319, (2013).

49 M. L. Richard J. Gowers, J. Barnoud, T. Reddy, M. N. Melo, S. Seyler, J. Domanski, David L. Dotson, Sébastien Buchoux, Ian M. Kenney, O. Beckstein MDAnalysis: A Python package for

4

the rapid analysis of molecular dynamics simulations. *Proceedings of the 15th Python in Science Conference*, 98-105, (2016).

50   C. Lee, W. Yang & R. G. Parr. Development of the Colle-Salvetti correlation-energy formula into a functional of the electron density. *Physical Review B* **37**, 785-789, (1988).

51   S. F. Boys & F. Bernardi. The calculation of small molecular interactions by the differences of separate total energies. Some procedures with reduced errors. *Molecular Physics* **100**, 65-73, (2002).

52   M. Frisch, G. Trucks, H. B. Schlegel, G. E. Scuseria, M. A. Robb, J. R. Cheeseman, G. Scalmani, V. Barone, B. Mennucci & G. J. I. Petersson, Wallingford CT. gaussian 09, Revision d. 01, Gaussian. **201**, (2009).

53   V. J. E. A. Gutmann. Empirical parameters for donor and acceptor properties of solvents. *Electrochimica Acta* **21**, 661-670, (1976).

54   O. Pecher, P. M. Bayley, H. Liu, Z. Liu, N. M. Trease & C. P. Grey. Automatic Tuning Matching Cycler (ATMC) in situ NMR spectroscopy as a novel approach for real-time investigations of Li- and Na-ion batteries. *Journal of Magnetic Resonance* **265**, 200-209, (2016).

55   A. B. Gunnarsdóttir, C. V. Amanchukwu, S. Menkin & C. P. Grey. Noninvasive In Situ NMR Study of "Dead Lithium" Formation and Lithium Corrosion in Full-Cell Lithium Metal Batteries. *Journal of the American Chemical Society* **142**, 20814-20827, (2020).

4

5. Unveiling co-intercalation-free high-entropy electrolytes for lithium-ion batteries

Abstract

Developing electrolytes has garnered significant attention for the diverse compositions that provide tunable performance for next-generation lithium (Li)-ion batteries (LIBs). The various compositions introduce complex solvation chemistry that assumes a crucial role in facilitating Li^+ transport and solid-electrolyte interphase (SEI) formation, presenting a landscape rich for exploration. Here, we show that by introducing multiple commercial Li salts, a long-standing challenge—namely, the co-intercalation of propylene carbonate (PC) into graphite anodes can be effectively addressed, which opens up new avenues for advancing electrolytes and boosting performance. This is rationalized by introducing multiple Li salts within PC solvent to formulate a standard 1 M high-entropy (HE) electrolyte. This composition remarkably alters solvation properties by shifting the predominant interaction from strong Li^+-solvent to increased Li^+-anion interactions. Consequently, the reduced barriers for Li^+ (de)solvation and the emergence of a salt-dominated solvation sheath are observed, enabling the growth of a protective, inorganic-rich layer on electrode surfaces, which effectively suppress solvent co-intercalation, mitigate mechanical strain of particles, prevent graphite exfoliation, and thereby curb rapid capacity decay. In contrast to conventional strategies, the HE multi-salt electrolyte exhibits an exceptional outcome, demonstrating significantly enhanced cycling stability and rate capabilities on both the state-of-the-art graphite and high-capacity silicon-graphite anodes. This achievement extends principles that can enable highly competitive PC electrolytes for more demanding battery chemistries, and underscores the potential of tailored electrolyte compositions.

5

5.1 Introduction

Lithium(Li)-ion batteries (LIBs) have revolutionized society by enabling the development of portable devices, electric vehicles, and space exploration[1]. However, the growing demand for higher energy storage necessitates the optimization of the current LIBs, with a particular focus on enhancing their energy density, safety, and cycling performance[2,3]. In this regard, the thermodynamics and kinetics processes at the interphase between the electrolyte and electrode are of paramount importance[4,5]. One promising approach to address these challenges is through the design of effective electrolytes that stabilize the interphases and facilitate ion and charge transport within batteries[6].

The most well-known example that underscores the relationship between the interphase and electrolyte is perhaps the "EC-PC disparity" in the history of LIBs development[7]. During the period from the 1950s to the 1990s, propylene carbonate (PC) emerged as the prevailing choice for non-aqueous electrolytes, facilitating the dissolution of various Li salts[8]. However, the course of LIBs development took an unforeseen turn when the introduction of the intercalation host, graphite, as an anode material, brought the limitations of PC to the forefront. The persistent reduction decomposition of PC occurring around 0.7 V leads to detrimental consequences, ultimately contributing to the exfoliation and structural collapse of the graphite electrode[9]. In contrast, ethylene carbonate (EC), distinguished by a mere methyl group variation in its molecular configuration, boasts a remarkable capability. It promotes the formation of a robust solid-electrolyte interphase (SEI) passivation layer, effectively curtailing electrolyte decomposition at lower potentials, thus facilitating the reversible Li^+ (de)intercalation within the graphite framework[10]. This divergence in performance places EC in important role within in the landscape of LIB technologies, despite its inherent drawbacks in contrast to its counterpart PC, including a comparatively elevated melting point, a restricted liquid range, and diminished anodic stability[11]. This historical episode serves as a vivid illustration of the intricate interplay between interphase phenomena and electrolyte choices in the performance of batteries, showing the intricate trade-offs and careful considerations inherent in the quest for advanced energy storage solutions.

5

Over the past three decades of research, the "Li$^+$-PC solvation–co-intercalation–decomposition" model has effectively elucidated the intricate relationships among PC electrolyte compositions, the Li$^+$ solvation sheath complex, and the resulting interphase chemistry on graphite anodes[12,13]. Meanwhile, investigations into the EC-PC disparity have highlighted a critical aspect of the Li$^+$ de-solvation process at electrode-electrolyte interfaces. This phenomenon hinges on the competitive solvation of Li$^+$ by anion and solvent molecules, ultimately determining whether an electrolyte can establish a protective interphase between EC-based and PC-based electrolytes[7]. Consequently, using higher salt concentrations in PC electrolytes, that augments the anion population or F-donation capability due to the increased salt-to-solvent ratio, has been demonstrated as a possible way to alter the Li$^+$ solvation from the PC solvent molecules to anion groups, thus reversing the observed disparity[14,15]. However, it is important to acknowledge that resorting to concentrated electrolytes unavoidably entails trade-offs, potentially sacrificing pivotal bulk electrolyte properties like ionic conductivity, viscosity, and cost, compromising their practical applicability[16]. In addition, researchers also investigated other strategies aimed at enhancing the interphase of graphite anodes in PC electrolytes, including the integration of film-forming additives and cosolvents (mostly≥50% in volume)[16-21], as well as graphite surface coatings[22,23]. Despite efforts, these methods have fallen short of either attaining performance that rivals that of EC-based electrolytes or compromising the electrolyte properties, such as ion transport and redox stability, as well as the charge/ion transfer at interphases[24]. Therefore, the pursuit of an approach that optimally retains the benefits of the PC solvent while avoiding to introduce negative effects holds of great significance for both current graphite anodes and the forthcoming generation of high-capacity graphite-containing anodes.

5
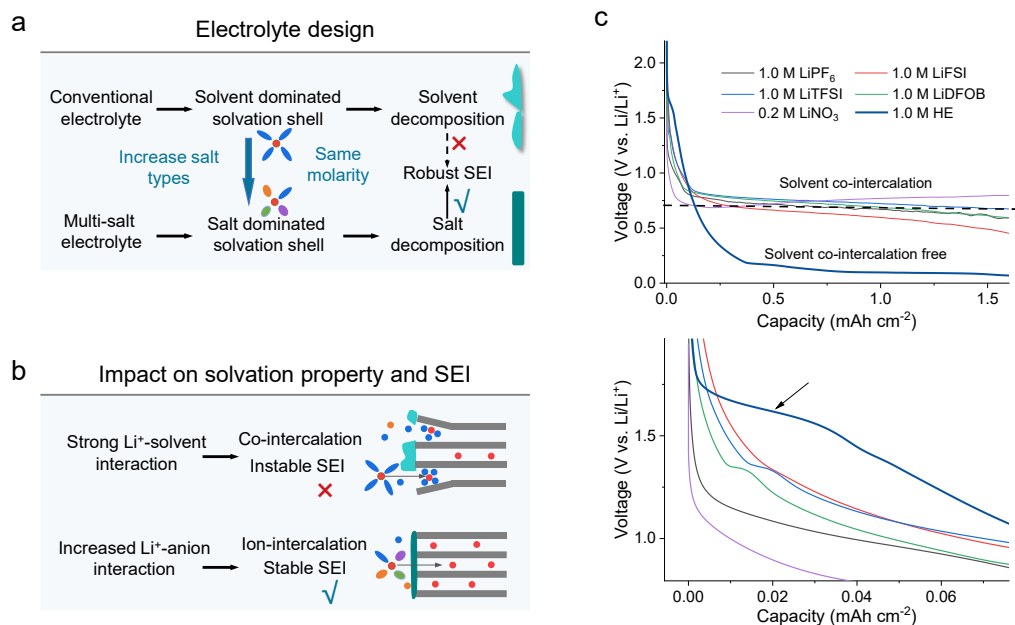
Fig. 5.1. Electrolyte design strategy and its impacts on solvation property and SEI. a, Electrolyte design strategy from conventional single/less-salt electrolyte to multi-salt electrolytes. With an equivalent salt concentration, the addition of diverse salt types can facilitate a transition from a solvent-dominated solvation shell to a salt-dominated solvation shell. **b**, Impacts on the solvation property and SEI on graphite anode. The strong Li⁺-solvent interaction results in solvent co-intercalation into the graphite layers with instable SEI, of which interaction can be decreased to prevent solvent from the intercalation. **c**, Discharge profiles of the graphite electrode at 0.1C for various salts electrolytes in PC solvent (0.2 M LiNO₃ is used because of its limited solubility). The enlarged profiles are shown in the bottom, where a short discharging plateau is observed at around 1.7 V in the HE multi-salt electrolyte. The corresponding dQ/dV plots are shown in Fig. S5.1.

Leveraging the vast chemical composition possibilities of electrolytes, this study presents compelling evidence that the synthesis of a PC solvent by combining various commercially available salts offers a straightforward yet highly efficient method to achieve the solvent-co-intercalation-free characteristic within graphite-containing anodes (Fig. 5.1). Differing from conventional knowledge[14,15], increasing the types of salts introduces the capacity to modulate the solvation interactions between Li⁺ and PC solvent towards the increased Li⁺-anion interactions (Fig. 5.1a), achieving the similar effect to the above-mentioned salt concentrated electrolytes but within a regular 1.0 M salt concentration. Furthermore, the intrinsically increasing the diversity of solvation species

by the participation of multi-salt anions demonstrates a higher Li$^+$ diffusion, decreased Li$^+$ and PC solvent interaction and lowered Li$^+$ de-solvation energy in this HE-PC electrolyte, consisting of equimolar 0.2 M LiPF$_6$/0.2 M LiTFSI/0.2 M LiFSI/0.2 M LiDFOB/0.2 M LiNO$_3$. Comprehensive studies from a combination of spectroscopic techniques, including cryogenic transmission electron microscopy (cryo-TEM), operando solid-state nuclear magnetic resonance (NMR) spectroscopy, indicate the electrolyte has an ability to facilitate the formation of a robust interphase, suppressing PC co-intercalation and graphite electrode degradation (Fig. 5.1b). Consequently, this effectively resolves the problem of incompatibility between individual salt-based PC electrolytes and graphite-based anodes (Fig. 5.1c), resulting in a significant improvement in cycling and rate performance. This improvement is notable even when these electrolytes are used alongside high-voltage layered oxide cathodes. In the context of typical high-energy NCM811‖graphite full cells, it maintains a capacity retention of approximately 94.0% after 600 cycles. Moving towards higher energy density, the NCM811‖Si/G450 (a capacity of 450 mAh g^{-1}) cells exhibit an initial Coulombic efficiency (CE) of 86.3% and maintain a capacity retention of about 94.5% after 300 cycles. Furthermore, the elevated-energy NCM811‖Si/G1000 full cells can demonstrate stable cycling with a capacity retention of approximately 90.0% after 300 cycles. Our study unravels the intricate solvation chemistry of the electrolytes through the incorporation of multiple salts within PC electrolytes, and elucidates how this controls the characteristics of the SEI on graphite-based anodes toward a high reversibility.

5.2 Electrochemical performance of HE multi-salt electrolyte in graphite anodes

To understand the impact of the different solvation chemistry and interphase property on the electrochemical performance, cycling tests were conducted using graphite anodes in the HE multi-salt electrolyte and a conventional LiPF$_6$-PC electrolyte (used as a reference in this context). It's important to note that the engineering exploration of different salt combinations and their respective ratios goes beyond the scope of the present study. Fig. 5.1c shows initial discharge-charge profiles of graphite‖Li cells in PC electrolytes with
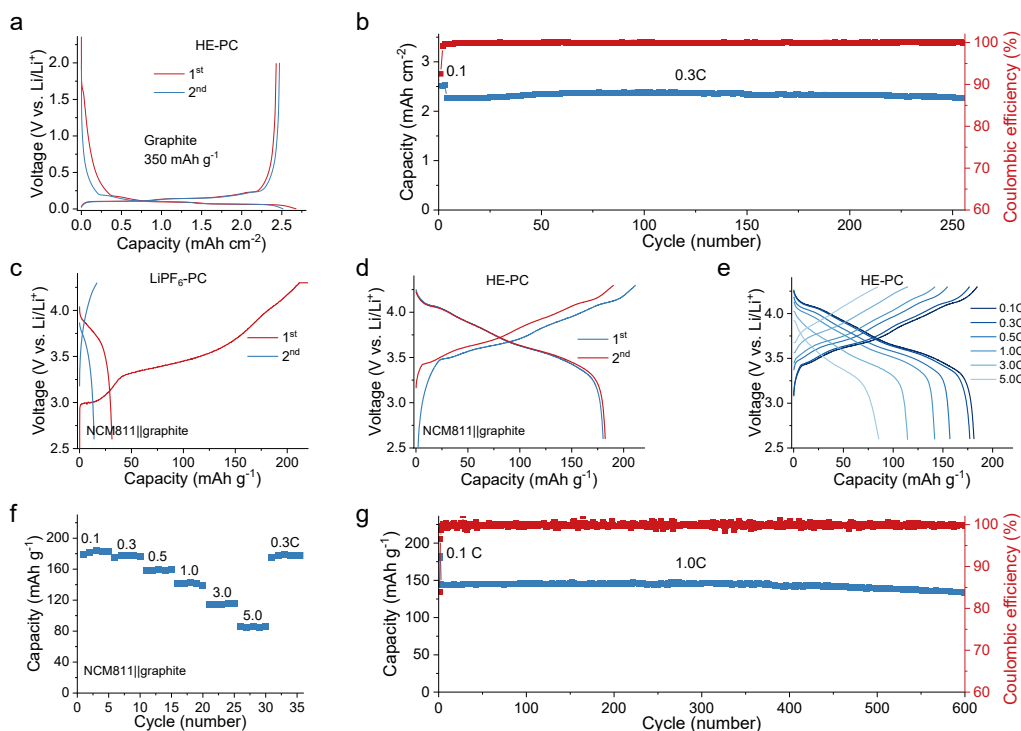
Fig. 5.2. Electrochemical performance of HE multi-salt electrolyte in graphite anode. a, Discharge/charge profiles of graphite anode in graphite∥Li cell with the HE multi-salt electrolyte in the voltage range 0.001-2.0 V vs. Li/Li$^+$. **b**, Long-term cycling performance at 0.1C for the first 3 cycles and 0.3C for following cycles. Electrochemical performance of full cells with graphite anode and NCM811 cathode in **c**, LiPF$_6$-PC electrolyte and **d**, HE multi-salt PC electrolyte cycled between 2.6-4.3 V at 0.1C. **e**, The charge/discharge profiles and **f**, discharge capacity retention of full cells at various rates from 0.1C to 5.0C of HE multi-salt electrolyte cycled between 2.6-4.3 V. **g**, Capacity retention of the NCM811∥graphite full cells cycled between 2.6-4.3 V. The discharge/charge rates are 0.1C for the first three cycles and 1.0C for the following cycles. The mass loading of graphite is around 2.5 mAh cm^{-2}, and the N/P (anode/cathode) ratios of the full cells are in the range of 1.1~1.15.

various single salt, where all exhibit a long plateau near 0.7 V, corresponding to continuous co-intercalation during the initial discharge process. The dQ/dV plots confirm the co-intercalation in conventional PC electrolytes (Fig. S5.1), which is held responsible for the low initial CE of around 40% as observed in the graphite∥Li cell using the LiPF$_6$-PC electrolyte (Fig. S5.2). Interestingly, even though the solvent is identical, the cells with multiple salts strongly promote the reversibility, displaying voltage plateaus between 0.001-0.25 V representing the different stages of Li$^+$-graphite intercalation (Fig. 5.2a). In

this case, the initial CE exceeds 90%, and at subsequent cycling at 0.3C rate 99% capacity is maintained after 256 cycles (Fig. 5.2b). Since salt decomposition takes place around ~1.5 V, whereas the decomposition of cyclic carbonate solvents occurs around 0.5 V[25], the SEI formation from salt decomposition turned out to be one of the factors to support the improved cycling stability, as indicated by a clear peak around ~1.7 V during the initial stages of the first discharge in the dQ/dV plots (Fig. S5.1). This is also supported by the redox peaks in cyclic voltammetry (CV) measurements in the Li||Cu cells (Fig. S5.3), where a wide reduction peak centered around 1.25 V in the HE-PC electrolyte emerges.

The high-voltage cathode compatibility of HE multi-salt PC electrolyte is also investigated in NCM811 ($LiNi_{0.8}Co_{0.1}Mn_{0.1}O_2$)||Li cells (Fig. S5.4). While a similar initial charge capacity is observed, the $LiPF_6$-PC electrolyte exhibits a slightly lower initial CE of approximately 80%, in contrast to the 83.6% achieved with the HE-PC electrolyte. During the follow cycling test, the capacity of the cells using $LiPF_6$-PC electrolyte fails after 100 cycles whereas the HE-PC electrolyte shows stable cycling with capacity retention of around 93% after 200 cycles. The result indicates that this electrolyte has a better compatibility with the high-voltage layered oxide cathodes. To further examine the practical feasibility, a full cell was assembled combining an NCM811 cathode with a graphite anode. The voltage profiles of the NCM811||graphite cell with the $LiPF_6$-PC electrolyte shows a first-stage slope during the first charge (Fig. 5.2c), which is consistent with the flat plateau observed in the graphite||Li cells, corresponding to Li^+-PC solvent co-intercalation. This co-intercalation in the $LiPF_6$-PC limits the reversible capacity to less than ~40 mAh g^{-1} from the second cycle, which comes along with rapid capacity fading. In contrast, the full cells with the HE-PC electrolyte show a reversible capacity of about 180 mAh g^{-1} with an initial CE of approximately 84% at 0.1C (Fig. 5.2d). The rate performance is also demonstrated by cycling at different current densities (Figs. 5.2e and 5.2f), where reversible capacities of ~181.2, 177.5, 159.7, 141.7, 116.1, and 85.6 mAh g^{-1} are obtained at rates of 0.1, 0.3 0.5, 1.0, 3.0, and 5.0C, respectively. After the rate cycling test, a reversible capacity of around 177.2 mAh g^{-1} is delivered at 0.3C, and the battery can be continued to cycle. The long-term cycling stability is further investigated (Fig. 5.2g), resulting in a capacity retention of around ~94.0% after 600 cycles at 1.0C with an average CE of about 99.9±0.2 %, demonstrating potential application for the current LIBs.

5.3 Solvation chemistry of HE multi-salt electrolyte
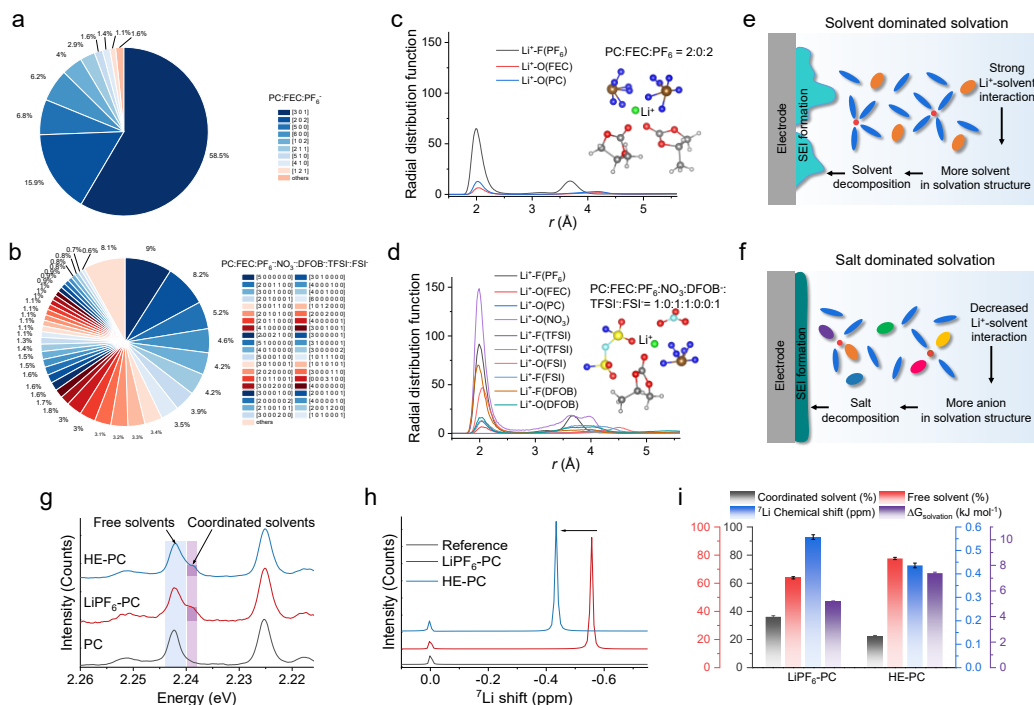
Fig. 5.3. Solvation structure characterizations. Li$^+$ coordination environments of **a,** single-salt LiPF$_6$-PC electrolyte and **b**, HE-PC electrolyte determined from MD simulations (detailed description in the Table S5.1 and S5.2). Simulation of the RDF for Li$^+$ in **c,** LiPF$_6$-PC electrolyte and in **d**, HE-PC electrolyte. **e,** Solvent dominated solvation structure. The strong solvent dominated solvation sheath results in an organic-rich and poorly passivated SEI, causing electrolyte consumption, low CE and irreversible capacity loss. **f,** Salt dominated solvation structure. The interaction between Li$^+$ and solvent is decreased, leading to more anions involve in the inner solvation structure. This leads to an inorganic-rich, robust SEI that passivates further decomposition. **g,** Raman spectra of PC solvent, single-salt LiPF$_6$-PC and HE-PC electrolyte. **h**, Liquid ^{7}Li NMR spectra of LiPF$_6$-PC and HE-PC electrolytes. The peaks were referenced to 1.0 M LiCl in D$_2$O at 0 ppm. **i,** Comparison of the Li solvation environment properties in LiPF$_6$-PC and HE-PC electrolytes. Each axis corresponds to the bar chart with the same color.

The solvation complex of electrolytes, that is the coordination of Li$^+$ to anions and PC solvent molecules, is responsible for the SEI formation and cycling reversibility[8]. To gain more insights into the solvation structures, classical molecular dynamics (MD) simulations were carried out (Figs. S5.5-S5.8). The various principal anion species in the

HE-PC electrolyte result in a rich diversity of Li^+ solvation environments, much more than in the single-salt $LiPF_6$-PC electrolyte (Figs. 5.3a, 5.3b and Table S5.1 and S5.2). According to the radial distribution function (RDF) results obtained from the MD simulations (Figs. 5.3c and 5.3d), the solvation sheath in HE-PC electrolyte promotes the presence of more anions in the inner solvation sheath of Li^+ compared with the $LiPF_6$-PC electrolyte, leading to more salt dominated solvation configurations. The difference between the two electrolytes presents two typical solvation categories, solvent dominated and salt dominated solvation (Figs. 5.3e and 5.3f). In a conventional $LiPF_6$-PC electrolyte, Li^+ is usually strongly solvated by polar solvents and most anions are excluded from the inner solvation sheath. Since the primary solvation sheath is the precursor for SEI formation, such solvation leads to solvent-derived organic-rich interphase chemistry and poorly passivated SEI, causing electrolyte consumption, low CE, and irreversible capacity loss[12,26]. In contrast, this multi-salts HE-PC electrolyte show the salt-dominated solvation interaction, where the primary solvation sheath around the Li^+ is dominated by anions, leading to an anion-derived inorganic-rich and robust SEI that passivates PC solvent co-intercalation and further electrolyte decomposition, enabling the good cycling of graphite anode[27]. This is in agreement with the lower amount of coordinated solvent observed in HE-PC than in $LiPF_6$-PC electrolytes from Raman measurements (Fig. 5.3g, Figs. S5.9 and S5.10).

The solvation strength is studied by ^7Li liquid NMR spectroscopy, where the chemical shift reflects the shielding of Li^+ as a result of their solvation environment. The HE-PC electrolyte experiences a decreased interaction between solvation sheath and Li^+ as reflected by the downfield chemical shift (~0.12 ppm) as shown in Fig. 5.3h, compared to the up-field shift for the $LiPF_6$-PC electrolyte indicating more shielded Li^+ due to the high electron density from the stronger solvation interactions[28]. This weaker solvation observed in HE-PC electrolyte also promotes Li^+ mobility as reflected by a higher simulated self-diffusion coefficient of 4.78×10^{-7} $cm^2 s^{-1}$ compared to $LiPF_6$-PC electrolyte (1.39×10^{-7} $cm^2 s^{-1}$) (Fig. S5.6). In addition, the solvation energy $\Delta G_{solvation}$ is investigated (Fig. 5.3i, see method for details), which represents an overall evaluation of the binding strength between Li^+ and solvating species (both solvent and anion). The more positive

$\mathit{\Delta}G_{solvation}$ suggests a weaker solvation interaction (thus lower Li^+-anion dissociation energy) of this HE-PC electrolyte[29]. Altogether, these findings indicate that this multi-salts HE-PC electrolyte, induced by the introduction of multiple salts in the PC solvent, can lead to a more diverse solvation environment and weaker Li^+-PC solvent coordination, that can be used to realize the solvent-co-intercalation-free property in the graphite anodes. It's worth noting that the introduction of multiple salts in a PC-solvent yields results similar to those observed in high-salt concentration electrolytes[16]. In both scenarios, there is a shift towards increased interaction between Li^+ and anions, leading to the dominance of salt-induced solvation sheaths and interphases[30]. However, they are fundamentally distinct: one involves increasing the salt-to-solvent ratio to enhance the Li^+-anion population, while the other conceptually resembles HE alloys[31,32], where the presence of multiple principal elements enhances configurational diversity while maintaining the same overall salt concentration[33-36]. This greater diversity of solvated species indicates the broadened possibility for Li^+ ion coordination with anions as observed in both the MD simulation and Raman measurement, because of the varying coordinating strengths and molecular structures of each salt. This result disrupts the customary local configurations between Li^+ and solvent; instead, it contributes to an increased potential for diverse local solvation complex configurations involving salts.

5.4 Capturing solvent-co-intercalation-free in electrodes

5

The TEM result of the pristine graphite material (Fig. 5.4a) shows the smooth-edged morphology before electrochemical cycling. After discharging to 0.5 V vs. Li/Li^+ in the single-salt $LiPF_6$-PC electrolyte, corresponding to the end of the Li^+-PC solvent co-intercalation, the expanded graphite layers are observed in Fig. 5.4b. It can be seen that certain regions depict disintegration of the graphite layers, resulting in a loss of connection with neighboring layers. In a sharp contrast, a good structural integrity of the electrode surface is observed in the HE-PC electrolyte (Fig. 5.4c), without graphite exfoliation after discharging. Cryo-STEM electron energy loss spectroscopy (EELS) mappings reveal a strong oxygen signal between the carbon layers in Fig. 5.4d, indicating the presence of the co-intercalation of the PC solvent molecules, which is more clearly observed by the

stacking map of C and O (Fig. S5.11). More areas of the graphite particle after co-intercalation can be found in Fig. S5.12. The bended graphite layers, marked in the C *K*-mapping is a result of residual stress that promotes the exfoliation of the graphene layers and formation of chunks of graphite, held responsible for the structural degradation. By comparison, the EELS mappings show a uniform distribution of elements in graphite of HE-PC electrolyte, and the high carbon counts are attributed to the highly reserved crystalline nature (Fig. 5.4e).
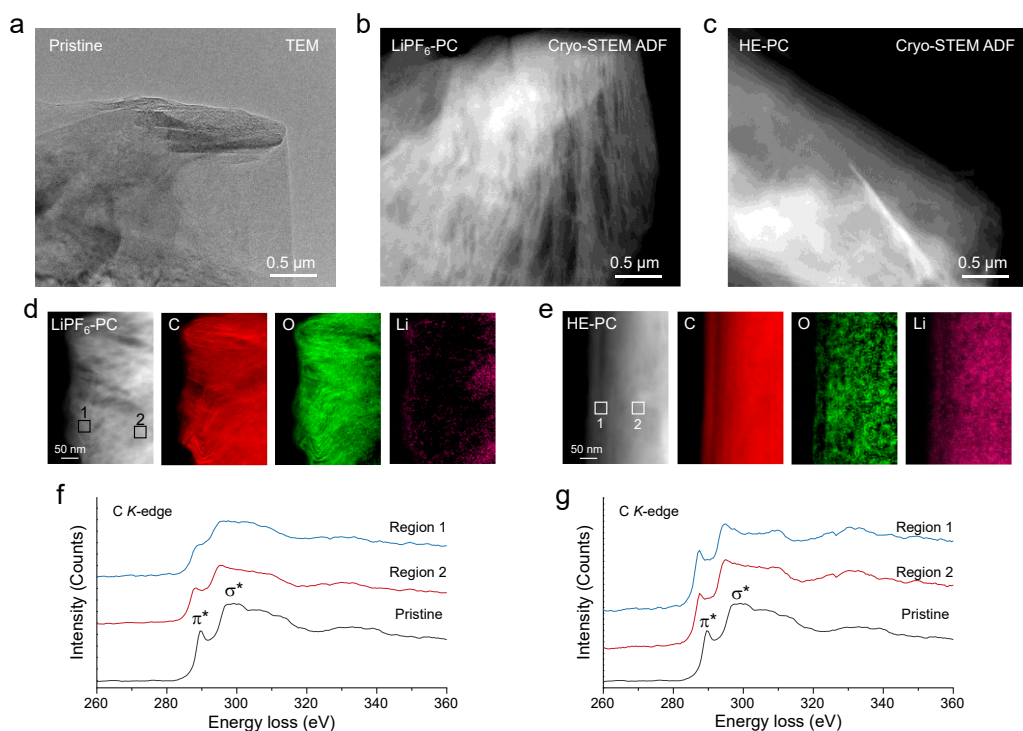
Fig. 5.4. Visualizing Li$^+$-solvent co-interaction in electrode using Cryo-STEM. a, TEM image of pristine graphite. Cryo-STEM-ADF image of graphite cycled in **b**, single-salt LiPF$_6$-PC and **c**, HE-PC electrolyte at 0.2C rate to the voltage of 0.5 V vs. Li/Li$^+$. Cryo-STEM EELS mappings of the graphite in **d**, single-salt LiPF$_6$-PC and **e**, HE-PC electrolytes. EELS of C *K*-edge fine structure of graphite cycled in **f**, single-salt LiPF$_6$-PC electrolyte and **g,** HE-PC electrolyte recorded at Region 1 and Region 2, respectively.

Moreover, employing cryo-STEM-EELS analysis of the C *K*-edge can provide valuable insights into the carbon bonding environment within different regions of the

graphite particle (Figs. 5.4f and 5.4g). At the near surface of graphite, the EELS profile of region 1 shows a decreased intensity of the π^* peak representing the sp^2 bonding, along with the broadening of the σ^* peak, which indicates the transition to a more amorphous structure after cycling in LiPF$_6$-PC electrolyte (Fig. 5.4f). At the bulk graphite, the EELS profile at region 2 presents the pristine-like edge shapes, indicating a relatively preserved structure. Hence, parts of the graphite surface experience profound structural degradation in LiPF$_6$-PC electrolyte. As for the electrode cycled in the HE-PC electrolyte, the bonding environment of the carbon molecules within graphite (Fig. 5.4g), shows similar π^* and σ^* bonding characteristics as compared to pristine graphite both in the region near the surface (Region 1) and the region in the bulk. The preserved graphite structure and the uniform Li and oxygen distribution suggest that Li$^+$ is uniformly intercalated into the graphite layer without co-intercalation, thus highlighting the ability of the stable SEI in the HE-PC electrolyte to effectively passivate the graphite surface during the initial cycle.

5.5 Interphase structure and chemistry evolution after cycling

Then cryo-TEM is used to probe the nanostructure of the SEI and its interface with graphite. The pristine graphite shows a well-defined layered crystal structure in Fig. 5.5a. After cycling, an amorphous SEI layer can be observed on the surface of the graphite in both electrolytes. The uneven SEI formed in the LiPF$_6$-PC electrolyte shows an average thickness larger than that formed in the HE-PC electrolyte, where the latter is uniform and homogeneous with a thickness of around 2.7 nm (Figs. 5.5b and 5.5c). Moreover, the distortion and expansion of the graphite layer are also observed in the cryo-TEM results after cycling in LiPF$_6$-PC electrolyte. In comparison with pristine graphite, graphite cycled in the LiPF$_6$-PC electrolyte shows an increased and irregular lattice spacing (Figs. 5.5d and 5.5e), reflecting the disorder due to co-intercalation. In contrast, the crystal structure of graphite cycled in the HE-PC electrolyte is well preserved (Figs. 5.5c and 5.5f).

5
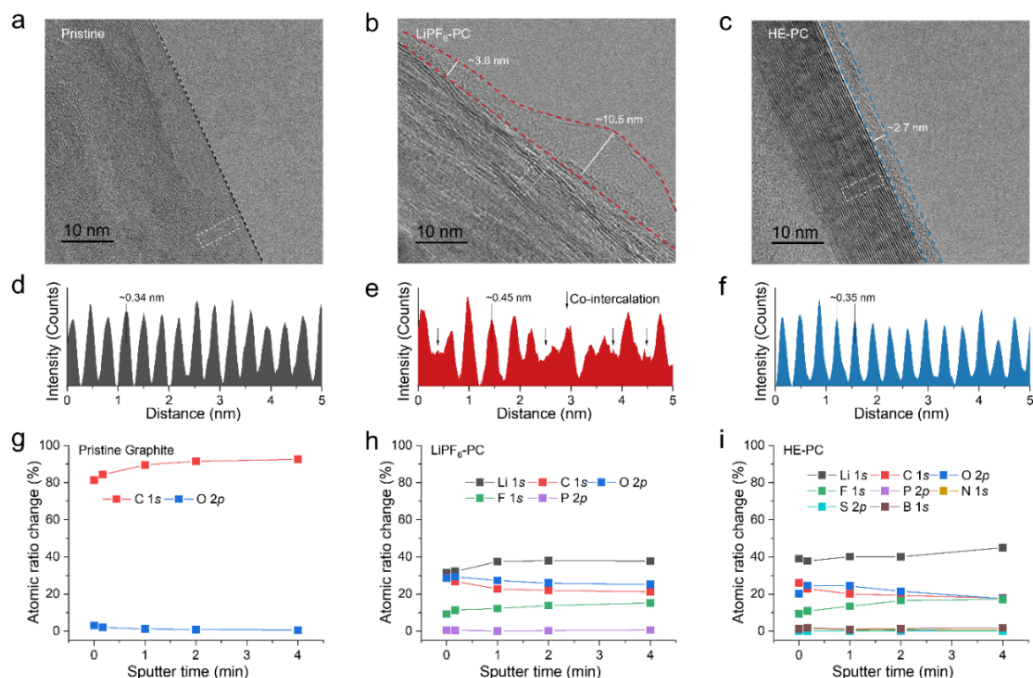
Fig. 5.5. SEI structures and chemistry. a, High-resolution TEM images of pristine graphite. High-resolution cryo-TEM images of graphite after cycling in **b**, single-salt LiPF$_6$-PC and **c**, HE-PC electrolytes. Integrated intensities of graphite lattice in the region indicated in **a-c** for **d**, pristine graphite **e**, graphite cycled in the single-salt LiPF$_6$-PC and **f**, graphite cycled in the HE-PC electrolytes. Quantified atomic composition ratios of the SEI at different sputtering times for **g,** pristine graphite **h**, graphite cycled in the LiPF$_6$-PC electrolyte, and **i,** graphite cycled in the HE-PC electrolyte from XPS spectra.

In addition, we further study the SEI composition using XPS measurements on graphite electrodes in the two electrolytes. The atomic concentration after different sputtering time reveals the SEI composition as a function of depth (Figs. 5.5g-5.5i, Figs. S5.13-S5.19). For the pristine graphite electrode, the surface contains a large amount of C and a small amount of O (Fig. 5.5g). After cycling in the LiPF$_6$-PC electrolyte, the SEI shows high C and O content, while less F content indicating solvent dominated decomposition in SEI formation (Fig. 5.5h). In contrast to the LiPF$_6$-PC electrolyte, the atomic composition of SEI in the HE-PC electrolyte shows lower C, O content and higher F content as well as N, B, and S, species that originate from salt decomposition (Fig. 5.5i). This implies that the SEI formed in the HE-PC electrolyte has more anion-derived

interfacial chemistry (Supplementary Note S5.1). This is further confirmed by the deconvolution of the C 1*s* and O 1*s* spectra (Figs. S5.13 and S5.14). The C 1*s* spectra of pristine graphite reveal four peaks, including C-C (from graphite), C-H, C-O, and π^*-π^* (from graphite). After cycling, the C=O species result from PC solvent decomposition appears. The peak intensities of C-O and C=O in the SEI from the HE-PC electrolyte is lower than that in the LiPF$_6$-PC electrolyte, confirming the more inorganic-rich SEI due to the anion-dominated solvation structure, which is held responsible for passivating, and thereby stabilizing the graphite electrode during cycling.

Considering the formation of a stable SEI is also an intriguing aspect when examining Li-metal anodes. Hence, the performance of the two electrolytes is assessed through electrochemical evaluation in Li∥Cu cells. In comparison to the LiPF$_6$-PC electrolyte, the HE-PC electrolyte demonstrates notably enhanced electrochemical compatibility with Li metal. This is evident in the reversible plating and stripping observed over 200 cycles, showing an average coulombic efficiency (CE) exceeding 99% (Fig. S5.20). Conversely, the cell employing the LiPF$_6$-PC electrolyte falters before reaching 100 cycles. This observation is corroborated by a refined approach[37], where the HE-PC electrolyte achieves an even higher CE of around 99%, contrasting the approximately 88.5% achieved with the LiPF$_6$-PC electrolyte (Fig. S5.21). Additionally, the overpotential associated with Li plating/stripping is diminished in the HE-PC electrolyte compared to the LiPF$_6$-PC electrolyte, suggesting smoother Li-ion transport facilitated by the inorganic-rich and robust SEI formed in the HE-PC electrolyte.

5

5.6 Electrode structure evolution upon cycling

The evolution of the corresponding electrode structure in various electrolytes is investigated using solid-state NMR, a potent tool offering insights into the changing chemical state and environment of specific nuclei[38-42]. In this context, operando ^{7}Li NMR is employed to observe the Li$^+$-solvent co-intercalation behavior within graphite∥Li cells utilizing different electrolytes. The setup for operando NMR measurements is illustrated in Fig. S5.22. Fig. 5.6a and Fig. S5.23 present the evolution of the ^{7}Li resonance in a graphite∥Li cell utilizing the LiPF$_6$-PC electrolyte, captured during the initial cycle. The
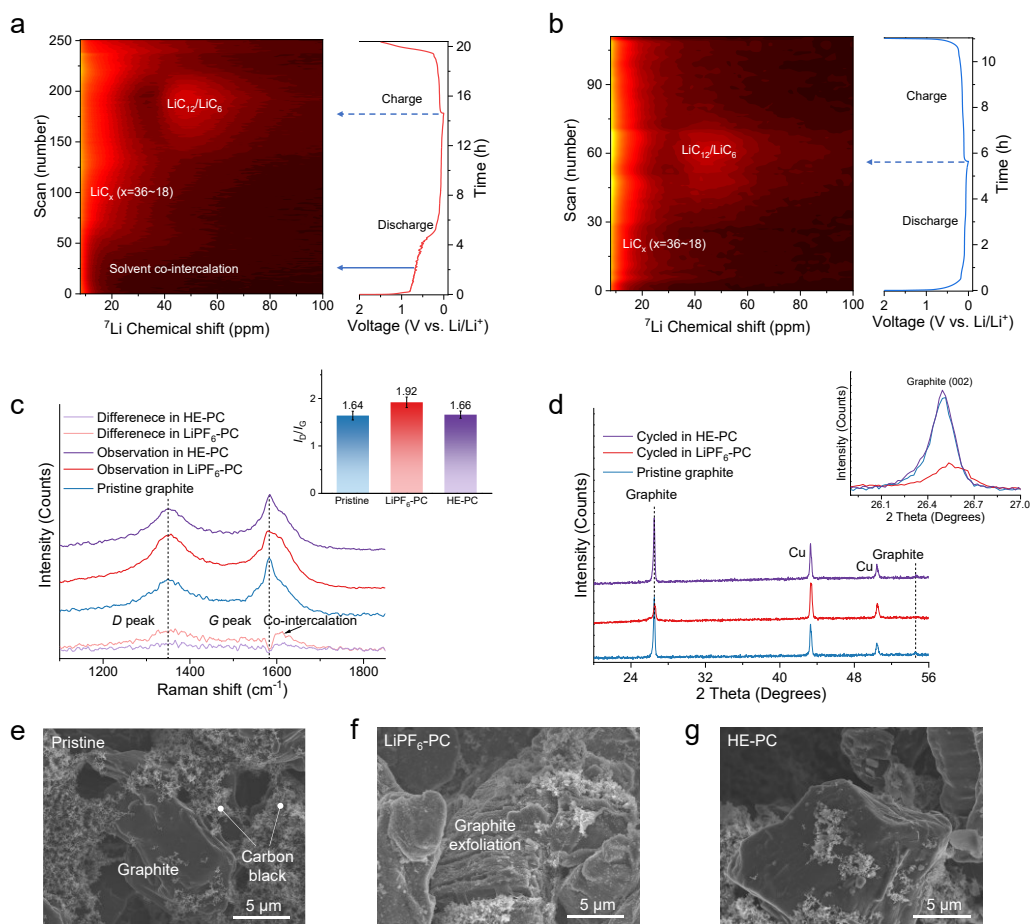
Fig. 5.6. Structure evolution of the graphite anode after cycling. Discharge/charge profile and contour plots of operando ^{7}Li NMR data of graphite∥Li cells between 0.001 and 2.0 V at 0.2C rate using **a**, single-salt LiPF$_6$-PC and **b**, HE-PC electrolytes. **c**, Raman spectra of graphite electrode before (pristine graphite) and after one cycle in LiPF$_6$-PC and HE-PC electrolytes. The light red and light purple lines at the bottom show the differential spectrum between the pristine graphite and cycled graphite, showing different degrees of structure degradation. Inset shows I_D/I_G ratio calculated by integrated intensity showing different degrees of graphitization and defects. **d**, XRD pattern of the graphite anode before and after cycling in LiPF$_6$-PC and HE-PC electrolytes. Inset shows the magnified image of the graphite (002) peak. **e**, SEM image of a pristine graphite anode. SEM image of graphite anode after cycling in **f**, LiPF$_6$-PC electrolyte and in **g**, HE-PC electrolytes.

extended voltage plateau attributable to solvent co-intercalation becomes evident around 0.7 V vs. Li/Li$^+$, during which the ^{7}Li chemical shift aligns near 0 ppm. This suggests a comparable Li$^+$ environment in the co-intercalated species when compared to the

electrolyte, making it indistinguishable from the strong electrolyte peak also around 0 ppm. Throughout the co-intercalation process, no novel Li^+ environment emerges, as discerned from the spectra captured at different discharge and charge stages (Fig. S5.24). Subsequent to co-intercalation, a ^7Li resonance emerges at around 15 ppm, growing in intensity and shifting to around 30 ppm. This observation aligns with the formation of LiC_x (18<x<36) compounds[43]. Additionally, an extra resonance emerges at approximately 50 ppm, attributed to LiC_{12}/LiC_6 compounds. Concurrently, the intensity within the 30-ppm region diminishes while shifting to a lower ppm value, indicating a transformation between these species. During charging, Li-deintercalation from the graphite leads to a decline in the LiC_{12}/LiC_6 resonance. Remarkably, at the end of charging at 2 V, the intensity of the resonance linked to LiC_x (18<x<36) remains significant, suggesting a substantial amount of trapped Li within the graphite. This finding elucidates the lower initial CE for the $LiPF_6$-PC electrolyte. Operando 7Li NMR analysis of the graphite‖Li cell using the HE-PC electrolyte is also conducted for comparison, as depicted in Fig. 5.6b and Fig. S5.23. As anticipated, there is no co-intercalation region observed, and the LiC_x (18<x<36) resonance emerges almost immediately upon discharge (Fig. S5.25). In this instance, the resonance shift occurs more continuously compared to the $LiPF_6$-PC electrolyte, suggesting a more uniform intercalation process. Furthermore, the lower intensity of the LiC_x resonance at the end of the charging process indicates superior reversibility of Li-intercalation for the HE-PC electrolyte in contrast to the $LiPF_6$-PC electrolyte.

5

To further investigate the changes in graphite structure upon cycling, Raman spectra were conducted on electrodes before (pristine graphite) and after cycling. The results are depicted in Fig. 5.6c and Fig. S5.26. The ratio of relative intensity between the D and G bands, denoted as I_D/I_G, around 1350 and 1580 cm^{-1}, respectively, serves as an indicator for assessing the extent of carbon structure defects. After cycling with the $LiPF_6$-PC electrolyte, this ratio significantly increases to 1.92 compared to pristine graphite (1.64), signifying a more defective structure and, consequently, a reduced degree of graphitization due to the co-intercalation. In contrast, the graphite cycled with the HE-PC electrolyte maintains a consistent I_D/I_G ratio of 1.66, indicating the preservation of its structure during cycling. Electrode structure analysis was further conducted using X-ray diffraction (XRD),

where the patterns of the graphite electrode before and after cycling in different electrolytes were captured (Fig. 5.6d). The (002) graphite peak at approximately 26.5° 2θ demonstrates a decrease in intensity and broadening after cycling in the $LiPF_6$-PC electrolyte, consistent with interlayer spacing expansion due to Li^+-PC co-intercalation. On the contrary, the graphite (002) peak remains unchanged after cycling with the HE-PC electrolyte, indicating structural stability. Further insights into electrode morphology and structure were obtained using scanning electron microscopy (SEM) as depicted in Figs. 5.6e-5.6g, with additional details in Fig. S5.27. The graphite anode cycled in the $LiPF_6$-PC electrolyte experiences extensive exfoliation, while the graphite particles remain intact with a smooth surface after cycling with the HE-PC electrolyte. Energy-dispersive spectroscopy (EDS) (Figs. S5.28-S5.30) findings reveal that the graphite surface cycled in the $LiPF_6$-PC electrolyte is enriched with oxygen, pointing to a solvent-dominated solid electrolyte interphase (SEI). Conversely, the O intensity is notably low for graphite cycled with the HE-PC electrolyte, whereas P, F, and S are more prominently present, indicating a salt-dominated SEI.

5.7 Electrochemical performance of HE multi-salt electrolyte in silicon-graphite composite anodes

Next, we extend the application of this HE-PC electrolyte to Si/graphite composite anodes, which offer a higher specific capacity to increase the battery energy density. Given the presence of graphite, conventional PC-based electrolytes are typically deemed incompatible. As illustrated in Fig. 5.7a, employing the $LiPF_6$-PC electrolyte in combination with a Si/graphite composite anode with a specific capacity of 450 mAh g^{-1} (Si/G450) yields a lower CE of approximately 51.0%, attributable to the co-intercalation. In contrast, utilizing the HE-PC electrolyte yields a significantly improved CE surpassing 95.0% (Fig. 5.7b). Furthermore, an anode with a higher Si fraction and a specific capacity of 1000 mAh g^{-1} (Si/G1000) demonstrates promising performance. It exhibits an initial CE exceeding 88.5% and maintains reversible cycling paired with the HE-PC electrolyte (Fig. 5.7c).
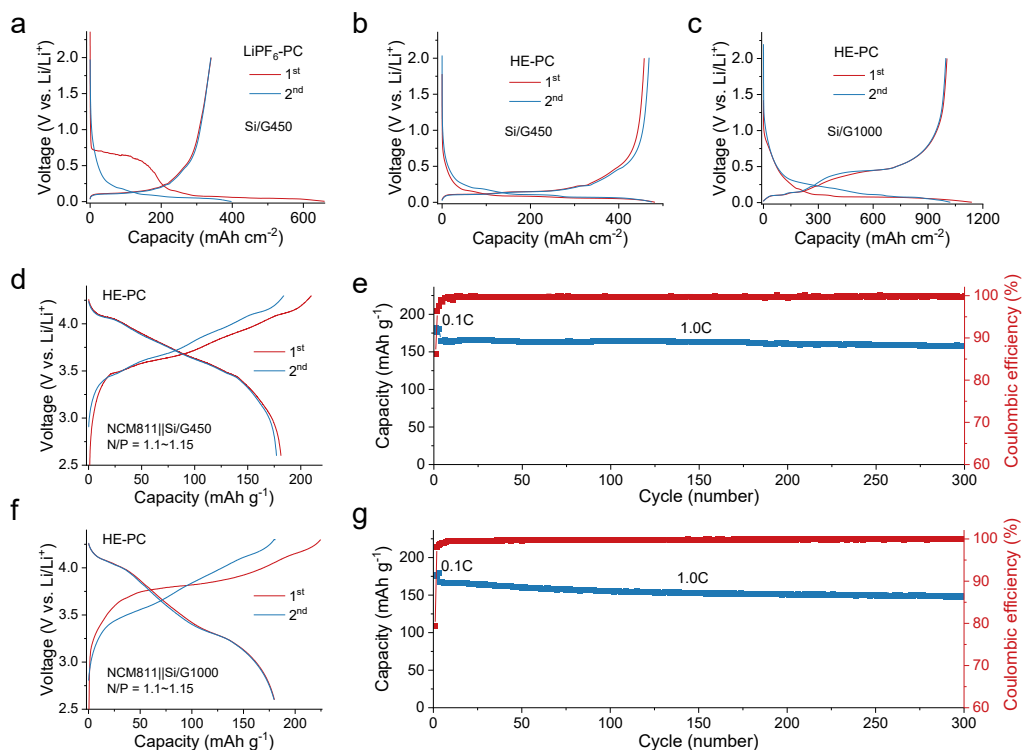
Fig. 5.7. Electrochemical performance of Si/graphite composite anodes. Charge/discharge profiles of Si/graphite‖Li cells with Si/G450 anode in **a**, LiPF$_6$-PC electrolyte and **b**, HE-PC electrolyte, and **c**, Si/G1000 anode in HE-PC electrolyte at 0.1C rate between 0.001-2.0 V vs. Li/Li$^+$. Cycling performance and corresponding voltage profiles of the full cells using the HE-PC electrolyte cycled between 2.6-4.3 V using **d, e,** Si/G450 anode and **f, g**, Si/G1000 anode. The discharge/charge rates are 0.1C for the first three cycles and 1.0C for the following cycles. The mass loading of Si/graphite composite anodes is around 2.5 mAh cm^{-2}, and the N/P (anode/cathode) ratios of the cells are in the range of 1.1~1.15.

5

To explore the application of the HE-PC electrolyte in cells with higher energy density, the electrochemical performance of NCM811‖Si/G450 full cells utilizing the HE-PC electrolyte is assessed (Fig. 5.7d). The cell exhibits an initial discharge capacity of approximately 180 mAh g^{-1}, accompanied by an initial CE of 86.3%. Following the initial cycles at 0.1C, the cell displays minimal degradation during subsequent cycles at a rate of 1.0C. The discharge capacity attains 162 mAh g^{-1} at the 150th cycle and 157 mAh g^{-1} at the 300th cycle, resulting in impressive capacity retentions of 97.5% and 94.5%, respectively (Fig. 5.7e). Furthermore, a noteworthy average CE of 99.8% ± 0.3% is

maintained throughout cycling. Expanding on this, cells with even higher energy density, employing NCM811||Si/G1000, are evaluated using the HE-PC electrolyte. The initial discharge capacity is approximately 180 mAh g^{-1} (Fig. 5.7f). The CE quickly reaches 99.5% within five cycles and maintains 99.9% ± 0.2% with a capacity retention of ~90.0% for 300 cycles (Fig. 5.7g).

5.8 Conclusions

In summary, our investigation shows the effectiveness of introducing multiple Li salts to engineer electrolyte compositions, thereby opening avenues for the advancement of next-generation high-energy LIBs. This HE multi-salt electrolyte has yielded intriguing results, particularly in realizing a reversed solvation chemistry, which enables a transformative shift from strong Li$^+$-solvent solvation to enhanced Li$^+$-anion interactions within the same total salt concentration. This alteration in solvation structure bears two significant outcomes. Firstly, it contributes to the reduction of de-solvation energy, which facilitates efficient Li$^+$ transport and accelerates charge transfer processes. Secondly, the prevalence of a salt-dominated solvation structure leads to the creation of a robust inorganic-rich SEI layer. This protective interphase acts as a barrier, effectively preventing continuous electrolyte decomposition and electrode deterioration. This strategy is realized by combining five-type commonly used salts in a PC solvent to formulate an electrolyte with a standard 1.0 M concentration. This approach successfully eliminates solvent co-intercalation in graphite-containing anodes, a distinct achievement not attainable in all single-salt electrolytes. Importantly, our approach departs from conventional methods. The introduction of various salts engenders solvation interactions between Li$^+$ ions, solvents, and anions, diverging from common strategies like incorporating film-forming additives or raising salt concentration to increase salt participation in solvation. The integration of multiple salts can increase the disorder (or entropy) of mixing[31,32], thereby expanding the realm of possibilities for Li$^+$-anion complexes within the solvation sheath. Through a practical illustration involving the PC-graphite system's inherent incompatibility, our study indicates the potential of altering solvation chemistry via mixing salts to address this long-standing challenge at electrode-electrolyte interphases.

The outcomes of this approach have yielded unexpected advancements in battery performance, also as demonstrated in higher capacity Si/Graphite anodes in combination with high capacity NMC811 cathodes. At last, we hope our study is a catalyst not only for reevaluating the utilization of materials such as PC solvent in this context but also for charting novel avenues in advanced electrolyte chemistry and beyond.

5.9 Methods

Materials

Solvent of propylene carbonate (PC) was purchased from Sigma-Aldrich with battery-grade purity, which was dehydrated with a 4 Å molecular sieve (Sigma-Aldrich) to eliminate the trace water. Lithium hexafluorophosphate (LiPF$_6$), lithium bis(fluorosulfonyl)imide (LiFSI), lithium bis(trifluoromethanesulfonyl) imide (LiTFSI), lithium difluoro(oxalato)borate (LiDFOB) were obtained from Sigma-Aldrich. Lithium nitrate (LiNO$_3$, >99.9%) was purchased from Shenzhen Capchem Technology Co., Ltd and used as-received. All the electrolytes were prepared by dissolving the specific amount of different Li salts in solvents in an Ar-filled glove box (H$_2$O < 0.1 ppm, O$_2$ < 0.1 ppm). Li-metal foils (thickness of 250 μm), Cu foils and Al foils were purchased from MTI Corporation. All Li-metal foils were washed 3 times with DMC solvent before use. Cu foils were immersed in diluted acetic acid for several minutes, subsequently washed by deionized water and acetone three times, separately, then they were quickly dried in the vacuum oven of glove box at room temperature.

LiNi$_{0.8}$Co$_{0.1}$Mn$_{0.1}$O$_2$ (NCM811) was synthesized using coprecipitation method. The certain amount of alkaline aqueous solution (NH$_4$OH and NaOH) was poured into deionized water (1.5 L) to form the base solution in a tank reactor under continuous stirring. Then, a 2 M solution of NiSO$_4$·6H$_2$O, CoSO$_4$·7H$_2$O and MnSO$_4$·H$_2$O with a molar ratio of 8:1:1 and an aqueous solution of 5 M NH$_4$OH and 10 M NaOH were added into the base solution in the tank reactor with a steady rate of 8 mL min^{-1}. The coprecipitation temperature was controlled at 50 °C, and pH value was maintained at around 11 by NH$_4$OH with stirring speed of 500 rpm under nitrogen atmosphere. The coprecipitated

5

$Ni_{0.8}Co_{0.1}Mn_{0.1}(OH)_2$ precursor was prepared, which was subsequently washed by deionized water and ethanol for four times and dried in a vacuum at 120 °C for 24 h. The apparent and tap density of $Ni_{0.8}Co_{0.1}Mn_{0.1}(OH)_2$ precursor are 1.88 g cm^{-3} and 2.06 g cm^{-3}, respectively. For preparation of NCM 811 materials, the as-obtained precursor was mixed with LiOH·H_2O at a molar ratio of 1:1.03; then heated at 500 °C for 5 h and subsequently calcined at 780 °C for 12 h in oxygen atmosphere. After cooling naturally, the obtained material was directly put into an Ar-filled glovebox to prevent any moisture exposition. The NCM811 electrodes were prepared by mixing active material, conductive carbon (Super P) and poly(vinylidene difluoride) (PVDF) binder in the mass ratio of 90: 5: 5 in N-methyl-2-pyrrolidone (NMP) solvent and cast on Al foil and then dried at 60 °C for 6 h, followed by drying in a vacuum oven at 120 °C overnight. Graphite was obtained from BTR New Material Group Co., Ltd. The graphite electrode was prepared by mixing active material, Super P, and PVDF conductive carbon in a weight ratio of 94:3:3. The resulting slurry was cast on the Cu foil then dried at 60 °C for 6 h, followed by drying overnight at 100 °C in a vacuum oven.

Preparation of electrolytes

The 1.0 mol L^{-1} (M) LiPF$_6$-PC is prepared by dissolving 1.0 M LiPF$_6$ in the PC solvent. The multi-salt HE-PC electrolyte was prepared by dissolving 0.2 M LiNO$_3$, 0.2 M LiFSI, 0.2 M LiPF$_6$, 0.2 M LiDFOB, 0.2 M LiTFSI in the PC solvent. LiNO$_3$ was firstly dissolved into PC under 60-80 °C, and then the other salts were added into this mixture. All the electrolytes contain 5% FEC in volume.

Electrochemical measurements

Electrochemical cycling tests of all batteries were based on CR2032 coin cells assembled in an Ar-filled glove box (H_2O < 0.1 ppm, O_2 < 0.1 ppm) with Solupor separator manufactured by DSM Solutech, unless stated otherwise. 70 μL electrolytes were injected into each coin cell for comparison. All coin cells were tested using multi-channel battery testing systems (Land CT2001A or Lanhe G340A). For Li‖Cu cells, 14 mm diameter Li-metal foils and 16 mm Cu foils were used, with the effective area for Li-metal deposition of 1.54 cm^2. Graphite‖Li cell were tested with graphite electrode with areal capacity of

2.5 mAh cm^{-2}, and Li-metal foils were used as counter electrodes. All full cells were cycled under a 0.1C rate for three cycles before cycling at 1C rate (1C=180 mA g^{-1}). The capacity ratio between the anode (the negative electrode) and cathode (the positive electrode), known as N/P ratio, is around 1.1~1.15. Cyclic voltammetry (CV) of Li∥Cu cells with different electrolytes were conducted at a scan rate of 0.8 mV s^{-1} from -0.1 to 2.5 V vs. Li/Li^{+}.

The solvation energy was measured with the method based on ref [29]. By measuring open circuit potential (OCV) in a cell with symmetric electrodes and asymmetric electrolytes, the effects of anions, and solvents on solvation energy across varied electrolytes can be quantitatively characterized. A home-made apparatus consisting of a T-shaped flange assembled between H-cell was used for the measurement. The apparatus is divided to three chambers containing test electrolyte, salt bridge electrolyte, and reference electrolyte, respectively. Solupor separators were used as porous junctions to separate the three chambers. Two pieces of fresh Li-metal foil were used as electrodes in both sides in the H-cell. Salt bridge (3.0 M LiTFSI in DOL/DME 1:1 in volume), reference electrolyte (1.0 M LiFSI in DEC) and experiment electrolyte were put in H-cell, and each chamber was capped to prevent evaporation. Each electrode was connected to a potentiometer (Biologic VMP3) to measure the OCV, and the voltage was recorded after stabilization of a few minutes. The solvation Gibbs free energy ($\Delta G_{solvation}$) was converted from the measured H-cell OCV using equation: $\Delta G = -nFE$.

5

Materials characterizations

Morphologies of electrodes were measured on a cold field scanning electron microscope (SEM, HITACH-S4800, SU8010) with energy-dispersive spectroscopy (EDS) for elemental analysis. Elemental composition on the surface of the electrodes was analyzed by X-ray photoelectron spectroscopy (XPS, PHI 5000 VersaProbe II) using a monochromatic Al Kα X-ray source. For depth profiling of the electrodes, argon sputtering for the XPS depth-profiling was carried out with beam energy of 1 kV and current of 0.5 μA. Peaks were fitted using MultiPak software calibrated with respect to carbon (284.8 eV). The above morphology and composition characterization were performed with cells being disassembled after specific cycles in an Ar-filled glove box

and rinsed with pure DMC solvent three times to remove residual electrolyte, followed by drying in a glove box for several hours at room temperature to remove the residual solvent. Then these electrodes were transferred into the vacuum transfer boxes for measurements to avoid air exposure. Raman spectroscopy was measured by Micro-laser confocal Raman spectrometer (Horiba LabRAM HR800 spectrometer) equipped with an Olympus BX microscope and an argon ion laser (532 nm) at room temperature. All the electrolytes were hermetically sealed in quartz cuvettes in a glovebox before measurement.

Cryo-transmission electron microscopy (cryo-TEM) characterization

Conventional and cryo-TEM experiments were performed on a scanning transmission electron microscope (STEM) (JEM-ARM300F, JEOL Ltd.) operated at 300 kV with a cold field emission gun and double Cs correctors. The microscope was equipped with Gatan OneView and K2 cameras for images recording. During image acquisition, the corresponding electron dose flux (units of number of electrons per square angström per second, e^- $Å^{-2}$ s^{-1}) was recorded. Conventional STEM images were taken with a dose rate of over 1000 e^- $Å^{-2}$ s^{-1} with an exposure time for each image of several seconds. Cryo-TEM images were obtained with an exposure time for each image of around 0.3 s with built-in drift correction function in GMS3 using the OneView and K2 camera. Cryo-TEM images were taken with an electron dose rate of 50 - 500 e^- $Å^{-2}$ s^{-1}. Short-exposure single-frame shots were used to estimate the defocus and make it as close as possible to Scherzer defocus. The EELS spectrum images were carried out with a camera length of 20 mm, and a pixel dwell time of 10 ms. Energy drift during spectrum imaging was corrected by centering the zero-loss peak to 0 eV at each pixel. Elemental maps were computed through a two-window method in a pre-edge window fitted to a power-law background and a post-edge window of 50-200 eV on the core-loss signal. Analysis of the spectra has been performed in Digital Micrograph.

For cryo-TEM preparation of graphite, graphite||Li cells were cycled at 0.2C and then disassembled in glovebox. After rinsing, a small piece of electrode was sealed in an airtight container with pure DMC inside. Then the sealed airtight container was taken out from glovebox and the sample was dispersed for three minutes by ultrasonic method. After that, the dispersed graphite was dropped on the TEM grids in glovebox and loaded into

the cryo-TEM holder for further measurement. The same specialized shutter was also used to prevent air exposure. All cryo-TEM images are taken at around -170 °C to reduce beam damage. For the conventional TEM experiments, the dispersed graphite sample was dropped on a copper grid, dried for three hours in a vacuum and loaded into the double-tilt holder. Then the TEM images were recorded at room temperature.

Liquid nuclear magnetic resonance (NMR) characterization

Liquid NMR spectra were recorded with an Agilent 400 MHz DD2 NMR spectrometer with 5 mm ONE NMR Probe at room temperature, which worked at 155.5 MHz on [7]Li. The chemical shift values are given in ppm. [7]Li chemical shift was referenced to the standard solution: 1 M LiCl in D_2O for [7]Li (0 ppm). All referenced solutions are measured in the enclosed internal capillary in D_2O. During measurement, all electrolytes were sealed into 5-mm Pyrex capillary tubes with PTFE caps, and then was inserted into an NMR tube containing the external standard solutions.

Solid-state NMR characterization

Operando solid-state NMR measurements were conducted on a wide-bore Bruker Ascend 500 system equipped with a NEO console with a magnetic field strength of 11.7T and a [7]Li resonance frequency being 194.37 MHz using a solenoidal Ag-coated Cu coil. Operando static ^{7}Li NMR measurements were performed using an automatic-tuning-and-matching probe (ATM VTX operando WB NMR probe, NMR Service) at room temperature which can allow for an automatic recalibration of the NMR radio-frequency (rf) circuit during an operando electrochemistry experiment. A highly shielded wire with low-pass filters was attached to the probe for electrochemical measurement, which could minimize the interferences between NMR and the electrochemistry circuit. Single-pulse with a π/2 pulse of 3 μs and recycle delay of 8.0 s was applied to acquire the 1D static spectrums. The electrochemical cell was simultaneously controlled by a Maccor battery testing system. A plastic capsule cell made out of polyether ether ketone (PEEK) was used for the operando NMR experiments. The cells were assembled using graphite and Li-metal foils as working and counter electrodes with both a piece of Celgard and a piece of Solupor separator as a separator. The operando capsule cell was aligned in an Ag-coated Cu coil

5

with graphite and Li-metal foil electrodes oriented perpendicular to B_0 and parallel with respect to the B_1 rf-field. During the static ^{7}Li NMR measurements, the cells were cycled at C/5 in the voltage range of 0.001-3 V. The chemical shift of ^{7}Li was referenced to 1 M aqueous solution of LiCl at 0 ppm. The spectra were processed in the Bruker Topspin software, using the automatic phase and baseline correction.

Molecular dynamics

Classical molecular dynamics (MD) simulations were conducted on electrolyte systems with different Li salts using the Groningen Machine for Chemical Simulations (GROMACS)[44-47]. Molecular forces were calculated using the generalized Amber force field (GAFF)[48]. Topology files and bonded and Lennard–Jones parameters were generated using the acpype script[49]. The optimization of the molecular geometries was performed via *gaussian 09* package at a level of B3LYP/6–311G+ (d, p). Partial charges were computed by fitting the molecular ESP at the atomic centers with the Møller–Plesset second-order perturbation method with the correlation-consistent polarized valence cc-pVTZ basis set[50]. Simulation boxes were constructed using the software Packmol[51] with the dimensions of $10\times10\times10$ nm^3. The single salt model contains 1000 PC, 50 FEC, 90 LiPF$_6$, while the multiple salts system contains 1000 PC, 50 FEC, 18 LiPF$_6$, 18 LiNO$_3$, 18 LiDFOB, 18 LiTFSI, 18 LiFSI. A cutoff distance of 1.0 nm was chosen for the Lennard-Jones interactions. The particle mesh Ewald method was used to calculate electrostatic interactions, with a Fourier spacing of 0.16 nm. Periodic boundary conditions were applied in all directions. The energy minimization on both simulation boxes was first performed using the steepest descent method. A time-step of 2 fs was chosen for the MD simulations performed after this point. Subsequently, both systems were equilibrated at room temperature using canonical ensemble simulations. Then, isothermal-isobaric ensemble simulations at 300 K was then performed in order to obtain the correct volumes of both systems. The final 20 ns of the production run were used for the analysis of the radial density functions and the diffusivities of the Li ions, which were computed using the MDAnalysis package[52]. The solvation structures for both electrolytes were analyzed with the final 1 ns using the script based on MDAnalysis package. Visualizations were generated with VESTA.

5

5.10 Supplementary information

Supplementary Notes

Supplementary Note S5.1

XPS analysis of SEI on graphite. The SEI derived from the LiPF$_6$-PC electrolyte contains high concentrations of C and O elements, compare to that in the HE-PC electrolyte, indicating a solvent derived SEI. In contrast, a higher content of F, B, N and S elements can be found in SEI from the HE-PC electrolyte, suggesting the decomposition of the anionic group. The detail spectrum in the C 1s region contains several peaks (Fig. S5.13). The first peak at 284.8 eV can be attribute to C-C/C-H species. The second peak of C-O species comes from the decomposition of solvents in the LiPF$_6$-PC electrolyte, while in the HE-PC electrolyte it comes from both solvent and C-O containing salts such as DFOB$^-$. The third peak at around 290.2 eV (assigned to C=O) are from ROCO$_2$Li formed by the decomposition of PC, where the higher peak intensity of this peaks in the LiPF$_6$-PC electrolyte is in agreement with more solvent decomposition as compared with the HE-PC electrolyte. Matching the C 1s features, signals of O=C (~533 eV) and C-O (~529.5 eV) species are also observed in the O 1s spectra (Fig. S5.14), where the LiPF$_6$-PC electrolyte shows higher content of these species than the HE-PC electrolyte. In addition, extra peaks attributed to B-O, N-O, SO$_x$ in the HE-PC electrolyte are observed due to the decomposition of multiple salts (Figs. S5.15-S5.17). In the F 1s spectra (Fig. S5.18), peaks due to Li-F (~685.5 eV) and P-F (~687.7 eV) species in both electrolytes are detected due to the decomposition of LiPF$_6$, while in the HE-PC electrolyte the C-F species contributed from other anionic group is also observed together with a decreased content of P-F species. Li-F content in both electrolytes accounted for a large proportion of the F-containing species, which is confirmed in Li-F peak (~56.5 eV) in the Li 1s spectra (Fig. S5.19).

5
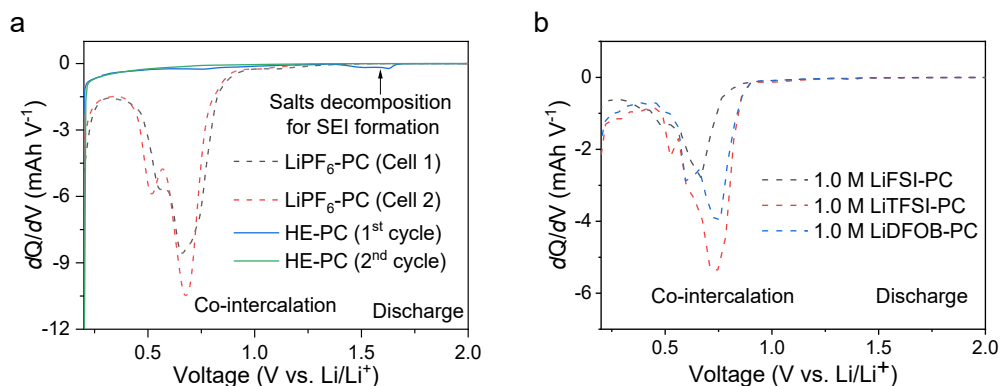
Fig. S5.1. *d*Q/*d*V plots of first lithiation for graphite‖Li cells using different electrolytes at 0.1C. a, *d*Q/*d*V plots for graphite‖Li cells using single-salt LiPF$_6$-PC and HE-PC electrolytes. Two cells using LiPF$_6$-PC electrolyte shows reduction peak at around 0.7 V vs. Li/Li$^+$ ascribed to PC co-intercalation. In contrast, the plot for cells using HE-PC electrolyte exhibit smooth curve without co-intercalation peak, and the additional peak at around 1.5 V vs. Li/Li$^+$ during first discharge, indicating SEI formation that is likely ascribed to salts decomposition. **b**, *d*Q/*d*V plots for the first lithiation of graphite‖Li cells using different single salt electrolytes with PC solvent. All these electrolytes show PC co-intercalation peak.
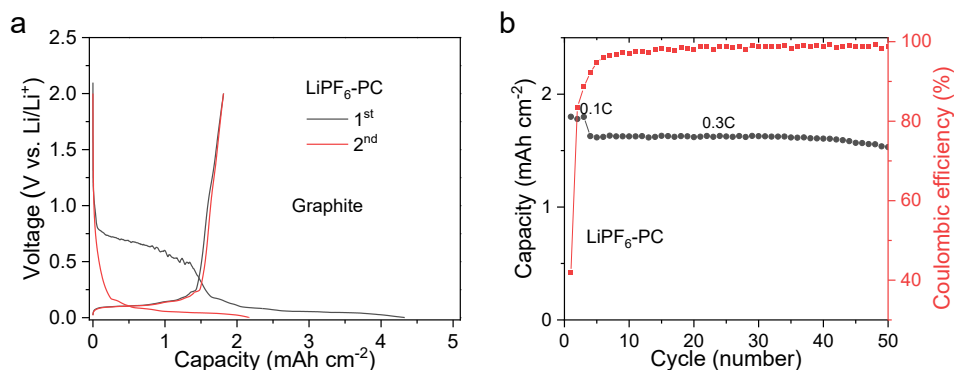
Fig. S5.2. Cycling stability of graphite‖Li cell using LiPF₆-PC electrolyte. Left: first two cycles voltage profiles of graphite electrodes in the voltage range of 0.001-2.0 V vs. Li/Li$^+$. The voltage plateau at around 0.7 V corresponds to the PC co-intercalation, leading to high irreversible capacity and consumption of active Li. Right: charge capacity retention of graphite‖Li cell at 0.1C for the first 3 cycles and 0.3C for the following cycles.
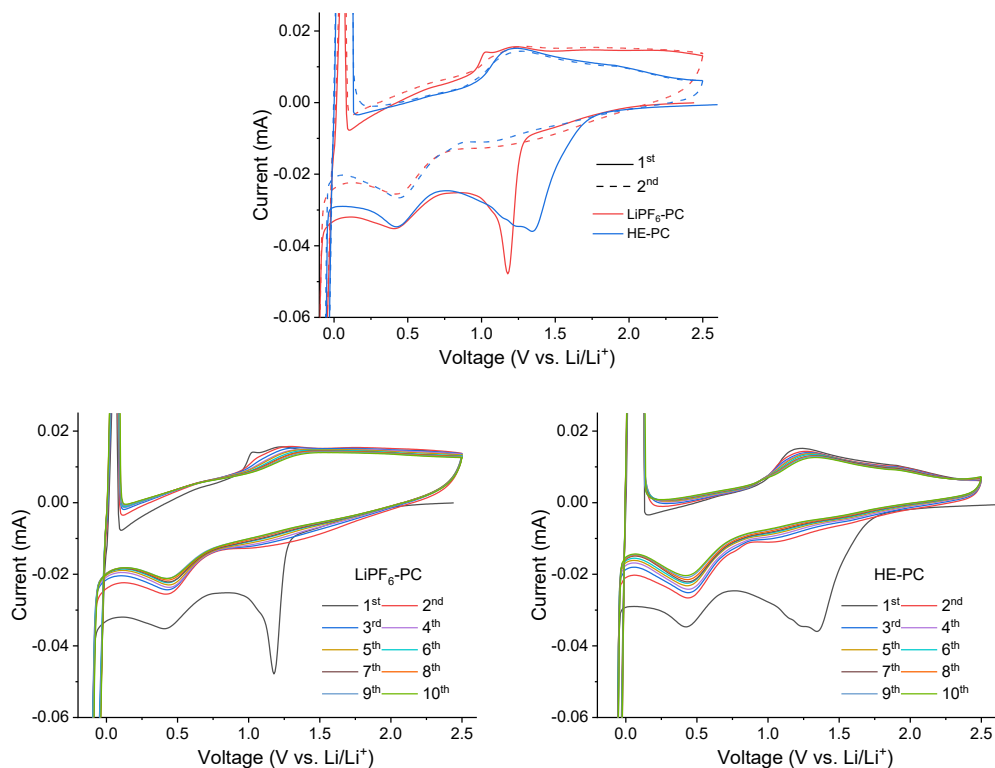
Fig. S5.3. CV curves of Li‖Cu cells in a voltage range of -0.1~2.5 V vs. Li/Li⁺ using single-salt LiPF₆-PC and HE-PC electrolytes. To investigate the decomposition of electrolyte at anode side, Li‖Cu cells were assembled, taking advantage of the more reactive nature of Li metal compared with graphite. The wide negative peak centered around 1.25 V in HE-PC electrolyte indicate the decomposition of multiple Li salts. The sharp peak in LiPF₆-PC electrolyte centered at 1.17 V represent the decomposition of LiPF₆, however, with much less electron transfer as compared to multiple salt decomposition in HE-PC electrolyte. At the same time, more solvent decomposition can be observed in LiPF₆-PC than HE-PC electrolyte indicated by the large integral intensity of the negative peak at around 0.4 V. The intensity of these decomposition peaks decreased in the following cycles, indicating the suppressed reaction due to the formation of SEI. The intensity of electrolyte decomposition peaks decreased in the following cycles, indicating the suppressed reaction due to the formation of SEI.

5
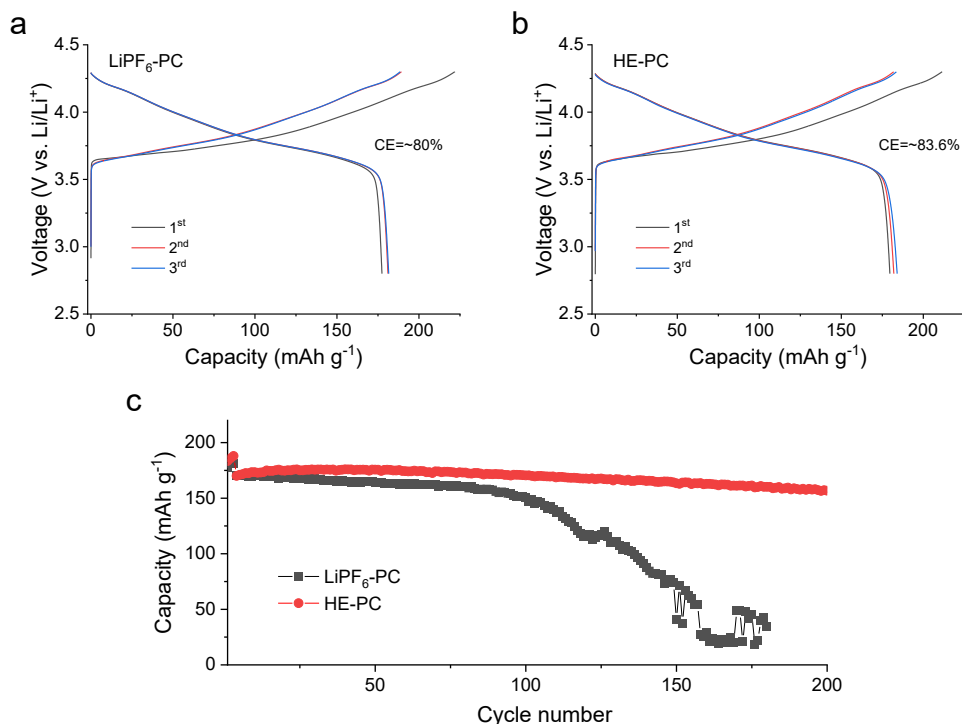
Fig. S5.4. Cycling performance of NCM811||Li cells using different electrolytes. a, **b**, Charge/discharge curves of the first three cycles at 0.1C at the voltage range of 2.8-4.3 V. **c**, Cycling stability of NCM811||Li cells at 0.1C for the first three cycles and 1.0 C for the following.
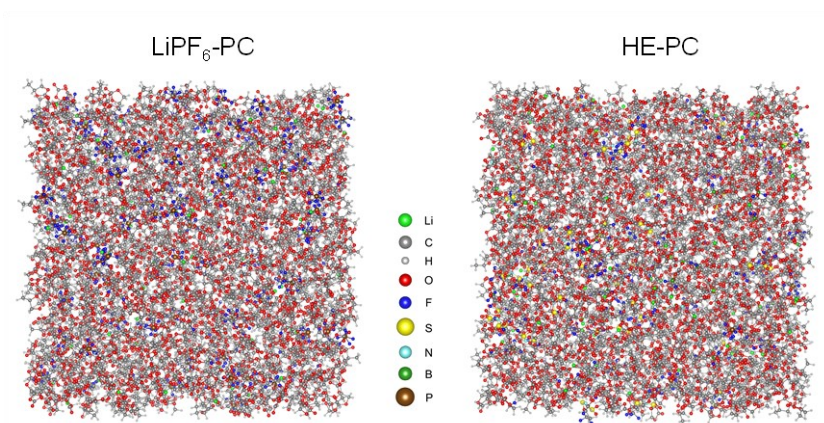
Fig. S5.5. Structure packing of electrolytes for MD simulations. See the method for details.
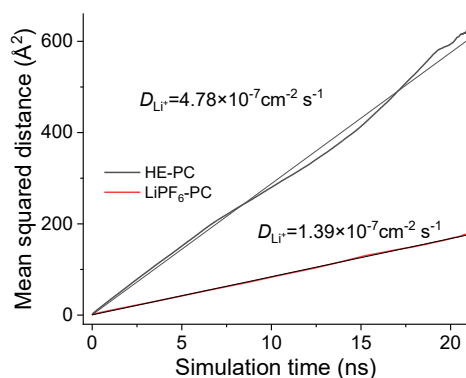
Fig. S5.6. The Li⁺ self-diffusion coefficient (D_{Li}) from the MD simulated mean squared displacement. The red is for the LiPF₆-PC electrolyte and the black is for the HE-PC electrolyte.
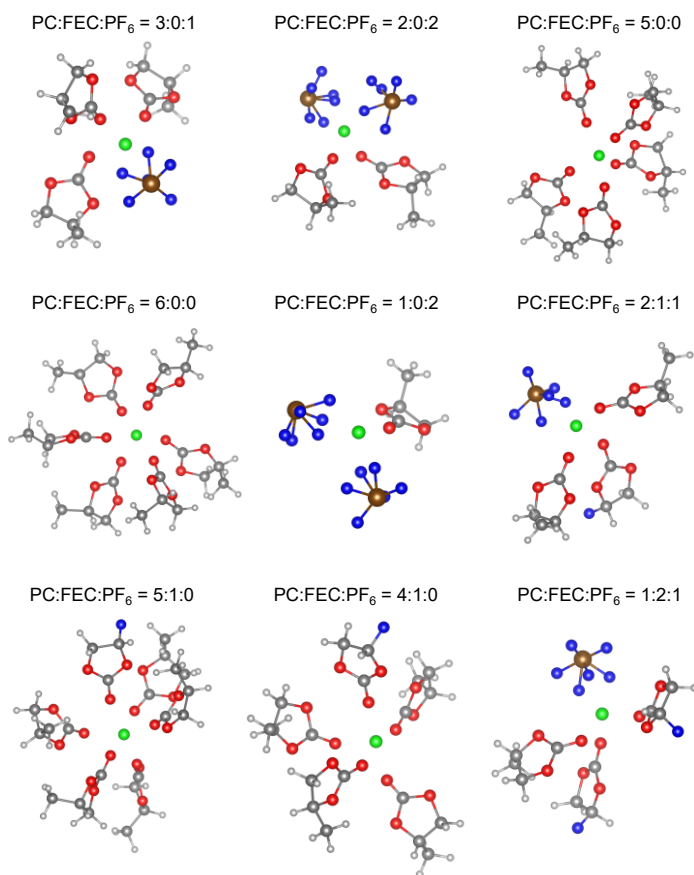
Fig. S5.7. The representative solvation structures in the LiPF₆-PC electrolyte. The detailed structures are shown in Table S5.1.
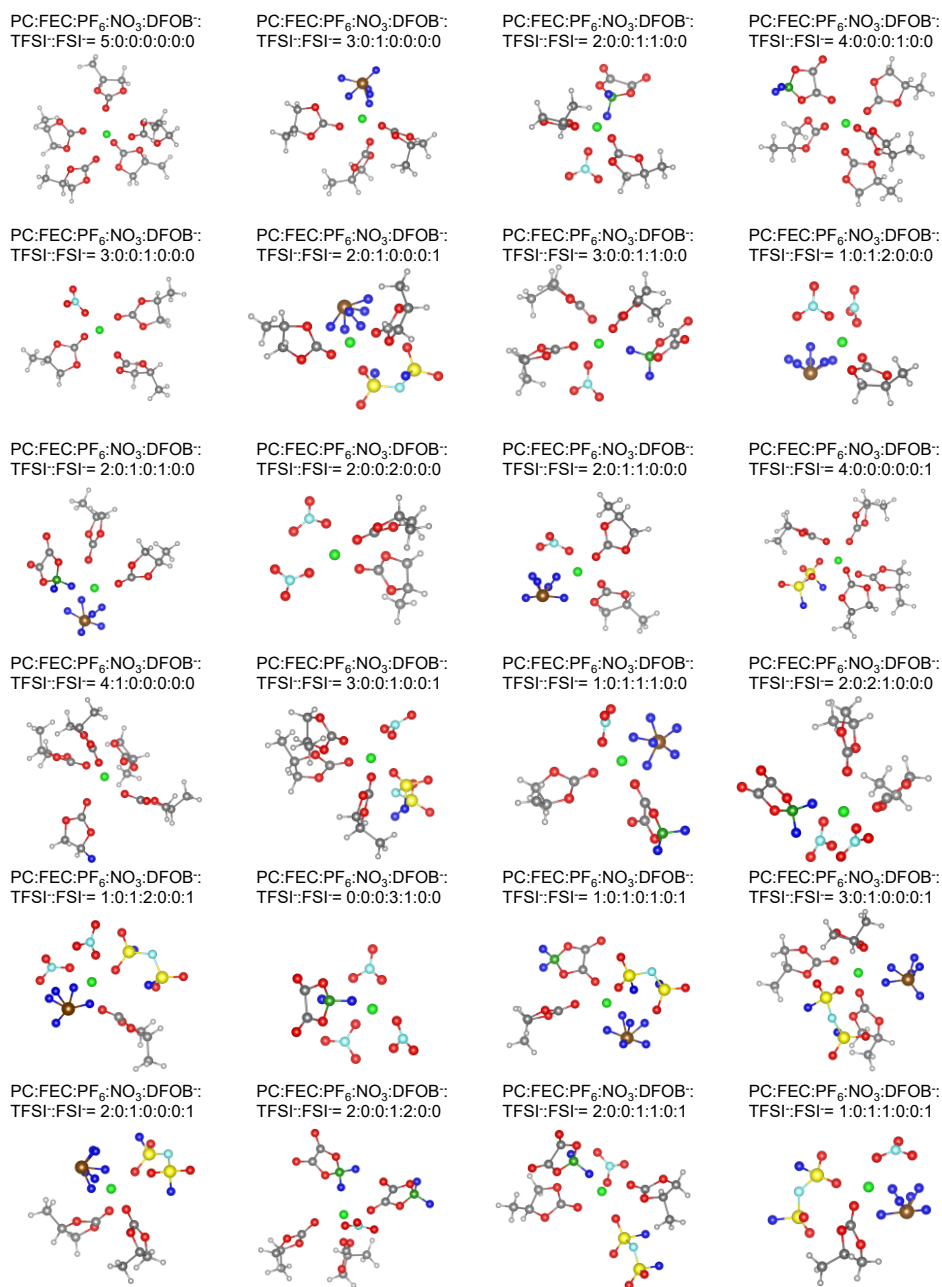
Fig. S5.8. The representative solvation structures in the HE-PC electrolyte. The detailed structures are shown in Table S5.2.
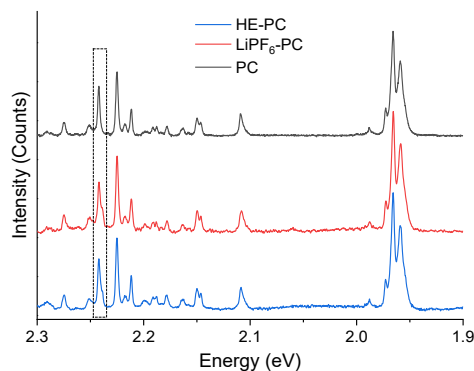
Fig. S5.9. Solvation structure analysis from Raman measurement. a, Full Raman spectra of neat PC solvent and different electrolytes.
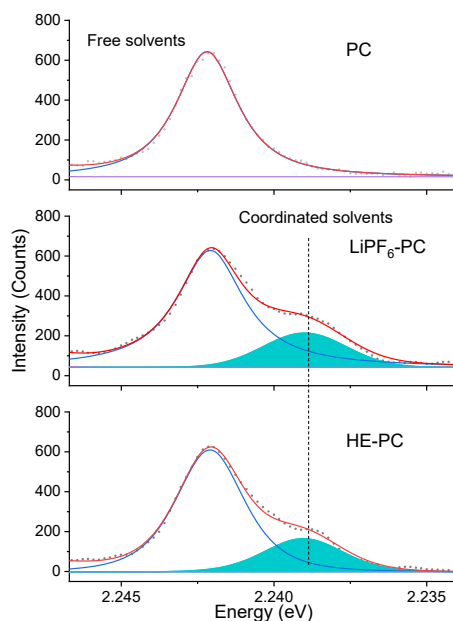
Fig. S5.10. The deconvoluted peaks of the Raman spectra. The LiPF$_6$-PC electrolyte shows larger intensity of the green peak, indicating more coordinated solvent compared to HE-PC electrolyte. The Raman spectra are collected for both electrolytes and the pure PC solvent as shown in Fig. S5.9. The peaks at 2.242 eV and 2.238 eV can be attributed to free PC molecules and solvating PC molecules, respectively[14]. With the increase of disorder, the relative contribution of free PC molecules increases and that of solvated PC molecules decreases, indicating decreased interaction between the solvent and the Li$^+$ in the HE-PC electrolyte.
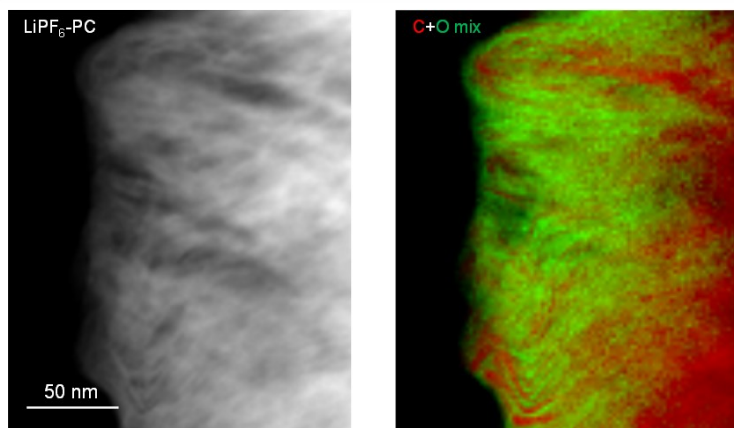
Fig. S5.11. Cryo-STEM EELS of the graphite after PC co-intercalation. The results show that carbon and oxygen can match in the lattice gap, showing solvent distribution.
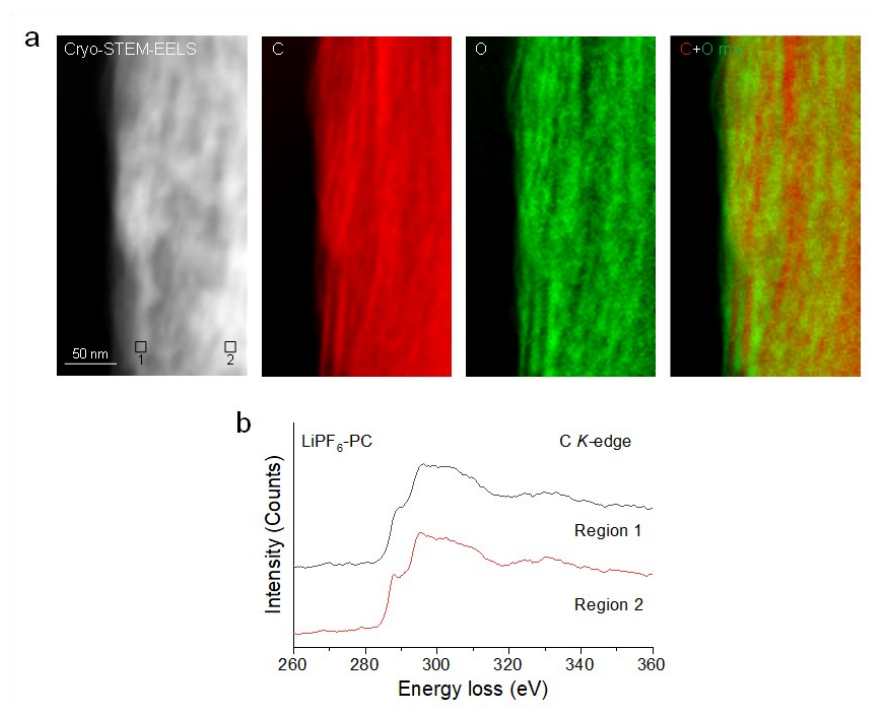
Fig. S5.12. Cryo-STEM EELS of the graphite after PC co-intercalation. a, Cryo-STEM-EELS maps of the graphite in LiPF$_6$-PC electrolyte. **b**, C K-edge fine structure of Region 1 and Region 2 indicated in **a.**
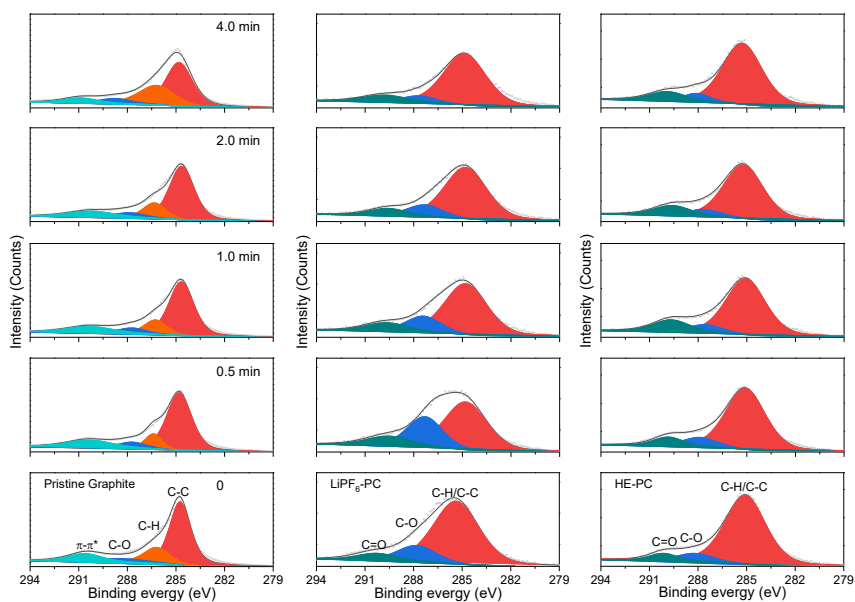
Fig. S5.13. C 1*s* spectra of pristine graphite and SEI on graphite electrodes in electrolytes at different depths.
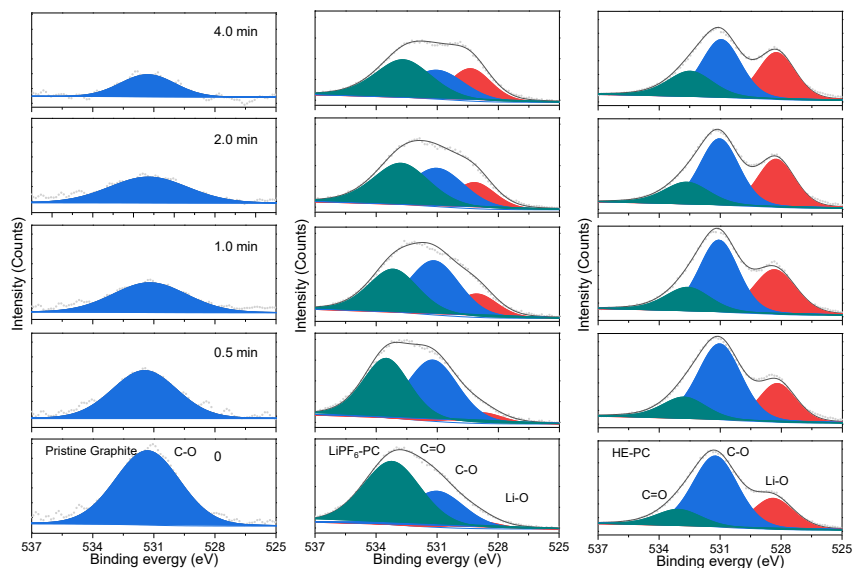
Fig. S5.14. O 1*s* spectra of pristine graphite and SEI on graphite electrodes in electrolytes at different depths.
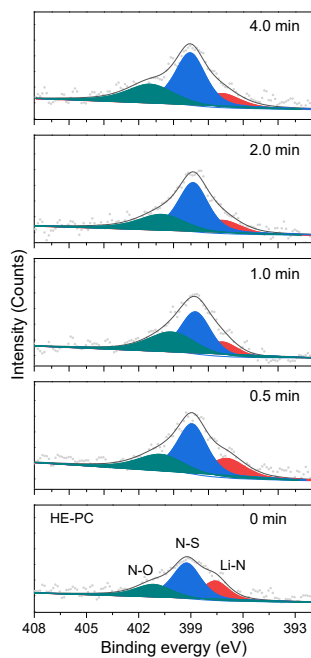
Fig. S5.15. N 1*s* spectra of SEI on graphite electrodes in HE-PC electrolyte at different depths.
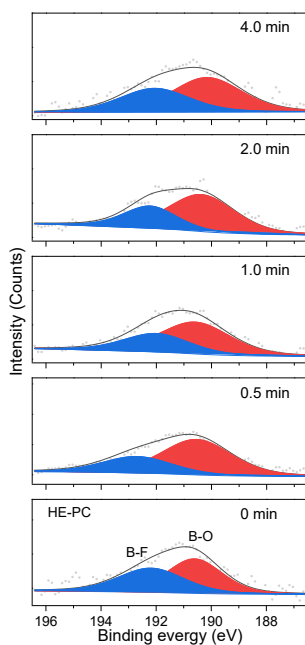
Fig. S5.16. B 1*s* spectra of SEI on graphite electrodes in HE-PC electrolyte at different depths.
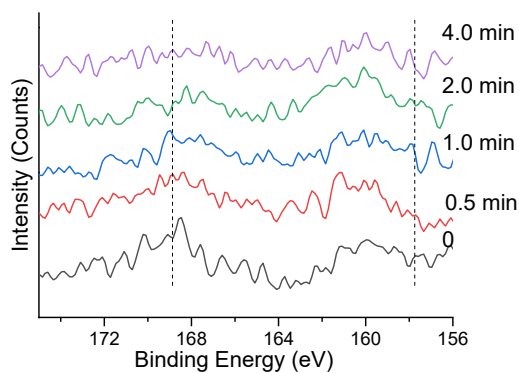
Fig. S5.17. S 2*p* spectra of SEI on graphite electrodes in HE-PC electrolyte at different depths.
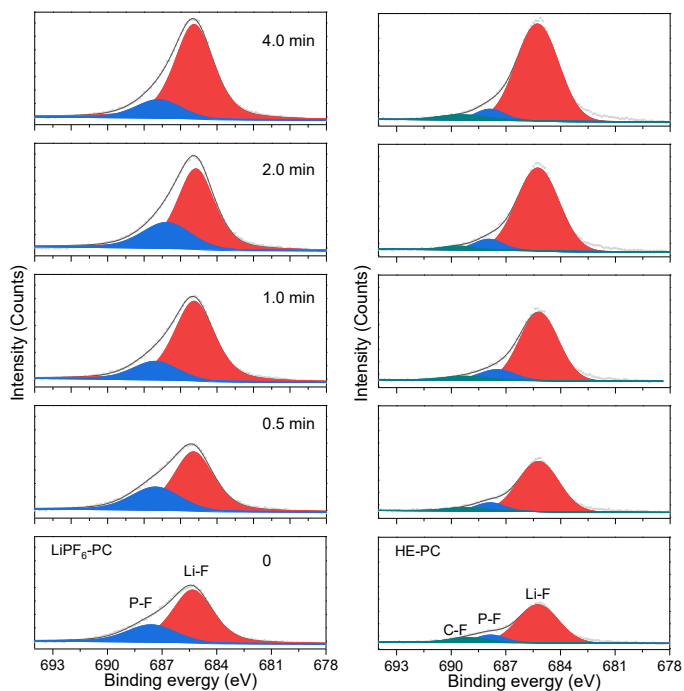
Fig. S5.18. F 1*s* spectra of SEI on graphite electrodes in electrolytes at different depths.
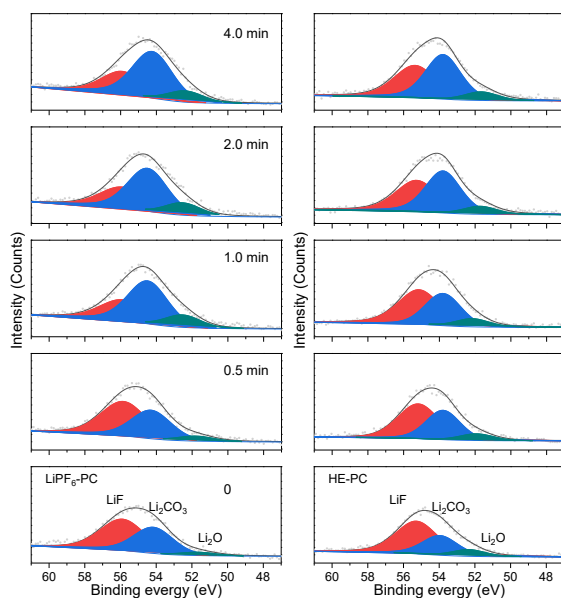
Fig. S5.19. Li 1*s* spectra of SEI on graphite electrodes in electrolytes at different depths.
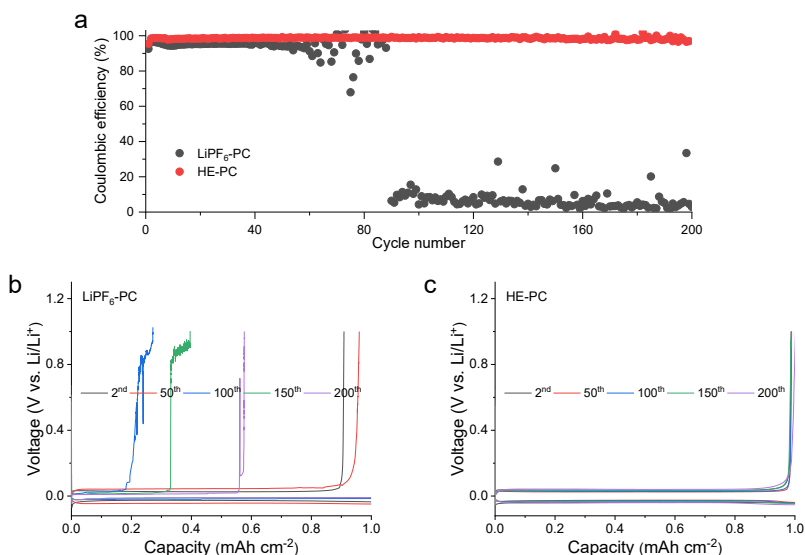
Fig. S5.20. Cycling performance of Li‖Cu cells using different electrolytes. a, CEs of Li‖Cu cells using different electrolytes. Galvanostatic Li plating/stripping profiles of Li‖Cu cells cycled in **b**, LiPF$_6$-PC and **c**, HE-PC electrolytes for selected cycles. at 0.5 mA cm^{-2} and 1 mAh cm^{-2}. Li was electrodeposited at 0.5 mA cm^{-2} to a capacity of 1 mAh cm^{-2}.
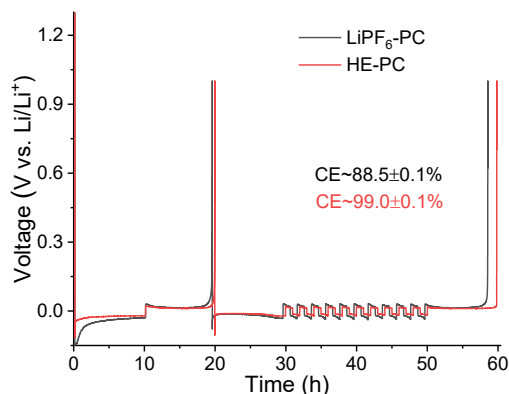
Fig. S5.21. An improved measurement[37,53] of Li metal CE in Li‖Cu cells using different electrolytes. The cell using the HE-PC electrolyte exhibits higher CE around 99.0% and lower overpotential both during initial nucleation and following cycles.
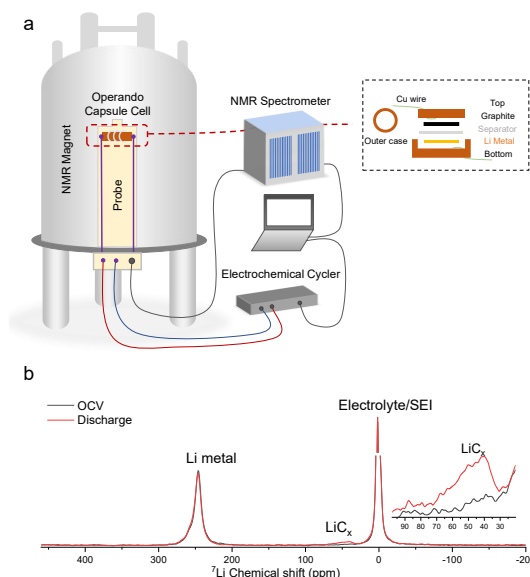
Fig. S5.22. Operando NMR to detect Li intercalation and co-intercalation into graphite. a, The schematic of the operando NMR setup[30]. The dashed box shows the operando capsule cell inserted in the NMR probe coil. The cylindrical casing to assemble electrochemical cells comprising of top, bottom and outer case. Graphite electrode and Li-metal foil counter electrode are connected to copper wires with a separator in between soaked with electrolyte. Then the outer capsule case is used for sealing and producing pressure. The cell is connected to electrochemical cycler for galvanostatic charging/discharging in the NMR magnet. **b**, Representative ^{7}Li NMR spectrum of the operando graphite‖Li cell during the formation of LiC_x showing the resonant frequencies of the Li metal, electrolyte and SEI and LiC_x
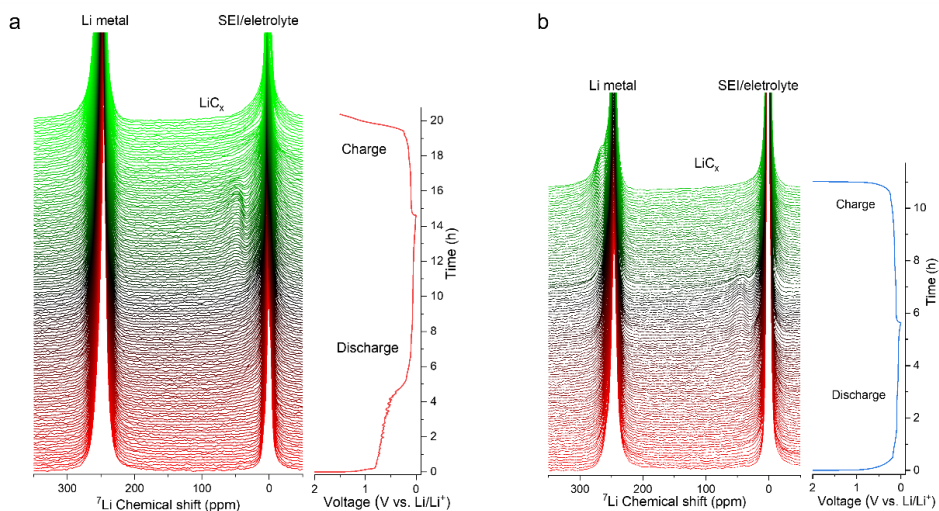
Fig. S5.23. Stacking plot of full ^{7}Li NMR spectra of graphite||Li cells. a is for LiPF$_6$-PC electrolyte and **b** is for HE-PC electrolyte**.**
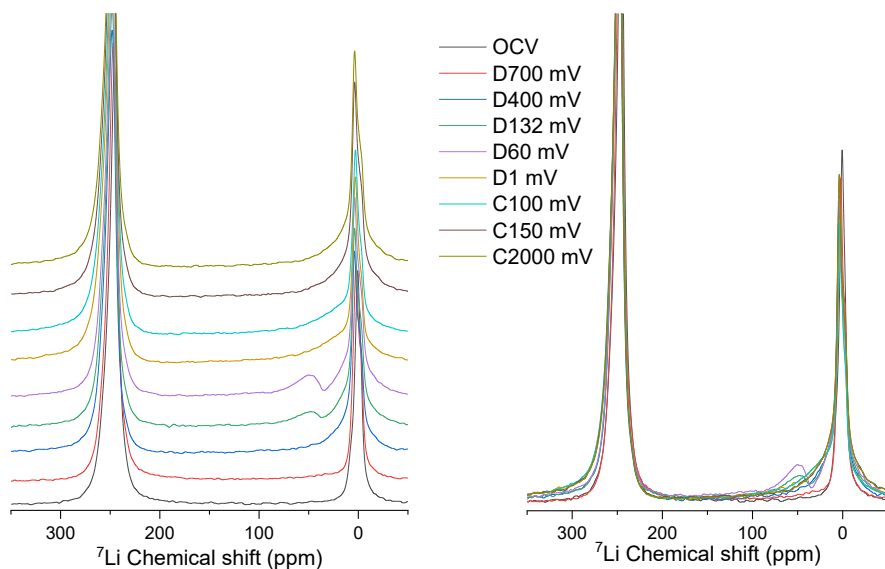
Fig. S5.24. Representative spectra of graphite||Li cell using LiPF$_6$-PC electrolyte extracted from the operando ^{7}Li NMR spectra as indicated by the different voltage.
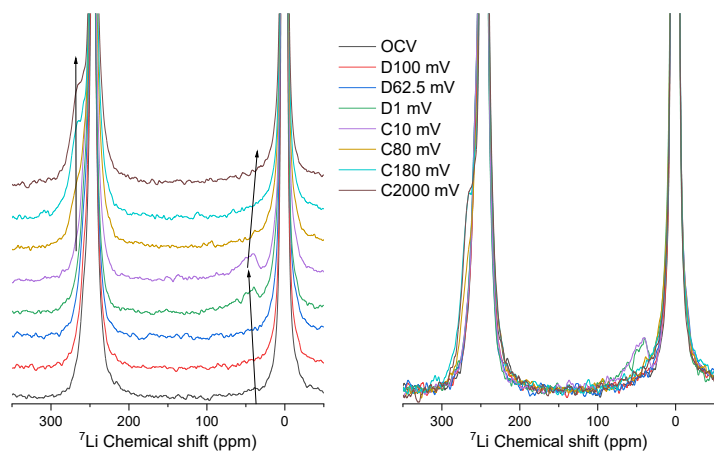
Fig. S5.25. Representative spectra of graphite||Li cell using HE-PC electrolyte extracted from the operando ^{7}Li NMR spectra as indicated by the different voltage.
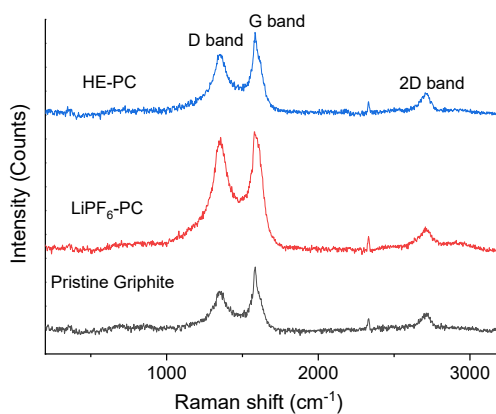
Fig. S5.26. Raman spectra of graphite anode before and after cycling in electrolytes.
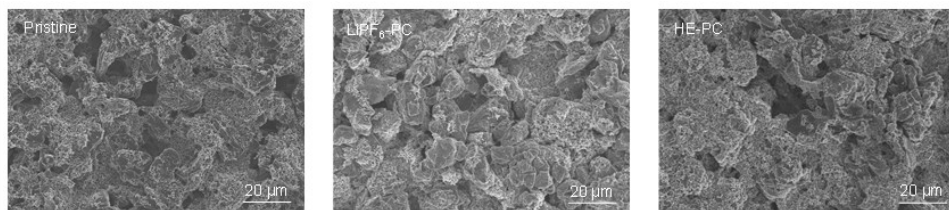
Fig. S5.27. Top-view SEM images at low magnification of graphite anode before and after cycling in different electrolytes.
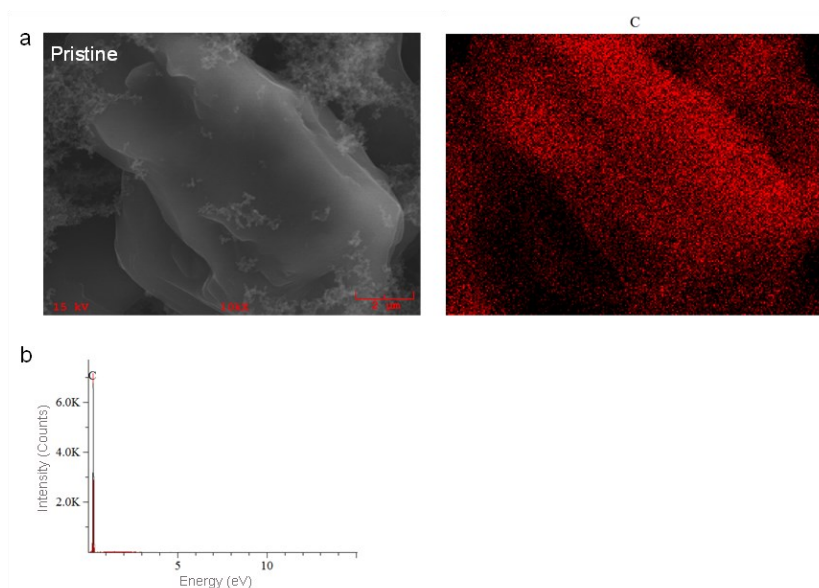
Fig. S5.28. SEM-EDS characterizations of the pristine graphite electrode. a, SEM-EDS mapping for the elemental distributions on pristine graphite electrode. **b**, SEM-EDS spectra in the regions shown in **a**.

5
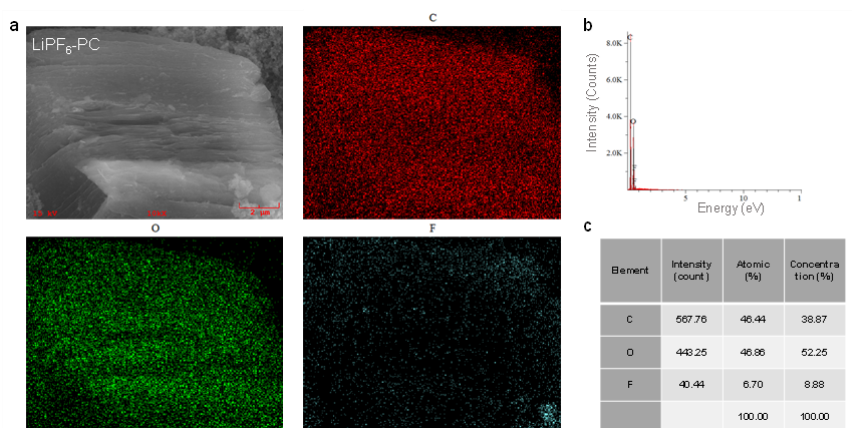
Fig. S5.29. SEM-EDS characterizations of the graphite cycled in LiPF$_6$-PC electrolyte. a, SEM-EDS mapping for the elemental distributions on graphite electrode after one cycle. **b**, SEM-EDS spectra in the regions shown in **a**. **c**, Elemental ratio from SEI based on the SEM-EDS.

Element	Intensity (count)	Atomic (%)	Concentration (%)
C	567.76	46.44	38.87
O	443.25	46.86	52.25
F	40.44	6.70	8.88
		100.00	100.00

Element	Intensity (count)	Atomic (%)	Concentration (%)
B	2.99	3.33	2.82
C	304.93	86.20	81.12
O	9.88	5.85	7.33
F	9.01	2.73	4.06
P	13.06	0.93	2.25
S	13.37	0.96	2.42
		100.00	100.00
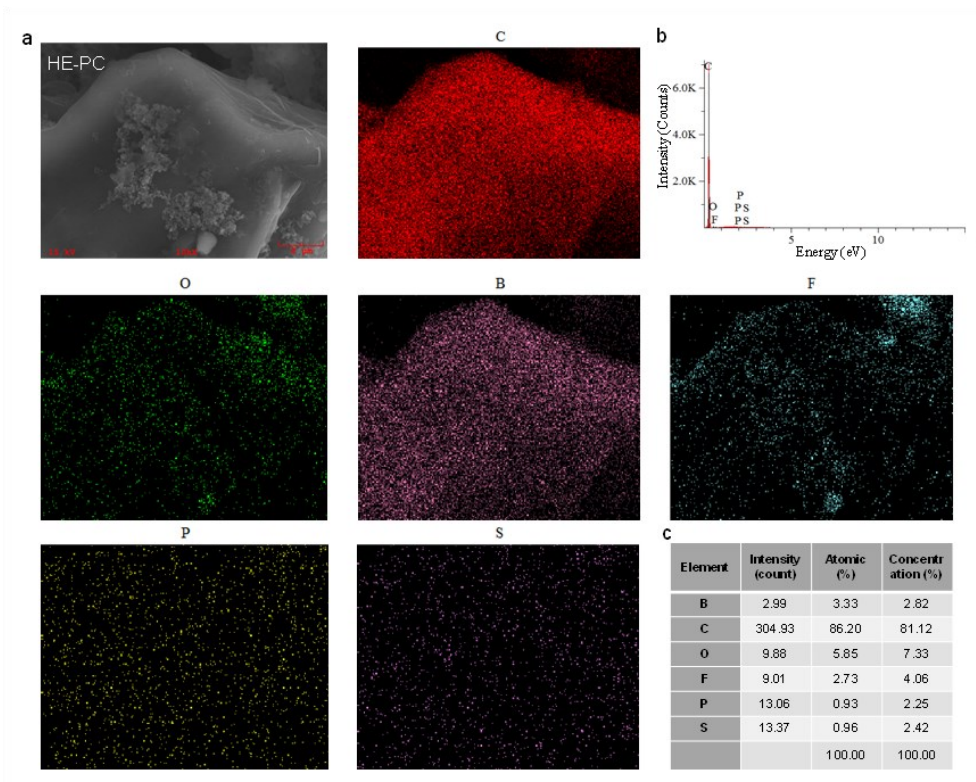
Fig. S5.30. SEM-EDS characterizations of the graphite cycled in HE-PC electrolyte. a, SEM-EDS mapping for the elemental distributions on graphite electrode after one cycle. **b**, SEM-EDS spectra in the regions shown in **a**. **c**, Elemental ratio from SEI based on the SEM-EDS.

5

Supplementary Tables

Table S5.1. The types of solvation structures and their corresponding proportion in the LiPF$_6$-PC electrolyte.

PC	FEC	PF$_6^-$	Percentage (%)
3	0	1	58.48
2	0	2	15.92
5	0	0	6.77
6	0	0	6.22
1	0	2	4.01
2	1	1	2.88
5	1	0	1.58
4	1	0	1.42
1	2	1	1.11
4	0	0	0.57
2	0	1	0.42
4	0	1	0.38
3	1	1	0.07
3	1	0	0.07
3	0	2	0.04
5	0	1	0.03
4	2	0	0.01
1	1	2	0.01
0	0	2	0.01

Table S5.2. The types of solvation structures and their corresponding proportion in the HE-PC electrolyte.

PC	FEC	PF$_6^-$	NO$_3^-$	DFOB$^-$	TFSI$^-$	FSI$^-$	Percentage (%)
5	0	0	0	0	0	0	9.01
3	0	1	0	0	0	0	8.17
2	0	0	1	1	0	0	5.24
4	0	0	0	1	0	0	4.62
3	0	0	1	0	0	0	4.24
4	0	0	1	0	0	0	4.16
2	0	1	0	0	0	1	3.94
6	0	0	0	0	0	0	3.46
3	0	0	1	1	0	0	3.39
1	0	1	2	0	0	0	3.27
2	0	1	0	1	0	0	3.24
2	0	0	2	0	0	0	3.13
2	0	1	1	0	0	0	3.03
4	0	0	0	0	0	1	2.96
4	1	0	0	0	0	0	1.79
3	0	0	1	0	0	1	1.67
2	0	0	2	1	0	0	1.64
3	0	0	0	0	0	1	1.62
5	1	0	0	0	0	0	1.58
3	1	0	0	0	0	1	1.52
4	0	1	0	0	0	0	1.51
3	0	0	0	0	0	2	1.41
5	0	0	0	1	0	0	1.29
1	0	1	1	1	0	0	1.11
3	0	1	0	0	0	1	1.10
1	0	1	0	1	0	1	1.09
2	0	2	0	0	0	0	1.09
3	0	0	0	1	1	0	1.08
1	0	1	1	0	0	1	1.06

0	0	0	3	1	0	0	1.01
3	0	0	2	0	0	0	0.97
4	0	0	0	0	0	0	0.97
3	0	0	0	1	0	0	0.92
2	0	0	1	0	0	1	0.92
2	0	0	0	0	0	2	0.91
4	0	0	0	0	1	0	0.83
2	1	0	0	1	0	1	0.82
2	0	0	1	2	0	0	0.76
3	0	0	0	2	0	0	0.73
1	0	1	0	0	0	1	0.63
2	0	0	1	1	0	1	0.57
3	0	0	1	0	1	0	0.51
2	0	0	1	0	1	0	0.46
1	0	0	1	1	0	1	0.40
3	1	0	1	0	0	0	0.37
2	0	0	0	2	0	0	0.36
1	0	0	1	2	0	0	0.34
2	1	0	2	0	0	0	0.32
2	2	0	0	0	0	1	0.30
5	0	0	0	0	0	1	0.29
4	0	0	0	0	0	2	0.29
4	2	0	0	0	0	0	0.27
4	0	0	0	1	0	1	0.26
1	0	0	2	1	0	0	0.26
2	1	0	0	0	0	1	0.23
1	1	0	0	1	0	1	0.23
3	0	1	1	0	0	0	0.22
3	0	0	0	1	0	1	0.20
4	1	0	0	0	0	1	0.19
3	2	0	0	0	0	0	0.18
2	0	1	0	0	0	0	0.11
5	0	0	0	0	1	0	0.11
3	1	0	0	0	0	0	0.10
1	0	0	3	1	0	0	0.10
2	0	0	1	1	1	0	0.09
4	0	0	1	1	0	0	0.09
1	0	1	0	1	0	0	0.08
5	0	0	1	0	0	0	0.07
2	0	0	2	0	0	1	0.07
2	0	1	2	0	0	0	0.07
3	0	0	0	0	1	0	0.07
2	0	0	0	1	1	0	0.06
3	0	0	2	1	0	0	0.06
1	1	0	2	0	0	0	0.06
3	1	0	0	1	0	1	0.04
4	0	0	1	0	0	1	0.04
2	1	0	2	1	0	0	0.04
2	1	0	1	1	0	0	0.04
3	1	0	0	0	1	0	0.04
4	1	0	0	0	1	0	0.04
4	0	0	0	1	1	0	0.03
4	0	0	2	0	0	0	0.03
1	0	2	0	0	0	0	0.03
2	0	0	0	0	0	1	0.03
2	0	0	1	0	0	0	0.03
3	0	0	2	0	0	1	0.02
3	1	1	0	0	0	0	0.02
4	1	1	0	0	0	0	0.02
1	1	0	0	0	0	1	0.02
1	0	1	1	0	0	0	0.02
5	0	1	0	0	0	0	0.02
1	0	1	2	0	0	1	0.02

5

1	1	0	0	2	0	0	0.01
1	2	0	0	0	0	1	0.01
2	1	0	0	2	0	0	0.01
2	1	0	1	0	0	0	0.01
2	0	1	1	0	0	1	0.01
3	1	0	0	1	0	0	0.01
3	2	0	0	0	0	1	0.01
2	0	0	0	1	0	0	0.01
0	0	1	1	0	0	1	0.01
4	0	0	1	0	1	0	0.01
2	2	0	0	0	0	0	0.01
3	0	1	0	1	0	0	0.01
7	0	0	0	0	0	0	0.01
1	0	0	1	1	0	0	0.01
1	0	0	0	0	0	2	0.01

5

References

1 J. M. Tarascon & M. Armand. Issues and challenges facing rechargeable lithium batteries. *Nature* **414**, 359-367, (2001).

2 D. Larcher & J. M. Tarascon. Towards greener and more sustainable batteries for electrical energy storage. *Nature Chemistry* **7**, 19-29, (2015).

3 J. W. Choi & D. Aurbach. Promise and reality of post-lithium-ion batteries with high energy densities. *Nature Reviews Materials* **1**, 16013, (2016).

4 W. Li, B. Song & A. Manthiram. High-voltage positive electrode materials for lithium-ion batteries. *Chemical Society Reviews* **46**, 3006-3059, (2017).

5 N. Nitta, F. Wu, J. T. Lee & G. Yushin. Li-ion battery materials: present and future. *Materials Today* **18**, 252-264, (2015).

6 M. Li, C. Wang, Z. Chen, K. Xu & J. Lu. New Concepts in Electrolytes. *Chemical Reviews* **120**, 6783-6819, (2020).

7 L. Xing, X. Zheng, M. Schroeder, J. Alvarado, A. von Wald Cresce, K. Xu, Q. Li & W. Li. Deciphering the Ethylene Carbonate–Propylene Carbonate Mystery in Li-Ion Batteries. *Accounts of Chemical Research* **51**, 282-289, (2018).

8 S. Hou, X. Ji, K. Gaskell, P. F. Wang, L. Wang, J. Xu, R. Sun, O. Borodin & C. Wang. Solvation sheath reorganization enables divalent metal batteries with fast interfacial charge transfer kinetics. *Science* **374**, 172-178, (2021).

9 M. Fujimoto, Y. Shoji, Y. Kida, R. Ohshita, T. Nohma & K. Nishio. Influence of solvent species on the charge–discharge characteristics of a natural graphite electrode. *Journal of Power Sources* **72**, 226-230, (1998).

10 K. Xu. Whether EC and PC Differ in Interphasial Chemistry on Graphitic Anode and How. *Journal of The Electrochemical Society* **156**, A751, (2009).

11 K. Xu. Electrolytes and Interphases in Li-Ion Batteries and Beyond. *Chemical Reviews* **114**, 11503-11618, (2014).

12 A. von Wald Cresce, O. Borodin & K. Xu. Correlating Li+ Solvation Sheath Structure with Interphasial Chemistry on Graphite. *The Journal of Physical Chemistry C* **116**, 26111-26117, (2012).

13 M. R. Wagner, J. H. Albering, K. C. Moeller, J. O. Besenhard & M. Winter. XRD evidence for the electrochemical formation of $Li^+(PC)_yC_n-$ in PC-based electrolytes. *Electrochemistry Communications* **7**, 947-952, (2005).

5

14 S.-K. Jeong, M. Inaba, Y. Iriyama, T. Abe & Z. Ogumi. Electrochemical Intercalation of Lithium Ion within Graphite from Propylene Carbonate Solutions. *Electrochemical and Solid-State Letters* **6**, A13, (2003).

15 G. Åvall, J. Wallenstein, G. Cheng, K. L. Gering, P. Johansson & D. P. Abraham. Highly Concentrated Electrolytes: Electrochemical and Physicochemical Characteristics of LiPF6 in Propylene Carbonate Solutions. *Journal of The Electrochemical Society* **168**, 050521, (2021).

16 S. S. Zhang, K. Xu & T. R. Jow. Enhanced performance of Li-ion cell with LiBF4-PC based electrolyte by addition of small amount of LiBOB. *Journal of Power Sources* **156**, 629-633, (2006).

17 B. Wang, Q. T. Qu, Q. Xia, Y. P. Wu, X. Li, C. L. Gan & T. van Ree. Effects of 3,5-bis(trifluoromethyl)benzeneboronic acid as an additive on electrochemical performance of propylene carbonate-based electrolytes for lithium ion batteries. *Electrochimica Acta* **54**, 816-820, (2008).

18 J. Demeaux, Y. Dong & B. L. Lucht. Reversible Graphite Anode Cycling with PC-Based Electrolytes Enabled by Added Sulfur Trioxide Complexes. *Journal of The Electrochemical Society* **164**, A1352, (2017).

19 M. Khasanov, E. Pazhetnov & W. Shin. Dicarboxylate-Substituted Ethylene Carbonate as an SEI-Forming Additive for Lithium-Ion Batteries. *Journal of the Electrochemical Society* **162**, A1892-A1898, (2015).

20 Y. Wang, S. Nakamura, K. Tasaki & P. B. Balbuena. Theoretical Studies To Understand Surface Chemistry on Carbon Anodes for Lithium-Ion Batteries: How Does Vinylene Carbonate Play Its Role as an Electrolyte Additive? *Journal of the American Chemical Society* **124**, 4408-4421, (2002).

21 S. S. Zhang. A review on electrolyte additives for lithium-ion batteries. *Journal of Power Sources* **162**, 1379-1394, (2006).

22 L. J. Fu, J. Gao, T. Zhang, Q. Cao, L. C. Yang, Y. P. Wu & R. Holze. Effect of Cu_2O coating on graphite as anode material of lithium ion battery in PC-based electrolyte. *Journal of Power Sources* **171**, 904-907, (2007).

23 H.-Y. Lee, J.-K. Baek, S.-W. Jang, S.-M. Lee, S.-T. Hong, K.-Y. Lee & M.-H. Kim. Characteristics of carbon-coated graphite prepared from mixture of graphite and polyvinylchloride as anode materials for lithium ion batteries. *Journal of Power Sources* **101**, 206-212, (2001).

5

24 K. Xu, A. von Cresce & U. Lee. Differentiating Contributions to "Ion Transfer" Barrier from Interphasial Resistance and Li+ Desolvation at Electrolyte/Graphite Interface. *Langmuir* **26**, 11538-11543, (2010).

25 H. Zhao, S.-J. Park, F. Shi, Y. Fu, V. Battaglia, P. N. Ross & G. Liu. Propylene Carbonate (PC)-Based Electrolytes with High Coulombic Efficiency for Lithium-Ion Batteries. *Journal of The Electrochemical Society* **161**, A194-A200, (2013).

26 A. von Cresce & K. Xu. Preferential Solvation of Li+ Directs Formation of Interphase on Graphitic Anode. *Electrochemical and Solid-State Letters* **14**, A154, (2011).

27 Y. Yamada, K. Furukawa, K. Sodeyama, K. Kikuchi, M. Yaegashi, Y. Tateyama & A. Yamada. Unusual Stability of Acetonitrile-Based Superconcentrated Electrolytes for Fast-Charging Lithium-Ion Batteries. *Journal of the American Chemical Society* **136**, 5039-5046, (2014).

28 B. Qiao, G. M. Leverick, W. Zhao, A. H. Flood, J. A. Johnson & Y. Shao-Horn. Supramolecular Regulation of Anions Enhances Conductivity and Transference Number of Lithium in Liquid Electrolytes. *Journal of the American Chemical Society* **140**, 10932-10936, (2018).

29 S. C. Kim, X. Kong, R. A. Vilá, W. Huang, Y. Chen, D. T. Boyle, Z. Yu, H. Wang, Z. Bao, J. Qin & Y. Cui. Potentiometric Measurement to Probe Solvation Energy and Its Correlation to Lithium Battery Cyclability. *Journal of the American Chemical Society* **143**, 10301-10308, (2021).

30 Q. Wang, C. Zhao, S. Wang, J. Wang, M. Liu, S. Ganapathy, X. Bai, B. Li & M. Wagemaker. Clarifying the Relationship between the Lithium Deposition Coverage and Microstructure in Lithium Metal Batteries. *Journal of the American Chemical Society* **144**, 21961-21971, (2022).

31 J. W. Yeh, S. K. Chen, S. J. Lin, J. Y. Gan, T. S. Chin, T. T. Shun, C. H. Tsau & S. Y. Chang. Nanostructured High-Entropy Alloys with Multiple Principal Elements: Novel Alloy Design Concepts and Outcomes. *Advanced Engineering Materials* **6**, 299-303, (2004).

32 B. Cantor, I. T. H. Chang, P. Knight & A. J. B. Vincent. Microstructural development in equiatomic multicomponent alloys. *Materials Science and Engineering: A* **375-377**, 213-218, (2004).

33 E. P. George, D. Raabe & R. O. Ritchie. High-entropy alloys. *Nature Reviews Materials* **4**, 515-534, (2019).

34 B. E. MacDonald, Z. Fu, B. Zheng, W. Chen, Y. Lin, F. Chen, L. Zhang, J. Ivanisenko, Y. Zhou, H. Hahn & E. J. Lavernia. Recent Progress in High Entropy Alloy Research. *JOM* **69**, 2024-2031, (2017).

5

35 L. R. Owen & N. G. Jones. Lattice distortions in high-entropy alloys. *Journal of Materials Research* **33**, 2954-2969, (2018).

36 D. B. Miracle & O. N. Senkov. A critical review of high entropy alloys and related concepts. *Acta Materialia* **122**, 448-511, (2017).

37 D. Aurbach, Y. Gofer & J. Langzam. The Correlation Between Surface Chemistry, Surface Morphology, and Cycling Efficiency of Lithium Electrodes in a Few Polar Aprotic Systems. *Journal of The Electrochemical Society* **136**, 3198-3205, (1989).

38 C. P. Grey & N. Dupré. NMR Studies of Cathode Materials for Lithium-Ion Rechargeable Batteries. *Chemical Reviews* **104**, 4493-4512, (2004).

39 N. M. Trease, T. K. J. Ko ster & C. P. Grey. In Situ NMR Studies of Lithium Ion Batteries. *Interface magazine* **20**, 69-73, (2011).

40 F. Chevallier, M. Letellier, M. Morcrette, J. M. Tarascon, E. Frackowiak, J. N. Rouzaud & F. Béguin. In Situ 7Li-Nuclear Magnetic Resonance Observation of Reversible Lithium Insertion into Disordered Carbons. *Electrochemical and Solid-State Letters* **6**, A225, (2003).

41 M. Letellier, F. Chevallier, F. Béguin, E. Frackowiak & J.-N. Rouzaud. The first in situ 7Li NMR study of the reversible lithium insertion mechanism in disorganised carbons. *Journal of Physics and Chemistry of Solids* **65**, 245-251, (2004).

42 M. Letellier, F. Chevallier & M. Morcrette. In situ 7Li nuclear magnetic resonance observation of the electrochemical intercalation of lithium in graphite; 1st cycle. *Carbon* **45**, 1025-1034, (2007).

43 J. L. Lorie Lopez, P. J. Grandinetti & A. C. Co. Enhancing the real-time detection of phase changes in lithium–graphite intercalated compounds through derivative operando (dOp) NMR cyclic voltammetry. *Journal of Materials Chemistry A* **6**, 231-243, (2018).

44 D. Van Der Spoel, E. Lindahl, B. Hess, G. Groenhof, A. E. Mark & H. J. C. Berendsen. GROMACS: Fast, flexible, and free. *Journal of Computational Chemistry* **26**, 1701-1718, (2005).

45 H. J. C. Berendsen, D. van der Spoel & R. van Drunen. GROMACS: A message-passing parallel molecular dynamics implementation. *Computer Physics Communications* **91**, 43-56, (1995).

46 E. Lindahl, B. Hess & D. van der Spoel. GROMACS 3.0: a package for molecular simulation and trajectory analysis. *Molecular modeling annual* **7**, 306-317, (2001).

5

47 M. J. Abraham, T. Murtola, R. Schulz, S. Páll, J. C. Smith, B. Hess & E. Lindahl. GROMACS: High performance molecular simulations through multi-level parallelism from laptops to supercomputers. *SoftwareX* **1-2**, 19-25, (2015).

48 J. Wang, R. M. Wolf, J. W. Caldwell, P. A. Kollman & D. A. Case. Development and testing of a general amber force field. *Journal of Computational Chemistry* **25**, 1157-1174, (2004).

49 A. W. Sousa da Silva & W. F. Vranken. ACPYPE - AnteChamber PYthon Parser interfacE. *BMC Research Notes* **5**, 367, (2012).

50 S. V. Sambasivarao & O. Acevedo. Development of OPLS-AA Force Field Parameters for 68 Unique Ionic Liquids. *Journal of Chemical Theory and Computation* **5**, 1038-1050, (2009).

51 L. Martínez, R. Andrade, E. G. Birgin & J. M. Martínez. PACKMOL: A package for building initial configurations for molecular dynamics simulations. *Journal of Computational Chemistry* **30**, 2157-2164, (2009).

52 R. Gowers, M. Linke, J. Barnoud, T. Reddy, M. Melo, S. L. Seyler, D. Dotson, J. Domanski, S. Buchoux & I. Kenney. in *Proceedings of the 15th Python in Science Conference*   (Austin, TX, 2016).

53 B. D. Adams, J. Zheng, X. Ren, W. Xu & J.-G. Zhang. Accurate Determination of Coulombic Efficiency for Lithium Metal Anodes and Lithium Metal Batteries. *Advanced Energy Materials* **8**, 1702097, (2018).

5

6. Directly engineering ion transport and stability in interphases for high-energy lithium batteries

This chapter has been submitted as Wang, Q. *et al.* Directly engineering ion transport and stability in interphases for high-energy lithium batteries. (2023).

Abstract

The formation of stable passivating interphases within carbonate solutions is crucial for commercial battery technology based on graphite anodes, supporting long cycle life and fast charging capabilities. However, next-generation high-capacity Li-metal/silicon anodes face challenges in controlling the interphases using the current carbonates, while the prevailing electrolyte engineering entails sacrificing crucial assets, like ionic conductivity and cost, compromising their practical applicability. Here we report and verify a competitive approach to realize effective electrode-electrolyte interphases through elevating the electrolyte components, achieved by introducing multiple salts into commercial carbonates. Results obtained from both multi-solvent and multi-salt electrolytes demonstrate that the latter can effectively balance the interactions between Li ions and solvent/salt species, leading to improved electrolyte ionic conductivity and the formation of multi-component inorganic-rich hybrid interphases. The resulting local microstructure in the interphase exhibits a substantial enhancement of ion transport by lowering migration barrier to approximately 22 kJ mol^{-1}, ensuring good electrode-electrolyte compatibility towards prolonged cycling life at high charge/discharge rates. Beyond the conventional knowledge, our comprehensive analysis reveals this directly engineered hybrid interphase, exclusively formed in low-cost carbonate electrolytes, shows remarkable electrochemical and chemical stability, enabling promising application using high-capacity thin-Li-metal, Si-based and anode-free anodes, respectively.

6

6.1 Introduction

The increasing demand for higher-energy-density lithium-ion batteries (LIBs) necessitates electrodes with higher specific capacities[1], such as nickel-rich oxide cathodes[2] combined with silicon-based/Li-metal anodes[3]. However, this poses challenges for electrode reversibility and cycle life due to the harsh conditions at the electrode-electrolyte interphases[4]. During battery operation, interphases form on electrode surface through electrochemical reactions with electrolytes. Consequently, the choice of electrolytes significantly impacts battery performance which require high ionic conductivity and the ability to form stable passivated layers on electrodes to prevent continuous electrolyte decomposition while maintain the electrochemical activity by allowing facile ion transport/charge transfer[4,5]. Several electrolyte strategies, including concentrated and/or fluorinated electrolytes have been developed[6,7], which alter the solvation environment of Li ions, manipulating interphase properties to form anion-derived and/or LiF-abundant components that improve battery performanced[8,9]. However, these electrolytes have a drawback in terms of lower ionic conductivity (e.g., ~1.5-4.0 mS cm^{-1}) due to high viscosity, resulting in performance degradation of cycling at high rates[10,11]. Additionally, they raise concerns about electrolyte cost and environmental sustainability due to the high fluorine[12,13]. Also, LiF is a common interphase component but presents a higher diffusion barrier compared to other inorganic interphase components (e.g., oxides)[8,14], while the report shows that removing LiF from interphase can improve rate and cycle capabilities of the batteries[15]. Therefore, exploring routes towards effective solid passivation layers and understanding the intricate relationships with electrolytes are essential to pursue.

The interphase, known as solid electrolyte interphases (SEI) for anodes and cathode-electrolyte interphases (CEI) for cathodes, was initially described by E. Peled[6], typically consisting of mixed organics (e.g., carbonates, polymers) and inorganics (e.g., oxides, carbonates, fluorides)[16-18]. However, understanding its Li-ion transport mechanisms is challenging due to its diverse and heterogeneous nature[19,20]. Peled et al.[21] provided evidence for Li-ion transport via interphase grain boundaries and other interfacial impedance terms in liquid nonaqueous and polymer electrolytes. Christensen et al.[22] developed a mathematical model to simulate the interphase growth and ion/electron

6

transport properties through vacancies and interstitials, highlighting the importance of grain boundaries for ion transport. Raguette et al.[23] used molecular dynamics to study interphase compositions and their impact on electrolyte structure and dynamics, indicating that the presence of amorphous organics leads to Li-ion accumulation, slowing down solvation dynamics, which can be improved with crystalline inorganic components. Indeed, the emerging family of hybrid/composite solid electrolytes shares similarities with the electrode-electrolyte interphases, as they both combine organic and inorganic components[24,25]. By incorporating inorganic fillers into the organic polymer electrolyte, the ionic conductivity of solid electrolytes can be improved, enhancing ion transport and promoting the compatibility between the electrodes/electrolyte[26,27]. This approach also improves the mechanical behavior, providing better stability and durability. Thus, design strategies developed for hybrid/composite solid electrolytes can potentially guide the design of the electrode-electrolyte interphase in liquid batteries, however, how to translate it into practical applications poses a significant challenge.

In this work, we investigate the formation of an effective hybrid electrode-electrolyte interphase by comparing multi-salt and multi-solvent electrolytes to maximize the possible grain boundaries for Li-ion transport, inspired by high-entropy strategies[28-30]. This allows us to unveil what and how affect the interphase structure and composition, influencing stability, local interphase kinetics, and charge transfer (see Fig. 6.1a). Using a new multi-salt electrolyte, we demonstrate its ability to tune the solvation structure, resulting in enhanced electrolyte ion conductivity (e.g., ~10.0 mS cm^{-1}) and Li-ion diffusion coefficients, facilitating ion/charge transfer[23,31]. Importantly, the interphases formed, including SEI and CEI, are notably more stable and offer higher Li-ion diffusivity. This combined approach presents a promising route towards addressing interphase challenges in next-generation high-energy-density electrodes with using commercial carbonate-based electrolytes, effectively reducing costs as well.

6.2 Electrolyte and its compatibility on Li metal anode

The study aims to utilize commercially available salts, namely LiPF$_6$, LiFSI, LiTFSI, LiNO$_3$, and LiDFOB, along with carbonate solvents including EC, DEC, PC, DMC, and

EMC to explore various interphase properties of the possible low-cost electrolytes. The baseline electrolyte, 1 M LiPF$_6$ in EC/DEC (1:1 by volume) is denoted as 1S-2Sol (1 Salt-2 Solvents). Another electrolyte was prepared using 1 M LiPF$_6$ with equal volume ratios of five commercial carbonate solvents, termed as 1S-5Sol. For the multi-salt electrolyte, the five salts (0.225 M LiFSI, 0.225 M LiPF$_6$, 0.225 M LiDFOB, 0.225 M LiTFSI, and 0.1 M LiNO$_3$) were optimized in EC/DEC, resulting in a total concentration of 1 M, and referred to as 5S-2Sol. Lastly, a multi-salt multi-solvent electrolyte was created by combining the five salts (with a total concentration of 1 M) with the five solvents in equal volume ratios. Li-ion solvation environment of electrolytes was initially investigated using liquid ^{7}Li nuclear magnetic resonance (NMR) spectroscopy (Fig. S6.1), in which the chemical shift in NMR spectra provides information about the Li-ion coordinating species in the solvation shell, revealing the solvation interactions. Compared to the baseline 1S-2Sol electrolyte at -0.36 ppm, increasing the number of solvent species or salt species results in slightly more positive chemical shifts at around -0.34 and -0.32 ppm, respectively. This indicates weaker shielding of Li-ions due to decreased local electron density, implying various solvation interactions[32,33]. The 5S-5Sol electrolyte exhibits a larger downfield shift at around -0.28 ppm, suggesting that increasing both the number of solvents and salt species further alters solvation interactions. The solvation structures were further examined using Raman spectroscopy (Figs. S6.2-S6.5). Increasing the number of salt species (not its concentration) decreases the amount of the Li-ion-coordinated solvents, as reflected by the weaker coordinated peak. Consequently, the ionic conductivities improve from 8.85 mS cm^{-1} of the baseline 1S-2Sol electrolyte to ~9.34 mS cm^{-1} for 1S-5Sol electrolyte, ~9.81 mS cm^{-1} for 5S-2Sol electrolyte and ~11.1 mS cm^{-1} for 5S-5Sol electrolyte (Fig. S6.6). Li-ion diffusion coefficients measured from the pulsed field gradient (PFG) NMR spectra also show improved local Li-ion diffusivities (Fig. S6.7). This improved kinetics can be explained by the excess entropy scaling in liquids[28,29], where the increasing number of components leads to a wider distribution in diffusional barriers from diverse solvation structures, enhancing diffusional channels via the available percolation network. Tafel plots show the changed charge transfer kinetics at the electrode interface, where an increase in exchange current densities is observed when more

6

salt/solvent components are introduced (Fig. S6.8). However, compared to the influence of solvents, increasing the number of salt species in the 5S-2Sol electrolyte shows a larger exchange current density of ~0.41 mA cm^{-2}, which is even higher than that of the 5S-5Sol electrolyte, suggesting the different interphase properties. This is evaluated using cyclic voltammetry (CV) measurements in Li‖Cu cells (Figs. S6.9 and S6.10), where the increasing reduction peaks at around 1.4 V indicate adding diverse salts allows to tune the reduction potentials of the electrolytes.

The enhanced electrolyte kinetics and charge transfer kinetics upon increasing the salt/solvent species can be held partially responsible for the higher CE and lower overpotentials shown for Li‖Cu cells (Fig. 6.1b). Raising the number of salt species appears more favourable compared to raising the solvent species as the best performance is offered by the 5S-2Sol multiple salt electrolyte, showing a higher plating/stripping reversibility with an average CE of ~99.1% and a lower overpotential of ~13 mV compared to the single-salt multi-solvent 1S-5Sol electrolyte of ~91.5% and ~27 mV (Fig. S6.11). This difference in cycling reversibility and overpotential is also observed in symmetric Li-metal cells, especially at higher current densities of 8.0 mA cm^{-2} (Figs. S6.12-S6.14). However, raising both the number of salt and solvent species in the 5S-5Sol electrolyte also increases the average CE but to a lesser extent compared to the 5S-2Sol electrolyte, resulting in more capacity fading within 200 cycles (Fig. 6.1b and Fig. S6.11). It is anticipated that this may be the consequence of more solvent-rich coordination sheaths around Li-ions, being expected to lower interphase stability (Figs. S6.2-S6.5).

We subsequently performed scanning electron microscopy (SEM) measurements to investigate the Li-metal plating/stripping morphologies associated with the enhanced performance of the electrolytes. In contrast to the highly porous and whisker-like Li-metal deposits in the 1S-5Sol (Fig. 6.1c) and 1S-2Sol electrolytes (Fig. S6.15), the deposits in the 5S-2Sol electrolyte are more compact and well-connected to the Cu substrate showing particle sizes up to ~12 μm (Figs. 6.1c and 6.1d). After stripping, a porous morphology with some residual dendritic Li is observed for the 1S-5Sol electrolyte (Fig. S6.16) whereas much less Li-metal appears to be left behind for the 5S-2Sol electrolyte, indicating more complete and homogenous stripping. Denser and better-connected Li-
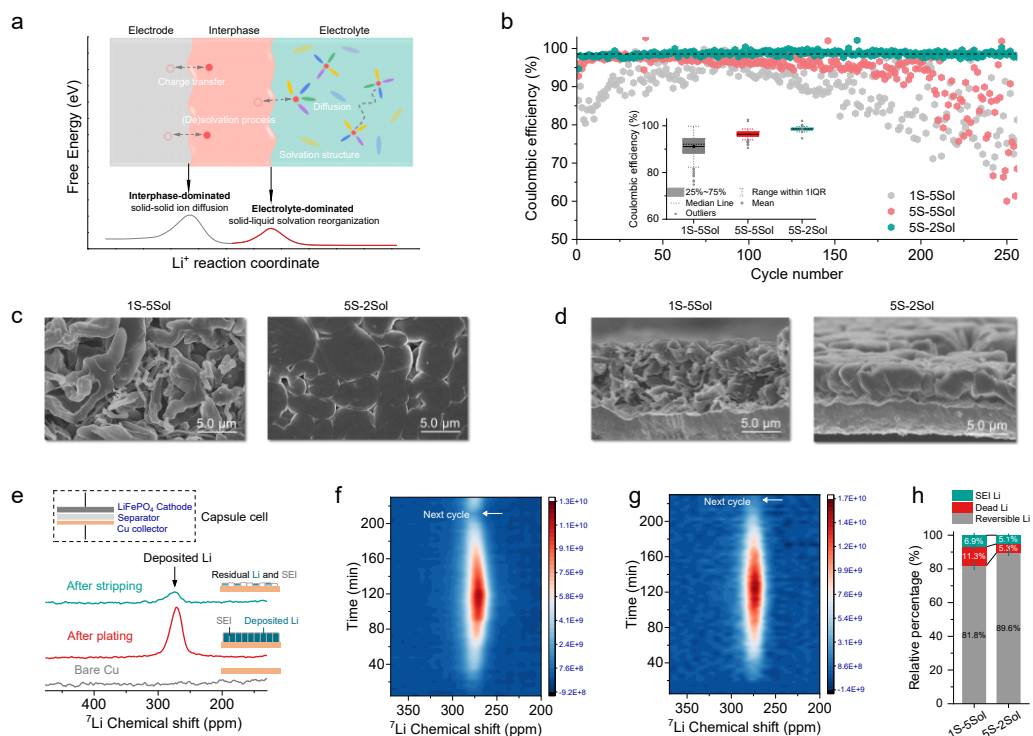
6

Fig. 6.1. Electrode-electrolyte interphase and electrolyte compatibility with Li-metal anode.
a, Schematic diagram of Li$^+$ transfer between electrode and electrolyte. The process involves two mechanisms: interphase-dominated, based on solid-solid ion diffusion between electrode-electrolyte interphases, and electrolyte-dominated, arising from solid-liquid ion solvation reorganization. **b,** CE in Li∥Cu cells. Cells were tested at the continuous cycling at 0.5 mA cm^{-2} for 2 h. The inset shows the statistical analysis of CEs with box plots showing the median, 25 and 75% quantiles, whiskers indicating the range of ±1.5×IQR, and outlying points plotted individually. **c,** SEM images of deposited Li metal on Cu foil at a current density of 0.5 mA cm^{-2} to 1 mAh cm^{-2}. Cells were first cycled ten cycles and then plated to 1 mAh cm^{-2}. **d**, Cross-sectional views of deposited Li metal. **e**, Schematics of operando ^{7}Li NMR measurement using anode-less Cu∥LiFePO$_4$ cells. **f,g,** Operando ^{7}Li NMR measurement during Cu∥LiFePO$_4$ cells cycling with 1S-5Sol with 5S-2Sol electrolytes at a current density of 0.5 mA cm^{-2} for 2 h. The arrow indicates the end of this cycle. **h**, Quantifying Li species, including Li species in SEI (blue bars), reversible Li metal (grey bars), and dead Li-metal residual (red bars) species, derived from the Li metal integrated intensity ratio and the electrochemical CE. Error bars are calculated from the parallel tests.

metal deposits are beneficial for electron transport, allowing more efficient stripping and thus suppressing the formation of residual dead Li[34]. Additionally, compact deposits

minimize the exposed surface area, leading to less electrolyte decomposition and, in turn, suppressing the formation of porous Li on subsequent cycling. This phenomenon is also observed in the 5S-5Sol electrolyte (Fig. S6.15), which implies that increasing the number of different salt species can effectively improve Li-metal plating/stripping reversibility, also upon increasing the number of solvent species. The relatively high average CE of 99.1% indicates that decent Li-metal plating/stripping reversibility can be achieved in low-cost carbonate electrolytes under typical cycling conditions, without relying on concentrated electrolytes and fluorinated electrolytes.

Operando solid-state ^{7}Li NMR as a non-invasive method can provide quantitative and temporal information on Li metal deposition, allowing monitoring of Li plating/stripping during an electrochemical measurement[35,36]. The chemical shifts of different Li resonances can be used to differentiate metallic Li (~260-280 ppm) and diamagnetic Li species in SEI/electrolyte (~0 ppm) via the Knight shift[36]. Thus, this measurement allows quantifying the amount of dead Li-metal after stripping. In combination with the CE from electrochemical cycling, it enables the calculation of the amount of Li in the SEI (see the method)[37]. Operando ^{7}Li NMR measurements are performed using a Cu||LiFePO$_4$ anode-less battery configuration[37] to evaluate the different electrolytes. Before charging the Cu||LiFePO$_4$ cell, the Li-metal resonance at ~275 ppm is absent (Fig. 6.1e). Upon charging, the Li-metal resonance grows as it is deposited, reaching a maximum at the end of the charge and subsequently shrinking during discharge (Figs. 6.1f and 6.1g). At the end of the discharge, the Li-metal resonance remains visible, signifying that some dead Li-metal remains (Fig. S6.17). Comparing the 1S-5Sol and 5S-2Sol electrolytes, the calculated fractions of reversible Li metal, dead Li-metal, and Li in the SEI are shown in Fig. 6.1h. The 1S-5Sol electrolyte exhibits a higher fraction of dead Li-metal (~11.3%) and Li species in the SEI (~6.9%). This indicates that the accumulation of dead Li is the primary reason for the lower reversibility observed, which is linked to the porous and whisker-like morphologies observed in SEM measurements. In contrast, the 5S-2Sol electrolyte shows less Li loss in both the dead Li-metal and the SEI during cycling which consequently increases the CE, and thus the capacity retention upon cycling. The Li-metal plating and stripping process involves passing through the covered SEI layers, making SEI formation

6

a decisive factor in determining Li-metal deposited morphology and species, that is significantly influenced by the electrolyte composition.

6.3 Interphasial microstructure and chemistry

The impact of electrolyte composition on the microstructure of Li-metal deposits and SEI structure was investigated using cryogenic transmission electron microscopy (cryo-TEM) where the cryogenic conditions protect the weakly bonded components from the high-energy electron-beam irradiation and environmental exposure[38]. In the low-magnification cryo-TEM images (Figs. 6.2a and 6.2b), whisker-like Li-metal deposits with a lateral diameter of around 0.6~1.5 μm are observed in the 1S-5Sol electrolyte. These deposits are covered with an uneven SEI layer, resulting in a porous structure and rougher surface. On the other hand, Li deposits in the 5S-2Sol electrolyte exhibit isotropic morphologies with a larger average diameter and a smoother surface. High-resolution images reveal that a thin and compact SEI layer of approximately 8±2 nm is formed on the surface of deposited Li metal in the 5S-2Sol electrolyte (Fig. 6.2b). A relatively thicker and non-uniform SEI layer of around 13±2.6 nm is observed in the 1S-5Sol and 1S-2Sol electrolytes (Fig. 6.2a and Fig. S6.18), consistent with the results from operando NMR and SEM that indicate the presence of more SEI species. Moreover, selected area electron diffraction (SAED) measurements show that the SEI layer in the 5S-2Sol electrolyte is crystalline/inorganic-dominant. This indicates that more anionic groups from the multi-component salts participate in the SEI formation, resulting in a more hybrid/composite multilayer SEI structure (Fig. 6.2b and Fig. S6.18). In contrast, the SEI layers formed in the multi-solvent 1S-5Sol electrolyte are dominated by amorphous components with a small number of crystalline domains randomly dispersed, forming a mosaic SEI structure (Fig. 6.2a and Fig. S6.18). The amorphous matrix likely represents organic species formed by solvent decomposition, which also leads to the formation of polycrystalline compounds embedded in the bulk deposits in the 1S-5Sol electrolyte[38].

The chemical composition of the Li-metal deposits is further analyzed using time-of-flight secondary ion mass spectrometry (TOF-SIMS) and X-ray photoelectron spectroscopy (XPS) measurements to gain a more detailed understanding of the elemental

6

spatial distribution and bonding states. In the 5S-2Sol electrolyte, Li-metal deposits show dominant distributions of O and F on the surface (Figs. 6.2d, 6.2f and Figs. S6.18-S6.20) while for the 1S-5Sol electrolyte, C and O
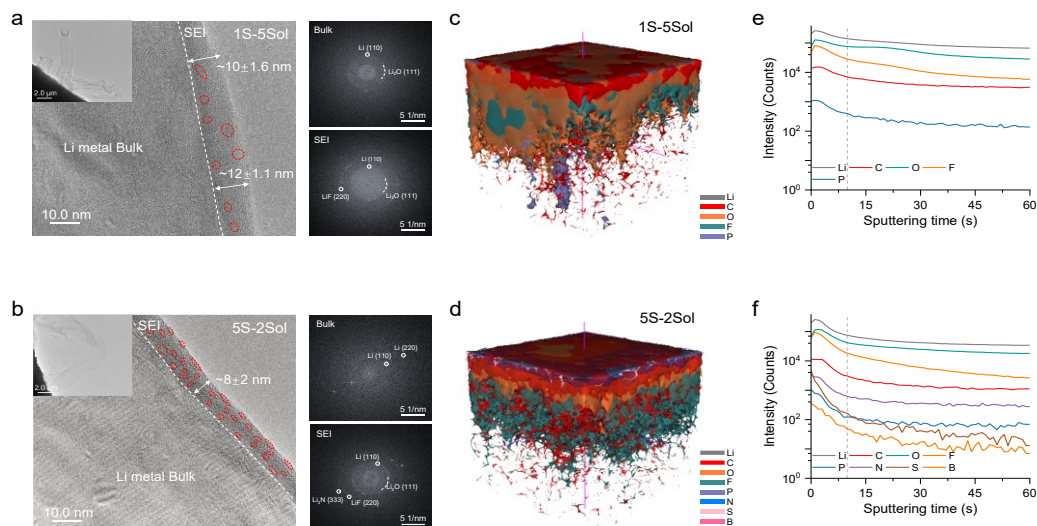

Fig. 6.2. Microstructure and chemistry of the interphase. a-b, Cryo-TEM micrographs displaying the microstructure of deposited Li metal and interfacial phase. Insets provide low magnification morphology and highlight inorganic region distribution in interphases (marked by lines). Corresponding SAED patterns of plated Li metal are shown in the SEI and Li metal bulk regions. **c-d**, TOF-SIMS analysis of Li metal deposits after 20 cycles at 0.5 mA cm^{-2} for 2 h in electrolytes. **e-f**, Depth profiles of various chemical species over time for the 1S-5Sol and 5S-2Sol electrolytes.

are the dominant, and more C is observed on the surface, extending into the bulk (Figs. 6.2c, 6.2e and Fig. S6.20). For the 5S-2Sol electrolyte also more S, N, and B elements are also observed to be uniformly distributed on the near-surface region, which is a consequence of the presence of the diversity of salt chemistries. XPS measurements are consistent with the TOF-SIMS analysis (Figs. S6.21-S6.24, showing that the SEI derived from the 5S-2Sol electrolyte contains a higher concentration of O and F elements, while the SEI in the 1S-5Sol electrolyte shows higher amounts of O and C elements (Figs. S6.21 and S6.22). The deconvoluted C 1s and O 1s profiles reveal larger fractions of C-O, C=O species in the 1S-5Sol electrolyte, indicating solvent-dominated SEI formation[39]. In the 5S-2Sol electrolyte, in addition to organic components from solvents, some C-SO$_x$ and

Poly(CO_3^{2-}) species are observed, suggesting that the anions of FSI⁻, TFSI⁻ and DFOB⁻ decomposition dominates the SEI formation process[40] (Fig. S6.21). The multi-salt derived SEI in the 5S-2Sol electrolyte is further supported by the presence of P, B, N, and S elements, where more Li-containing inorganic components, including Li_2O, Li_xN, and LiF, have been found in Li 1*s*, O 1*s*, F 1*s* and N 1*s* spectra (Figs. S6.22-S6.24), consistent with the increasing redox peak observed at ~1.4 V from CV measurements (Figs. S6.7 and S6.8). In addition, extra peaks attributed to B-O, B-F, N-O, and SO_x in 5S-2Sol electrolyte are observed due to the decomposition of multiple salts. In the F 1*s* spectra, Li-F and P-F species are detected in both electrolytes, most likely due to $LiPF_6$ decomposition, however, in the 5S-2Sol electrolyte the C-F species may originate from other anionic groups[41] also observed together with an increased amount of Li-F species, which is confirmed by the Li-F peak the Li 1*s* spectra (Fig. S6.22). The observed element distributions directly relate to the intrinsic characteristics of the different electrolytes where the multi-salt 5S-2Sol electrolyte results in various anion-derived interphase components contributing to the formation of a more inorganic-dominated hybrid interphase.

6.4 Interphasial ion transport

Li-ion transport through the SEI is anticipated to depend on the composition/structure of the interphase, which is however poorly studied owing to the challenge of directly probing the local ion diffusivity. A powerful method to investigate the ion transport across the SEI in its native state (see method) is NMR chemical exchange saturation transfer (CEST), commonly used in high-resolution ¹H NMR and magnetic resonance imaging to quantify exchange rates between different chemical environments[42-44]. The exchange between SEI and Li metal deposits can be considered as the exchange between two pools of Li, where the Li metal presents a large pool and the SEI a small pool of exchangeable Li ions. The basic principle of CEST is schematically shown in Fig. S6.25. The CEST experiment applies a long saturation pulse to the small pool, during which the continuous exchange will lead to the accumulation of transferred saturation, and the resonance
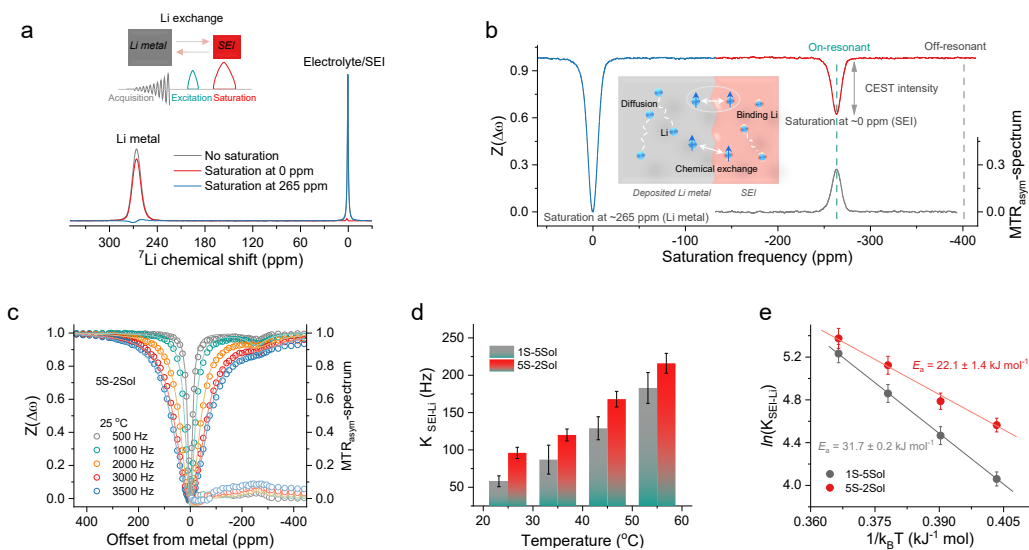
6

Fig. 6.3. Interphase Li-ion kinetics. a, Illustration of CEST approach. ^{7}Li NMR spectra of Li-metal deposits immersed in electrolyte (grey) and acquired with a saturation pulse of 0.2 s and 3500 Hz at the SEI resonance (~0 ppm, red) and the deposited Li (~265 ppm, blue). The inset demonstrates Li exchange during a CEST pulse sequence, where a saturation pulse is applied to the SEI site followed by an excitation on the resonance of Li metal. **b**, Z-spectra obtained from Li-metal deposits as a function of saturation frequencies and MTR$_{asym}$ quantitative analysis. $\Delta\omega$ represents the applied frequency away from the Li-metal peak. Data were fitted using the two-pool BMC equation. The inset presents the schematic diagram of the CEST effect on the "deposited Li metal and SEI" two-pool system. Through applying a soft saturation pulse on the SEI resonance (~0 ppm, Pool I) at a certain cross-relaxation, Li exchange occurs between SEI and deposited Li (~265 ppm, Pool II.), resulting in the decrease of the deposited Li signal (CEST intensity). **c**, Z-spectra obtained from Li-metal deposits with a saturation time of 0.2 s at 25 °C with various saturation powers. **d**, Exchange rates of Li metal deposits via fitting the Z-spectra from the two-pool BMC equation. **e**, Li exchange rates and activation energy as a function of temperature. The activation barrier was obtained by fitting the Arrhenius equation.

of the large pool will be detected (Fig. 6.3a)[45,46]. Applying a saturation pulse to the Li metal frequency can lead to a substantial signal reduction due to direct saturation. However, when the exchanging pool is saturated via selective radiofrequency (rf) irradiation at the SEI frequency, the saturation is transferred to the Li metal via chemical exchange thus decreasing the signal of the metal peak. To quantitatively analyse the Li exchange between Li metal and the SEI, the normalized Li-metal signal intensity is monitored against the frequency of the off-resonance saturation: the so-called Z-

spectrum[47] (Fig. 6.3b and Fig. S6.26). The magnetisation transfer ratio asymmetry (MTR$_{asym}$) signal derived from Z-spectrum (see method) can be used to qualitatively compare the exchange rate in different SEI-Li-metal systems[48]. For determining the exchange rate between SEI and Li metal in different electrolytes, Z-spectra with various RF saturation amplitudes ranging from 500 Hz to 3500 Hz are collected under temperatures from 25°C to 55°C for the Li-metal-SEI formed in the different electrolytes (Fig. 6.3c and Fig. S6.27). In all cases, the CEST effect increases with saturation amplitude B_1 and temperature, which also can be observed from the MTR$_{asym}$ signal evolution.

A qualitative comparison of the results suggests that the SEI formed in the 5S-2Sol electrolyte leads to a larger CEST than the SEI in the 1S-5Sol electrolyte under the same condition, indicating enhanced exchange between the SEI and Li-metal in the former. To quantify these differences, we employed the two-pool Bloch-McConnell (BMC) differential equation and fitted the Z-spectra acquired with multiple B_1 simultaneously (see method and Table S6.1)[49-51]. The resulting interphase exchange rates (Fig. 6.3e and Table S6.2) increase almost linearly with temperature in both cases, with the 5S-2Sol electrolyte showing a higher exchange rate than the 1S-5Sol electrolyte. This suggests that the inorganic-dominated hybrid/composite interphase formed in the 5S-2Sol electrolyte facilitates Li-ion transport, contributing to its more uniform Li deposition and better cycling performance. Furthermore, the activation energy for Li-ion transport across the metal–SEI interface was determined using variable temperature measurements on CEST, (Fig. 6.3h). The direct determination of the energy barrier for the SEI in its native form shows the SEI in the 5S-2Sol electrolyte has a lower activation barrier for Li-ion exchange around 22.1 kJ mol^{-1} as compared to the 1S-5Sol electrolyte with an activation barrier around 31.7 kJ mol^{-1}, further reflecting the higher Li-ion permeability of the 5S-2Sol electrolyte. Additionally, the interphase resistance measured by EIS and analyzed by distribution of relaxation times (DRT) after cycles (Figs. S6.28 and S6.29) show that the overall impedance of cells using 5S-2Sol electrolyte is lower than the 1S-5Sol electrolyte. Specifically, the interphase impedance, with a timescale of 10^{-4} to 10^{-2} s[52], for the 5S-2Sol electrolyte is around 13 Ω, much smaller than that of the 1S-5Sol electrolyte with a value

6

of around 27 Ω. Together with the improved exchange rate, this provides consistent evidence of the better Li-ion conductivity of the SEI in the 5S-2Sol electrolyte.

6.5 Interphasial Stability

We then assessed the stability of hybrid interphase using an intermittent electrochemical test protocol including a calendar aging step (Fig. 6.4a), which can account for the chemical corrosion, thermodynamic driving force on interphase degradation, and the electrolyte/electrode consumption during the storage beyond continuous electrochemical cycling[53]. In addition, the CE during the recover cycle allows us to distinguish to some extent if Li is lost as dead Li-metal or if it is lost in SEI-forming species. Intermittent cycling of Li∥Cu cells with aging times ranging from 12 h to 144 h was performed for different electrolytes (Fig. 6.4b, Figs. S6.30-S6.32). During this intermittent cycling, the 5S-2Sol and 5S-5Sol electrolyte displayed small CE fluctuations between the aging and the recover cycles, along with a higher average CE, while the 1S-5Sol electrolyte exhibited significant fluctuations and a lower average CE (Fig. 6.4b, Figs. S6.30 and S6.31). Analysis of the CE statistics for different aging times revealed two capacity loss mechanisms for the electrolytes (Fig. S6.32). Firstly, in all three electrolytes, dead Li formed during each aging step, but it could be recovered in the next cycle, reflected by a CE larger than 100%. However, the 1S-5Sol electrolyte suffered more significant capacity losses (approximately 65%) during aging cycles, especially at 12 h and 24 h, indicating the formation of more irreversible Li-containing SEI products due to chemical corrosion. By comparison, the multiple-salt (5S-2Sol and 5S-5Sol) electrolytes showed smaller capacity losses, with more capacity being recovered (Fig. 6.4b, Figs. S6.31 and S6.32). The enhanced cycling stability and reduced CE fluctuations suggest that the multiple-salt-derived hybrid/composite interphase from the 5S-2Sol electrolyte experiences less chemical decomposition and dead Li-metal formation during each aging step. Cells using the 5S-2Sol electrolyte exhibited higher capacity retention and a higher average CE during continuous electrochemical cycling (Fig. 6.4c). Similarly, intermittent electrochemical cycling of Cu∥LiFePO₄ cells revealed larger CE fluctuations and capacity loss upon aging for the 1S-5Sol electrolyte compared to the 5S-2Sol electrolyte. This observation can be

attributed to the limited Li inventory from LiFePO$_4$, which fails to compensate for Li loss during aging, leading to rapid capacity decay and fluctuations.
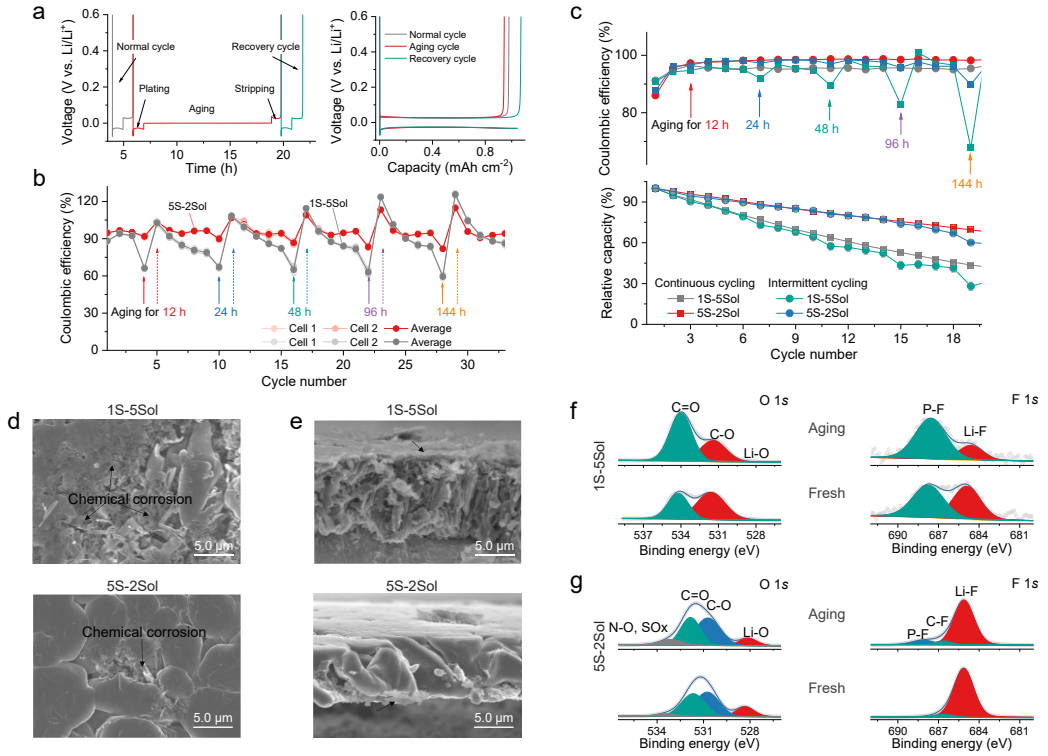

Fig. 6.4. Interphase stability. a, Illustration of the intermittent cycling protocol. Li‖Cu cells undergo three cycles of continuous cycling at 1.0 mA cm^{-2} for 1 h to represent the normal cycle. Subsequently, Li metal is plated at 1.0 mA cm^{-2} for 1 h and aged for various periods before being stripped at 1.0 mA cm^{-2} to the cut-off voltage of 1.0 V, representing the aging cycle. Following the aging cycle, Li-metal is plated and stripped at the same current density, representing the recovery cycle. **b**, Intermittent CE of the electrolytes for different aging times. **c**, Relative discharge capacity retention and the corresponding CE of Cu‖LiFePO$_4$ cells cycled at C/5 with different electrolytes using continuous and intermittent electrochemical cycling protocols. Cu‖LiFePO$_4$ cells undergo two cycles of continuous charge-discharge at C/5, followed by aging for various periods and then three continuous cycles using the same current density. **d**, SEM images of deposited Li after aging 120 h. Cells were cycled at 1.0 mA cm^{-2} for 1 h (1.0 mA h cm^{-2}) after twenty cycles and then plated for 1 h. **e**, Images of deposited Li metal on Cu foil from a cross-sectional view. **f-g**, XPS profiles of O 1s and F 1s profiles spectra after cycling in electrolytes. Fresh samples represent cells measured after 20 cycles, while aging samples represent cells aged for 120 h.

To investigate the underlying mechanisms responsible for the observed electrochemical properties, we examined the morphologies and surface chemistry of the deposited Li after aging. Fig. 6.4d illustrates that Li metal deposited in the 1S-5Sol electrolyte undergoes severe chemical corrosion during aging, resulting in the formation of extensive side-reaction products on the surface when compared to the fresh samples shown in Fig. 6.1c. In contrast, the deposits in the 5S-2Sol electrolyte maintain a cleaner and smoother surface with fewer corrosion species. SEM energy dispersive spectroscopy (EDS) mappings (Figs. S6.34 and S6.35) indicate that the corrosion products mainly consist of C- and O-containing species derived from reactions with solvents. Intriguingly, cross-section SEM images (Fig. 6.4e) reveal the presence of corrosion hotspots: in the 1S-5Sol electrolyte, the products mainly form on the top of corroded Li metal, while in the 5S-2Sol electrolyte, the corrosion is observed near the current collector. Thus, the observed corrosion processes in these two electrolytes can be attributed to different categories: top corrosion, associated with irreversible Li-containing products, and root corrosion, linked to dead Li formation. The latter mechanism also indicates a dead Li generation process for Li deposits with whisker-like diameters.

Further analysis of the chemical species in the interphase formed during aging is conducted through XPS measurements (Figs. 6.4f, 6.4g, and Figs. S6.36-S6.41). In the 1S-5Sol electrolyte, compared to the fresh Li deposits measured immediately after cycling (Fig. S6.37), significant changes are observed in the C 1s, O 1s, Li 1s, and F 1s spectra during the resting period. This suggests the accumulation of organic species, such as C=O in the O 1s spectra, on the surface of Li metal, consistent with solvent decomposition seen in previous EDS mapping. Additionally, species related to salt decomposition, like the Li-F peak in F 1s spectra, are reduced compared to the fresh sample confirming that solvent-driven corrosion dominates the process in the 1S-5Sol electrolyte. On the other hand, the spectra of the 5S-2Sol electrolyte remain relatively stable before and after aging, with slight increases in peaks such as N-O, SO$_x$, B-O, and S-N related to salt decomposition. This indicates a higher stability of the interphase, suppressing corrosion during aging. The results above demonstrate the multi-component inorganic-rich interphase obtained in the

multiple-salt (5S-2Sol) electrolyte exhibits superior electrochemical and chemical stability, effectively slowing down corrosion and prolonging the cycling life of the cells.

6.6 Performance of full cells

We further identified the interphase properties in combination with high-capacity cathode materials, where the oxidation stability of the 5S-2Sol and 1S-5Sol electrolytes was first evaluated with CV measurements on Li‖Al cells. The multi-salt 5S-2Sol electrolyte presents an electrochemical stability window up to ~4.7 V vs. Li/Li$^+$ as shown in Fig. 6.5a. In addition, the potentiostatic polarization measurements show that the oxidation leakage current of 5S-2Sol electrolyte reached a minimum value of ~0.27 μA cm^{-2} after holding for 8 h at 4.3 V, which is lower than that of ~0.48 μA cm^{-2} in 1S-5Sol electrolyte (Fig. S6.42). The corrosion of the multi-component electrolytes on Al current collectors was also tested, where both electrolytes demonstrated smooth morphologies on Al foils after polarization, indicating potential compatibility with nickel-rich layered cathodes (insets of Fig. 6.5a). Subsequently, the electrolytes were evaluated in combination with LiNi$_{0.8}$Co$_{0.1}$Mn$_{0.1}$O$_2$ (NCM811) cathodes in Li‖NCM811 cells in 2.8-4.3 V with an NCM811 areal capacity of 2.5 mAh cm^{-2} and a 50-μm Li-metal anode. During the initial cycles at 0.1C, both electrolytes present a similar discharge capacity (Figs. 6.5b and 6.5c), however, during the long-term cycling, cells using the 5S-2Sol electrolyte show significantly better stability with a capacity retention of around 95% after 200 cycles at 1.0C and more than 83% capacity can still be maintained after 400 cycles (Fig. 6.5d), outperforming the 1S-5Sol electrolyte that has capacity retention of around 73% after 200 cycles. These results suggest that the CEI layer formed in the 5S-2Sol electrolyte is more compatible with high-voltage cathodes. Additionally, the cells using the 5S-2Sol electrolyte exhibited promising rate performance, with capacity retentions of approximately 94.2%, 84.5%, 70.0%, and 60.6% at 1.0, 2.0, 4.0, and 6.0C, respectively, which were higher than the capacity retentions of 89.8%, 77.2%, 50.3%, and 10.5% achieved in the 1S-5Sol electrolyte (Fig. 6.5e and Fig. S6.43). Despite having similar ionic conductivities of ~9.81 vs. ~9.34 mS cm^{-1}, the improved interphase properties, including

6

higher ionic transport kinetics and better stability, are suggested to be responsible for the outstanding electrochemical performance of the 5S-2Sol electrolyte.
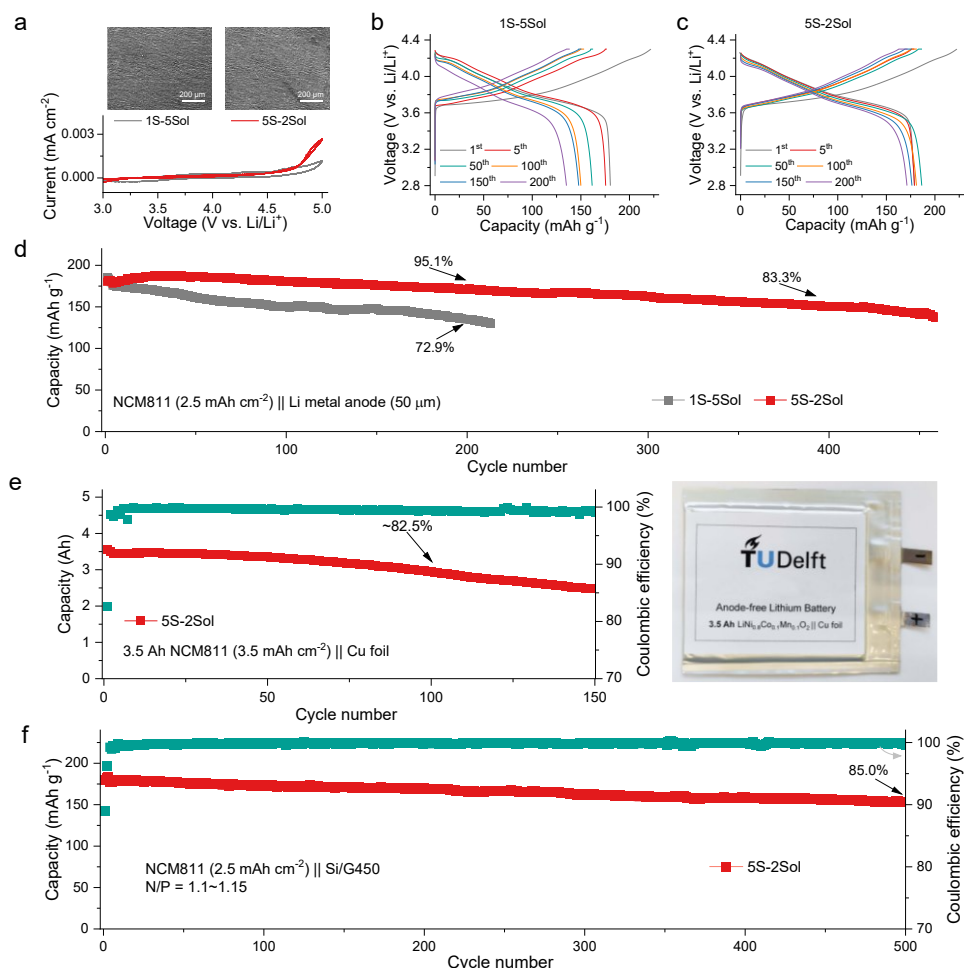

Fig. 6.5. Electrochemical performance of multi-salt and multi-solvent electrolytes. a, CV curves of Li‖Al cells with a scan rate of 0.8 mV s^{-1} from 3.0 to 5.0 V. Insets show the morphologies of the Al current collector after corrosion. **b-c**, Galvanostatic charge/discharge curves of NCM811 cells. **d**, Capacity retention of Li‖NCM811 cells with different electrolytes cycled between 2.8-4.3 V with 0.1C for three cycles and 1.0C for the following cycles. **e**, Cycling performance of anode-free 3.5-Ah pouch cells. Cells were tested with double-sided coating NMC811 cathode and bare Cu foils with E/C of ~2 g Ah^{-1} and cycled between 2.6-4.4 V with 0.1C for three cycles and 0.5C for the following cycles. **f**, Capacity retention of NCM811‖Si/graphite cells cycled between 2.6-4.3 V at 0.1C rate for the first three cycles and 1.0C for the following cycles. The capacity ratio of the negative over positive electrode is in 1.1~1.15. Si/G450 represents the Si/graphite composite anode with a capacity of 450 mAh g^{-1}.

6

To further assess the compatibility of the multi-component hybrid interphase formed in the 5S-2Sol electrolyte, more demanding anode-free pouch cells were assembled and cycled under harsh conditions, with zero-excess Li-metal, a high cathode loading of 3.5 mAh cm^{-2}, and a less amount of electrolyte with an electrolyte/cathode ratio (E/C) of ~2 g Ah^{-1} (Fig. 6.5e, Fig. S6.44, and Table S6.3). Even under these challenging cycling conditions, the prototype Li-metal pouch cell maintained good cycling stability with a capacity retention of around 82.5% after 100 cycles at a 0.5C rate, comparable to the performance achieved with optimized electrolytes reported in literature (Table S6.4). This competitive performance, based on commercial carbonate electrolytes under aggressive cycling conditions, further confirms the promising properties of this engineered hybrid interphase derived from the multi-salt electrolyte. To verify its practical application in higher energy density Li-ion cells, the electrochemical performance of NCM811||Si/G450 full cells was evaluated using the 5S-2Sol electrolyte. Fig. 6.5f shows the cycling performance of full cells cycled between 2.6-4.3 V at a 0.1C rate for the first three cycles and 1.0C for the following cycles. The capacity ratio of the negative over the positive electrode was in the range of 1.1~1.15, and the areal capacity of NCM811 cathode was 2.5 mAh cm^{-2}. Specifically, the full cells using the 5S-2Sol electrolyte exhibited a capacity retention of around 94.0%, 88.0%, and 85.0% after 200, 400, and 500 cycles, respectively, with an average CE of ~99.9%. The rate performance of the NCM811||Si/G450 full cells was also tested, delivering a capacity retention of around 98.3% at 0.3C, 86.5% at 1.0C, 70.2% at 3.0C, and 52.6% at 5.0C (Figs. S6.45 and S6.46), respectively. These promising performances in full cells suggest that the 5S-2Sol electrolyte results in more stable and highly Li-ion conductive interphases, making it highly promising for practical application.

The interphase chemistry between the cathode and electrolyte was further investigated using SEM and TEM measurements. The NCM811 cathode cycled in the 1S-5Sol electrolyte was found to be covered by an uneven CEI layer with a thickness of around 8~16 nm (Fig. S6.47). In contrast, a uniform CEI layer with a thickness of around 10 nm was formed on the surface of the cycled cathode in the 5S-2Sol electrolyte. Additionally, the CEI formed in the 5S-2Sol electrolyte contributed to restraining the cracks and pulverization of the NCM811 secondary particles, unlike the cathode cycled in

6

the 1S-5Sol electrolyte (Fig. S6.48). The suppression of microstructural degradation in the cathode particles likely reduces side reactions, preventing massive electrolyte consumption. Furthermore, the chemical composition of CEI layers was investigated by electron energy loss spectroscopy (EELS) measurements. Comparing the Ni *K*-edge spectra in CEI layers from both electrolytes, we can observe there exists the Ni element dissolution in the 1S-5Sol electrolyte (Fig. S6.49), which plays a vital role in cathode degradation. The dissolved transition metals may also mitigate to the anode side, resulting in the damage of SEI integrity via the cross-over effects[54], which eventually compromises the cycling stability of cells. In contrast, the CEI layer formed in the 5S-2Sol electrolyte is found to be the F-rich (Fig. S6.50), which can be held responsible for the high-voltage stability of the CEI layer[34]. These results demonstrate that the multi-salt 5S-2Sol electrolyte, through the formation of the inorganic-rich interphase hybrid, contributes to a homogeneous and stable CEI protective layer, thereby enhancing the electrochemical performance of the full cells.

6.7 Conclusions

In summary, we report a route towards more stable electrode-electrolyte interphases in Li-ion batteries through multiple-salt electrolytes, combining five commercially available salts in conventional carbonate solvents. The result is an anion-rich multi-component hybrid/composite interphase that exhibits enhanced stability under cycling/storing and provides higher Li-ion conductivity (Fig. 6.6). We compared multi-salt and multi-solvent electrolytes with the same regular 1 M total salt concentration, analyzing the interphase properties on all length scales through a comprehensive range of operando, in-situ, and ex-situ experimental techniques. The results demonstrated both the multi-component electrolytes have an ability to enhance bulk ionic conductivities by balancing Li-solvent/salt interactions and increasing solvation structure diversity. However, the multi-salt electrolyte results in the formation of a superior interphase, consisting of multiple inorganic components embedded in the typical amorphous organic components. The diversified and heterogenous interphase compositions maximize the percolating pathway
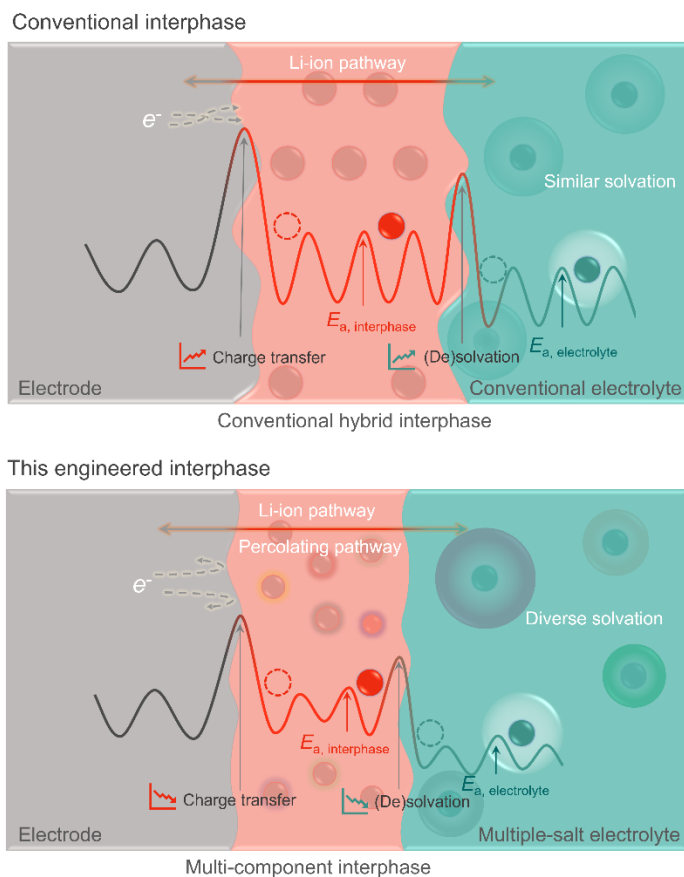
6

Fig. 6.6. Schematics of the engineered interphases in batteries. The transport of Li-ions across the electrode/electrolyte interphase contribute to the overall battery performance, which is determined by the activation energy in various dominating processes. $E_{a, electrolyte}$ is Li-ion diffusion barrier in electrolyte, which can be effectively reduced by increasing the diversity in solvation structure, facilitating improved liquid phase transport and de-solvation at the electrolyte/interphase interface. $E_{a, interphase}$ is Li-ion diffusion barrier in solid interphase, which is influenced by the interphase structure/composition. Unlike conventional interphases formed in typical electrolytes, this new interphase resulting from multiple-salt electrolytes is thinner and robust with a wide range of anion-rich hybrid/composite components. This diversity maximizes the percolating pathway, lowering the energy barrier, facilitating de-solvation and enhancing ion interphasial transport. Meanwhile, this interphase significantly improves interphase stability against electrochemical/chemical reactions, benefiting for the long cycling stability.

of grain boundaries, boosting a substantial enhancement of ion transport across the interphase with a lower migration barrier (Fig. 6.6). The improved interphase kinetics

6

effectively facilitates the solid-solid ion diffusion between electrode and interphase as well as the solid-liquid ion solvation reorganization between interphase and electrolyte, contributing to the higher charge/discharge rate capability. On the other hand, the inorganic-dominated multi-component hybrid interphase presents higher interphase stability against electrochemical/chemical reactions, supporting a long cycle and long calendar aging life. This work paves the way for designing effective electrode-electrolyte interphase, enabling long-cycling and high-stability batteries through the utilization of low-cost electrolytes (Fig. S6.51, Table S6.4-S6.7), signifying a step towards higher sustainability in batteries.

6.8 Methods

Materials

Solvents of ethylene carbonate (EC), dimethyl carbonate (DMC), fluoroethylene carbonate (FEC), propylene carbonate (PC), diethyl carbonate (DEC), ethyl methyl carbonate (EMC), were purchased with battery-grade purity, which was dehydrated with a 4 Å molecular sieve (Sigma-Aldrich) to eliminate the trace water. Lithium hexafluorophosphate (LiPF$_6$), lithium bis(fluorosulfonyl)imide (LiFSI), lithium bis(trifluoromethanesulfonyl) imide (LiTFSI), lithium difluoro(oxalato)borate (LiDFOB) were dried in the vacuum oven of glovebox 80 °C overnight. The suppliers are shown in the Table S6.5 and S6.6. Lithium nitrate (LiNO$_3$, >99.9%) was purchased from Shenzhen Capchem Technology Co., Ltd and used as received. Lithium metal foils (thickness of 250 µm), Cu foils, and Al foils were purchased from MTI Corporation, and lithium metal foils (50 µm) were purchased from China Energy Lithium Co., Ltd. All lithium metal foils were washed 3 times with DMC solvent before use. Cu foils were immersed in diluted acetic acid for several minutes, subsequently washed with deionized water and acetone three times, separately, then they were quickly dried in the vacuum oven of the glovebox at room temperature. All the electrolytes were prepared by dissolving the specific amount of different lithium salts in solvents in an Ar-filled glovebox (H$_2$O < 0.1 ppm, O$_2$ < 0.1 ppm).

6

The 1.0 mol L^{-1} (M) $LiPF_6$-EC/DEC (1S-1Sol) was prepared by dissolving 1.0 M $LiPF_6$ in the EC/DEC mixing solvents in the volume of 1:1. The 1.0 mol L^{-1} (M) $LiPF_6$-EC/DEC/PC/DMC/EMC (1S-5Sol) was prepared by dissolving 1.0 M $LiPF_6$ in the mixing solvents with the equal volume ratio. The 5S-2Sol electrolyte was prepared by dissolving 0.225 M LiFSI, 0.225 M $LiPF_6$, 0.225 M LiDFOB, 0.225 M LiTFSI, and 0.1 M $LiNO_3$ in the EC/DEC mixing solvents in a volume of 1:1, where $LiNO_3$ was firstly dissolved into EC solvent under 60-80 °C under the assistance of a touch mixer machine, and then the other salts were added into this mixture. The 5S-5Sol electrolyte was prepared by dissolving 0.225 M LiFSI, 0.225 M $LiPF_6$, 0.225 M LiDFOB, 0.225 M LiTFSI, and 0.1 M $LiNO_3$ in the EC/DEC/PC/DMC/EMC mixing solvents with the equal volume ratio, where $LiNO_3$ was firstly dissolved into EC/PC mixing solvents under 60-80°C under the assistance of a touch mixer machine, and then the other salts and solvents were added into this mixture. Finally, 5% FEC in volume was added to all the electrolytes.

$LiFePO_4$ was obtained from Leneng Technology for which the cathodes were prepared by mixing $LiFePO_4$ material, poly(vinylidene difluoride) (PVDF, MTI) binder, and Super P (Alfa Aesar) conductive carbon in a weight ratio of 92:4:4. The resulting slurry was cast on the Al foil then dried at 60 °C for 6 h, followed by drying overnight at 120 °C in a vacuum oven.

$LiNi_{0.8}Co_{0.1}Mn_{0.1}O_2$ (NCM811) was synthesized using the coprecipitation method. A certain amount of alkaline aqueous solution (NH_4OH and NaOH) was poured into deionized water (1.5 L) to form the base solution in a tank reactor under continuous stirring. Then, a 2 M solution of $NiSO_4 \cdot 6H_2O$, $CoSO_4 \cdot 7H_2O$, and $MnSO_4 \cdot H_2O$ with a molar ratio of 8:1:1 and an aqueous solution of 5 M NH_4OH and 10 M NaOH was added into the base solution in the tank reactor with a steady rate of 8 mL min^{-1}. The coprecipitation temperature was controlled at 50 °C, and the pH value was maintained at around 11 by NH_4OH with a stirring speed of 500 rpm under a nitrogen atmosphere. The coprecipitated $Ni_{0.8}Co_{0.1}Mn_{0.1}(OH)_2$ precursor was prepared, which was subsequently washed with deionized water and ethanol four times and dried in a vacuum at 120 °C for 24 h. The apparent and tap density of $Ni_{0.8}Co_{0.1}Mn_{0.1}(OH)_2$ precursors are 1.88 g cm^{-3} and 2.06 g cm^{-3}, respectively. For the preparation of NCM811 materials, the as-obtained precursor was

6

mixed with LiOH·H$_2$O at a molar ratio of 1:1.03; then firstly heated at 500 °C for 5 h and subsequently calcined at 780 °C for 12 h in an oxygen atmosphere. After cooling naturally, the obtained material was directly put into an Ar-filled glovebox to prevent any moisture exposition. The NCM811 electrodes were prepared by mixing the active material, Super P, and PVDF binder in the mass ratio of 90: 5: 5 in N-methyl-2-pyrrolidone (NMP) solvent and cast on Al foil and then dried at 60 °C for 6 h, followed by drying in a vacuum oven at 120 °C overnight. X-ray diffraction pattern demonstrates the pure phase of this prepared NCM811 material.

Si/G450 electrode material was purchased from BTR (China) and Si/G1000 was purchased from Showa Denko Materials (Japan). The Si/G450 and Si/G1000 electrodes were prepared by mixing the active material, Super P, and PVDF binder in the mass ratio of 94: 3: 3 in NMP solvent and cast on Cu foil, and then dried at 80 °C for 6 h, followed by drying in a vacuum oven at 120 °C overnight.

Materials characterization

Morphologies of electrodes were measured on a cold field scanning electron microscope (SEM, HITACH-S4800, SU8010). Elemental composition on the surface of the electrodes was analyzed by X-ray photoelectron spectroscopy (XPS, PHI 5000 VersaProbe II) using a monochromatic Al Kα X-ray source with X-ray settings being 100 μm 25 W 15 kV. Peaks were fitted using MultiPak software calibrated with respect to carbon (284.8 eV). The above morphology and composition characterization was performed with cells being disassembled after specific cycles in an Ar-filled glovebox and rinsed with pure DMC solvent three times to remove residual electrolyte, followed by drying in a glovebox for several hours at room temperature to remove the residual solvent. For the sample characterizations obtained through continuous electrochemical cycling, the samples were collected immediately after the cells were finished. For the sample characterizations obtained through intermittent electrochemical cycling, the samples were collected after the cells aged to a certain time. Then these electrodes were transferred into the vacuum transfer boxes for measurements to avoid air exposure. Raman spectroscopy was measured by Micro-laser confocal Raman spectrometer (Horiba LabRAM HR800 spectrometer) equipped with an Olympus BX microscope and an argon ion laser (532 nm)

6

at room temperature. All the electrolytes were hermetically sealed in quartz cuvettes in a glovebox before measurement.

Cryo-transmission electron microscopy (cryo-TEM) characterization

Conventional and cryo-(S)TEM experiments were performed on a scanning transmission electron microscope (STEM) (JEM-ARM300F, JEOL Ltd.) operated at 300 kV with a cold field emission gun and double Cs correctors. During image acquisition, the corresponding electron dose flux (units of number of electrons per square angström per second, $e^- \text{Å}^{-2} \text{s}^{-1}$) was recorded. Conventional STEM images were taken with a dose rate of over 1000 $e^- \text{Å}^{-2} \text{s}^{-1}$ with an exposure time for each image of several seconds. Cryo-TEM images were obtained with an exposure time for each image of around 0.3 s with a built-in drift correction function using the OneView and K2 cameras. Cryo-TEM images were taken with an electron dose rate of 50-500 $e^- \text{Å}^{-2} \text{s}^{-1}$. Short-exposure single-frame shots were used to estimate the defocus and make it as close as possible to Scherzer defocus. EELS spectra were acquired on a GIF Quantum camera with a dispersion of 1 eV/channel, utilizing the Dual EELS capability to correct for drift in the low-loss centered on the zero-loss peak and core-loss centered on the C K-edge. The EELS spectrum images were carried out with a camera length of 20 mm, and a pixel dwell time of 10 ms. Energy drift during spectrum imaging was corrected by centering the zero-loss peak to 0 eV at each pixel. Elemental maps were computed through a two-window method in a pre-edge window fitted to a power-law background and a post-edge window of 50-200 eV on the core-loss signal. Analysis of the spectra has been performed in Gatan microscopy suite software. For cryo-TEM sample preparation and transfer, cells were disassembled immediately in an argon-filled glovebox after cycling and then both lithium metal anodes and NCM811 cathodes were rinsed with pure DMC three times to remove lithium salts, followed by drying in the glovebox for one hour at room temperature to remove the residual solvent. During the washing procedure, approximately 10 mL DMC was carefully dropped onto each of the electrodes one time to reduce additional artifacts on the electrodes.

For cryo-TEM preparation of lithium metal anode, a lacey carbon TEM grid was put on a Cu foil working electrode and assembled into Li‖Cu cells in an argon-filled glovebox.

6

The cells were discharged at a constant current density of 1.0 mA cm^{-2} for 15 min, after which the TEM grid was taken out by disassembling the cells for measurement. The TEM grid was carefully transferred into the cryo-TEM holder in the glovebox with a specialized shutter to prevent air exposure and ice condensation onto the sample introducing any side reactions. Once the cryo-TEM holder was transferred into the TEM column, the temperature was maintained at around -170 °C using liquid nitrogen.

^{7}Li chemical exchange saturation transfer (CEST)

The measurements of ^{7}Li CEST were performed on a wide-bore Bruker Ascend 500 system equipped with a NEO console with a magnetic field strength of 11.7 T and Larmor frequencies for ^{7}Li being 194.37 MHz. The saturation pulse of the CEST experiment lasted for 0.5s and the RF amplitude was from 500 Hz to 3500 Hz. The saturation offset frequency ω was in the range of +500 ppm to -500 ppm with respect to the Li metal resonance, where the probe tuning was stable over the entire range. The recycle delay was set to 8s in all experiments to avoid the influence of RF heating. The longitudinal and transverse relaxation rates were determined for the lithium dendrites and the electrolyte using inversion-recovery and Carr–Purcell–Meiboom–Gill experiments, respectively. The spectra were initially processed using Bruker Topspin software including phase and baseline corrections. Further processing and analysis of the data were carried out in MATLAB (version 2022a).

The CEST effect was analyzed using a Z-spectrum, generated with the normalized Li metal signal intensity, $Z(\Delta\omega)$, as a function of the saturation frequency $\Delta\omega$[55,56]. $Z(\Delta\omega)$ is given by the following equation:

$$Z(\Delta\omega) = \frac{S_{metal}(\Delta\omega)}{S_{metal}} \tag{6.1}$$

where $\Delta\omega$ is the offset with respect to the Li metal frequency ($\Delta\omega = \omega_{sat} - \omega_{metal}$), and $S_{metal}(\Delta\omega)$ is the intensity of the Li metal signal with saturation on $\Delta\omega$.

When irradiating the Li metal at around 265 ppm, the signal disappears due to direct saturation (DS). This frequency is assigned to 0 ppm in Z-spectra. This DS may interfere with the detection of CEST effects, which is addressed by employing the symmetry of the

DS through a so-called magnetization transfer ratio (MTR) asymmetry analysis[48], using the following equation:

$$\text{MTR}_{\text{asym}} = \frac{S_{\text{metal}}(-\Delta\omega) - S_{\text{metal}}(\Delta\omega)}{S_0} \tag{6.2}$$

where S_0 corresponds to the Li metal signal without saturation.

The Z-spectra of the four electrolyte systems were analyzed using the two pools exchange model with abundant pool (Li metal pool) and rare pool (SEI pool), where f_{SEI} corresponds to the ratio between the SEI and Li metal pool concentrations. Separating the exchange rate from the concentration of the exchanging pools requires the simultaneous fitting of multiple B_1 Z-spectra[57-59]. Therefore, the Z-spectra acquired with varying saturation amplitude B_1 were fitted with two-pool Bloch-McConnell (BMC) differential equations which are six coupled first-order linear differential equations[49-51]:

$$\frac{d\vec{M}}{dt} = A\vec{M} + \vec{C} \tag{6.3}$$

$$A = \begin{bmatrix} L_m - f_s K & K \\ f_s K & L_s - K \end{bmatrix} \tag{6.4}$$

where m and s stands for Li metal and SEI, and $\vec{M}$ is magnetization vector described by:

$$\vec{M} = \left(M_{m,x} + M_{m,y} + M_{m,z} + M_{s,x} + M_{s,y} + M_{s,z} \right)^T \tag{6.5}$$

$$L_i = \begin{pmatrix} -R_{2i} & -\Delta\omega_i & 0 \\ \Delta\omega_i & -R_{2i} & \omega_1 \\ 0 & -\omega_1 & -R_{1i} \end{pmatrix} \tag{6.6}$$

$$K = \begin{pmatrix} k_s & 0 & 0 \\ 0 & k_s & 0 \\ 0 & 0 & k_s \end{pmatrix} \tag{6.7}$$

$$\vec{C} = \left(0,0, R_{1m}M_{m,0}, 0,0, R_{1s}M_{s,0} \right)^T \tag{6.8}$$

where i=m,s, $\omega 1 = \gamma B_1$ where γ is the nuclear gyromagnetic ratio and B_1 the saturation amplitude, $\Delta\omega i$ the saturation frequency $k_s = k_{SEI-metal}$. $\Delta\omega$ represent the frequency offset relative to the Larmor frequency of Li metal.

6

Finally, the equation was fitted with an analytical solution, and Lorentzian line shape for both pools[44,51], and the fitting parameters and boundaries are shown in Table S6.1. The value of f_{SEI} was fixed to 0.01 with all other parameters free and the results of this fit are summarized in Table S6.2.

The samples of deposited Li metal in various electrolytes for Li exchange detection were prepared in Li||Cu CR2032 coin cells with a PTFE ring (thickness around 0.5mm) on the Cu side and a Celgard 2500 separator on the Li metal side. A current density of 1 mA cm^{-2} and a capacity of 6 mAh were used for Li metal plating on the Cu current collector. After Li plating, the Li||Cu cells were disassembled, and Li metal deposition was transferred into a 4 mm rotor together with 50 ul corresponding electrolyte to keep the in-situ situation in an Ar-filled glove box (H_2O < 0.1 ppm, O_2 < 0.1 ppm). Then the rotor was sealed with a Vespel cap and taken to the nuclear magnetic resonance (NMR) characterization.

Liquid nuclear magnetic resonance (NMR) characterization

Liquid NMR spectra were recorded with an Agilent 400 MHz DD2 NMR spectrometer with a 5 mm ONE NMR Probe at room temperature, which worked at 155.5 MHz on ^{7}Li. The chemical shift values are given in ppm. ^{7}Li chemical shift was referenced to the standard solution: 1 M LiCl in D_2O for ^{7}Li (0 ppm). The external standard solutions were sealed into WILMAD coaxial insert tubes and inserted into the 5-mm KONTES tubes with electrolytes, and sealed with PTFE caps. Mestrelab Research Mnova software was used for data processing.

Solid-state NMR characterization

Operando solid-state NMR measurements were conducted on a wide-bore Bruker Ascend 500 system equipped with a NEO console in a magnetic field strength of 11.7T and a ^{7}Li resonance frequency being 194.37 MHz using a solenoidal Ag-coated Cu coil. Operando static ^{7}Li NMR measurements were performed using an automatic-tuning-and-matching probe (ATM VT X operando WB NMR probe, NMR Service) at room temperature which can allow for an automatic recalibration of the NMR radio-frequency (rf) circuit during an operando electrochemistry experiment. A highly shielded wire with low-pass filters was attached to the probe for electrochemical measurement, which could minimize the interferences between NMR and the electrochemistry circuit. Single-pulse with a π/2 pulse of 4 μs and recycle delay of 1.0 s was applied to acquire the 1D static spectrums. A recycle delay of three times of T_1 was used each time, where T_1 was determined using saturation

recovery experiments. The electrochemical cell was simultaneously controlled by a Maccor battery testing system. A plastic capsule cell made out of polyether ether ketone (PEEK) was used for the operando NMR experiments. The cells were assembled using LiFePO$_4$ cathode (areal capacity is 2.0 mAh cm^{-2}) and Cu foils as working and counter electrodes with both a piece of Celgard and a piece of Glass fiber (Whatman GF/A) as a separator. Before measurements, the assembled cells were rested for 2 h in the glove box. The operando capsule cell was aligned in an Ag-coated Cu coil with LiFePO$_4$ and Cu foil electrodes oriented perpendicular to B_0 and parallel with respect to the B_1 rf field. During the static ^{7}Li NMR measurements, the cells were charged to the capacity of 1 mAh cm^{-2} at a current density of 0.5 mA cm^{-2}. During the charge-discharge process, NMR spectra were continuously acquired. The chemical shift of ^{7}Li was referenced to 1 M aqueous solution of LiCl at 0 ppm. The spectra were processed in the Bruker Topspin software, using the automatic phase and baseline correction. Mestrelab Research Mnova software was used for data analysis.

Time-of-flight secondary ion mass spectrometry (TOF-SIMS) characterization

The TOF-SIMS characterization was carried out on PHI nanoTOF II (ULVAC-PHI, Japan), with a Bi^{3+} beam (30 kV, 2 nA) used as the primary beam to detect the samples, and the sputter etching was performed using an Ar$^+$ beam (3 kV, 100 nA) to obtain the desired depth profile. The area of analysis was 60 μm × 60 μm, while the sputtering area was 400 μm × 400 μm. In the process of sample transfer, a special transfer vessel is used, which can directly transfer the sample from the glove box to the TOF-SIMS vacuum chamber without being exposed to the ambient air. The analysis chamber is maintained in an ultra-high vacuum with pressures below 2×10^{-9} mbar. The samples were prepared on Li metal deposits after 20 cycles at 0.5 mA cm^{-2} for 2 h in different electrolytes. After the cycles finished, the samples were collected immediately in an Ar-filled glovebox and rinsed with pure DMC solvent three times to remove residual electrolyte, followed by drying in a glovebox for several hours at room temperature to remove the residual solvent. TOF-DR software was used for data processing and analysis.

Electrochemical measurements

6

Electrochemical cycling tests of all batteries were based on CR2032 coin cells assembled in an Ar-filled glovebox (H_2O < 0.1 ppm, O_2 < 0.1 ppm) with Celgard 2500 separator and tested at room temperature, unless stated otherwise. 70 μL electrolytes were injected into each coin cell for comparison. All coin cells were tested using multi-channel battery testing systems (Land CT2001A or Lanhe G340A) at room temperature. Symmetric Li‖Li cells were assembled to study the cycling stability under different current densities with various electrolytes. 15.6 mm diameter lithium metal foils with 250 μm thickness were used as both the working and counter electrodes. For Li‖Cu cells, 14 mm diameter lithium metal foils were used as the reference, while 16 mm Cu foils were used as a working electrode with an effective area for lithium deposition of 1.54 cm^2. The electrochemical cycling performance of NCM811 is with an areal capacity of ~2.5 mAh cm^{-2} tested with lithium metal foils with a thickness of 50 μm as the counter electrode. The electrochemical cycling performance of $LiFePO_4$ is with an areal capacity of 2 mAh cm^{-2} tested with lithium metal foils with a thickness of 50 μm as the counter electrode. Full cell electrochemical cycling performance of NCM811‖Si/G450 was tested between 2.6-4.3 V. Cells were cycled under a 0.1C rate for three cycles before cycling at a 1.0C rate. The areal capacity of NCM811 cathode used in full cell is ~2.5 mAh cm^{-2}, and the capacity ratio between the anode (the negative electrode) and cathode (the positive electrode), known as N/P ratio, is around 1.1~1.15.

Cyclic voltammetry (CV) of Li‖Cu cells with various electrolytes was conducted at a scan rate of 0.8 mV s^{-1} from -0.1 to 2.5 V vs. Li/Li^+. CV of Li‖Al cells with various electrolytes was conducted at a scan rate of 0.8 mV s^{-1} from 3.0 to 5.0 V vs. Li/Li^+. Electrochemical impedance spectra (EIS) of the symmetric cells were collected on an Autolab (PGSTAT302N) in the frequency range of 0.1 Hz–1 MHz with a potential amplitude of 10 mV. The distribution of relaxation times (DRT) was applied to the investigations of the individual relaxation processes occurring in the system and their corresponding relaxation frequencies based on the EIS data using the below expression[60].

$$Z_{DRT}(\omega) = R_0 + \int_{-\infty}^{+\infty} \frac{\gamma}{1+i\omega\tau} d(\ln\tau) \qquad (6.9)$$

where R_0 is the ohmic resistance, γ is distribution function that describes the relaxation time, ω is the angular frequency and τ is the relaxation time.

6.9 Supplementary information

Supplementary Figures
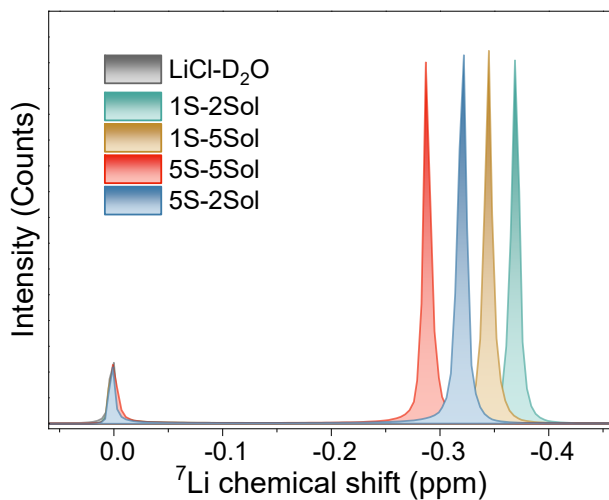
Fig. S6.1. Liquid ^{7}Li nuclear magnetic resonance (NMR) spectra of electrolytes. 1 M LiCl in D_2O is used as a reference.
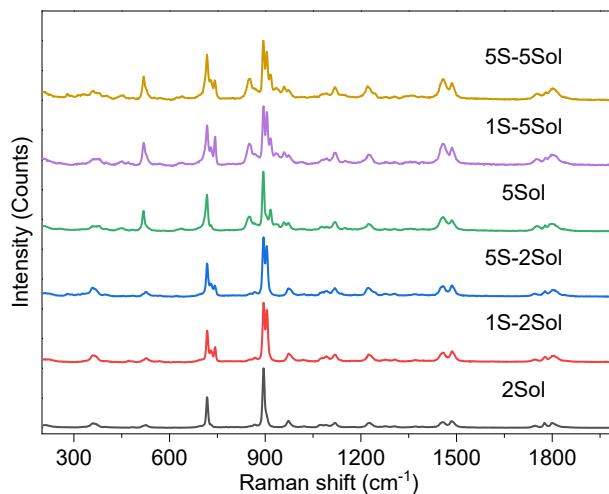

Fig. S6.2. Raman spectra of different electrolytes. The solvent mixtures are shown as a reference.
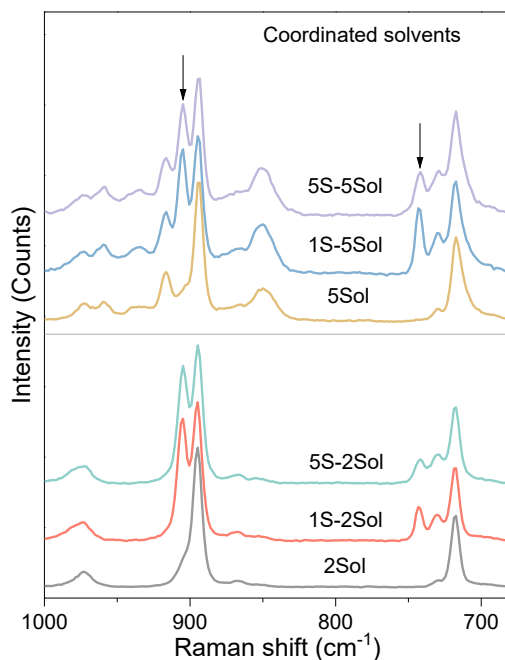
6

Fig. S6.3. Raman spectra of the solvents and electrolytes. The black arrows mark the peaks that represent the coordinated to solvents.
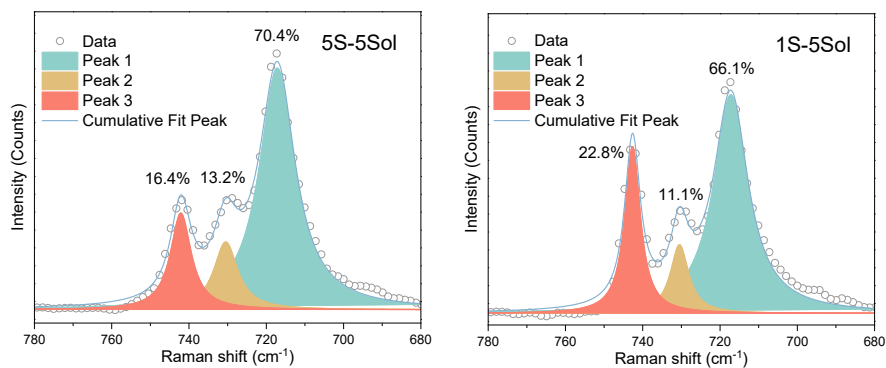

Fig. S6.4. Raman spectra for different electrolytes. The deconvoluted peak 3 represents the Li-ion coordination to solvents. In the same solvent composition, increasing the types of salts can decrease the amount of coordinated Li-ion to solvents.
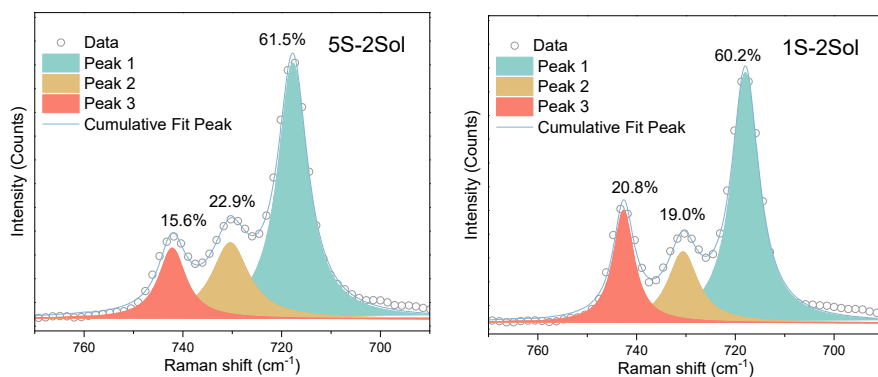
Fig. S6.5. Raman spectra for different electrolytes. The deconvoluted peak 3 represents the Li-ion coordination to solvents. In the same solvent composition, increasing the types of salts can decrease the amount of coordinated Li-ion to solvents.
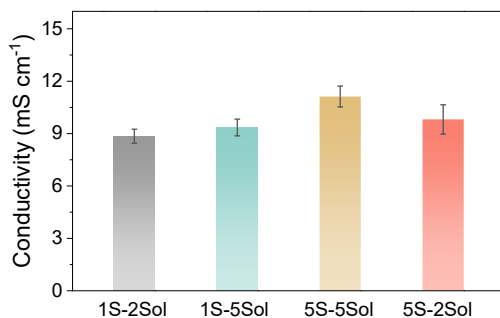
Fig. S6.6. Li-ion conductivity of different electrolytes. The test temperature is 25 °C.
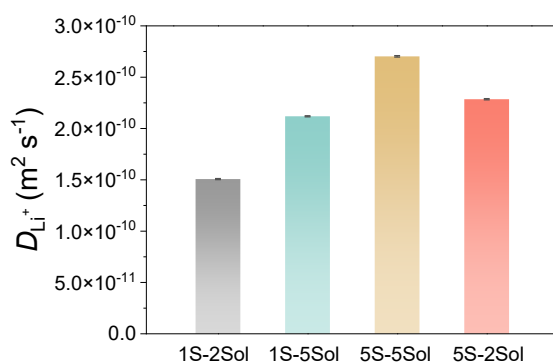
Fig. S6.7. Li-ion diffusion from ⁷Li pulsed field gradient (PFG) NMR spectroscopy. The test temperature is 25 °C.
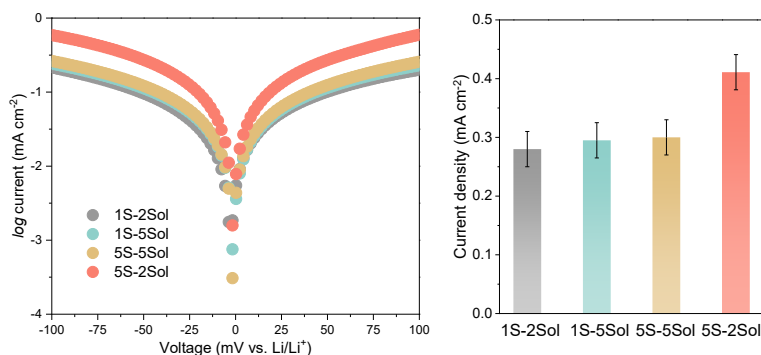
Fig. S6.8. Exchange current density from Tafel plots. Left: Galvanostatic Li plating/stripping using Li‖Li cells in different electrolytes; right: the exchange current density is obtained from the linear fitting of the Tafel curves.
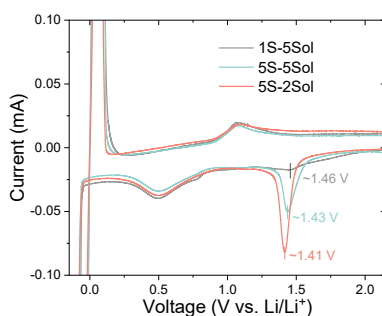
Fig. S6.9. Cyclic voltammetry (CV) curves of Li‖Cu cells. The measurements were carried out at a scan rate of 0.8 mV s^{-1} from -0.1 to 2.5 V vs. Li/Li$^+$ for different electrolytes.
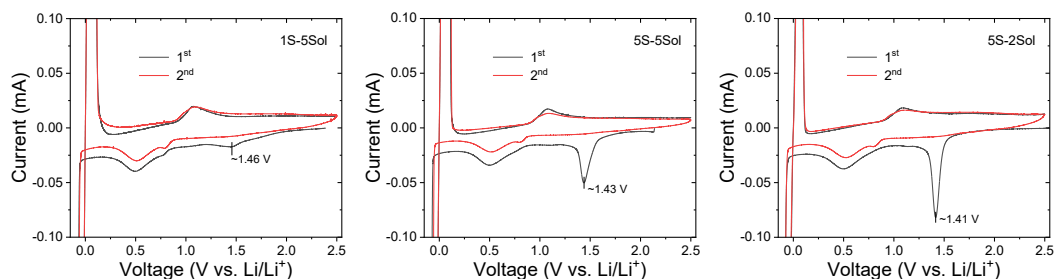
Fig. S6.10. CV curves of Li‖Cu cells. The measurements were carried out at a scan rate of 0.8 mV s^{-1} from -0.1 to 2.5 V vs. Li/Li$^+$ for different electrolytes.
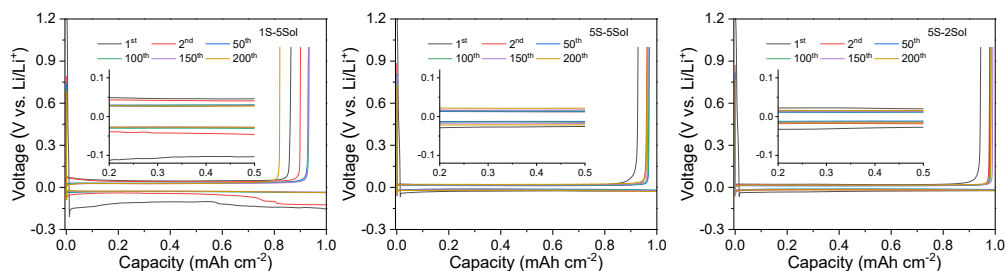
Fig. S6.11. Galvanostatic Li plating/stripping profiles of Li∥Cu cells. Cells were tested at the continuous cycling at 0.5 mA cm^{-2} for 2 h (1.0 mA h cm^{-2}). The inserts show the zoomed-in voltage curves of selected cycles.
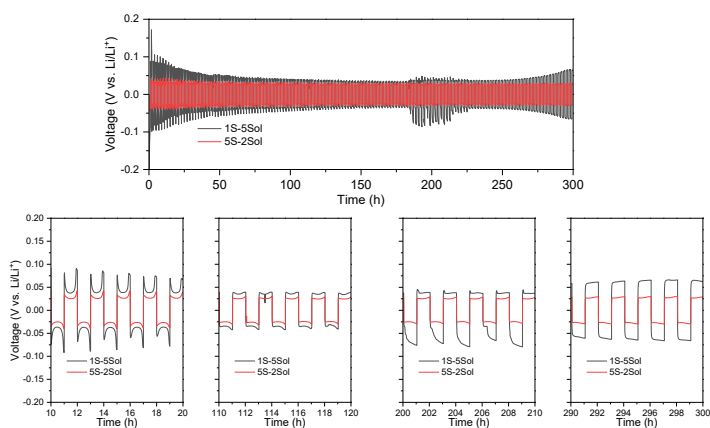
Fig. S6.12. Galvanostatic Li plating/stripping in Li∥Li cells. Cycling of Li∥Li cells are tested in different electrolytes at 1.0 mA cm^{-2} to a capacity of 1.0 mAh cm^{-2} and the overpotential of Li∥Li cells in different electrolytes at a different stage of cycling are shown.
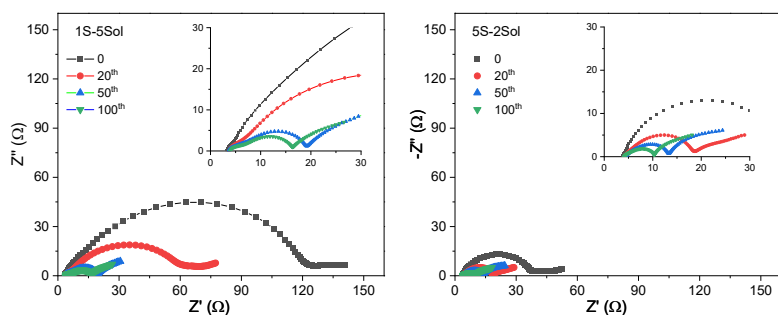
Fig. S6.13. Electrochemical impedance spectra (EIS) of Li∥Li symmetric cells in different electrolytes. The Li∥Li symmetric cells were cycled under a current density of 1 mA cm^{-2} with each plating/stripping time of 1 h.
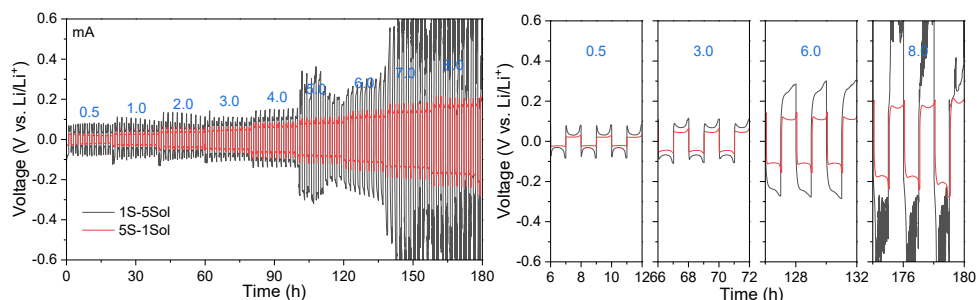
Fig. S6.14. Rate profiles for symmetric cells with different electrolytes. Li‖Li cells at a current density from 0.5 to 5 mA cm⁻² with each plating/stripping time of 1 h. Li‖Li cells at a current density from 0.5 to 5 mA cm⁻² with each plating/stripping time of 1 h. When the current density increases to 5.0 mA cm⁻², a short circuit occurred for the cells using the 1S-5Sol electrolyte. In contrast, the 5S-2Sol electrolyte can support the cells to cycle at a higher current density of 8.0 mA cm⁻² (Fig. S6.14), demonstrating the competitive reaction kinetics of this multi-salt electrolyte. This is consistent with the lower electrochemical impedance as observed during the extended cycles (Fig. S6.13).
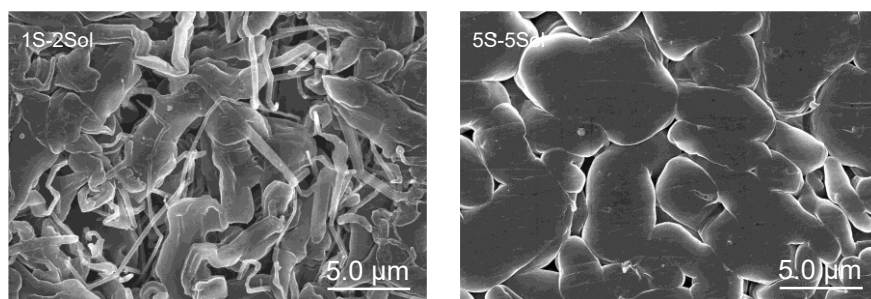
Fig. S6.15. Scanning electron microscope (SEM) images of Cu foil after plating in 1S-2Sol and 5S-5Sol electrolytes. Cells were cycled at a current density of 0.5 mA cm⁻² to 1 mAh cm⁻² in different electrolytes for ten cycles.
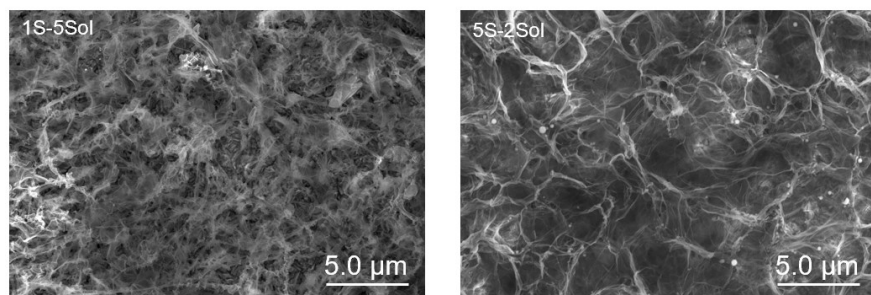

Fig. S6.16. SEM images of Cu foil after Li metal stripping. Cells were cycled at a current density of 0.5 mA cm⁻² to 1 mAh cm⁻² in different electrolytes for ten cycles.
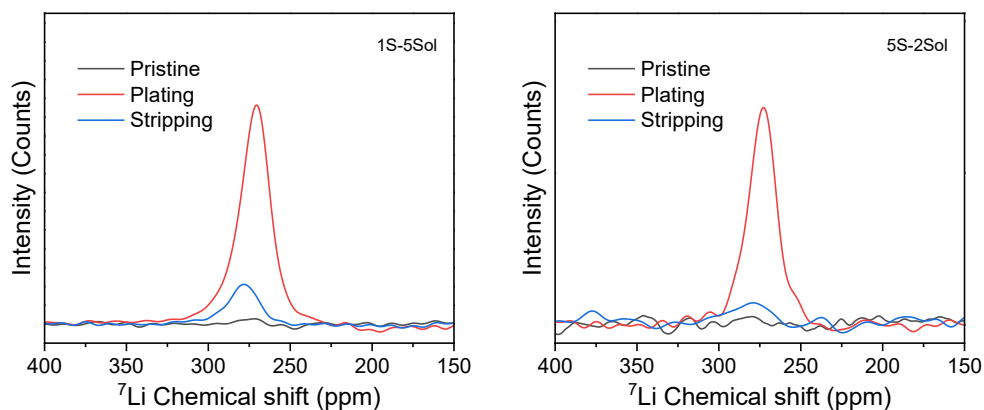
6

Fig. S6.17. ^{7}Li solid-state NMR spectra after different states during cycling. Comparison of the Li-metal resonance in the ^{7}Li NMR spectra are shown from the Cu‖LiFePO$_4$ cells before (pristine). after Li plating (charged), and after Li stripping (discharged).
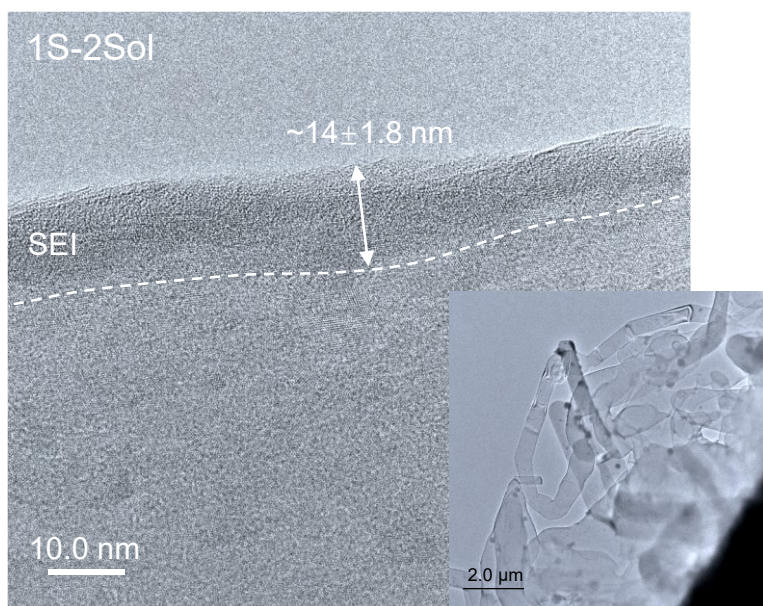

Fig. S6.18. Microstructure of deposited Li metal and interfacial phase from cryo-transmission electron microscopy (Cryo-TEM) from different electrolytes. The insets show the morphology of Li metal deposits at low magnification
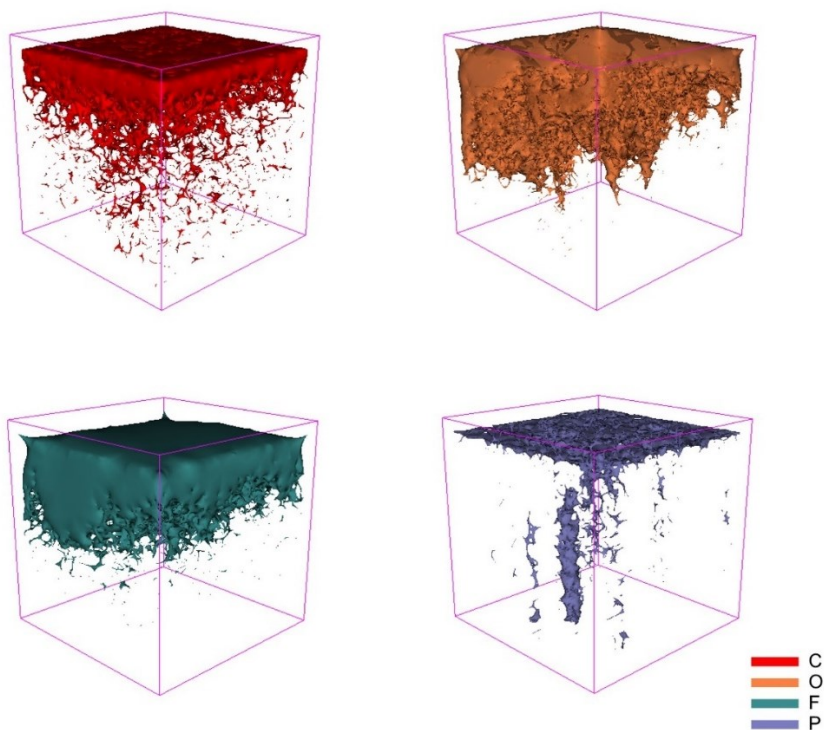
Fig. S6.19. Time-of-flight secondary ion mass spectrometry (TOF-SIMS) analysis of Li metal deposits after 20 cycles at 0.5 mA cm^{-2} for 2 h in 1S-5Sol electrolyte.
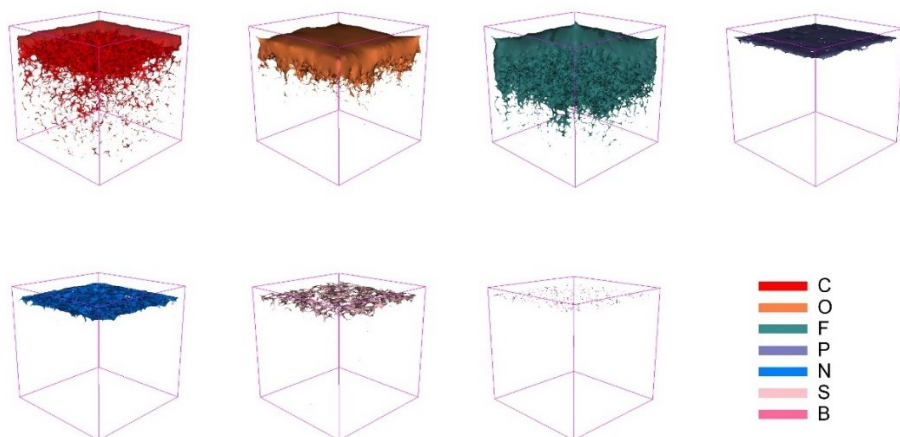

Fig. S6.20. TOF-SIMS analysis of Li metal deposits after 20 cycles at 0.5 mA cm^{-2} for 2 h in 5S-2Sol electrolyte.
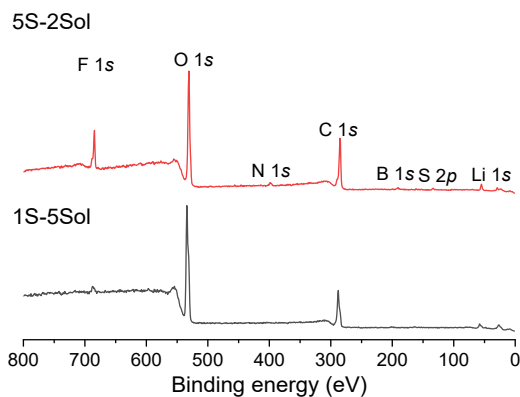
Fig. S6.21. Surveys of X-ray photoelectron spectroscopy (XPS) spectra of deposited Li metal in different electrolytes. Spectra were recorded immediately after 20 cycles from the surface of Cu foils.
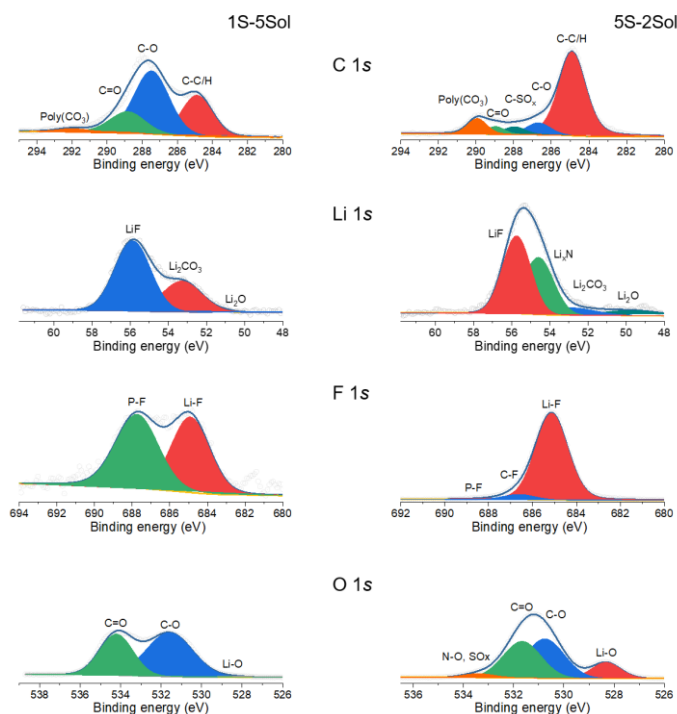

Fig. S6.22. XPS spectra on the surface of the Cu electrodes. The left panel is from the 1S-5Sol electrolyte and the right panel is from the 5S-2Sol electrolyte.
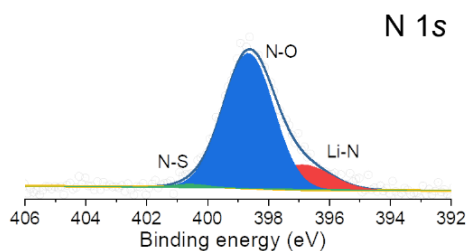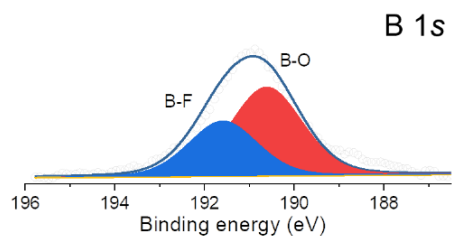
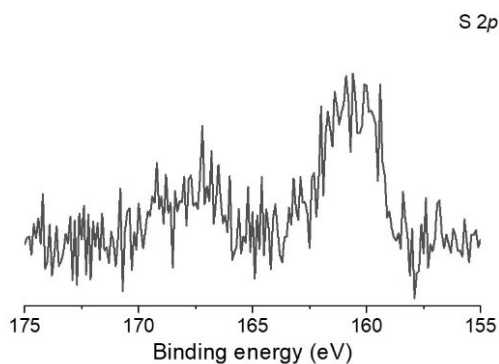**Fig. S6.23. XPS spectra on the surface of the Cu electrode in 5S-2Sol electrolyte.**

Fig. S6.24. S 2*p* spectrum on the surface of the Cu electrode in 5S-2Sol electrolyte.
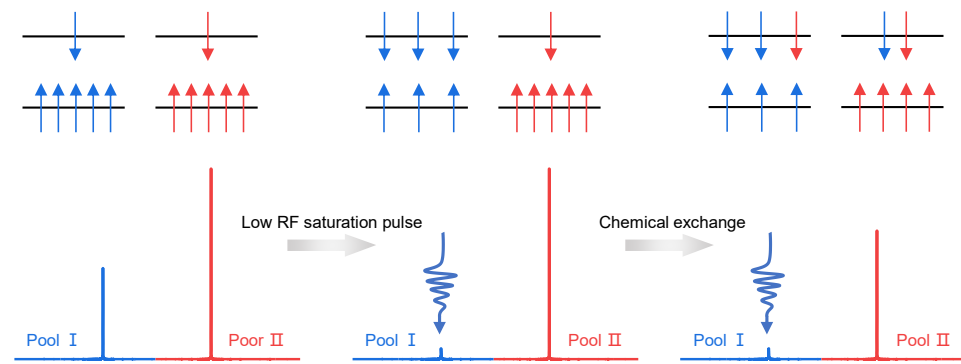
6

Fig. S6.25. Principles of chemical exchange saturation transfer (CEST) approach. For a two-pool system that has the same species at a specific resonance frequency (rf) (i.e., ^{7}Li in metal and SEI), one pool is directly invisible by NMR detection of the low-concentration "Pool I", the other is directly NMR detectable of the large "Pool II". Typically, a soft saturation pulse is applied on Pool I, and the signal in Pool II will decrease due to the chemical exchange with Pool I, where accounting for the change of the Pool II signal, allows probing the properties of Pool I in higher sensitivity.
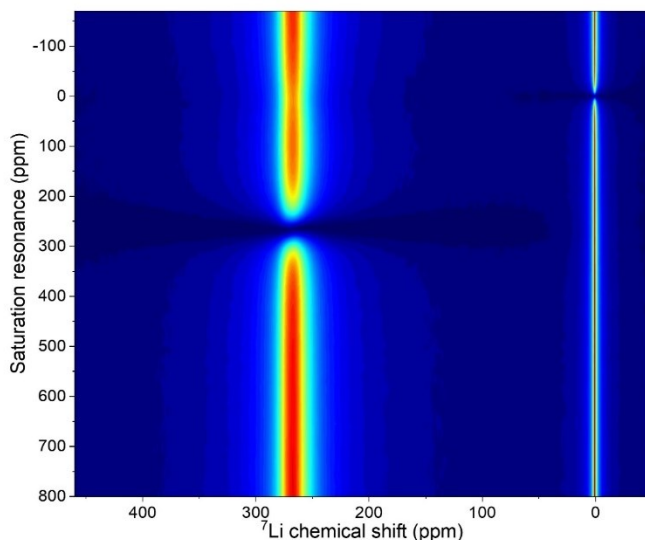

Fig. S6.26. Z-spectra obtained from Li metal deposits as a function of saturation frequencies in 5S-2Sol electrolyte. These spectra are acquired with a saturation pulse of 0.2 s in 3500 Hz as a function of saturation frequencies.
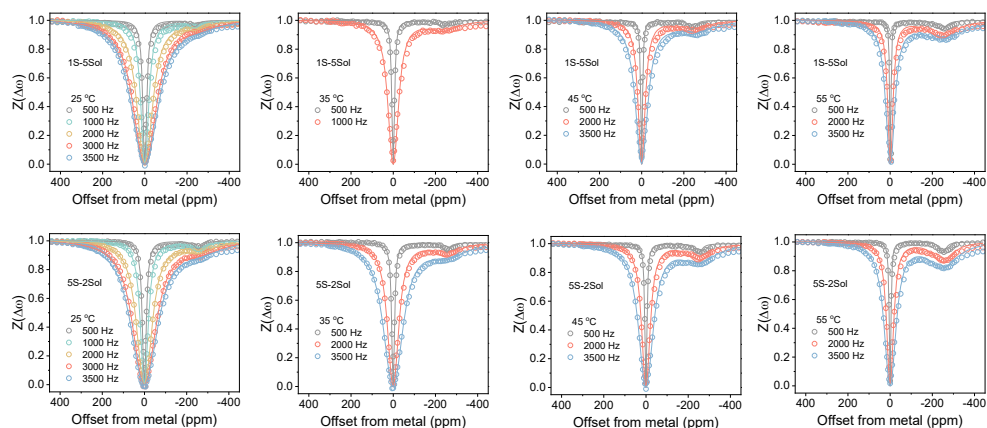
Fig. S6.27. *Z*-spectra obtained from Li metal deposits as a function of saturation frequencies for different electrolytes. *Z*-spectra obtained from Li metal deposits with a saturation time of 0.2 s at different temperatures with various saturation powers from 500 to 3500 Hz.

Fig. S6.28. EIS of Li‖Cu cells in different electrolytes. The Li‖Cu cells are cycled at the continuous Li plating/stripping at 1.0 mA cm^{-2} for 1 h (1.0 mAh cm^{-2}) for 20 cycles.
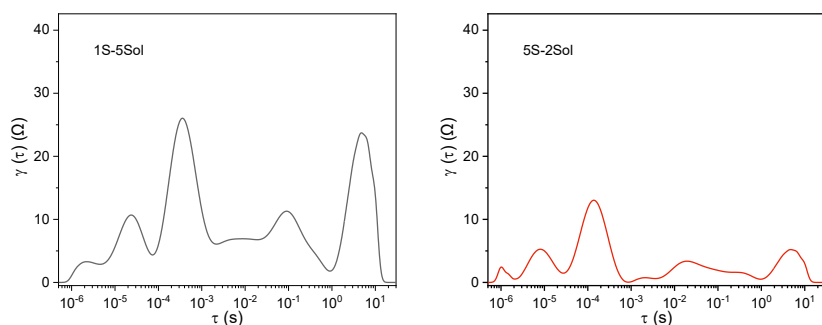
Fig. S6.29. Distribution of relaxation times (DRT) analysis of the cells. The Li‖Cu cells are firstly cycled at the continuous Li plating/stripping at 1.0 mA cm^{-2} for 1 h (1.0 mAh cm^{-2}) for 20 cycles.

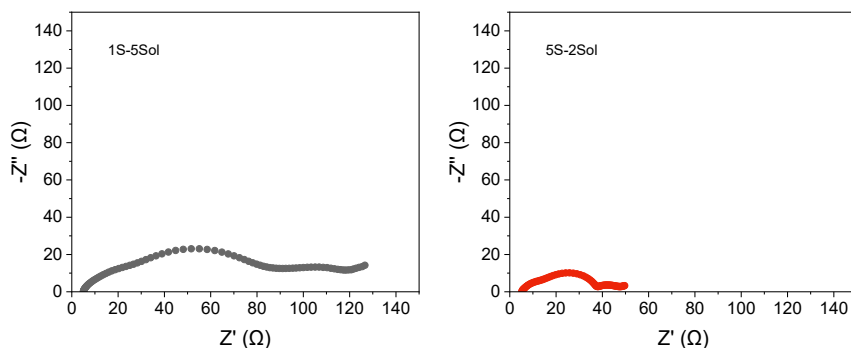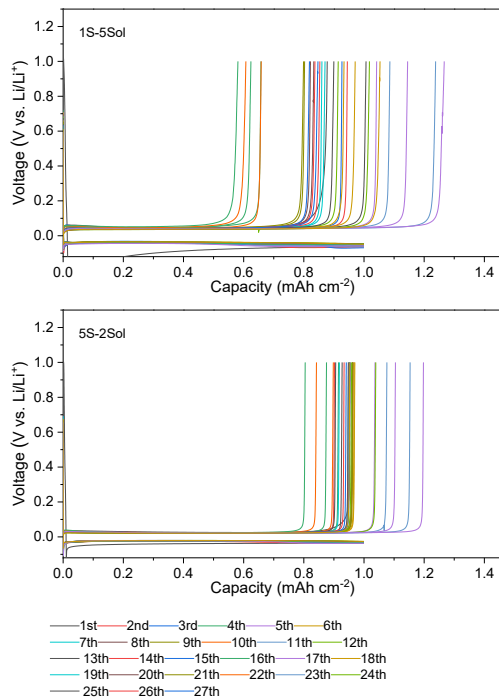**Fig. S6.30. Intermittent charge-discharge curves of Cu‖LiFePO₄ cells.** Cell is cycled at C/5 in different electrolytes The Cu‖LiFePO₄ cells are firstly cycled at the continuous charge-discharge at C/5 for two cycles then aged for different periods, and after those three continuous cycles using the same current density.
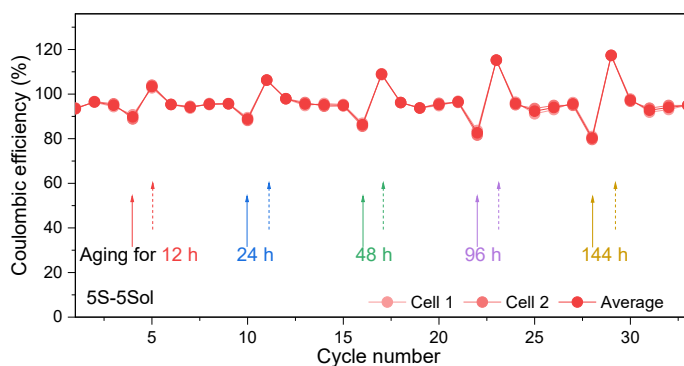
Fig. S6.31. Intermittent CE of electrolytes at different processes and various aging times in 5S-5Sol electrolyte.
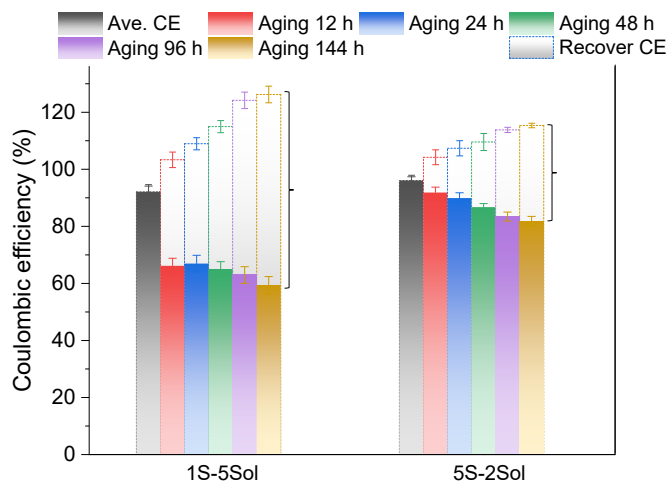
Fig. S6.32. Intermittent CE of electrolytes at different processes and various aging times. Brackets show the CE difference between the recover cycle and the aging cycle at various aging times.
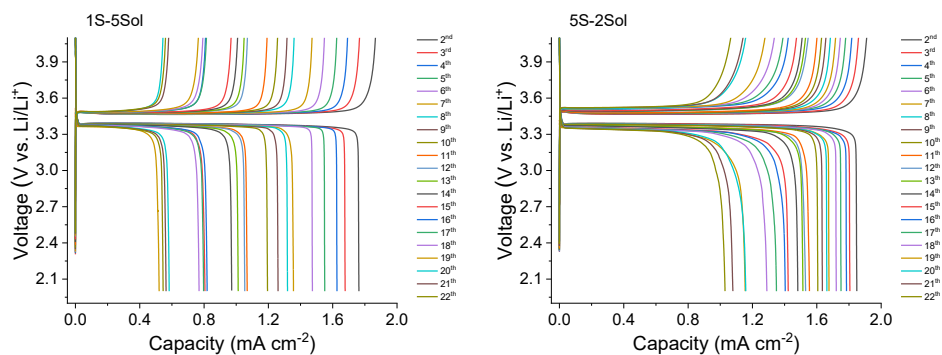
Fig. S6.33. Intermittent charge-discharge curves of Cu||LiFePO₄ cells. The Cu||LiFePO$_4$ cells are firstly cycled at the continuous charge-discharge at C/5 for two cycles then aged for different periods, and after those three continuous cycles using the same current density.

6
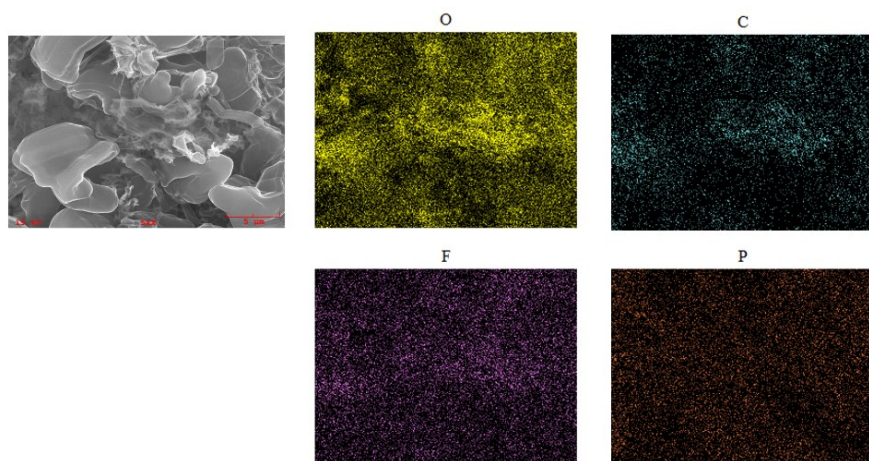
Fig. S6.34. SEM image and energy dispersive spectroscopy (EDS) mappings of deposited Li after aging 120 h from 1S-5Sol electrolyte. Cells were cycled at 1.0 mA cm^{-2} for 1 h (1.0 mA h cm^{-2}) after twenty cycles and then plated for 1 h.
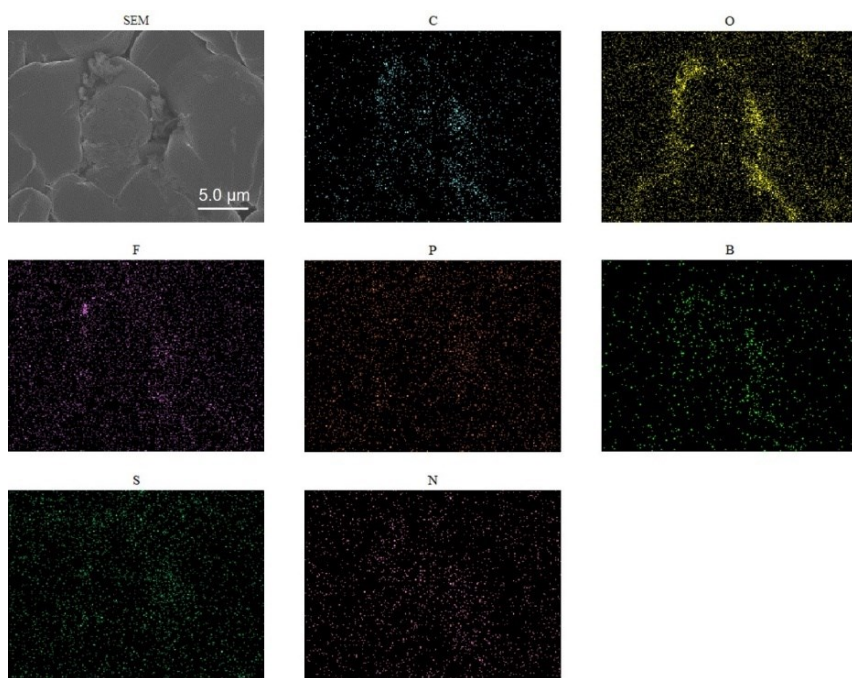
Fig. S6.35. SEM image and energy dispersive spectroscopy (EDS) mappings of deposited Li after aging 120 h from 5S-2Sol electrolyte. Cells were cycled at 1.0 mA cm^{-2} for 1 h (1.0 mA h cm^{-2}) after twenty cycles and then plated for 1 h.

6
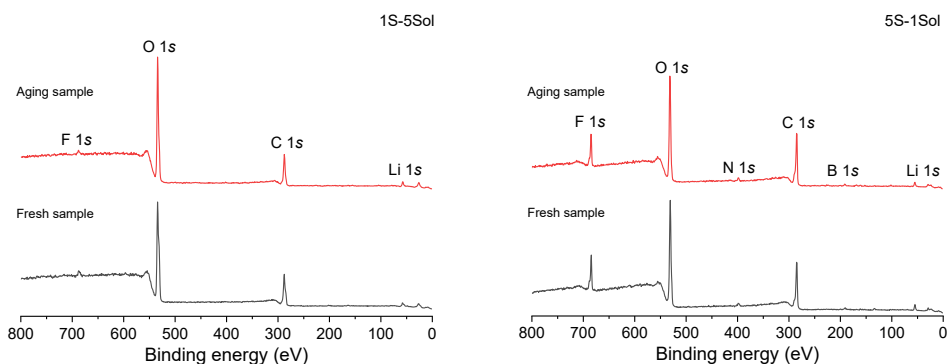
Fig. S6.36. Surveys XPS spectra of deposited Li metal in different electrolytes. The fresh samples were recorded immediately after 20 cycles from the surface of Cu foils and the aging samples present the Li‖Cu cells aged for 120 h after 20 cycles at 0.5 mA cm^{-2} for 1.0 mAh cm^{-2}.
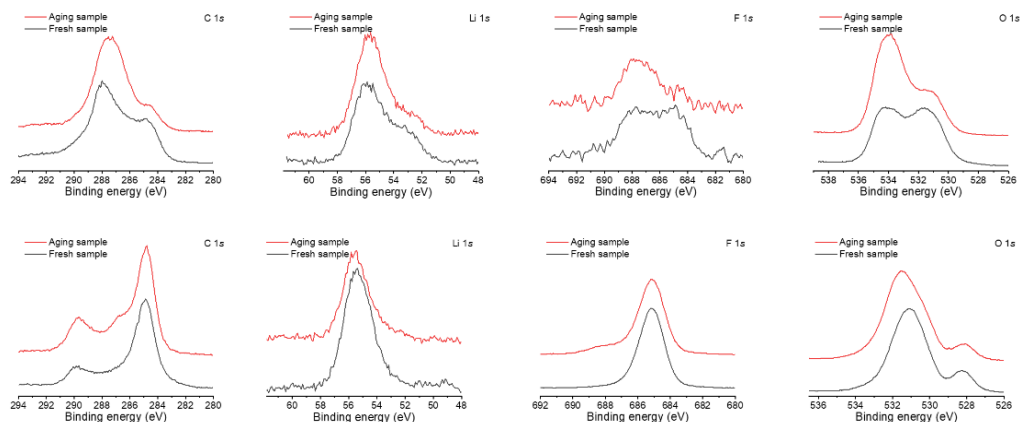
Fig. S6.37. Surveys XPS spectra of deposited Li metal in different electrolytes. The spectra of the Li metal deposition with and without resting period are collected. The top panel shows the spectra from the samples in the 1S-5Sol electrolyte, and the bottom panel shows the spectra from the samples in the 5S-2Sol electrolyte.

6
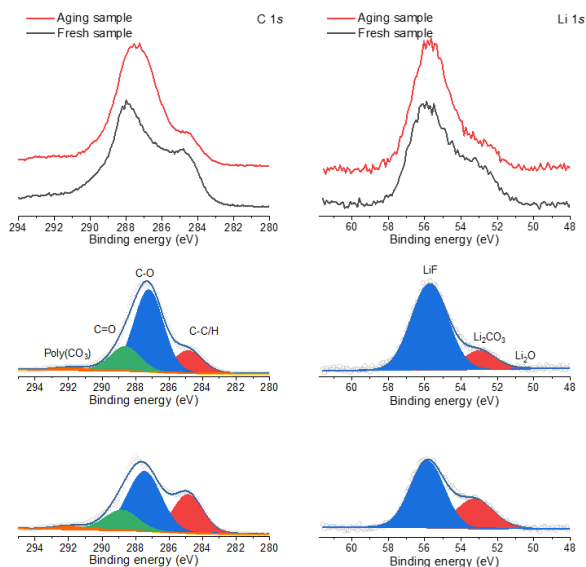
Fig. S6.38. XPS spectra on the surface of the Cu electrodes 1S-5Sol electrolyte. The panel in the middle is the peak deconvolution of the spectra after aging, and the bottom panel is the peak deconvolution of the spectra for the fresh sample.
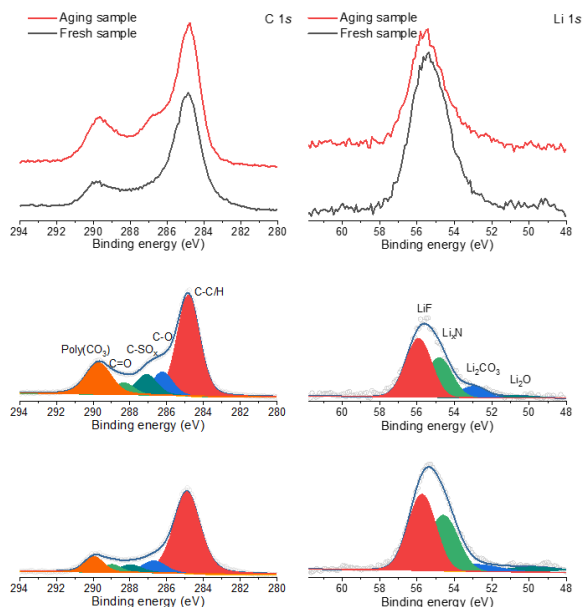
Fig. S6.39. XPS spectra on the surface of the Cu electrodes 5S-2Sol electrolyte. The panel in the middle is the peak deconvolution of the spectra after aging, and the bottom panel is the peak deconvolution of the spectra for the fresh sample.

6
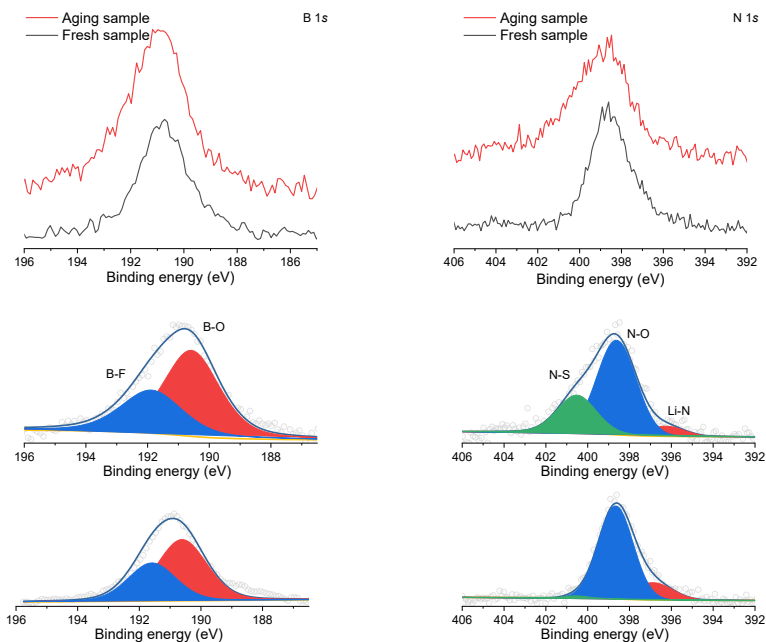
Fig. S6.40. B 1*s* and N 1*s* XPS spectra on the surface of the Cu electrode in 5S-2Sol electrolyte. The panel in the middle is the peak deconvolution of the spectra after aging, and the bottom panel is the peak deconvolution of the spectra for the fresh sample.
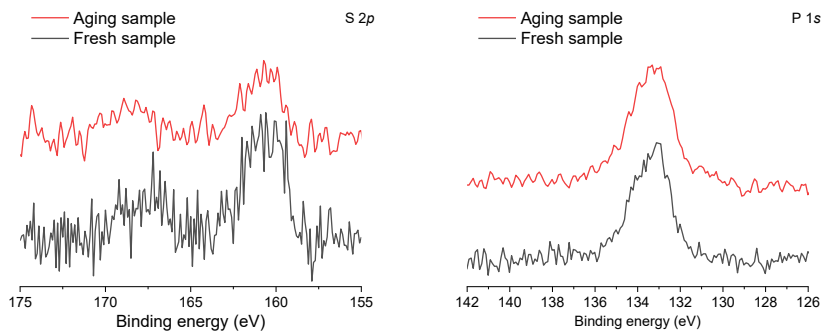
Fig. S6.41. S 2*p* and P 1*s* XPS spectra on the surface of the Cu electrode in 5S-2Sol electrolyte.

6
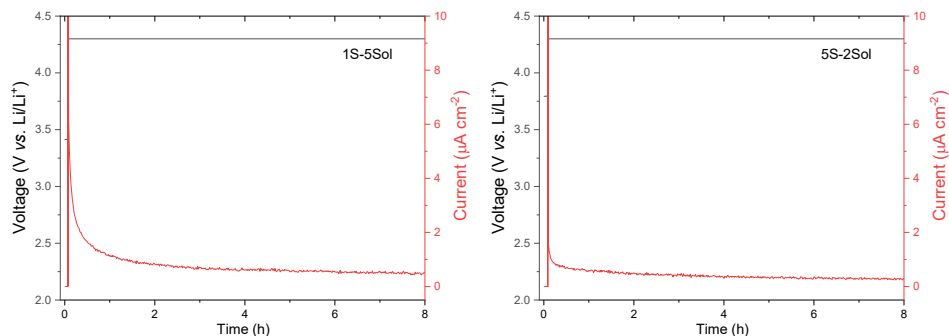
Fig. S6.42. Potentiostatic charge profiles. Li‖Al coin cells were used to study the corrosion current in different electrolytes at the polarization potential of 4.3 V vs. Li/Li$^+$ for 8 h, where both electrolytes show a stable anodic current under the same conditions.
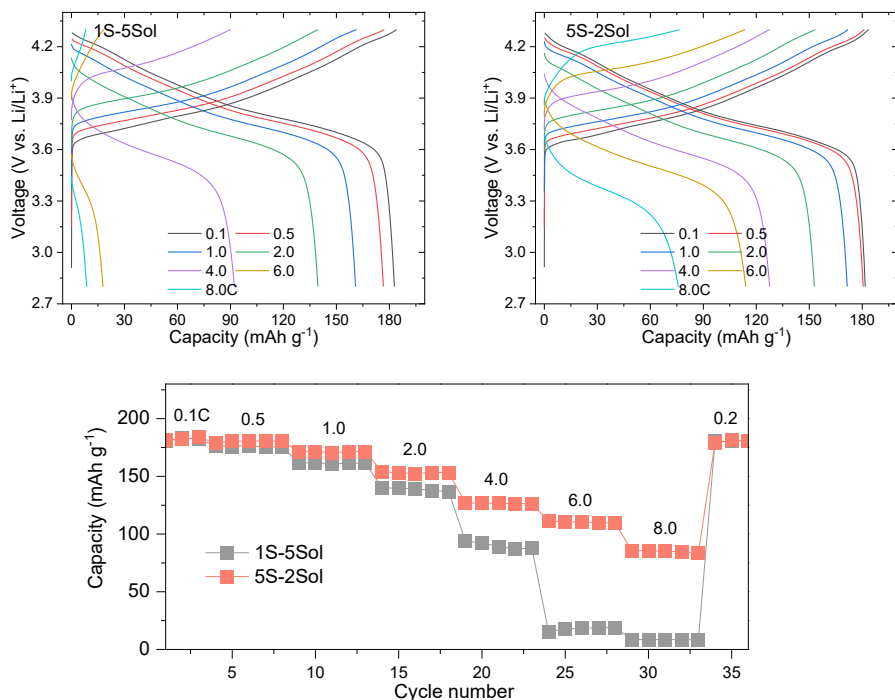
Fig. S6.43. Rate performance of Li‖NMC811 cells cycled between 2.8-4.3 V under various current densities in different electrolytes. Galvanostatic charge/discharge curves and the discharge capacities are shown under various current densities in different electrolytes.

Fig. S6.44. Anode-free NCM811||Cu pouch cell. The anode-free NCM811||Cu pouch cell is after preparation.
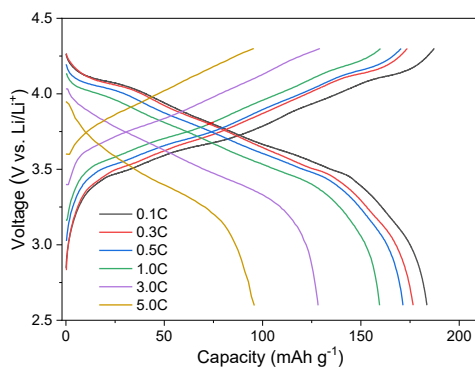
Fig. S6.45. Galvanostatic charge/discharge curves of NCM811||Si/graphite cells in the voltage range of 2.6-4.3 V. The capacity ratio of the negative over the positive electrode is in the range of 1.1~1.15. Si/G presents the Si/graphite composite anode with a capacity of 450 mAh g^{-1}.
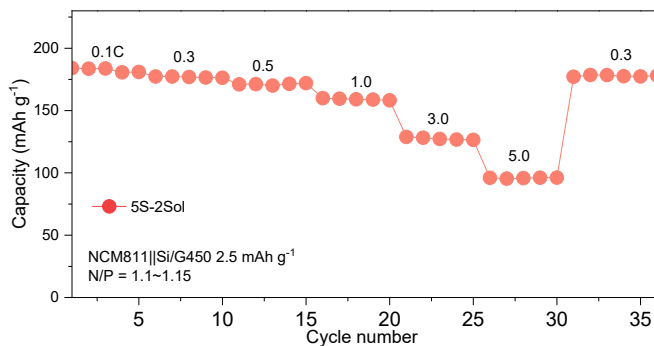
Fig. S6.46. Rate performance of NCM811||Si/graphite cells cycled between 2.6-4.3 V under various current densities. The capacity ratio of the negative over the positive electrode is in the range of 1.1~1.15. Si/G presents the Si/graphite composite anode with a capacity of 450 mAh g^{-1}.
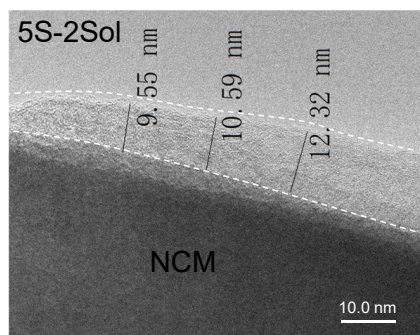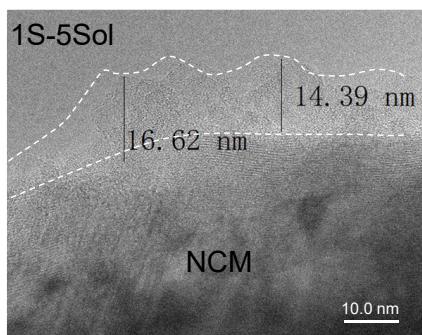
Fig. S6.47. High-resolution scanning transmission electron microscopy (STEM) images of NCM811 cathode after cycling in different electrolytes.
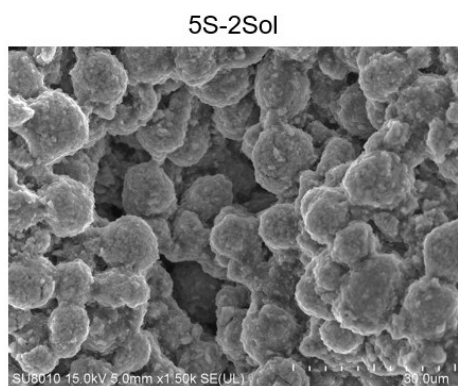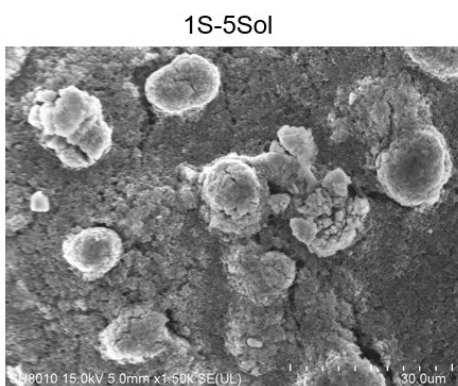
Fig. S6.48. SEM images of NCM811 cathode after 50 cycles. It can be observed that the secondary particles are damaged during cycling in 1S-5Sol electrolyte.
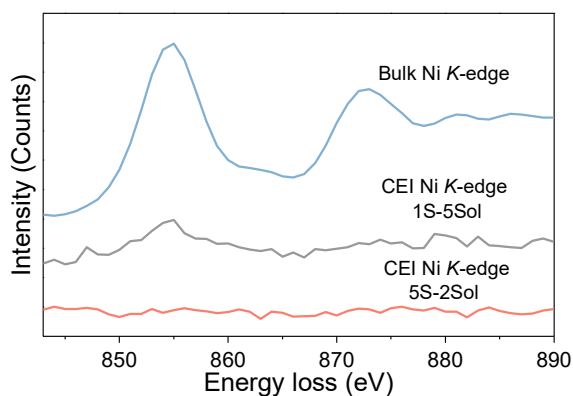
Fig. S6.49. Electron energy loss spectroscopy (EELS) of Ni *K*-edge in CEI after cycling in different electrolytes and the bulk.
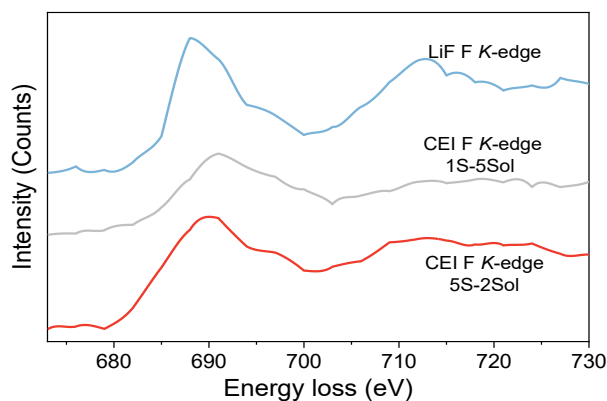
Fig. S6.50. EELS of F *K*-edge in CEI after cycling in different electrolytes. LiF is used as a reference.
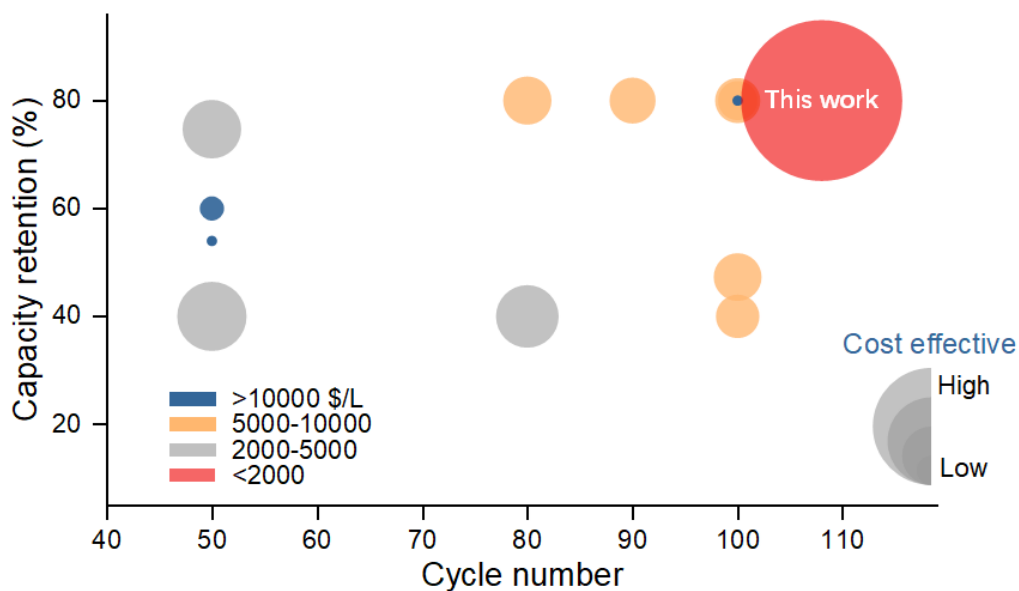
Fig. S6.51. Comparative analysis of electrolyte cost and battery performance in anode-free cells. The data are based on a selection of electrolytes in Table S6.3. The color scale indicates various cost levels according to Table S6.4. Bubble size reflects the cost effectiveness, determined by the total cost of each electrolyte relative to the highest cost among all the electrolytes considered. It can be noted that this work shows largest advantage in cost effectiveness and best cycling performance compared to other electrolytes.

Supplementary Tables

Table S6.1. Fitting parameters and boundaries.

Parameter	Starting value	Lower boundary	Upper boundary
$\Delta\omega_{Li}$ [ppm]	0	-5	5
$R_{2,\,Li}$ [s^{-1}]	1000	0.5	2×10^4
$\Delta\omega_{SEI}$ [ppm]	-265	-215	315
K_{SEI-Li} [Hz]	1000	1	1×10^6
f_{SEI}	0.01	0	2
$R_{2,\,SEI}$ [s^{-1}]	50	0	7×10^4

Table S6.2. Relaxation parameters from experiments and fitting two-pool BMC solution.

Electrolyte	T (°C)	R1$_{Metal-E}$ (Hz)	R2$_{Metal-E}$ (Hz)	K$_{SEI-Metal}$ (Hz)	R2$_{Metal-F}$ (Hz)	R2$_{SEI-F}$ (kHz)	GOF(R^2)
	25	7.0	1360	58±7	936±25	30±11	0.76
	35	7.5	780	87±19	492±31	33±15	0.84
1S-5Sol	45	7.8	512	129±15	240±12	39±22	0.78
	55	8.2	366	183±21	125±9	41±25	0.73
	25	7.2	1200	96±8	984±17	28±10	0.86
	35	7.6	820	120±8	511±19	30±14	0.84
5S-2Sol	45	8.1	504	168±10	298±12	38±14	0.83
	55	8.4	328	216±13	191±8	40±13	0.83

6

Table S6.3. Parameters of anode-free 3.5-Ah pouch cell.

Cell component	Specification	Parameters
Cathode (NCM with Al current collector)	Active material ratio	93
	Size (cm×cm)	7×6
	Number	12
	Weight (g)	17.216
	Thickness (μm)	6
Collector (Cu)	Size (cm×cm)	7.1×6.1
	Number	13
	Weight (g)	3.16
Electrolyte	Electrolyte/Capacity (g Ah^{-1})	2.0
	Weight (g)	7.0
Separator	Weight (g)	0.825
Package and tabs	Weight (g)	3
	N/P	0
Full cell	Discharge capacity (Ah)	3.5
	Discharge energy (Wh)	13.475
	Total weight (g)	31.55
	Specific energy (Wh kg^{-1})	427.1

6

Table S6.4. Comparison of anode-free Li-metal battery performance with different electrolytes.

Electrolyte	Cathode	Anode	Cycles	Capacity retention	Ref.
2 M LiPF$_6$ EC/DEC/FEC (1:1:2.5)	NCM111 1.6 mAh cm^{-2}	Cu	50	40%	[61]
1 M LiTFSI+2 M LiFSI+0.6 M LiNO$_3$ DME/DOL (1:1)	LiFePO$_4$ 5 mg cm^{-2}	Cu	100	40%	[62]
4 M LiFSI DME	LiFePO$_4$ 1.7 mAh cm^{-2}	Cu	50	60%	[63]
1 M LiFSI DME/HFE (1:2)	NCM811 3.0 mAh cm^{-2}	Cu	50	74.7%	[64]
0.6 M LiDFOB + 0.6 M LiBF$_4$ FEC/DEC (1:2)	NCM523 16 mg cm^{-2}	Cu	80	80%	[65]
1 M LiPF$_6$ FEC/TTE/EMC (3:5:2)	NCM111 12 mg cm^{-2}	Cu	80	40%	[66]
1.5 M LiFSI DME/TTE (1.2:3 by molar)	NMC622 4.0 mAh cm^{-2}	Cu	100	80%	[67]
1.8 M LiDFOB + 0.4 M LiBF$_4$ FEC/DEC (1:2)	NCM523 16 mg cm^{-2}	Cu	90	80%	[68]
7 M LiFSI FEC	LiNi$_{0.5}$Mn$_{1.5}$O$_2$ 1.83 mAh cm^{-2}	Cu	50	54%	[69]
1 M LiFSI FDMB	NCM811 4.2 mAh cm^{-2}	Cu	100	80%	[70]
1 M LiBF4 + 1 M LiDFOB FEP/FEC (1:2)	NCM811 4.64 mAh cm^{-2}	Cu	100	80%	[71]
2 M LiFSI+2 M LiNO$_3$ DME	NCM622 2.0 mAh cm^{-2}	Cu	100	47.3%	[72]
5S-2Sol	NCM811 3.5 mAh cm^{-2}	Cu	100	82%	This work

6

Table S6.5. Comparison of the prices for Li salts used in the reported liquid electrolytes for Li-metal batteries.

Salt	Chemical name	Product Number	Size (g)	Price ($)	Unit price, ($/kg)
LiPF$_6$	thium Hexafluorophosphate	L0146	100	261.00	2610
LiClO$_4$	thium Perchlorate	L0379	500	240.00	480
LiFSI	thium Bis(fluorosulfonyl)imide	L0281	25	357.00	14280
LiTFSI	thium Bis(trifluoromethanesulfonyl)imide	B2542	250	495.00	1980
LiTFO	thium Trifluoromethanesulfonate	T1548	25	68.00	2720
LiDFOB*	thium difluoro(oxalato)borate	774138	25	335.00	13400
LiBOB	thium Bis(oxalate)borate	L0367	25	205.00	8200
LiBF$_4$	thium Tetrafluoroborate	L0133	25	142.00	5680
LiPF$_2$O$_2$	thium Phosphorodifluoridate	L0375	25	247.00	9880
LiNO$_3$*	thium nitrate	227986	1000	227.00	227

All prices listed here are based on TCI pricing data unless noted specifically.
*Price data are from MilliporeSigma.

6

Table S6.6. Comparison of the prices for solvents used for the reported liquid electrolytes in Li-metal batteries. All prices listed here are from TCI unless indicated specifically.

Solvent	Chemical name	Product Number	Size (ml)	Price ($)	Unit price, ($/L)
EC	:hylene carbonate	E0076	500	29.00	58
DMC	imethyl carbonate	C0053	500	43.00	86
DEC	iethyl carbonate	C0041	500	40.00	80
EMC	hyl methyl carbonate	C1342	25	113.00	4520
VC	inylene carbonate	V0015	25	237.00	9480
PC	ropylene carbonate	P0525	500	43.00	86
FEC	uoroethylene carbonate	F0731	25	147.00	5880
DME	imethoxyethane	D0634	500	57.00	114
DEGDME	iethylene glycol dimethyl ether	B0498	500	49.00	98
DOL	3-Dioxolane	D5539	500	47.00	94
TMP	rimethyl phosphate	P0271	500	53.00	106
TEP	iethyl phosphate	P0270	500	48.00	96
DMSO	imethyl sulfoxide	D5293	500	66.00	132
THF	etrahydrofuran	T0104	500	26.00	52
FEMC	ethyl 2,2,2-trifluoroethyl carbonate	M3376	25	454.00	18160
FEP	ethyl 3,3,3-Trifluoropropionate	M2783	5	272.00	54400
HFE	1,2,2-tetrafluoroethyl-2,2,2-trifluoroethyl ether	T3057	25	66.00	2640
TTE	etrafluoroethyl-2,2,3,3-Tetrafluoropropyl Ether	T3069	25	56.00	2240
BTFE	is(2,2,2-trifluoroethyl) ether	B1293	5	140.00	28000
TFEO*	ris(2,2,2-trilfuoroethyl) orthoformate	ATE517251825	1	353.60	353600

*They are taken from MilliporeSigma.

6

Table S6.7. Cost analysis of various electrolytes.

Electrolyte	Salt cost ($/L)	Solvent cost ($/L)	Total cost ($/L)	Ref.
2 M LiPF$_6$ EC/DEC/FEC (1:1:2.5)	792.94	2995.20	3788.14	[61]
1 M LiTFSI+2 M LiFSI+0.6 M LiNO$_3$ DME/DOL (1:1)	5920.52	104.00	6024.52	[62]
4 M LiFSI DME	10685.44	114.00	10799.44	[63]
1 M LiFSI DME/HFE(1:2)	2671.36	1798.00	4469.36	[64]
0.6 M LiDFOB + 0.6 M LiBF$_4$ FEC/DEC (1:2)	1475.40	3946.67	5422.06	[65]
1 M LiPF$_6$ FEC/TTE/EMC (3:5:2)	396.47	3788.00	4184.47	[66]
1.5 M LiFSI DME/TTE (1:3.65)	4007.04	1782.80	5789.84	[67]
1.8 M LiDFOB + 0.4 M LiBF$_4$ FEC/DEC (1:2)	3680.72	2013.33	5694.06	[68]
7 M LiFSI FEC	18699.52	5880.00	24579.52	[69]
1 M LiFSI FDMB[a]	2671.36	~4000	6671.36	[70]
1 M LiBF$_4$ + 1 M LiDFOB FEP/FEC (1:2)	2459.00	22053.33	24512.33	[71]
2 M LiFSI+2 M LiNO$_3$ DME	5374.02	114.00	5488.02	[72]
5S-2Sol	1267.27	359.55	1626.82	This work

[a]The price of this solvent is calculated based on average level of the fluorinated solvent.

6

References

1   J. B. Goodenough & Y. Kim. Challenges for Rechargeable Li Batteries. *Chemistry of Materials* **22**, 587-603, (2010).

2   W. Li, B. Song & A. Manthiram. High-voltage positive electrode materials for lithium-ion batteries. *Chemical Society Reviews* **46**, 3006-3059, (2017).

3   M. N. Obrovac & L. Christensen. Structural Changes in Silicon Anodes during Lithium Insertion/Extraction. *Electrochemical and Solid-State Letters* **7**, A93, (2004).

4   E. Peled. The Electrochemical Behavior of Alkali and Alkaline Earth Metals in Nonaqueous Battery Systems—The Solid Electrolyte Interphase Model. *Journal of The Electrochemical Society* **126**, 2047, (1979).

5   E. Peled & S. Menkin. Review—SEI: Past, Present and Future. *Journal of The Electrochemical Society* **164**, A1703, (2017).

6   L. Suo, O. Borodin, T. Gao, M. Olguin, J. Ho, X. Fan, C. Luo, C. Wang & K. Xu. "Water-in-salt" electrolyte enables high-voltage aqueous lithium-ion chemistries. *Science* **350**, 938-943, (2015).

7   C. Wang, Y. S. Meng & K. Xu. Perspective—Fluorinating Interphases. *Journal of The Electrochemical Society* **166**, A5184, (2019).

8   Q. Zhao, S. Stalin & L. A. Archer. Stabilizing metal battery anodes through the design of solid electrolyte interphases. *Joule* **5**, 1119-1142, (2021).

9   K. Xu. Interfaces and interphases in batteries. *Journal of Power Sources* **559**, 232652, (2023).

10 Y. Yamada, K. Furukawa, K. Sodeyama, K. Kikuchi, M. Yaegashi, Y. Tateyama & A. Yamada. Unusual Stability of Acetonitrile-Based Superconcentrated Electrolytes for Fast-Charging Lithium-Ion Batteries. *Journal of the American Chemical Society* **136**, 5039-5046, (2014).

11 Q. Wang, C. Zhao, S. Wang, J. Wang, M. Liu, S. Ganapathy, X. Bai, B. Li & M. Wagemaker. Clarifying the Relationship between the Lithium Deposition Coverage and Microstructure in Lithium Metal Batteries. *Journal of the American Chemical Society* **144**, 21961-21971, (2022).

12 J. Han, L. Kiss, H. Mei, A. M. Remete, M. Ponikvar-Svet, D. M. Sedgwick, R. Roman, S. Fustero, H. Moriwaki & V. A. Soloshonok. Chemical Aspects of Human and Environmental Overload with Fluorine. *Chemical Reviews* **121**, 4678-4742, (2021).

13 G. Hernández, R. Mogensen, R. Younesi & J. Mindemark. Fluorine-Free Electrolytes for Lithium and Sodium Batteries. *Batteries & Supercaps* **5**, e202100373, (2022).

14 M. D. Tikekar, S. Choudhury, Z. Tu & L. A. Archer. Design principles for electrolytes and interfaces for stable lithium-metal batteries. *Nature Energy* **1**, 16114, (2016).

6

15 Y. Qin, Z. Chen, J. Liu & K. Amine. Lithium Tetrafluoro Oxalato Phosphate as Electrolyte Additive for Lithium-Ion Cells. *Electrochemical and Solid-State Letters* **13**, A11, (2010).

16 P. Lu & S. J. Harris. Lithium transport within the solid electrolyte interphase. *Electrochemistry Communications* **13**, 1035-1037, (2011).

17 K. Xu. Nonaqueous Liquid Electrolytes for Lithium-Based Rechargeable Batteries. *Chemical Reviews* **104**, 4303-4418, (2004).

18 D. Aurbach. Review of selected electrode–solution interactions which determine the performance of Li and Li ion batteries. *Journal of Power Sources* **89**, 206-218, (2000).

19 Q. Zhang, J. Pan, P. Lu, Z. Liu, M. W. Verbrugge, B. W. Sheldon, Y.-T. Cheng, Y. Qi & X. Xiao. Synergetic Effects of Inorganic Components in Solid Electrolyte Interphase on High Cycle Efficiency of Lithium Ion Batteries. *Nano Letters* **16**, 2011-2016, (2016).

20 A. Wang, S. Kadam, H. Li, S. Shi & Y. Qi. Review on modeling of the anode solid electrolyte interphase (SEI) for lithium-ion batteries. *npj Computational Materials* **4**, 15, (2018).

21 E. Peled, D. Golodnitsky & G. Ardel. Advanced Model for Solid Electrolyte Interphase Electrodes in Liquid and Polymer Electrolytes. *Journal of The Electrochemical Society* **144**, L208, (1997).

22 J. Christensen & J. Newman. A Mathematical Model for the Lithium-Ion Negative Electrode Solid Electrolyte Interphase. *Journal of The Electrochemical Society* **151**, A1977, (2004).

23 L. Raguette & R. Jorn. Ion Solvation and Dynamics at Solid Electrolyte Interphases: A Long Way from Bulk? *The Journal of Physical Chemistry C* **122**, 3219-3232, (2018).

24 J. Janek & W. G. Zeier. A solid future for battery development. *Nature Energy* **1**, 16141, (2016).

25 I. Gurevitch, R. Buonsanti, A. A. Teran, B. Gludovatz, R. O. Ritchie, J. Cabana & N. P. Balsara. Nanocomposites of Titanium Dioxide and Polystyrene-Poly(ethylene oxide) Block Copolymer as Solid-State Electrolytes for Lithium Metal Batteries. *Journal of The Electrochemical Society* **160**, A1611, (2013).

26 J. Zheng, M. Tang & Y.-Y. Hu. Lithium Ion Pathway within Li$_7$La$_3$Zr$_2$O$_{12}$-Polyethylene Oxide Composite Electrolytes. *Angewandte Chemie International Edition* **55**, 12538-12542, (2016).

27 J. W. Fergus. Ceramic and polymeric solid electrolytes for lithium-ion batteries. *Journal of Power Sources* **195**, 4554-4569, (2010).

28 Y. Rosenfeld. Relation between the transport coefficients and the internal entropy of simple systems. *Physical Review A* **15**, 2545-2549, (1977).

6

29 J. C. Dyre. Perspective: Excess-entropy scaling. *The Journal of Chemical Physics* **149**, 210901, (2018).

30 J. Luo & N. Zhou. High-entropy grain boundaries. *Communications Materials* **4**, 7, (2023).

31 R. A. Marcus & N. Sutin. Electron transfers in chemistry and biology. *Biochimica et Biophysica Acta (BBA) - Reviews on Bioenergetics* **811**, 265-322, (1985).

32 Q. Wang, C. Zhao, J. Wang, Z. Yao, S. Wang, S. G. H. Kumar, S. Ganapathy, S. Eustace, X. Bai, B. Li & M. Wagemaker. High entropy liquid electrolytes for lithium batteries. *Nature Communications* **14**, 440, (2023).

33 C. V. Amanchukwu, Z. Yu, X. Kong, J. Qin, Y. Cui & Z. Bao. A New Class of Ionically Conducting Fluorinated Ether Electrolytes with High Electrochemical Stability. *Journal of the American Chemical Society* **142**, 7393-7403, (2020).

34 Q. Wang, Z. Yao, C. Zhao, T. Verhallen, D. P. Tabor, M. Liu, F. Ooms, F. Kang, A. Aspuru-Guzik, Y.-S. Hu, M. Wagemaker & B. Li. Interface chemistry of an amide electrolyte for highly reversible lithium metal batteries. *Nature Communications* **11**, 4188, (2020).

35 H. J. Chang, A. J. Ilott, N. M. Trease, M. Mohammadi, A. Jerschow & C. P. Grey. Correlating Microstructural Lithium Metal Growth with Electrolyte Salt Depletion in Lithium Batteries Using 7Li MRI. *Journal of the American Chemical Society* **137**, 15209-15216, (2015).

36 R. Bhattacharyya, B. Key, H. Chen, A. S. Best, A. F. Hollenkamp & C. P. Grey. In situ NMR observation of the formation of metallic lithium microstructures in lithium batteries. *Nature Materials* **9**, 504-510, (2010).

37 A. B. Gunnarsdóttir, C. V. Amanchukwu, S. Menkin & C. P. Grey. Noninvasive In Situ NMR Study of "Dead Lithium" Formation and Lithium Corrosion in Full-Cell Lithium Metal Batteries. *Journal of the American Chemical Society* **142**, 20814-20827, (2020).

38 X. Wang, Y. Li & Y. S. Meng. Cryogenic Electron Microscopy for Characterizing and Diagnosing Batteries. *Joule* **2**, 2225-2234, (2018).

39 J.-H. Song, J.-T. Yeon, J.-Y. Jang, J.-G. Han, S.-M. Lee & N.-S. Choi. Effect of Fluoroethylene Carbonate on Electrochemical Performances of Lithium Electrodes and Lithium-Sulfur Batteries. *Journal of The Electrochemical Society* **160**, A873, (2013).

40 S. Jiao, X. Ren, R. Cao, M. H. Engelhard, Y. Liu, D. Hu, D. Mei, J. Zheng, W. Zhao, Q. Li, N. Liu, B. D. Adams, C. Ma, J. Liu, J.-G. Zhang & W. Xu. Stable cycling of high-voltage lithium metal batteries in ether electrolytes. *Nature Energy* **3**, 739-746, (2018).

6

41 S. Leroy, H. Martinez, R. Dedryvère, D. Lemordant & D. Gonbeau. Influence of the lithium salt nature over the surface film formation on a graphite electrode in Li-ion batteries: An XPS study. *Applied Surface Science* **253**, 4895-4905, (2007).

42 S. Forsén & R. A. Hoffman. Study of Moderately Rapid Chemical Exchange Reactions by Means of Nuclear Magnetic Double Resonance. *The Journal of Chemical Physics* **39**, 2892-2901, (1963).

43 K. M. Ward, A. H. Aletras & R. S. Balaban. A New Class of Contrast Agents for MRI Based on Proton Chemical Exchange Dependent Saturation Transfer (CEST). *Journal of Magnetic Resonance* **143**, 79-87, (2000).

44 D. Columbus, V. Arunachalam, F. Glang, L. Avram, S. Haber, A. Zohar, M. Zaiss & M. Leskes. Direct Detection of Lithium Exchange across the Solid Electrolyte Interphase by 7Li Chemical Exchange Saturation Transfer. *Journal of the American Chemical Society* **144**, 9836-9844, (2022).

45 M. Zaiss & P. Bachert. Chemical exchange saturation transfer (CEST) and MR Z-spectroscopy in vivo: a review of theoretical approaches and methods. *Physics in Medicine & Biology* **58**, R221, (2013).

46 E. Vinogradov, A. D. Sherry & R. E. Lenkinski. CEST: From basic principles to applications, challenges and opportunities. *Journal of Magnetic Resonance* **229**, 155-172, (2013).

47 R. G. Bryant. The dynamics of water-protein interactions. *Annual review of biophysics biomolecular structure* **25**, 29-53, (1996).

48 V. Guivel-Scharen, T. Sinnwell, S. D. Wolff & R. S. Balaban. Detection of Proton Chemical Exchange between Metabolites and Water in Biological Tissues. *Journal of Magnetic Resonance* **133**, 36-45, (1998).

49 H. M. McConnell. Reaction Rates by Nuclear Magnetic Resonance. *The Journal of Chemical Physics* **28**, 430-431, (1958).

50 D. E. Woessner, S. Zhang, M. E. Merritt & A. D. Sherry. Numerical solution of the Bloch equations provides insights into the optimum design of PARACEST agents for MRI. *Magnetic Resonance in Medicine* **53**, 790-799, (2005).

51 M. Zaiss & P. Bachert. Exchange-dependent relaxation in the rotating frame for slow and intermediate exchange – modeling off-resonant spin-lock and chemical exchange saturation transfer. *NMR in Biomedicine* **26**, 507-518, (2013).

52 Y. Lu, C.-Z. Zhao, J.-Q. Huang & Q. Zhang. The timescale identification decoupling complicated kinetic processes in lithium batteries. *Joule* **6**, 1172-1198, (2022).

6

53 P. Keil, S. F. Schuster, J. Wilhelm, J. Travi, A. Hauser, R. C. Karl & A. Jossen. Calendar Aging of Lithium-Ion Batteries. *Journal of The Electrochemical Society* **163**, A1872, (2016).

54 C. Zhan, T. Wu, J. Lu & K. Amine. Dissolution, migration, and deposition of transition metal ions in Li-ion batteries exemplified by Mn-based cathodes – a critical review. *Energy & Environmental Science* **11**, 243-257, (2018).

55 R. G. Bryant. The dynamics of water-protein interactions. *Annu Rev Biophys Biomol Struct* **25**, 29-53, (1996).

56 P. C. M. van Zijl & N. N. Yadav. Chemical exchange saturation transfer (CEST): What is in a name and what isn't? *Magnetic Resonance in Medicine* **65**, 927-948, (2011).

57 M. Zaiss, G. Angelovski, E. Demetriou, M. T. McMahon, X. Golay & K. Scheffler. QUESP and QUEST revisited – fast and accurate quantitative CEST experiments. *Magnetic Resonance in Medicine* **79**, 1708-1721, (2018).

58 M. Zaiss, M. Schnurr & P. Bachert. Analytical solution for the depolarization of hyperpolarized nuclei by chemical exchange saturation transfer between free and encapsulated xenon (HyperCEST). *The Journal of Chemical Physics* **136**, 144106, (2012).

59 S. Goerke, M. Zaiss & P. Bachert. Characterization of creatine guanidinium proton exchange by water-exchange (WEX) spectroscopy for absolute-pH CEST imaging in vitro. *NMR in Biomedicine* **27**, 507-518, (2014).

60 T. H. Wan, M. Saccoccio, C. Chen & F. Ciucci. Influence of the Discretization Methods on the Distribution of Relaxation Times Deconvolution: Implementing Radial Basis Functions with DRTtools. *Electrochimica Acta* **184**, 483-499, (2015).

61 T. T. Hagos, B. Thirumalraj, C.-J. Huang, L. H. Abrha, T. M. Hagos, G. B. Berhe, H. K. Bezabh, J. Cherng, S.-F. Chiu, W.-N. Su & B.-J. Hwang. Locally Concentrated LiPF6 in a Carbonate-Based Electrolyte with Fluoroethylene Carbonate as a Diluent for Anode-Free Lithium Metal Batteries. *ACS Applied Materials & Interfaces* **11**, 9955-9963, (2019).

62 F. Qiu, X. Li, H. Deng, D. Wang, X. Mu, P. He & H. Zhou. A Concentrated Ternary-Salts Electrolyte for High Reversible Li Metal Battery with Slight Excess Li. *Advanced Energy Materials* **9**, 1803372, (2019).

63 J. Qian, B. D. Adams, J. Zheng, W. Xu, W. A. Henderson, J. Wang, M. E. Bowden, S. Xu, J. Hu & J.-G. Zhang. Anode-Free Rechargeable Lithium Metal Batteries. *Advanced Functional Materials* **26**, 7094-7102, (2016).

6

64 J. Zhang, H. Zhang, L. Deng, Y. Yang, L. Tan, X. Niu, Y. Chen, L. Zeng, X. Fan & Y. Zhu. An additive-enabled ether-based electrolyte to realize stable cycling of high-voltage anode-free lithium metal batteries. *Energy Storage Materials* **54**, 450-460, (2023).

65 R. Weber, M. Genovese, A. J. Louli, S. Hames, C. Martin, I. G. Hill & J. R. Dahn. Long cycle life and dendrite-free lithium morphology in anode-free lithium pouch cells enabled by a dual-salt liquid electrolyte. *Nature Energy* **4**, 683-689, (2019).

66 T. M. Hagos, T. T. Hagos, H. K. Bezabh, G. B. Berhe, L. H. Abrha, S.-F. Chiu, C.-J. Huang, W.-N. Su, H. Dai & B. J. Hwang. Resolving the Phase Instability of a Fluorinated Ether, Carbonate-Based Electrolyte for the Safe Operation of an Anode-Free Lithium Metal Battery. *ACS Applied Energy Materials* **3**, 10722-10733, (2020).

67 C. Niu, D. Liu, J. A. Lochala, C. S. Anderson, X. Cao, M. E. Gross, W. Xu, J.-G. Zhang, M. S. Whittingham, J. Xiao & J. Liu. Balancing interfacial reactions to achieve long cycle life in high-energy lithium metal batteries. *Nature Energy* **6**, 723-732, (2021).

68 M. Genovese, A. J. Louli, R. Weber, C. Martin, T. Taskovic & J. R. Dahn. Hot Formation for Improved Low Temperature Cycling of Anode-Free Lithium Metal Batteries. *Journal of The Electrochemical Society* **166**, A3342, (2019).

69 L. Suo, W. Xue, M. Gobet, S. G. Greenbaum, C. Wang, Y. Chen, W. Yang, Y. Li & J. Li. Fluorine-donating electrolytes enable highly reversible 5-V-class Li metal batteries. *Proceedings of the National Academy of Sciences* **115**, 1156, (2018).

70 Z. Yu, H. Wang, X. Kong, W. Huang, Y. Tsao, D. G. Mackanic, K. Wang, X. Wang, W. Huang, S. Choudhury, Y. Zheng, C. V. Amanchukwu, S. T. Hung, Y. Ma, E. G. Lomeli, J. Qin, Y. Cui & Z. Bao. Molecular design for electrolyte solvents enabling energy-dense and long-cycling lithium metal batteries. *Nature Energy* **5**, 526-533, (2020).

71 M. Mao, X. Ji, Q. Wang, Z. Lin, M. Li, T. Liu, C. Wang, Y.-S. Hu, H. Li, X. Huang, L. Chen & L. Suo. Anion-enrichment interface enables high-voltage anode-free lithium metal batteries. *Nature Communications* **14**, 1082, (2023).

72 D. W. Kang, J. Moon, H.-Y. Choi, H.-C. Shin & B. G. Kim. Stable cycling and uniform lithium deposition in anode-free lithium-metal batteries enabled by a high-concentration dual-salt electrolyte with high $LiNO_3$ content. *Journal of Power Sources* **490**, 229504, (2021).

6

Summary

The ever-growing demand of today's energy storage and power applications requires batteries with higher energy density, which has prompted the development of lithium (Li)-metal anodes. Li metal having an ultrahigh theoretical specific capacity and a low electrochemical redox potential has gained increasing attention. However, the most negative electrochemical potential of Li metal leads to the challenges, that the extreme activity makes Li metal react with all electrolytes, resulting in the formation of SEI. The consequence is that only in the presence of the favourable SEI can the reversible electrochemical reactions of Li metal operate far away from the chemical equilibrium, defined by its thermodynamics. To increase Li cycling reversibility, various electrolyte solutions have been studied, including local/high-salt concentrated and fluorinated additives. These electrolytes modify the Li-ion solvation sheath structure, which leads to the change in interphase components through the decomposition of the salt anions/fluoridated solvents, improving the battery's performance. However, the ionic conductivity of such electrolytes (e.g., ~1.5-4.0 mS cm^{-1}) is largely reduced due to the high viscosity and high fluorination (e.g., poor dissociation ability of salts), leading to the performance degradation of batteries at long cycling and high charge/discharge rates. Hence, this work explores a new class of liquid electrolytes based on the entropy-impacted concept for Li batteries, in which how increasing entropy impacts the thermodynamic/kinetic properties in liquids and the fundamental relationship between entropy-dominated solvation structures and interphasial ionic transport are investigated, bringing forward high-entropy (HE) electrolytes as composition-rich materials for Li batteries and beyond.

In Chapter 2, Li-metal deposited morphology and SEI are systematically investigated as a function of electrolyte concentration using a combination of operando, in-situ, and ex-situ experimental techniques, which formulates a comprehensive picture of the relationship between Li deposition coverage and microstructure in Li metal batteries. The higher deposition coverages can be formed in the dilute electrolytes, which provides a favourable starting point for dense Li-metal deposition. However, the formation of the

organic-rich mosaic SEI, also a consequence of salt depletion at the Li-metal surface, prevents the growth of large Li deposits and dense Li-metal deposition. In contrast, higher concentrated electrolytes induce a thin and stable SEI, which induces large Li deposits' growth. In this case, however, the relatively small deposition coverage limits the final density of the Li-metal deposition. These results imply the importance of deposition coverage in the microstructure of Li metal. Furthermore, the deposition coverage can be improved through the substrate surface structure, making it possible to combine the favourable aspects of low-concentration electrolytes with those of highly concentrated electrolytes. For intermediate-concentration electrolytes, the combination of the high deposition coverage with stable SEI derived from the functional additives or alternative salts/solvents provides a promising research direction for practical applications, which has been also demonstrated by the commercial carbonate electrolytes.

In Chapter 3, the electrolyte engineering strategy, that HE electrolytes by introducing multiple salts (e.g., LiFSI, LiTFSI, LiDFOB and LiNO$_3$) in an ether solvent, has been prepared for the proof of concept, which exhibits higher reversibility for Li metal plating/stripping and higher oxidation stability for Ni-rich cathode charging to a high cut-off voltage and results in improved rate performance. Despite the low salt concentration (0.6 M) and the poor oxidation stability of DME, the HE endows the solution with the demonstrated promising electrolyte properties. The results show that more salt anions participate in the solvation structures of the low-concentration HE electrolyte, resulting in a thinner and inorganic-rich SEI compared to the single salt electrolyte. The improved interphase properties enhance anodic and cathodic electrochemical stability and result in more compact Li metal plating and higher oxidative stability of ether-based solvents for 4 V-class Li batteries. This rationalizes the improved reversibility of the charge/discharge cycles and improved rate performance that exceeds these of conventional electrolytes. Moreover, the observed weaker solvation strengths between Li ions and the solvents/anions, as compared to the commonly single-salt low- and high-concentration electrolytes, is held responsible for the enhanced charge transfer and the improved electrolyte conductivity. This is the consequence of the increased entropy of mixing leading to more diverse solvation structure and more facile solvation rearrangements.

Chapter 4 shows that increasing the entropy of mixing, by introducing multiple solutes, can be used to increase the stability of solvent-solute combinations, offering an attractive strategy to develop advanced electrolytes for (non)aqueous batteries. The resulting electrolytes show improved Li-ion kinetics and strongly altered solvation interactions due to the disordered solvation structure by mixing several salts. This leads to the formation of more stable and inorganic-rich interphases on the electrodes, strongly improving the electrochemical performance of batteries with practical applicability. Another aspect of the higher solvation-structure entropy is the lowering of the electrolyte melting point to some extent, thereby improving low-temperature performance.

This work using commercial carbonate electrolytes (i.e., $LiPF_6$-EC/DMC) as starting point, should be considered as a prototype study towards the general impact of increasing entropy induced by multiple salts, where strategies using advanced salts and/or solvents in combination with fluorine-rich or salt-concentrated can be expected to provide more opportunities for further improve these electrolytes. Conceptually different to change the chemical and physical properties by tuning salt concentrations of the electrolyte, the present work demonstrates that raising the entropy by using multiple salts, induces a general and fundamental change in solvation interaction and structure, that (along with the specific salt chemistry) can be used to improve electrolyte properties. As liquids are widely utilized as reaction media in the synthesis of functional materials and drugs, introducing multiple components forming the HE solutions, can be considered an interesting route to alter the inter-molecular interactions such that it can impact mass transfer processes relevant to preparation processes.

In Chapter 5, the solvation structure of HE electrolytes has been studied by using a PC solvent in graphite-containing anodes. Results show that by introducing multiple commercial Li salts, a long-standing challenge—the co-intercalation of PC into graphite anodes can be effectively addressed. By creating a standard 1 M HE electrolyte containing various Li salts in PC, the result achieves a reversed solvation chemistry. This shift enhances Li^+-anion interactions over Li^+-solvent solvation within the same total salt concentration. Consequently, it reduces de-solvation energy, facilitating Li^+ transport and expediting charge transfer. Moreover, this alteration leads to the formation of a robust

inorganic-rich SEI layer that safeguards against electrolyte decomposition and electrode deterioration. Diverging from common methods, like incorporating film-forming additives or raising salt concentration to increase salt participation in solvation, The integration of multiple salts can increase the disorder (or entropy) of mixing, thereby expanding the realm of possibilities for Li^+-anion complexes within the solvation sheath. This effectively resolves the problem of incompatibility between individual salt-based PC electrolytes and graphite-based anodes, resulting in a significant improvement in cycling and rate performance, even used alongside high-voltage layered oxide cathodes. In the typical high-energy NCM811‖graphite full cells, it maintains a capacity retention of approximately 94.0% after 600 cycles. Moving towards higher energy density, the NCM811‖Si/G450 (a capacity of 450 mAh g^{-1}) cells exhibit an initial CE of 86.3% and maintain a capacity retention of about 94.5% after 300 cycles. Furthermore, the elevated-energy NCM811‖Si/G1000 full cells can demonstrate stable cycling with a capacity retention of approximately 90.0% after 300 cycles. This work unravels the intricate solvation chemistry of the electrolytes through the incorporation of multiple salts within PC electrolytes, and elucidates how this controls the characteristics of the SEI on graphite-based anodes toward a high reversibility.

Chapter 6 revealed a route towards more stable electrode-electrolyte interphases in Li-ion batteries through multiple-salt or high salt entropy electrolytes, combining five commercially available salts in carbonate solvents. The result is an anion-rich hybrid/composite interphase that is more stable under cycling and aging and provides better Li-ion conductivity. This is demonstrated by the systematic comparison between multi-salt versus multi-solvent electrolytes (having the same regular 1 M total salt concentration) using a comprehensive combination of operando, in-situ, and ex-situ experimental techniques that probe the interphase properties on all length scales. The results demonstrated both the multi-component electrolytes have the ability to increase the bulk ionic conductivities through balancing Li-solvent/salt interactions to form a larger diversity in solvation structures. However, the multi-salt electrolyte results in the formation of a better interphase, consisting of multiple inorganic components embedded in the typical amorphous organic components. The diversified and heterogenous

interphase compositions maximize the percolating pathway of grain boundaries, boosting a substantial enhancement of ion transport across the interphase with a lower migration barrier of approximately 22 kJ mol^{-1}. This improved interphase kinetics effectively facilitates the solid-solid ion diffusion between electrode and interphase as well as the solid-liquid ion solvation reorganization between interphase and electrolyte, contributing to the higher charge/discharge rate capability. On the other hand, this inorganic-dominated multi-component hybrid interphase presents higher interphase stability against the electrochemical/chemical reactions, supporting the long cycle life and long calendar aging life. NCM811‖Li cells with a 50 μm Li metal anode shows a higher capacity retention of >83% after 400 cycles. Moreover, 3.5-Ah anode-free NCM811‖Cu pouch cells using zero-excess Li-metal anode maintain a cycling retention of over 80% after 100 cycles, presenting highly competitive performance based on commercially available salts and carbonate solvents. The resulting hybrid/composite interphase also supports good cycling capability of the practical higher-energy NCM811‖Si/G450 Li-ion full cells, retaining more than 85.0% capacity over 500 cycles with an average CE of more than 99.9%. This work paves the way for designing hybrid interphase for long-cycling, and high-stability batteries under practical conditions.

The composition-rich liquid electrolytes have abilities to provide a broader exploration space for both basic scientific research and future industrial applications. This work investigates HE electrolytes, including increasing the components to increase the entropy of mixing and increasing entropy to form a homogeneous solution, explores their potential characteristics that weaken Li-ion solvation strengths between, facilitating Li-ion diffusivity, and induce salt anions participating in the formation of stable interphase passivation layers. Hoping that this exploration motivates more fundamental and systematic research, which is of general scientific importance and will guide the development of better electrolyte systems and beyond. However, there are some questions that need to be further considered for the HE electrolytes in the future study and practical application.

1. How can we assess entropy in liquids?
2. How to select the appropriate salt/solvent and their ratio towards the better properties?

3. How to evaluate the application of salt-concentrated electrolytes and/or fluorinated electrolytes in practice?
4. How to effectively employ Marcus theory for the comprehensive theoretical and experimental analysis of the Li-ion transport in batteries?
5. What does the actual energy landscape of Li-ion transport from the electrolyte to the electrode look like, and which methods are considered reliable for conducting this study?
6. What are the specific reaction schemes that occur in HE electrolytes at the electrode interfaces?

Finally, I hope that the research in this thesis can further promote the development of liquid electrolytes for batteries and related technologies.

Samenvatting

De gestaag groeiende eisen van de huidige energieopslag- en hoogvermogen-apparatuur vergen batterijen met hogere energiedichtheid, wat aanleiding is geweest voor de ontwikkeling van lithiummetaalanoden. Li-metaal, dat een zeer hoge theoretische specifieke capaciteit en een lage elektrochemische redoxpotentiaal bezit, heeft toenemend aandacht gekregen. De uiterst negatieve elektrochemische potentiaal van Li-metaal komt met de uitdaging, dat de extreme activiteit Li-metaal doet reageren met alle elektrolyten, wat resulteert in de vorming van SEI. Het gevolg is dat alleen in de aanwezigheid van een gunstige SEI de reversibele elektrochemische reacties van Li-metaal ver van chemisch evenwicht kunnen werken, zoals gedefinieerd door zijn thermodynamica. Om de reversibiliteit van Li onder cycli te laten toenemen zijn verscheidene elektrolytoplossingen met lokaal hoge zoutconcentratie en gefluorideerde additieven bestudeerd. Deze elektrolyten veranderen de omhulling van het Li-ion in oplossing, wat leidt tot een verandering in grensfasecomponenten door het uiteenvallen van de zoutanionen/gefluorideerde oplosmiddelen, waardoor de prestatie van de batterijen verhoogd wordt. Echter, de ionengeleiding van zulke elektrolyten (~1.5-5.0 mS cm^{-1}) wordt grotendeels gereduceerd door de hoge viscositeit en hoge fluoridering (slecht dissociatievermogen van zouten), wat leidt tot prestatievermindering van batterijen na vele cycli en bij hoog lading/ontladingstempo. Daarom verkent dit werk een nieuwe klasse vloeibare elektrolyten gebaseerd op het concept van entropieinvloed op Li batterijen, waarin wordt bestudeerd, hoe entropietoename de thermodynamische/kinetische eigenschappen in vloeistoffen en het fundamentele verband tussen door entropie gedomineerde solvatiestructuren en grensfase ionentransport beïnvloedt, wat hoge-entropie elektrolyten als materialen met rijke samenstelling voor Li batterijen en andere toepassingen suggereert.

In Hoofdstuk 2 worden de morfologie van Li-metaal afzettingen en SEI systematisch onderzocht als functie van elektrolytconcentratie met gebruik van een combinatie van operando, in-situ en ex-situ experimentele technieken, wat leidt tot een omvattend beeld van de relatie tussen Li-depositiebedekking en microstructuur in Li-metaal batterijen. De

hogere depositiebedekkingen kunnen gevormd worden in verdunde elektrolyten, wat een gunstig startpunt voor dichte Li-metaal depositie oplevert. Echter, de vorming van het organisch-rijke mozaïsche SEI, ook een gevolg van zoutdepletie bij het Li-metaal oppervlak, voorkomt de groei van grote Li afzettingen en dichte Li-metaaldepositie. In tegenstelling daartoe induceren sterker geconcentreerde elektrolyten een dun en stabiel SEI, wat de groei van grote Li afzettingen teweegbrengt. In dit geval echter beperkt de relatief kleine bedekking met afzetting de uiteindelijke dichtheid van de Li-metaalafzetting. Deze resultaten impliceren het belang van afzettingsbedekking in de microstructuur van Li-metaal. Bovendien kan de afzettingsbedekking verbeterd worden door de oppervlaktestructuur van het substraat, waardoor het mogelijk wordt de gunstige aspecten van elektrolyten met lage concentratie te combineren met die van sterk-geconcentreerde elektrolyten. Voor intermediair-geconcentreerde elektrolyten, biedt de combinatie van de hoge afzettingsbedekking met stabiel SEI ontleend aan de functionele additieven of alternatieve zouten/oplosmiddelen een veelbelovende onderzoeksrichting voor praktische toepassingen, wat ook is aangetoond door de commerciële carbonaatelektrolyten.

In Hoofdstuk 3 is een elektrolytsamenstellingsstrategie, die HE elektrolyten door multipele zouten (e.g., LiFSI, LiTFSI, LiDFOB and $LiNO_3$) in een ether oplosmiddel te introduceren, voorbereid voor het bewijs van het principe, wat hogere reversibiliteit aantoont voor Li-metaal afzetting/verwijdering en hogere oxidatiestabiliteit voor het laden van Ni-rijke kathoden tot een hoog afsnijvoltage en resulteert in een verbeterde tempoprestatie. Ondanks de lage zoutconcentratie (0.6 M) en de slechte oxidatiestabiliteit van DME begiftigt de hoge entropie de oplossing met de aangetoonde veelbelovende elektrolyteigenschappen. De resultaten laten zien dat meer zout-anionen participeren in de solvatiestructuren van het lage-concentratie HE elektrolyt, resulterend in een dunner en anorganisch componentenrijke SEI vergeleken met het elektrolyt met een enkel zout. De verbeterde eigenschappen van de grensfase verhogen anodische en kathodische elektrochemische stabiliteit en resulteren in compactere Li-metaallagen en hogere oxidatieve stabiliteit van ether-gebaseerde oplosmiddelen voor 4 V-klasse Li batterijen. Dit verklaart de verbeterde reversibiliteit van de lading/ontladingscycli en verbeterde

tempoprestatie, wat die van conventionele elektrolyten overtreft. Bovendien worden de waargenomen zwakkere oplossingskrachten tussen Li-ionen en de oplosmiddelen/anionen, vergeleken met de gebruikelijke elektrolyten met een enkel zout in lage of hoge concentratie, verantwoordelijk gehouden voor de verhoogde ladingsoverdracht en de verbeterde geleidbaarheid van het elektrolyt. Dit is het gevolg van de toegenomen mengentropie, wat leidt tot meer diverse en gemakkelijker oplossingsherschikking.

Hoofdstuk 4 laat zien dat verhoging van de mengentropie, door meer opgeloste stoffen te introduceren, gebruikt kan worden om de stabiliteit te doen toenemen van combinaties van oplosmiddel en opgeloste stof, wat een aantrekkelijke strategie aanreikt om geavanceerde elektrolyten te ontwikkelen voor al dan niet water-bevattende batterijen. De resulterende elektrolyten vertonen betere Li-ionen kinetiek en sterk veranderde oplossingsinteracties door de wanordelijke oplossingsstructuur dankzij het mengen van verscheidene zouten. Dit leidt tot de vorming van grensfasen op de electrode, die stabieler zijn en rijker aan anorganische stoffen, waarmee de elektrochemische prestatie van batterijen met praktische toepasbaarheid verbeterd wordt. Een ander aspect van de hogere entropie van de oplossingsstructuur is de verlaging van het smeltpunt van het elektrolyt tot op zekere hoogte, waardoor de prestatie bij lage temperatuur verbeterd wordt.

Dit werk, dat gebruik maakt van commerciële carbonaatelektrolyten (b.v., $LiPF_6$-EC/DMC) als startpunt, zou beschouwd moeten worden als prototype studie naar de impact van entropieverhoging geïnduceerd door gebruik van meer zouten in het algemeen, waar strategieën die gebruik maken van geavanceerde zouten en/of oplosmiddelen in combinatie met fluorrijk of geconcentreerd zout, verwacht mogen worden meer gelegenheid te bieden voor verdere verbetering van deze elektrolyten. Conceptueel anders dan het veranderen van de chemische en fysische eigenschappen door zoutconcentraties van het elektrolyt af te stemmen, toont dit werk aan dat het verhogen van de entropie door meer zouten te gebruiken een algemene en fundamentele verandering in oplossingsinteractie en structuur induceert, die (samen met de specifieke zoutchemie) gebruikt kan worden om de eigenschappen van het elektrolyt te verbeteren. Daar vloeistoffen breed gebruikt worden als reactiemedia bij de synthese van functionele materialen en geneesmiddelen, kan het introduceren van meer componenten bij de

vorming van de HE oplossing beschouwd worden als een interessante route om de intermoleculaire interacties zo te veranderen, dat dit de processen voor massaoverdracht, die relevant zijn voor de bereidingsprocessen, kan beïnvloeden.

In Hoofdstuk 5 is de oplosstructuur van HE-elektrolyten bestudeerd door gebruik te maken van een PC-oplosmiddel in grafietbevattende anodes. Resultaten tonen aan dat door meerdere commerciële Li-zouten te introduceren, een langdurige uitdaging-de co-intercalatie van PC in grafietanodes-effectief kan worden aangepakt. Door een standaard 1 M HE-elektrolyt te creëren met verschillende Li-zouten in PC, wordt het resultaat bereikt van een omgekeerde oploschemie. Deze verschuiving verbetert Li^+-anion interacties ten opzichte van Li^+-oplosmiddelsolvatie binnen dezelfde totale zoutconcentratie. Hierdoor wordt de de-solvatie-energie verminderd, wat Li^+-transport vergemakkelijkt en de ladingsoverdracht versnelt. Bovendien leidt deze verandering tot de vorming van een robuuste anorganische SEI-laag die beschermt tegen elektrolytdecompositie en elektrodedegradatie. Afwijkend van gangbare methoden, zoals het opnemen van filmvormende additieven of het verhogen van de zoutconcentratie om zoutdeelname in oplossing te vergroten, kan de integratie van meerdere zouten de wanorde (of entropie) van menging vergroten, waardoor het bereik van mogelijkheden voor Li^+-anioncomplexen binnen de oplosschede wordt uitgebreid. Dit lost effectief het probleem van onverenigbaarheid op tussen individuele zoutgebaseerde PC-elektrolyten en grafietgebaseerde anodes, wat resulteert in een aanzienlijke verbetering van de cyclische en prestaties bij hoge snelheid, zelfs wanneer ze samen worden gebruikt met kathodes van hoogspanningsgelaagd oxide. In de typische high-energy NCM811||grafiet volledige cellen behoudt het een capaciteitsbehoud van ongeveer 94.0% na 600 cycli. Naar een hogere energiedichtheid toe bewegend, vertonen de NCM811||Si/G450 (een capaciteit van 450 mAh g^{-1}) cellen een initiële CE van 86.3% en behouden ze een capaciteitsbehoud van ongeveer 94.5% na 300 cycli. Bovendien kunnen de hoogenergetische NCM811||Si/G1000 volledige cellen stabiel cyclen met een capaciteitsbehoud van ongeveer 90.0% na 300 cycli. Dit werk ontrafelt de complexe oploschemie van de elektrolyten door de incorporatie van meerdere zouten binnen PC-elektrolyten, en

verduidelijkt hoe dit de kenmerken van de SEI op grafietgebaseerde anodes beheerst richting een hoge omkeerbaarheid

Hoofdstuk 6 onthulde een weg naar stabielere electrode-elektrolyt grensfasen in Li-ionen batterijen door multipel-zout of hoge-zout-entropie elektrolyten door combinatie van vijf commercieel beschikbare zouten in carbonaat oplosmiddelen. Het resultaat is een anionenrijke hybride/samengestelde grensfase, die stabieler is onder cycli en veroudering en betere Li-ionengeleiding biedt. Dit wordt aangetoond door de systematische vergelijking tussen multi-zout versus multi-oplosmiddel elektrolyten (beide met dezelfde gebruikelijke 1 M totale zoutconcentratie) met gebruik van een veelomvattende combinatie van operando, in-situ en ex-situ experimentele technieken, die de eigenschappen van de grensfase op alle lengteschalen onderzoeken. De resultaten lieten zien dat beide elektrolyten met meer componenten het vermogen hebben de bulk ionengeleiding te doen toenemen door Li-oplosmiddel/zout interacties in balans te brengen om een grotere diversiteit in solvatiestructuren te vormen. Echter, het multi-zout elektrolyt resulteert in de vorming van een betere grensfase, bestaande uit multipele anorganische componenten ingebed in de typisch amorfe organische componenten. De gediversifieerde en heterogene grensfasesamenstellingen maximaliseren het percolerende pad van korrelgrenzen, wat een substantiële verhoging van ionentransport over de grensfase met een lagere migratiedrempel van ongeveer 22 kJ mol^{-1} stimuleert. Deze verbeterde grensfasekinetiek faciliteert de vaste-stof-vaste-stof ionendiffusie tussen electrode en grensfase effectief zowel als de vaste-stof-vloeistof ionensolvatie-reorganisatie tussen grensfase en elektrolyt, wat bijdraagt tot de geschiktheid voor een hoger lading/ontladingstempo. Aan de andere kant vertoont deze anorganisch-gedomineerde meercomponenten hybride grensfase hogere grensfasestabiliteit tegen electrochemische/chemische reacties, waardoor het de lange levensduur onder cycli en lange levensduur onder veroudering steunt. NCM811‖Li cellen met een 50 μm Li-metaal anode vertonen een hoger capaciteitsbehoud van >83% na 400 cycli. Bovendien behouden 3.5-Ah anode-vrije NCM811‖Cu knoopcellen met een nul-overschot Li-metaal anode overschrijden 80% na 100 cycli en vertonen een sterk competitieve prestatie gebaseerd op commercieel beschikbare zouten en carbonaat oplosmiddelen. De resulterende

hybride/samengestelde grensfase ondersteunt ook een goed vermogen cycli te doorstaan van de praktische hogere-energie NCM811||Si/G450 Li-ion complete cellen, die meer dan 85.0% capaciteit behouden over 500 cycli met een gemiddelde CE van meer dan 99.9%. Dit werk baant het pad om een hoog-entropische hybride grensfase te ontwerpen voor batterijen met veel ladingscycli en hoge stabiliteit onder praktische omstandigheden.

De vloeibare elektrolyten met een rijke samenstelling hebben het vermogen een grotere verkenningsruimte te bieden voor zowel fundamenteel onderzoek als toekomstige industriële toepassingen. Dit werk onderzoekt hoog-entropische elektrolyten, waaronder verhogen van het aantal componenten om de mengentropie te doen toenemen en entropieverhoging om een homogene oplossing te vormen, verkent hun potentiele karakteristieken, die de krachten tussen het Li-ion en de solvatielaag verzwakken, Li-ionendiffusiviteit faciliteren en zoutanionen er toe brengen te participeren in de vorming van stabiele grensfasepassivatielagen. Hopend dat deze verkenning de motivatie vormt voor meer fundamenteel en systematisch onderzoek, dat van algemeen wetenschappelijke importantie is, de weg zal wijzen naar de ontwikkeling van betere elektrolytsystemen en verder. Er zijn echter een paar punten, die nader beschouwd dienen te worden voor de HE elektrolyten in praktische toepassing.

1. Hoe kunnen we entropie in vloeistoffen beoordelen?
2. Hoe selecteer je het geschikte zout/oplosmiddel en hun verhouding voor betere eigenschappen?
3. Hoe de toepassing van zoutgeconcentreerde elektrolyten en/of gefluoreerde elektrolyten in de praktijk te evalueren?
4. Hoe de Marcus-theorie effectief te gebruiken voor een allesomvattende theoretische en experimentele analyse van het Li-ionentransportproces in batterijen?
5. Hoe ziet het feitelijke energielandschap van Li-ionen transport van het elektrolyt naar de elektrode eruit, en welke methoden worden beschouwd als betrouwbaar voor het uitvoeren van dit onderzoek?
6. Wat zijn de specifieke reactieschema's die optreden in HE-elektrolyten aan de elektrode-interfaces?

Tenslotte hoop ik, dat het onderzoek in dit proefschrift de ontwikkeling van vloeibare elektrolyten voor batterijen en verwante technologieën kan bevorderen.

List of publications

Publications related to this thesis

1. **Qidi Wang**, Chenglong Zhao, Shuwei Wang, Jianlin Wang, Ming Liu, Swapna Ganapathy, Xuedong Bai, Baohua Li & Marnix Wagemaker. Clarifying the Relationship between the Lithium Deposition Coverage and Microstructure in Lithium Metal Batteries. *Journal of the American Chemical Society* 144, 21961-21971 (2022).

2. **Qidi Wang**, Chenglong Zhao, Jianlin Wang, Zhenpeng Yao, Shuwei Wang, Sai Govind Hari Kumar, Swapna Ganapathy, Stephen Eustace, Xuedong Bai, Baohua Li & Marnix Wagemaker. High entropy liquid electrolytes for lithium batteries. *Nature Communications* 14, 440 (2023).

3. **Qidi Wang**, Chenglong Zhao, Zhenpeng Yao, Jianlin Wang, Fangting Wu, Sai Govind Hari Kumar, Swapna Ganapathy, Stephen Eustace, Xuedong Bai, Baohua Li, Jun Lu & Marnix Wagemaker. Entropy-Driven Liquid Electrolytes for Lithium Batteries. *Advanced Materials* 35, 2210677 (2023).

4. **Qidi Wang**, Jianlin Wang, Jouke Heringa, Xuedong Bai, Baohua Li & Marnix Wagemaker. Unveiling co-intercalation-free high-entropy electrolytes for lithium-ion batteries. *Under review*.

5. **Qidi Wang**, Xia Hu, Jianlin Wang, Jouke Heringa, Swapna Ganapathy, Stephen Eustace, Xuedong Bai, Baohua Li, Doron Aurbach & Marnix Wagemaker. Directly engineering ion transport and stability in interphases for high-energy lithium batteries. *Under review*.

Patent related to this thesis

Qidi Wang, Chenglong Zhao & Marnix Wagemaker. High entropy liquid electrolytes for Li-ion or Na-ion batteries. No. P100843NL00. 08/12/2022.

Acknowledgements

Looking back at my PhD years, I would like to sincerely thank all the people who helped me on both science and life during my stay in the Netherlands.

First of all, I am deeply grateful to my promoter Prof. Marnix Wagemaker. Thank you for your support. I learned a lot from the discussions with you, and thank you for the guidance of scientific thinking and writing. You always interested in the new ideas, so I can get a chance to do broad studies on interesting topics. It is an unforgettable experience being in your group, and the diverse and multicultural atmosphere has enriched our office dynamics. Also thank you for your wisdom regarding a healthy work-life balance. I have good memories of the group dinners, and had fun times playing with Maya and Jeva, which is a very warm experience.

I would also like to thank all the thesis committee members for their effort on evaluation and suggestions for this thesis.

Thanks to my master supervisor Prof. Baohua Li. I started my research on batteries and learned a lot in his advanced lab. Even during my PhD in Netherlands, you still offer strong support to the works. I am also very thankful for the chance to be an exchange student in Marnix's group, which is a turning point for both my life and career.

Thanks for my co-promoter, Dr. Swapna Ganapathy. Thank you for all your guidance and help about solid-state NMR. You are always very patient in improving the experiments, and sometimes even sitting in the NMR room for a whole day with me to get a good measurement that I really appreciate.

Thanks for my daily supervisor, Dr. Chenglong Zhao, for all the support in experiments and writing. Your passion in the research field have significantly extend my comprehension of different subjects, and helped me to improve this thesis to a much deeper level.

Thank for the Dr. Nicola from shell global solutions international B.V for discussions.

To all the group members and friends in RID, thanks for Pier, Remco, Alex, Hanan, Eveline, Victor, Mark, Chao Wang, Zhaolong, Shengnan, Anastasia, Pranav, Martijn, Chaofan, Xuehang, Lars, Pedro, Biffo, Ajay, Xavier, Theo, Tammo, Viola, Tomas, Ziying,

Thanks for Dr. Deniz Wong and Dr. Götz Schuck from Helmholtz Zentrum Berlin für Materialien und Energie Hahn-Meitner-Platz for their support and help in the synchrotron radiation absorption spectrum and the resonant inelastic X-ray scattering spectrum measurements.

Thanks for Dr. Fu Sun and Dr. Xia Zhang from Helmholtz-Zentrum Berlin Institute of applied materials on synchrotron X-Ray tomography measurements.

Thanks for Dr. Zhou Jin, Dr. MengyuTian and Prof. Xuejie Huang from the Institute of Physics, Chinese Academy of Sciences for providing $LiFePO_4$ materials.

Finally, I would like to express my heartily love to my family for your strong support and help, that continuously inspire and encourage me.

<div align="right">

王启迪

Qidi Wang

</div>

Curriculum Vitae

Qidi Wang

06-04-1994, Shandong, China

Education

2021-2023 Doctor of

        Delft University of Technology, the Netherlands

2017-2020 Master of

        Materials Science and Engineering

        Tsinghua University, China

2013-2017 Bachelor of

        1) Geology

        2) Business Administration

        China University of Geosciences, Beijing, China